

Polymer controlled mineralization of zinc phosphate hydrates and applications in Corrosion Protection, Catalysis and Biomedicine

Dissertation

Zur Erlangerung des Grades

“Doktor der Naturwissenschaften”

am Fachbereich Chemie und Pharmazie
der Johannes-Gutenberg-Universität Mainz

vorgelegt von

Laurent Herschke

Mainz, 2004

Die vorliegende Arbeit wurde unter der Betreuung von Prof. Dr. G. Wegner in der Zeit von Oktober 2001 bis Juni 2004 am Max-Planck-Institut für Polymerforschung durchgeführt.

Tag der mündlichen Prüfung: 29 / 10 / 2004

Note: Summa Cum Lauda

Zusammenfassung

Die Tauglichkeit von Hybridmaterialien auf der Basis von Zinkphosphathydrat-Zementen zum Einsatz als korrosionshemmende anorganische Pigmente oder zur prothetischen und konservierenden Knochen- und Zahntherapie wird weltweit empirisch seit den neunziger Jahren intensiv erforscht.

In der vorliegenden Arbeit wurden zuerst Referenzproben, d.h. α - und β -Hopeite (Abk. α -, β -ZPT) dank eines hydrothermalen Kristallisationsverfahrens in wässrigem Milieu bei 20°C und 90°C hergestellt. Die Kristallstruktur beider Polymorphe des Zinkphosphattetrahydrats $\text{Zn}_3(\text{PO}_4)_2 \cdot 4 \text{H}_2\text{O}$ wurde komplett bestimmt. Einkristallstrukturanalyse zeigt, daß der Hauptunterschied zwischen der α - und β -Form des Zinkphosphattetrahydrats in zwei verschiedenen Anordnungen der Wasserstoffbrücken liegt. Die entsprechenden drei- und zweidimensionalen Anordnungen der Wasserstoffbrücken der α - und β -ZPT induzieren jeweils unterschiedliches thermisches Verhalten beim Aufwärmen. Während die α -Form ihr Kristallwasser in zwei definierten Stufen verliert, erzeugt die β -Form instabile Dehydratationsprodukte, z.B. Zinkphosphattrihydrat und -monohydrat. Dieses entspricht zwei unabhängigen, aber nebeneinander ablaufenden Dehydratationsmechanismen: (i) bei niedrigen Heizraten einen zweidimensionalen Johnson-Mehl-Avrami (JMA) Mechanismus auf der (011) Ebene, der einerseits bevorzugt an Kristallkanten stattfindet und andererseits von existierenden Kristalldefekten auf Oberflächen gesteuert wird; (ii) bei hohen Heizraten einem zweidimensionalen Diffusionsmechanismus (D_2), der zuerst auf der (101) Ebene und dann auf der (110) Ebene erfolgt. Durch die Betrachtung der ZPT Dehydratation als irreversible heterogene Festkörperstufenreaktion wurde dank eines „ähnlichen Endprodukt“-Protokolls das Dehydratationsphasendiagramm aufgestellt. Es beschreibt die möglichen Zusammenhänge zwischen den verschiedenen Hydratationszuständen und weist auf die Existenz eines Übergangszustandes um 170°C (d.h. Reaktion β -ZPT \rightarrow α -ZPT) hin. Daneben wurde auch ein gezieltes chemisches Ätzverfahren mit verdünnten H_3PO_4 - und NH_3 Lösungen angewendet, um die ersten Stufe des Herauslösens von Zinkphosphat genau zu untersuchen. Allerdings zeigen α - und β -Hopeite charakteristische hexagonale und kubische Ätzgruben, die sich unter kristallographischer Kontrolle verbreitern. Eine zuverlässige Beschreibung der Oberflächenchemie und Topologie konnte nur durch AFM und FFM Experimente erfolgen. Gleichzeitig konnte in dieser Weise die Oberflächendefektdichte und -verteilung und die Volumenauflösungsrate von α - und β -Hopeite bestimmt werden.

Auf einem zweiten Weg wurde eine innovative Strategie zur Herstellung von basischen Zinkphosphatpigmenten erster und zweiter Generation (d.h. $\text{NaZnPO}_4 \cdot 1\text{H}_2\text{O}$ und $\text{Na}_2\text{ZnPO}_4(\text{OH}) \cdot 2\text{H}_2\text{O}$) mit dem Einsatz von einerseits oberflächenmodifizierten Polystyrolatices (z.B. produziert durch ein Miniemulsionspolymerisationsverfahren) und andererseits von Dendrimeren auf der Basis von Polyamidoamid (PAMAM) besprochen. Die erhaltene Zeolithstruktur (ZPO) hat in Abhängigkeit von steigendem Natrium und Wassergehalt unterschiedliche kontrollierte Morphologie: hexagonal, würfelförmig, herzförmig, sechsarmige Sterne, lanzettenförmige Dendrite, usw. Zur quantitativen Evaluierung des Polymereinbaus in der Kristallstruktur wurden carboxylierte fluoreszenzmarkierte Latices eingesetzt. Es zeigt sich, daß Polymeradditive nicht nur das Wachstum bis zu $8 \mu\text{m}\cdot\text{min}^{-1}$ reduzierten. Trotzdem scheint es auch als starker Nukleationsbeschleuniger zu wirken. Dank der Koordinationschemie (d.h. Bildung eines sechszentigen Komplexes $\text{L-COO}^- \cdots \text{Zn-PO}_4 \cdots \text{H}_2\text{O}_{\text{Kristall}}$ mit Ligandenaustausch) konnten zwei einfache Mechanismen zur Wirkung von Latexpartikeln bei der ZPO Kristallisation aufgezeigt werden: (i) ein Intrakorona- und (ii) ein Extrakorona-Keimbildungsmechanismus.

Weiterhin wurde die Effizienz eines Kurzzeit- und Langzeitkorrosionsschutzes durch maßgeschneiderte ZPO/ZPT Pigmente und kontrollierte Freisetzung von Phosphationen in zwei Näherungen des Auslösungsgleichgewichts abgeschätzt: (i) durch eine Auswaschungsmethode (thermodynamischer Prozess) und (ii) durch eine pH-Impulsmethode (kinetischer Prozess). In dieser Perspektive stellt jedes Pigment eine unerwartete pH-Abhängigkeit der Löslichkeit in „W-Form“ dar, die einen von der Säuredissoziationskonstante K_{a_i} (i.e. β_i) der Phosphorsäure gesteuerten Auflösungsprozess (d.h. Puffereffekt) ausdrückt. Besonders deutlich wird der Ausflösungs-Fällungsmechanismus (d.h. der Metamorphismus). Die wesentliche Rolle der Natriumionen bei der Korrosionshemmung wird durch ein passendes zusammensetzungsabhängiges Auflösungsmodell (ZAAM) beschrieben, das mit dem Befund des Salzsprühtests und der Feuchtigkeitskammertests konsistent ist.

Schließlich zeigt diese Arbeit das herausragende Potential funktionalisierter Latices (Polymer) bei der kontrollierten Mineralisation zur Herstellung maßgeschneiderter Zinkphosphat Materialien. Solche Hybridmaterialien werden dringend in der Entwicklung umweltfreundlicher Korrosionsschutzpigmente sowie in der Dentalmedizin benötigt.

List of most used abbreviation and Symbols

Methods and related acronyms

XRD	X-ray diffraction
SAD	Selected Area Diffraction
FT-Raman	Fourier transform Raman spectroscopy
DRIFT	Infrared spectroscopy in diffuse reflectance
DSC	Differential scanning calorimetry
TGA-MS	Thermogravimetry coupled with mass spectrometry
DTGA	Differential thermogravimetry
SEM	Scanning electron microscopy
TEM	Transmission electron microscopy
LM	Polarized light microscopy
DLS	Dynamic light scattering
MALDI-Tof	Matrix assisted laser/desorption ionization spectroscopy combined with time-of-flight detection
ICP-MS	Inductively coupled plasma mass spectrometry
AAS	Atom absorption spectroscopy
GPC	Gel permeation chromatography
MAS NMR	Nuclear magnetic resonance spectroscopy at magic angle spinning
BET	Brunauer-Emmet-Teller adsorption method
ADSA	Automated axisymmetric drop shape analysis
GOF	Goodness of fitting
JMA	Johnson-Mehl-Avrami model
D ₂	Two dimensional diffusional model
WFO	Wall-Flynn-Ozawa integral method
LJ	Lutz-Jung correlation (Chapter 2)
EQS	Equation-of-state model for surface tension calculation (chapter 4)
IEP	Isoelectric point

Monomers, Polymers and chemical

SAM	Self-assembled monolayer
TMAOH	Tetramethylammonium hydroxide
MAA	Methacrylic acid
CA	Crotonic acid
AA	Acrylic acid
VPO	Vinylphosphonic acid
VBTC	1-vinylbenzyl-6-trimethylammonium chloride
VPO	Vinylphosphonic acid
MATMAC	2-(methacryloyloxy) trimethylammonium chloride
PEO	Poly(ethylene oxide)
PPO	Poly(propylene oxide)
Lutensol AT50	C ₁₆ /C ₁₈ -PEO ₅₀
Pluronic PE6800	(PEO) ₁₂₃ - <i>block</i> -(PPO) ₂₄
DHBCs	Double hydrophilic block copolymer
EA3007	C ₁₂ H ₂₅ -(MAA) ₈ -(PEO) ₆₈
PS- <i>g</i> -PAA	Poly(styrene- <i>graft</i> -acrylic acid)
PS- <i>g</i> -PNaSS	Poly(styrene- <i>graft</i> -styryl sulfonic acid sodium salt)
PDADMAC	Poly(dimethyldiallyl-ammonium chloride)
PAMAM	Polyamidoamine starburst dendrimer
PAM	Poly(acrylamide)
ZPT	Zinc phosphate tetrahydrate
ZPD	Zinc phosphate dihydrate
ZPA	Zinc phosphate anhydrate
ZPO	Organically modified zinc phosphate
ZHPT	Zinc hydrogen phosphate trihydrate
ZPC	Zinc phosphate cement
NaZP	Basic zinc phosphate: NaZnPO ₄ · 1 H ₂ O
Na ₂ ZPOH	Basic zinc phosphate: Na ₂ ZnPO ₄ (OH) · 2 H ₂ O
HAP	Hydroxyapatite
DA	Calcium deficient HAP
DCPD	Calcium dihydrogen phosphate dihydrate
OCP	Octacalciumphosphate
ACP	Amorphous calcium phosphate
ACC	Amorphous calcium carbonate

Symbols

Chapter 2

(hkl)	Crystal face or plane using Miller's indices
$[hkl], \{hkl\}$	Crystallographic direction using Miller's indices
Γ_{vibr}	Irreducible representation of internal vibration modes (Space group theory)
ν	Stretching vibrational mode (1 to 4 for phosphate ions)
δ	Bending vibrational mode
2θ	Diffraction angle ($^{\circ}$)
β	Heating rate ($K \cdot min^{-1}$)
a,b,c	Lattice parameters (unit-cell lengths) (\AA)
α, β, γ	Lattice parameters (unit-cell angles) ($^{\circ}$)
V_m	Molar volume ($m^3 \cdot mol^{-1}$)
Z	Unit-cell compacity
D_x	Density determined by single crystal X-ray analysis

Chapter 3

T_i	Initial temperature of transition (K)
T_f	Final temperature of transition (K)
dm or dw	Mass change (g)
X or α	Degree of conversion
Y	Apparent mass fraction
ΔQ or HF	Heat flow (mW)
ΔT	Temperature change ($^{\circ}C$)
C_p	Molar heat capacity ($J \cdot K^{-1} \cdot mol^{-1}$)
ΔH	Enthalpy variation associated with a phase transition ($kJ \cdot mol^{-1}$)
ΔS	Entropy variation associated with a phase transition ($kJ \cdot mol^{-1} \cdot K^{-1}$)
ΔG	Gibbs' free energy variation associated with a phase transition ($kJ \cdot mol^{-1}$)
E_a	Activation energy ($kJ \cdot mol^{-1}$)
n	Order of a solid state reaction
k	Kinetic constant of solid state reaction
A	Frequency factor
S	Kissinger's shape index
$f(\alpha)$	Numerical curve fit
$g(\alpha)$	Reciprocal function of $f(\alpha)$
δ	Chemical shift (ppm)

Chapter 4

PSD	Particle size distribution
EPSD	Etch pit size distribution
CSD	Crystal size distribution
σ^2	Variance of the CSD
θ	Monolayer capacity (i.e. coverage)
\vec{h}	Burger's vector
r_0	Dislocation core radius (Å)
γ	Surface tension (mJ.m ⁻²)
γ_{SL}, γ_{LV}	Solid-liquid and liquid-vapour interfacial tension (mJ.m ⁻²)
γ^d	Disperse component of the surface energy
γ^{di}	Surface tension component due to hydrogen and dipole bonding (mJ.m ⁻²)
g	Free energy of dissolution (kJ.mol ⁻¹)
C	Concentration of the dissolving species
C_0 or s	Equilibrium solubility
τ	Shear modulus (MPa)
ν	Poisson's coefficient
J	Rate of formation of etch pits per unit area (m ⁻² .s ⁻¹)
X_d	Fraction of surface sites intersected by dislocations
$n(L)$	Etch pit population density function
$N(L)$	Number of pit per unit area per unit length (m ⁻² .m ⁻¹)
ΔL	Length interval (µm)
G	Pit growth rate (m.s ⁻¹)
W_{I-0}	Corrected pit width
θ	Etch pit wall slope (°)
d	Etch pit depth (µm)
L_F	Average transition length from pointed to bottom-flat pit geometry
L_F	Average transition length from pointed to bottom-flat pit geometry
τ_p	Mean pit lifetime (s)
\dot{a}	Rate of pit removal by annihilation (e.g. coalescence) (s ⁻¹)
m_i	Moment of the EPSD of order i
$G_{1,2}$	First of second etch pit population
$R(L)$	Bulk dissolution rate (mol.cm ⁻² .s ⁻¹)
ν_b, ν_c	Etch pit half-length (i.e. half-width) opening rate along <i>b</i> -axis or <i>c</i> -axis
L_F	Average transition length from pointed to bottom-flat pit geometry (µm)
D_i	Diffusion coefficient (m ² .s ⁻¹)
q	Growth step flux (s ⁻¹)
λ	Distance between two steps (nm)

p	Slope of a surface or plane (hkl)
$\rho_n(L)$	Impurity concentration frequency for a linear distribution (m^{-1})
δ	Lattice misfit
θ_Y	Young's contact angle ($^\circ$)
σ	Line tension
π_e	Equilibrium spreading pressure of a liquid (Pa)
l/κ	Debye length
a	Radius of a particle (μm)
σ	Surface charge density ($\mu C.m^{-2}$)
ψ_0	Surface potential (V)
ε	Dielectric constant
ζ	Zeta-potential (mV)
μ	Electrophoretic mobility ($m^2.V^{-1}.s^{-1}$)
$f(\kappa a)$	Henry's function
η	Viscosity of a fluid (Pa.s)

Chapter 5

F	Faraday's constant
a	Latex particle radius (nm)
ϕ	Particle volume fraction (% V/V)
PDI	Polydispersity index of a PSD
f	Emulsion solid content (wt%)
Z	Number of charge/functional groups per latex particle
σ	Surface charge density ($\mu C.m^{-2}$)
κ	Electric conductivity ($mS.cm^{-1}$)
R	Crystal aspect ratio or shape factor length/width
$E_{attach.}^{hkl}$	Attachment energy to a face (hkl) (Hartman-Perdok theory) ($kJ.mol^{-1}$)
$K_{app}^{growin}(L)$	Apparent growth rate constant ($\mu m.min^{-1}$)
$P(L_i(t))$	Normalized population frequency of of crystals of length L_i ,
$n_i^{crystal}$	Number of crystals of length L_i ,
L_{min}	Length of the smallest crystal (μm)
A, B	Adjustable parameter of the CSD related to the amplitude and width of the
$(t_{nr}-t_n)$	Relative induction time (s)
t_{no}	Initial time of nuclei formation (S)
t_{ni}	time of nuclei formation growing to a length L_i (s)
t_{nf}	Final time of nuclei formation growing to a length L_{min} (s)
n_{ni}	number of nuclei grown at t_{ni}
S	Supersaturation
[Latex]	Structure controlling agent (Latex) concentration (ppm)

$D_{\text{eff}}(r)$	Spatially dependent spin-diffusion coefficient
T_2	Transverse relaxation time (ms)
$t_m^{s,0}$	Mixing or transfer time ($\text{ms}^{1/2}$)
λ_{max}	Wavelength of maximum absorption (nm)
N	Number of latex particles incorporated per crystal

Chapter 6

μ_i	Chemical potential of the species i
ν_a	Stoichiometric numbers in a formula unit of the dissolving phase
a_i	Activity of the ion i
γ_i	Activity coefficient of the ion
C_i	Concentration of the ion I (mol.L^{-1})
z^i	Charges (valencies) of the ion i
σ	Relative supersaturation
S	Supersaturation
K_s	Thermodynamic solubility product
IP	Ionic activity product
I	Ionic strength (mol.L^{-1})
α_i	Immobilized phosphate and zinc amounts (mol.L^{-1})
Φ_i	Relative fraction of reacting phosphate ions (mol.L^{-1})
Λ_0	Molar conductivity of a solution at infinite dilution ($\text{mS.cm}^{-1}.\text{mol}^{-1}$)
Λ_0	Molar conductivity of the ion I ($\text{mS.cm}^{-1}.\text{mol}^{-1}$)
K_{measured}	Measured solution conductivity (mS.cm^{-1})

Content

ZUSAMMENFASSUNG	I
LIST OF MOST USED ABBREVIATION AND SYMBOLS	III
METHODS AND RELATED ACRONYMS	III
MONOMERS, POLYMERS AND CHEMICALS	IV
SYMBOLS	V
CONTENT	IX
1. INTRODUCTION	1
1.1. ZINC PHOSPHATE: AN INDUSTRIAL PRODUCT OF HIGH TECHNICALITY	1
1.1.1. <i>Protective coatings and corrosion inhibitors based on zinc phosphates</i>	1
1.1.2. <i>Novel applications of zinc phosphates</i>	4
1.2. MINERALIZATION OF PIGMENTS BASED ON ZINC PHOSPHATE HYDRATES	6
1.2.1. <i>Biom mineralization</i>	6
1.2.2. <i>Polymer controlled mineralization</i>	8
1.3. STRATEGIES OF INVESTIGATION: MATERIALS BY DESIGN	10
1.4. REFERENCES	11
2. CRYSTAL STRUCTURES AND BULK PROPERTIES OF ZINC PHOSPHATE HYDRATES	15
2.1. INTRODUCTION	15
2.2. SYNTHESIS OF ZINC PHOSPHATE TETRAHYDRATE (ZPT)	17
2.2.1. <i>P₂O₅-ZnO-H₂O phase diagram and synthesis temperature</i>	17
2.2.2. <i>Strategies for the synthesis of ZPT polymorphs</i>	20
2.2.3. <i>Proposed syntheses of micro- and microcrystals of ZPT polymorphs</i>	21
2.2.3.1. <i>α-,β-zinc phosphate tetrahydrate (ZPT) microcrystals</i>	21
2.2.3.2. <i>α-,β-zinc phosphate tetrahydrate (ZPT) crystalline powders</i>	22
2.2.3.3. <i>Zinc hydrogen phosphate trihydrate (ZHPT) microcrystals</i>	22
2.3. POLYMORPHISM OF ZINC PHOSPHATE TETRAHYDRATE (ZPT)	23
2.4. DETERMINATION AND COMPARISON OF THE CRYSTAL STRUCTURE OF HOPEITE POLYMORPHS AND ZHPT	29
2.5. SPECTROSCOPIC INVESTIGATION OF THE STRUCTURAL STABILITY OF ZPT POLYMORPHS	37
2.5.1. <i>Investigation of the molecular stability of crystal water and hydrogen bonding pattern by means of DRIFT and FT-Raman spectroscopy in ZPT polymorphs</i>	37
2.5.2. <i>General investigation of the relative structural stability of ZPT polymorphs</i>	41
2.6. CONCLUSION	49
2.7. REFERENCES	50

3. THERMAL BEHAVIOUR AND KINETICS OF DEHYDRATION OF ZINC PHOSPHATE HYDRATES.....	54
3.1. INTRODUCTION.....	55
3.2. PRINCIPLES OF DSC AND DTGA, TWO COMPLEMENTARY METHODS.....	56
3.2.1. <i>Principles of thermogravimetry (TG/TGA) and differential thermogravimetry (DTGA)</i>	56
3.2.1.1. Principle of thermogravimetry (TG/TGA).....	57
3.2.1.2. Principle of differential thermogravimetry (DTGA).....	57
3.2.1.3. Factors affecting thermogravimetric curves.....	59
3.2.2. <i>Principle of differential scanning microcalorimetry</i>	60
3.2.2.1. Principle of differential scanning calorimetry (DSC).....	60
3.2.2.2. Effects of the calibration and heating rate on DCS curves.....	62
3.2.3. <i>Quantitative analysis in DSC</i>	64
3.3. THERMAL STABILITY OF ZINC AND CALCIUM PHOSPHATES HYDRATES: DESCRIPTIVE APPROACH.....	66
3.3.1. <i>Structural differentiation between α- and β-hopeite, and α-, β- zinc phosphate dihydrate by SEM and XRD</i>	66
3.3.2. <i>Structural differentiation between α- and β-hopeite, and α-, β- zinc phosphate dihydrate by thermoanalysis</i>	71
3.4. THERMODYNAMIC STABILITY OF α - AND β -HOPEITE AND THEIR RELATIVE HYDRATES.....	73
3.4.1. <i>Validity of non isothermal measurements and isoconversional methods</i>	73
3.4.2. <i>Heating rate dependence of peak characteristics - Validity of Arrhenius law</i>	74
3.4.3. <i>Thermodynamic order of phase transition and irreversibility during dehydration of hopeite polymorphs</i>	77
3.4.4. <i>Comparison of the thermal stability of zinc phosphate hydrates</i>	79
3.5. KINETICS OF DEHYDRATION OF ZINC PHOSPHATE TETRAHYDRATES.....	84
3.5.1. <i>Non-isothermal methods</i>	84
3.5.2. <i>Heterogeneous solid state reactions</i>	85
3.5.3. <i>Degree of conversion and basic kinetic equation</i>	86
3.5.4. <i>Classical empirical methods of kinetic analysis</i>	87
3.5.4.1. Dehydration reactions of first order – Newkirk method.....	87
3.5.4.2. Differential method of Freeman and Carroll (FC method).....	88
3.5.4.3. Approximate method of Kissinger.....	88
3.5.4.4. Approximate method of Coats and Redfern (CR method).....	90
3.5.4.5. Corrected Integral method of Valuska and Voboril (VV method).....	90
3.5.4.6. Integral method of Doyle.....	91
3.5.4.7. Integral method of Friedman.....	92
3.5.4.8. Integral method of Ozawa.....	92
3.5.4.9. Flynn-Wall Ozawa integral method (WFO method).....	93
3.5.5. <i>Formal kinetics analysis of processes in solid state</i>	94
3.5.5.1. Master data methodology and isoconversional methodology.....	94
3.5.5.2. Kinetics analysis in solid phase: standard kinetic methodology.....	94
3.5.5.3. Mechanisms of solid state reactions for non-isothermal isocon- versional kinetics.....	96
3.5.6. <i>Methodology for the selection of the kinetic model</i>	98
3.5.7. <i>Descriptive approach of the dehydration kinetics of ZPT polymorphs: Activation energy E_a and order of reaction. Correlation / significance of the global order of reaction with regards to their crystallographic structures</i>	99
3.5.8. <i>Temptative determination of the kinetic mechanisms of dehydration of α-,β-hopeite and α-,β-ZPD</i>	106
3.6. CONCLUSION.....	118
3.7. REFERENCES.....	120

4. CHEMICAL REACTIVITY OF METAL (Zn²⁺, Ca²⁺) PHOSPHATE HYDRATES AT SURFACES AND INTERFACES	124
4.1. INTRODUCTION	124
4.2. MORPHOLOGICAL STUDIES	126
4.2.1. <i>Morphology and structure (topology) of surfaces</i>	126
4.2.2. <i>Surface reactivity and chemical etching</i>	131
4.2.2.1. Theory of etch pit formation applied to hopeite	132
4.2.2.1.1. Thermodynamic approach	132
4.2.2.1.2. Kinetic approach and etch pit size distribution (PDS model)	137
4.2.2.2. Chemical Etching of metal phosphate crystals followed by SEM	139
4.2.2.2.1. pH-dependence on the efficiency of treatment by chemical etching	139
4.2.2.2.2. Time-dependence on the efficiency of treatment by NH ₃ chemical etching	141
4.2.3. <i>Topology, surface inhomogeneities and local disorder followed by AFM</i>	145
4.2.4. <i>E-beam irradiation and electron induced chemical reaction</i>	154
4.3. FROM STRUCTURAL TO SURFACE PROPERTIES	157
4.3.1. <i>Wettability and contact angle measurement</i>	157
4.3.1.1. Fowkes approach and extended Fowkes approach	159
4.3.1.2. Lifshitz-Van der Waals / Acid-Base (van Oss) approach (STC method)	160
4.3.1.3. Equation of state approach (EQS method)	160
4.3.2. <i>Wetting envelop of ZPT polymorphs</i>	162
4.3.3. <i>Suspension stability and zeta-potential measurements</i>	166
4.3.3.1. Interfacial electrophoretic phenomena	166
4.3.3.2. Electrokinetic properties of ZPT pigments and suspension stability	169
4.4. CONCLUSION	174
4.5. REFERENCES	175
5. POLYMER CONTROLLED MINERALIZATION OF ZINC PHOSPHATE HYDRATES	180
5.1. INTRODUCTION	180
5.2. SELECTED CRYSTALLIZATION ADDITIVES	183
5.2.1. <i>Latexes obtained by miniemulsion polymerization</i>	183
5.2.2. <i>Dendrimers</i>	190
5.3. POLYMER (LATEX) CONTROLLED MINERALIZATION OF ZINC PHOSPHATE HYDRATES: 1 ST GENERATION OF BASIC ZPO	191
5.3.1. <i>Effect of the addition of a carboxylated latex on ZPT crystallization</i>	191
5.3.2. <i>Effect of the size of a carboxylated latex on ZPT/ZPO crystallization</i>	194
5.3.3. <i>Effect of the corona thickness of a phosphonated latex on the crystallization mechanism of ZPO</i>	197
5.3.4. <i>Effect of the chemical function of latex on ZPT crystallization</i>	199
5.3.5. <i>Effect of the presence of a positively charged latex on the fractal growth of ZPO – Crystal growth controlled by latex absorption mechanism</i>	209
5.3.6. <i>Effect of the pH and ionic strength on ZPO crystallization in presence of a negatively charged and polar latex template</i>	213
5.3.7. <i>Kinetics of ZPO crystallization</i>	216
5.3.8. <i>Effect of concentration of a carboxylated latex on ZPT crystallization</i>	219
5.3.9. <i>Characterization of 1st generation basic zinc phosphate and selective incorporation of latex particles</i>	225
5.3.10. <i>Quantitative determination of the incorporation of latex particles in NaZnPO₄ · 1 H₂O, a basic zinc phosphate (1st generation ZPO)</i>	235
5.3.11. <i>Mechanisms of interactions between a growing basic ZPT crystal and a latex particle</i>	238
5.4. DENDRIMER CONTROLLED MINERALIZATION AND ZPOS OF 2 ND GENERATION: Na ₂ ZnPO ₄ (OH) · 2 H ₂ O	244
5.4.1. <i>Effect of the chemical functionalization of PAMAM based dendrimers on ZPO crystallization</i>	245

5.4.2.	<i>Effects of increasing polymer concentration and crystallization time on PAMAM based dendrimer controlled ZPO crystallization</i>	248
5.4.3.	<i>Selective incorporation of NH₂-/COOH-functionalized dendrimer in ZPO zeolitic structures</i>	250
5.5.	CONCLUSION	255
5.6.	REFERENCES.....	258
6.	SOLUBILITY AND DISSOLUTION KINETICS OF ZINC PHOSPHATE HYDRATE BASED PIGMENTS FOR ANTICORROSION AND POTENTIAL BIOMEDICAL APPLICATIONS.....	266
6.1.	INTRODUCTION	267
6.2.	SOLUBILITY MODELS	269
6.2.1.	<i>Sparingly soluble salts, supersaturation and dissolution process</i>	269
6.2.1.1.	Basic concepts of solubility.....	269
6.2.1.2.	Unusual dissolution and solubility phenomena	270
6.2.1.3.	Solution Thermodynamics.....	271
6.2.2.	<i>Turbidity phase diagram and metastability domain</i>	275
6.2.2.1.	Thermodynamic approach of supersaturation	275
6.2.2.2.	Experimental determination of supersaturation limits	278
6.2.3.	<i>Predominance diagrams of ions species</i>	279
6.2.4.	<i>Zinc phosphate dissolution mechanism and chemical composition dependent models</i>	282
6.2.4.1.	Hopeite dissolution model.....	282
6.2.4.2.	Composition dependent dissolution model.....	285
6.3.	METHODS DEVELOPMENTS.....	287
6.3.1.	<i>Strategies for the investigation of dissolution mechanisms: forced release and achievement of a thermodynamic equilibrium</i>	287
6.3.2.	<i>Dissolution conditions: Choice of the experimental parameters</i>	288
6.3.3.	<i>Conductivity measurements</i>	290
6.3.4.	<i>Supernatant analysis and complexometric measurements</i>	292
6.3.4.1.	Determination of the zinc concentration $[Zn^{2+}]_{total}$	292
6.3.4.2.	Determination of the total phosphate concentration $[PO_4^{3-}]_{total}$	293
6.4.	SOLUBILITY ISOTHERMS AND PH DEPENDENCE OF DISSOLUTION PROFILES.....	294
6.4.1.	<i>Solubility isotherms</i>	294
6.4.1.1.	pH fluctuations	295
6.4.1.2.	Gravimetric monitoring of ZP dissolution.....	296
6.4.1.3.	Comparative techniques for monitoring ZP dissolution.....	300
6.4.1.4.	Hopeite model and composition dependent dissolution model.....	302
6.4.2.	<i>Synergy of competing dissolution-precipitation mechanisms</i>	304
6.4.3.	<i>Metamorphism of basic zinc phosphates: NaZnPO₄·1H₂O, Na₂Zn(PO₄)(OH)·2H₂O</i>	306
6.4.4.	<i>Applications: standardized corrosion inhibition tests</i>	309
6.4.4.1.	Sodium effect in basic zinc phosphate pigments	309
6.4.4.2.	Combined effects of the state of hydration and polymorphy on ZP anticorrosion efficiency	311
6.5.	CONCLUSION	314
6.6.	REFERENCES.....	316
7.	SUMMARY AND FURTHER OUTLOOK.....	321
8.	ACKNOWLEDGEMENTS.....	323
9.	CURRICULUM VITAE.....	325

1. Introduction

“There is no such things as applied sciences, only applications of science”,
Louis Pasteur, 11. September 1872

1.1. Zinc Phosphate: an industrial product of high technicality

1.1.1. Protective coatings and corrosion inhibitors based on zinc phosphates

Protection of metal from corrosion presents a heavy problem of both economical and ecological nature [1] and solely in year 2003, damages and related costs ascribed to corrosion are evaluated to 300 bn € by European insurers and policy makers. Both points of view are addressed partially by the technical progress in the anticorrosion protection of metals [2]. At present the use of organic coatings based on binder soluble in organic solvents (aliphatic or aromatic), known as *primer*, and pigmented with red lead or zinc chromate, is not only one of the determining step in the application of painting systems, but above all is one of the most extensively used and efficient techniques for the protection of ferrous surfaces against corrosion. Notwithstanding this, their use has been severely restricted since 1990, mainly due to their high toxicity. The concern of meeting both modern ecological and socio-economical requirements and consequently of rapidly replacing these extremely polluting pigments has led to the rise of large research programs aimed at developing *active* “green” anticorrosive pigments [3-6], of equal or better efficiency for corrosion control than achieved by lead or zinc chromate, that further necessarily exhibit exceptional synergetic performance with waterborne coatings (i.e. substitution of alkyd and epoxy paints with styrene-acrylate dispersions) [7]. Among several non-toxic anticorrosive pigments so far developed, European researchers [8-10] and manufacturers [11-12] have mainly focused their attention to highly promising zinc phosphate hydrates, albeit their anticorrosion mechanisms are not yet fully understood. According to Kalendová et al. [13-15] their short-to-mid-term anticorrosive efficiency bases on the so-called *barrier effect* [16] (Fig. 1.1), in which microcrystals embedded in a protective organic coating can stop the water diffusion onto a steel surface. In a candid way they even

lately suggested that only the zinc phosphate dihydrate may be an *passive* corrosion inhibitor, since it might have the capacity to uptake water before dissolving as water penetrates the protective coating.

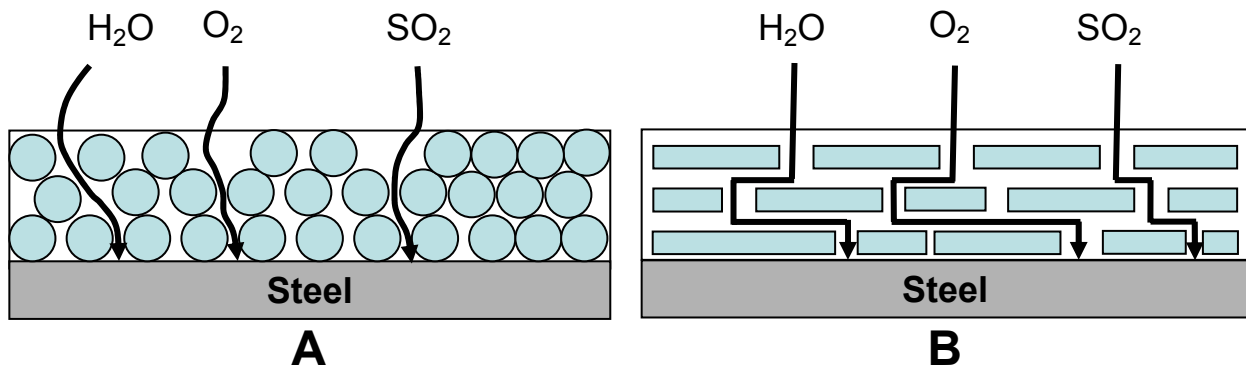


Figure 1.1: Principle of the pigment barrier effect and scheme of diffusion of a corrosive medium through a waterborne paint (protective coating) pigmented with isometric (A) and non-isometric (B) particles.

However, it is not clear if this selective water uptake is first a beneficial effect uniquely in the case of a zinc phosphate dihydrate and secondly if a strictly limited water uptake regarding zinc phosphate tetrahydrate based pigments is utmost expectable.

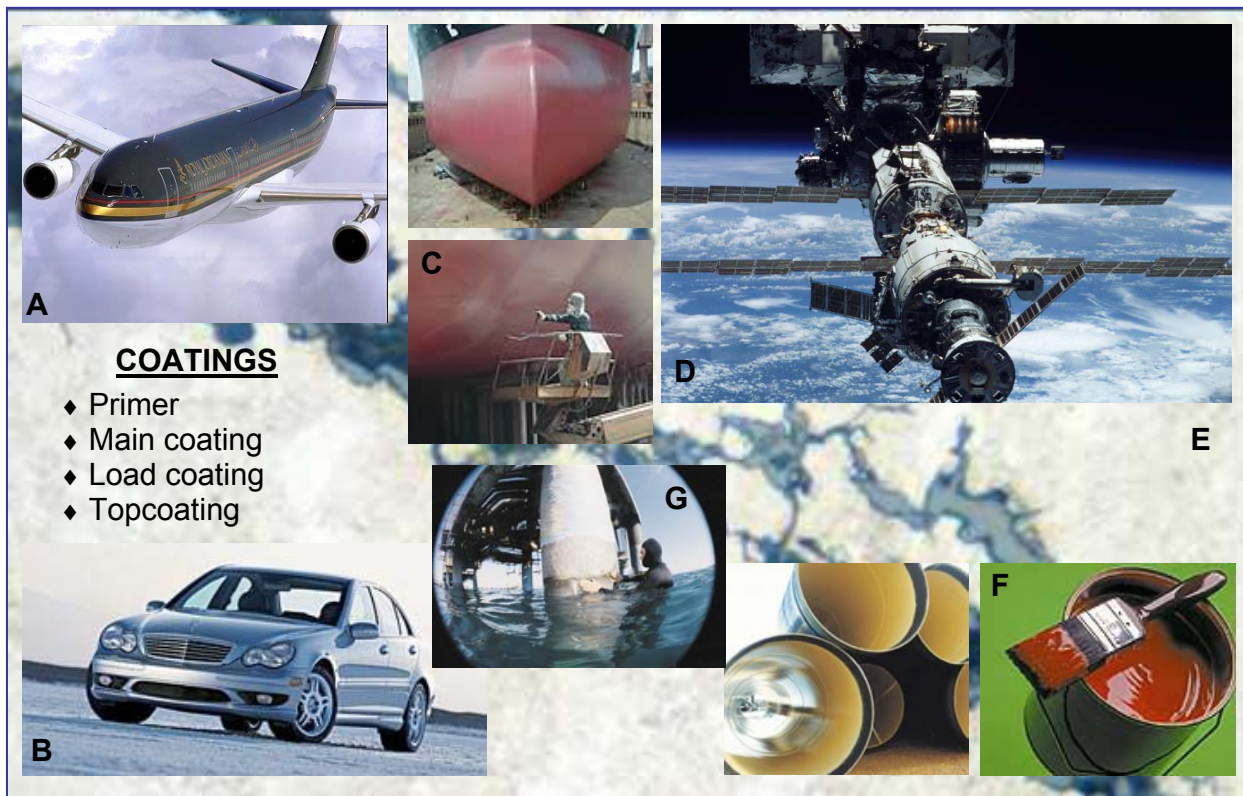


Figure 1.2: Some applications related to public and goods transportation in which corrosion inhibition is a primary issue: (A) air, (B) automobile, and marine (C) transportations. Even the international space station may corrode (D). (E) Chloride stress corrosion cracking (SCC) on the water cooling side of a stainless steel exchange tube. Application of multilayer coatings on pipe elements (F,G). A 100 μm thick multilayer coating is composed of four main layers (From McDanel's [17]).

Furthermore, while absorbed water diffuses through the coating, zinc phosphate dihydrate may also convert partially in zinc phosphate tetrahydrate. Therefore, for example, mixed zinc phosphate tetrahydrate/dihydrate pigments are broadly used as *passive* corrosion inhibitor in the formulation of marine and automotive paints [18] (Fig. 1.2). For such industrial applications, where prolonged exposure to heat/cold and where geometric thermomechanical stability are of major concerns, a thorough study of the hydration process, the determination of the hydration phase diagram and a precise quantification of the relative stability of zinc phosphate tetrahydrate (ZPT), zinc phosphate dihydrate (ZPD) and zinc phosphate anhydrate (ZPA) might be necessary. Besides, zinc phosphate tetrahydrate exists in nature in two structures, orthorhombic hopeite and parahopeite, its triclinic polymorph [19]. Although the phase system P_2O_5 -ZnO- H_2O has been studied for a very long time [20-22], the precise structure of the two orthorhombic modifications, α - and β -hopeite, is not yet known. Moreover, it seems that the long-term protective mechanism against corrosion results first from the formation of coordination-complexes with the acrylate binder components, as early suggested by Meyer [23] and secondly from metal substrate phosphatization or *passivation* [24-25] (Fig. 1.3 A,B) via slow controlled release and diffusion of phosphate ions (i.e. *active anticorrosion*) through the coating layers [26].

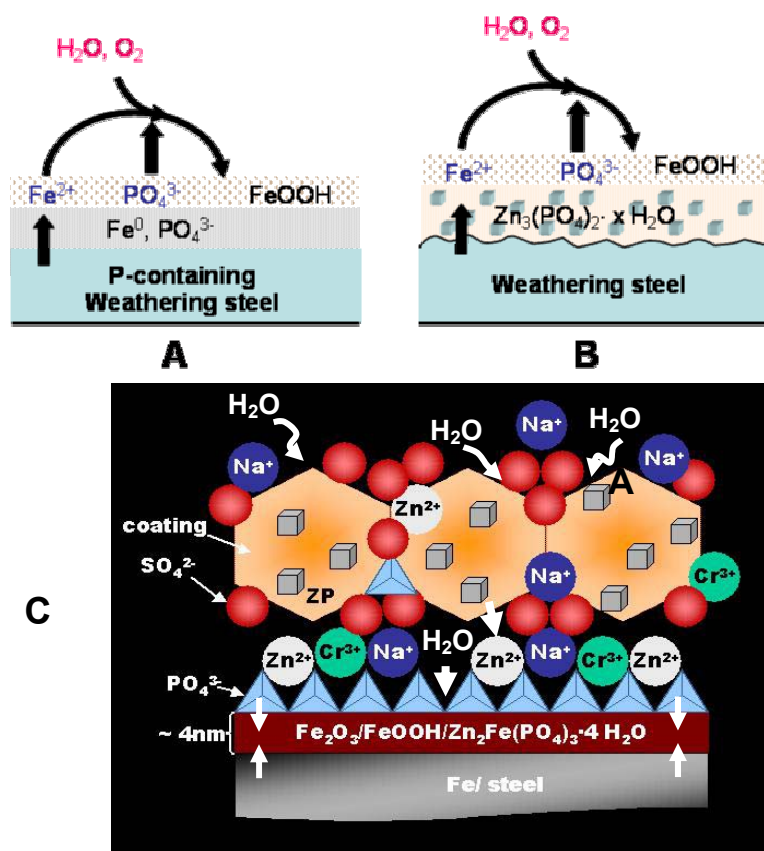


Figure 1.3: Schematic cut of a primer coating layer, containing either a phosphate layer [protection thanks to phosphatizing (■) in (A)] or loaded with zinc phosphate based pigments (B) releasing phosphate ions upon partial dissolution; thus avoiding the disastrous formation of goethite (α -FeOOH) to the benefit of a passive layer of phosphophyllite ($FeZn_2(PO_4)_2 \cdot 4H_2O$) (■) (C) in the intermediate zone (interface) between the dispersion coating (■) and the steel surface (■). This scheme also emphasizes the substitution of CrO_4^{2-} by PO_4^{3-} ions in a corroding (i.e. complex electrochemical) environment; from Schindler [27] and Matijevic [28].

Such compounds react with oxidation products, e.g. Fe^{2+} , yielding an adherent layer of sparingly soluble phosphophyllite [$FeZn_2(PO_4)_2 \cdot 4H_2O$] (Fig. 1.3 C) on the metal surface [29-30]. In that sense, it has been controversially argued that one of the major limitations of zinc phosphate

pigments as corrosion inhibitors might be their poor solubility [31-32] and the difficulties to control both the desired hydration state [33] and the synthesized crystal phase (polymorphy) on industrial scale.

1.1.2. Novel applications of zinc phosphates

In addition to its appealing anticorrosion application and its common use in protective coating technology, hopeite is also one of the main crystalline reaction components of dental cements and prosthodontic luting agents [34-36] and therefore leads to a new generation of dental ceramics formulations: the zinc phosphate cements (ZPC), as extensively reviewed by Pawlig [37-40]. Active research has been recently conducted in dental medicine to obtain materials suitable for the fabrication of esthetic single crowns or fixed partial dentures as permanent restoration of teeth [41-43]. Zinc phosphate based cements and glass ionomer/phosphate based cements generally perform well because of high fracture toughness [44-45], excellent dimensional stability [46], low solubility in an aggressive biological environment [47], as well as a high bonding i.e. retentive strength with any other adhesive cement or with bone substrate conferring a good chemical stability [47], durability and low cytotoxicity, i.e. excellent biocompatibility. In addition, great advances have been recently achieved in combining hydroxyapatite ($\text{Ca}_5(\text{PO}_4)_3\text{OH}$) with zinc phosphate cements [48]. Accordingly, an implant with desired long term biostability and low cytotoxicity may be obtained in controlling the crystal size and the hydration state of zinc (ZP) and/or calcium phosphate containing materials [50-52]. Beyond, retention of dental restoration to the tooth substance and sealing of the marginal gap between the restoration and tooth are also dependent on one hand on the surface and bonding properties of ZP cements that critically control the adhesion stability and longevity of the restoration and on the other hand on the Ca+Zn to PO_4 ratio [53-56]. Therefore many studies focus on the synthesis of biphasic zinc phosphate ceramics through various raw materials [57] and processes [58-59]. However numerous long term clinical studies comparing different potential dental materials show that the antagonistic optimization of the elastic modulus versus fracture toughness in parallel with a dramatic lowering of the solubility for a better workability and extended service-lifetime are still needed [60-62].

In addition, since the first microporous zinc phosphates with zeolite-like topologies were reported by Gier and Stucky [63], a large number of zincophosphates (ZnPOs) with 1D, 2D and 3D open framework structures and tunable pore geometries have been synthesized by sol-gel process or hydrothermal precipitation (typically 20 bars, 150-200°C) in the presence of organic templates, mostly small molecules containing amine or amino groups [64-65]. In this line and albeit the harsh synthesis conditions, pharmaceutical interests toward basic zinc phosphates

(e.g. $\text{Na}_6(\text{ZnPO}_4)_6 \cdot 8 \text{H}_2\text{O}$, soladite) has recently arisen due to the perspectives of enantioselective separation (Fig. 1.4) and/or crystallization of active substances and proteins. Besides, ZPA and zeolite NaZnPO_4 in its monohydrate and anhydrate were reported to exhibit an excellent catalytic activity, i.e. $\text{Zn}_3(\text{PO}_4)_2$ yields cyclohexene from cyclohexanol, whereas, under the same reaction conditions, NaZnPO_4 produces a ketone selectivity [66]. Furthermore, thanks to their ion-exchange and retention abilities and intrinsic basicity, zeolite β such as $\text{NaZnPO}_4 \cdot 1 \text{H}_2\text{O}$ and $\text{Na}_2\text{ZnPO}_4(\text{OH}) \cdot 2 \text{H}_2\text{O}$ could also perform well as corrosion inhibitors in basic conditions and may represent an expansion of the classical ZPT family, since they are expected to display a satisfying water retention capacity (passive anticorrosion) and very low solubility above pH 8. But in spite of several hypotheses, the mechanism of formation of complex two and three dimensional open framework structure, especially zeolite β containing sodium ions, is still poorly understood. Until now, hopeite is believed to be one of the precursor of zinc phosphate based zeolites, in that it is gradually transformed into ladder-like and layered three dimensional structures by substantial incorporation of the respective template agent, thus strongly involving hydrogen bonding [67-68].

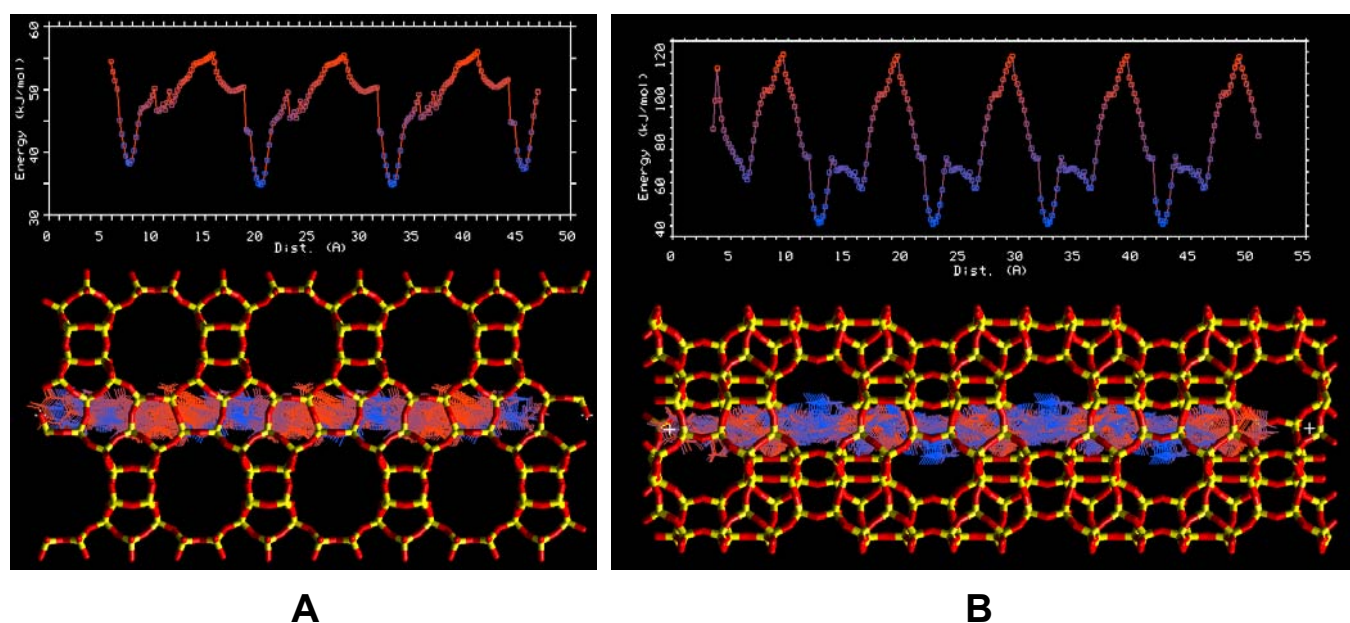


Figure 1.4: Superimposed snapshots (stick representation) of the diffusion of cumene in large and medium pore zeolites BEA (A) and MFI (B), including the corresponding energy plot (above). The computed energy barrier with CATALYSIS modelization package for diffusion of cumene in those open-framework structures is 77.9 kJ.mol^{-1} and 20.9 kJ.mol^{-1} for MFI and BEA (A-polymorph of zeolite β) respectively. Exert from: http://www.accelrys.com/cases/eniricerche_full.html

All these materials geared towards advanced applications share the common feature that, concerning synthesis and purity, the type of zinc phosphate hydrates (tetrahydrate: α , β -hopeite, parahopeite, trihydrate: $\text{Zn}_3(\text{HPO}_4)_3 \cdot 3\text{H}_2\text{O}$ or ZHPT, $\text{NaZnPO}_4 \cdot 1\text{H}_2\text{O}$, etc.) has dramatic influence on pigment activation [69-71], bioactivity [72-73] and the resulting macrostructure.

Furthermore, the pigment surface reactivity and crystal/paint compatibility can be tuned in reducing dramatically the crystal size and narrowing the crystal size distribution, which in turn govern the specific surface area and surface energy values. One way of achieving this consists of designing zinc phosphate pigments “on purpose”, employing an innovating strategy combining low temperature precipitation in aqueous medium and mineralization control by functionalized polymers.

1.2. Mineralization of pigments based on zinc phosphate hydrates

1.2.1. Biomineralization

Nature is adept at controlling mineralization processes. Many living organisms synthesize simultaneously amorphous and polycrystalline organic/inorganic composite materials for the generation of protective structures, e.g. mollusc shells, skeletons, teeth, etc. (Fig. 1.5). They exert exceptional control over the gross morphology, physical properties and hierarchical structuring of these materials on several length scales (i.e. from the Ångstrom to the cm scale), often creating shapes that defy the strict geometrical restrictions of the 230 classical space groups [74-75]. This precisely encompasses the term *biomineralization* [76].

In recent years much interest in biomineralization has been generated due to the perspectives of unique combination of strength and elasticity, the resistance both to fracture and to drastic environmental conditions, and other desirable properties of biomaterials [77]. Additionally, the participation of biomolecules in the nucleation and growth of crystals raises interesting questions with respect to molecular recognition [78] and chirality transfer [79]. Most notably, the proteins involved in directing the shape of these biomaterials have often evolved to recognize and bind selectively to one or more faces of the growing crystal. Because of clear potential applications such as bone substitutes for hydroxyapatitic materials [80-81] and the opportunity to unravel this fascinating process (e.g. stabilization of intermediary phases: amorphous calcium carbonate (ACC) [82-85], amorphous calcium phosphate (ACP) and supposedly amorphous zinc phosphate (AZP) [86-87]), in the last ten years research into the design of supramolecular, organic assemblies to assist the growth “in-vitro” of inorganic crystals has increased significantly [88-89].

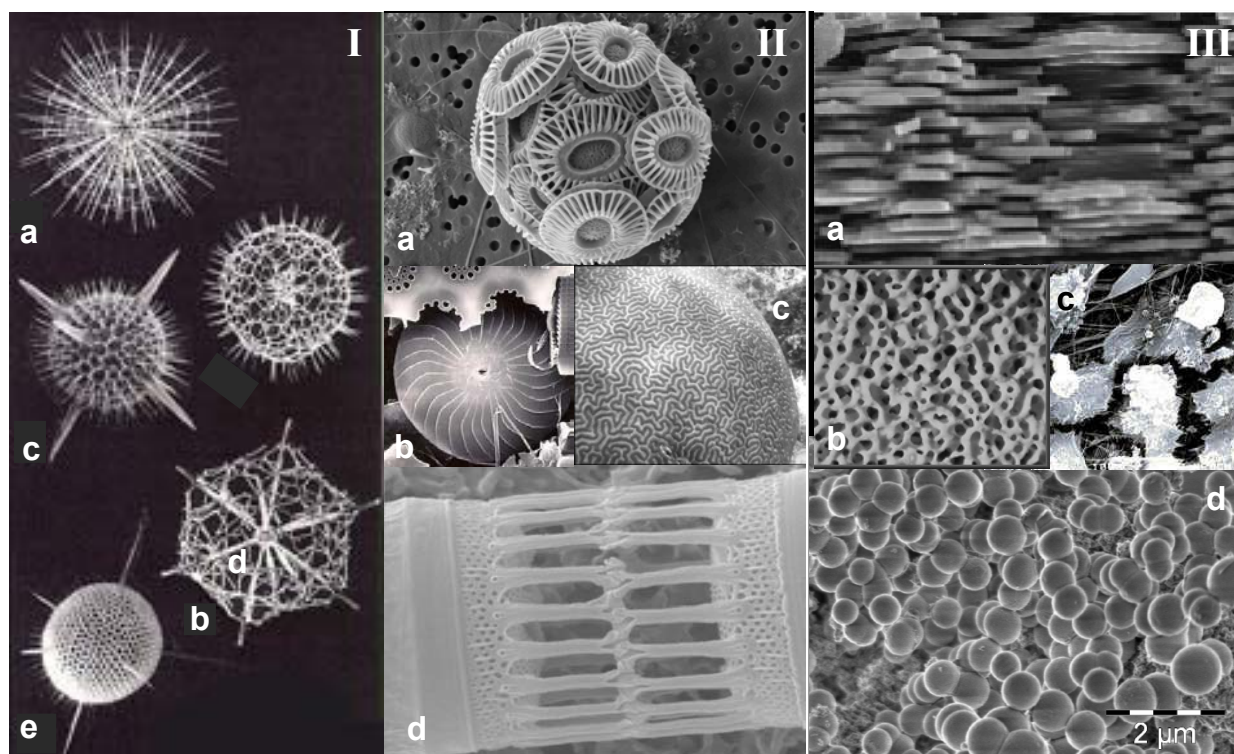


Figure 1.5: Crystals, symmetry and life - Scanning electron microscopy images of biomaterials. (I) skeletons of some radiolaria showing the remarkably diverse shapes composed of silicate. Some have very small central shells and long spines (a,d), while others have very large lattice-like shells (b) and other species produce very robust thickened shells and massive short spines (c,e) with shells varying in size from less than 100 μm to nearly 1 mm; (II) skeletons made from calcium carbonate of coccolithosphere arrangement (a) and single coccolith (*Heteroccolith Emiliana Huxley*) [90] (b), giant brain coral (c), diatom skeletonema (x 6000) (d); (III) calcium containing organized hybrid structures pointing toward nano-bioengineering: columnar nacre of *Turbo Undulatus* [91] (a), synthetic amorphous CaCO_3 nanospheres [92] (d), natural and synthetic hydroxyapatitic bone (b,c).

1.2.2. Polymer controlled mineralization

Inspired from biomineralization, polymer-mediated mineralization of inorganic materials has been the subject of intense research for the same reasons. Many authors have thoroughly investigated the influence of synthetic polymers [93-96] and biopolymers [97-99], supramolecular assemblies [100-101], self-assembled films [102-103], gels [104-105] and inverse emulsions (i.e. nanoreactors) [106-108] on the mineralization process, as summarized in Fig. 1.6. However these studies are mainly restricted to simple model systems such as ZnO or BaTiO_3 mainly due to the presence of a single crystal phase [108], and more recently were extended first to semi-conducting nanopowders and finally to the complex calcium carbonate and calcium phosphate systems [110-115]. Notably, several descriptive studies have clearly shown that polymeric additives control not only the particle shape (e.g. morphology and surface topology), size and size distribution [116-122] but also the crystal phase [123-124] and the crystal state of hydration [125] or even the crystal chirality (introduced by the organic host) [126-

128]. Hence, precipitation reactions from aqueous media in particular are a versatile and non-polluting method for the formation monodisperse and uniform inorganic powders, and highly ordered composite architectures in the nanometer up to the micron scale. In addition to the chemical nature of the polymeric additive of mineralization, numerous “physical” parameters such as temperature, ionic strength and the pH of the reaction solution or the stirring process itself drastically influence the crystallization process and thus the resulting powder substances [129]. Although immense progress has been made in understanding the role of the polymeric additives on nucleation and crystal growth during precipitation, and aging process (e.g. aggregation, phase transformation) especially in dependence of the polymer composition [130-131]) and concentration, few studies have carefully addressed the question of the precise crystal growth mechanisms [132-137] on the basis other than systematically investigating morphologies of the final products. In this line, a new class of functional polymers, the so-called double-hydrophilic block copolymers (polyelectrolytic DHBCs) has been recently developed in parallel by Weiner, Antonietti and Cölfen for mineralization purpose [138-140].

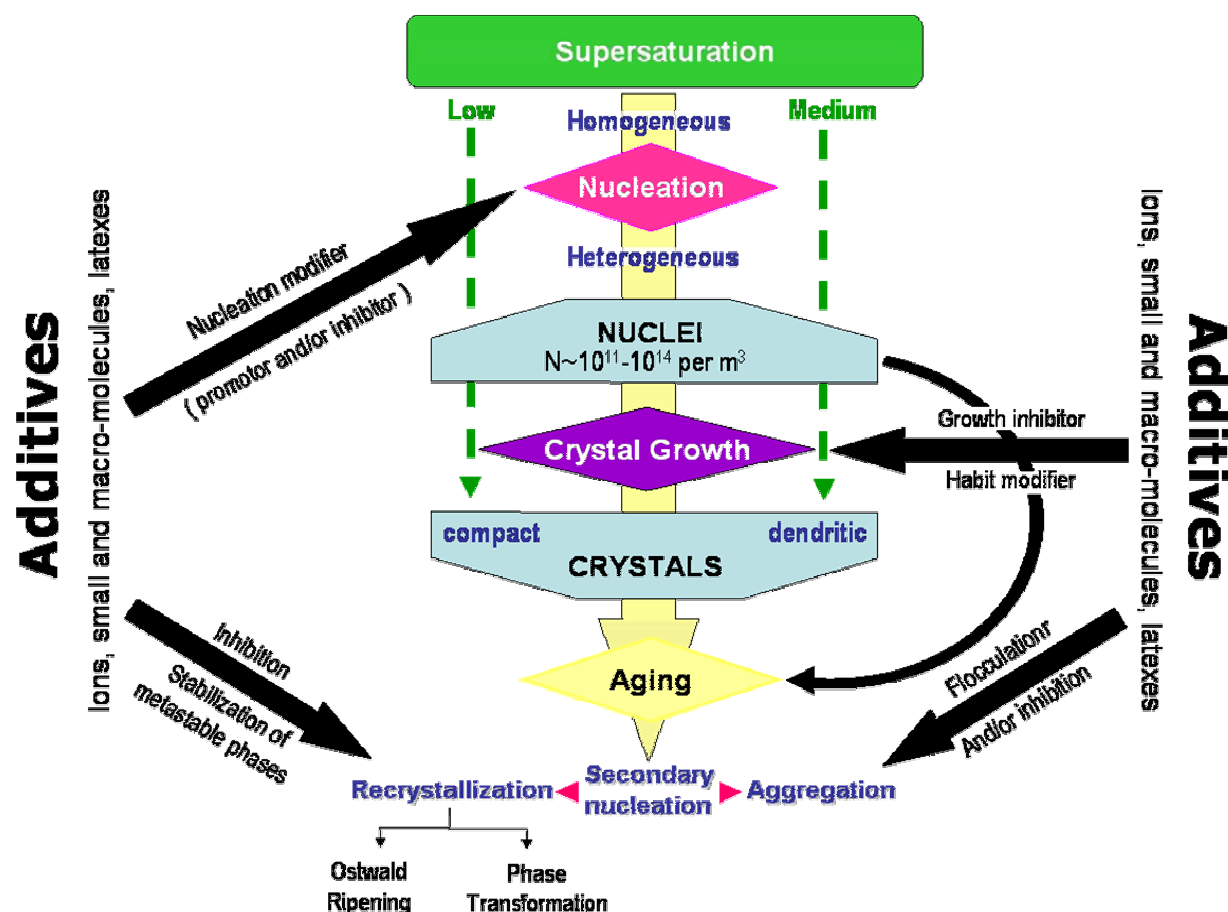


Figure 1.6: Schematic representation emphasizing the possible role of polymeric additives in the aqueous precipitation of sparingly soluble salts such as zinc phosphate hydrates and initiates by heterogeneous nucleation.

These polymers consist of one charged and hydrophilic (e.g. poly(meth)acrylic) block designed to interact strongly with the appropriate inorganic materials and surfaces, and another hydrophilic block that does not interact (or only weakly and mainly promotes steric stabilization or solubilisation in water). The potential of poly(meth)acrylics and poly(meth)acrylates in nucleation and growth processes was identified rather early by the pioneering work of Henglein et al. [141]. Owing to the separation of the solvating moieties, DHBCs are “improved or optimized versions” of the poly(meth)acrylics and turned out to be incredibly effective in the crystallization control for zinc oxide [142] and calcium carbonate [143], where tuned morphologies varying from rods, tubes, wires, cubes, spheres, drumlike, to donuts and pancakes were easily achieved [144-145].

Furthermore, latexes combine a rigid core inducing a shape persistence or geometric invariance necessary during the nucleation stage [150] and a flexible corona, that can change its conformation and local charge density in order to roughly fit the ionic group (i.e. of opposite charge to the polymer) distribution of characteristic planes of the zinc phosphate crystals [151-152]. Such templates display also striking similarities with P(S-*b*-MAA) and P(EO-*b*-MAA) DHBCs [153] used in model crystallization systems. In addition, these latexes may be conveniently produced by one-step synthesis, i.e. direct miniemulsion polymerization [154-158], which is an very reliable process (e.g. highly reproducible, product stable over months), that delivers monodisperse structured particles of adjustable size (range 50 nm - 1 μ m), composition (choice of the hydrophilic comonomer on acrylate basis) and surface charge density. Furthermore, such latexes are obtained on industrial scale and are currently used as the most promising substitute primer to more classical but toxic organic anticorrosive coatings. Moreover, understanding the molecular and supramolecular processes that lead to a specific phosphate containing product is however a pivotal issue for enabling the design and fabrication on large scale of tailored materials, such as *basic* zinc phosphate based corrosion inhibitors (i.e. $\text{NaZnPO}_4 \cdot 1\text{H}_2\text{O}$, $\text{Na}_2\text{Zn}(\text{PO}_4)(\text{OH}) \cdot 2\text{H}_2\text{O}$).

1.3. Strategies of investigation: Materials by design

In a first step, the first three chapters of this thesis are realized in order to shed some necessary light on the reactivity of ZPT crystals at surfaces and interfaces, depending (i) on the aggressive chemical environment and surrounding temperature (Chapter 4), (ii) on their polymorphism (Chapter 2) and respective state of hydration (Chapter 3). Especially, while Chapter 2 focuses on the identification of hopeite polymorphs (α -, β -ZPT) and the refinement of their respective crystal structure in comparison to a metastable precursor $\text{Zn}_3(\text{HPO}_4)_3 \cdot 3\text{H}_2\text{O}$, Chapter 3 aims at

determining the zinc phosphate phase diagram of hydration and investigates both the thermodynamic interrelations between zinc phosphate pigments of different state of hydration and the dehydration mechanisms. Besides, Chapter 4 offers information of paramount importance regarding the chemical reactivity of ZPT crystals at surfaces and interfaces, which are urgently needed for an efficient polymer mediated crystallization (e.g. adsorption mechanisms) and for an accurate estimation of pigment bulk dissolution rates. In addition, the systematic investigation of the parameters governing an efficient latex-controlled mineralization in Chapter 5 is expected to offer first key information regarding ZPT crystallization mechanism and secondly an efficient process for large scale synthesis of polymer modified ZPO pigments. Tentative latex-crystal interaction mechanisms based on coordination chemistry and modern heterogeneous nucleation theories are consequently proposed. Further in Chapter 6, the anticorrosion efficiency of the pigments described in Chapters 2 and 5 is evaluated in comparison to commercially available zinc phosphate pigments and general dissolution mechanisms depending on the pigment chemical composition will be outlined.

1.4. References

- [1] S.C. DeVito, *Prog. Org. Coat.* **35** (1999) 55
- [2] W. Funke, *Prog. Org. Coat.* **31** (1997) 5
- [3] I.M. Zin, S.B. Lyon, S.J. Badger, J.D. Scantlebury, V.I. Pokhmurskii, *J. Corros. Sci. Eng.* **2** (1999) 21
- [4] L. Veleva, J. Chin, B. Del Amo, *Prog. Org. Coat.* **36** (1999) 211
- [5] C.H. Hare., *J. Prot. Coat. Minings* **15** (1998) 31
- [6] G.A. Howard, *Pigment Resins Tech.* **29** (2000) 325.
- [7] A. Bittner, *Surf. Coat. Int. J.O.C.C.A* **4** (1988) 97
- [8] W. Funke, *J. Coat. Technol.* **58** (1986) 741
- [9] A. Amirudin, C. Barreau, R. Hellouin, D. Thierry, *Prog. Org. Coat.* **25** (1995) 339
- [10] A. Kalendová, P. Kalendá, *Farbe + Lacke* **110**(3) (2004) 22
- [11] A. Bittner, *J. Coat. Technol.* **61**(777) (1989) 111
- [12] <http://www.heubachcolor.de>
- [13] A. Kalendová, *Prog. Org. Coat.* **44** (2001) 201
- [14] A. Kalendová, P. Kalendá, *Farbe + Lacke* **109**(11) (2003) 62
- [15] H. Leidheiser, *J. Coat. Technol.* **53** (1981) 29
- [16] P. Kalendá, A. Kalendová, V. Štengl, P. Antoš, J. Šubrt, Z. Kváča, S. Barkardjieva, *Prog. Org. Coat.* **49** (2004) 137
- [17] S. J. McDanel, *An Overview of Fatigue and Other Metallurgical Failure Modes and Analysis at the Kennedy Space Center*, Flammability and Sensitivity of Materials in Oxygen-Enriched Atmospheres: 8th Volume, ASTM STP 1319, W. T. Royals, T. C. Chou, and T.A. Steinberg, Eds., American Society for Testing and Materials, 1997.
- [18] J.B. Harrison, *Corrosion and Coatings* **3** (1976) 11
- [19] G. Chao, *Z. Kristallogr. Krisr.* **130**(4-6) (1969) 261
- [20] M.V. Goloshchapov, T.N. Filatova, *Russ. J. Inorg. Chem.* **14**(3) (1969) 424
- [21] E.A. Nikonenko, I.N. Marenkova, *Russ. J. Inorg. Chem.* **31**(1986) 397
- [22] A. Whitaker, *J. Appl. Cryst.* **6** (1973) 495
- [23] G. Meyer, *Farbe + Lacke* **71** (1965) 113
- [24] G. Meyer, *Farbe + Lacke* **69** (1963) 528
- [25] M.F. Clay, G.H. Cox, *J. Oil Col. Chem. Assoc* **56** (1973) 13
- [26] G. Adrian, A. Bittner, *J. Coat. Technol.* **58** (1986) 59
- [27] P.W. Schindler, W. Stumm, *The surface chemistry of oxides, hydroxides and oxide minerals*, in Aquatic Surface Chemistry, W. Stumm Ed., Wiley (NY) (1987) p.83
- [28] E. Matijevic, EPRI-NP2606 (October 1982) p.1
- [29] R. Romagnoli, V.F. Vetere, *Corrosion* **51**(2) (1995) 216
- [30] H. Nakano, M. Urai, M. Iwai, *Surf. Coat. Int. J.O.C.C.A -Tetsu to Hagane* **85**(1) (1999) 39
- [31] J.A. Burkill, J.E.O. Mayne, *Surf. Coat. Int. J.O.C.C.A* **71** (1988) 275
- [32] B. Del Amo, R. Romagnoli, V.F. Vetere, L.S. Hernández, *Prog. Org. Coat.* **33** (1998) 28
- [33] H.M.A. Al-Maydama, P.J. Gardner, I.W. McAra, *Thermochim. Acta* **192** (1992) 117
- [34] M. Eisenberger, M. Addy, A. Roszbach, *J. Dentistry* **31**(2) (2003) 137
- [35] R. Nomoto, K. Uchida, Y. Momoi, J.F. McCabe, *Dent. Mater.* **19**(3) (2003) 240
- [36] Y. Yamada, Y. Tsubota, S. Fukushima, *Int. J. Prosthodont.* **17**(1) (2004) 94
- [37] R.G. Craig, in *Restorative Dental Materials*, Mosby, St Louis (1993)
- [38] A.D. Wilson, J.W. Nicholson, in *Chemistry of Solid State Material, Vol.3: Acid-based cements, their biomedical and industrial applications*, University Press (Cambridge) (1993)
- [39] C.L. Davidson, *Adv. Eng. Mater.* **3**(10) (2001) 763
- [40] O. Pawlig, *PhD Thesis*, University of Mainz (Germany) (2001)
- [41] R.S. Squier, J.R. Agar, J.P. Duncan et al., *Int. J. Oral Max. Impl.* **16**(6) (2001) 793

- [42] F. Bohlsen, M. Kern, *Quintessence Int.* **34**(7) (2003) 493
- [43] S. Peirada, J. Cavalheiro, R. Branco, A. Afonso, M. Vasconcelos, *Key Eng. Mat.* **254**(2) (2004) 659
- [44] N. Attar, L.E. Tam, D. McComb, *J. Prothet. Dent.* **89**(2) (2003) 127
- [45] K.A. Proos, M.V. Swain, J. Ironside et al, *Int. J. Prosthodont.* **16**(1) (2003) 82
- [46] S. Haussühl, M. Friedrich, *Cryst. Res. Technol.* **28**(4) (2003) 437
- [47] B. Czarnecka, H. Limanowska-Shaw, J.W. Nicholson, *J. Mater. Sci.-Mater. Med.* **14**(7) (2003) 601
- [48] S.O. Hedlund, N.G. Johansson, G. Sjogren, *Br. Dent. J.* **195**(3) (2003) 155
- [49] M. Otsuka, S. Marunaka, Y. Matsuda, A. Ito, P. Layrolle, H. Naito, N. Ichinose, *J. Biomed. Mater. Res.* **52**(4) (2000) 819
- [50] M. Uo, G. Sjoren, A. Sundh; F. Watari, M. Bergnman, U. Lerner, *Dent. Mater.* **19** (2003) 487
- [51] A. Piwowarezyk, H.C. Laue, *Oper. Dent.* **28**(5) (2003) 535
- [52] A. Ito, H. Kawamura, M. Otsuka, M. Ikeuchi, H. Ohgushi, K. Ishikawa, K. Onuma, N. Kanzaki, S. Sogo, N. Ichinose, *Mater. Sci. Eng. C –Bio. S.* **22**(1) (2002) 21
- [53] A.J. Coleman, H.H.D. Rickerby, L.R. Antonoff, *Quintessence Int.* **32**(10) (2001) 811
- [54] G.J.P. Fleming, O. Narayan, *Dent. Mater.* **19**(1) (2003) 69
- [55] M.M. Piemjai, *Int. J. Prosthodont.* **14**(5), (2001) 412
- [56] R. Nomoto, J.F. McCabe, *Dent. Mater.* **17**(1) (2001) 53
- [57] A.D. Wilson, J.W. Nicholson, *Phosphate bonded cements*, in A.D. Wilson and J.W. Nicholson Eds., *Acid-base cements: their biomedical and industrial applications*, Cambridge University Press (1993)
- [58] W.W. Brackett, S. Rosen, *Oper. Dent.* **19** (1994) 106
- [59] J. Li, S. Forberg, R. Söremark, *Acta. Otolol. Scand.* **52** (1994) 209
- [60] K. Sunnegardh-Gronberg, A. Peutzfeldt, J.W.V. van Dijken, *J. Dent. Res.* **81** - Sp. Iss. B (2002) 361
- [61] E. Mezzomo, F. Massa, S. Libera, *Quintessence Int.* **34**(4) (2003) 301
- [62] M. Eisenberger, M. Addy, A. Roszbach, *J. Dent.* **31**(2) (2003) 137
- [63] T.E. Gier, G.D. Stucky, *Nature* **349** (1991) 508
- [64] W. Liu, Y. Liu, Z. Shi, W. Pang, *J. Mater. Chem.* **10** (2000) 451
- [65] A.K. Cheetam, G. Ferey, T. Loiseau, *Angew. Chem. Int. Ed.* **38** (1999) 3268
- [66] M.A. Aramendía, V. Boreau, C. Jiménez, J.M. Marinas et al., *J. Catalysis* **151** (1995) 44
- [67] S. Oliver, A. Kuperman, G.A. Ozin, *Angew. Chem. Int. Ed.* **37** (1998) 46
- [68] J. Li, J. Yu, W. Yan, Y. Xu, W. Xu, S. Qiu, R. Xu, *Chem. Mater.* **11** (1999) 2600
- [69] L.S. Hernández, G. Garcia, C. López, B. Del Amo, R. Romagnoli, *Surf. Coat. Int. J.O.C.C.A.* **81** (1998) 19.
- [70] P.J. Gardner, I.W. McArn, V. Bartob, G.M. Seydt, *Surf. Coat. Int. J.O.C.C.A.* **74** (1990) 16
- [71] O. Pawlig, R. Trettin, *Mat. Res. Bull.* **34**(12-13) (1999) 1959
- [72] N. Ewoldsen, R.S. Demke, *Am. J. Orthod. Dentofac.* **120**(1) (2001) 45
- [73] C.A. Mitchell, M. Abbariki, J.F. Orr, *Dent. Mater.* **16**(3) (2000) 198
- [74] S. Mann, J. Webb, R.J.P. Williams, *Biomineralization: Chemical and biochemical perspectives*, Wiley VCH (NY) (1989) p. 541
- [75] H.A. Lowenstram, S. Weiner, *On biomineralization*, Oxford University Press (NY) (1989)
- [76] J.J.J.M. Donners, PhD Thesis, University of Eindhoven (Netherlands) (2002)
- [77] (a) S. Mann, D.D. Archibal, J.M. Didymus, T. Douglas, B.R. Heywood, F.C. Meldrum, N.J. Reeves, *Science* **261** (1993) 1286; (b) S. Mann, *J. Chem. Soc.: Dalton Trans.* (1997) 3953
- [78] (a) L. Addadi, S. Weiner, *Stereochemical and structural relations between molecules and crystals in biomineralization*, S. Mann Ed, Wiley VCH (NY) (1989) p. 133; (b) R.J. Davey, S.N. Black, L.A. Bromley, D. Cotter et al., *Nature* **353** (1991) 549
- [79] (a) C.A. Orme, A. Noy, A. Wierzbicki, M.T. McBride et al., *Nature* **411** (2001) 773; (b) L. Addadi, S. Weiner; *Nature* **411** (2001) 753

- [80] J.E. Barrelet, K.J. Lilley, L.M. Grover, D.F. Farrar, C. Ansell, U. Gbureck, *J. Mater. Sci.: Mater. Med.* **15**(4) (2004) 407
- [81] S. Kim, H.S. Ryu, F.S. Jung, K.S. Hong, *Met. Mater. Int.* **10**(2) (2004) 171
- [82] E. Loste, R.M. Wilson, R. Seshadri, F.C. Meldrum, *J. Cryst. Growth* **254**(1-2) (2003) 206
- [83] L. Addadi, S. Raz, S. Weiner, *Adv. Mater.* **15**(12) (2003) 960
- [84] E. Loste, R.M. Wilson, R. Seshadri, F.C. Meldrum, *J. Cryst. Growth* **154**(1-2) (2003) 206
- [85] S. Weiner, P.M. Dove, *Rev. Mineral. Geochem.* **54** (2003) 1
- [86] R.K. Tag, C.A. Ormes, G.H. Nancollas, *J. Phys. Chem. B* **107**(38) (2003) 10653
- [87] L.M. Grover, J.C. Knowles, G.J.P. Fleming, J.E. Barrelet, *Biomaterials* **24**(23) (2003) 4133
- [88] S. Mann, *Angew. Chem. Int. Ed.* **39** (2000) 3392
- [89] L.A. Estroff, A.D. Hamilton, *Chem. Mater.* **13** (2001) 3227
- [90] (a) J.R. Young, J.M. Didymus, P.R. Brown, S. Mann et al., *Nature* **356** (1992) 516; (b) K. Henriksen, S.L.S. Stipp, J.R. Young, P.R. Brown, *Am. Mineralogist* **88** (2003) 2040
- [91] M. Rousseau, E. Lopez, A. Coute, G. Mascarel et al., *Key Eng. Mat.* **254**(2) (2004) 1009
- [92] M. Faatz, F. Groehn, G. Wegner, *Adv. Mater.* **16**(12) (2004) 996
- [93] C.G. Göltner, M. Antonietti, *Adv. Mater.* **9** (1997) 431
- [94] (a) H. Cölfen, M. Antonietti, *Langmuir* **14** (1998) 582, (b) H. Cölfen, Q. Limin, *Chem. Eur. J.* **7** (2000) 106
- [95] L. M. Qi, H. Cölfen, M. Antonietti, *Chem. Mater.* **12** (2000) 2392
- [96] H. Cölfen, *Macromol. Rapid. Commun.* **22** (2001) 587
- [97] J. Aizenberg, J. Hanson, T.F. Koetzle, S. Weiner et al., *Chem. Eur. J.* **1** (1995) 414
- [98] S. Weiner, L. Addadi, *J. Mater. Chem.* **7** (1997) 689
- [99] (a) N. Kröger, G. Lehmann, R. Rachel, M. Sumper, *Eur. J. Biochem.* **250** (1997) 99; (b) N. Kröger, R. Deutzmann, M. Sumper, *Science* **286** (1999) 1129
- [100] B.R. Heywood, S. Mann, *Adv. Mater.* **6** (1994) 9
- [101] (a) S. Mann, *J. Mater. Chem.* **5** (1995) 935, (b) S. Mann, S.L. Burkett, S.A. Davis, C.E. Fowler et al., *Chem. Mater.* **9** (1997) 2300
- [102] J. Kuether, M. Bartz, R. Seshadri, G.B.M. Vaughn, W. Tremel, *J. Mater. Chem.* **11** (2001) 503
- [103] P.A. Ngankam, P. Lavalley, J.C. Voegel, L. Szyk, G. Decher et al., *J. Am. Chem. Soc.* **122** (2000) 8998
- [104] S.M. D'Souza, C. Alexander, S.W. Carr, A.M. Waller et al., *Nature* **398** (1999) 312
- [105] G. Falini, S. Fermani, M. Gazzano, A. Ripamonti, *J. Chem. Soc.: Dalton Trans.* **21** (2000) 3983
- [106] M. Willert, R. Rothe, K. Landfester, M. Antonietti, *Chem. Mater.* **13** (2001) 4681
- [107] (a) M.P. Pileni, *Cryst. Res. Technol.* **33** (1998) 1155; (b) M. Antonietti, E. Wenz, L. Bronstein, M. Seregina, *Adv. Mater.* **7** (1995) 1000
- [108] J.P. Cason, M.E. Miller, J.B. Thompson, C.B. Roberts, *J. Phys. Chem. B* **105**(12) (2001) 2297
- [109] (a) A.F. Hollemann, N. Wiberg, *Lehrbuch der anorganische Chemie*, 91-100th Ed., W. DeGruyter (Berlin) (1985), (b) A.R. West, *Grundlagen der Festkörperchemie*, Wiley VCH (Weinheim) (1992)
- [111] J.M. Marentette, J. Norwig, E. Stockelmann, W.H. Meyer, G. Wegner, *Adv. Mater.* **9**(8) (1997) 647
- [112] M. Oner, J. Norwig, W.H. Meyer, G. Wegner, *Chem. Mater.* **10**(2) (1998) 460
- [113] H. Cölfen, *Z. Anorg. All. Chem.* **629** (2003) 2305
- [114] F. Peters, M. Epple, *J. Chem. Soc.: Dalton Trans.* **X** (2001) 3585
- [115] A. Becker, W. Becker, J.C. Marsen, M. Epple, *Z. Anorg. Allg. Chem.* **629** (2003) 2305
- [116] M. Antonietti, M. Breulmann, C.G. Göltner, H. Cölfen, *Chem. Eur. J.* **4**(12) (1998) 2493
- [117] H. Kawaguchi, H. Hirai, K. Sakai, S. Sera et al., *Colloid. Polym. Sci.* **270** (1992) 1176
- [118] L. Qi, H. Cölfen, M. Antonietti, M. Li et al., *Chem. Eur. J.* **7** (2001) 3526
- [119] A. Bigi, E. Banini, G. Cojazzi, G. Falini et al., *Cryst. Growth Des.* **1** (2001) 239
- [120] J.H. Adair, E. Suvaci, *Curr. Opin. Colloid Interface Sci.* **5** (2000) 160
- [121] (a) E. Matijevic, *Chem. Mater.* **5** (1993) 412; (b) E. Matijevic, *Curr. Opin. Colloid Interface Sci.* **1** (1996) 176

- [122] M. Sastry, A. Kumar, C. Damle, S.R. Sainkar et al., *CrystEngComm*. **1** (2001) 21
- [123] M. Sedláč, H. Cölfen, *Macromol. Chem. Phys.* **202** (2001) 587
- [124] (a) C. M. Zaremba, A. M. Belcher, M. Fritz, Y. Li et al., *Chem. Mater.* **8** (1996) 679, (b) C. M. Zaremba, D.E. Morse, S. Mann, P.K. Hansma et al., *Chem. Mater* **10** (1998) 3814
- [125] J.B. Thompson, G.T. Plaoczi, J.H. Kindt, M. Michenfelder et al., *Biophys. J.* **79** (2000) 3307
- [126] J. Nyvlt, J. Ulrich, *Admixtures in Crystallization*, Weinheim VCH (1995)
- [127] Y. Mastai, M. Sedláč, H. Völfen, M. Antonietti, *Chem. Eur. J.* **8**(11) (2002) 2430
- [128] Y. Wang, J. Yu, Y. Li, Z. Shi et al., *Chem., Eur. J.* **9** (2003) 5048
- [129] E. Yahima, K. Maeda, T. Nishimura, *Chem. Eur. J.* **10** (2004) 42
- [130] (a) E. Matijevic, *Langmuir* **2** (1986) 12; (b) E. Matijevic, *Chem. Mater.* **5** (1993) 412
- [131] P. Baum, *PhD Thesis*, University of Mainz (Germany) (2000)
- [132] G. Wegner, P. Baum, M. Muller, J. Norwig et al., *Macromol. Symp.* **175** (2001) 349
- [133] R.L. Penn, J.F. Banfield, *Science* **281** (1998) 969
- [134] A.P. Alivisatos, *Science* **289** (2000) 736
- [135] S. Bush, H. Dolhaine, A. DuChesne, T. Weiland et al., *Eur. J. Inorg. Chem.* **10** (1999) 1643
- [136] J.F. Banfield, S.A. Welch, H. Zhang, T. Thomsen-Ebert et al., *Science* **289** (2000) 751
- [137] J. Rieger, J. Thieme, C. Schmidt, *Langmuir* **16** (2000) 8300
- [138] N. Bouropoulos, S. Weiner, L. Addadi, *Chem. Eur. J.* **7** (2001) 1881
- [139] (a) C. Seitz, *PhD. Thesis*, University of Mainz (Germany) (1999); (b) S. Förster, M. Antonietti, *Adv. Mater.* **10**(3) (1998) 195
- [140] H. Cölfen, *Macromol. Rapid Commun.* **22**(4) (2001) 219
- [141] P. Kašparová, *PhD Thesis*, University of Potsdam (Germany) (2002) and references therein
- [142] (a) M. Gutierrez, A. Henglein, *J. Phys. Chem.* **100**(18) (1996) 7656; G.B. Ershov, A. Henglein, *J. Phys. Chem.* **B102**(52) (1998) 10663
- [143] S.H. Yu, H. Cölfen, M. Antonietti, *J. Phys. Chem.* **B107**(30) (2003) 7396
- [144] A. Taubert, D. Palms, Ö. Weiss, M.T. Piccini, *Chem. Mater.* **14** (2002) 2594
- [145] A. Taubert, G. Glasser, D. Palms, *Langmuir* **18**(11) (2002) 4488
- [146] D. Braga, *J. Chem. Soc.: Dalton Trans.* **21** (2000) 3705
- [147] K. Landfester, N. Bechthold, F. Tiarks, M. Antonietti, *Macromolecules* **32**(8) (1999) 2679
- [148] S. Kirsch, K. Landfester, O. Schaffer, M.S. El-Aasser, *Acta Polym.* **50**(10) (1999) 347
- [149] D. Vaihinger, K. Landfester, I. Kräuter, H. Brunner et al., *Macromol. Chem. Phys.* **203** (2002) 1965
- [150] (a) M. Antonietti, K. Tauer, *Macromol. Chem. Phys.* **204**(2) (2003) 297; (b) M. Willert, K. Landfester, *Macromol. Chem. Phys.* **203**(5-6) (2002) 825
- [151] P.A. Ngankam, Ph. Lavalley, J.C. Voegel, L. Szyk et al., *J. Am. Chem. Soc.* **122** (2000) 8998
- [152] L. Addadi, S. Weiner, *Proc. Natl. Acad. Sci. USA* **82** (1985) 4110
- [153] J.J.J.M. Donners, R.J.M. Noltes, N.A.J.M. Sommerdijk, *J. Am. Chem. Soc.* **124** (2002) 9700
- [154] N. Bechthold, F. Tiarks, M. Willert, K. Landfester et al., *Macromol. Symp.* **151** (2000) 549
- [155] M. Antonietti, K. Landfester, *Prog. Polym. Sci.* **27** (2002) 689
- [156] J.M. Asua, *Prog. Polym. Sci.* **27** (2002) 1283
- [157] K. Landfester, *Top. Curr. Chem.* **227** (2003) 75
- [158] K. Landfester, N. Bechthold, F. Tiarks, M. Antonietti, *Macromolecules* **32**(16) (1999) 5222

2. Crystal structures and bulk properties of zinc phosphate hydrates

“Where observation is concerned, chance favours only the prepared mind”, *Louis Pasteur, address given on the inauguration of the Faculty of Science, University of Lille, 7 December 1854.*

2.1. Introduction

Protection of metal from corrosion presents a heavy problem of both economical and ecological nature [1]. Both points of view are solved partially by the technical progress in the anticorrosion protection of metals [2]. At present the use of organic coatings based on binder [3] soluble in organic solvents (aliphatic or aromatic), known as *primer*, and pigmented with red lead or zinc chromate, is not only one of the determining step in the application of painting systems, but above all is one of the most extensively used and efficient techniques for the protection of ferrous surfaces against corrosion. Notwithstanding this, their use has been severely restricted since 1990, mainly due to their high toxicity and the potential chemical hazard they represent for the environment. The concern of meeting both modern ecological and socio-economical requirements and consequently of rapidly replacing these extremely polluting pigments has led to the rise of large research programs aimed at developing “active green” anticorrosive pigments [4-7], of equal or better efficiency for corrosion control than achieved by lead or zinc chromate, that further necessarily exhibit exceptional synergic performance with waterborne coatings (substitution of alkyd and epoxy paints with styrene-acrylate dispersions) [8].

Among several non-toxic anticorrosive pigments so far developed, European researchers [9-11] and manufacturers [12-13] have mainly focused their attention to highly promising zinc phosphate hydrates, albeit their anticorrosion mechanisms are not yet fully understood. It appears that the protective mechanism results from metal substrate phosphatization or *passivation* [14-15] and to the formation of coordination-complexes with the acrylate binder components, as early suggested by Meyer [16]. Such compounds react with oxidation products, e.g. Fe^{2+} , yielding an adherent layer of sparingly soluble phosphophyllite $[\text{FeZn}_2(\text{PO}_4)_2 \cdot 4 \text{H}_2\text{O}]$ on the metal surface [17-19]. According to Kalendova et al. [20-21] their anticorrosive efficiency, either a long-term controlled

release of phosphate ions [22] or the so-called *barrier effect* [23] (c.f. Chapter 1), depend on selective water uptake, on one hand a beneficial hydration in the case of a zinc phosphate dihydrate and on the other hand a strictly limited water uptake regarding zinc phosphate tetrahydrate based pigments. In that sense, it has been controversially argued that one of the major limitations of zinc phosphate pigments as corrosion inhibitors might be their poor solubility [24-25] and the difficulties to control both the desired hydration state [26] and the synthesized crystal phase (polymorphy) on industrial scale.

In addition to its appealing anticorrosion application and its common use in protective coating technology, hopeite is also one of the main crystalline reaction components of dental cements and prosthodontic luting agents [27-29] and therefore leads to a new generation of dental ceramics formulations: the zinc phosphate cements (ZPC), as extensively reviewed by Pawlig [30-33]. Active research has been recently conducted in dental medicine to obtain materials suitable for the fabrication of esthetic single crowns or fixed partial dentures as permanent restoration of teeth [34-36]. Zinc phosphate based cements and glass ionomer/phosphate based cements generally perform well because of high fracture toughness [37-38], excellent dimensional stability [39], low solubility in an aggressive biological environment [40], as well as a high bonding i.e. retentive strength with any other adhesive cement or with bone substrate conferring a good chemical stability [41], durability and low cytotoxicity, i.e. excellent biocompatibility. Nevertheless, numerous long term clinical studies comparing different potential dental materials show that the antagonistic optimization of the elastic modulus versus fracture toughness in parallel with a dramatic lowering of the solubility for a better workability and extended service-lifetime are still necessary [42-44].

Since the first microporous zinc phosphates with zeolite-like topologies were reported by Gier and Stucky [45], a large number of zincophosphates (ZnPOs) with 1D, 2D and 3D structures have been synthesized in the presence of organic templates [46-47]. In spite of several hypotheses, the mechanism of formation of complex two and three dimensional open framework structure is still poorly understood. But hopeite is believed to be one of the precursor of zinc phosphate based zeolites, in that it is gradually transformed into ladder-like and layered three dimensional structures by substantial incorporation of the respective template agent, thus strongly involving hydrogen bonding [48-49].

All these materials geared towards advanced applications share the common feature that, concerning synthesis and purity, the type of zinc phosphate hydrates (tetrahydrate: α , β -hopeite, parahopeite, trihydrate: $\text{Zn}_3(\text{HPO}_4)_3 \cdot 3\text{H}_2\text{O}$ or ZHPT) has dramatic influence on pigment activation [50-52], bioactivity [53-54] and the resulting macrostructure.

In nature zinc phosphate tetrahydrate exists in two structures, orthorhombic hopeite and parahopeite, its triclinic polymorph [55]. Although the phase system P_2O_5 -ZnO- H_2O has been studied for a very long time [56-57], the precise structure of the two orthorhombic modifications, α - and β -hopeite, is not precisely known.

Therefore this second chapter is focused on the systematic and unambiguous identification of the two most stable polymorphs of zinc phosphate tetrahydrate, namely α - and β -hopeite, their synthesis either as monodisperse powder on large scale or as millimetric “macrocrystals” of highest purity, the comparison with the on purpose synthesized precursor $Zn_3(HPO_4)_3 \cdot 3H_2O$ and the refinement of their respective crystal structure [58], finally allowing a direct correlation between structure and bulk properties. The structural stability of the Zn-P infinite framework and the molecular environment of phosphate tetrahedra are thoroughly evaluated using a combination of powerful spectroscopic techniques, including Solid State NMR, DRIFT and FT-Raman. The careful identification of the hydrogen bonding network in the different zinc phosphate forms is expected to offer a starting point for the basic understanding of their intrinsic thermal stability, their surface reactivity and solubility in various environmental conditions. This may also lead to future efficient modifications of zinc phosphate based materials such as dental cements, catalysts based on zeolite technology and “clean” anticorrosion inhibitors.

2.2. Synthesis of zinc phosphate tetrahydrate (ZPT)

2.2.1. P_2O_5 -ZnO- H_2O phase diagram and synthesis temperature

Of the infinite variety of shape and patterns one observe in nature, an intriguing part lies inside the structure of inorganic crystals. Linear, island, layer-like and intricate three-dimensional closed and porous structures are generously produced by systems like the metal phosphates, where zeolite represent protruding examples [59]. The zinc phosphate (ZP) system, on its own, portrays another instance illustrating this exuberance. Indeed, the P_2O_5 -ZnO- H_2O phase diagram is rather complex since multiple solid phases of varying composition (hydrogen phosphate, polyhydrate, e.g. $Zn_3(PO_4)_2 \cdot 4H_2O$, $ZnHPO_4 \cdot 3H_2O$, $ZnHPO_4 \cdot H_2O$ [60], $Zn(H_2PO_4)_2 \cdot 2H_2O$ [61] and $Zn(H_2PO_4)_2 \cdot 1.5H_2O$) are encountered depending principally on initial relative Zn/P concentration, reaction pH and temperature. Such a phase diagram was first determined at room temperature by Eberly et al. [62] and then extended by Goloshchapov and Filatova [63] to a broader range (0-60°C) of temperature of practical interest in connection with the use of ZP compounds. Albeit zinc phosphate tetrahydrate is thermodynamically the most stable structure of the phase diagram, as confirmed in Chapter 3, fundamental aspects regarding the temperature of formation of ZPT

polymorphs, the corresponding mechanism of formation and their intrinsic structural difference still need to be discovered.

Historically Spencer [64] mentioned the observation of two polymorphs on natural ZPT crystal, designed as α - and β -ZPT, based on slight variations of specific gravity, birefringence and singular thermal behaviour, assumingly correlated with the water content of the crystal. As shown in Figure 2.1, Goloshchapov and Filatova doubtfully concluded that as temperature is raised from 0°C to 60°C, the phosphate incorporation in the crystal structure is facilitated at 25.0°C in comparison to higher temperature, leading to α -ZPT at 0°C and β -ZPT at 60°C due first to decreasing solubility with temperature (see Chapter 6) and secondly to the preferential decomposition and subsequent condensation of $\text{ZnHPO}_4 \cdot 3 \text{H}_2\text{O}$ and $\text{ZnHPO}_4 \cdot 1 \text{H}_2\text{O}$ at pH 4 and 25.0°C in the liquid phase. While β -ZPT stems from the monosubstituted $\text{ZnHPO}_4 \cdot x \text{H}_2\text{O}$ salt, parahopeite may be obtained by decomposition of the disubstituted $\text{Zn}(\text{H}_2\text{PO}_4)_2 \cdot 2\text{H}_2\text{O}$ salt. In complete opposition the results of Salmon and Terrey [65] and lately Pawlig et al. [66] suggested (i) that the formation of α -hopeite occurs at 90.0°C, (ii) in diluted aqueous solution (salt concentration $\approx 1. \text{mol.L}^{-1}$) and not directly from concentrated medium ($> 60 \text{ wt}\%$) and (iii) results from the consecutive decomposition of a metastable zinc monohydrogen phosphate monohydrate into a metastable zinc monohydrogen phosphate trihydrate, as follows:



Scheme 2.1: Most probable reactional mechanism of step-decomposition of zinc hydrogen phosphate hydrate leading to hopeite.

In addition, thanks to a detailed thermodynamical investigation of the phase diagram of dehydration of ZPT, Al-Maydama et al. [26] succeeded first in proving the existence of a third modification of zinc phosphate tetrahydrate, and secondly in isolating the γ -ZPT from rehydration of a suspension of a possible α -ZPD (α -zinc phosphate dihydrate) monitored in-situ by isoperibole microcalorimetry (refer to Chapter 3).

In the frame of this studies, the existence of a zinc phosphate hexahydrate obtained in following the procedure described in § 2.2.3.2 at 3°C precisely and not appearing in this phase diagram (Fig. 2.1) has also to be reported for the first time.

Nevertheless the conditions of formation of synthetic β -ZPT [67] remain unknown and the structural differences between α -ZPT and β -ZPT uncertain [68].

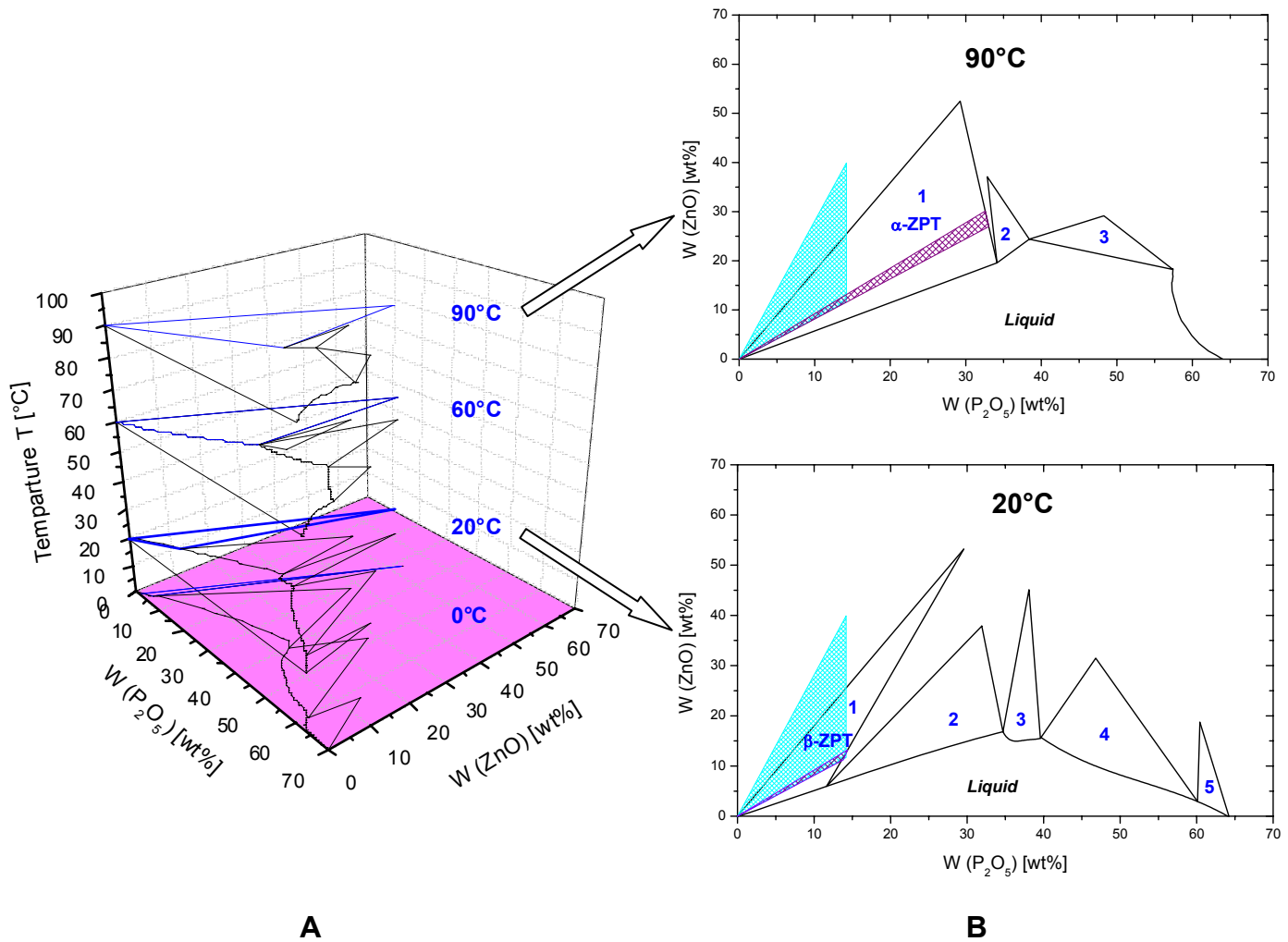


Figure 2.1: Temperature dependence of the phase diagram of ZnO-P₂O₅-H₂O (A) compiled from data of Eberly et al. and Goloshchapov et al, enabling the extrapolation of solidus-liquidus curves at 20°C and 90°C (B). These temperatures are identified as formation temperature of β -ZPT and α -ZPT, respectively. The indexation corresponds to: (1) Zn₃(PO₄)₂·4H₂O, (2) ZnHPO₄·3H₂O, (3) ZnHPO₄·1H₂O, (4) Zn(H₂PO₄)₂·2H₂O, (5) Zn(H₂PO₄)₂·2H₃PO₄. The synthesis domain of pure ZPT polymorphs corresponds to a molar stoichiometry [Zn]/[P] = 0.95-1.05 (violet area) while the domain of industrial synthesis of ZPT based pigments corresponds to a stoichiometry [Zn]/[P] = 0.95-1.5. Unfortunately this last domain locates partly outside the existence domain of ZPT.

2.2.2. Strategies for the synthesis of ZPT polymorphs

For a reliable crystal structure determination and the use a standard materials, synthetic crystals ZPT polymorphs of highest purity obtained in normal laboratory conditions are required. Therefore all methods generating residual impurities ranging from template assisted mineralization, (e.g. employing for example organic phosphates [69-70]), sol-gel method [71-72] to inverse microemulsion [73-74] and other unconventional methods [75-78] and high pressure crystallization [79] are automatically disregarded. Similarly a growth process from a melt is

considered as unrealistic owing to the decomposition of hopeite under temperatures above 130°C. In this line, epitaxial growth of single crystal is as well challenging and thus neglected [80]. Moreover in more conventional approaches by aqueous precipitation crystallization, other problems may arise because the seemingly trivial synthesis from plain zinc oxide and orthophosphoric acid (Table. 2.1 A) leads inevitably to the formation of a mixture of α -, β - and γ -ZPT in most cases due assumingly to an imprecise control of reaction conditions, e.g. temperature and time [26, 81]. Furthermore this method involves multiple reaction steps including first the partial dissolution by a 1 mol.L⁻¹ acetic acid solution of zinc oxide aggregates (15-50 wt%) in aqueous suspension at room temperature, generating a mixture of zinc hydroxide and zinc acetate, that secondly reacts with a solution of concentrated phosphoric acid (min. 5 mol% acid excess) at 95°C for hours until a pH drop from approximately 4 to 6 is achieved, finally followed by an hazardous crystal recovery employing filtration and drying in hot air flow (130-160°C) for numerous hours. Consequently, this last step may produce an uncontrolled amount of zinc phosphate dihydrate (α -, β - ZPD). For instance this synthesis route is derived from the original procedure developed by Bishop [82] and represents the most widely used process for industrial production of ZPT based corrosion inhibitors [83-84]. Even, Komrska et al. [85-86] investigated the kinetics of such reaction by means of X-ray analysis at 37°C under conditions of high humidity. The preferentially selected synthesis method of zinc phosphate tetrahydrate consists in its precipitation from aqueous solution using zinc sulphate or zinc chloride and sodium phosphate or sodium dihydrogen phosphate as reagents and urea as pH control agent according to the reactions (B) and (C) listed in Table 2.1.

Suspension reaction	
$3 \text{ZnO} + 2 \text{H}_3\text{PO}_4 + \text{H}_2\text{O} \rightarrow \text{Zn}_3(\text{PO}_4)_2 \cdot 4\text{H}_2\text{O}$	(A)
Solution reaction	
Standard synthesis routes	
$3 \text{ZnCl}_2 + 2 \text{Na}_3\text{PO}_4 \cdot 12 \text{H}_2\text{O} \rightarrow \text{Zn}_3(\text{PO}_4)_2 \cdot 4\text{H}_2\text{O} + 6 \text{NaCl} + 20 \text{H}_2\text{O}$	(B)
$3 \text{ZnSO}_4 \cdot 7\text{H}_2\text{O} + 2 \text{Na}_2\text{HPO}_4 \cdot 2 \text{H}_2\text{O} \rightarrow \text{Zn}_3(\text{PO}_4)_2 \cdot 4\text{H}_2\text{O} + \text{H}_2\text{SO}_4 + 2 \text{Na}_2\text{SO}_4 + 21 \text{H}_2\text{O}$	(C)
Proposed synthesis route	
$3 \text{Zn}(\text{CH}_3\text{COO})_2 \cdot 2\text{H}_2\text{O} + 2 \text{H}_3\text{PO}_4 \rightarrow \text{Zn}_3(\text{PO}_4)_2 \cdot 4\text{H}_2\text{O} + 6 \text{CH}_3\text{COOH} + 6 \text{H}_2\text{O}$	(D)

Table 2.1: Summary of four classical synthesis strategies of ZPT from aqueous precipitation

However these two strategies depicted in Table 2.1 B and C are time consuming and generate unavoidable side products (i.e. NaCl, Na₂SO₄) and an inopportune high ionic strength and hence suffer from a low efficiency of reaction. Pohl [87] also reported an expected maximum reaction yield of 60% that could not be exceeded after 48 hours. Further in direct relation to Figure 2.1, such syntheses may lead to a mixture of α - and β -ZPT micrometric crystals. In addition, employing the reaction scheme given in Table 2.1 B and C, Haussühl and Friedrich [88] claimed to obtain the

first synthetic millimetric crystals of hopeite, apparently α -ZPT, by critical pH method (Chapter 6) and controlled diffusion of gaseous NH_3 in the solution mixture at 97°C over several weeks. The long decomposition of tetramethylammoniumhydroxide (TMAOH) above 95°C suggested by Grohe [89] may also present the advantage of eliminating possible contaminations (sealed crystallization reactor) in casting off the use of alkali hydroxides while stabilizing the reaction pH at around 4.

On contrary, the philosophy of the method developed in Fig. 2.2 D is favoured due to the use extremely pure and defined starting materials, and thus presents the advantage of eliminating the necessity for extensive purification of the products while benefiting of an interesting buffer effect of acetic acid. In addition this reaction is sensitive to changes of reaction temperature and authorizes the synthesis of appreciable quantities of pure α - and β -ZPT crystals of tunable size.

2.2.3. Proposed syntheses of micro- and macrocrystals of ZPT polymorphs

A rigorous description of the developed syntheses of crystals of different size of α - and β -ZPT and a so-far not isolated intermediary compound ZHPT ($\text{Zn}_3(\text{HPO}_4)_3 \cdot 3\text{H}_2\text{O}$) is presented hereunder employing the strategy described in Table 2.1 D.

2.2.3.1. α -, β -zinc phosphate tetrahydrate (ZPT) macrocrystals

100 mL of a buffered solution of concentrated phosphoric acid was prepared by slowly adding 26.98 mL of 10 times diluted ammonia solution in water (25 wt% solution) to 73.02 mL of a four times diluted phosphoric acid solution in water (85 wt% solution), so that 50 mol% of H_3PO_4 reacts with ammonia to give a 0.792 mol.L^{-1} solution of ammonium hydrogen phosphate. The mixture was vigorously stirred for 2 hours at 0°C . Another 0.114 mol.L^{-1} aqueous solution prepared from 5g zinc acetate (previously dried overnight at 70°C) and 100 mL water (Millipore grade, $18.6 \text{ M}\Omega/\text{cm}$) was transferred into a sealed crystallization reactor and kept there for 2 hours at 90.0°C ($\pm 0.1^\circ\text{C}$) precisely under reflux under inert gas atmosphere (argon). 30.17 mL of the partially neutralized phosphate solution was added in order to achieve the following molar ratio $\text{Zn}:\text{PO}_4:\text{NH}_4 = 1:1.05:0.52$. A white precipitate forms and redissolves quickly as pH reaches 1.45 while stirring at 1250 rpm. Then a 4 mol.L^{-1} NaOH solution, prepared from NaOH pellets, is added drop-wise over a period of five days to the reaction mixture without stirring to yield a white precipitate. During aging and after 2 days the first transparent crystals of hopeite appear at the

precipitation front-solution interface, corresponding to a slow change in pH from 1.5 to approximately 2.6. Further addition of NaOH gives rise to slowly growing α -hopeite (i.e. α -ZPT) crystals. At pH 6 the reaction was finally stopped and crystals of the product were recovered from their mother liquor by filtration and washed to neutral pH and dried at room temperature for 12 hours.

β -zinc phosphate tetrahydrate (commonly designed as β -hopeite or β -ZPT) crystals were obtained in following the same procedure with a $57 \cdot 10^{-3} \text{ mol}\cdot\text{L}^{-1}$ L zinc acetate solution. Crystallization temperature was fixed at $20.0 \pm 0.1^\circ\text{C}$.

2.2.3.2. α -, β -zinc phosphate tetrahydrate (ZPT) crystalline powders

The synthesis described above yields α - and β -hopeite macrocrystals which then were used for single crystal determination. All other analyses were performed using a well dried crystal powder obtained by mixing 100 mL of $0.114 \text{ mol}\cdot\text{L}^{-1}$ zinc acetate (dried overnight at 70°C) solution with 5.5 mL of a four times diluted phosphoric acid solution (85 wt% solution) during two hours at pH 4 and mild stirring (250 rpm) at 90.0°C and 20.0°C for α - and β -ZPT, respectively.

2.2.3.3. Zinc hydrogen phosphate trihydrate (ZHPT) macrocrystals

Large crystals of zinc hydrogen phosphate trihydrate (ZHPT) can be obtained by slightly changing the above described procedure of the α -hopeite synthesis. 100 mL of a buffered solution of 6.13 mol/L concentrated phosphoric acid was prepared as for the α -hopeite synthesis but with neutralization up to 70 mol% of H_3PO_4 with ammonia. 150 mL of a $2.5 \text{ mol}\cdot\text{L}^{-1}$ zinc acetate solution were stored in a sealed crystallization reactor for 2 hours at 90.0°C to achieve a thermal equilibrium. After adding successively 62.5 mL of the phosphate solution and 10 mL of a $5 \text{ mol}\cdot\text{L}^{-1}$ nitric acid solution (65 wt% solution) a pH of 0.25 is reached. In adding drop-wise 37 mL of a $5 \text{ mol}\cdot\text{L}^{-1}$ NaOH in 2 days, flat needle shaped ZHPT crystals will form. For a mass transfer crystal (diffusion dependant) growth, only 3 mL of triethanolamine (98 wt%) have to be added in the reaction medium, thus allowing the growth of $\text{Zn}_3(\text{HPO}_4)_3\cdot 3\text{H}_2\text{O}$ crystals up to millimeter size [90].

2.3. Polymorphism of zinc phosphate tetrahydrate (ZPT)

Since macrocrystals of absolutely pure ZPT polymorphs can be now synthesized without restriction, it is actually of interest to analyse their corresponding bulk properties. It is expected

that the identification and the understanding of the origin of the sound differences between α - and β -ZPT, i.e. polymorphy, may greatly facilitate or at least orientate the identification of the crystal structure of each hopeite polymorph (e.g. their singular hydrogen bonding pattern).

First of all, the exact stoichiometric composition must be determined before any further investigation of the crystal bulk properties.

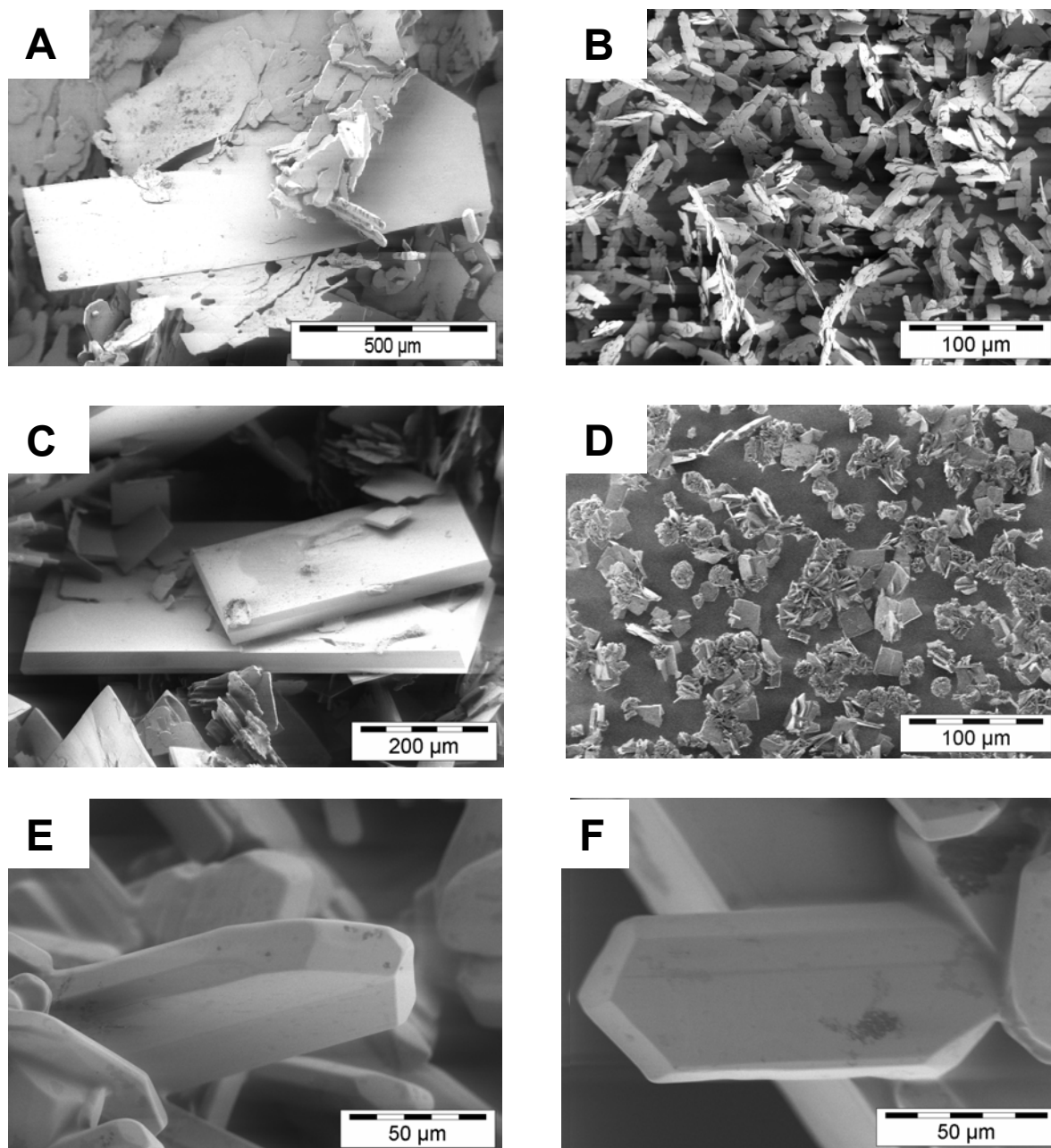


Figure 2.2: SEM images of macrocrystals suitable for single crystal analysis of: (A) α -hopeite (B) β -hopeite, (E) and (F) $\text{Zn}_3(\text{HPO}_4)_3 \cdot 3\text{H}_2\text{O}$. SEM images of samples suitable for X-ray powder diffraction: (B) α -hopeite (D) β -hopeite, (E) $\text{Zn}_3(\text{HPO}_4)_3 \cdot 3\text{H}_2\text{O}$.

This was easily done by elemental analysis in combination with thermogravimetry (e.g. detection of crystal water) and colorimetric molybdophosphate method [91] with an estimated error reduced to less than 1mol%. Hence, the crystal stoichiometry was calculated as follows: α -hopeite: $Zn_3(PO_4)_{1.95} \cdot 3.98 H_2O$, β -hopeite: $Zn_3(PO_4)_{1.98} \cdot 3.96 H_2O$, ZHPT: $Zn_3(HPO_4)_{3.02} \cdot 2.99 H_2O$. In the case of α -, β -hopeite these values match nearly perfectly with the zinc phosphate tetrahydrate stoichiometry. This confirms the high purity of the ZPT standards. So, the subtle variations in bulk properties of pure α - and β -ZPT can be presently carefully analysed.

Therefore Figure 2.2 shows the SEM micrographs of the ZPT and ZHPT crystals and powders used in this study. α -hopeite crystals (Fig. 2.2 A) present the classical plate shape and are reasonably uniformly sized of about $1000 \times 250 \times 0.5 \mu m^3$, whereas β -hopeite crystals (Fig. 2.2 C) were not as well defined and slightly smaller and partially agglomerated. The development of the faces of α -hopeite crystals is sometimes irregular and the crystals may simulate disphenoidal or hemimorphic symmetry. The β -hopeite sample presents two different habits: tabular $\{010\}$ to prismatic $\{001\}$. This plate-like habitus of hopeite crystal corresponds to a layered structure, the b axis being the crystal-plate normal [92]. The zinc hydrogen phosphate trihydrate crystals (Fig. 2.2 E and F) present themselves as elongated $\{001\}$ and tabular $\{100\}$ plates of vitreous appearance and cleaved planes $\{010\}$.

In addition, all specimen are examined using powder x-ray diffraction [93] and also on purpose of validating the synthesis method. Hence, Figure 2.3 A and B show by comparison that the two main polymorphs of the tetrahydrate are not distinguishable by XRD. It may be concluded that the non-hydrogen atom positions within the crystal structures are essentially identical. Therefore, the differentiation of α - and β -hopeite may need methods offering a good selectivity regarding the local changes in the sphere of coordination of phosphate entities and the hydrogen atom bondings: DRIFT measurements and thermogravimetry.

Moreover, Diffuse Reflectance Infrared Fourier Transform (DRIFT) allows a sensitive and fast detection of the two forms of zinc phosphate tetrahydrate. The symmetry of a "free" PO_4^{3-} ion is T_d and the nine modes of internal vibrations span the representation $\Gamma_{vibr}(T_d) = A_1 + E + 2 F_2$ [94-95]. Here A_1 represents the symmetric stretching mode $\nu_s(P-O)$, located at $\approx 980 \text{ cm}^{-1}$. E represents the symmetric bending mode $\delta_s(OPO)$ at $\approx 420 \text{ cm}^{-1}$, and the triply degenerated modes F_2 represent the antisymmetric bending mode $\delta_{as}(OPO)$, located at $\approx 560 \text{ cm}^{-1}$. However slight shifts from known spectra of α -hopeite have to be noticed in Figure 2.4 due to solid-state effects and specificities of DRIFT technique [96]. In Fig. 2.4 a and Fig. 2.4 b, below 1200 cm^{-1} (phosphate region), α - and β -hopeite show very similar spectra, confirming the uniformity of the non-hydrogen framework.

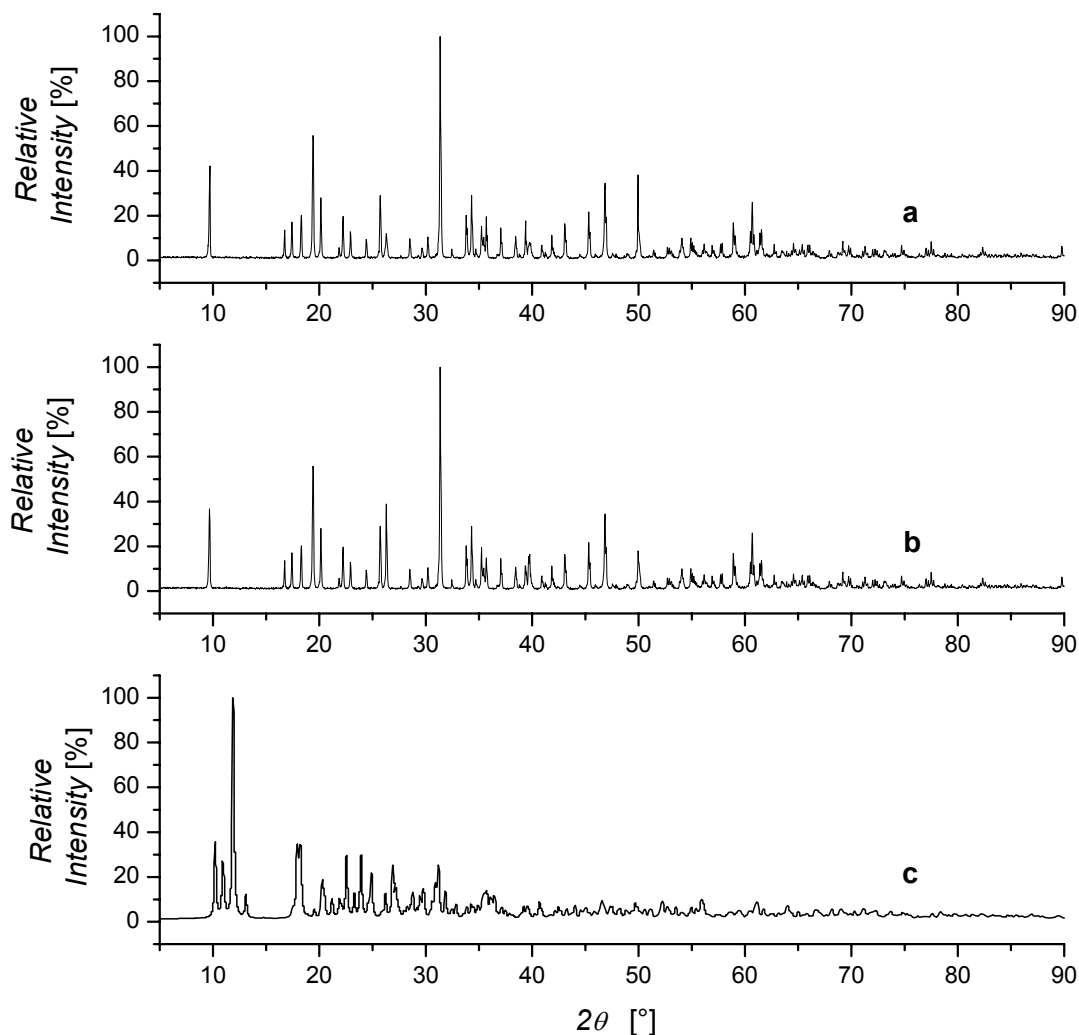


Figure 2.3: X-ray powder pattern of: (a) α -hopeite; (b) β -hopeite and (c) $\text{Zn}_3(\text{HPO}_4)_3 \cdot 3\text{H}_2\text{O}$. No significant differences in the diffractograms of α -hopeite and β -hopeite are to be reported.

The observed bands at 1102-1068-1005, 945-928, 635-584, and 414 cm^{-1} (last band not shown in Fig. 2.4) are assigned to $\nu_{\text{as}}(\text{P-O})(\nu_3)$, $\nu_{\text{s}}(\text{P-O})(\nu_1)$, $\delta_{\text{as}}(\text{OPO})(\nu_4)$ and $\delta_{\text{s}}(\text{OPO})(\nu_2)$, respectively. In comparison to α -hopeite (orthorhombic) the ν_1 mode of the intermediary compound (ZHPT) is stronger, sharper and shifted to 911 cm^{-1} , indicating a more open or distorted sphere of coordination of phosphate groups [57-58]. Multiple ν_3 vibrations in the region between 1220 and 1123 cm^{-1} indicate that the zinc hydrogen phosphate trihydrate belongs to a less ordered space group (triclinic).

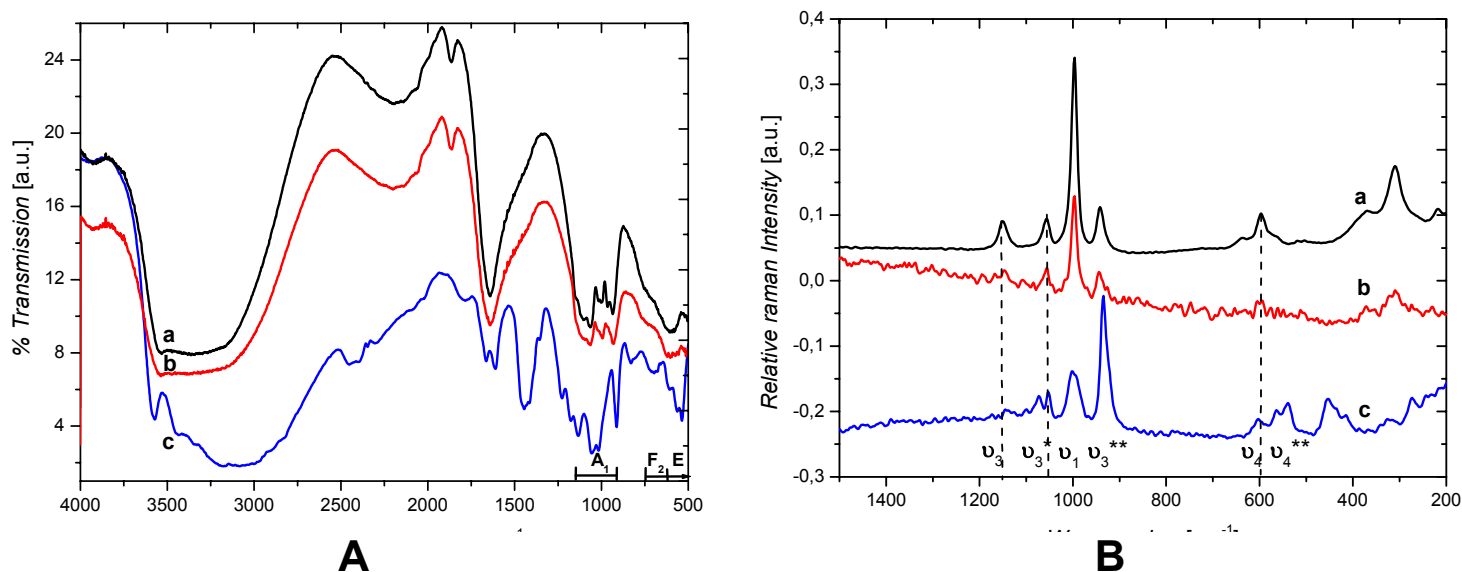


Figure 2.4: Comparison of (A) DRIFT and (B) FT-Raman spectra of macrocrystals of the two polymorphs of zinc phosphate tetrahydrates (a) α -hopeite; (b) β -hopeite and of a precursor compound (c) $\text{Zn}_3(\text{HPO}_4)_3 \cdot 3\text{H}_2\text{O}$, presented in a fine crystalline powder form. For FT-Raman analysis refer to Fig. 2.14.

The “free” H_2O group has three modes of internal vibrations occurring at frequencies 3765, 3652 and 1640 cm^{-1} [99]. The large peak around 1640 cm^{-1} in the α -hopeite spectrum corresponds to the internal bending (ν_3) vibration of crystal water molecules while the broad, very strong band centered around 3300 cm^{-1} represents stretching (ν_1 and ν_3) modes, shifted to lower frequencies from their ideal value due to hydrogen bonding. In this regard, it is interesting to compare the spectrum of α - and β -hopeite: the β form shows a broader band than the α -hopeite at 1639 cm^{-1} . As depicted in Fig. 2.4 c, the shape of the H_2O stretching region of ZHPT is significantly different from those of α - and β -hopeite, with a decoupling of bands at 1601 and 1673 cm^{-1} indicating at least two types of water molecules [100]. In addition, the ZHPT form presents a strong peak at 3580 cm^{-1} , constituting additional evidence for the variability of hydrogen bonding schemes within the framework of the two polymorphs of zinc phosphate tetrahydrate and its precursors.

Another well documented way of distinguishing both forms of hopeite is to investigate their unique thermal behaviour, and to carefully analyse the slightest dissimilarities between α - and β -ZPT [26, 64]. Direct influence of surface effects due to varying size (micro- and macrosized samples) are neglected in the following discussion. Moreover, the formation of zinc phosphate dihydrates and anhydrites on dehydration of ZPT polymorphs is discussed in detail in Chapter 3. Thus both orthorhombic modifications of $\text{Zn}_3(\text{PO}_4)_2 \cdot 4\text{H}_2\text{O}$ show dehydration starting above 100°C and appearing to be complete at about 400°C (Fig. 2.5 and Fig. 2.6). The thermogravimetric (TGA-MS) curves given in Fig. 2.6 show that α -hopeite powder loses crystal water in two well defined stages: two molecules at 146°C and the remaining two at 330°C ; this is the characteristic behaviour of α -hopeite. Similarly the DSC measurement gives two well separated peaks but

slightly displaced: one sharp peak at 182°C and a “double” peak at 278 and 298°C which may indicate the starting point for the loss of two types of water molecules. At about 220°C, i.e. after loss of 2.02 H₂O, a pseudo-stabilization of the structure is reached; the water loss increases slowly, indicating the existence of a dihydrate structure. In the light of these results, one can confirm that the first step corresponds to the transition Tetrahydrate-Dihydrate while the second step to the transition Dihydrate-Anhydrate [101-102].

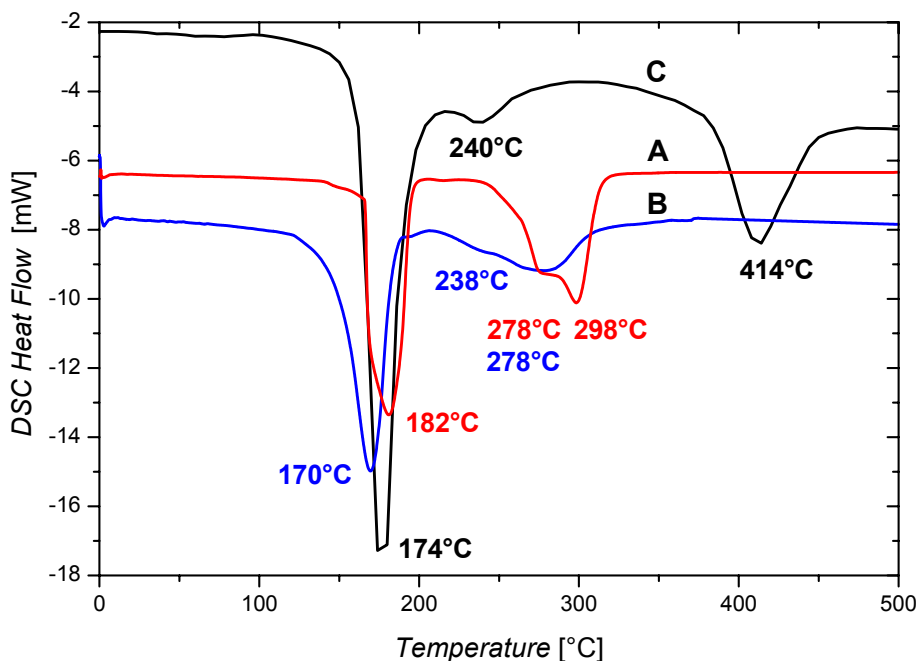


Figure 2.5: DSC curves taken at a heating rate β of 10 K.min⁻¹ of: macrocrystals of (A) α -hopeite; (B) β -hopeite and (C) Zn₃(HPO₄)₃·3H₂O.

The TGA-MS thermogram of the β -hopeite shows significant differences compared to the α -phase. β -hopeite seems to have lower activation energy of dehydration (refer Chapter 3) compared to the α -hopeite pointing toward a lower symmetry of the four water molecules contained in the crystal. This is confirmed by DSC where the onset point of the thermal decomposition appears at 115°C for the β -form (Fig. 2.5B) and 130°C for the α -form (Fig. 2.5A).

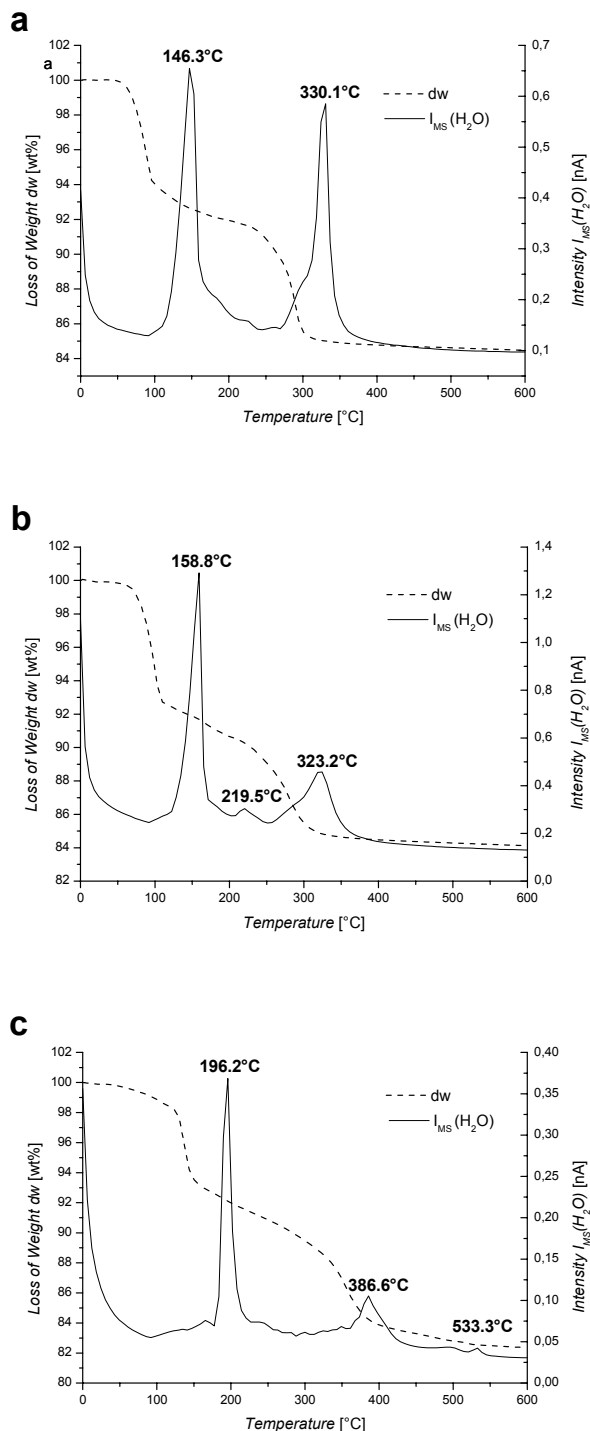


Figure 2.6: Typical TGA-MS curves of: (a) α -hopeite; (b) β -hopeite and (c) $Zn_3(HPO_4)_3 \cdot 3H_2O$ taken at a heating rate β of $10 \text{ K} \cdot \text{min}^{-1}$ with approximately 25 mg of micro-sized sample.

While no graduation is clearly observable on the TGA-weight loss curve of β -hopeite between the dihydrate and the anhydrous salt, the DSC curve (Fig. 2.5B) presents two peaks at 238°C and 278°C , and one can see a shoulder on the TGA-curve at a water content corresponding to the monohydrate [85]. Surprisingly, this transition at 238°C corresponds also to the temperature where the dihydrate starting from α - $Zn_3(PO_4)_2 \cdot 4H_2O$ is formed. Thus, we can observe the loss of

two water molecules in the transformation from dihydrate to anhydrous salt, but the transformation from β -hopeite to " β -dihydrate" is different. In this last case, a shoulder appears both in TGA-MS and DSC curves at 130°C which may be attributed to the formation of an unstable trihydrate. A broad endothermic peak detected by DSC at 170°C, accompanies the removal of 1.69 water molecules [103]. In conclusion, the β -hopeite loses its four water molecules one after another in four consecutive steps. These results are in partial disagreement with the thermal behaviour of β -hopeite previously reported in the literature [81].

For the last compound (ZHPT), the dehydration process is also notably different from that of α -hopeite: after a non-uniform dehydration between 100 and 220°C, corresponding to the loss of 0.99 water molecules, successive peaks occur at 386 and 533°C, corresponding to the loss of 1.53 and 0.47 H₂O molecules, respectively. However DSC data exhibit two peaks at 174°C and 240°C, related to the formation of a dihydrate and a further single dehydration peak at 414°C. This thermal anomaly, similar to the one observed for the β -hopeite at 238°C but at a higher temperature, may be interpreted by the intermediate formation of a compound whose water content varies from dihydrate (α -, β -form: 214°C) and from monohydrate (α -, β -form: 286°C) [59] or by the transformation of the monohydrogen phosphate group to a phosphate group [104].

From all these analyses, it may be concluded that the non-hydrogen atom positions within the crystal structures are essentially identical (DRIFT) and therefore the marked difference in thermal response of the two polymorphs of zinc phosphate tetrahydrate primarily involve changes in hydrogen bonding pattern alone [57, 105]. Furthermore, these last observations are sustained by the differences in thermodynamic stability measured by P.J. Gardner et al. [106] for α - and β -hopeite.

2.4. Determination and comparison of the crystal structure of hopeite polymorphs and ZHPT

The structure of α -hopeite was previously reported [57,107-108] but not completely described due to the missing the hydrogen atom locations. Early descriptions of an epitaxial growth of the β -phase of zinc phosphate tetrahydrates on a zinc crystal were given by Omori and Okabe [109]. They reported similar values of lattice parameters as those found by Gamidov and Galovachev [110]. However, all previous studies could not distinguish the α -form and the β -form of zinc phosphate tetrahydrate from a crystallographic point of view.

Structure	α -hopeite	α -hopeite	β -hopeite	ZHPT
Reference	Ref. [57]			
Crystal data				
Chemical formula	$Zn_3(PO_4)_2 \cdot 4H_2O$	$Zn_3(PO_4)_2 \cdot 4H_2O$	$Zn_3(PO_4)_2 \cdot 4H_2O$	$Zn_3(HPO_4)_3 \cdot 3H_2O$
Formula weight M_r (g.mol ⁻¹)	458.11	458.11	458.11	538.08
Temperature (°K)	290	230	290	290
Wavelength (Å)	0.71070	0.071073	0.071073	0.071073
Crystal system	Orthorhombic	Orthorhombic	Orthorhombic	Triclinic
Space group	Pnma	Pbnm	Pbnm	P1
<i>a</i> (Å)	10.629	5.0135 (3)	5.0266 (2)	8.4746 (4)
<i>b</i> (Å)	18.339	10.6044 (5)	10.6060 (4)	9.8688 (5)
<i>c</i> (Å)	5.040	18.2828 (7)	18.2946 (5)	9.8895 (5)
α (°)	90.0	90.0	90.0	112.0618 (13)
β (°)	90.0	90.0	90.0	111.9702 (13)
γ (°)	90.0	90.0	90.0	96.9953 (12)
<i>V</i> (Å ³)	982.4	972.0 (1)	975.3 (1)	676.9 (1)
Z (formula unit/cell)	4	8	8	2
D_x (g.cm ⁻³)	3.096	3.1301	3.1223	2.6396
Refinement				
	Full-matrix least-squares on F^2	Full-matrix least-squares on F^2	Full-matrix least-squares on F^2	Full-matrix least-squares on F^2
No. measured reflexions	1471	16792	11249	8100
No. independent reflections	1415	1582	1369	3535
No. refined parameters	-	85	85	187
No. unobserved reflexions ($I > 3\sigma(F^2)$)	1415	857	857	2514
R_{int}	0.064	0.065	0.041	0.0025
R	0.064	0.0277	0.0290	0.0492
R_w	0.068	0.0384	0.0327	0.0523
Goodness of fit (GOF)	-	1.068	1.368	1.011

Table 2.2: Lattice parameters, data collection and structure refinement of hopeite polymorphs and its precursor. Calculated standard deviations in parentheses.

For the structure determination of the three zinc phosphate polymorphs (single crystal diffraction method), a suitable crystal with dimension 100 x 50 x 50 μm^3 was used. The hydrogen atoms were located in difference fourier maps and refined isotropically in the riding mode.

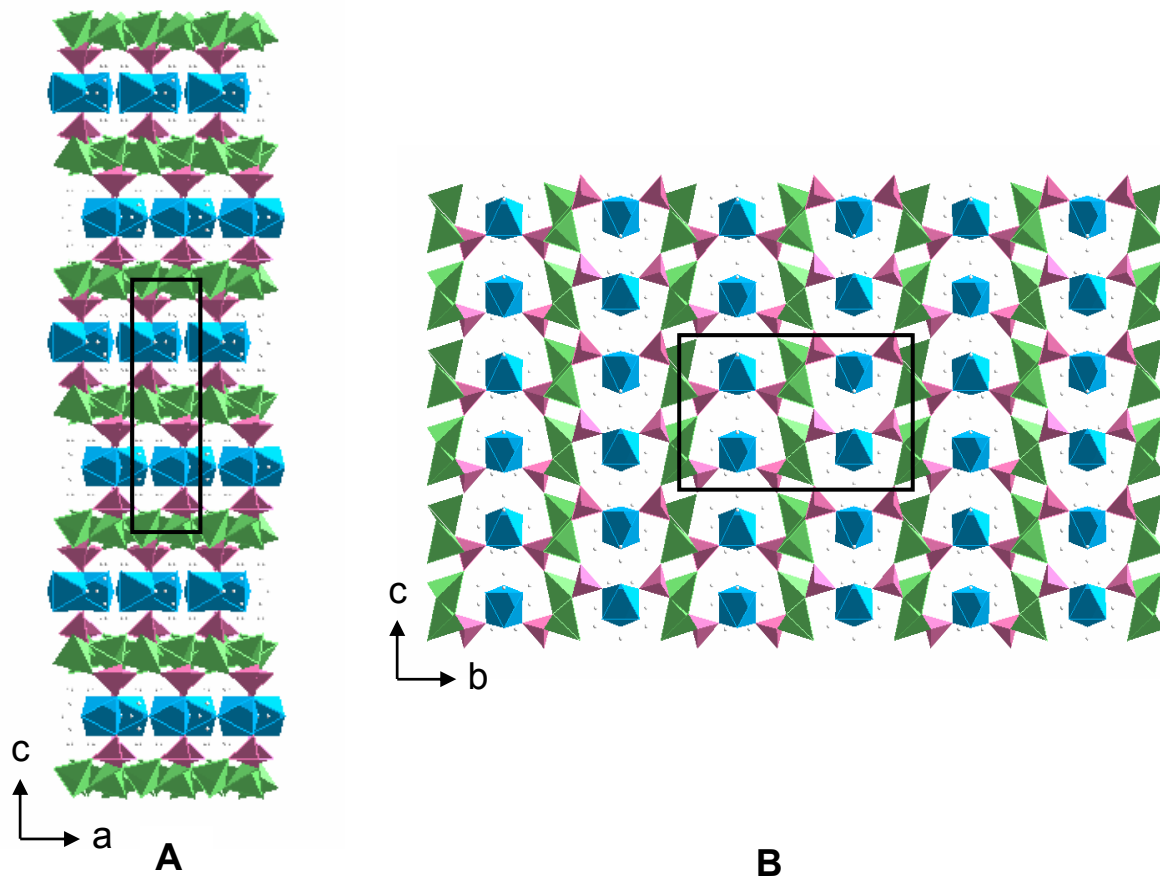


Figure 2.7: Sheet arrangement of cation (Zn^{II})-centered polyhedra and phosphate tetrahedra in zinc phosphate tetrahydrate. The framework is identical for α - and β -hopeite. The connectivity is emphasized in projections along $[010]$ (A) and $[100]$ (B). The green and magenta tetrahedra describe ZnO_4 (coordination 4) and PO_4 groups respectively. The blue octahedron symbolizes the ZnO_6 (coordination 6) groups. Hydrogen atoms are depicted in white.

The crystal structure of many minerals can be understood by the representation of the framework of coordination polyhedra, as shown in Figure 2.7. In this representation the structural similarities of a group of related structures can be made visible. Thus in a number of quite different compounds, e.g. in the family of apatites and hydroxyapatites [111] crystal structures can be derived from one aristotype and the crystal chemistry can be systematized as variations of one common structural principle. In apatites the wealth of different structures also arises from the possibility of non-stoichiometric compositions. This is not the case with the zinc phosphates studied here. There is no experimental evidence for deviations from the integral stoichiometries. In Table 2.2, the pertinent crystallographic data are summarized for α and β -Hopeite, ZHPT and a comparison with reliable reference data regarding the α -form is given.

The crystal structures of zinc phosphates can be described in terms of a framework built by ZnO_6 octahedra, ZnO_4 tetrahedra and PO_4 tetrahedra. The other known hydration states [112-113] as well as zinc hydrogen phosphates can be understood using this approach. Two projections of the hopeite structure in the planes ac and bc are shown in Fig. 2.7. In this structure ZnO_6 octahedra contain the four water molecules. The remaining two oxygen atoms share corners with two PO_4 tetrahedra. These share corners with two ZnO_4 tetrahedra and an edge with a third. The hopeite structure can thus be characterized as a layer structure in which layers of the closely connected PO_4 and ZnO_4 tetrahedra are separated by ZnO_6 octahedra. Alternatively the structure of hopeite can be described as tetrahedral sheets of zig-zag chains of corner-sharing ZnO_4 moieties connected by shared corners with PO_4 and thus with ZnO_6 to produce a complex sheet of three and four membered rings. This layer character is well visible in the ac projection (Fig. 2.7 B).

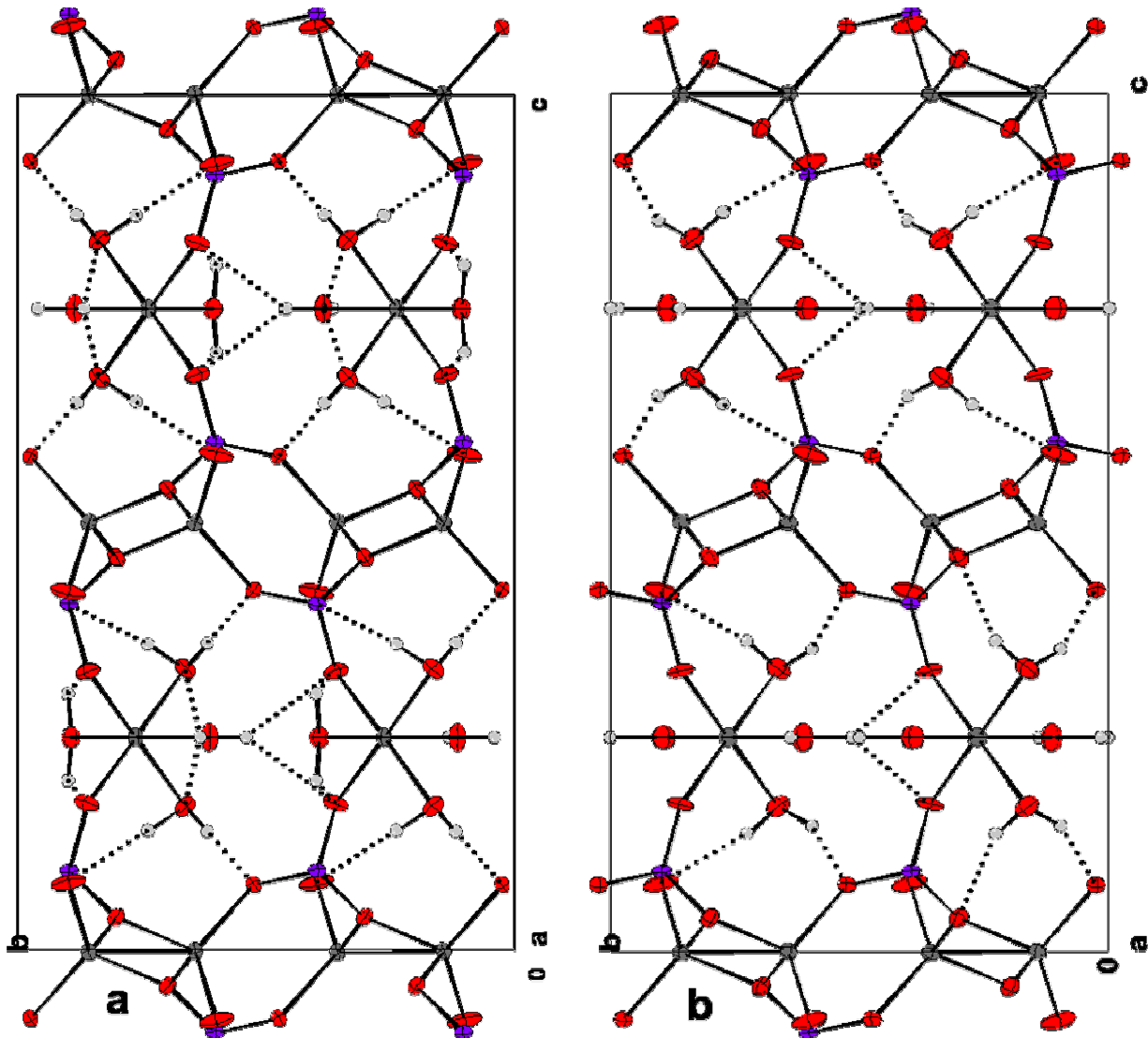


Figure 2.8: Unit cell diagram of: (a) the α - $\text{Zn}_3(\text{PO}_4)_2 \cdot 4\text{H}_2\text{O}$ and (b) β - $\text{Zn}_3(\text{PO}_4)_2 \cdot 4\text{H}_2\text{O}$ structures are shown in projection onto the bc plane (50% thermal displacement ellipsoids). The Zn cations are shown in dark grey, the phosphorus atoms in violet, the oxygen atoms in red and the hydrogen atoms in light grey. Dashed lines represent hydrogen bonds.

The connection between the layers is comparatively weak, with the exception of the above-mentioned corner sharing oxygen atoms it is formed by hydrogen bonds. The main cleavage plane of hopeite crystals is found to be parallel to this interface. However, this interface contains no voids which could be used to include additional atoms or ions. The high packing density of hopeite is also reflected by the high crystal density [64a]. It should be noted that unlike to the case of the above-mentioned apatites in zinc phosphates hydrogen bonds play a dominant role in the packing and crystal chemistry. In α - and β - hopeite all non-hydrogen atoms are found on identical positions. This leads to the surprising result that both forms which exhibit markedly different thermal behaviour differ only in the position of a few hydrogen atoms, i.e. in the orientation in which water molecules are coordinated in the ZnO_6 octahedra. The different water orientations give rise to different hydrogen bonding patterns. Accordingly, different Fourier maps enable to locate all hydrogen atoms in the α - and β -hopeite structures.

Consequently, the crystal structures of α and β -hopeite are shown in Figure 2.8. In the β -form the two water molecules which are located on the mirror plane (O(8) and O(9), respectively) are oriented so that the molecular plane coincides with the mirror plane. In α -Hopeite one of these O(8) is oriented perpendicular to the mirror plane.

Hydrogen bonding			Distances (Å)			Angles (°)		
Donor		Receptor						
O_a (water)	H_i	O_b (PO_4)	$\text{O}_a\text{-O}_b$	$\text{O}_a\text{-H}$	H-O_b	$\text{O}_b\text{-O}_a\text{-O}_b^*$	$\text{O}_a\text{-H-O}_b$	$\text{H-O}_a\text{-H}$
α-Hopeite								
O (8)	H (8)	O (6)	2.781	0.793	1.719	147.69	112.77	99.91
O (10)	H (10-1)	O (4)	2.706	0.873	1.833	72.02	58.20	108.34 ^a
O (10)	H (10-2)	O (5)	3.017	0.950	2.067	82.16 ^d	179.88	92.25
O (9)	H (9-1)	O (10)	2.889	0.747	2.227	116.19 ^b	39.63	108.34 ^a
O (9)	H (9-2)	O (8)	3.060	1.210	2.455	31.67 ^b	124.09	108.34 ^c
O (9)	H (9-2)	O (6)	3.121	0.793	2.455	49.14 ^b	142.37	108.34 ^{a,c}
β-Hopeite^e								
O (10)	H (10-1)	O (2)	2.714	0.995	1.781	104.21	154.74	47.85
O (10)	H (10-2)	O (5)	3.025	0.895	2.142	73.60	168.65	60.31 ^f
O (9)	H (9-2)	O (6)	3.116	1.100	2.200	59.64	139.18	73.38
O (8)	H (8)	O (10)	3.225	1.145	2.337	51.39	135.49	82.01

Table 2.3: Distances and angles involved in hydrogen bonds for α - and β -Hopeite. Measurement errors are for the lengths and angles as follows: ± 0.001 Å, $\pm 0.01^\circ$.

- (a) Angle H(10-1)-O(10)-H(10-2) considered.
 (b) Angle given with O_b^* , symmetric of O_b through ac plane as mirror plane. Other angles are obtained in using bc plane as mirror plane.
 (c) For H(9-2)-O(9)-H(8), the angle value is 55.71° .
 (d) Observing O(5) as symmetric of O(5) through the ac plane, the angle value is 60.49° for O(5)-O(9)-O(5).
 (e) All angles are measured with O_b^* , symmetric of O_b through bc plane as mirror plane.
 (f) For the following angle: H(10-2)-O(10)-H(10-1), the measured value is 99.91° .

In this orientation a strong intra-octahedral hydrogen bond is formed which may account for the higher thermal stability of the α -form. The other hydrogen bonds are inter-octahedral or to neighbouring ZnO_4 or PO_4 tetrahedra and do not differ significantly in the two crystal forms. Comparison of hydrogen bonding geometry, including bond lengths and contact angles, is given in Table 2.3 following the definitions of Figure 2.9, concerning the labelling of hydrogen atoms.

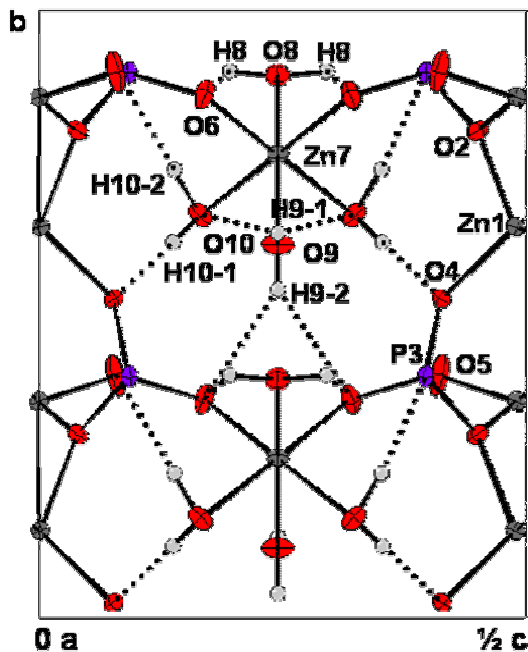


Figure 2.9: Projection of half of the asymmetric unit cell along the a-axis. This representation is valid for both α - and β -zinc phosphate tetrahydrate.

For α - and β -hopeite, values of distances and angles involved in both hydrogen bonding schemes lies well within the well accepted range of hydrogen bond length (Pimentel & McClellan), whereas the interatomic distances (donor-acceptor) for O(9)-O(6) (α -Hopeite) and O(8)-O(10) (β -Hopeite) are near the end of the range (2.2-3.1 Å). Corrected values of hydrogen bonds are higher than those obtained by Whitaker for α -Hopeite [107] 1.719 Å in comparison to 1.54 Å for the shortest length, due to thermal distortion effects. Although the angles subtended by the hydrogen at the water oxygen are noticeably fluctuating between 45° and 90° for β -Hopeite and between 90° and 110° with a maximum at 108.34° for α -Hopeite, both geometries are nearly tetrahedral. It was found that the hydrogen bonds were never collinear in α -Hopeite so that the H atoms subtended an angle of 109° at the donor oxygen although the acceptors did not. However in the view of the O(9)-H(9-1)-O(10) angle (179.88°) existing uniquely in the α -ZPT, substantial structural stabilisation is achieved in assuring contact between zinc octahedra and tetrahedra.

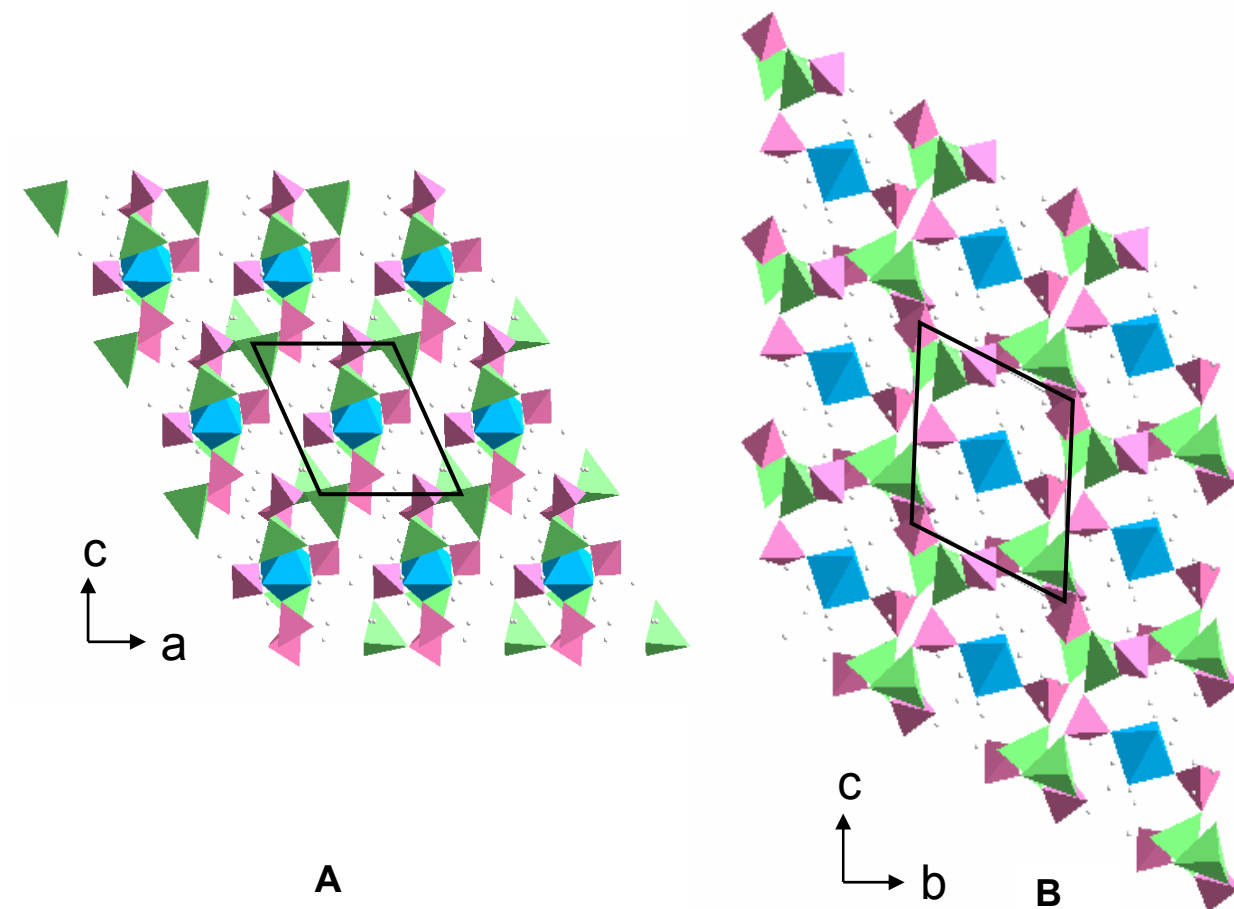


Figure 2.10: Sheet arrangement of cation (Zn^{II})-centered polyhedra and phosphate tetrahedra in zinc hydrogen phosphate trihydrate (ZHPT). The connectivity is emphasized in projections along $[010]$ (A) and $[100]$ (B). The green and magenta tetrahedra describe ZnO_4 (coordination 4) and PO_4 groups respectively. The blue octahedron symbolizes the ZnO_6 (coordination 6) groups.

A projection of the crystal structure of ZHPT is shown in Fig. 2.10. The sheet structure consists of ZnO_6 octahedra which are located on symmetry centers and contain 4 water molecules. The remaining two oxygen atoms share a corner with PO_4 tetrahedra. Three of the oxygens of the PO_3OH groups share a corner with ZnO_4 tetrahedra. This network geometry of Zn- PO_4 bondings (continuous six-ring channels) presents clearly some similarities with other compounds of the ZnO- P_2O_7 - H_2O system such as the parahopeite [55,113]. This arrangement of cation centered polyhedra and phosphate tetrahedra is emphasized in Fig. 2.10 A and Fig. 2.10 B. The structure contains one additional water molecule which is not coordinated to zinc. All water molecules and OH groups take part in hydrogen bonds creating a three-dimensional network which is not shown in Fig. 2.11 for clarity, but can easily explain the high dehydration temperatures documented in the DSC thermogram.

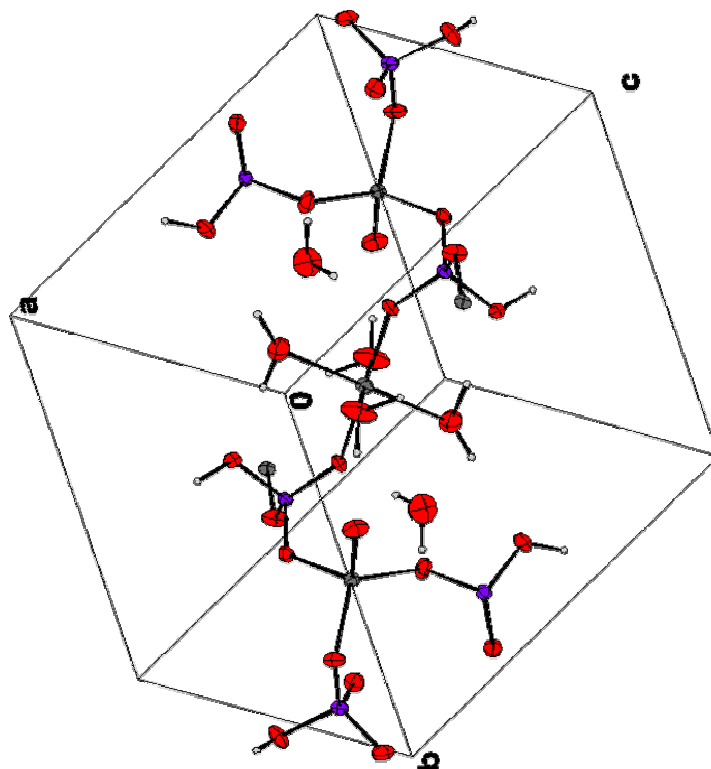


Figure 2.11: Unit cell diagram of $\text{Zn}_3(\text{HPO}_4)_3 \cdot 3\text{H}_2\text{O}$ crystal structure (with 50% thermal probability ellipsoids). Note the inversion center of symmetry passing through the octahedrally coordinated zinc. The Zn cations are shown in dark grey, the phosphorus atoms in violet, the oxygen atoms in red and the hydrogen atoms in light grey.

In conclusion of this crystallographic study, the crystal structure of these polymorphic forms of zinc phosphate tetrahydrate (ZPT) $\text{Zn}_3(\text{PO}_4)_2 \cdot 4\text{H}_2\text{O}$ is entirely resolved for the first time, in comparison with a so-far not yet isolated intermediary compound $\text{Zn}_3(\text{HPO}_4)_3 \cdot 3\text{H}_2\text{O}$ of the hopeite (ZHPT). The single crystal study realized above proves that the main difference between the α - and β -form of zinc phosphate tetrahydrate is caused by the orientation of one of the water molecules in the ZnO_6 octahedral network, indicating two different hydrogen bonding patterns: one bidimensional (β -ZPT) and one three dimensional (α -ZPT) hydrogen bond pattern. This is also confirmed unambiguously by analysis of their unique thermal behaviour and by correlation with FT-IR spectroscopy data at room temperature. Undoubtedly, this part assists to a better understanding of the mechanism of formation of zinc phosphate compounds, and provides the first evidence of their thermodynamic interrelation, that are further detailed in Chapter 3. Nevertheless, a careful spectroscopic analysis of the local sphere of coordination of the phosphate ions in relation with the flexibility of Zn-P-O framework at varying temperatures is still necessary. By correlation with the above realized crystallographic study, this may definitively validate the preceding conclusions.

2.5. Spectroscopic investigation of the structural stability of ZPT polymorphs

Besides analytical techniques such as X-Ray Photoelectron Spectroscopy (XPS), X-Ray Diffraction Spectroscopy (XRD), Secondary Ion Mass Spectroscopy (SIMS), Electron energy Loss Spectroscopy (EELS) and Electrochemical Spectroscopy (EIS), which have been frequently used to study structural and morphological properties, especially infrared, Raman and solid state NMR spectroscopy (^1H , ^{31}P MAS-NMR) have revealed to be very adequate methods for qualitative and quantitative characterization of zinc phosphate surfaces [109-113]. Vibrational techniques may give precious information about the structural changes that take place in crystals of hopeite polymorphs upon heating ($\text{OH} \rightarrow \text{H}_2\text{O}$ and $\text{HPO}_4 \rightarrow \text{PO}_4$) (Chapter 3), chemical doping (zinc exchanged with Na, Ca, Ni, Mo) (Chapter 5) or chemical etching (Chapter 4). Besides, for comparison with other metal phosphates of interest for their potential use as fast developing dental cement products, namely biogenic hydroxyapatite (HAP) and one of its metastable precursors, a calcium dihydrogen phosphate dihydrate (DCPD) or Brushite (in correspondence to ZHPT) are presently used to underline the resulting oriented distortion, under temperature variation, of the zinc phosphate tetrahedra, in accordance with their respective molecular tetrahedral linkage scheme.

2.5.1. Investigation of the molecular stability of crystal water and hydrogen bonding pattern by means of DRIFT and FT-Raman spectroscopy in ZPT polymorphs

For instance, DRIFT combined with FT-Raman allows a sensitive and fast detection of the two forms of zinc phosphate tetrahydrate in dependence of temperature. As already mentioned in § 2.3, the symmetry of a “free” PO_4^{3-} ion is T_d and the nine modes of internal vibrations span the irreducible representation $\Gamma_{\text{vibr}}(T_d) = A_1 + E + 2 F_2$, as depicted bellow in Figure 2.12. Moreover, the 300 vibration modes of the unit cell of hopeite decompose in 150 only Raman active modes and 111 IR active only modes. Since the crystal structure of both α - and β -hopeite are centrosymmetric, the Raman modes display g -symmetry and their IR counterparts u -symmetry (mutual exclusion principle). The PO_4^{3-} ions contribute 27 IR and 36 Raman modes to the 106 active internal vibrations. The diverse kinds of hydrate H_2O molecules give rise to 19 IR and 24 Raman modes.

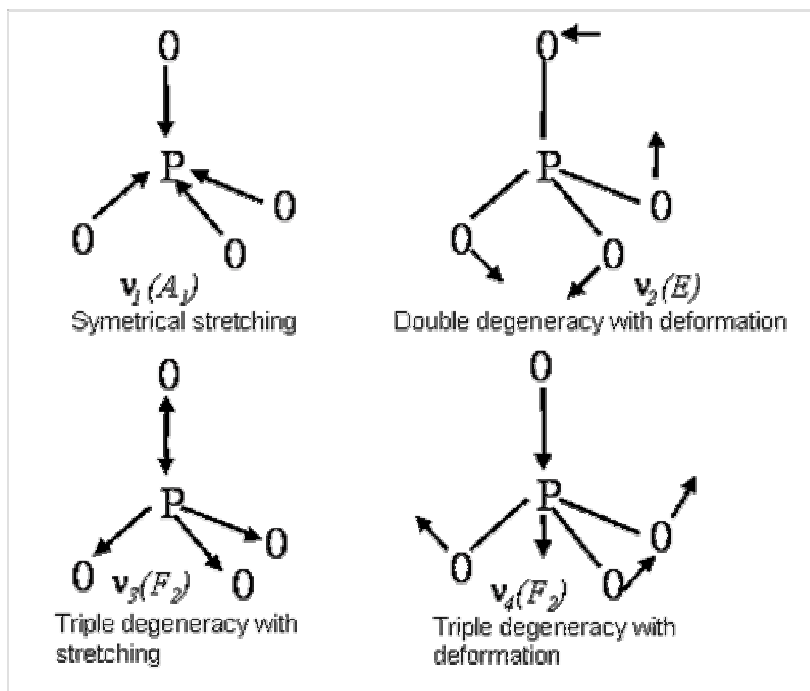


Figure 2.12: Structural representation of the basic modes of vibration of PO_4^{3-} groups.

In solid hydrates, the three translations and the three rotations of the crystal water molecules become frustrated and thus give rise to external H_2O librations and translational modes (lattice vibrations) in addition to internal stretching and bending vibrations [115-116]. The librations usually show bands in the range $900-300\text{ cm}^{-1}$, and the translational modes between 350 and 100 cm^{-1} [117]. In ionic crystals, the H_2O molecules being strongly involved in hydrogen bonding, the stretching modes are generally redshifted and hence can be usually observed in the range $3000-3600\text{ cm}^{-1}$. It is well established that the H_2O bending modes are less sensitive to site symmetry effects and extent distortion of H_2O molecules, and thus are observed in the range $1560-1660\text{ cm}^{-1}$. For studying the local distortional geometry and evaluating the bond strengths of H_2O molecules, the DRIFT spectra of isotopically diluted samples (0, 25, 50 and 75% D) recorded at low Temperature (90 K) and room temperature (Fig. 2.13) are very informative. They display uncoupled OD stretching modes of matrix isolated HDO and D_2O molecules. Hence each band observed in the spectra is due to a distinct hydrogen position in the structure. On one hand the peak frequency can be correlated with bond length and on the other hand the band width is in direct correlation with local bond geometry (angles). Splitting of degenerated or coupled or overlapped modes succeeds in performing high resolution measurements at low temperature.

From a systematic study of crystal water, Lutz [99] assigned confidently the characteristic peak frequencies at 3765 , 3652 and 1640 cm^{-1} to three of the modes of internal vibrations of “free” H_2O molecules. At room temperature, in Figure 2.13, the large peak around 1640 cm^{-1} in the α -hopeite spectrum corresponds to the internal bending (ν_3) vibration of crystal water molecules while the broad, very strong band centered around 3300 cm^{-1} represents stretching (ν_1 and ν_3) modes,

shifted to lower frequencies from their ideal value due to hydrogen bonding. It is possible to determine the number of crystallographic non-equivalent type of water molecule from the frequency components at 3000-3600 cm^{-1} (asymmetrical and symmetrical valence vibrations of OH groups). While only two and three types of crystalline water can be identified within β - and α -hopeite respectively at 25°C, the increasing partial substitution (up to 75%) of water with D_2O at 90 K may indicate the existence of four non-energetically equivalent hydrogen bonds, i.e two crystallographically different H_2O molecules in β -hopeite (3519, 3450, 3374 and 3222 cm^{-1}) and six for α -hopeite (3451, 3388, 3322, 3275, 3213, 3136 cm^{-1}).

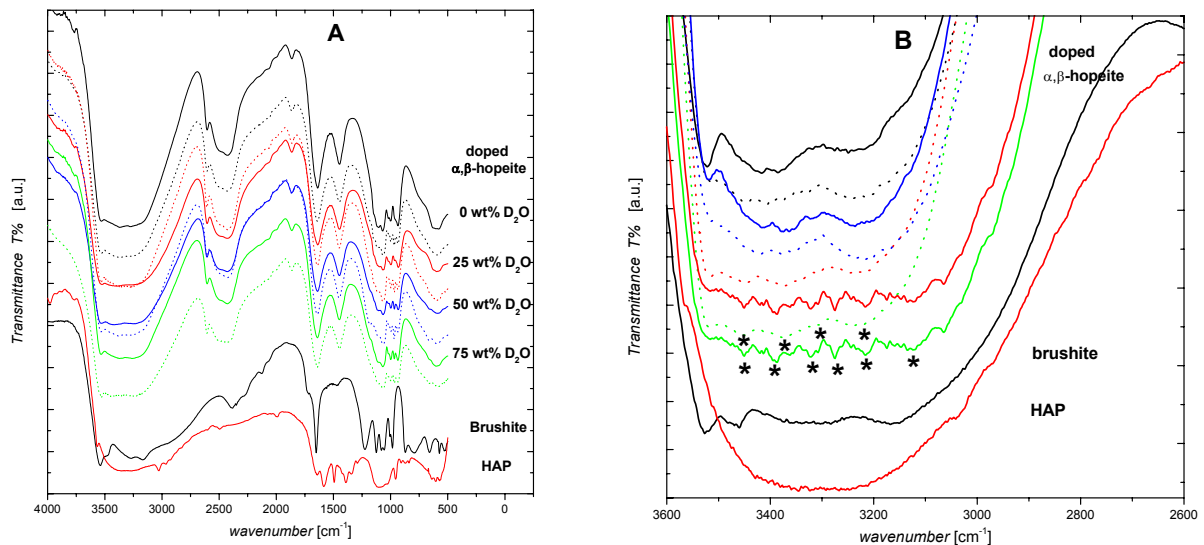


Figure 2.13: FTIR reflection spectra of orthorhombic α -Hopeite [full line], β -Hopeite [dash line], doped with increasing concentrations of D_2O at 25°C (A). Comparison with monoclinic Brushite ($\text{CaHPO}_4 \cdot 2\text{H}_2\text{O}$) [black line] and hexagonal Hydroxyapatite ($\text{Ca}_5(\text{PO}_4)_3(\text{OH})$) [red line]. (B) Details of the hydroxyl region at 90 K. Stars labelled peaks refer to wavenumbers used for correlation calculation of bond lengths.

This results correlate completely with crystallographic data since among the three different crystal water of α -hopeite, two occupy a site of C_s symmetry and thus four uncoupled OD stretching modes are expected at least. In addition, bands at 3521, 631 and 352 cm^{-1} are assigned to stretching modes (ν_s), libration mode (ν_L) and translational mode (ν_T) respectively, of the hydroxyl group alone [117-118]. Therefore, HAP displays a broad shoulder in the region 3462-3033 cm^{-1} and near 3542 cm^{-1} , indicating a vertical oscillation of the hydroxyl groups along the crystallographic c -axis approaching and going away from the neighbouring plane defined by three calcium ions [120]. Such patterns do not exist for the hopeite polymorphs. In consequence only a sharp peak at 3518 cm^{-1} is to be noticed. The shape of the H_2O stretching region of brushite and hydroxyapatite are significantly different from those of α - and β -hopeite, with one band decoupling at 1647 and 1671 cm^{-1} indicating at least two types of water molecules [121] in the case of brushite and two separated narrow peaks at 1635 and 1584 cm^{-1} indicating one type of well stabilized OH group in the HAP structure [122]. While α, β -hopeite possess a broad shoulder in

the range 623-575 cm^{-1} , brushite exhibits one well defined peaks at 658 cm^{-1} and HAP at 668 cm^{-1} , corresponding to OH libration frequencies.

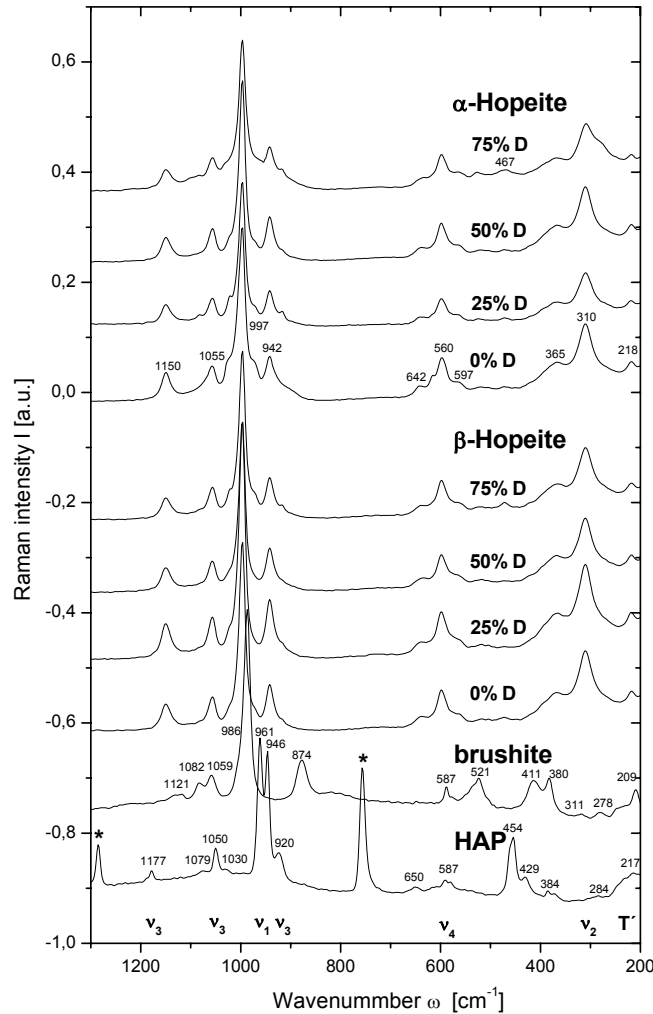


Figure 2.14: Influence of the partial substitution of crystal water by D_2O on the FT-Raman spectra of orthorhombic α - and β - $\text{Zn}_3(\text{PO}_4)_2 \cdot 4 \text{H}_2\text{O}$ (α - and β -ZPT) in the extended phosphate region 1300-200 cm^{-1} , at room temperature. Comparison with brushite and hydroxyapatite

The Raman spectral analysis (Fig. 2.14) shows a band at 310 cm^{-1} on the hopeite polymorphs, at 311 cm^{-1} for Brushite and a weak band at 333 cm^{-1} for HAP, attributed respectively to Zn-OH and Ca-OH bonds. The latter one may indicate that the Ca-OH bond is partially covalent, in reference to Fowler's data on HAP (343 cm^{-1}) [120]. The 630 or 655 cm^{-1} bands (hydroxyl libration mode) appearing well separated from PO_4^{3-} vibration in the HAP Raman spectrum, is seen slightly shifted in α -, β -hopeite compounds due to structure stabilization via hydrogen bonding. Distinction between α - and β -hopeite also succeeds in observing a weak band at 3207 cm^{-1} (α -form, 0%D), displaced at 3223 cm^{-1} with 75% hydrogen substitution for α -hopeite, and 3218 cm^{-1} for β -hopeite. Similarly well identified peaks appear at 3082 cm^{-1} in the case of brushite and at 3554 and 3225 cm^{-1} for HAP, attributed by Freund et al. [122] to H_2O librations and valence vibration.

Hydrogen bonding				Distances (Å)					
Donor O _a (water)	H _i	Receptor O _b (PO ₄)	ν_{OD} 298°K (cm ⁻¹)	a O _a -O _b	a O _a -H	a H-O _b	b O _a -O _b	c O _a -H	b H-O _b
<i>α</i>-Hopeite									
O (8)	H (8)	O (6)	3174	2.781	0.793	1.719	2.658	0.954	1.699
O (10)	H (10-1)	O (4)	3244	2.706	0.873	1.833	2.715	0.958	1.759
O (10)	H (10-2)	O (5)	3362	3.017	0.950	2.067	2.769	0.961	1.816
O (9)	H (9-1)	O (10)	3386	2.889	0.747	2.227	2.832	0.967	1.882
O (9)	H (9-2)	O (8)	3419	3.060	1.210	2.455	2.861	0.974	1.913
O (9)	H (9-2)	O (6)	3519	3.121	0.793	2.455	2.967	0.983	2.017
<i>β</i>-Hopeite									
O (10)	H (10-1)	O (2)	3172	2.714	0.995	1.781	2.667	0.954	1.709
O (10)	H (10-2)	O (5)	3273	3.025	0.895	2.142	2.720	0.963	1.764
O (9)	H (9-2)	O (6)	3358	3.116	1.100	2.200	2.798	0.974	1.847
O (8)	H (8)	O (10)	3517	3.225	1.145	2.337	2.966	0.981	2.023

Table 2.4: Distances of OD...O hydrogen bonds in *α*- and *β*-Hopeite: Comparison between crystallographic data and correlations from averaged OD stretching modes ν_{OD} (cm⁻¹) (DRIFT/FT-Raman) of matrix isolated HDO molecules in dilute samples (50%D). Measurement errors are for the lengths (DRIFT-XRD) are as follows: ± 0.001 Å, ± 0.01 Å.

- (a) X-ray single crystal analysis.
- (b) Calculated from the wavenumbers of the uncoupled OD stretching modes by using the correlation developed by Mikenda.
- (c) Calculated from the wavenumbers of the uncoupled OD stretching modes using LJ method.

A conclusive assignment of the uncoupled OD stretching modes of *α*- and *β*-hopeite (Fig. 2.13 and Fig. 2.14) to their six and four crystallographically different hydrogen positions is shown in Table 2.4. The assignment of the hydrogen bonds reported in [67] is mainly confirmed. The O-O, O-D and D...O distances calculated from the wavenumbers of the uncoupled OD stretching modes by FT-Raman and DRIFT characterization, by using the correlation curves of Lutz-Jung (LJ method) [123-124] and Mikenda [125], are in good agreement with crystallographic data obtained in paragraph 2.4, principally for strong hydrogen bond.

2.5.2. General investigation of the relative structural stability of ZPT polymorphs

It is interesting to consider the spectral modifications related to the restructuring of phosphate anions in the possible conformational evolution from *β*-hopeite to *α*-hopeite. A lowering of tetrahedron symmetry (from T_d to C₁), due to the dynamic interactions of ions in the unit cell, caused by the formation of hydrogen bonds between the water molecules and PO₄³⁻ ions or the coordination via the Zn²⁺ cations, is easily observed by Raman spectroscopy since the ν_1 and ν_2

modes are prohibited in the IR spectrum by the selection rules. Further information can be gained by solid-state Nuclear Magnetic Resonance (NMR) and by comparison with Brushite (presence of HPO_4^{2-}) and hydroxyapatite (PO_4^{3-} -OH interactions).

Thus in Figure 2.13 below 1200 cm^{-1} (phosphate region) α - and β -hopeite show very similar IR spectra, confirming the uniformity of the non-hydrogen framework. The observed bands at 1102-1068-1005, 945-928, 635-584, and 414 cm^{-1} (last band not shown in Fig. 2.13) are assigned to $\nu_{\text{as}}(\text{P-O})(\nu_3)$, $\nu_{\text{s}}(\text{P-O})(\nu_1)$, $\delta_{\text{as}}(\text{OPO})(\nu_4)$ and $\delta_{\text{s}}(\text{OPO})(\nu_2)$, respectively. In comparison to α -hopeite (orthorhombic) the ν_1 mode of the HAP intermediary compound (Brushite) is stronger, sharper and shifted to 911 cm^{-1} , indicating a more open or distorted sphere of coordination of phosphate groups [126-127]. Multiple ν_3 vibrations in the region between 1220 and 1123 cm^{-1} , and characteristic peaks at 2480, 1722, 868 and 875 cm^{-1} [128-132] indicate that the calcium hydrogen phosphate dihydrate (Brushite) belongs to a less ordered space group (monoclinic) [133].

Lattice modes		Internal PO_4^{3-} modes							
		ν_1		ν_2		ν_3		ν_4	
ω	Γ	ω	Γ	ω	Γ	ω	Γ	ω	Γ
<i>α-Hopeite</i>									
218 ^{sh}	22	997	20	365 ^{sh}	89	942	17	560	31
310 ^b	41			471 ^w	23	1055	21	597	35
				503 ^w	10	1150	21	642 ^{sh}	26
				519 ^w	26				
<i>β-Hopeite</i>									
217 ^{sh}	26	996	16	366 ^{sh}	94	941	29	562	31
309	50			471 ^w	18	1057	21	598	28
				502 ^w	9	1148	26	637 ^{sh}	38
				515 ^w	28				

Table 2.5 : Frequencies and widths (in cm^{-1}) of the peaks observed in the Raman spectra of α - and β -hopeite ^a.

- (a) The full widths at half height have been determined from Lorentzian fits to the observed peaks. [(sh) = shoulder, (w) = weak].
 (b) A broad band is observed in this frequency region.

In particular, in Figure 2.14, well defined Raman scattering bands can be observed close to the frequencies of the free PO_4^{3-} modes. The centers of the PO_4^{3-} internal bands are shifted to higher energy by 10 - 15 cm^{-1} (one ν_1 at 997 cm^{-1} and three ν_3 modes at 1150 , 1055 and 942 cm^{-1}) in relation to the free PO_4^{3-} ion frequencies, suggesting a strong crystalline site field in the α - and β -hopeite [134-135].

In Table 2.5, the frequencies and widths of the Raman peaks of α - and β -hopeite determined from high resolution scans of the Raman scattering bands observed in the spectra of Figure 2.14. In respect to ν_1 and ν_3 modes, β -hopeite has broader peaks (20% for ν_1 and 30% on ν_3 in average) than α -hopeite due to (1) the different strength of the various P-O bonds as shown from the corresponding P-O decreasing distances, viz. 1.567/1.571 (P₃-O₂), 1.534/1.1.537 (P₃-O₄), 1.519/1.520 (P₃-O₅) and 1.515/1.517 Å [using atom definition of Fig. 2.9], (2) the different contributing coupling with Zn-O stretching vibration to the adjacent metal oxygen polyhedra such as ZnO₂(H₂O)₄ in the case of α -hopeite. Similarly, group theory predicts 42 Raman modes originating from the ν_2 tetrahedron modes. As can be seen from Fig. 2.13, in the frequency region 365-520 cm⁻¹ where those modes occur, four broad peaks are detected at 365, 471, 503 and 519 cm⁻¹. Considering the high sensitivity of the ν_2 mode to O-P-O bond angles, the large widths of the peaks observed in this region (see Table 2.5) suggests contribution from ν_2 internal modes very close in energy due to small disorder-induced angular distortions of the tetrahedra, and weak coupling between ν_2 modes of different tetrahedra. It is well known that the tetrahedron ν_2 modes are of purely bond-bending character, whereas the ν_4 modes contain also a small stretching component [136]. Taking into account that the relative bond angle variation in α -, β -hopeite is about 5 to 10% while the relative variation of bond length is only 3%, the ν_2 modes of α -, β -hopeite, whose energy is determined by interactions depending on the O-P-O angles, are expected to be more sensitive to small variations of the O-P-O angles than the ν_4 -type mode for which the energy contains also a bond-stretching contribution. Therefore with 75%D substitution, the relative ratio $\{[\nu_2(75\%D)/\nu_1(75\%D)] / [\nu_2(0\%D)/\nu_1(0\%D)]\}$ of the peak areas taken at 519 (515) and 997(996) cm⁻¹ for the α -form and β -form respectively, is 1.47 and 3.48, and is a direct quantification of O-P-O angles fluctuations and bond flexibility.

Moreover, NMR spectroscopy can be applied not exclusively for liquids but also for solids. It gives a complete view of the crystal structure and particularly of the phosphate chain geometry at a molecular level [137-138]. In solids, broadening interactions of nuclear spins are no longer averaged, consequently the solid NMR spectra are characteristically broadened. In principle, the line width in amorphous and crystalline materials is related to the chemical environment and the local mobility with the sample investigated, and thus gives complementary information to FT-Raman and DRIFT spectroscopy. The lines width of ¹H and ³¹P spectra in solid state NMR can be reduced by spinning the sample at the magic angle (Magic Angle Spinning, MAS) where typical rotation frequencies are currently in the range of 2 to 35 kHz.

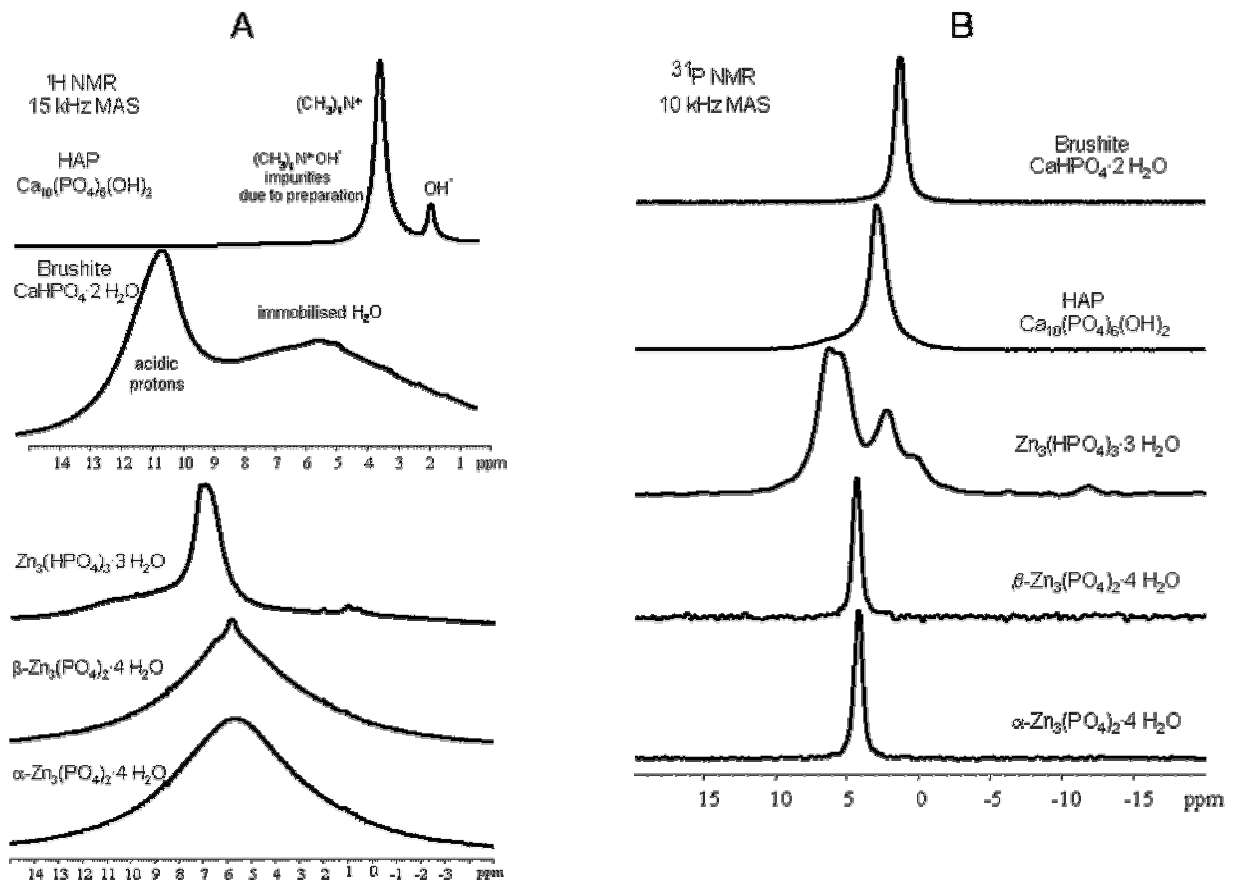


Figure 2.15 : Slow spinning ^1H MAS NMR spectra (A) and ^{31}P MAS NMR spectra (B) of α - and β -hopeite, compared with $\text{Zn}_3(\text{HPO}_4)_3 \cdot 3\text{H}_2\text{O}$, Brushite and Hydroxyapatite. All ^{31}P NMR spectra were referenced with respect to 85% H_3PO_4 (0 ppm), with upfield shifts taken as negative. Note that liquid water is generally found to resonate at 4.7 ppm in a sharp resonance frequency.

Figure 2.15 depicts the ^1H and ^{31}P MAS NMR spectra of various zinc and calcium phosphate hydrates. Despite their same chemical composition, it is possible to distinguish the α -hopeite from the β -hopeite, as they were found to resonate 4.52 ppm and 4.34 ppm in a single peak, indicating the presence of only one type of chemically equivalent phosphorus atom in both structures. Similarly, Sato [139] mentioned a main chemical shift of 4.59 ppm for hopeite coatings, which is in good agreement with the chemical shift $\delta [^{31}\text{P}]$ (namely σ_{iso}) of α -hopeite. In addition, the ^{31}P MAS NMR spectra of hopeite polymorphs show one isotropic resonance with a corresponding array of sidebands separated at a sample spinning speed of 10 kHz. While zinc hydrogen phosphate show multiple ^{31}P NMR signals (2.3, 5.5 and 6.5 ppm), hydroxyapatite and particularly Brushite (calcium hydrogen phosphate) display broad singlets at 3.1 and 1.3 ppm respectively. Besides ^{31}P MAS NMR, a method sensitive to the chemical structural environment of phosphate, ^1H MAS NMR additionally monitors inhomogeneities in the mobility of the components, between bulk components and adsorbed ones. While most components of α -hopeite, distincts from the β -hopeite, are quite rigid (crystal water) and contribute to broad resonances at 5.7 and 5.8 ppm, the

β -form displays a second sharp resonance at 6.5 ppm, corresponding presumably to preferentially oriented hydrogen bonds (see Table 2.6).

Phosphate compounds	^1H NMR signals δ_{iso} (ppm)
$\text{Ca}_{10}(\text{PO}_4)_6(\text{OH})_2$	1.5 (OH ⁻), 3.2 ((CH ₃) ₄ N ⁺)
$\text{CaHPO}_4 \cdot 2 \text{H}_2\text{O}$	5.0 (H ₂ O), 10.3 (acidic H)
$\text{Zn}_3(\text{PO}_4)_2 \cdot 4 \text{H}_2\text{O}$	7.0 (acidic H)
$\alpha\text{-Zn}_3(\text{PO}_4)_2 \cdot 4 \text{H}_2\text{O}$	5.7 (H ₂ O)
$\beta\text{-Zn}_3(\text{PO}_4)_2 \cdot 4 \text{H}_2\text{O}$	5.8 (H ₂ O)

Table 2.6: List of chemical shifts from ^1H NMR signals for zinc and calcium phosphate hydrates.

Concerning HAP, the peak at 1.5 ppm corresponds to the OH groups located in the HAP channels along the *c*-axis, and shifted from its known value of 0.2 ppm [140] due to the presence of TMA. Yesinowski and Eckert [141] observed at nearly the same position in the case of fluoroapatite and assigned it to hydroxyls in the neighbourhood of fluorine. The broad peak centered at 3.2 ppm is assigned to synthesis additive (tetramethylammonium hydroxide) and to adsorbed and/or structural water. The corresponding IR bands could be found at 3547 and 3541 cm^{-1} as shown in Fig. 2.13 [142]. Thus ^1H MAS NMR spectroscopy can distinguish different ^1H chemical state more definitely, as compared with DRIFT or FT-Raman spectroscopy.

Further it is possible to resolve resonances from nearly crystallographically equivalent atoms that have different local environments. Therefore, using the ^{31}P MAS spectra collected at low spinning frequency (Fig. 2.16), the shielding tensor components σ_{ii} , the anisotropy δ and asymmetry parameter ρ are extracted from sidebands intensities by methods developed successively by Maricq et Waugh [143] and Herzfeld et Berger [144]. These parameters are intrinsically connected with structural changes at a molecular level. Neglecting the σ -bonds of PO_4 tetrahedron, Grimmer [145] found that the different values of the chemical shift anisotropy are related to the π -bond character/order of the P-O bond around the phosphorus atom and therefore extremely sensitive to the cation charge (i.e cation electronegativity) and radius fluctuations. Table 2.7 displays the results of bond length calculations analysis. It indicates that α -hopeite, showing a decreased bond length comparing to β -hopeite, has a higher π -bond order and consequently a higher stability. Further, this is confirmed with the higher deviation of the averaged bond angle from perfect PO_4 tetrahedron (in solution) for β -hopeite than α -hopeite.

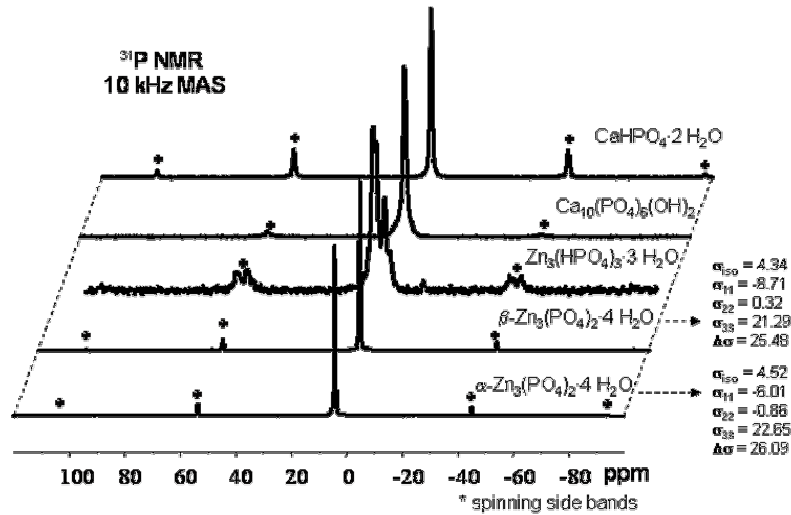


Figure 2.16: Overview ³¹P MAS NMR spectra of hopeite polymorphs compared to Hydroxyapatite and Brushite, with adjacent chemical shifts (ppm) for each resonance. There is one set of sidebands, separated by the spinning speed f (10 kHz) and indicated by the crosses, at each side of the central resonance, occurring at the isotropical shift σ_{iso} . The anisotropical shifts σ_{ij} are calculated from the sideband intensities [143-144] and the chemical shift anisotropy from $\Delta\sigma = \sigma_{33} - \frac{1}{2}(\sigma_{11} + \sigma_{22})$.

The Wiesenberg MAS NMR method [146-147] is used to access more detailed O-P-O angle fluctuations [$\Delta\alpha_{O-P-O \text{ min-max}}$] occurring in α -, β -hopeite, allowing the identification of privileged PO₄ bridging directions. A good agreement with XRD measurements is achieved since both methods give similar angle fluctuations values as shown in Table 2.7 for α -hopeite (4.090 vs 3.465°). Since the two hopeite forms display a reduced bond angle in the O(2)-P(3)-O(4) direction due to hydrogen bonding along the b -axis of the unit cell, the principal structural distinction between α - and β -hopeite comes from the P(3) tetrahedra stretching preferentially in the O(4)-P(3)-O(5) direction in the case of α -hopeite and in the O(2)-P(3)-O(5) for β -hopeite, as confirmed crystallographically and shown schematically in Fig. 2.9. Moreover, the band valence method, based on a modified second Pauling rule, may confirm these observed slight tetrahedron distortion differences between α - and β -hopeite, because it requires the exact fulfilment of the valence balance with due regard for the empirical bond valence-bond strength-bond length relations developed by Brown, Shannon et al [148-150] and completed by Mohri [151]. A shift of the position of the layered PO₄ anions from the mirror plane (ac plane) causes an increase of the distortion of the phosphate tetrahedron both in terms of quadratic elongation and bond angle variation (Table 2.7), and results in a systematic decrease of the stretching frequencies (ν_1 , ν_3) vibrational modes and a clear increase of splittings of degeneracy (ν_2 , ν_4) Raman and IR active modes.

Structural property	α -hopeite	β -hopeite	Method
Bond length^a			
$r_{\text{P-O Avg}} (\text{\AA})$	1.594(2)	1.594(6)	MAS-NMR ^b
$r_{\text{P-O Avg}} (\text{\AA})$	1.523(5)	1.523(3)	MAS-NMR ^c
$r_{\text{P-O Avg}} (\text{\AA})$	1.535(9)	1.534(8)	XRD ^d
O-P-O bond angle fluctuation/deviation^f			
$\Delta\alpha_{\text{O-P-O min-max}} (^{\circ})$	4.090	7.161	MAS-NMR ^e
$\alpha [\text{O}(2)\text{-P}(3)\text{-O}(4)] (^{\circ})$	105.37	102.32	
$\alpha [\text{O}(4)\text{-P}(3)\text{-O}(5)] (^{\circ})$	113.55	-	
$\alpha [\text{O}(2)\text{-P}(3)\text{-O}(5)] (^{\circ})$	-	116.61	
$\Delta\alpha_{\text{O-P-O Avg}} (^{\circ})$	3.465	3.230	XRD ^d
$\alpha [\text{O}(2)\text{-P}(3)\text{-O}(4)] (^{\circ})$	105.26	105.37	
$\alpha [\text{O}(4)\text{-P}(3)\text{-O}(5)] (^{\circ})$	112.19	-	
$\alpha [\text{O}(2)\text{-P}(3)\text{-O}(5)] (^{\circ})$	-	112.02	
$\Delta\alpha_{\text{O-P-O Avg}} (^{\circ})$	0.0168	0.0172	MAS-NMR ^e
$\Delta\alpha_{\text{O-P-O Avg}} (^{\circ})$	0.1309	0.1341	MAS-NMR ^c
$\Delta\alpha_{\text{O-P-O Avg}} (^{\circ})$	0.0496	0.0499	XRD ^d

Table 2.7: Structural parameters of PO_4 tetrahedron in hopeite polymorphs.

- (a) Estimated bond length error $r \pm 0.0006 \text{ \AA}$
 (b) Calculated from Grimmer correlation. (Ref. [145])
 (c) Calculated from Oldfield correlation. (Ref. [146])
 (d) Calculated from § 2.4
 (e) Calculated from Wiesenfeld correlation (Ref. [147])
 (f) Estimated angular error $\alpha \pm 0.03^{\circ}$

Thus thanks first to Ray et Callender correlations [152-153] between the sum of P-O bond strengths, expressed in terms of average number of electron pairs per bond, localized on the phosphorus and oxygen atoms, and the fundamental PO_4 stretching frequencies, and secondly thanks to Jackeman and Cheetham's correlation [154-155] between the chemical shift and the P-O bond strength, a reliable prediction of the PO_4 coordination tetrahedron distortion may be given. The results of Table 2.7 indicate that for all methods employed (MAS-NMR, Raman, XRD) the bond strengths are concordant and that on a phosphate subunit level, the vibrational frequency shifts of nearly 3 cm^{-1} (measured from Raman spectra in Fig. 2.14), is a direct consequence of the tetrahedral bond length or volume variation.

Internal property	α -hopeite	β -hopeite	Method
P-O phosphorus bond strength $S(P^{5+})$^a			
$\Sigma [S(P)]$	4.897	4.8980	MAS-NMR ^b
$\Sigma [S(P)]$	4.955	4.950	Raman ^c
$\Sigma [S(P)]$	4.952	4.894	XRD ^d
P-O oxygen bond strength $S(O^{8-})$^a			
$\Sigma [S(O)]$	7.932	7.929	MAS-NMR ^b
$\Sigma [S(O)]$	7.914	7.924	Raman ^c
$\Sigma [S(O)]$	7.936	7.954	XRD ^e

Table 2.8: Distortion-Reorientation of phosphate units in solid zinc phosphate tetrahydrates. This is characterized with the deviation of the sums of all bond strengths of phosphate tetrahedrons from the valence state (from formal oxidation states of O^{2-} , P^{5+}) and monitored by XRD, MAS-NMR and FT-Raman spectroscopy.

- (a) Estimated bond strength error $S \pm 0.005$, given in valence unit (v.u.).
- (b) Calculated from Cheetham correlation. (Ref. [155])
- (c) Calculated from Callender correlation. (Ref. [152])
- (d) Calculated from Brown correlation. (Ref. [149])
- (e) Calculated from Cheetham correlation combined with Brown correlation.

In contrast, changes of the values of Raman and MAS-NMR splitting do not result simply from dipole-dipole interaction between the phosphate ions and the unit-cell, but also from the presence of strong hydrogen bonds. This is first marked in Table 2.8 by the general concordance of the sums $\Sigma [S(P)]$, $\Sigma [S(O)]$ with their respective valency in a simplistic approach, and secondly by the fact that the P-O bond electrons are slightly and more preferentially localized around the oxygen for the α -hopeite (7.936 vs 7.954) and around the phosphorus for β -hopeite (4.952 vs 4.893). A systematic MAS-NMR study focused on the localization of hydrogen bonds in the hopeite structure may be envisioned in similarities with the calcium phosphate system [156-159].

2.6. Conclusion

In conclusion, a new simple method to synthesize pure macrocrystals of two zinc phosphate tetrahydrates: α -, β -hopeite has been demonstrated. XRD proves that the non-hydrogen atom positions within the crystal structures are essentially identical. However, the differentiation of the two phases becomes possible using advanced investigation methods including thermoanalysis (e.g. DSC, TGA-MS) and spectroscopic techniques (e.g. DRIFT, FT-Raman, MAS-NMR). The marked difference in thermal response primarily involves changes in hydrogen atom bonding alone. Single crystal analysis proves that the main difference between the α - and β -form of zinc phosphate tetrahydrate is caused by the orientation of one of the water molecules in the ZnO_6 octaetra. While in the β -hopeite two water molecules are located on the mirror plane (O(8) and O(9), respectively) and are oriented so that the molecular plane coincides with the mirror plane (two dimension hydrogen bond pattern), in α -Hopeite one of these (O(8)) is oriented perpendicular to the mirror plane (three dimensional hydrogen bond pattern). Further, the zinc hydrogen phosphate trihydrate (ZHPT) structure shows striking similarities with another zinc phosphate tetrahydrate: the parahopeite. Besides, solid state NMR, FT-Raman and DRIFT deliver concordant information about the slightly lower flexibility of the Zn-P-O structure framework (distortion of the phosphate tetrahedron given both in terms of quadratic elongation and O-P-O bond angle variation) of β -hopeite compared to α -hopeite and are in excellent agreement with the corresponding crystallographic data.

Inasmuch as crystallographic study by the analysis and understanding of the role of hydrogen bonding in seemingly simple zinc phosphate structures was a prerequisite for a first differentiation of α - and β -hopeite, a deep understanding of the intrinsic bulk properties of zinc phosphate tetrahydrates on a molecular level may offer a starting point to gain exclusive knowledge of properties of the respective surfaces (Chapter 4). Further, the thoroughful thermodynamic characterization (Chapter 3) of the two hopeite polymorphs in comparison with their calcium phosphate homologues might also well lead to tremendous progress in the characterization of their corresponding surface dynamics (i.e. solubilisation, anion and molecules or polymer adsorption for precise surface modification (Chapter 5), etc.) and the respective dissolution behaviour and consequent anticorrosion efficiency (Chapter 6).

2.7. References

- [1] S.C. DeVito, *Prog. Org. Coat.* **35** (1999) 55
- [2] W. Funke, *Prog. Org. Coat.* **31** (1997) 5
- [3] M. Zubielewicz, W. Gnot, *Prog. Org. Coat.* **49** (2004) 358
- [4] I.M. Zin, S.B. Lyon, S.J. Badger, J.D. Scantlebury, V.I. Pokhmurskii, *J. Corros. Sci. Eng.* **2** (1999) 21
- [5] L. Veleva, J. Chin, B. Del Amo, *Prog. Org. Coat.* **36** (1999) 211
- [6] C.H. Hare., *J. Prot. Coat. Minings* **15** (1998) 31
- [7] G.A. Howard, *Pigment Resins Tech.* **29** (2000) 325.
- [8] A. Bittner, *Surf. Coat. Int. J.O.C.C.A.* **4** (1988) 97
- [9] W. Funke, *J. Coat. Technol.* **58** (1986) 741
- [10] A. Amirudin, C. Barreau, R. Hellouin, D. Thierry, *Prog. Org. Coat.* **25** (1995) 339
- [11] A. Kalendová, P. Kalendá, *Farbe + Lacke* **110**(3) (2004) 22
- [12] A. Bittner, *J. Coat. Technol.* **61**(777) (1989) 111
- [13] <http://www.heubachcolor.de>
- [14] G. Meyer, *Farbe + Lacke* **69** (1963) 528
- [15] M.F. Clay, G.H. Cox, *J. Oil Col. Chem. Assoc* **56** (1973) 13
- [16] G. Meyer, *Farbe + Lacke* **71** (1965) 113
- [17] G. Adrian, A. Bittner, *J. Coat. Technol.* **58** (1986) 59
- [18] R. Romagnoli, V.F. Vetere, *Corrosion* **51**(2) (1995) 216
- [19] H. Nakano, M. Urai, M. Iwai, *Surf. Coat. Int. J.O.C.C.A. Tetsu to Hagane* **85**(1) (1999) 39
- [20] A. Kalendová, *Prog. Org. Coat.* **44** (2001) 201
- [21] A. Kalendová, P. Kalendá, *Farbe + Lacke* **109**(11) (2003) 62
- [22] H. Leidheiser, *J. Coat. Technol.* **53** (1981) 29
- [23] P. Kalendá, A. Kalendová, V. Štengl, P. Antoř, J. Šubrt, Z. Kváča, S. Barkardjieva, *Prog. Org. Coat.* **49** (2004) 137
- [24] J.A. Burkill, J.E.O. Mayne, *Surf. Coat. Int. J.O.C.C.A* **71** (1988) 275
- [25] B. Del Amo, R. Romagnoli, V.F. Vetere, L.S. Hernández, *Prog. Org. Coat.* **33** (1998) 28
- [26] H.M.A. Al-Maydama, P.J. Gardner, I.W. McAra, *Thermochim. Acta* **192** (1992) 117
- [27] M. Eisenberger, M. Addy, A. Rossbach, *J. Dentistry* **31**(2) (2003) 137
- [28] R. Nomoto, K. Uchida, Y. Momoi, J.F. McCabe, *Dent. Mater.* **19**(3) (2003) 240
- [29] Y. Yamada, Y. Tsubota, S. Fukushima, *Int. J. Prosthodont.* **17**(1) (2004) 94
- [30] R.G. Craig, in *Restorative Dental Materials*, Mosby, St Louis (1993)
- [31] A.D. Wilson, J.W. Nicholson, in *Chemistry of Solid State Material, Vol.3: Acid-based cements, their biomedical and industrial applications*, University Press, Cambridge (1993)
- [32] C.L. Davidson, *Adv. Eng. Mater.* **3**(10) (2001) 763
- [33] O. Pawlig, *PhD Thesis*, University of Mainz (Germany) (2001)
- [34] R.S. Squier, J.R. Agar, J.P. Duncan et al., *Int. J. Oral Max Impl.* **16**(6) (2001) 793
- [35] F. Bohlsen, M. Kern, *Quintessence Int.* **34**(7) (2003) 493
- [36] S. Peirada, J. Cavalheiro, R. Branco, A. Afonso, M. Vasconcelos, *Key Eng. Mat.* **254**(2) (2004) 659
- [37] N. Attar, L.E. Tam, D. McComb, *J. Prothet. Dent.* **89**(2) (2003) 127
- [38] K.A. Proos, M.V. Swain, J. Ironside et al, *Int. J. Prosthodont.* **16**(1) (2003) 82
- [39] S. Haussühl, M. Friedrich, *Cryst. Res. Technol.* **28**(4) (2003) 437
- [40] B. Czarnecka, H. Limanowska-Shaw, J.W. Nicholson, *J. Mater. Sci.-Mater. Med.* **14**(7) (2003) 601
- [41] S.O. Hedlund, N.G. Johansson, G. Sjogren, *Br. Dent. J.* **195**(3) (2003) 155
- [42] K. Sunnegardh-Gronberg K, A. Peutzfeldt, J.W.V. van Dijken, *J. Dent. Res.* **81** - Sp. Iss. B (2002) 361
- [43] E. Mezzomo, F. Massa, S. Libera, *Quintessence Int.* **34**(4) (2003) 301
- [44] M. Eisenberger, M. Addy, A. Rossbach, *J. Dent.* **31**(2) (2003) 137
- [45] T.E. Gier, G.D. Stucky, *Nature* **349** (1991) 508
- [46] W. Liu, Y. Liu, Z. Shi, W. Pang, *J. Mater. Chem.* **10** (2000) 451

- [47] A.K. Cheetham, G. Ferey, T. Loiseau, *Angew. Chem. Int. Ed.* **38** (1999) 3268
- [48] S. Oliver, A. Kuperman, G.A. Ozin, *Angew. Chem. Int. Ed.* **37** (1998) 46
- [49] J. Li, J. Yu, W. Yan, Y. Xu, W. Xu, S. Qiu, R. Xu, *Chem. Mater.* **11** (1999) 2600
- [50] L.S. Hernández, G. Garcia, C. López, B. Del Amo, R. Romagnoli, *Surf. Coat. Int. J.O.C.C.A.* **81** (1998) 19.
- [51] P.J. Gardner, I.W. McArn, V. Bartob, G.M. Seydt, *Surf. Coat. Int. J.O.C.C.A.* **74** (1990) 16
- [52] O. Pawlig, R. Trettin, *Mat. Res. Bull.* **34**(12-13) (1999) 1959
- [53] N. Ewoldsen, R.S. Demke, *Am. J. Orthod. Dentofac.* **120**(1) (2001) 45
- [54] C.A. Mitchell, M. Abbariki, J.F. Orr, *Dent. Mater.* **16**(3) (2000) 198
- [55] G. Chao, *Z. Kristallogr. Krisr.* **130**(4-6) (1969) 261
- [56] M.V. Goloshchapov, T.N. Filatova, *Russ. J. Inorg. Chem.* **14**(3) (1969) 424
- [57] E.A. Nikonenko, I.N. Marenkova, *Russ. J. Inorg. Chem.* **31** (1986) 397
- [58] A. Whitaker, *J. Appl. Cryst.* **6** (1973) 495
- [59] M.E. Davis, R.F. Lobo, *Chem. Mater.* **4** (1992) 756
- [60] Y. Cudennec, A. Lecerf, A. Riou, Y. Gérault, *C.R. Acad. Sci. Fr.* **301**(2) (1985) 93
- [61] M.T. Averbuch-Pouchot, *J. Appl. Cryst.* **7** (1974) 511
- [62] N.E. Eberby, C.V. Gross, W.S. Crowell, *J. Am. Chem. Soc.* **42** (1920) 1433
- [63] M.V. Goloshchapov, T.N. Filatova, *Russ. J. Inorg. Chem.* **14**(3) (1969) 424
- [64] (a) E. Spencer, *Min. Mag.* **15** (1908) 1; (b) J.D. Dana, E.S. Dana, R.Y. Gaines, *Dana's New Mineralogy: The System of Mineralogy of James Dwight Dana and Edward Salisbury Dana*, 8th Ed. (1997) Wiley (NY)
- [65] J.E. Salmon, H.T. Terrey, *J. Chem. Soc.* (1950) 2813
- [66] O. Pawlig, R. Trettin, *Mat. Res. Bull.* **41**(12-13) (1999) 1959
- [67] K. Yoshioka, *Tetsu to Hagane* **70**(13) (1984) 1070
- [68] M. Takahashi, A. Kawahara, Y. Takano, *Acta. Cryst.* **A28**, Suppl. (1972) 68
- [69] S. Neeraj, A.K. Cheetham, *Chem. Comm.* **16** (2002) 1738
- [70] R. Singh, J. Doolittle, Jr., P.K. Dutta, *J. Phys. Chem.* **B106** (2002) 2146
- [71] S. Feng, T. Bein, *Nature* **368** (1994) 834
- [72] W. Wallau, J. Patarin, I. Widmer, P. Caulet, J.L. Guth, *Zeolites* **14** (1994) 402
- [73] I. Lisiecki, M. Björling, L. Motte, B. Ninham, M.P. Pileni, *Langmuir* **11** (1995) 2385
- [74] J.P. Cason, M.E. Miller, J.B. Thompson, C.B. Roberts, *J. Phys. Chem.* **B105** (2001) 2297
- [75] B.Z. Putliz, K. Landfester, H. Fischer, M. Antonietti, *Adv. Mater.* **13**(7) (2001) 500
- [76] T. Sugama, T. Takahashi, *J. Mater. Sci.* **30** (1995) 809
- [77] Y.H. Koh, N.J. park, J.H. Choi, *Mater. Sci. Forum* **273-275** (1998) 635
- [78] X. Yang, T.K. Chaki, *Mater. Sci. Eng.* **B39** (1996) 123
- [79] C.K. Park, M.R. Sisbee, D.M. Coy, *Cement Concrete Res.* **28**(1) (1998) 141
- [80] A. Okuwari, J. Ninagawa, T. Okabe, K. Omori, *Bull. Chem. Soc. Jp.* **45** (1972) 1720
- [81] E.A. Nikonenko, I.I. Olikov, I.N. Marenkova, L.N. Margolin, L.A. Reznikova, *Russ. J. Inorg. Chem.* **30** (1985) 25
- [82] D. Bishop, *British Rail Technical Center*, Derby, priv. comm. (1985)
- [83] (a) Patent CH603486 (15-08-1978); (b) Patent DT2842150 (10-04-1980)
- [84] (a) Patent JP-2000124010-A (06-06-2000); (b) Patent RU2177488 (27-12-2001)
- [85] J. Komrska, V. Šatava, *Silikáty* **13** (1969) 135
- [86] J. Komrska, V. Šatava, *Dtsch. Zahärztl.* **25** (1970) 914
- [87] M. Pohl, *PhD Thesis*, University of Duisburg (Germany) (1992)
- [88] S. Haussühl, M. Friedrich, *Cryst. Res. Technol.* **28**(4) (1993) 437
- [89] B. Grohe, *PhD Thesis*, University of Mainz (Germany) (1999)
- [90] A. Echavaria, A. Simon-Masseron, J.L. Paillaud, V. Gramlich, C. Saldarriaga, *Inorg. Chim. Acta* **343** (2003) 51
- [91] J.E. Harwood, R.A. Van Steederen, A.L. Kühn, *Water Res.* **3** (1969) 417
- [92] O.V. Yakubovich, O.V. Karmova, O.V. Dimitrova, W. Massa, *Acta. Cryst.* **C55** (1999) 151
- [93] Cards N°37-465 and 39-1352, JCPDS-ICDD database, FIZ Karlsruhe (1996)
- [94] O. Pawlig, V. Schellenberger, H.D. Lutz, R. Trettin, *Spectrochim. Acta* **A57** (2001) 581
- [95] K. Nakamoto, in *IR and Raman Spectra of Inorganic and Coordination Compounds*, J. Wiley & Sons (NY) (1986)
- [96] R.J. Hill, J.B. Jones, *Am. Mineral.* **61** (1976) 987

- [97] H.D. Lutz, J. Himmrich, M. Schmidt, *J. Alloys Compd.* **241** (1996) 1
- [98] V. Perusevski, B. Soptrajanov, *J. Mol. Struct.* **17** (1988) 349
- [99] H.D. Lutz, *Struct. Bonding* (Berlin) **69** (1988) 7
- [100] O. Pawlig, R. Trettin, *Chem. Mater.* **12** (2000) 1279
- [101] Y. Arnaud, E. Sahakian, M. Romand, J.C. Charbonnier, *Appl. Surf. Sci.* **32** (1988) 281
- [102] Y. Arnaud, E. Sahakian, J. Lenoir, A. Roche, *Appl. Surf. Sci.* **32** (1988) 296
- [103] H. Haidara, *PhD. Thesis*, University of Muhlhouse, (France) (1985)
- [104] A. Bensalem, *J. Solid State Chem.* **162**(1) (2001) 29
- [105] A.B. Yaroslavtsev, Z.N. Prozorokskaya, V.F. Chuvaev, *Zhurnal Neorganicheskoi Khimii* **34**(8) (1989) 2036
- [106] M.A. Al-Maydama, P.J. Gardner, I.W. McAra, *Thermochim. Acta* **196** (1992) 117
- [107] A. Whitaker, *Acta Crystallogr. Sect. B* **31** (1975) 2026
- [108] R.J. Hill, J.B. Jones, *Am. Mineralogist* **61**(9-10) (1975) 987
- [109] A. Okuwary, J. Ninagawa, T. Okabe, K. Omori, *Bull. Chem. Soc. Japan* **45** (1972) 1720
- [110] R.S. Gamidov, V.P. Galovachev, *Dokl. Akad. Nauk. USSR* **150** (1963) 381
- [111] T.J. White, D. Zhili, *Acta Crystallogr. Sect. B* **59** (2003) 1
- [112] J.S. Stephens, C. Calvo, *Canadian J. Chem.* **45** (1957) 2303
- [113] J.S. Stephens, C. Calvo, *Canadian J. Chem.* **43** (1965) 436
- [114] I. Kumbasar, J.J. Finney, *J. Mineralogical. Soc.* **36**(281) (1968) 88
- [115] L.M. Rodriguez-Lorenzo, J.N. Harn, K.A. Gross, *J. Phys. Chem. B* **107**(33) (2003) 8316
- [116] M. Grodziki, G. Amthauer, *Phys. Chem. Min.* **27**(10) (2000) 694
- [117] H.D. Lutz, *Struct. Bonding* **82** (1988) 97
- [118] J. Arends, J. Christoffersen, M.R. Christoffersen, H. Eckert, B. O. Fowler, J. C. Heughebaert, G.H. Nancollas, *J. Cryst. Growth* **84** (1987) 512
- [119] J.J. Stuttmann, J.D. Termine, A.S. Posner, *Trans. NY Acad. Sci.* **27** (1965) 669
- [120] B.O. Fowler, *Inorg. Chem.* **13** (1974) 194
- [121] B.O. Fowler, E.C. Moreno, W.E. Brown, *Arch. Oral. Biol.* **11** (1966) 477
- [122] F. Freund, R.M. Knobel, *J. Chem. Soc.* **6** (1977) 1136
- [123] H.D. Lutz, *Struct. Bonding* (Berlin) **82** (1995) 85
- [124] H.D. Lutz, C. Jung, *J. Mol. Struct.* **404** (1997) 63
- [125] W. Mikenda, *J. Mol. Struct.* **147** (1986) 1
- [126] H.D. Lutz, J. Himmrich, M. Schmidt, *J. Alloys Compd.* **241** (1996) 1
- [127] V. Perusevski, B. Soptrajanov, *J. Mol. Struct.* **17** (1988) 349
- [128] E.E. Berry, C.B. Baddiel, *Spectrochim. Acta A* **23** (1967) 537
- [129] A.C. Chapman, D.A. Long, D.L. Jones, *Spectrochim. Acta A* **21** (1965) 633
- [130] J.A.S. Bett, L.G. Christner, W. Keith Hall, *J. Am. Chem. Soc.* **89** (1967) 5535
- [131] G. Socrates, in *Infrared Characteristic Group Frequencies*, J. Wiley & Sons (Chichester) (1980)
- [132] A.Y.U. Malysheva, B.I. Beletskii, *Glass and Ceram.* **58**(3) (2001) 147
- [133] A. Hina, G.H. Nancollas, M. Grynpas, *J. Cryst. Growth* **223** (2001) 213
- [134] H.D. Lutz, H. Haeuseler, *Trends Appl. Spectrosc.* **2** (1998) 59
- [135] H.D. Lutz, H. Haeuseler, *J. Mol. Struct.* **511**(512) (1999) 69
- [136] G. Herzberg, in *Molecular Spectra and Molecular Structure II: Infra-Red & Raman Spectra of Polyatomic Molecules*, D. Van Nostrand Ed. (Princeton) (1945)
- [137] T.H.W. Claridge, *High-Resolution NMR Techniques*, in *Organic Chemistry*, Tetrahedron Organic Chemistry Series, Vol. **19**, Pergamon (Oxford) (1999)
- [138] M.H. Levitt, *Spin dynamics: Basics of Nuclear Magnetic Resonance*, Wiley (NY) (2002)
- [139] N. Sato, *J. Mater. Sci. Lett.* **10**(2) (1991) 115
- [140] T. Isobe, S. Nakamura, R. Nemoto, M. Senna, *J. Phys. Chem. B* **106** (2002) 5169
- [141] J.P. Yesinowski, H. Eckert, *J. Am. Chem. Soc.* **109** (1987) 6274
- [142] A. Baumer, M. Ganteaume, W. E. Klee, *Bull. Mineral.* **108** (1985) 145
- [143] M.M. Maricq, J.S. Waugh, *J. Phys. Chem.* **70**(7) (1979) 3300
- [144] J. Herzfeld, E. Berger, *J. Phys. Chem.* **73**(2) (1980) 6021
- [145] A.R. Grimmer, *Spectrochim. Acta A* **34** (1978) 941
- [146] G.L. Turner, K.A. Smith, R.J. Kirkpatrick, E. Oldfield, *J. Magnet. Reson.* **70** (1986) 408
- [147] J.P. Dustata, J.B. Robert, L. Wiesenfeld, *Chem. Phys. Letters* **77**(2) (1981) 336

- [148] I.D. Brown, K.K. Wu, *Acta Cryst. B* **32** (1976) 1957
[149] I.D. Brown, R.D. Shannon, *Acta Cryst. A* **29** (1973) 266
[150] R.D. Shannon, C.T. Prewitt, *Acta Cryst. B* **25** (1969) 925
[151] F. Mohri, *Acta Cryst. B* **56** (2000) 626
[152] W.J. Ray, J.W. Burgner, H. Deng, R. Callender, *Biochemistry* **32** (1993) 12977
[153] W.J. Ray, J. Wang, H. Deng, R. Callender, *J. Phys. Chem. B* **102** (1998) 3617
[154] R.J.B. Jackeman, A. K. Cheetham, N. J. Clayden, C. M. Dobson, *J. Am. Chem. Soc.* **107** (1985) 6249
[155] A. K. Cheetham, N. J. Clayden, C.M. Dobson, R. J. B. Jackeman, *J. Chem. Soc. Chem. Commun.* **3** (1986) 195
[156] J. P. Yesinowski, H. Eckert, G.R. Rossman, *J. Am. Chem. Soc.* **110** (1988) 1367
[157] E. Brunner, H. H. Karge, H. Pfeifer, *Z. Phys. Chem.- Int. J. Res. Phys. Chem. & Chem. Phys.* **176** (1992) 173
[158] U. Sternberg, E. Brunner, *J. Magnet. Reson. A* **108** (1994) 142
[159] E. Brunner, E. Sternberg, *J. Prog. Nucl. Magnet. Res. Spectr.* **32** (1998) 21

3. Thermal behaviour and kinetics of dehydration of zinc phosphate hydrates

“The way to succeed is to keep one’s courage and patience and to work on energetically”
Vincent Van Gogh to Theo, February 1886

3.1. Introduction

Thermal behaviour, though an important issue in the area of micro and nano-crystalline materials science has not been studied as extensively as the formation of these materials. Many microcrystalline materials, especially metal phosphate hydrates and metal phosphate of the open framework type, possess metastable structures and evolve to more stable, condensed structures via solid state reaction or dissolution.

Since zinc phosphate pigments are widely used in numerous industrial applications where prolonged exposure to heat/cold and where geometric thermomechanical stability are of major concerns, a thorough study of the hydration/dehydration process, the determination of the hydration phase diagram and a precise quantification of the relative stability of zinc phosphate tetrahydrates (ZPT), zinc phosphate dihydrates (ZPD) and zinc phosphate anhydrates (ZPA) are still necessary. For example, mixed zinc phosphate tetrahydrate/dihydrate pigments are broadly used as *passive* corrosion inhibitor in the formulation of marine paints [1]. First Clay and Cox [2] and lately Meyer [3] proposed an anticorrosion mechanism of hopeite with a “barrier effect”, in which microcrystals embedded in a protective organic coating can stop the water diffusion onto a steel surface. In a candid way Kalendova and Kalenda suggested that only the zinc phosphate dihydrate may be an *active* corrosion inhibitor, since it might have the capacity to take water up before dissolving as water penetrates the protective coating [4]. Furthermore, α -zinc phosphate tetrahydrate is of considerable importance, since it has been observed as a growing phase on the surface of zinc phosphate dental cements [5]. For a versatile use of zinc phosphate based cement (ZPC) as cohesive material for partial or permanent restoration of bone and teeth, a fast solid state crystallization process involving incorporation of water in the product material is highly desired. However the fundamental aspects of hydration (crystallization) and dehydration of either pure zinc

phosphate hydrates or of the corresponding chemically modified cements are not yet reported. In a satisfactory manner Nevertheless tentative analyses of the thermal behaviour of ZPC cements were recently provided by Pawlig [6].

As early as 1969, Goloshchapov and Filatova [7] studied the solid phase stability relationships in the system $\text{ZnO-P}_2\text{O}_5\text{-H}_3\text{PO}_4$. While they determined that *pure* hopeite was the most stable phase in the temperature range 0-60°C, their study did not distinguish between various polymorphs of zinc phosphate tetrahydrates. Recently, Perez and Nancollas [8] studied the crystallization reaction of α -hopeite using a dissolution reaction approach (at solid-liquid interphase) monitored by microcalorimetry. They pointed out that hopeite precipitated without participation of precursors at 40°C and at higher temperature but did not exclude the involvement of intermediary phosphate hydrate salts at lower temperature, particularly around 20°C. This is the temperature of formation of β -zinc phosphate tetrahydrate. They suggested a surface controlled growth mechanism involving factors such as exchange of water molecules at a zinc ion or incorporation of growth units stabilized via hydrogen bondings at growth spirals (dislocations) on the crystal surface. However, little is known concerning water exchange at solid interfaces. Using a similar strategy than Nancollas, Al-Maydama, Gardner and McAra [9] focused their interest on the determination of the enthalpy of formation of α - and β -zinc phosphate tetrahydrates by isoperibol solution-reaction calorimetry and batch microcalorimetry. But their solid-liquid approach did not offer satisfying experimental results regarding: (i) the stability difference between α -ZPT and β -ZPT and the corresponding dihydrates, (ii) the following solid state reaction $\alpha\text{-ZPT} \rightarrow \beta\text{-ZPT}$, (iii) the corresponding critical temperature of transition, (iv) the existence of hydrates of other stoichiometries, for example the trihydrate [10] and the monohydrate [11], (v) the reversibility of the dehydration reaction, (vi) the kinetics of dehydration and the related complex mechanisms of dehydration. Therefore a solid-gas approach of the thermal behaviour of all known polymorphs of zinc phosphate hydrates (α -, β -ZPT) [12-17] is presently preferred. Due to their high sensitivity Thermogravimetry (TG), Differential Thermogravimetry (DTG) coupled with Mass Spectrometry (DTGA-MS) and Differential Scanning Calorimetry (DSC) are the methods of choice for the investigation of the thermodynamic interrelation of zinc phosphate hydrates and for the determination of their respective but specific dehydration kinetics.

3.2. Principles of DSC and DTGA, two complementary methods

The currently accepted definition of *thermal analysis*, as given by Mackenzie [18-19] and the International Confederation for Thermal Analysis (ICTA) is: “ a group of techniques in which a physical property of a substance and/or its reaction products is measured as a function of temperature whilst the substance is subjected to a controlled temperature program”. Ample details relative to various types of thermal analysis methods (TG, DTA, DSC, TMA, evolved gas detection

EGD, emanation thermal analysis ETA etc.) and their applications in solid state chemistry have successively been published by Wendland [20], Dunn [21] and Liptay [22]. Therefore the principles and specificities of each of the used thermoanalytical techniques (D-TGA, DSC) are discussed herunder.

3.2.1. Principles of thermogravimetry (TG/TGA) and differential thermogravimetry (DTGA)

3.2.1.1. Principle of thermogravimetry (TG/TGA)

The thermal analysis technique of thermogravimetry (TGA) is one in which the change in sample mass (mass-loss or gain) is determined as a function of temperature and/or time. Three methods of thermogravimetry are commonly used: (a) isothermal gravimetry, in which the sample is recorded as a function of time at constant temperature, (b) quasi-isothermal thermogravimetry, in which the sample is heated to constant mass at each of a series of increasing temperatures, and (c) dynamic thermogravimetry, in which the sample is heated in an environment whose temperature is changing in a predetermined manner, preferably at a linear heating rate β .

The characteristics of a single-stage mass-loss curve are illustrated in Figure 3.1. Two temperatures are considered characteristic of a single-stage non-isothermal reaction: T_i , the *initial temperature* or procedural decomposition temperature (pdt) or onset temperature, which is the temperature at which a cumulative mass-change reaches a magnitude that the balance can detect,; and T_f , the *final temperature*, which is the temperature at which the cumulative mass-change first reaches its maximal value dm , corresponding to complete reaction.

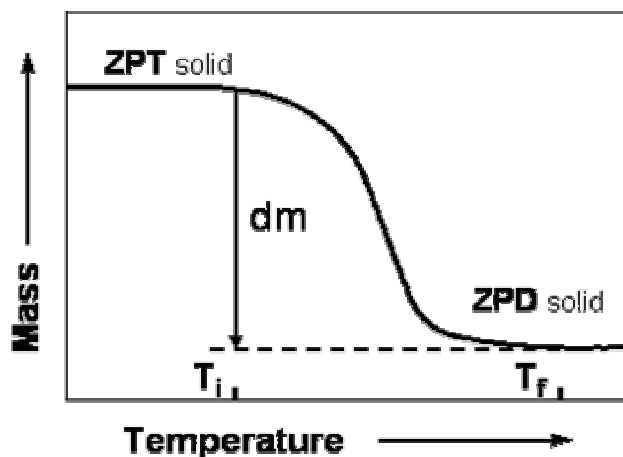
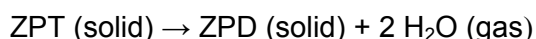


Figure 3.1: Characteristics of TGA curve for a single-stage reaction as for example



The thermal stability domain of a solid such as α -ZPT is defined as a general term by Duval [23] indicating the ability of a substance to maintain its properties (ex. weight) as nearly unchanged as possible on heating (i.e. temperature range).

3.2.1.2. Principle of differential thermogravimetry (DTGA)

In conventional thermogravimetry, the mass of a sample m is continuously recorded as a function of temperature T , or time t ,

$$m = f(T, t) \quad (3.1)$$

Quantitative measurements of the mass-change are possible by determination of the distance on the curve mass axis, between the two points of interest or between the two horizontal mass levels. As De Keyser [24] first suggested, followed by Erdey et al. [25] and then Waters [26] in differential thermogravimetry, the derivative of the mass change with respect to time, i.e. temperature, is recorded as a function of time or temperature,

$$\frac{dm}{dt} = \frac{1}{\beta} \cdot \frac{dm}{dT} = f(T \text{ or } t) \quad (3.2)$$

the resulting curve is the first derivate of the mass mass-change curve. A series of peaks are obtained instead of the stepwise curve, in which the area under the peak is proportional to the total mass-change of the sample. A horizontal plateau in the TGA curve gives a well defined corresponding plateau in the DTGA curve because $dm/dt = 0$. A maximum in the DTGA curve is obtained when the TGA curve has an inflexion point where mass is being lost most rapidly.

A comparison between *conventional* and *derivative* mass-loss curve is given in Figure 3.2.

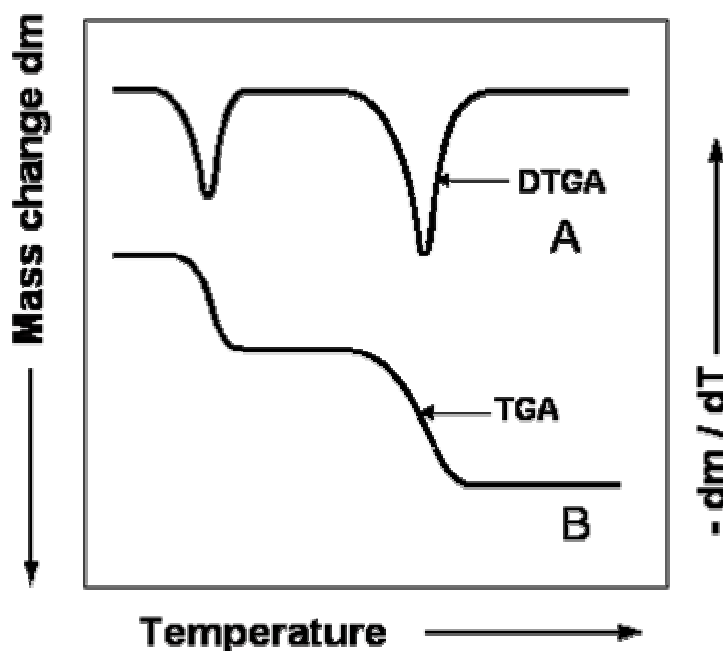


Figure 3.2: Comparison between (A) Integral (TGA) and (B) differential (DTGA) mass-loss curves

An increasing interest has been shown by Dunn [27-28], who first discussed the numerous advantages of using DTGA for a precise separation of overlapping reactions. Reactions that occur within the same temperature range give TGA curves that appear to consist of one continuous mass-loss. However, DTGA curves are discontinuous lines, and hence subtle mass-changes are emphasized. Four different TGA curves and their corresponding DTGA curves are shown in Figure 3.3. Curve (A) is a single reaction that occurs over a small temperature range; curve (B) consists of two reactions that are partially overlapping; curve (C) describes two reactions, the first of which occurs slowly, followed by a fast reaction; and curve (D) is one in which minor reactions occur during or near a major reaction. In the latter case by using an extrapolation procedure (multiple Gaussian or Lorentzian peak fitting), it may be possible to determine the temperature at which the second reaction precisely begins. All these curves represent cases encountered in the thermal analysis of zinc phosphate hydrate crystalline powders.

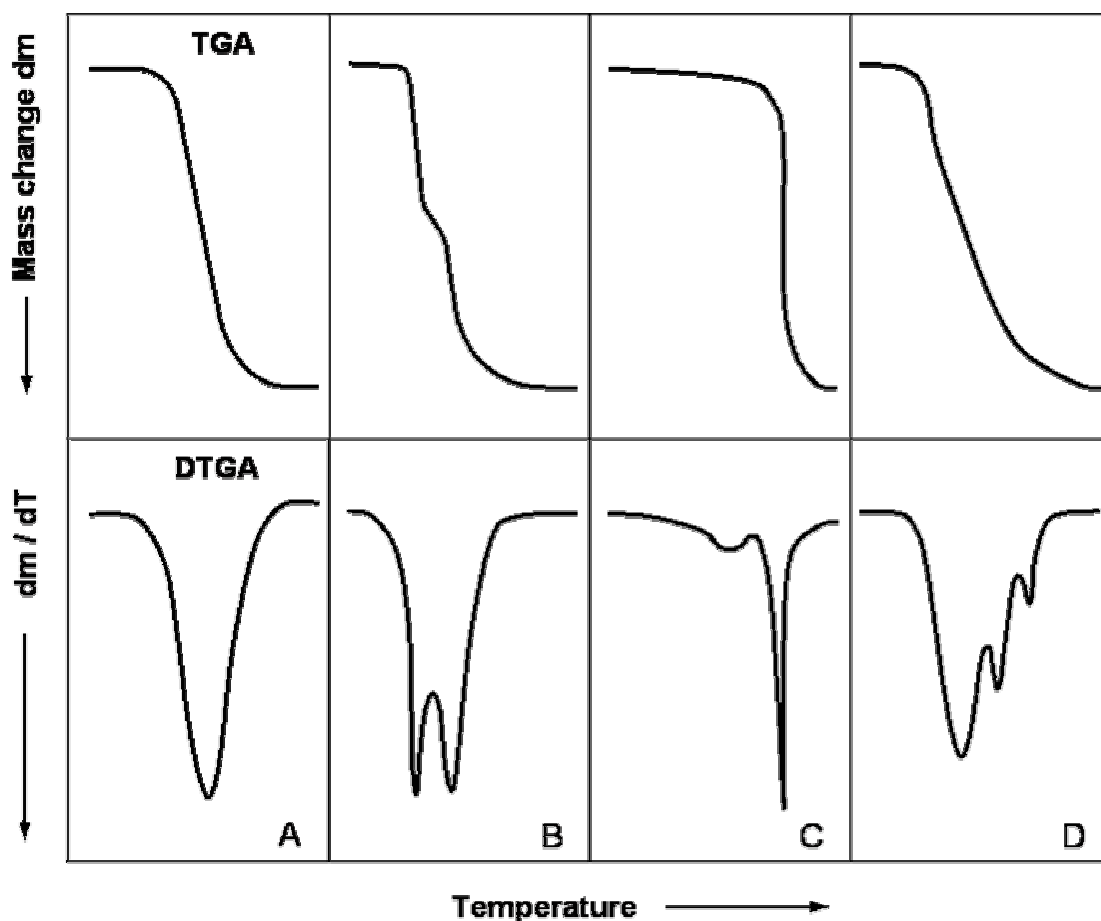


Figure 3.3: Comparison of TGA and DTGA mass-loss curves. (A) single stage reaction, (B), (C), (D) various overlapping reactions depending on their respective kinetics.

3.2.1.3. Factors affecting thermogravimetric curves

As with any instrumental technique, numerous factors influence the precision and accuracy of thermogravimetric results. Duval [29] summarized the most important parameters and classified them in two categories

<i>Instrumental (thermobalance) factors</i>	<i>Sample characteristics</i>
a. Furnace heating rate β	a. Amount of sample m_0
b. Furnace atmosphere (air/N ₂ /argon)	b. Particle size and particle size distribution
c. Geometry of sample holder (i.e. 40mg Alu. pin)	c. Sample packing
d. Geometry of furnace (cylindric)	d. Nature of the sample
e. Sensitivity of the of the recording mechanism	e. Heat of reaction
	f. Thermal conductivity
	g. Solubility of evolved gases in sample

Table 3.1: List of experimental parameters influencing the thermogravimetric curves.

Particularly the effect of heating rate on the onset temperature of a sample has been widely discussed by Simons and Newkirk [30-31], Simons and Wendlandt [32] Redfern and co-workers [33] and finally by DeVries and Gellings [34]. With increasing heating rate, the onset temperature T_i and the final temperature T_f are displaced to higher temperatures. On one hand the difference ($T_f - T_i$) increases with increasing heating rate, but on the other hand for any given *reaction temperature interval* ($T_f - T_i$) the extent of decomposition and the induced resolution decreases. Thus if very small amount of sample is used, very fast heating rates may be employed and one may still be able to detect the presence of intermediary compounds (for example a zinc phosphate trihydrate) formed during the decomposition (dehydration) reaction. Further, the resolving power of DTGA has been fully reviewed lately by Criado et al. [35]

Among all the factors bound to the sample characteristics one of the most significant is the sample particle size. Its effect on the TG curve is has been little studied compared to the effect of heating rate. Various particle sizes may cause a change in the diffusion of product gases (here outgoing crystal water), which may alter the reaction rate and hence the curve shape. Most of the studies in this area that have been reported have been concerned with the effect of particle size on kinetics parameters [33, 36]. In comparing the thermal decomposition curves of calcium carbonate hydrates, Richer and Vallet [37] found that while large crystals (size > 1mm) may decrepitate causing sudden mass-loss in the TGA curve, smaller particles (50 μm < size < 200 μm) minimize advert surface effects and increases the extent to which equilibrium is reached, and, at any given temperature the extent of decomposition.

3.2.2. Principle of differential scanning microcalorimetry

3.2.2.1. Principle of differential scanning calorimetry (DSC)

In a broad sense Differential Scanning Calorimetry (DSC) is a thermal technique, which as defined by Warrington, Höhne and Hemminger [38-39] can be operated in two modes: the *Power Compensated* DSC mode (generally assimilated to DSC) [40] and the *Heat Flow* DSC mode, [41-42] sometimes abusively assimilated to Differential Thermal Analysis (DTA). Both modes can also be operated as a temperature-modulated mode (TM-DSC). The *Power Compensated* DSC mode is a technique in which the difference of *heat flow* (HF), i.e. the amount of energy, exchanged between the sample and the apparatus, compared with the heat flow exchanged between the reference (an inert material) and the apparatus, is measured in function of the temperature and/or time, while the temperatures of the sample and reference, being placed in separated micro-ovens are kept equal for a given temperature program. By contrast, the principle of the Differential Thermal Analysis is the detection of the temperature difference between sample and reference as a function of the sample, reference or furnace temperature for a given temperature program. Since all chemical reaction and many physical changes (i.e. dehydration, phase transformation) are associated with the uptake or release of heat, the quantitative investigation of heat exchange is a relative simple and universal method but complementary, compared to thermogravimetry for characterizing particular complex processes.

The fundamental equation of calorimetry describes the relationship between heat exchanged ΔQ (J) with a calorimeter substance and a corresponding temperature range ΔT (K) :

$$\Delta Q = C_p(T) \cdot \Delta T \quad (3.3)$$

where the proportionality factor is the heat capacity C_p of the sample. Generally the temperature dependence of the heat capacity stands in the way of a linear relationship. The exact theory of DSC was given by O'Neill [43], and discussed by numerous authors such as Gray [44], Baxter [45] and then Flynn [46] and Davis [47]. The heat of reaction is then defined as follows:

$$\frac{dH}{dt} = -\frac{dQ}{dt} + (C_{ps} - C_{pr}) \frac{dT_p}{dt} - RC_{ps} \frac{d^2Q}{dt^2} \quad (3.4)$$

C_{ps} and C_{pr} are the total heat capacities of the sample (plus the container) and reference. R corresponds to the controlling thermal resistance over the temperature range, describing the geometry of the calorimeter and the efficiency of the heat exchanges in the system. In the power compensated mode, temperature changes in the calorimeter substance are avoided by supplying or dissipating heat exactly equal in magnitude (but opposite) in sign to the associated process under investigation. As a rule electrical energy is used to provide this compensation, either in the form of Joulean heat or dissipation through Peltier effect. This method of compensation is advantageous

since it permits measurements to be carried out under quasi-isothermal conditions. In quasi-static conditions, the heat flow rate is defined as follows:

$$\dot{Q} = \Phi(T) = \frac{dQ}{dt} \approx C_p(T) \cdot \frac{dT}{dt} \quad (3.5)$$

where the real quantities heat flow rate Φ (in Watt) and temperature changes (heating rate β) are strictly proportional. A typical DSC curve is illustrated in Figure 3.4. Excluding the Initial HF deflection due to the sample's heat capacity (A), five types of transitions are described: (B) glass transition of amorphous fraction of the sample or second order transition in which a change in the horizontal baseline (D) is detected, (C) an endothermic peak curve caused by fusion or melting transition, (E) an endothermic peak due to a decomposition or dissociation (e.g. dehydration) reaction, (F) an exothermic peak curve of crystallization or caused by a crystalline phase change and (G) a sharp increase of heat flow due to an oxidative degradation (for example the decomposition of phosphate into pyrophosphate).

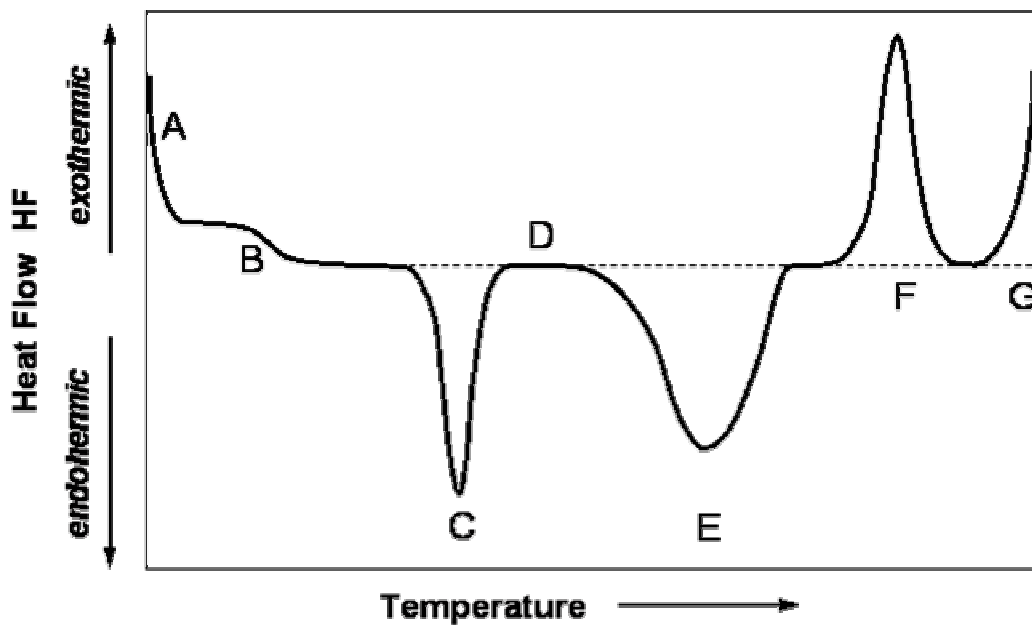


Figure 3.4: Typical DSC curve.

For precise measurements it is necessary to correct (calibrate) the measured heat flow magnitude (see equation 3.5) and phase shift for influence from the apparatus, as well as from the heat transport, which is a time-dependent process and therefore influence the measured heat flow rate function, as prescribed by Höhne [48].

3.2.2.2. Effects of the calibration and heating rate on DCS curves

Numerous factors similar to those affecting the TGA curves influence the DSC results [49]. Nevertheless since any temperature difference between the sample and the reference is directly

proportional to the corresponding differential flow rate, the proportionality constant or calibration factor for the calorimeter K is itself a function of the thermal conductivity of the sample and therefore temperature dependent:

$$\Phi(T) = K(T) \cdot \Delta T \quad (3.6)$$

Moreover, temperature difference between the sample and the reference results in variable amounts of heat loss to the surroundings via inevitable heat leaks. Consequently, the sample characteristics such as mass, thermal conductivity and heat capacity and specific enthalpy difference strongly influence the calibration factor in non-linear way in respect to the temperature [50]. Successively David [51], Curell [52] and finally Ozawa [53] expressed K as a polynomial function of the temperature T varying with the power 4 in respect to T . Recently Hensel and Schick discussed the linearity of the calibration function for time/temperature-dependent processes [54].

Besides the calibration factor, although the effects of heating rate on the onset and endset temperatures and on the peak temperature of a reaction peak have been known for many years, only in 1969 were Melling et al. able to explain these changes in details [55]. In general an increase in heating rate will displace T_i , T_f and the difference $(T_f - T_i)$ to higher temperature; the latter corresponding to a peak broadening effect as shown in Figure 3.5 b.

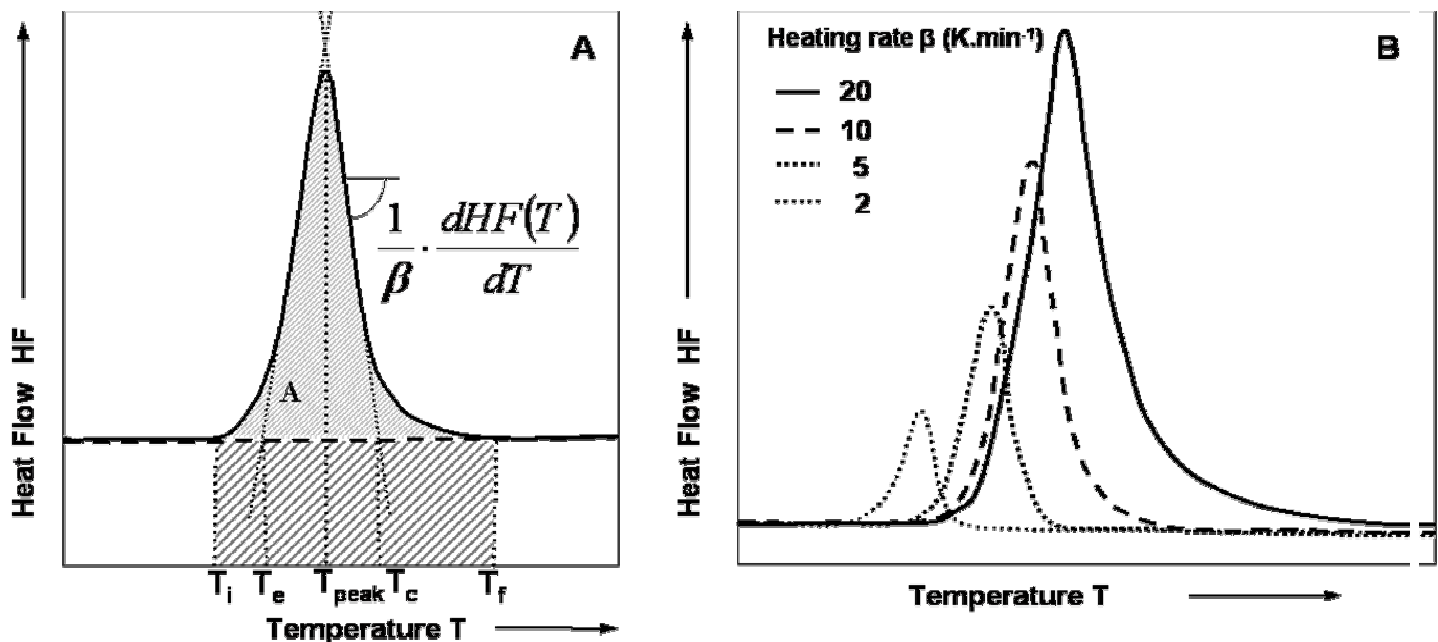


Figure 3.5: (A) Typical DSC curve exhibiting a horizontal baseline due to a constant c_p during the concerned exothermic transition. The peak area corrected from the baseline is designed as A . T_e and T_c design the extrapolated peak onset and endset temperatures, intersects of the auxiliary peak lines with the baseline. T_e onset (i.e. onset) slope is also given here (B) effect of the heating rate on the shape of a DSC peak.

Excluding the effects generated by the particle size and its packing (surface effects), Garn [56] showed that if the heating rate remains constant during the reaction, the peak area is linearly proportional to the heating rate as shown in Figure 3.5 a.

However at high heating rate the resolution of two adjacent peaks diminishes dramatically, thereby obscuring one of the peaks. This effect is particularly well illustrated by Barall and Rogers [57] for the dehydration of sodium hydrogen carbonate. Kissinger [58-59] has shown that the onset temperature and the peak temperature T_{\max} or T_{peak} are dependent on the heating rate β according to:

$$\frac{d[\text{Ln}(\beta/T_p^2)]}{d(1/T_p)} = -\frac{E_a}{R} = \text{constant} \quad (3.7)$$

where E_a is the activation energy and R is the ideal gas constant with $R = 8,31441 \text{ J.K}^{-1}.\text{mol}^{-1}$.

Besides, Smyth's calculations permit the overall description of the shape of the differential peak in taking into account varying heating rates but assuming that density, specific heat and thermal conductivity all remained constant during the considered transition [60].

Both heating rate and the change of heat capacity and/or the extent of heat transfer to the sample holder during a reaction contribute to changes in the baseline. This in turn means that the area corresponding to the heat of reaction and the associated thermodynamic parameters cannot be determined exactly. Therefore the choice of the type of baseline as shown in Figure 3.5 is crucial for an efficient thermodynamic analysis.

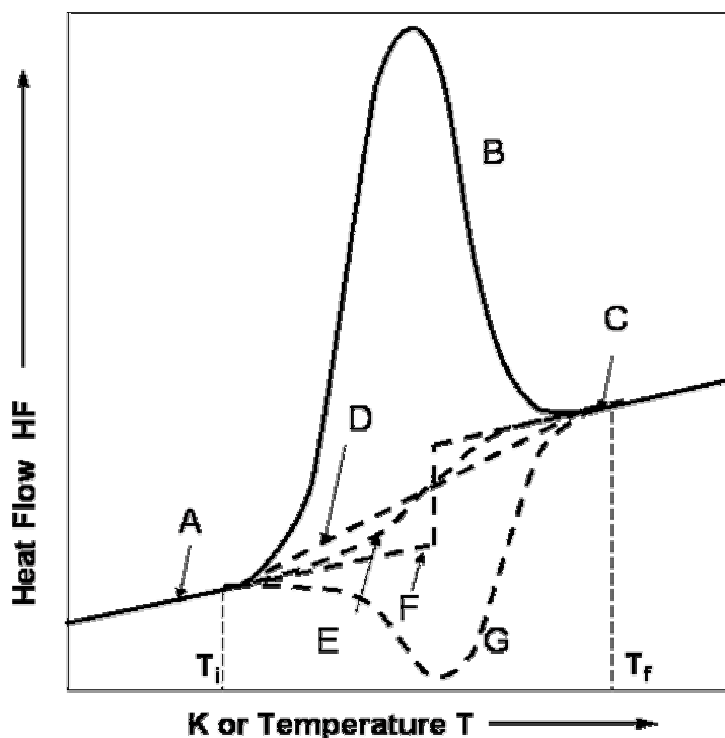


Figure 3.6: DSC curve showing a shift in baseline caused by a variability in either C_p or the coefficient of heat transfer $\lambda(T)$. T_i and T_f are corresponding to onset and endset temperatures of reaction transition. Diverse type of baselines are considered for a peak (B): (A) tangential left, (C) tangential right, (D) line, (E) spline, (F) tangential, (G) integral.

3.2.3. Quantitative analysis in DSC

Various thermodynamic functions (enthalpy, entropy, free energy, etc.) can be determined by integration of the DSC curves on the basis of specific heat capacities. The accurate establishment of specific heat capacities at constant pressure c_p , as a function of temperature is thus of fundamental importance. Accurate results are obtained using isothermal calorimeters or Calvet-Tian scanning / isoperibolic calorimeters [61-62], or by direct comparison with the c_p value of a known substance, e.g. sapphire, in a specific transition temperature range [63]. Phase transitions in solid mixtures can be followed directly by DSC, i.e. vapor pressures associated with the components are so low that vaporization plays virtually no role and therefore does not interfere. In the theory developed by Speil et al. [64] and modified by Keir et Kulp [65] the area enclosed by the differential curve as shown in Fig. 3.5 a represents the heat of reaction or the transition enthalpy ΔH_r :

$$\Delta H_r = \frac{KM}{m_0} \cdot \int_{t_i}^{t_f} \Delta HF(t) dt = \frac{KM}{\beta \cdot m_0} \cdot \int_{T_i}^{T_f} \Delta HF(T) dT \quad (3.8)$$

where m_0 is the mass of the sample measured, M its molar mass, K the calibration constant of the DSC apparatus, T_i and T_f are the integration limits of the differential curve. The baseline function is of utmost importance for a correct determination of the enthalpy of reaction, since it is included in the integration of the peak area. The choice of the baseline (also possibly temperature dependent) depends strongly of the shape of the thermal peak and of the appearance of a singularity at T_{peak} , corresponding to a discontinuity in the $\Delta c_p(T)$ [66]. Thus from the DSC curve it is possible to calculate the variation of heat capacity $\Delta c_p(T)$, which correspond to the first derivate of the heat flow $HF(T)$ assuming that the crystal water sublimates [67]:

$$C_p(T) = \left. \frac{dHF(T)}{dT} \right|_p \quad \text{and} \quad \Delta C_p(T) = \left. \frac{d\Delta HF(T)}{dT} \right|_p \quad (3.9)$$

Using the second thermodynamic principle for a given transition, the determination of the $\Delta c_p(T)$ gives access to the entropy of reaction $\Delta S_{reaction}$:

$$\Delta S(T) = \int_{T_i}^{T_f} \frac{\Delta C_p(T)}{T} \cdot dT \quad (3.10)$$

Applying the Gibbs-Helmholtz equation, the free energy variation associated with the observed transition is given as follows:

$$\Delta G(T) = \Delta H(T) - T \cdot \Delta S(T) \quad (3.11)$$

Based on Mraw's model [68], only valid for a first-order phase transition, Saito et al. defined a numerical procedure to determine the thermodynamic functions from the analysis of the slope of the DSC peak [69]. Tanake [70] and later Hatta et al. [71] offer several methods for the precise determination of the non-linear temperature dependence of the heat capacity, necessary for the analysis of all other cases, including thermodynamic transitions of first order accompanied by a

sudden release of latent heat at the transition temperature T_0 , second-order phase transition and time/temperature-dependent processes (irreversible process).

Despite the advanced development of electronic instrumentations currently employed in thermoanalysis, the great majority of investigators present numerical data without relevant qualification as the precision or accuracy. In order to minimize uncertainties about the determination of thermodynamic functions, a systematic statistical approach was discussed by Schwenker and Whitwell [72] for the DSC and Sturm [73] for the DTA. Averaging over eight random measurements, these authors found an error of less than 2% within a predicted confidence limit of 95% on $\Delta H_{\text{reaction}}$.

3.3. Thermal stability of zinc and calcium phosphates hydrates: descriptive approach

The crystal structure of the zinc phosphate polymorphs, α - and β -hopeite differ by the hydrogen bonding pattern as demonstrated in Chapter 2, leading to characteristic differences in thermal behaviour. In agreement with extensive characterizations conducted first by Yaglov and Volkov [74-75] and more recently by Gardner and McAra [76], it must be concluded that the α -hopeite is the most stable phase and therefore may possess a higher activation energy of dehydration than β -hopeite. The studies of zinc phosphate hydrates has so far suffered from a lack of accuracy and contradictory information on the dehydration processes of the pure hopeite polymorphs. This gave reason to carry out a detailed study of the dehydration of structurally pure α - and β -hopeite. To a greater extent, since it was possible to obtain the pure ZPT polymorphs, a focused comparison with more complicated structures like biological calcium phosphate hydroxyhydrates (brushite and hydroxyapatite) is expected to help to perceive better the unique thermal properties of zinc phosphate tetrahydrates.

3.3.1. Structural differentiation between α -and β -hopeite, and α -, β - zinc phosphate dihydrate by SEM and XRD

Scanning Electron Microscopy (SEM) and Powder X-ray diffraction (XRD) are required as complementary techniques to thermoanalysis in order to give light about the possible pathways of solid state reactions of dehydration (e.g. coexistence of ZPT and ZPD, continuous transformation of ZPT in ZPD). A rapid preliminary morphological characterization has been done on the effects of thermal treatment at 200°C and 600°C, allowing the formation of the zinc phosphate dihydrates and anhydrates of both forms of zinc phosphate. Figure 3.7 shows SEM images taken of α -and β -zinc

phosphate tetrahydrates after a storage of 24 hours at room temperature (Fig. 3.7 A,B and Fig. 3.8 A,B) and successively calcined at 200°C (Fig. 3.7 C,D and Fig. 3.8 C,D) and 600°C (Fig. 3.7 E,F

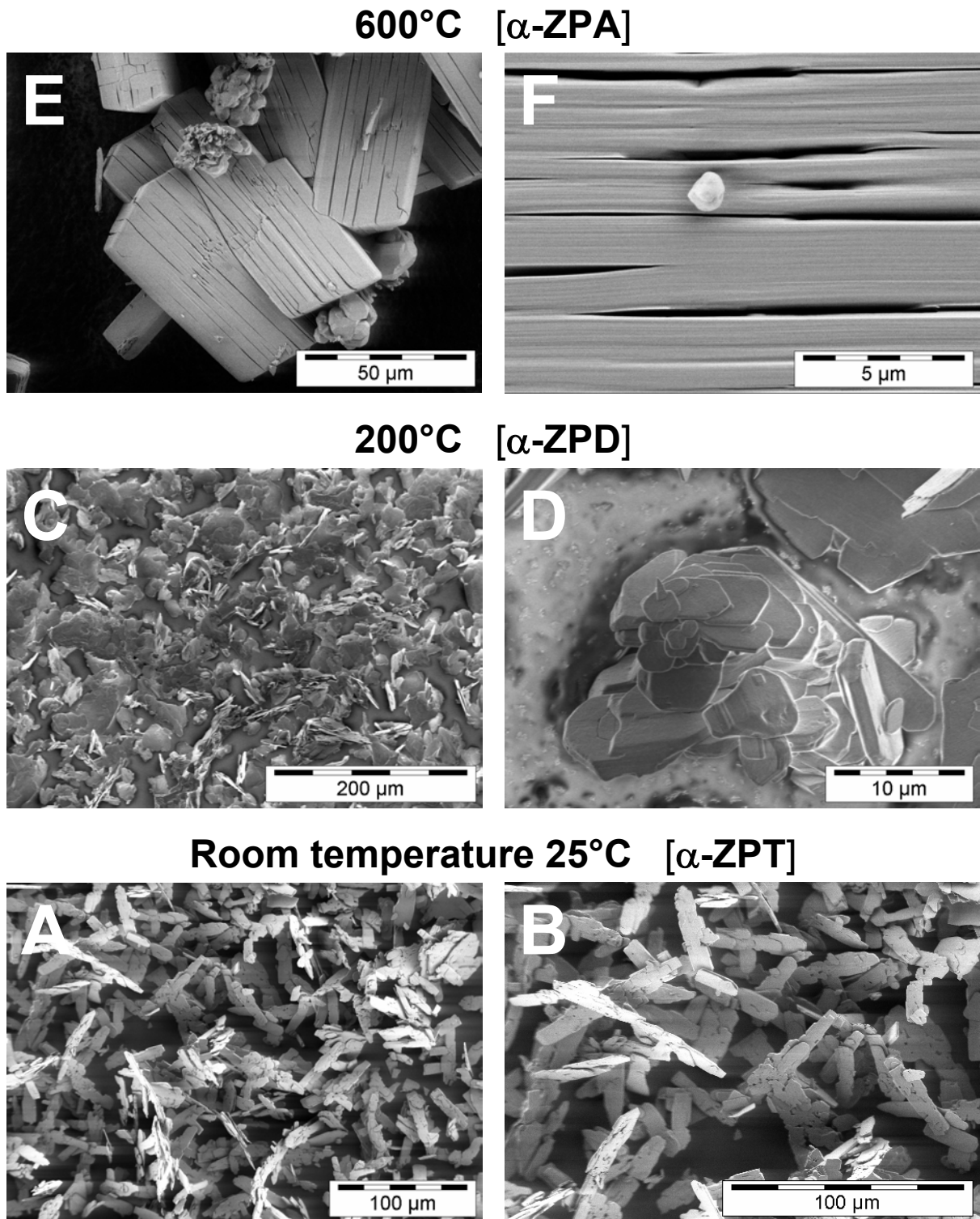


Figure 3.7: SEM images taken of α -zinc phosphate tetrahydrate: (A,B) stored 24 hours at room temperature, (B,C) thermally dihydrated at 200°C for 24 hours under inert gas (N_2) atmosphere, (E,F) thermally treated at 200°C for 24 hours under inert gas (N_2) atmosphere.

and Fig. 3.8 E,F). The size, particle size polydispersity (PSD) and morphology of these crystals seem to be approximately conserved on thermal treatment since no dramatic ruptures due to

mechanical constraints generated thermally (residual strains) are observed in each of the zinc phosphate polymorphs.

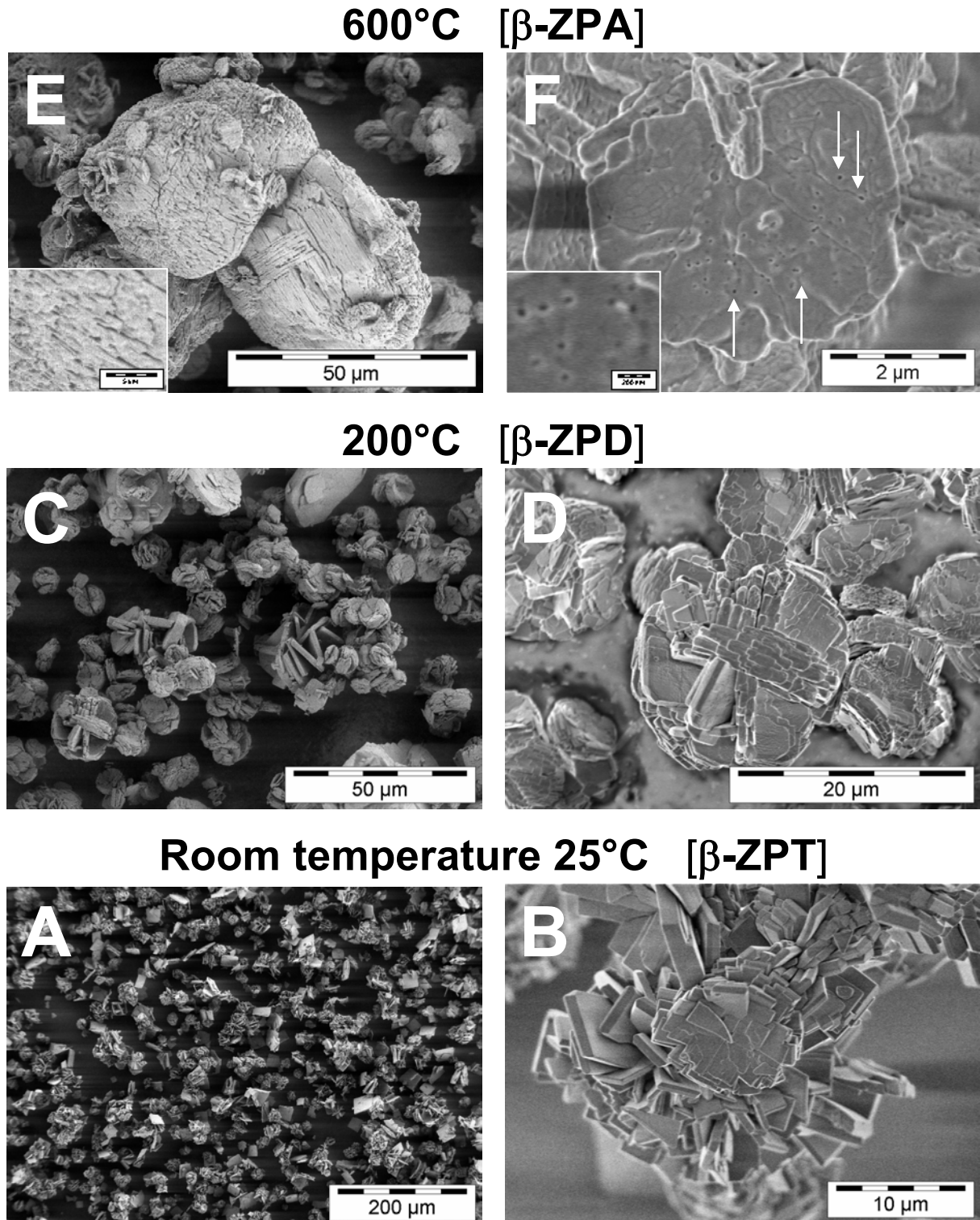


Figure 3.8: SEM images taken of β -zinc phosphate tetrahydrate: (A,B) stored 24 hours at room temperature, (B,C) thermally dihydrated at 200°C for 24 hours under inert gas (N_2) atmosphere, (E,F) thermally treated at 200°C for 24 hours under inert gas (N_2) atmosphere.

However with increasing temperature large crystals of α -ZPT (Fig. 3.7 A) tend to be a bit smaller and exhibit superficial roughening and rounding of the crystal edges (Fig. 3.7 D). A detailed

characterization of the crystal surface (prominent plane [100]) shows that both polymorphs of the dihydrate (α -, β -ZPD) and anhydrate (α -, β -ZPA) exhibit cracks (Fig. 3.7 E,F and Fig. 3.8 E) of circa 1-10 μm in length and 30 nm in width and of some tens to hundredth nanometers in depth, located in parallel planes (surface (110)). These cracks cannot correspond to propagating lattice imperfections due to the length scale involved. On contrary it is supposed to correspond to the formation of water channels of evaporation (Fig. 3.8 F and thereby insert) since the crystal water of hopeite is located in a alternating sheet structure with zinc phosphate polyhedra (surface (110)) [77]. Similarly, Thus, Figure 3.9 displays the successive dehydration steps of α -hopeite (Fig. 1a) and β -hopeite (Fig. 1b) at 220°C and 600°C in terms of XRD.

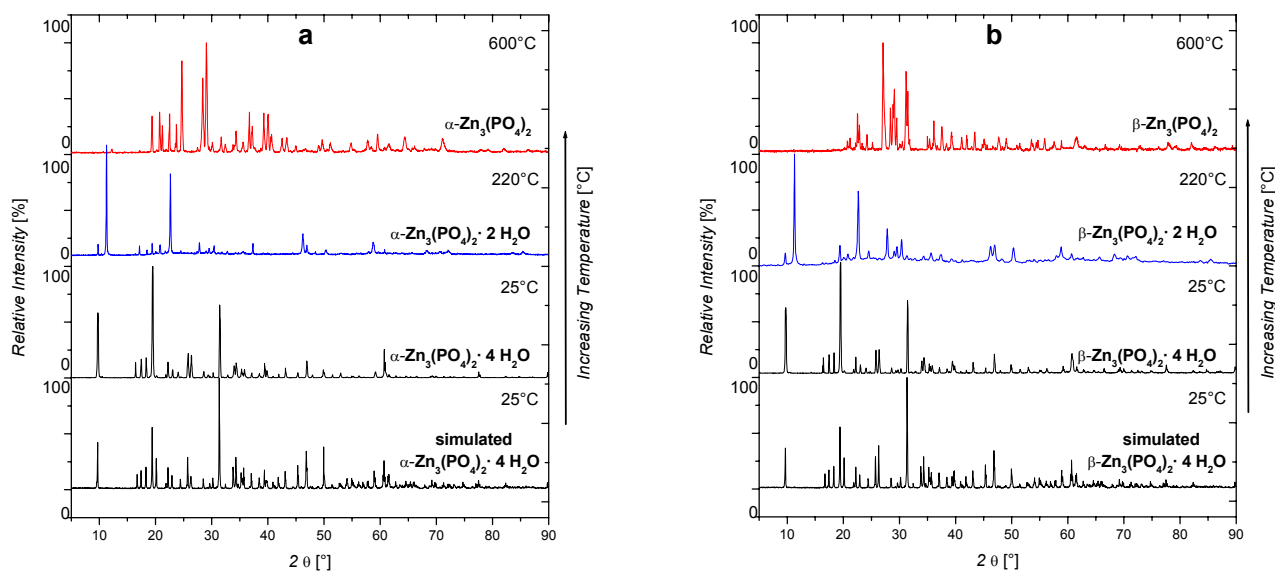


Figure 3.9: X-ray powder pattern of: (a) α -hopeite; (b) β -hopeite, at various temperatures corresponding to their respective hydrated phases. At room temperature, comparison between experimental and simulated spectra.

The starting materials were chemically pure and their measured powder diffractograms correspond very well with the simulated powder diffractograms (MSI, Cerius 2 (2001)) using the previously determined crystallographic data for each phase [78]. The stoichiometric composition was calculated as follows within the limits of analytical error (elemental analysis and thermogravimetry): α -hopeite: $\text{Zn}_3(\text{PO}_4)_2 \cdot 4\text{H}_2\text{O}$, β -hopeite: $\text{Zn}_3(\text{PO}_4)_2 \cdot 4\text{H}_2\text{O}$, Brushite: $\text{Ca}_1(\text{HPO}_4)_1 \cdot 2\text{H}_2\text{O}$ and Hydroxyapatite $\text{Ca}_5(\text{PO}_4)_3(\text{OH})$. In the case of α -, β -hopeite, these values match nearly perfectly with the zinc phosphate tetrahydrate stoichiometry. Thanks to preliminary DSC experiments (§ 3.3.2), one may conclude that the zinc phosphate dihydrate exist between 200 and 240°C, and that the anhydrate is stable above 600°C until 650°C without occurrence of reversible metamorphism, as it was duly noted by Calvo [79]. The diffractograms obtained at 200°C and above do not correspond to known intermediary structures such as zinc phosphate trihydrate or monohydrate [80] and are not exactly

identical to earlier published results of G erault et al. about zinc phosphate dihydrate [81-82]. At 600 C, the XRD data are similar to those of α -, β -Zn₃(PO₄)₂ [83].

Kotlova et al. [84] have prepared a dihydrate polymorph and have characterized it by XRD and thermal analysis. They designated this polymorph as “active” form or β -dihydrate in that it behaves more hygroscopically than the “normal” dihydrate, also called α -zinc phosphate dihydrate, and abusively α -dihydrate. They affirmed that this β -form, also produced by McAra [76] in another way (room temperature and reduced pressure), converts into the α -dihydrate at approximately 150 C until 200 C at ambient pressure. In contradiction to these results, our XRD studies confirm that there is no spontaneous transformation from the β -dihydrate to the α -dihydrate. α - and β -zinc phosphate dihydrates possess different powder diffractograms, thus indicating different crystal structures, and the kinetics of the thermal dehydration discussed later in this chapter (  3.6) speak against such an assumption. In addition, Arnaud et al. [85] determined the structure of the α -dihydrate from powder diffractogram. However, the crystal structure of β -dihydrate has not been yet determined.

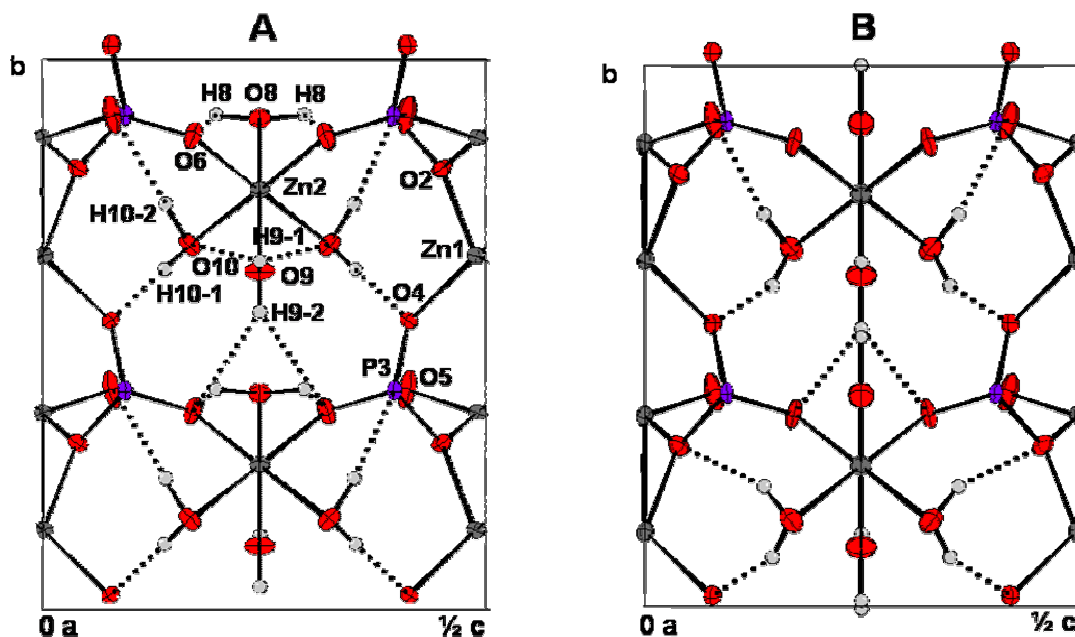


Figure 3.10: Composition of a half asymmetric unit cell of (A) α -hopeite and (B) β -hopeite projected along the *a*-axis. The same nomenclature is used for β -hopeite. Dash lines represent hydrogen bonds (c.f. Chapter 2).

During dehydration from tetrahydrate to dihydrate, the alteration of the structure occurs in planes parallel to (001)_{dh} of the dihydrate which corresponds to (010)_{hop}. Justified by the fact that the **a** and **b** cell parameters remain practically unchanged during dehydration, the structural contraction occurs only in the (010)_{hop} plane within the PO₄³⁻-Zn(1)-PO₄³⁻ sequence (Figure 3.10). In consequence, the Zn(1)-type zinc atoms [86] undergo a change of coordination from octahedral to tetrahedral during dehydration, and this configuration is stabilized by hydrogen bonding along the

(001)_{dh}-axis. Therefore, in analogy to the structural difference between α - and β -hopeite, the crystallographic difference between α - and β -zinc phosphate dihydrates may lie similarly in the hydrogen bonding pattern. Using DSC and TGA-MS experiments as follows, this conclusion will be confirmed.

3.3.2. Structural differentiation between α - and β -hopeite, and α -, β - zinc phosphate dihydrate by thermoanalysis

Both orthorhombic modifications of $\text{Zn}_3(\text{PO}_4)_2 \cdot 4 \text{H}_2\text{O}$ show dehydration starting above 100°C and appearing to be complete at about 400°C as shown by DSC and TGA-MS in Figures 3.12 and 3.11. At higher temperatures, decomposition or “condensation” of phosphate and hydrogen phosphate groups in pyrophosphate groups are expected (438°C for the hopeite polymorphs and above 467°C for the brushite crystals) [85].

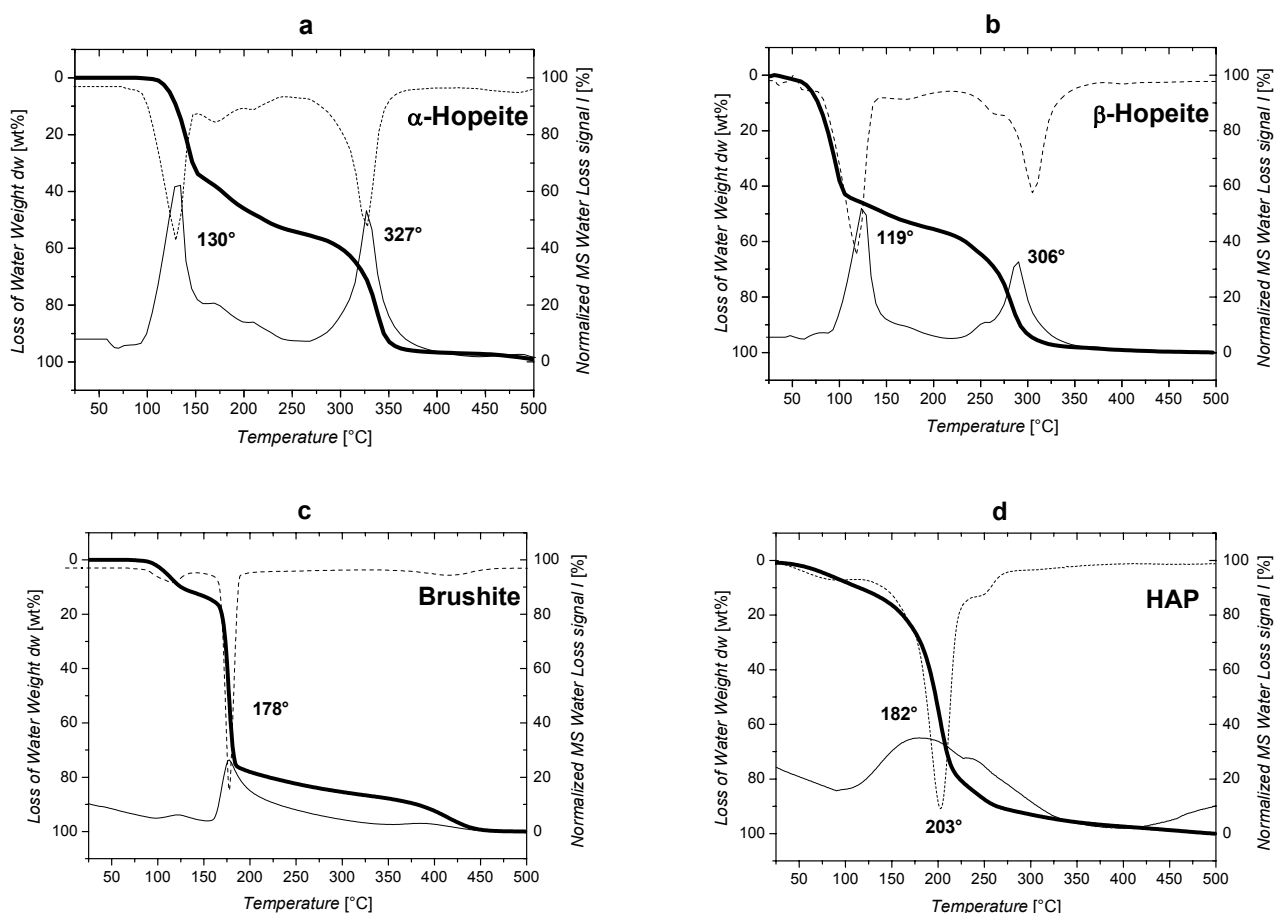


Figure 3.11 : Comparison of TGA-MS thermograms of (a) α -hopeite, (b) β -hopeite, (c) Brushite, (d) Hydroxyapatite taken at $10 \text{ K} \cdot \text{min}^{-1}$. Weight loss (thick line), First order derivate (dash line) of the weight loss curves and MS water signal (m/s : 18, dark line) are given as normalized to 100%. This corresponds to the loss of four water molecules for the hopeite samples. Similarly, it describes the loss of one and two water molecules for HAP and brushite samples.

The thermogravimetric curves (Fig. 3.11) show that α -hopeite loses crystal water in two well defined stages: two molecules at 130°C and the remaining two at 327°C; this is the characteristic behaviour of α -hopeite. Similarly the DSC measurement (Fig. 3.12) gives two well separated peaks but slightly displaced: one sharp peak at 182°C and another one at 289°C which may indicate the starting point for the loss of two types of water molecules. At about 220°C, i.e. after loss of 2 H₂O, a pseudo-stabilization of the structure is reached; the water loss increases slowly, indicating the existence of a dihydrate structure. In the light of these results, one can confirm that the first step corresponds to the transition Tetrahydrate-Dihydrate while the second step to the transition Dihydrate-Anhydrate [77,83].

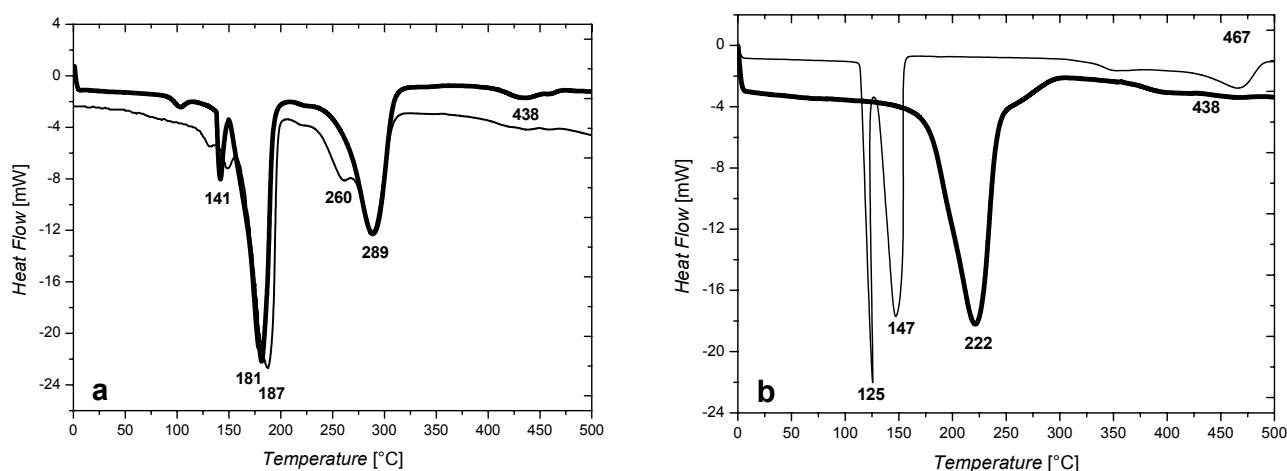


Figure 3.12: Comparison of DSC curves taken at a heating rate of 10 K.min⁻¹ of (a): α -, β -hopeite and of (b) : Brushite and HAP. While α -hopeite and HAP are described with thick black lines, β -hopeite and Brushite are shown in thin line. Peak temperatures measured are also given.

In opposition, the thermograms of the β -hopeite show significant differences compared to the α -phase. β -hopeite seems to have lower activation energy of dehydration compared to the α -hopeite pointing toward a lower symmetry of the four water molecules contained in the crystal, as it will be show in § 3.5.7. This is confirmed by DSC where the onset point of the thermal decomposition appears at 115°C for the β -form and 130°C for the α -form (Fig. 3.12 a). A four-step dehydration starts with the loss of one water molecule, corresponding to an unstable trihydrate intermediary structure at 141°C, rapidly followed by the loss of a second water molecule (removal of 1.96 H₂O), marked by a broad endothermic peak at 181°C. While no graduation is clearly observable on the TGA-weight loss curve of β -hopeite between the dihydrate and the anhydrous salt, the DSC curve presents two peaks 260°C and 289°C, and one can see a shoulder on the TGA-curve at a water content corresponding to the monohydrate [79]. Surprisingly, the weak transition at 238°C may indicate a conformational rearrangement of the β -dihydrate since no water is lost at that temperature, and corresponds also to the temperature where the dihydrate starting from α -

$\text{Zn}_3(\text{PO}_4)_2 \cdot 4 \text{H}_2\text{O}$ is well formed [86]. In conclusion, the β -hopeite loses its four water molecules one after another in four consecutive steps. These results are in partial disagreement with the thermal behaviour of β -hopeite previously reported in the literature [87].

Similarly to β -hopeite, brushite loses its two crystal water molecules (exactly $1.97 \pm 0.05 \text{H}_2\text{O}$) successively at 125°C and 147°C (Fig. 3.11 b), as indicated by a broad water peak on the TGA-MS thermogram (Fig. 3.11 c) [88]. Furthermore, the weight loss curve showing a drastic change and its first order derivate displaying a sharp peak at 178°C , this suggests that the two crystal waters of brushite are not energetically equivalent. Hydroxyapatite shows a single well-defined dehydration peak detected at 222°C in DSC (Fig. 3.12 b) and 182°C in TGA (Fig. 3.11 d), corresponding only to the collapse the structure into octacalcium phosphate, on grounds that this happens exactly in the existence domain of α -zinc phosphate dihydrate, a more stable structure. In contrast, Kumar et al. [89] reported that the thermal dehydration of brushite at 147°C is related to a gradual transformation of the crystal surface into hydroxyapatite, thus explaining the broad peak in the MS (m/z 18) signal of TGA thermogram of brushite.

These marked thermal behaviour differences observed for α -, β -hopeite on one side and for brushite / HAP on the other side can be correlated either to crystallographic and thermodynamic differences relative to the hydrogen bonding pattern, or to a purely kinetic effect. In order to elucidate this, a thermodynamic-kinetic study focused on the dehydration reaction of α -and β -hopeite has been conducted.

3.4. Thermodynamic stability of α - and β -hopeite and their relative hydrates

3.4.1. Validity of non isothermal measurements and isoconversional methods

The non isothermal methods of kinetic analysis of thermal dehydration (decomposition) has been widely accepted, since among other advantages, experiments can be carried out rapidly over the whole conversion range, also covering a wide range of temperature [90-91], thus allowing the simultaneous characterization of both reactions $\text{ZPT}(\text{solid}) \rightarrow \text{ZPD}(\text{solid})$ and $\text{ZPD}(\text{solid}) \rightarrow \text{ZPA}(\text{solid})$. Some authors think that the number of experimental runs, necessary in a kinetic study is smaller for the non-isothermal methods [92]. However others, accepting the advantages of non-

isothermal analysis perform the experiments in isothermal conditions [93] because of the difficulties of separating temperature and conversion influence in non-isothermal studies. De Bruijn et al. [94] consider necessary to use isothermal methods in kinetic analysis, suggesting that it is not possible to obtain the right conversion influence, the right values of the activation energy E_a and solid state reaction order n by using dynamic methods. Tang [95] solved partially this issue in proving that the conversion influence has to be determined using at least one isothermal experiment. O'Brien and Ross [96] pointed out that the determination of kinetic parameters for calcium oxalate dehydration by non-isothermal methods is likely to be unreliable; while Guler et al. [97] consider the agreement between isothermal and non-isothermal results to be reasonable, albeit the adequate heat flow fitting function $f(\alpha)$ cannot always be chosen for non-isothermal experiments. Gorbachev, Calvo and then Segal [98-100] conclusively demonstrated using mathematical analysis [101-102] that kinetic parameters with linear temperature programming (constant heating rate) are perfectly identical to those obtained from isothermal experiments when the chemical transformation is irreversible; which is the case of the dehydration reaction of zinc phosphate hydrates. However a similar statement cannot be made for reversible non-isothermal transformations, since kinetic parameters depend then on the heating rate. The influence of heating rate on non-isothermal kinetics was fully investigated and modeled by Urbanovici and Segal [103].

3.4.2. Heating rate dependence of peak characteristics - Validity of Arrhenius law

The effect of heating rate on T_i and T_{peak} was followed by DSC and TGA for α - and β -hopeite (Fig. 3.13). According to last-square extrapolations to zero-heating rate, it is possible to obtain an evaluation of the absolute value of the onset and peak temperatures of dehydration of zinc phosphate hydrates near equilibrium. Thus one should apply the "tangent method" of Newkirk to DTGA curves for a precise determination of the onset temperature at increasing heating rate [104]. As shown in Fig. 3.13 A and Fig. 3.13 B the linear dependence of onset temperature T_i on heating rate in both DSC and DTGA techniques is in good agreement with the observation of Melling et al. [105]. The peak temperature of the two consecutive dehydration reactions ZPT (solid) \rightarrow ZPD (solid) and ZPD (solid) \rightarrow ZPA (solid) are also linear with the heating rate as proven by DTGA (Fig. 3.13 A) and confirmed by DSC (Fig. 3.13 C).

From a general point of view, the estimated onset temperature of dehydration should be found to be higher in TGA than in DSC for the reason that one should give thermal energy (monitored in DSC) to the crystal in order to break the hydrogen bonds of the outgoing crystal water. Thus due to diffusion mechanism of water molecules in the zinc phosphate crystals and at the crystal surface, the water loss is detected in TGA at a higher temperature than in DSC. This is confirmed for the

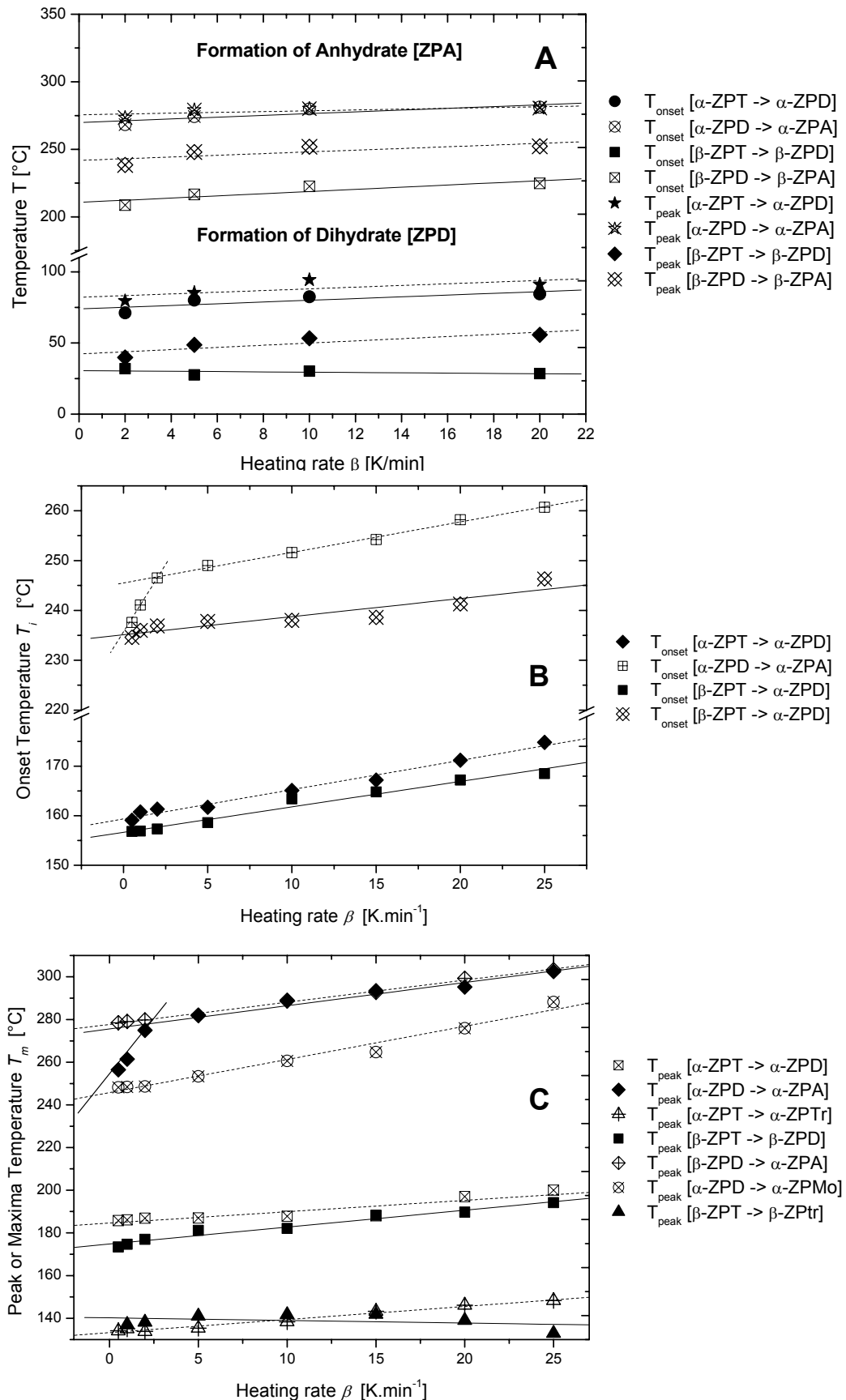


Figure 3.13: Last-square extrapolations of onset temperature and peak temperatures to zero heating rate measured from: (A) DTGA data set, (B) and (C) DSC data set. ZPT_r and ZPMo describe the following intermediary zinc phosphate hydrate products: trihydrate and monohydrate.

ZPD \rightarrow ZPA transition, but not for ZPT \rightarrow ZPD transition, outwardly due to the detection of adsorbed surface water in DTGA. The presence of diffusive process of water evaporation at the crystal surface is supported by the presence of water channels on SEM photographs in Figure 3.7 and Figure 3.8. On contrary, the peak temperature appears to be lower in TGA compared to DSC due to a molecular rearrangement of the crystal structure.

A certain amount of crystal water, at least one water molecule per stoichiometric formula $Zn_3(PO_4)_2 \cdot 4 H_2O_{(cr)}$ and marked by a peak minima in DTGA, must be lost before any molecular rearrangement, i.e. collapse of the crystal structure followed by a “recrystallization” in a new ordered crystal structure such as zinc phosphate dihydrate or anhydrate takes place. At very low heating rates (0.2 and 0.5 K.min⁻¹) the linearity of the peak temperature with the heating rate is not completely verified due to the stabilization on intermediary hydrates (i.e monohydrate) in the case of the α -ZPD. From Table 3.2 on basis of DTGA and DSC results one can conclude that the β -form of zinc phosphate, either the tetrahydrate or the dihydrate, losses its water at lower temperature than the α -form of zinc phosphate. This indicates a lower stability of β -zinc phosphate tetrahydrate (β -ZPD) in comparison to α -zinc phosphate tetrahydrate (α -ZPD). At high temperature, the peak temperatures of the following transitions α -ZPD \rightarrow α -ZPA and β -ZPD \rightarrow β -ZPA are practically identical, suggesting structures of zinc phosphate anhydrates of similar thermal stability. Furthermore, its is well known that the temperature lag, i.e. the difference of onset and peak temperature, is a estimation of the peak area [106]. In reason of the linearity of the onset and peak temperature with the heating rate, one can affirm that the Arrhenius law is here verified. Also using Kissinger’s approach discussed here above for the, a plot of $\ln(\beta/T^2)$ versus $1/T$ should yield a curve with a constant slop of E_a/R and therefore also prove the validity of the Arrhenius law. However this method should not be used for precise determination of an activation energy.

Observed transition	Onset temperature	Peak temperature
	T_i [°C]	T_{peak} [°C]
DTGA		
α -ZPT \rightarrow α -ZPD	76	82
α -ZPD \rightarrow α -ZPA	269	276
β -ZPT \rightarrow β -ZPD	34	43
β -ZPD \rightarrow β -ZPA	211	242
DSC		
α -ZPT \rightarrow α -ZPD	160	183
α -ZPD \rightarrow α -ZPA	245 (234)	278 (255)
β -ZPT \rightarrow β -ZPD	157	174
β -ZPD \rightarrow β -ZPA	235	275

Table 3.2: Onset and peak temperatures of dehydration obtained from last-squares extrapolations to zero heating rates. Estimated errors $\pm 1^\circ\text{C}$. The values in parentheses correspond to the zinc phosphate monohydrate.

3.4.3. Thermodynamic order of phase transition and irreversibility during dehydration of hopeite polymorphs

Phase transformations such as the reaction of dehydration in a solid state can be broadly classified in two categories. A reaction that takes place more or less simultaneously in all part of a crystal is regarded as an *homogeneous* transformation. The second category of phase transformations is *heterogenous* and of the nucleation-and-growth type. Tiny volumes of the product phase or nuclei, often assumed to be the same in structure and composition as the transformation product, form first. A sharp boundary delineates the nuclei from the surrounding matrix. These small regions subsequently grow by the outward movement of the boundary, with corresponding changes in composition and crystal structure behind the advancing front. (Avrami-Erofeev mechanism). Following the Mass Action Law, reversible phase changes are endothermal and in consequence, exothermal transformation must be irreversible [107].

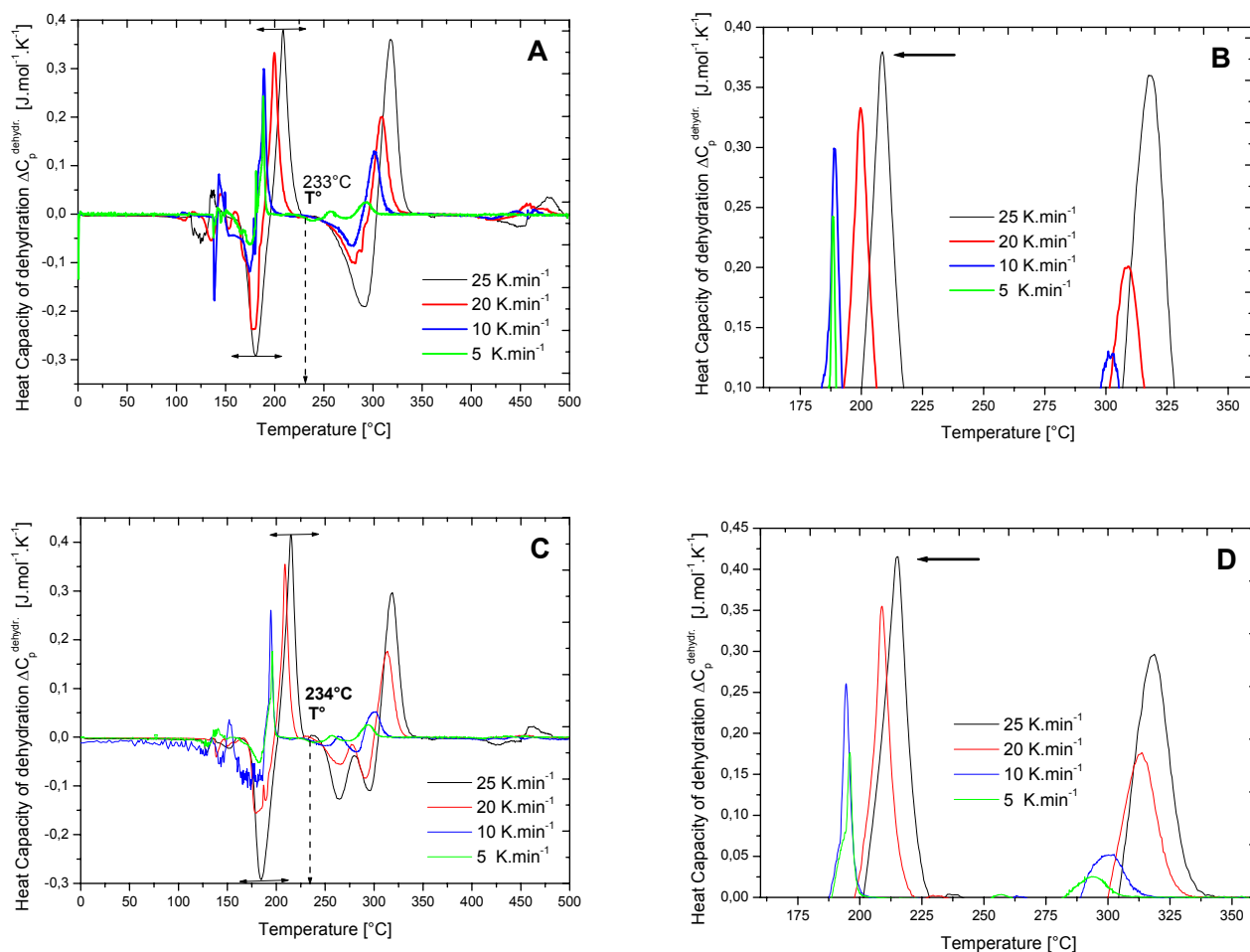


Figure 3.14: Dependence of the variation of heat capacity during dehydration ΔC_p of the reaction temperature for: (A) α -hopeite, (B) β -hopeite, considering the effect of the heating rate. Zoom showing the discontinuity of ΔC_p with increasing temperature (arrow: singular point) for the transition ZPT \rightarrow ZPD while no discontinuity is observed for the transition ZPD \rightarrow ZPA for: (C) α -hopeite, (D) β -hopeite.

Chemical reaction and crystalline rearrangement are a common cause of exothermal effects. Dehydration is a solid state phase transformation with composition change of the system undergoing the transformation. Therefore dehydration is considered here an *irreversible* reaction. Applied to the zinc phosphate system, the transformation Tetrahydrate \rightarrow Dihydrate \rightarrow Anhydrate exhibit at low heating rate ($0.1\text{-}0.2\text{ K}\cdot\text{min}^{-1}$) in near steady state conditions small exothermal crystallization peaks, especially around 220°C , due to local molecular reorganization following the release of crystal water molecules. A transformation is considered thermodynamically of first order if the Gibbs free energy $\Delta G_{\text{reaction}}$, the associated entropy change, specific volume and the molar heat capacity of the system vary continuously through the transformation and particularly at the transition (equilibrium) temperature T_c and pressure P_c . Nevertheless the first derivative of $\Delta G_{\text{reaction}}$ with respect to temperature (i.e. pressure) often have a discontinuity at T_c (i.e. P_c). A thermodynamic second-order transition is one in which the free energy and its first derivatives change continuously through the equilibrium transition temperature and pressure but the second order derivatives still exhibit discontinuities. These discontinuities in second order derivatives of $\Delta G_{\text{reaction}}$, represent abrupt changes in specific heat, molar heat capacity, thermal retraction and volume coefficient of thermal expansion [108].

The existence and stability domains of zinc phosphate dihydrate crystals (ZPD) is well illustrated in Fig. 3.14 A and Fig. 3.14 C as no significant variation of heat capacity of the products of reaction is to be noticed. α -ZPD and β -ZPD exhibit very similar domain of thermal stability around 233°C .

Using the results displayed in Figure 3.14 it is possible to affirm that from a thermodynamic point of view the transition $\alpha,\beta\text{-ZPT} \rightarrow \alpha,\beta\text{-ZPD}$ is of second order and that the transition $\alpha,\beta\text{-ZPD} \rightarrow \alpha,\beta\text{-ZPA}$ is of first order. Indeed during the dehydration reaction the heat capacity difference ΔC_p displays a double inflexion point (critical temperatures corresponding to a gain or loss of entropy) at 175°C and 188°C (heating rate β : $10\text{ K}\cdot\text{min}^{-1}$) for the dehydration reaction $\alpha\text{-ZPT} \rightarrow \alpha\text{-ZPD}$ in Fig. 3.14 A. Similarly one can find 173°C and 184°C for the dehydration reaction $\beta\text{-ZPT} \rightarrow \beta\text{-ZPD}$ (Fig. 3.14 C). On the opposite broad transition peaks are observed for both α - and β -hopeite regarding the second dehydration reaction: $\text{ZPD} \rightarrow \text{ZPA}$. Therefore one should investigate separately the two dehydration reactions as two consecutive step reactions: first $\text{ZPT} \rightarrow \text{ZPD}$ and secondly $\text{ZPD} \rightarrow \text{ZPA}$.

This conclusion is reaffirmed by the following experiment: if one heats independently α - and β -hopeite to 220°C for at least 24 hours, stability temperature of zinc phosphate dihydrate, and cools to room temperature the obtained structures, the obtaining of a single broad dehydration peak either in DTGA or DSC at around 260°C and 280°C (see Fig. 3.15 A and Fig. 3.15 B,C) is a proof first that only the-one step reactions $\beta\text{-ZPD} \rightarrow \beta\text{-ZPA}$ and $\alpha\text{-ZPD} \rightarrow \alpha\text{-ZPA}$ take place respectively, and secondly that one must consider the dehydration of zinc phosphate tetrahydrate polymorphs as a

two step reaction with different thermodynamic and kinetic properties for each step reaction. As accurately suggested by Ashcroft [109] one may confirm this in further measuring the partial saturating vapour pressure generated by sublimation of crystal water after the first dehydration of ZPT at 220°C.

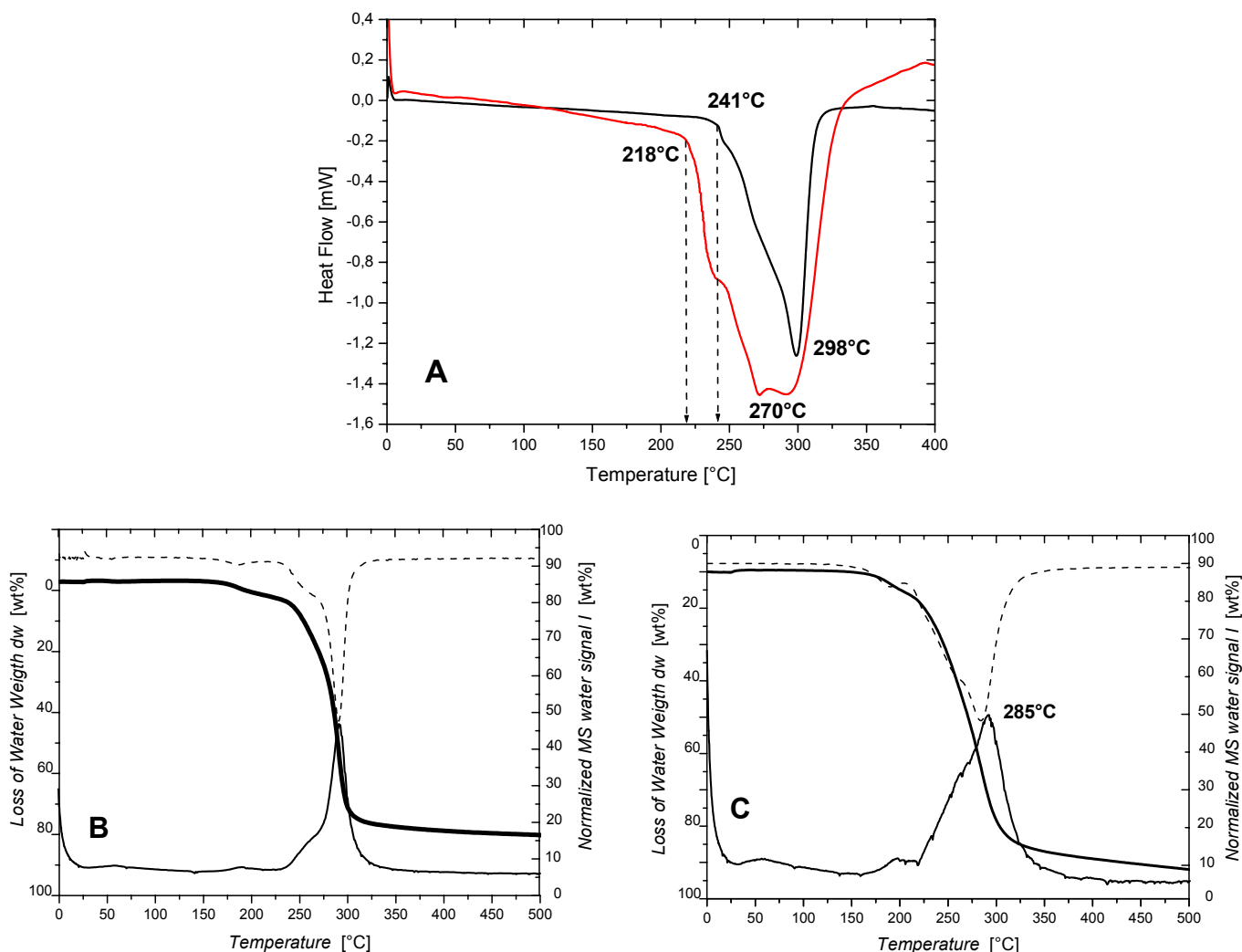


Figure 3.15: (A) DSC curves and (B) TGA-MS curves taken at a heating rate of 10 K.min⁻¹ of α -ZPD (black) and β -ZPD (red) obtained from isothermal dehydration of α -ZPT and β -ZPT at 220°C for 24 hours. TGA-MS curves of (B) α -ZPD and (C) β -ZPD also taken at 10 K.min⁻¹. Weight Loss (thick line), First order derivate (dash line) of the weight loss curves and MS water signal (m/z : 18, dark line) are given as normalized to 100%. This corresponds to the loss of two water molecules for the zinc phosphate dihydrate samples.

3.4.4. Comparison of the thermal stability of zinc phosphate hydrates

The standard enthalpies ($\Delta H^{\text{dehydr.}}$), entropies ($\Delta S^{\text{dehydr.}}$) and free energies ($\Delta G^{\text{dehydr.}}$) of dehydration of the zinc phosphate tetrahydrates to anhydrites, depending on their crystallographic phase, have

been generated from independent DSC measurements in averaging over 8 runs at linear increasing heating rates [0.5, 1, 2, 5, 10, 15, 20, 25 K.min⁻¹] as shown in Figure 3.16.

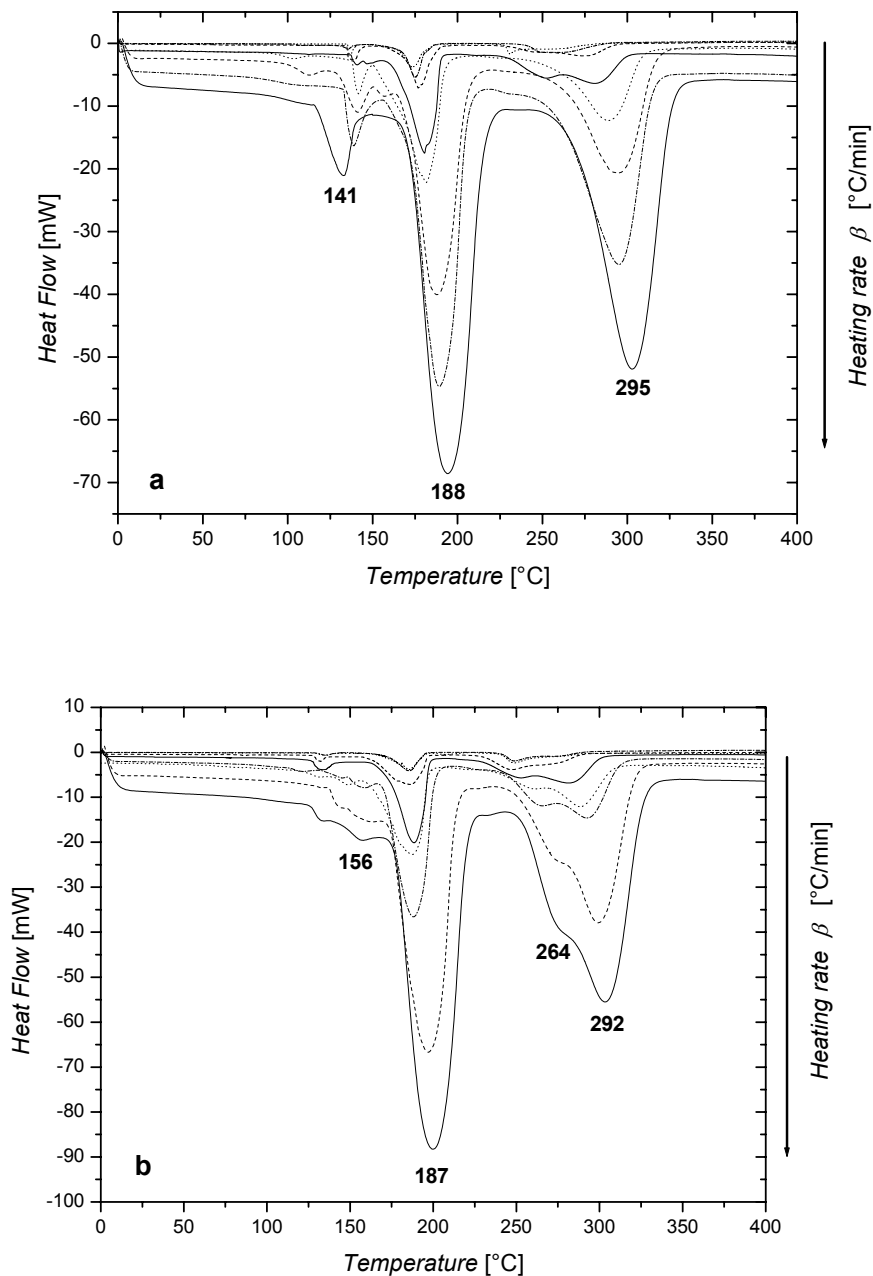


Figure 3.16: Characteristics DSC thermograms of: (a) α -hopeite and (b) β -hopeite at various heating rates (25, 20, 15, 10, 5, 2, 1, 0.5 K.min⁻¹). Peak temperatures measured at 10°C.min⁻¹ are also given.

In a simple approximation one can notice that the values of ΔH , ΔS and ΔG are linearly dependent of the heating rate as shown in Fig. 3.17. This means that before and after the dehydration, the heat capacity of the product and educt (for example α -ZPD and α -ZPT in the reaction α -ZPT \rightarrow α -ZPD +

$2\text{H}_2\text{O}$) are constant with the temperature. However during dehydration, a change of entropy is observed and the heat capacity varies as shown in Fig. 3.14 B.

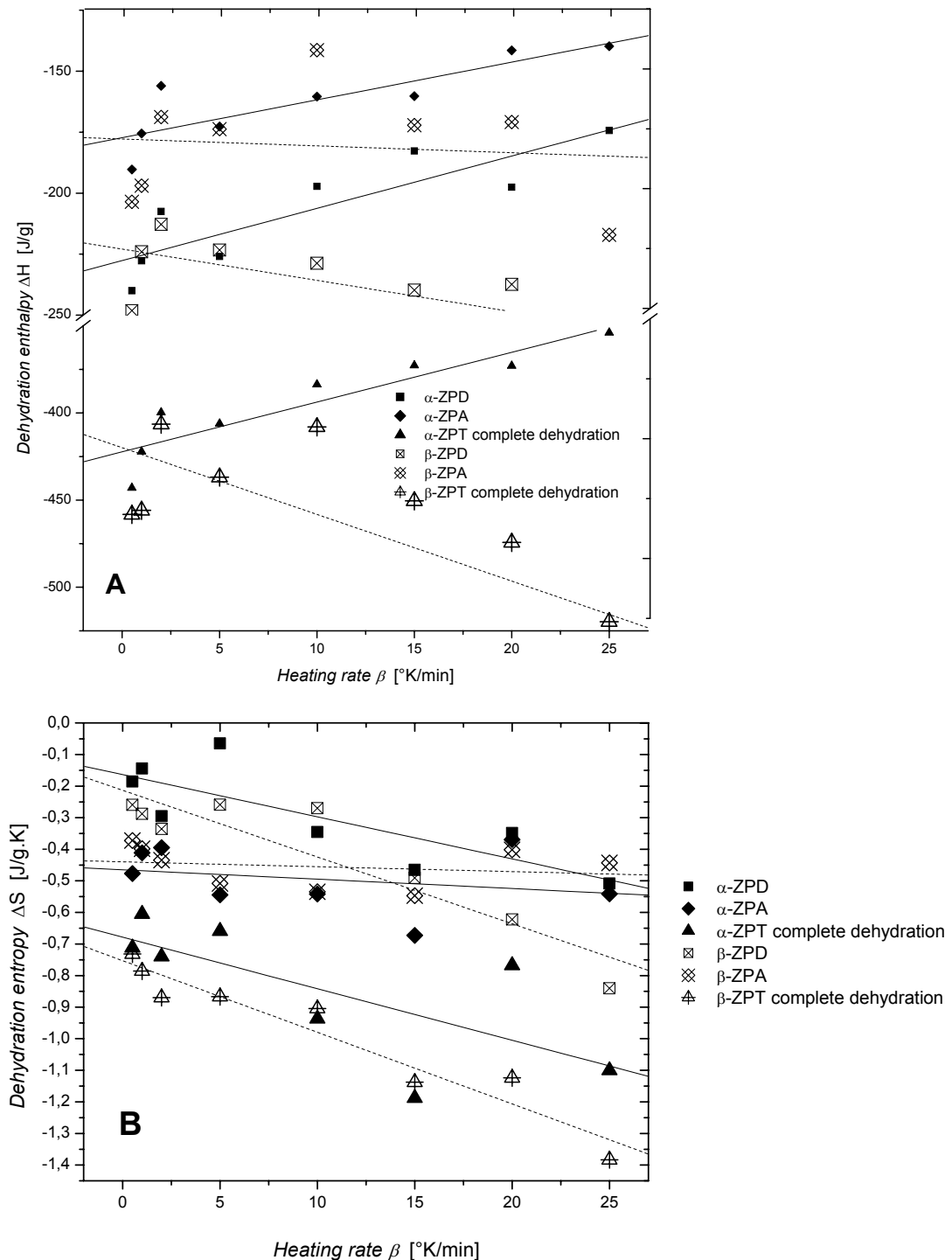
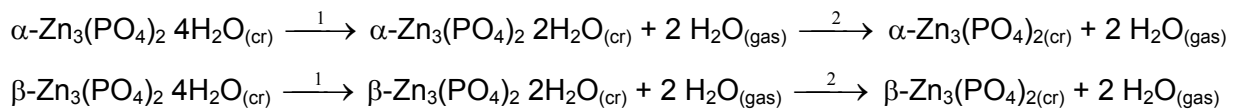


Figure 3.17: Master curves of the enthalpy (A) and the entropy (B) of dehydration for the two successive step reactions $\text{ZPT}_{cr} \rightarrow \text{ZPD}_{cr} + 2\text{H}_2\text{O}_g$ and $\text{ZPD}_{cr} \rightarrow \text{ZPA}_{cr} + 2\text{H}_2\text{O}_g$.

By extrapolation to zero heating rate from Figure 3.17 A,B , it is possible to obtain the values of the thermodynamic state functions at the transition temperatures, using the Kirchoff's equation. These values of ΔH , ΔS and ΔG calculated at transition temperature are similar to the solubilisation

enthalpies obtained for by McAra et al. [110] for a rehydration from $\text{Zn}_3(\text{PO}_4)_2 \cdot 2\text{H}_2\text{O}_{(l)}$ to $\text{Zn}_3(\text{PO}_4)_2 \cdot 4\text{H}_2\text{O}_{(cr)}$. Surprisingly, by selective dissolution reaction calorimetry, Yaglov [111-112] and then Volkov [113-114] obtained separately a set of thermodynamical data for α, β -hopeite (α, β -ZPT or α, β -tetrahydrate) that vary as much as 25% with our measured $\Delta H^{\text{dehydr.}}$ values, especially concerning the dihydrate state (α, β -ZPD or α, β -dihydrate) (Table 3.3). This is certainly due to impurities contained in the starting material (zinc oxide, zinc hydrogen phosphate). This could also originate from the “same final thermodynamic state” procedure, described as a solid-liquid reaction, while the present method use a solid-gas reaction ($\Delta H^{\circ}_{\text{form.}}(\text{H}_2\text{O}) = -241.8 \text{ kJ}\cdot\text{mol}^{-1}$, $S^{\circ}_{\text{form.}}(\text{H}_2\text{O}) = -228.6 \text{ J}\cdot\text{mol}^{-1}\cdot\text{K}^{-1}$) [115-117] as shown hereunder in the two-step solid-gas reactions mechanism:



Further Dollimore [118] discussed the pertinence of the choice of this type of solid state reaction based on structural considerations (surface effects and negation of the concept of rigid structure)

Table 3.3: Extrapolated thermodynamic values of dehydration process from DSC curves at a heating rate β of zero $\text{K}\cdot\text{min}^{-1}$ given at transition temperature for the two zinc phosphate tetrahydrate polymorphs.

Hydration state of crystals	Transition temp. T_{max} [$^{\circ}\text{C}$]	$\Delta H^{\text{dehydr. c}}$ [kJ/mol]	$\Delta H^{\text{dehydr. Lit c}}$ [kJ/mol]	$\Delta S^{\text{dehydr. c}}$ [kJ/mol.K]	$\Delta G^{\text{dehydr. d}}$ [kJ/mol]	$\Delta G^{\text{dehydr. Lit}}$ [kJ/mol]
α -dihydrate ^a	174.7	-111	-102 ^e	-0.33	36	30
α -anhydrate	266.1	-75	-125 ^e	-0.20	32	29
β -dihydrate ^b	184.6	-105	-94 ^f	-0.30	30	29
β -anhydrate	277.5	-75	-120 ^f	-0.19	27	27

(a) mass of zinc phosphate tetrahydrate in vacuo : 458.11 g/mol.

(b) mass of zinc phosphate dihydrate in vacuo : 422.11 g/mol.

(c) estimated errors $T \pm 0.1^{\circ}\text{C}$, $\Delta H \pm 0.5 \text{ kJ}\cdot\text{mol}^{-1}$.

(d) ΔG calculated at transition temperature, experimental error $\pm 1.0 \text{ kJ}\cdot\text{mol}^{-1}$.

(e) from references [79,86].

(f) from references [77, 79].

A certain fluctuation of the results may also arise from the considered molecular weight of the various involved products of reaction. Here are considered the following molecular weight $M(\text{ZPT})$: $487.57 \text{ g}\cdot\text{mol}^{-1}$, $M(\text{ZPD})$: $422.57 \text{ g}\cdot\text{mol}^{-1}$, $M(\text{ZPA})$: $356.59 \text{ g}\cdot\text{mol}^{-1}$.

One should conclude first that the enthalpy plays a very limited role as one component of the global transition energy at the transition temperature, due to the primary involvement of thermal breaking of a few hydrogen bonds in the crystal structure, thus allowing a direct comparison of the relative thermodynamic stabilities between α - and β -hopeite. As a strong parallel, α - and β - $\text{Ca}_3(\text{PO}_4)_2$ (α, β -

TCP) originating from the dehydration of Hydroxyapatite [119-121] have not only nearly identical free energy as α,β -hopeite (-4120/-4109 in comparison with -4102/-4091 kJ.mol⁻¹) [122], but also possess similar entropy (0.249/0.236 kJ.mol⁻¹.K⁻¹ for α,β -TCP). Secondly, the enthalpy has a preponderant influence in that process at 25°C. One can assume the obtaining of the same anhydrate state from α - and β -hopeite (tetrahydrates) (see Figure 3.18) since Stephens and Calvo [123] showed that there is a reversible crystallographic interconversion between the α -Zn₃(PO₄)₂ and the β -Zn₃(PO₄)₂. Using carefully this assumption and based on the measured variations of ΔH^{dehydr} (Table 3.4), the stability difference for the α -, β -form of dihydrate and tetrahydrate are evaluated to 6.1 and 31.1 kJ.mol⁻¹ respectively. These values are significantly higher than the experimental error and once again in good agreement with the estimates from the early works of McAra et al. They obtained respectively 4.1 and 5.4 kJ.mol⁻¹. Finally, the comparison of this set of data with the numerous values published in the literature [124-127] seems to point out that the transitions of dehydration are involving a strong surface effect due to the similarities between our measured values for a dehydration in the crystalline state (in contact with argon) and those of I.W. McAra et al. for the rehydration of a crystal immersed in a concentrated H₃PO₄ solution or in liquid water. In Table 3.4, the marked differences of absolute entropy of formation for the α - and β -forms of zinc phosphate tetrahydrates/dihydrates first prove that the α -form is more stable than the β -form, due to the lower entropy (i.e an higher absolute value of $|\Delta S_{\text{dehydr.}}|$) entropy of the α -form, and secondly in correlation with the ΔS^{dehydr} of Table 3.3 that the crystal order is partly (up to 50% stat.) assured by hydrogen bonding.

Table 3.4: Standard thermodynamic values of formation of zinc orthophosphates and its hydrates, calculated from dehydration reaction at 25°C.

Hydration state of crystals	$\Delta H^{\circ}_{\text{form.}}$ [kJ.mol ⁻¹]*	$\Delta H^{\circ}_{\text{form. Lit}}$ [kJ.mol ⁻¹]*	$\Delta G^{\circ}_{\text{form}}$ [kJ.mol ⁻¹]*	$\Delta G^{\circ}_{\text{form Lit}}$ [kJ.mol ⁻¹]*	S°_{form} [J.mol ⁻¹ .K ⁻¹]*
α -tetrahydrate	- 4086	- 4093 ^a	- 3613	-3628 ^f	253
β -tetrahydrate	- 4055	- 4091 ^c	- 3605	- 3616 ^f	291
α -dihydrate	- 3486	- 3492 ^a	- 3126	-	451
β -dihydrate	- 3480	- 3487 ^a	- 3120	-	477
anhydrate	- 2891 ^b	- 2891 ^d	-	- 2633 ^e	779 ^g

(a) from Ref. [128].

(b) recalculated from Ref. [21] using $\Delta H^{\circ}_{\text{form}}[\text{ZnO,c}] = -350.4$ kJ.mol⁻¹ and $\Delta H^{\circ}_{\text{form}}[\text{PO}_4^{3-},\text{liq.}] = -1277.4$ kJ.mol⁻¹

(c) from Ref. [125].

(d) from Ref. [85].

(e) from Ref. [83].

(f) from ref. [126].

(g) recalculated from Ref.[87] for a ionic crystal using $S^{\circ}_{\text{form}}[\text{Zn}^{2+}] = 153.8$ J.mol⁻¹.K⁻¹ and $S^{\circ}_{\text{form}}[\text{PO}_4^{3-}] = 159.0$ J.mol⁻¹.K⁻¹

(*) estimated errors $T \pm 0.1^{\circ}\text{C}$, $\Delta H \pm 0.5$ kJ.mol⁻¹, $\Delta G \pm 1.0$ kJ.mol⁻¹ and $S^{\circ} \pm 4$ J.mol⁻¹.K⁻¹

It is now possible to describe a thermal stability diagram of the two forms of hopeite as they dehydrate and compare their relative stability with those of zinc phosphate dihydrate and anhydrate. Figure 3.15 describes the thermodynamic interrelation between the three types of zinc phosphate

hydrate. With increasing temperature, the crystal structures are more and more ordered since their entropy of formation increases as shown in Table 3.4, but their crystal structure display less symmetry elements: ZPT/orthorhombic \rightarrow ZPD/monoclinic \rightarrow ZPA/mono-clinic [129-130]. The following order of decreasing thermodynamic stability ($\Delta G^{\text{formation}}$) is thus obtained:

$$\begin{array}{ll} \text{Hydration state:} & \text{ZPD} > \text{ZPD} > \text{ZPA} \\ \text{and polymorphy:} & \alpha\text{-form} > \beta\text{-form} > \gamma\text{-form} \quad [123,131] \end{array}$$

On the basis of the close connection between thermal stability and hydrogen bond strength, one may conclude that the evaluation of the activation energy of dehydration is a direct measure of the hydrogen bond strength, thus confirming the crystallographic and thermodynamic interrelation of α - and β -zinc phosphate tetrahydrates.

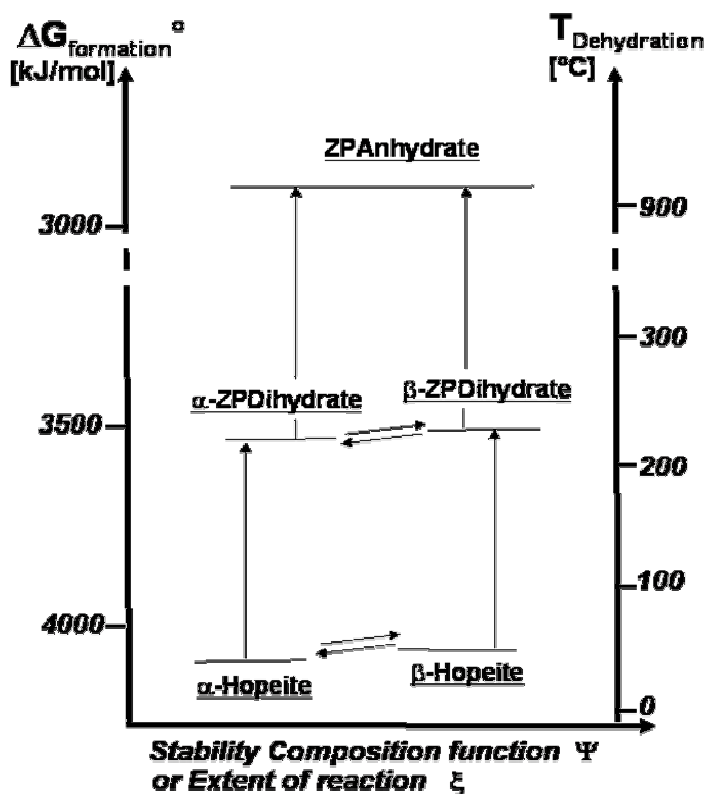


Figure 3.18: Scheme describing the thermodynamic interrelationship between polymorphy and hydration state of the most stable zinc phosphate phases. Note the thermodynamic interconversion from a β -form to an α -form for a given hydration state.

3.5. Kinetics of dehydration of zinc phosphate tetrahydrates

3.5.1. Non-isothermal methods

Non isothermal methods are widely used to investigate the kinetics of thermal decomposition

reactions. Among the numerous advantages already described in § 3.4.1 of this procedure compared to conventional isothermal studies is that the reaction onset temperature can be determined very precisely and therefore the zero-time error is absent. Hence a considerable portion of the sample is likely to undergo some reaction during the initial heat-up of isothermal experiment, particularly when the onset of reaction is lower than the isothermal temperature. This is particularly true for the dehydration of hopeite starting around 130°C with a dehydration reaction observed only in a reasonable measurement window around 180°C. In this case the degree of advancement or degree of conversion X will not be zero at $t = 0$ for an isothermal experiment. However a decided disadvantage of non-isothermal compared with isothermal methods is the uncertainty surrounding the determination of the reaction mechanism, and hence the meanings of the activation energy, the order of reaction and the frequency factor.

3.5.2. Heterogeneous solid state reactions

While most crystallographic phase transitions and decomposition reactions proceed rapidly, others like the dehydration reaction of zinc phosphate may evolve gently under controlled heating rate. One of the most frequently quoted approaches is that of Borchardt and Daniels [132-134] for homogeneous reactions. Therein must be “systems in the liquid phase” understood. Six assumptions must be made: (i) the homogeneity conditions. This means that the temperature of the sample and the reference are considered to be uniform. However in solids, since a propagating temperature front proceeds from the surface inward in solids, the uniform temperature assumption is out of question and therefore the extension to solids of the Borchardt and Daniels is automatically void; (ii) the heat-transfer coefficients of the reactants and products are equal; (iii) the heat capacities of the reactants and products are equal; (iv) the above-mentioned quantities and the heat of reaction do not change over the temperature range of reaction. Assumption (ii) depends greatly of the nature of the material, as just in solids the nature of the solid interfaces governs dramatically the dehydration reaction. Assumption (iii) is not reasonably valid in the zinc phosphate system, since one may suppose that the possible simultaneous coexistence of two phases (for example ZPT and ZPD) which have very different heat capacities. Assumption (iv) is related to this last effect, since desolvation and desorption (in liquids) and moreover (water) desorption from the solid surface would be temperature-sensitive. Assumption (v) describes that the heat effect as measured by DTA is proportional to the number of molecules reacting in unit time on the basis that assumption (i) is verified. This may be true in a liquid state where two reacting molecules A and B may diffuse and combine (described by a frequency factor) but not in a solid state. Assumption (vi) stipulates that a reaction kinetics can be described by a single rate constant and the activation energy does not vary with temperature. Therefore, the dehydration reaction of more complicated solid systems such as zinc phosphate hydrates may be approached as a *heterogeneous*

decomposition reaction and the simple theory of Borchardt and Daniels must not be applied. Subsequently, specific theories for solid state reactions have been written and are introduced in § 3.5.5.3.

3.5.3. Degree of conversion and basic kinetic equation

The foundations for the calculation of kinetic data from a DTGA or a DSC curve are similar and based on the formal kinetic equation with an empirical reaction model of order n :

$$-\frac{dX}{dt} = k(T) \cdot f(X) = k(T) \cdot X^n \quad (3.12)$$

where X is the degree of conversion, i.e. the (relative) amount of sample undergoing reaction, n is the order of reaction and k the specific rate constant. As pointed out by Sestak [135] this equation describes very well the thermal decomposition of solids, such as endothermic reactions of metal oxalate and the dehydration reactions. The relationship of X to the weight-loss, w (i.e. dm) is described here:

$$-dX = \frac{w_0}{w_\infty} \cdot dw \quad (3.13)$$

where w_0 is the initial mass of the sample and w_∞ is the maximal mass loss. By integration of this equation it follows for a time window t_i or a temperature interval of measurement T_i :

$$X = X_i = \frac{w_\infty}{w_0} \cdot (w_\infty - w_i) \quad (3.14)$$

The temperature dependence of the specific rate constant is expressed by the Arrhenius equation:

$$k = A \cdot \exp(-E_a/RT) \quad (3.15)$$

where A is the preexponential factor, E_a is the activation energy and R is the gas law constant.

The mathematical treatment of kinetic equations generally makes use of one of the following three methods of evaluation: (1) differential, (2) integral, (3) approximate. By substitution of the equations (3.14) and (3.15) into equation (3.12), and by differentiation the logarithmic form, an expression is obtained which is the fundament of the differential methods: the Freeman and Carroll method [136]. In opposition integral methods use the integrate form of equation (3.12) after the transposition of the mass-loss w in the equations (3.14) and (3.15).

$$\left(\frac{w_0}{w_\infty}\right)^{1-n} \int_0^w (w_\infty - w)^{-n} dw = \frac{A}{\Phi} \cdot \int_{T_i}^{T_f} \exp\left(\frac{-E_a}{RT}\right) dT \quad (3.16)$$

The right-hand side is generally resolved numerically and the solution is an infinite series of which the first two terms are often considered. This is the fundament of the methods developed by Doyle [137] and Coats and Redfern [138]. Approximation methods, developed by Horowitz and Metzger

[139] solve equation (3.16) by an approximation using the temperature T_m , corresponding to the maximum dehydration rate.

3.5.4. Classical empirical methods of kinetic analysis

3.5.4.1. Dehydration reactions of first order – Newkirk method

From a set of single TGA curve taken at different heating rates, Newkirk [140] obtained rate constants or the dehydration reaction as illustrated in Figure 3.19. For a series of temperature T_1 and T_2 , the sample mass remaining w_0-w_1 and w_0-w_2 (i.e. X_1 and X_2 in DTGA) and corresponding dehydration rate $(dw/dt)_1$ and $(dw/dt)_2$ (i.e. $(dX/dt)_1$ and $(dX/dt)_2$ in DTGA), were obtained by tangents to the curve at time t_1 and t_2 (i.e. temperatures T_1 and T_2) This method is often used since it allows evaluating quickly in first approach the kinetic order of reaction n , and therefore serves as *first criterion* for evaluating if a reaction kinetics is of first order or not. If the reaction is kinetically of first order, with a kinetic equation similar to:

$$\frac{dX}{dt} = \beta \cdot \frac{dX}{dT} = kX \quad (3.17)$$

then the logarithm of the reaction rate constant k , when plotted against $1/T$ should yield a straight line. For increasing heating, these lines should be parallel.

The method of Newkirk was extended to reactions of kinetic order higher than one by Reich and Stilava [141]. The same principle, requiring two pairs of values of X and T , applied to equation (3.19) allows calculating the activation energy for arbitrary selected values of n . The resulting arbitrary values of E_a may be plotted against corresponding values of n and the region bounded by intersecting curves used simultaneously to estimate actual values of E_a and n . When this process is repeated for different heating rates, one may distinguish different reaction mechanisms involved in the dehydration process. For a pair of values of X and T ,

$$\text{Log} \left[\frac{1 - (1 - \alpha_1)^{1-n}}{1 - (1 - \alpha_2)^{1-n}} \cdot \left(\frac{T_2}{T_1} \right)^2 \right] = \frac{E_a}{R} \cdot \left(\frac{1}{T_1} - \frac{1}{T_2} \right) \quad (3.18)$$

Hence the frequency factor can be calculated depending on the heating rate β from this equation for given values of X and T . It comes:

$$\text{Ln } K = \text{Ln} \left[\frac{1 - (1 - X)^{1-n}}{T^2} \right] + \frac{E_a}{RT} \quad \text{and} \quad K = \frac{A(1-n)R}{\beta E_a} \quad (3.19-3.20)$$

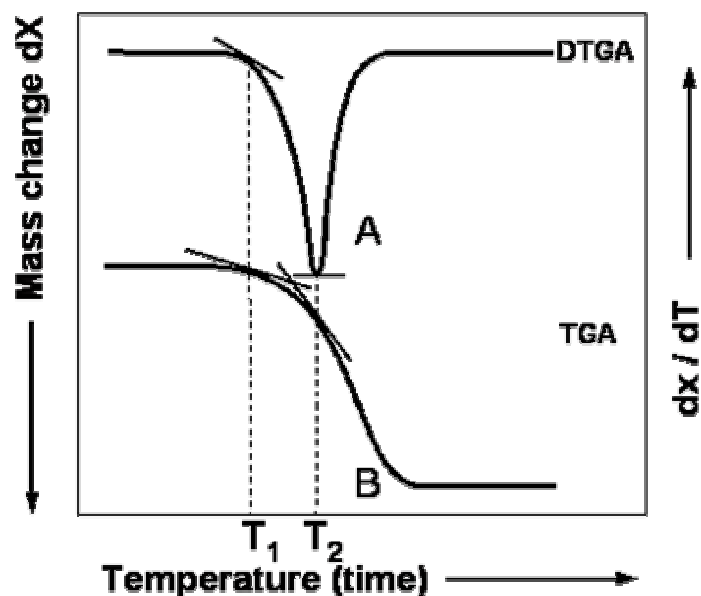


Figure 3.19: Determination of the reaction rate, the extent of reaction from a DTGA curve. Criteria of Newkirk for a dehydration reaction with a first order kinetics.

Reich and Stilava [142] further extended the preceding method to the different solid state reaction mechanisms (§ 3.5.5.3) [143-144] using an iteration technique [145] and various algorithms [146-147].

3.5.4.2. Differential method of Freeman and Carroll (FC method)

The most widely used kinetics method was developed by Freeman and Carroll in 1958 [148]. The advantage of this method is to consider a kinetics over an entire temperature range in a continuous manner without any missing regions. Therefore the kinetic transition between the two step reactions $ZPT \rightarrow ZPD$ and $ZPD \rightarrow ZPA$ can be investigated. In addition, where a sample undergoes a considerable reaction of dehydration in being raised to the temperature of interest (i.e. $T_{\text{dehydration}}$), the results obtained by isothermal method are often questionable. The order of reaction n , and the activation energy E_a are calculated from the following equation in using the definition given in the relation (3.13):

$$-(E_a/2.306 R) \cdot \frac{d(1/T)}{d\text{Log}w_r} = -n + \frac{d\text{Log}(dw/dt)}{d\text{Log}w_r} \quad (3.21)$$

where $w_r = w_c - w$, in which w_c is the maximum mass-loss.

3.5.4.3. Approximate method of Kissinger

Kissinger [149-150] developed a method relating the shape of a DSC or DTGA peak to the order of the decomposition kinetics. To his point of view for a quasi-steady state heating, the local heating

rate fluctuations is related to the local temperature or heat flow fluctuations in a solid sample for a fixed sample geometry, as follows:

$$\frac{dT}{dt} = f\left(\frac{d\beta}{dt}\right) \cdot \frac{d^2\beta}{dt^2} \quad (3.22)$$

Since $d^2\beta/dt^2 = 0$ implies maximum rate of reaction and $dT/dt = 0$ a maximum temperature (i.e. heat flow) variation, the peak deflection in the DSC must occur at the maximum rate of reaction. However this method ascertains that homogeneity condition is validated in the vicinity of the thermocouple and at ZP crystal surface and that no effect of partial supersaturating water pressure (one dimensional diffusion mechanism) on the heating rate fluctuations is occurring. Differentiating the expression of Valuska and Voboril (see equation 3.28) and setting the expression to zero, Kissinger obtained:

$$\frac{E_a}{RT_{peak}^2} = \left(\frac{An}{\beta}\right) \cdot (1 - \alpha_{prak})^{n-1} \cdot \exp(-E_a/RT_{peak}) \quad (3.23)$$

This expression means that the order of dehydration n becomes smaller as the quantity of material dehydrated at T_{peak} diminishes. A modified form of this expression is given in equation (3.7) for $n=1$. For $n \neq 0$ (reversible transformation) and $n \neq 1$, an approximated expression of equation (3.23) has been given:

$$n \cdot (1 - \alpha_{peak})^{n-1} \approx 1 + (n-1) \left(\frac{2RT_{max}}{E_q}\right) \quad (3.24)$$

Employing various substitutions, Kissinger finally proved that equation (3.7) was independent of the order of reaction. Therefore, from the variation of α at T_{peak} with the order of reaction, Kissinger proposed to evaluate n from a "shape index" S of the DSC or DTGA peak. This parameter defines the absolute ratio of the slope of the tangents to the DSC peak at the inflexion points so as given in Figure 3.20,

$$\begin{cases} S = a/b \\ n = 1.26 \cdot S^{1/2} \end{cases} \quad (3.25-3.26)$$

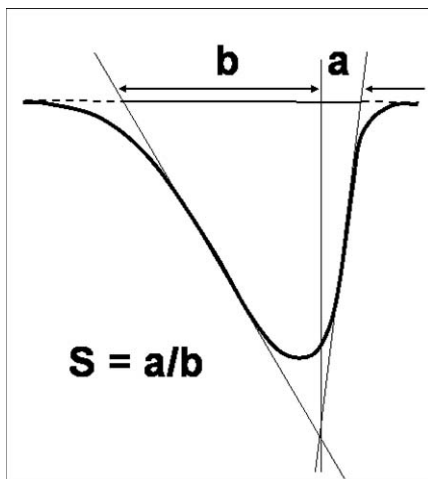


Figure 3.20: Method of Kissinger for measuring the asymmetry in an endothermic DSC peak, and deducing an order of reaction n .

Kissinger may be used as a rough guide to determine the apparent order of the dehydration reactions of zinc phosphate hydrates.

3.5.4.4. Approximate method of Coats and Redfern (CR method)

For a reaction in which the kinetic order is unknown, Coats and Redfern [151] derived the following expression:

$$\text{Log} \left\{ \frac{1 - (1 - X)^{1-n}}{T^2 \cdot (1-n)} \right\} = \text{Log} \left(\frac{AR}{\beta E_a} \cdot \left[1 - \frac{2RT}{E_a} \right] \right) - \frac{E_a}{2.306 RT} \quad (3.27)$$

Reporting the left-arm of this expression for increasing heating rates against $1/T$ leads to straight lines of slope $-E_a/2.306 R$ for the correct value of n . Generally, the quantity $\text{Log} (AR/\beta E_a [1-2RT/E_a])$ appears to be reasonably constant in the temperature range over which the dehydration reaction occurs.

Sharp and Wentworth [152] evaluated this method for the thermal decomposition of calcium carbonate under various conditions and concluded that this method best suited for diffusion-controlled and order-of-reaction mechanisms. Further Galladher and Johnson [153] found for the same reaction that this method fits well the contracting geometry law and the Avrami-Erofeev mechanism for $n = 2$. Besides, in investigating the dehydration kinetics of calcium oxalate hydrate, Callada compared two methods based on the maximum rate temperature such as the Kissinger and the Carroll, and concluded that these two methods could not distinguish between overlapping reactions or mechanisms. For example, Criado [154] found that it was impossible in the Coats and Redfern method to distinguish between an interface chemical reaction-controlled mechanism (called R_3) and the three dimensional Jander-diffusion mechanism (called D_3).

3.5.4.5. Corrected Integral method of Valuska and Voboril (VV method)

The main advantage of this method [155] is to consider fully the validity of the Arrhenius equation in taking into account the thermal effects of the dehydration reactions which result in a deviation of the sample temperature from the programmed values of the linear heating. Further taking into account the fact all zinc phosphate tetrahydrate (ZPT) crystals do not dehydrate at the same decomposition rates, ZPT and ZPD products may coexist below 230°C and similarly ZPD and ZPA may coexist below 350°C (see Fig. 3.13). Very often this is the case for thick crystals like the zinc phosphate hydrate samples. Papazian [156] and then Andonyi [157] approaches therefore describe the specific rate constant as dependent of the unconverted fraction $(1-X)$. Starting from the differential equation:

$$-\frac{dX}{dt} = A(1-X)^n \cdot \exp\left[\frac{-E_a}{RT}\right] \quad (3.28)$$

one finds that by differentiating with respect to the time and considering that the degree of conversion X and the temperature T are function of time (i.e. evaluation of the local fluctuations of the heating rate),

$$\frac{d^2X/dt^2}{dX/dt} = -\frac{n}{1-X} \left(\frac{dX}{dt}\right) + \frac{E_a}{RT^2} \left(\frac{dT}{dt}\right) \quad (3.29)$$

By rearrangement a linear equation is obtained by means of which the reaction order n can be calculated from the slope with precision and the intercept gives the activation energy. This method yields to kinetic results astonishingly close to those obtained from isothermal measurements.

3.5.4.6. Integral method of Doyle

Doyle [158] discussed in detail the kinetics of volatilization of polymers. This can be applied to crystal powders, which contain hydration water that may be easily destabilized and evaporated.

If Y is the apparent mass fraction calculated on the initial mass, the apparent mass fraction evaporated Y is : $Y = 1-w$. The apparent evaporation rate is found to by multiplying the TGA curve slop $-dw / dT$ by the constant heating rate β . However for a particular dehydration step the appropriate residual mass fraction is the exact one, defined from the area of the DTGA peak and calculated on the total fraction α volatilized during the step , rather than on the initial mass:

$$\alpha = \frac{w-G}{H} \quad (3.30)$$

where H is the total apparent mass fraction volatilizing during the dehydration step and G is the apparent weight fraction remaining after the step has been completed. One should note that in the case of crystal dehydration reaction, α may be assimilated to X defined in equation (3.14)

$$\frac{dY}{dt} = -H \cdot \frac{d\alpha}{dt} \cong -\beta \cdot \frac{dw}{dt} \quad (3.31)$$

Another difficulty arises from the need to take into account the nature of the kinetic process. In general, applying the Arrhenius equation for the dehydration process it comes:

$$-\frac{d\alpha}{dt} = k_\alpha(T) \cdot f(\alpha) = A \cdot \exp\left(\frac{-E_a}{RT}\right) \cdot f(\alpha) \quad (3.32)$$

where $f(\alpha)$ is a function describing numerically the DTGA curve. $f(\alpha)$ is strongly related to a reaction mechanism. For example, for a parabolic law, $\alpha^2 = kt$, which applies to many diffusion controlled reactions, $f(\alpha) = \alpha/2$.

Zsako [159] has attempted to simplify Doyle's trial-and-error method of $f(\alpha)$ by linearizing the Arrhenius equation a discretized temperature range:

$$p(\alpha) = \frac{AE_a}{R\beta} f(\alpha) \quad (3.33)$$

and taking the logarithm, one obtains,

$$\text{Log} \frac{AE_a}{R\beta} = \text{Log} p(\alpha) - \text{Log} f(\alpha) = B \quad (3.34)$$

where B depends only of the nature of the sample (via A and E_a) and on the heating rate. This method ensures that the activation energy is obtained with a maximum of consistency regarding to B since on a selected temperature range. By varying the heating rate, one can separate parallel reactions occurring with different kinetics (rate determining step).

3.5.4.7. Integral method of Friedman

Friedman [160] proposed to use an isoconversional approach (§ 3.5.5.1) based on the following relationship:

$$\text{Ln} \left(\frac{d\alpha}{dt} \right) = -\frac{E_a}{RT} + \text{Ln}[A \cdot f(\alpha)] \quad (3.35)$$

which may be converted to:

$$\text{Ln} t = \frac{E_a}{RT} + \text{Ln}[g(\alpha)/A] \quad (3.36)$$

If one consider values of $d\alpha/dt$, T and t , at which in different DSC experiments the same value of the degree of conversion is reached ($\alpha = \alpha_k = \text{constant}$), the activation energy can be calculated from the slope of the linear relationship $\text{Ln} (d\alpha/dt)_{ik}$ versus $1/T_{ik}$ or $\text{Ln} t_{ik}$ versus $1/T_{ik}$

3.5.4.8. Integral method of Ozawa

Ozawa [161] proposed an approximate integral method similar to, but much simpler than, that of Doyle. Besides, Ozawa found that the Freeman and Carroll, the Coats and Redfern and the Sharp methods cannot be applied to second-order reactions, scission of polymer chains or a system of two parallel competitive first-order reactions [162]. In his method the fractional weight w , of a reacting material, here a zinc phosphate tetrahydrate, is expressed as a fraction of a structural quantity such as four departing water molecules two by two, which is represented by α :

$$w = h(\alpha) \quad (3.37)$$

where x changes according to the kinetics described in equation (3.23). By integration of equation (3.23) for various heating rates β , it follows:

$$-\int_{\alpha_0}^{\alpha} \frac{d\alpha}{f(\alpha)} = \frac{A}{\beta} \cdot \int_{T_0}^T \exp\left(\frac{-E_a}{RT}\right) dT \quad (3.38)$$

where α is equal to the value of α_0 and T to the value of T_0 at $t = t_0$ (onset of dehydration). The two following approximations are made:

(i) Ordinary, the rate of reaction (dehydration) is very low at low temperature

(ii) The value of the right-hand side in equation (3.34) is expressed by Doyle as a function $p(\alpha)$

Thus it appears:

$$\int_{T_0}^T \exp\left(\frac{-E_a}{RT}\right) dT \stackrel{(i)}{=} \int_{T_0}^T \exp\left(\frac{-E_a}{RT}\right) dT \stackrel{(ii)}{=} \frac{E_a}{R} \cdot p\left(\frac{E_a}{RT}\right) \quad (3.39)$$

The boundary condition is then, that if a weight fraction decreases at a temperature T_1 for a heating rate β_1 , at T_2 for β_2 , and so on, at T_i for β_i , the equation obtained by combination of (3.38) and (3.39) is:

$$\frac{AE_a}{\beta_1 R} \cdot p\left(\frac{E_a}{RT_1}\right) = \frac{AE_a}{\beta_2 R} \cdot p\left(\frac{E_a}{T_2}\right) = \frac{AE_a}{\beta_i R} \cdot p\left(\frac{E_a}{RT_i}\right) \quad (3.40)$$

Ozawa proposed that for E_a/RT larger than 20, $p(E_a/RT)$ may be approximated (developed in series only to the first order) with:

$$\text{Log } p\left(\frac{E_a}{RT}\right) \approx -2.315 - 0.4567 \frac{E_a}{RT} + o(T) \quad (3.41)$$

Thus using the expressions (3.38) and (3.39) the $\text{Log } \beta$ versus $1/T$ for a given value of w (i.e. α) must be a straight line, from which slope the activation energy may be determined. If the TGA curves (i.e. DTGA curves) are given as plot of w or $f(\alpha)$ versus $1/T$, the curves superimpose upon each by shifting them along the abscissa proportionally to the logarithm of the heating rate of the considered curve [163-164].

3.5.4.9. Flynn-Wall Ozawa integral method (WFO method)

Flynn and Wall [165] and then Ozawa [166] have proposed a method, the so-called FWO method, based on the following equation:

$$\text{Ln } \beta = -1.05 \frac{E_a}{RT} + \text{Ln}\left(\frac{E_a}{RT}\right) - 5.33 - \text{Ln } g(\alpha) \quad (3.42)$$

For $\alpha = \alpha_k = \text{constant}$ the plot of $\text{Ln } \beta_i$ versus $1/T_{ik}$, obtained for different heating rate β_i , should be a straight line.

3.5.5. Formal kinetics analysis of processes in solid state

3.5.5.1. Master data methodology and isoconversional methodology

Jones [167] used the reduced time developed by Sharp [168] in which the experimental kinetics data $f(\alpha)$ is plotted against the master data $g(\alpha)$ or $g(t)$ in such a way to produce a linear plot. The experimental data is first expressed in form of degree of conversion α_e and corresponding reaction rate $f(\alpha_e)$ as a function of reduced time $(t/t_{1/2})_e$, where e refers to the experimental data.

Two equivalent procedures are possible:

(1) The experimental value of α_e at which $g(t/t_{1/2})_e$ has the same value as in the master data $g(t/t_{1/2})_m$ is plotted against the master value of α (designated α_m). If $\alpha_e = \alpha_m$ the resulting plot will be a straight line through the origin with a slope α_e/α_m equal to unity.

The experimental value of may be plotted against $g(t/t_{1/2})_m$ for common values of α_e and α_m . (2) The resulting plot should be a straight line through the origin with a slope $(t/t_{1/2})_m \times (t/t_{1/2})_e$ equal to unity for absolute correlation. Trying this procedure systematically for various values of α_e constitutes the principle of isoconversional methods [169].

3.5.5.2. Kinetics analysis in solid phase: standard kinetic methodology

The kinetic for heterogeneous systems is traditionally described by the a modification of the kinetic equations for homogeneous systems (assumption 1) represented in term of degree of conversion, X or α , using the general equation (3.32), where $f(\alpha)$ depends on the reaction mechanism. Deduction of the mechanism of reaction by use of non-isothermal kinetics has been primary discussed by Sestak and Berggren [169] and Satava [170]. The most widely accepted procedure of Satava is based on the assumption that the non-isothermal reaction proceeds in an infinitesimal time interval isothermally (assumption 2). At constant (linear) heating rate, one transforms the function $f(\alpha)$ in an integrated form $g(\alpha)$ as follows:

$$\frac{d\alpha}{dt} = k(T) \cdot f(\alpha) = A \cdot e^{-x} f(\alpha) \quad (3.43)$$

$$\int_0^{\alpha} \frac{d\alpha}{f(\alpha)} = g(\alpha) = \frac{E_a}{R \beta} \cdot p(x) = k(T) \cdot t \quad (3.44)$$

where $p(x)$ is based on the definition of Doyle (3.33). It comes:

$$p(x) = \frac{e^{-x}}{x} - \int_{-x}^{\infty} \frac{e^{-u}}{u} du = \frac{e^{-x}}{x} + E(-x) \quad (3.45)$$

where the reduced activation energy u , $x = E_a/RT$ and where $E(x)$ describes the statistical averaging function of the activation energy. Using the approach of Doyle, in taking the logarithmic form of equation (3.32) and combining it to (3.33) one obtains:

$$\text{Log } g(\alpha) - \text{Log } p(x) = \text{Log } \frac{AE_a}{R\beta} \quad (3.46)$$

It can be seen that similarly to the Doyle's method, the left-hand side is temperature dependent, while the right-hand side is temperature independent, but nevertheless heating rate dependent. For a third approximation, (Doyle-Zsako's method), the function $\text{Log } p(x)$ is a linear function of $1/T_\alpha$ if x is sufficiently large ($x > 20$) and thus $\text{Log } g(\alpha)$ must be also a linear function of $1/T_\alpha$. For a *correct reaction mechanism*, the validity criterion is that $\text{Log } p(x)$ versus $1/T_\alpha$ must be a straight line. For incorrect mechanisms a polynomial deviation of higher order is expected. Lately Baitalow et al. [171] introduced a modified form of the equations (3.26) and (3.27),

$$p(x) = \pi(x) \cdot \frac{e^{-x}}{x} \quad (3.47)$$

Where $\pi(x)$ is the temperature integral approximation. There are many approximate expressions of the $\pi(x)$ function in the literature. Often is the relation of Senum and Yang [172] sufficient:

$$\pi(x) = \frac{x^3 + 18x^2 + 88x + 96}{x^4 + 20x^3 + 120x^2} + 240x + 120 \quad (3.48)$$

The attraction of these two methods stems from the possibility of being able to determine the *apparent activation energy* as a function of α for certain identifiable prerequisites without knowing the kinetic model of the reaction mechanism. Except the Friedman and WFO analysis all methods above-mentioned are mechanism (model) dependent via the choice of the functions $f(\alpha)$ and $g(\alpha)$. Moreover the conventional methods of kinetic analysis are based on a *mechanism (model) discrimination* : the selection of the form of the functions $f(\alpha)$ and $g(\alpha)$ as best describing experimental data. However, the determination of the *true values* of the activation energy E_a and the order of reaction n only succeeds if the selected forms of the $f(\alpha)$ and $g(\alpha)$ functions also describe the data sets generated from isothermal measurements at various temperatures, but only for processes with a single rate-limiting step [173]. Baitalow et al. [174] affirmed that even if the actual form of $f(\alpha)$ may be unknown, i.e. no solid state reaction mechanism is favoured, the selected mechanism i.e. the function $f(\alpha)$ must be the same (*invariance criterion*) for all measurements. However, to my point of view the statement of Baitalow should be observed with

special care, since at high heating rate a reaction mechanism may be predominant while another, basically very different of the last one may be found at low heating rate or approaching the thermodynamic equilibrium. If the basic invariance assumption is not fulfilled, an apparent set of values of E_a and n is generated, which differs greatly from the true set of values. The invariance criterion validity can be examined by comparison of α with reduced time plots (master data methodology). These reduced time plots may be obtained from isothermal runs [175] followed by XRD. For non-isothermal measurements, the set of reduced functions proposed by Malek may be useful [176-177].

3.5.5.3. Mechanisms of solid state reactions for non-isothermal isoconversional kinetics

The types of kinetic mechanisms most frequently encountered in solid state chemistry are described hereunder in Table 3.5 (empirical models) and in Table 3.6 (solid state mechanisms). The Tables 3.5 and 3.6 set out a variety of relationships in differential ($f(\alpha)$ functions) and integrated ($g(\alpha)$ functions) forms and therefore can be used advantageously in identifying the mathematical equation which will describe the kinetic data. However to identify the equations with models is a wrong approach.

Model	Symbol	Function $g(\alpha)$	Function $f(\alpha)$
<i>Reaction order (Acceleratory α-t curves)</i>			
Reaction order n	RO(n)	$(n-1)[1/(1-\alpha)]^{n-1}$	$(1-\alpha)^n$
First order (simple autocatalytic)	RO ₁	$-Ln(1-\alpha)$	$1-\alpha$
Second order	RO ₂	$1/(1-\alpha)$	$(1-\alpha)^2$
Third order	RO ₃	$2[1/(1-\alpha)]^2$	$(1-\alpha)^3$
Degree reaction	DR(n)	$(n-1)[1/\alpha]^{n-1}$	α^n
Šesták-Berggren (binomial law)	SB(m.n) or B _i	$\alpha^m(1-\alpha)^n$	-
Autocatalytic reaction			
Power law	P ₁	$\alpha^{1/n}$	$n\alpha^{(n-1)/n}$
Exponential law	E ₁	$Ln\alpha$	α

Table 3.5: Exhaustive list of empirical kinetic models

Function	Function $g(\alpha)$	Rate-controlling mechanism
<i>Diffusion (Deceleratory α-t curves)</i>		
D ₁	$\alpha^2/2$	One dimensional diffusion
D ₂	$(1-\alpha) \ln(1-\alpha) + \alpha$	Two-dimensional diffusion, cylindrical symmetry
D ₃	$\cdot [1 - (1-\alpha)^{1/3}]^2$	Three-dimensional diffusion, spherical geometry, Jander equation
D ₄	$(1 - 2\alpha/3) - (1-\alpha)^{2/3}$	Three-dimensional diffusion cylindrical geometry, Ginsting-Brounshtein equation
<i>Nucleation and nuclei growth (Sigmoidal α-t curves)</i>		
A ₁ / F ₁	$-\ln(1-\alpha)$	1 D random nucleation, one nucleus/particle
A ₂ / F ₂	$[-\ln(1-\alpha)]^{1/2}$	2 D random nucleation: Avrami equation I (JMA) ^a
A ₃ / F ₃	$[-\ln(1-\alpha)]^{1/3}$	3 D random nucleation: Avrami equation II (JMA) ^a
A ₄	$[-\ln(1-\alpha)]^{1/4}$	Avrami-Erofeev model
B ₁	$\ln(\alpha/(1-\alpha)) + C$	Prout-Tompinks model
<i>Phase boundary reaction (Deceleratory α-t curves)</i>		
R ₁	α	1 D phase boundary reaction
R ₂	$1 - (1-\alpha)^{1/2}$	2 D phase boundary reaction, cylindrical symmetry ^c
R ₃	$1 - (1-\alpha)^{1/3}$	3 D phase boundary reaction, spherical symmetry ^c
Symbol	Function $f(\alpha)$	Rate-controlling mechanism
<i>Diffusion (Deceleratory α-t curves)</i>		
D ₁	α^{-1}	One dimensional diffusion
D ₂	$[-\ln(1-\alpha)]^{-1}$	Two-dimensional diffusion, cylindrical symmetry
D ₃	$3/2 \cdot (1-\alpha)^{2/3} \cdot [1 - (1-\alpha)^{-1/3}]^{-1}$	Three-dimensional diffusion, spherical geometry, Jander equation
D ₄	$3/2 \cdot [(1-\alpha)^{-1/3} - 1]^{-1}$	Three-dimensional diffusion cylindrical geometry, Ginsting-Brounshtein equation
<i>Nucleation and nuclei growth (Sigmoidal α-t curves)</i>		
A ₁ / F ₁	$1 - \alpha$	1 D random nucleation, one nucleus/particle
A ₂ / F ₂	$2(1-\alpha)[- \ln(1-\alpha)]^{1/2}$	2 D random nucleation: Avrami equation I (JMA) ^a
A ₃ / F ₃	$3(1-\alpha)[- \ln(1-\alpha)]^{2/3}$	3 D random nucleation: Avrami equation II (JMA) ^a
A ₄	$4(1-\alpha)[- \ln(1-\alpha)]^{3/4}$	Avrami-Erofeev model
B ₁	$\alpha(1-\alpha)$	Prout-Tompinks model
<i>Phase boundary reaction (Deceleratory α-t curves)</i>		
R ₁	<i>constant</i>	1 D phase boundary reaction
R ₂	$2(1-\alpha)^{1/2}$	2 D phase boundary reaction, cylindrical symmetry ^c
R ₃	$3(1-\alpha)^{2/3}$	3 D phase boundary reaction, spherical symmetry ^c

Table 3.6: List of basic kinetic models and corresponding conversion functions $f(\alpha)$ and $g(\alpha)$

- (a) JMA: Johnson-Mehl-Avrami model.
 (b) the RO(n) model in Table 3.18 includes the R₂ and R₃ mechanism for for $n = 1/2$ and $n = 1/3$ respectively.
 (c) based on geometric model with contracting dimensions.

Most of the models in solid state decomposition use the concept of the formation of a nuclei, and their subsequent growth via a reaction interface (JMA based models). It is in this reaction interface that the structural rearrangements occur. The idea of this reaction interface should be considered as a reaction zone having a definite volume as explored by Hill [178] and there are structure features as given in § 3.5.8 which would support this concept. A consequence of experimental treatment is that nucleation most often occurs at the crystal surface. The progress of the reaction interface then reflects the geometry of the crystal shape as the interface contracts inward away from the surface [179]. Further Mulpert [180] explored the effects of additional diffusion of species (model D_i) away from or towards the reaction interface.

The classical models used by Mapel [181], Erofeev [182] and Avrami [183] show that each model can give rise to numerous mathematical relationship. The exponent n in the Johnson-Mehl-Avrami equation depends on the mechanism of the nucleation-growth process [184-186]. In most cases which have been until now been studied the exponent n remains constant through the greater part of the reaction but may greatly vary with changes of heating rate [187]. In addition to basic kinetic models which correspond to a certain geometry of the interface, there are also empirical models (Table 3.7). The kinetic exponent n can be an integer or a fraction for both $RO(n)$ and $SB(n,m)$ models. It is evident that the $RO(n)$ model includes both R_2 and R_3 models for $n = 1/2$ and $n = 1/3$ respectively. It was shown by Malek et al. [188] that acceptable values of the parameter m for the $SB(n,m)$ model are confined to the interval $0 < m < 1$.

Further a full description of all assumptions made in the different basic kinetic models and a valuable discussion about their relative physical meanings in relation with the fast developing theories in the field of solid state chemistry may be found in the *Treatise on Solid State Chemistry* of N.B. Hannay [189] and in the revised monography *Chemical Kinetics of Solids* of H. Schmalzried [190].

3.5.6. Methodology for the selection of the kinetic model

The nature of the multiple reaction is a function of the rates of conversion of the individual reactions (sequential approach), the heating rate and the initial composition of the reaction mixture: Depending on the heating rate and/or the initial composition of the reaction mixture, the multiple reaction may exhibit various pseudo orders of reaction and even multiple peaks. Thus Agrawal affirms that “modelling multiple reactions with the “pseudo” order of reaction approach contributes generally little to the understanding of the behaviour of a complex reaction such as the dehydration of zinc phosphate tetrahydrate” [191].

One important problem of kinetic analysis is the mathematical correctness of inverse task positioning, i.e. the existence and single value of the inverse task solution $f(\alpha)$ for an arbitrary set of experimental data and solution stability by small data variations. The existence of a solution is guaranteed first if the number of parameters of the model is a finite quantity and their determination range is well defined and secondly if the global mechanism to determine is not so complex and does not combine more than two or three effects (nucleation effect, diffusion, phase boundary reaction). Therefore a simpler approach correlated to the physico-chemical significance of the proposed mechanism(s) was used here for a tentative determination of the competitive dehydration mechanisms. In a similar but extended concept as Kissinger, Dollimore [192] proposed the extensive use of characteristic features of the plot $d\alpha/dT$ versus T , i.e. the maximum of the degree of conversion α_{\max} and the peak half-width $w_{1/2}$. Figure 3.21 provides an outline of the mechanism selection scheme:

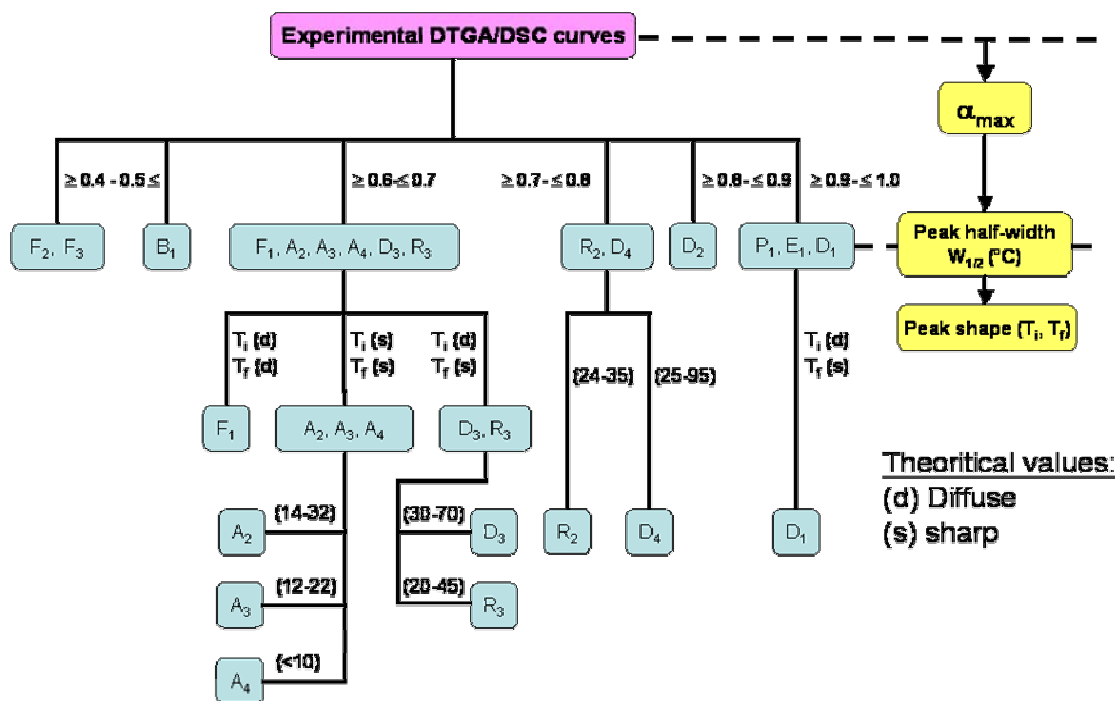


Figure 3.18: Outline of scheme to identify kinetic mechanisms $[f(\alpha)]$ from plot $d\alpha/dT$ versus T .

3.5.7. Descriptive approach of the dehydration kinetics of ZPT polymorphs: Activation energy E_a and order of reaction. Correlation / significance of the global order of reaction with regards to their crystallographic structures

Considering the dehydration process of solids as a purely heterogeneous decomposition reaction, it is possible to calculate first the activation energy and the order of reaction of such multi-step

processes by simply varying the heating rate during thermo-analysis as recommended by Málek [193], and applying some of the empirical models listed in Table 3.5 or detailed in § 3.5.4. Several approaches have been evaluated, since many assumptions are necessary. Four of these assumptions have major influence of the final results: (1) the homogeneity condition, where reference and sample have continually uniform temperature, (2) the heat transfer coefficients of reactants and products are equal, (3) the heat capacities of reactants and products are equal, and (4) these quantities, plus the heat of reaction, do not change over the temperature range of reaction. The first two assumptions depend greatly on the nature of the solid and its grain size, as heat transfer in solid is also governed by the nature of interfaces. The two last assumptions are related to a reduction of the heat of solvation / desorption of crystal water at the solid surface. Studying the dehydration of various samples of Kaolin, Brindley et Nakahira [194] verified that the water desorption does not play an important role in the dehydration process. As Murray and White [195-196] suggested, this may be easily done in plotting the temperature at which the reaction proceeds most rapidly T_{Max} in function of the heating rate β . As Sewell [197-198] pointed out, for each hydration state and also for the intermediary state (trihydrate, monohydrate), this last assumption is judged valid as long as a linear relationship is found. This is our case for heating rates in the range 5-25 K.min⁻¹. However a strong divergence from the linearity has to be duly noticed for $\beta < 5$ K.min⁻¹ suggesting the coexistence of concurring mechanisms. In the light of these considerations, the activation energy of dehydration of α - and β -hopeite (Table 3.7) was measured.

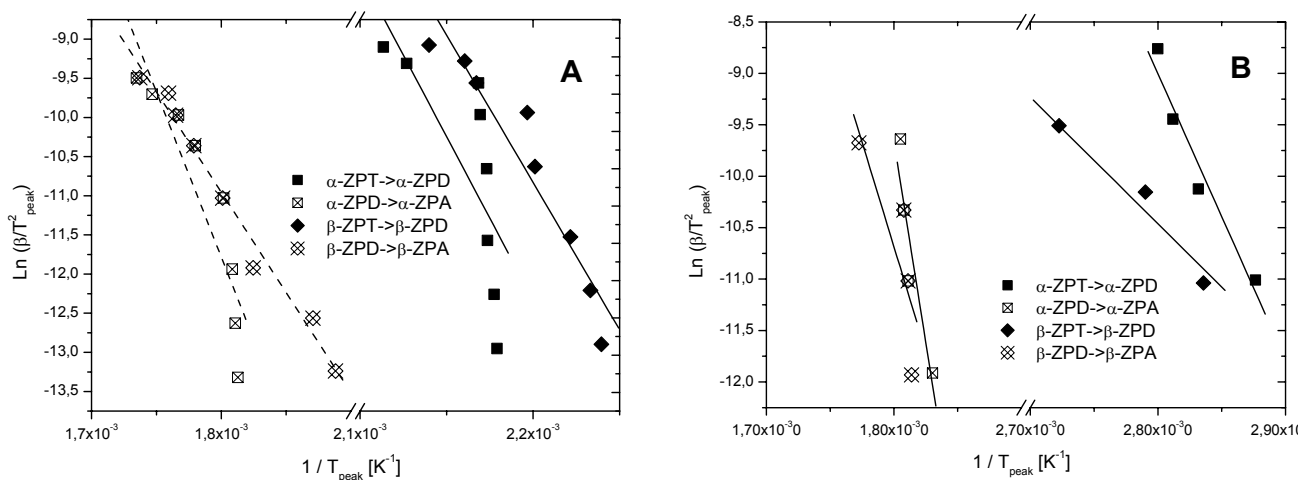


Figure 3.22: Determination of E_a of dehydration using Kissinger method on (A) DSC curves, (B) DTGA curves.

Thanks to a classical approach consisting in the description of a heterogeneous dehydration as a sum of homogeneous steps in terms of degree of conversion α (self-consistent method), the first results are obtained using Kissinger analysis applied to DSC curves (Fig. 3.22 and corresponding Table 3.7) and compared to results obtained from non-isothermal DSC experiments derived from

the simple isoconversional method of Friedman [199] for $\alpha = 0.25, 0.5$ and 0.75 . Kissinger and then Caroll and Friedman [200] developed as similar approach for TGA and DTGA experiments.

Phase	Hydration state $\text{Zn}_3(\text{PO}_4)_2 \cdot x \text{H}_2\text{O}$	DSC *			TGA *		Global order of reaction n_{app}^c
		E_a (Kissinger) [kJ.mol ⁻¹] ^a	E_a (Friedmann) [kJ.mol ⁻¹] ^b	E_a (WFO) [kJ.mol ⁻¹]	E_a (Kissinger) ^a [kJ.mol ⁻¹]	E_a (Caroll) ^c [kJ.mol ⁻¹]	
α	2	175.1	144.4	125.9	115.5	191.3	-
β	2	156.1	117.2	114.7	51.1	191.3	-
α	0	173.2	109.4	112.8	166.6	81.1	8/2
β	0	146.1	98.3	97.2	162.8	78.1	6/4

Table 3.7: Mean activation energy of dehydration of two zinc orthophosphates and its hydrates, calculated with a degree of conversion α of 25, 50 and 75 %.

- (a) averaged value obtained on extrapolation to zero heating rate.
 (b) averaged value for different degree of conversion ($\alpha = 0.25, 0.5$ and 0.75).
 (c) by extension of the method of Caroll [94], mean average of for experiments at increasing heating rate (1, 2, 5, 10 and 20 K.min⁻¹).
 (c) the global order of reaction $\text{Zn}_3(\text{PO}_4)_2 \cdot 4\text{H}_2\text{O}_{(cr)} \rightarrow \text{Zn}_3(\text{PO}_4)_2_{(cr)} + 4 \text{H}_2\text{O}_{(g)}$ is given. The first mentioned order corresponds to a calculated value at a heating rate of 20 K.min⁻¹ and the second value to the extrapolated reaction order at a heating rate of 0 K.min⁻¹ (thermodynamic equilibrium).
 (*) estimated errors $E_a \pm 5.00$ kJ.mol⁻¹ (DSC) and $E_a \pm 10.00$ kJ.mol⁻¹ (TGA).

Additionally, Flynn-Wall [201] and Ozawa [202] have proposed a method (so called WFO method) delivering less ambiguous characteristics of the dehydration dynamics in combining order of reaction and activation energy. An Arrhenius plot supporting this idea may only be obtained in selecting a dehydration model (curve Ln k versus T). As displayed in Table 3.7 Kissinger's approach delivers higher values of the apparent activation energy E_a than other methods (Friedmann, WFO) in DSC. The values are slightly smaller for β -ZPD (i.e. β -ZPA) than α -ZPD (α -ZPA). Using DTGA curves, the selectivity of Kissinger analysis seems to be catastrophic, since it tends to show that it the obtaining of a zinc phosphate dihydrate (~ 50 - 115 kJ.mol⁻¹) requires less thermal energy than a zinc phosphate anhydrate structure (~ 160 kJ.mol⁻¹), in complete opposition with the trend given by the Carroll's method. In Table 3.7 (DSC), the transformation starting from α -, β -hopeite (zinc phosphate tetrahydrate or ZPT) to α -, β -zinc phosphate dihydrate (α -, β -dihydrate or ZPD) involves an activation energy higher for the α -hopeite (144 kJ.mol⁻¹) than the β -hopeite (117 kJ.mol⁻¹), thus confirming the higher stability of the α -form of zinc phosphate. Similarly, the α -ZPD has a more stable crystalline structure (109 kJ.mol⁻¹) than the β -ZPD with 98 kJ.mol⁻¹, in good agreement with the classification of ΔG^{Dehydr} values given in Table 3.4 and of ΔG^{form} of Table 3.4. The drawing of a classical Arrhenius plot (log k vs. $1/T$) seems attractive to support this conclusion but may necessitate the knowledge of the frequency factor for each dehydration reaction, whose calculation requires the choice of an adequate solid state reaction model. At this step of the discussion, such choice may not be wise and therefore not recommended.

Nevertheless, from a pragmatic point of view [203], one may consider the description of crystal structures of many minerals as divided in two parts: (1) the structural unit, an array of high-bond valence polyhedra that is usually of ionic character (here PO_4^{3-} groups) and (2) an interstitial complex, an array of large low valence cations (here Zn^{2+}) and H_2O groups that is usually cationic in character. Interstitial complexes link the structural unit by weak cation-anion interactions and hydrogen bonds into a continuous structure, and the breakdown of a structure is controlled by strength of the weak bonds that link the structural unit together. If one examines a series of structures with the same structure unit, implicitly α,β -hopeite, α,β -zinc phosphate dihydrate and α,β - $\text{Zn}_3(\text{PO}_4)_2$, it is evident that the average coordination of the Zn atoms (Type 1, octahedrally coordinated) of the structural unit varies slightly from one structure to the other, producing a range of Lewis basicity for this specific structural unit. In that way, the Zn- H_2O specific unit is stable over a definite range of temperature (Fig. 3.9: RT-200°C and 240-500°C) and possesses characteristic activation energies of dehydration. Therefore, in analogy to Werner's theory of coordination chemistry [204], the consumption of two crystal water via dehydration from α - $\text{Zn}_3(\text{PO}_4)_2 \cdot 4\text{H}_2\text{O}$ to α - $\text{Zn}_3(\text{PO}_4)_2 \cdot 2\text{H}_2\text{O}$ for example, may involve an activation energy at least of $60 \text{ kJ}\cdot\text{mol}^{-1}$ [205-206] and, more probably, $120 \text{ kJ}\cdot\text{mol}^{-1}$ as estimated by Hsu for brushite minerals [208]. Concordingly, the interdependence between the wavenumber shift of FTIR stretching vibration band relative to free binding hydroxyl groups (see chapter 2) and the hydrogen bond energy indicates values higher than $70 \text{ kJ}\cdot\text{mol}^{-1}$ according to Lippicott and Shroeder [209].

Furthermore, using the X-ray diffraction method developed by Heal and Mikura [210], Trillat [211] evaluated this activation energy to the nearly similar value of $104 \text{ kJ}\cdot\text{mol}^{-1}$. The values calculated with the WFO method with DSC data and with the Carroll method for TGA, are also in the same range. Astonishingly the Carroll method indicates no difference of activation energy between α - and β -hopeite, while the Friedman method based on the same model shows a difference of $27 \text{ kJ}\cdot\text{mol}^{-1}$ between α - and β -hopeite and the WFO method a difference just of $12 \text{ kJ}\cdot\text{mol}^{-1}$. This difference in activation energy is as much conserved in the course of dehydration as the difference in ΔG . On contrary the entropy ΔS^{dehydr} ($\text{ZPT} \rightarrow \text{ZPD}$) fluctuates as much as 10%, confirming the conformational origin of the structural difference (hydrogen bond pattern) between α - and β -hopeite.

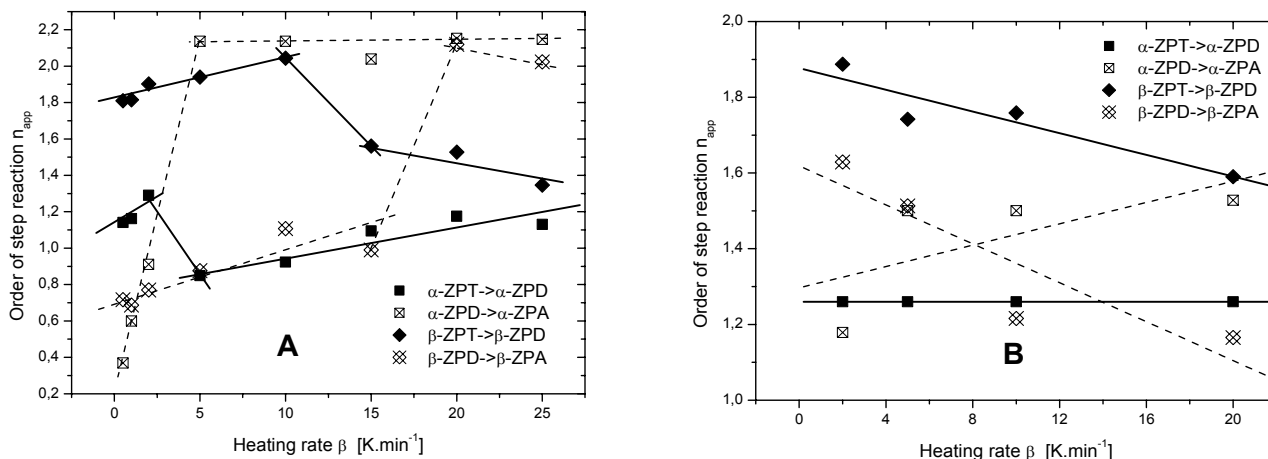


Figure 3.23: Kissinger's approach for the calculation of the apparent order of the step-reaction of dehydration in (A) DSC and (B) DTGA at varying heating rate. Estimated errors $n_{app} \pm 0.1$

This can not be the case of the α - and β -zinc phosphate dihydrate. Their respective XRD diffractograms not only show crystallographic difference of hydrogen bonding networks but also of the structural unit (region of 2θ : 15-20° (311) and (241) peaks of dihydrate). Indeed, the global order of dehydration (Table 3.7) gives an estimate of the temperature stability of the crystal structure. The α -hopeite possesses a 3D hydrogen bond network stabilizing the structural units while the β -hopeite has only a 2D- hydrogen bonding pattern. So, on heating the structure of α -hopeite is destabilized in such a way that it transforms itself automatically to a dihydrate and to an anhydrate at higher temperature. Therefore, a global order of dehydration of 2 (extrapolated at β : 0 K.min⁻¹) for the α -hopeite is found and explains the release of crystal water two by two, as monitored in DSC. On contrary, β -hopeite shows a global order of reaction, extrapolated at a zero °C per min heating rate, of 4.

Partial order of reaction n_{app}^i		Method	Proposed mechanism
Low heating rate ($\beta < 10$ K.min ⁻¹)	High heating rate ($\beta > 20$ K.min ⁻¹)		
$\alpha\text{-ZPT} \xrightarrow{1} \alpha\text{-ZPD}$ and $\alpha\text{-ZPD} \xrightarrow{2} \alpha\text{-ZPA}$			
1 + 0.3	1 + 2	DSC	D ₁ -D ₂ /A ₃ -D ₃ /D ₂ /RO ₂
1 + 1.5	1 + 1	DTGA	D ₁ -D ₂ / A ₁ -R ₂ /A ₁ -D ₂
$\beta\text{-ZPT} \xrightarrow{1} \beta\text{-ZPD}$ and $\beta\text{-ZPD} \xrightarrow{2} \beta\text{-ZPA}$			
1.9 + 0.6	1.5 + 2	DSC	RO ₂ /A ₃ /A ₂ -D ₂ -R ₂ /RO ₂
1.9 + 1.6	1.7 + 1.2	DTGA	RO ₂ /A ₂ -D ₂ -R ₂ /RO ₂

Table 3.8: Partial order of reaction evaluated from thermoanalysis and corresponding proposed mechanisms.

It can be interpreted as follows: the hydrogen bonds in the β -hopeite are all conformationally and energetically equivalent, so that the thermally induced breaking of one bond does not destabilize the whole crystal structure; four transient dehydration peaks are observed in the DSC thermogram. At high heating rate, the global order of reaction tends to degenerate as the phosphate groups may pyrolyze. Besides, a selective analysis of the apparent reaction order is well illustrated in Figure 3.23 using Kissinger's approach of the shape of dehydration peaks. Figure 3.23 suggests that the α -ZPT dehydrates successively in α -ZPD and α -ZPA with n_{app} values of 1 + 1 (DTGA) and 1 + 2 (DSC) thus confirming Carroll's value of the global order of reaction at zero heating rate. Comparingly, one finds for β -ZPT dehydration values of n_{app} of 2 + 1.5 (DTGA) and 2 + 0.5 (DSC) [see Table 3.8]. This also corroborates the Carroll's value of the global order of reaction at zero heating rate. However to my point of view the discrepancies of Figure 3.23 are not completely originating from errors of measurements. This may well point out that on one hand the surface effects via diffusive release of crystal water might become preponderant at low heating rate (mechanisms D_1 or D_2) for β -ZPT and on the other hand that a nucleation and growth process (Avrami A_2 or A_3 mechanisms) controls the dehydration of α -ZPD. A critical heating rate can be estimated as the values at which the activation energy and the apparent order of reaction switch from one statistical value to another one. This may lie around $7 \text{ k}\cdot\text{min}^{-1}$. Thus it gives a reason explaining why a basic approach like the one of Newkirk can only deliver unsatisfying values of n_{app} . In fact no linear relation has been obtained between $\beta \cdot d\alpha/dT$ and $1/T$ for $n_{app} = 1$ (RO_1 model).

Furthermore the rate constant k is strongly influenced by the shape of the crystals. In studying the dehydroxylation of kaolinite. First Murray and White [212] and then Holt, Cutler and Wadworth [213] demonstrated that in an infinitely thin system, the dehydration kinetics should follow a first-order law, since the dehydration is reduced to a one dimensional diffusion mechanism as shown in Table 3.8. Strong support concerning the second step dehydration reaction $ZPD \rightarrow ZPA$ stems from the fact that the DSC data set at various heating rates (Fig. 3.16) is nearly identical with the simulated heat flow curves of Opfermann and Kaisersberger [214] for a two-step dehydration reaction of first order (F_1 mechanism) using the FWO method. A low heating rate ($\beta = 0.1\text{-}0.5 \text{ K}\cdot\text{min}^{-1}$) the DSC thermograms exhibit two distinct peaks. This suggests the stabilization of a zinc phosphate trihydrate structure and the dehydration of ZPD in ZPA as two consecutive reactions. In conclusion, these results first suggest that the isothermal transition from the "metastable" β -form of ZPT to the most stable form α , is thermodynamically possible but kinetically not favoured and secondly that α -ZPT can only dehydrate into α -ZPD (i.e. β -ZPT \rightarrow β -ZPD). To understand this dehydration mechanism clearly, a description with an intermediary state is necessary (Fig. 3.25). This is precisely illustrated by the fact that albeit submitting β -hopeite crystals to water pressure at 90°C for one year, no crystallographic changes to α -hopeite occurs.

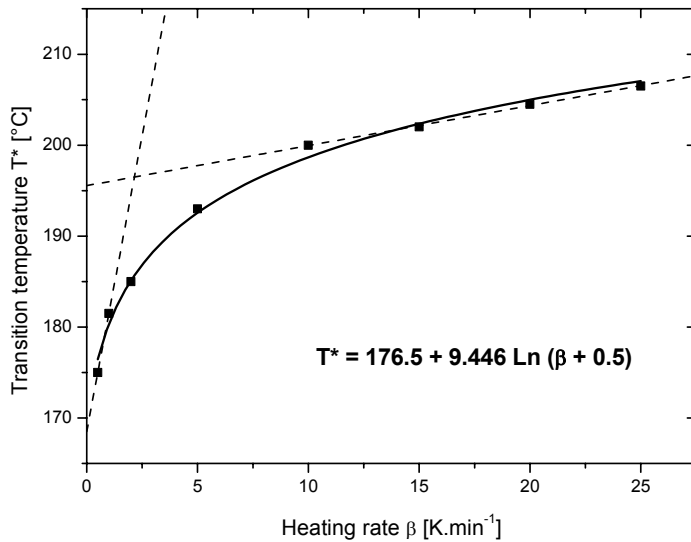


Figure 3.24: Extrapolation to zero heating of the transition temperature, corresponding to the maximum dehydration rate in a second order kinetics (model RO(2)).

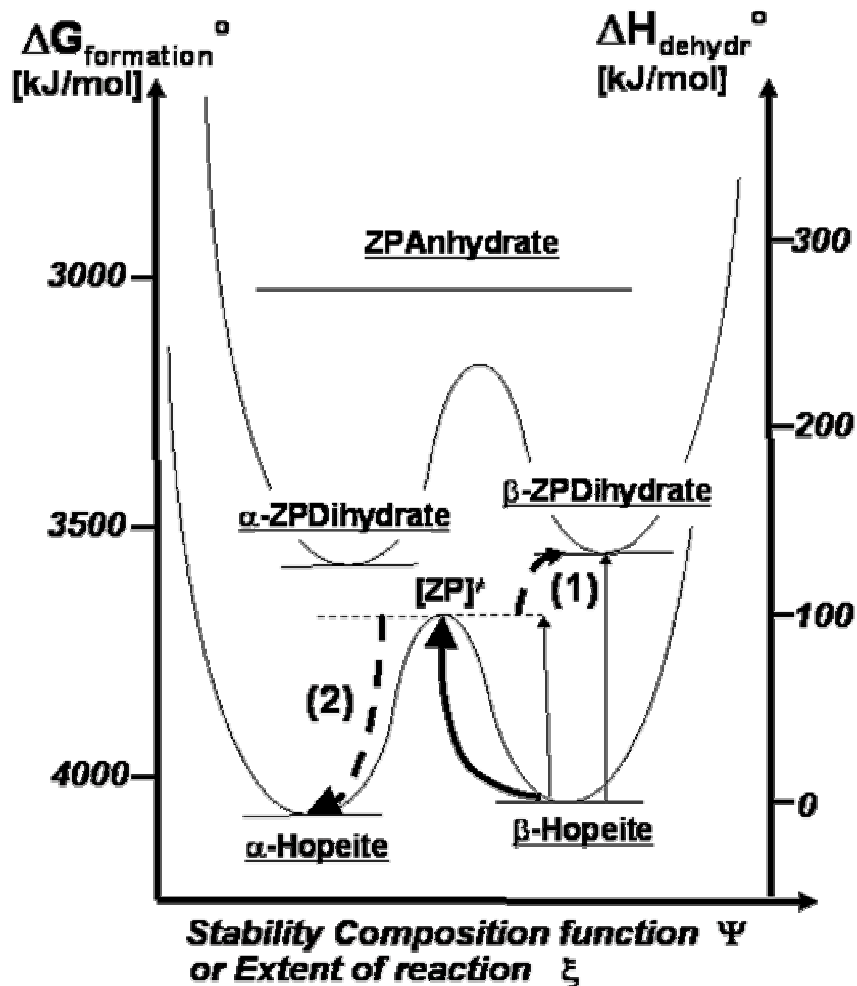


Figure 3.25: Representation of the thermodynamic-kinetic interrelations between the different zinc phosphate anhydrates, dihydrates and tetrahydrates. From Hess law cycles, the stability difference (ΔG° formation) between α - and β -ZPT and between α - and β -ZPD are 8.7 and 6.5 kJ/mol respectively. Upon heating, the β -ZPT is destabilized and two pathways are possible: a fast kinetic pathway (1) and a slow kinetic pathway or thermodynamic pathway (2).

Therefore the free energy of the β -ZPT \rightarrow α -ZPT isothermal reaction (at 90°C, synthesis temperature of α -hopeite) and the thermal activation energy of the reaction β -ZPT \rightarrow β -ZPD must be nearly identical at a temperature of transition T^{\neq} above 90°C and under 220°C, the stability temperature of β -zinc phosphate dihydrate, determined by DSC [215]. A statistical thermodynamics approach of the “activated complex theory” has been employed with the boundary condition, that the reaction β -ZPT \rightarrow β -ZPD has a second order kinetics due to a stepwise loss of two water molecules, as proven by DSC. The extension to a null heating rate of the maximum dehydration rate versus heating rate directly converges logarithmically to a characteristic value T^{\neq} (β -ZPT \rightarrow α -ZPT) of 168.5°C [216] as shown in Figure 3.24. At that precise temperature, an isothermal conversion of β -hopeite into α -hopeite is not only thermodynamically possible but also kinetically favoured.

3.5.8. Tentative determination of the kinetic mechanisms of dehydration of α -, β -hopeite and α -, β -ZPD

A tentative determination of the complex multi-step dehydration reaction involving most probably competitive mechanisms depending on the heating rate was done using the approach of Dollimore described in § 3.5.6. The first step of this sequential analysis is the generation of the global degree of conversion α versus temperature and corresponding first derivative $d\alpha/dt$ versus temperature plots using experimental data of DSC (Fig. 3.26) and DTGA (Fig. 3.27).

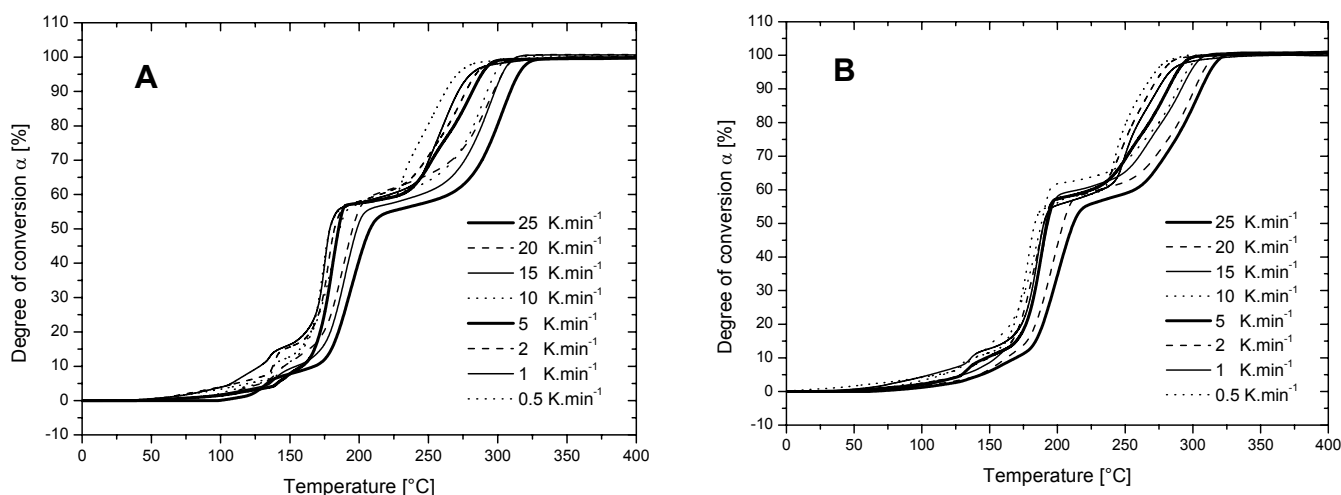


Figure 3.26: Curves of the degree of conversion versus temperature generated by DSC for (A) α -hopeite and (B) β -hopeite and dependence of heating rate in the range 0.5-25 K.min⁻¹.

Due to mathematical difficulties appearing in the processing of data (generation of a suitable baseline for partial integration avoiding a deflection effect [217]), the values of the degree of

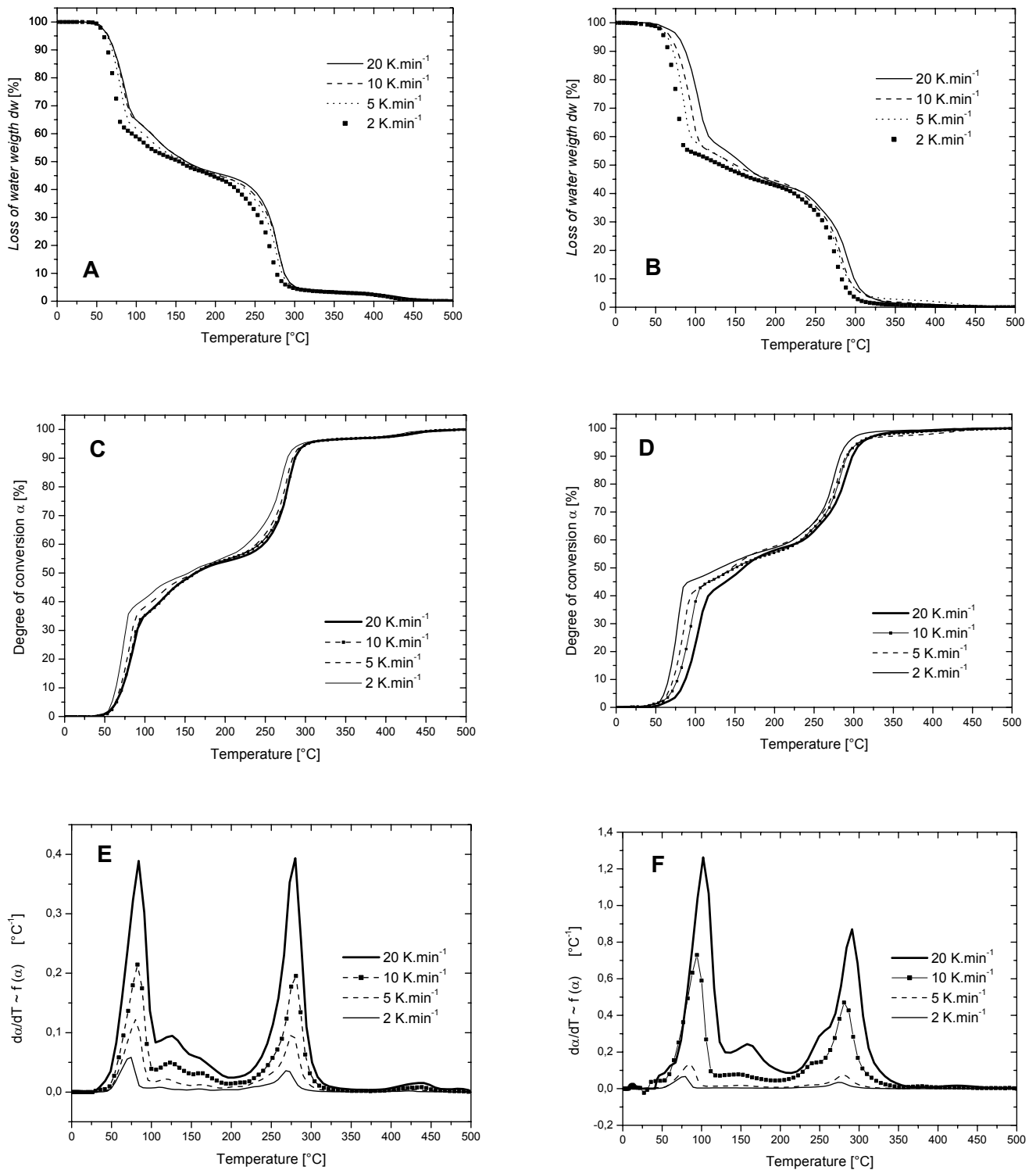


Figure 3.27: Heating rate dependence of TGA curves used for the identification of the dehydration mechanism: Weight-loss curves of (A) α -ZPT, (B) β -ZPT; Degree of conversion curves of (C) α -ZPT, (D) β -ZPT; rate of conversion curves (E) α -ZPT, (F) β -ZPT

conversion of 20% below 160°C in DSC (Fig. 3.26) are considered only partly reliable. However these curves α vs. T have the classical shape of a two-step reaction using both thermo-analytical

methods. Especially Fig. 3.27 display the building of master data from DTGA with the monitoring of the normalized water weight loss (Fig. 3.27 A,B), the degree of conversion (proportional to $f(\alpha)$ -Fig. 3.27 C,D) and its first order derivate in respect to time or temperature (proportional to $g(\alpha)$ -Fig. 3.27 E,F).

A Results of DTGA							
Heating rate β [K.min ⁻¹]	α_{max} ^a [%]	$\bar{\omega}_{1/2}$ [°C]	Proposed mechanism	Heating rate β [K.min ⁻¹]	α_{max} ^a [%]	$\bar{\omega}_{1/2}$ [°C]	Proposed mechanism
α -ZPT _{cr} → α -ZPD _{cr} + 2H ₂ O _g				α -ZPD _{cr} → α -ZPA _{cr} + 2H ₂ O _g			
20	49.1	16.5	F ₂ / F ₃	20	92.0	26.3	D ₂
10	44.5	20.5	F ₂ / F ₃	10	87.3	25.6	D ₂
5	40.7	24.5	F ₂ / F ₃	5	82.9	23.7	D ₂
2	39.9	26.9	F ₂ / F ₃	2	80.4	23.4	D ₂
β -ZPT _{cr} → β -ZPD _{cr} + 2H ₂ O _g				β -ZPD _{cr} → β -ZPA _{cr} + 2H ₂ O _g			
20	45.4	30.6	F ₂ / F ₃	20	88.4	29.4	D ₂
10	45.3	26.3	F ₂ / F ₃	10	86.6	32.6	D ₂
5	42.5	21.9	F ₂ / F ₃	5	82.3	77	D ₂
2	42.7	21.1	F ₂ / F ₃	2	81.7	85	D ₂
B Results of DSC							
Heating rate β [K.min ⁻¹]	α_{max} ^a [%]	$\bar{\omega}_{1/2}$ [°C]	Proposed mechanism	Heating rate β [K.min ⁻¹]	α_{max} ^a [%]	$\bar{\omega}_{1/2}$ [°C]	Proposed mechanism
α -ZPT _{cr} → α -ZPD _{cr} + 2H ₂ O _g				α -ZPD _{cr} → α -ZPA _{cr} + 2H ₂ O _g			
25	60.3	29.5	A ₂	25	99.6	35.0	D ₁
20	60.9	24.6	A ₂	20	99.6	36.5	D ₁
15	61.1	23.1	A ₂	15	99.1	34.7	D ₁
10	61.2	21.1	A ₂ / A ₃	10	99.0	33.5	D ₁
5	60.8	16.8	A ₂ / A ₃	5	98.7	43.7	D ₁
2	60.6	9.4	A ₄	2	98.4	46.8	D ₁
1	60.3	8.7	A ₄	1	98.1	34.8	D ₁
0.5	58.4	8.1	A ₄	0.5	97.6	34.0	D ₁
β -ZPT _{cr} → β -ZPD _{cr} + 2H ₂ O _g				β -ZPD _{cr} → β -ZPA _{cr} + 2H ₂ O _g			
25	62.2	31.0	A ₂	25	99.9	50.7	D ₁
20	62.1	29.5	A ₂	20	99.5	44.5	D ₁
15	60.6	24.6	A ₂	15	99.3	30.4	D ₁
10	60.4	21.8	A ₂ / A ₃	10	99.1	44	D ₁
5	60.4	17.9	A ₂ / A ₃	5	98.8	54.5	D ₁
2	60.2	22.	A ₂ / A ₃	2	98.5	44.1	D ₁
1	59.9	15.0	A ₂ / A ₃	1	98.1	33.3	D ₁
0.5	59.7	13.2	A ₂ / A ₃	0.5	97.7	24.1	D ₁

Table 3.9: Peak analysis of the rate of dehydration vs. T curves (Dollimore's approach) and deduced dehydration mechanisms.

- (a) maximum of the degree of conversion.
 (b) width of the peak at half-height of the $d\alpha/dt$ versus temperature T curve.

Since nearly all crystal water is released above 350°C and that the formation of a partially stabilized zinc phosphate anhydrate structure for both α - and β -polymorphs occurs above 320°C, one should expect to find a “global” degree of conversion higher than 95% for the dehydration of ZPT in ZPA ($ZPT \xrightarrow{1} ZPD$ and $ZPD \xrightarrow{2} ZPA$) in DSC and in the range 85-90% in DTGA as shown in Figure 3.26 and Figure 3.27 (C,D). The calculated “partial” degree of conversion of ZPT in ZPD should be used carefully, because of the consideration of two possible approaches: (1) $ZPT \xrightarrow{1} ZPD$ and $ZPD \xrightarrow{2} ZPA$ are consecutive and independent reactions; (2) $ZPT \xrightarrow{1} ZPD$ and $ZPD \xrightarrow{2} ZPA$ are partly concurring reactions in the stability domain of ZPD. In the first case the degree of conversion of both reactions vary up to 100% and in the second case, the degree of conversion of the first step reaction $ZPT \xrightarrow{1} ZPD$ may not exceed 60% of the total amount of water to dehydrate. This has two consequences: first that any fluctuations of α between 50% and 60% either indicates that the second step reaction partially overlaps the first one and two mechanisms of dehydration are concurring or that after obtaining a ZPD product the crystal structure evolves in a less ordered structure of type $Zn_3(PO_4)_2 \cdot 2.5 H_2O$, sometimes mentioned in the literature.

Table 3.9 displays the peak analysis on the $d\alpha/dT$ vs. T curves in DTGA (Table 3.9 A) and DSC (Table 3.9 B) and the resulting deduced mechanisms of dehydration using Dollimore’s theory and a two-step reaction with concurring dehydration mechanisms. Both thermo-analytical techniques give for each step reaction two types of dehydration mechanism that are nevertheless common for both polymorphs of hopeite. Since DTGA curves have lower onset temperature T_i than their corresponding DSC curves for a given heating rate, the proposed mechanism of dehydration for the first step-reaction $\alpha\text{-ZPT}_{cr} \rightarrow \alpha\text{-ZPD}_{cr}$ slips from a two- or three-dimensional Avrami Nucleation & Growth mechanism to a mechanism F_2 / F_3 emphasizing a change or “fluctuation” in the bulk nucleation mechanism of embryo of ZPD in a ZPT matrix. For this last reaction at very low heating rate ($\beta < 0.5 \text{ K}\cdot\text{min}^{-1}$), DSC data even suggest an Avrami-Erofeev (A_4) mechanism. The second step reaction can be observed in terms of diffusion controlled mechanism of dehydration either in one dimension (DSC) or in two dimensions (DTGA) as shown in Table 3.9.

In order to clarify the possible mechanisms of dehydration and their simultaneous occurrence, scanning electron microscopy combined with polarized light microscopy and powder diffractometry were used as complementary techniques to thermo-analysis. SEM allows characterizing with high resolution the topology of each face and the temperature induced morphological changes of an orthorhombic zinc phosphate tetrahydrate, which appears usually in a plate-like morphology. Thus the reaction $ZPT \xrightarrow{1} ZPD$ was of special interest and an isothermal dehydration of α -hopeite at 160°C was selected. Figure 3.28 shows ex-situ the selective dehydration of ZPT, preferentially in the (ac) planes. No induction time due to diffusion of heat in the crystal is noticed here. Therefore not so well defined striations appear shortly after 1 min in the (ac) planes. From an already

discussed crystallographic point of view, the appearance of striation has to be correlated with the rupture of hydrogen bonds along the *b*-axis and then *c*-axis (see Figure 3.29). The appearance of striations perpendicular to the *b*-axis may qualify this dehydration reaction as a “displacement reaction” following Wagner’s mechanism [218-219]. The exact origin of these striations has never discussed before but some crystallographic explanations might be proposed.

Since at 220°C complete dehydration is achieved as indicated by DSC thermograms (Fig. 3.16), these alternating layers displayed in Fig. 3.28 H cannot come from an incomplete reaction of dehydration where α -ZPT and α -ZPD might coexist in alternation. Besides, upon dehydration two crystal water molecules are released through the breaking of the weakest hydrogen bonds (H10-1 and H10-2) of the α -ZPT structure corresponding to two H₂O molecules of the octahedrally coordinated Zn(2) atom (see Fig. 3.10). Thus dehydration creates voids in the α -ZPT orthorhombic structure as water release progresses and consequently forces the crystal structure to collapse and thus to condense in a α -ZPD monoclinic structure. This ultimately induces a change of coordination of Zn(2) atoms from octahedral to tetrahedral, and represents a volume decrease of 14% of a unit cell. Figure 3.25 shows the diffraction patterns on selected surfaces ((011) and (101)) of a α -ZPT and its comparison with α -ZPD. Figure 3.28 A and B and also C and D are superimposable, indicating first similar crystal structures on each face of each hydrated phase and secondly the conservation of two lattice parameters during dehydration [α -ZPT: *a*: 10.62 Å, *b*: 18.40 Å, *c*: 5.05 Å; α -ZPD: *a*: 10.41 Å, *b*: 5.04 Å, *c*: 31.44 Å]. The formation of striations of dehydration appearing characteristically on the (101) face of α -ZPD is clearly shown in Fig. 3.28 A with emerging diffuse halos along diffraction lines and in comparison do not exist in the pristine structure (α -ZPT, Fig. 3.28 C). Thus upon dehydration contact-twin plate-like structure namely *gauche* (structure 2) and *droite* (structure 3) of zinc phosphate dihydrate may be formed in successive alternating layers paralleling the prominent (011) plane of α -ZPT as schematically presented in Fig. 3.30. Their existence of twin crystals of α -ZPD along the *a*-axis of α -ZPT strongly indicates a one dimensional diffusion process of dehydration. Further this can be observed since the resulting thermomechanical stress may delaminate the crystal as shown in Fig. 3.28 B. This remarkable cohesive rupture of the material may occur as dehydration generates crystal mismatch between a ZPT lower layer and a growing ZPD upper layer. This is often observed in single crystal XRD analysis and gives reason why no precise structure of ZPD crystals is yet reported in the scientific literature. Similar dehydration patterns also appear in the (*ab*) planes after a delay of approximately 10 min. Since no dramatic deformations (Fig. 3.28 I) of the plate-like topology ([011] surface) is monitored, which would have suggested a dehydration mechanism corresponding to an Avrami Nucleation & Growth mechanism, SEM results indicate first that the α -ZPT is completely destabilized and thus may recrystallize in a dihydrate form (α -ZPD) at that moment and secondly that a second direction for a one dimensional diffusion mechanism of dehydration along the *c*-axis is privileged. This

conclusively indicates a two dimensional diffusion mechanism of dehydration of the zinc phosphate tetrahydrates.

Further if one measures the time dependence of the number of striations and their thickness relatively to the crystal thickness, one can show that the striation thickness (or its variation $\Delta d_i/\Delta t$) decreases inversely logarithmically with time, confirming the two-dimension diffusion mechanism of dehydration of α -zinc phosphate tetrahydrate (Fig. 3.32). The same mechanism may be involved in the dehydration of β -ZPT. The rate constant k is strongly influenced by the shape of the crystals.

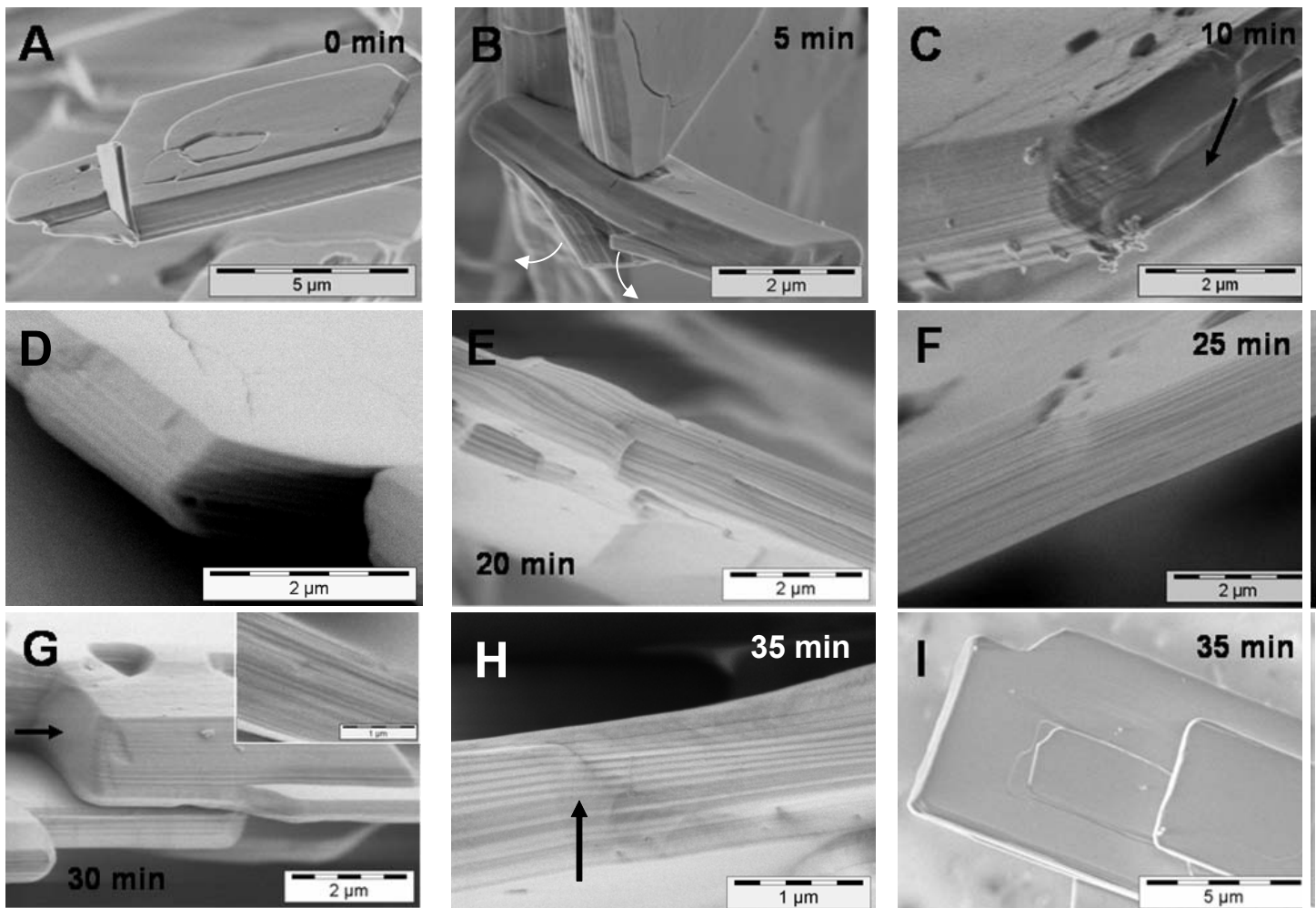


Figure 3.28: Isothermal dehydration of α -ZPT (tetrahydrate) followed by ex-situ SEM measurements every 5 min. Note the selective dehydration on specific $[011]$ crystal faces, characterized by the appearance of striation of denser α -ZPD. The $[110]$ faces exhibit dehydration patterns after ca. 10 min while only a slight deformation of the $[101]$ has been monitored.

In studying the dehydroxylation of kaolinite first Murray and White [220] and then Holt, Cutler and Wadworth [221] demonstrated that in an infinitely thin system, the dehydration kinetics should follow a first-order law, since the dehydration is reduced to a one dimensional diffusion mechanism.

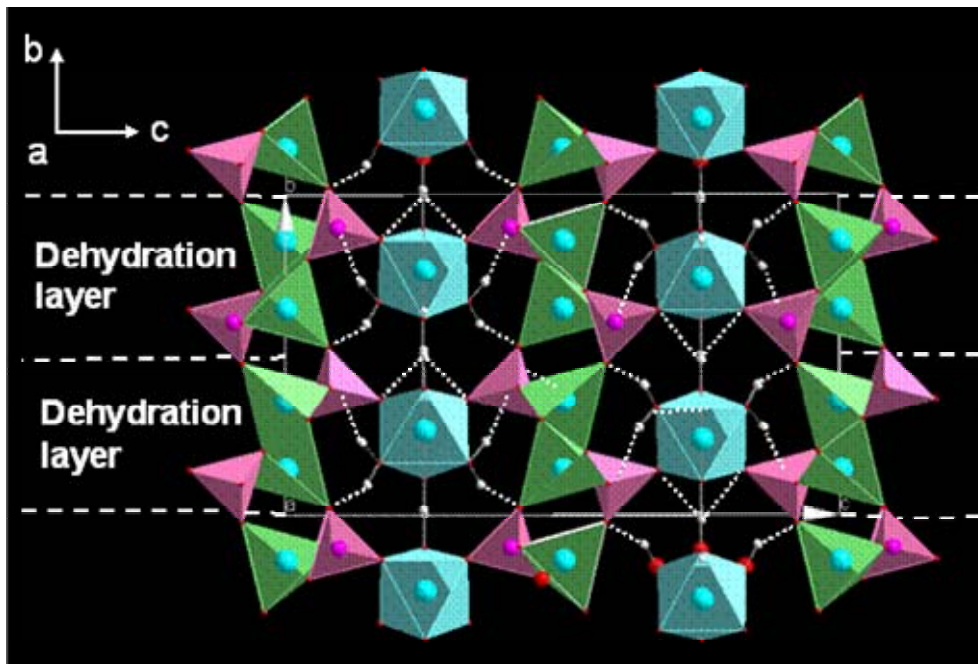


Fig 3.29: Schematic example pointing out the layered structure of β -hopeite, where hydrated layers indicated with their corresponding hydrogen bonding network along the b -axis, alternate with the zinc phosphate polyhedra structure (pink tetrahedra: PO_4 , blue and green: $Zn(I)$ and $Zn(II)$). Upon dehydration thermally induced rupture of the hydrogen bonds along b -axis causes the rearrangement (collapse) of the β -ZPT crystal in a more compact structure in the (101) plane, perpendicular to b -axis. This characteristic feature can easily be observed in SEM.

Besides one should notice that the thickness of one striation corresponds approximately to 20 unit cells of ZPD [222]. In fact because of the lamellar morphology arising, a considerable part of the decrease in free energy may be absorbed as interfacial free energy between two product phases. Therefore it can be shown that the decreasing rate of variation of the thickness of striations (interlamellar spacing) corresponds also to a maximum growth rate of ZPD.

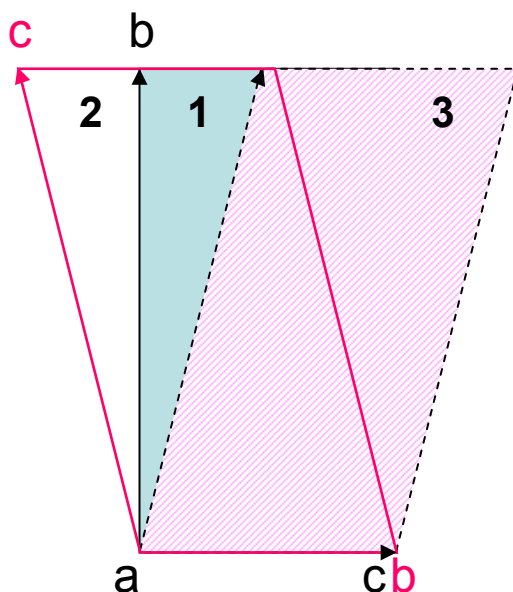


Figure 3.30: Schematic representation of the formation of contact-twin crystals (2: gauche structure in red and 3: droite structure in black, dash line) of α -ZPD along a -axis during dehydration of α -ZPT.

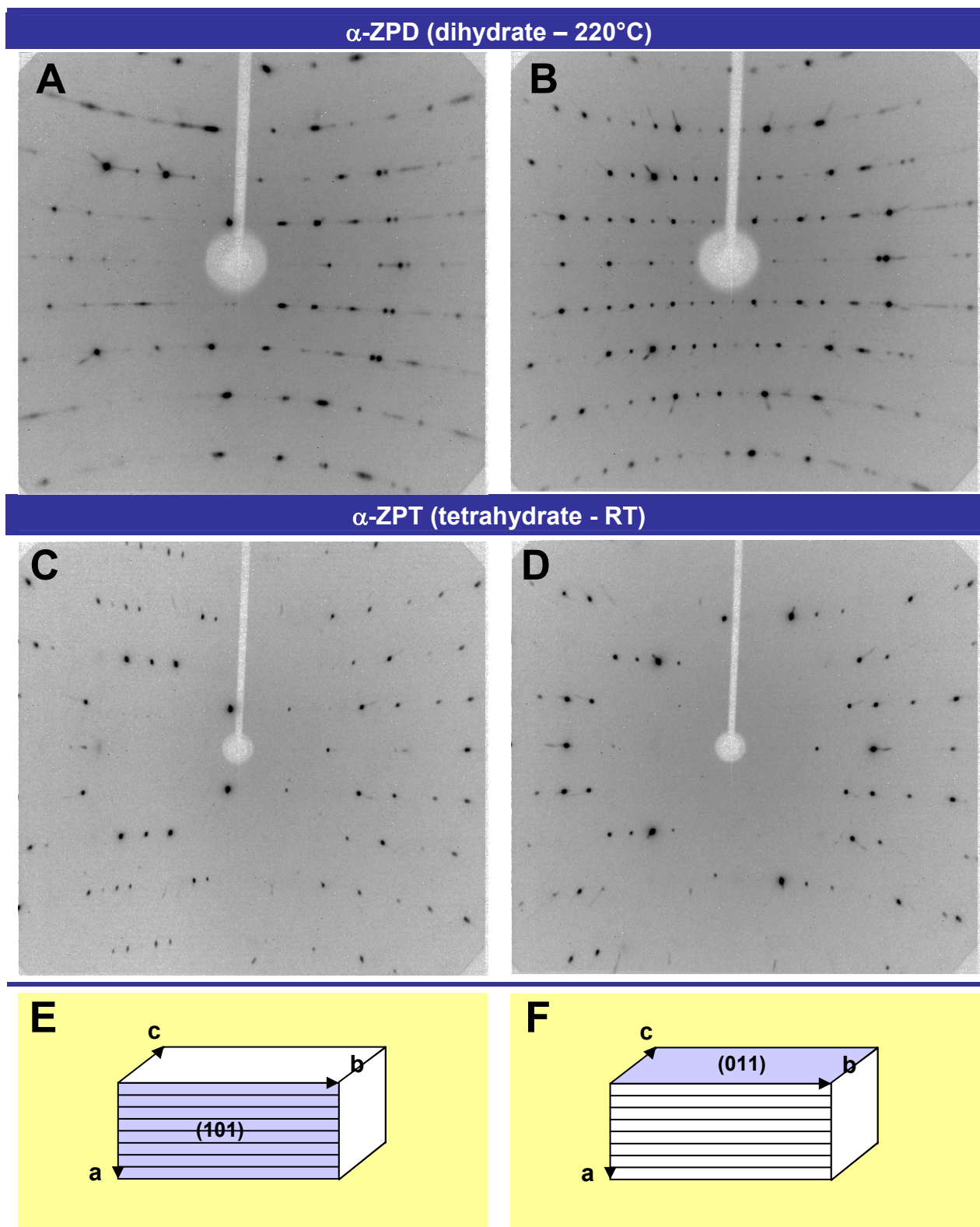


Figure 3.31: XRD single crystal diffraction patterns on selected surfaces (011) (B, D) and (101) (A, C) of α -zinc phosphate tetrahydrate and α -zinc phosphate dihydrate. The Bragg reflexes of the two planes either in the tetrahydrate (α -ZPT) or in the dihydrate (α -ZPD) crystals are very similar (superimposable) indicating that the bulk and the surface crystal structures for each hydrated phase are identical and that two of the cell parameters remain constant upon dehydration. Note the diffuse halos in (A), reflecting the one dimensional collapse of the ZPT structure (rupture of the hydrogen bonds of two crystal water molecules along c-axis, change of coordination sphere of Zn(II): octahedric \rightarrow tetrahedric) parallel to the plane (011) and the

growth of twin layers of α -ZPD. This explains on atomic scale the appearance of striations of dehydration in (101) planes of α -ZPD.

A further indication that this 2D-diffusional mechanism is the preponderant dehydration mechanism compared to a “hypothetical” dehydration mechanism (JMA mechanism) of the (bc) plane is given by XRD. Thus the isothermal dehydration of α -hopeite was followed at 150°C as displayed in Figure 3.26. At 150°C the starting material (Fig. 3.31 B) is unambiguously identified as having the structure of α -ZPT by comparison with the pure product (Fig. 3.31 A). Identically the identification of the final product succeeds in comparing Fig. 3.31 F and Fig. 3.33 G. One obtains a powder of α -ZPD. Figure 3.33 C shows that after one hour α -hopeite has transformed and evolved in a crystalline intermediary product (supposedly a trihydrate: α -ZPT_r). This products then transforms in a more and more crystalline structure of the α -ZPD as time elapses (Fig. 3.28 D to F). It must be noticed that at any moment of the reaction the α -ZPT and the α -ZPD do not coexist. This has strong implications on the mechanism of dehydration, since it excludes the possibility of a Avrami Nucleation and Growth mechanism and broadly contradicts the conclusions of thermoanalysis. On contrary this indicates a diffusional mechanism of dehydration.

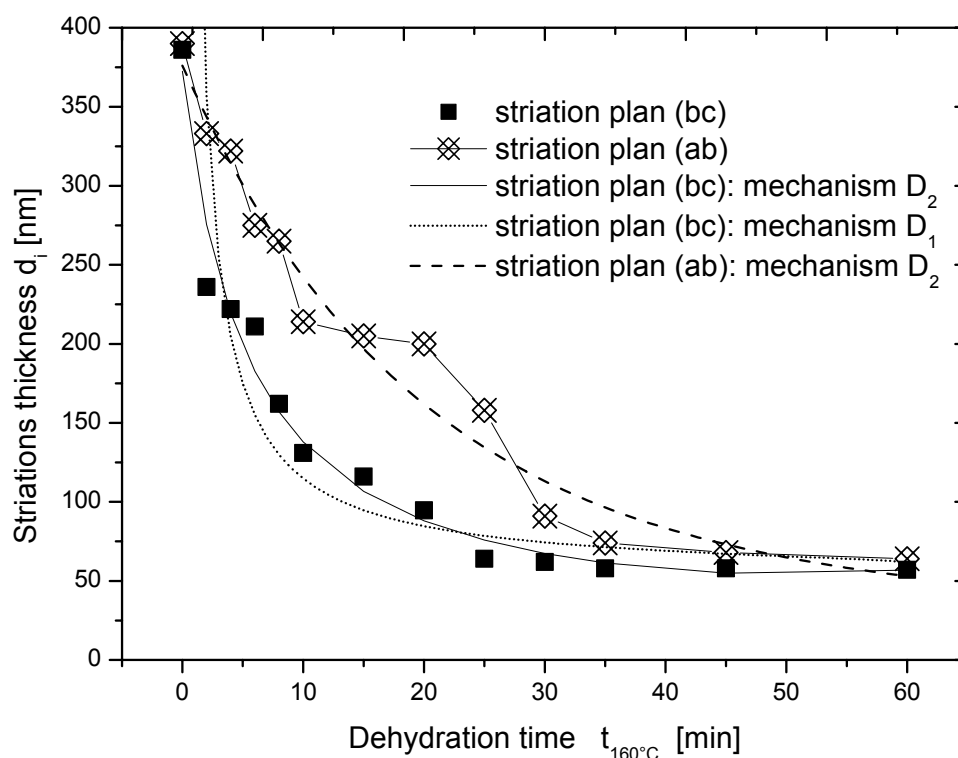


Figure 3.32: Isothermal time variations of the thickness of the striations in crystallographic planes (ab) and (ac) of α -ZPT at 160°C, evaluated from SEM images. A strong correlation with a bi-dimensional diffuse mechanism of dehydration is found without showing evidence of any induction time effect due to thermal conduction in solid state.

Before rejecting definitively the possibility of a concurring Avrami nucleation and growth mechanism to two dimensional diffusion mechanism of dehydration for the reaction reaction α -ZPT $\xrightarrow{1}$ α -ZPD,

the [011] surface (prominent face on the platelets of ZPT) was characterized by polarized microscopy (LM). The changes of contrast of an LM observation in reflection modus are proportional to changes of surface topology (essentially variations of height). The changes of contrast of an LM observation in transmission modus are proportional to changes of refraction index and therefore to changes of chemical composition.

Since zinc phosphate tetrahydrate and dihydrate crystallize in very different structures (orthorhombic and monoclinic), it is assumed that a change of density may induce a change of refractive index. Thus in transmission modus, the coexistence of both ZPT and ZPD phases in bulk and at the surface can be monitored. In order to confirm or infirm this information obtained from DSC and DTGA, the non isothermal dehydration of α -hopeite at constant heating rate ($10 \text{ K}\cdot\text{min}^{-1}$)

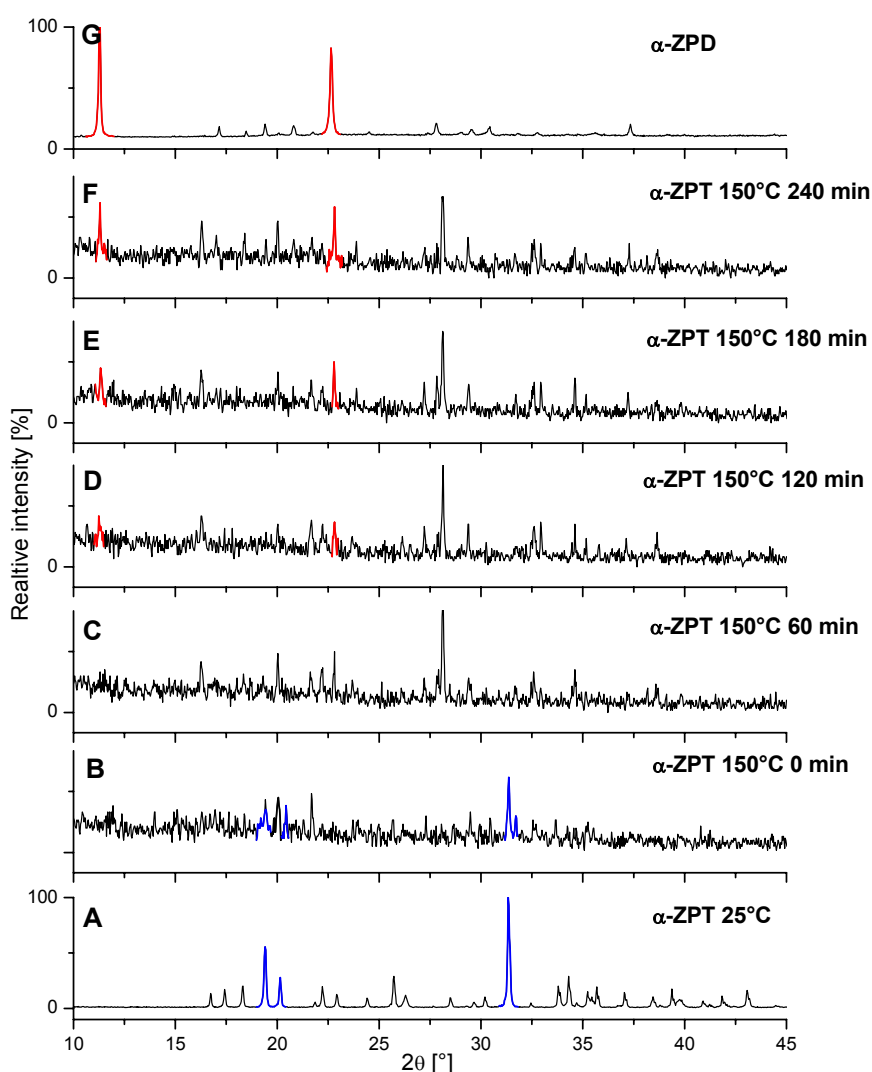


Figure 3.33: Isothermal dehydration of α -ZPT followed by Powder diffraction at 150°C . The continual transformation of α -ZPT in α -ZPD is illustrated with the RXD curves (B) to (F), indicating only very partial coexistence of both phases and the presence of a crystalline intermediary product after 1 hour (C). Pure α -ZPT (A) and α -ZPD (G) are also given as reference. Characteristic features are coloured in blue (α -ZPT) and red (α -ZPD).

in the range 100-240°C was followed by polarized light microscopy in reflection and transmission. At room temperature α -ZPT exhibits an important surface roughness as shown in reflection (Fig. 3.34 A - 25°C) and no compositional changes are noticed as illustrated in transmission in Fig. 3.43 D (25°C). This means that the crystal is composed of a pure α -ZPT phase. After heating to 240°C for one hour, second order interference patterns are observed in reflection (Fig. 3.43 A – 240°C). The variation of colours between 25°C and 240°C suggest a slight deformation of the surface occurring during dehydration and not monitored in SEM (Fig. 3.28 I) or the effects of residual thermal stresses on the (101) surface. In transmission during dehydration a lightly marked change of coloration (contrast yellow-red-green) is noticed. This indicates either a nearly continuous phase transformation of ZPT in ZPD with spots of different colours spread on the crystal surface where also a change of crystal thickness was notified or a uniform repartition of variation of refractive index. At 240°C the stabilization of the ZPD structure is completely achieved since no changes of refractive index are to be noticed in Fig. 3.34 D (240°C). This is also confirmed by XRD spectra in Fig. 3.9 A. Further using the same experimental conditions the analysis of reflected polarized light a careful observation of surface changes gives finally some proof of a slowly occurring surface dehydration process following the Avrami (JMA) mechanism. This is well illustrated in Fig. 3.28. Following the changes of contrasts especially in spot 1 of the (101) surface, one notices the appearance and the broadening of circular to elliptic white dots as temperature increases. Below 120°C, no dehydration points are to be reported. If one sets apart or neglects the constant changes of surface topology (quantifiable from Fig. 3.35); the broadening of white spots corresponds directly to a change of refractive index on the crystal surface (Fig. 3.35 180°C-210°C).

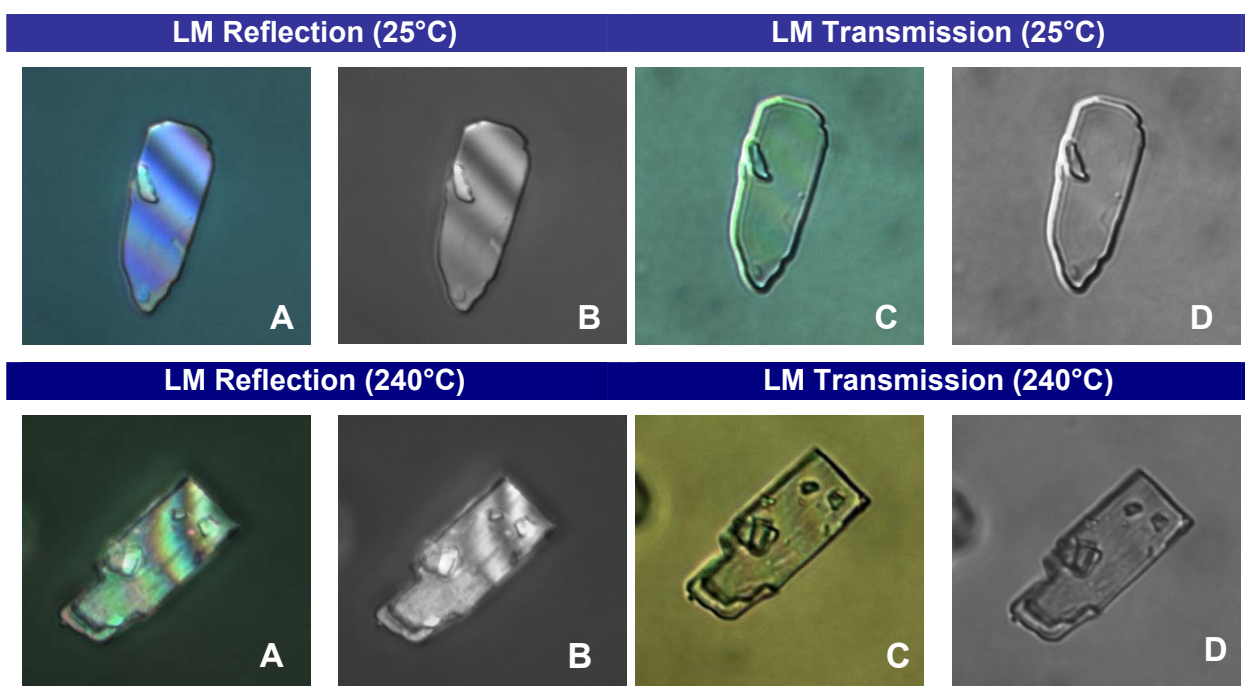


Table 3.34: Polarized Light Microscopy study of the dehydration reaction α -ZPT \rightarrow α -ZPD in zoom \times 1000. Coloured image (non analyzed light), Grey image (analyzed light)

It is evident that the first crystal layers of ZPT are first converting to ZPD as temperature increases and then the bulk is transforming. It is assumed that surface defects generated during crystallization (for example screw dislocations) are privileged locations to give birth to these dehydration spots. This idea may be supported by the work of Haussuhl and Friedrich [223] on the systematic determination of the elastic and thermoelastic constants of α -ZPT (hopeite) by means of ultrasonic resonance frequency analysis. In respect to longitudinal elastic stiffness α -ZPT behaves quasi isotropically but the elastic shear stiffness shows a large anisotropy (factor 2.5) and an anomalous temperature dependence (C66 component). Further they show that the α -ZPT contracts along a -axis and expands along c -axis, thus creating remnant thermal stresses suitable and favourable to initiation (non random nucleation) of surface dehydration as described by Nabbaro [224] and Fischer et al. [225]. This confirms that the JMA mechanism on the [011] surface is concurring with a two-dimensional diffusive mechanism on the [101] and [110] surfaces in the dehydration of α -ZPT. This statement is most probably also valid for the β -form of ZPT.

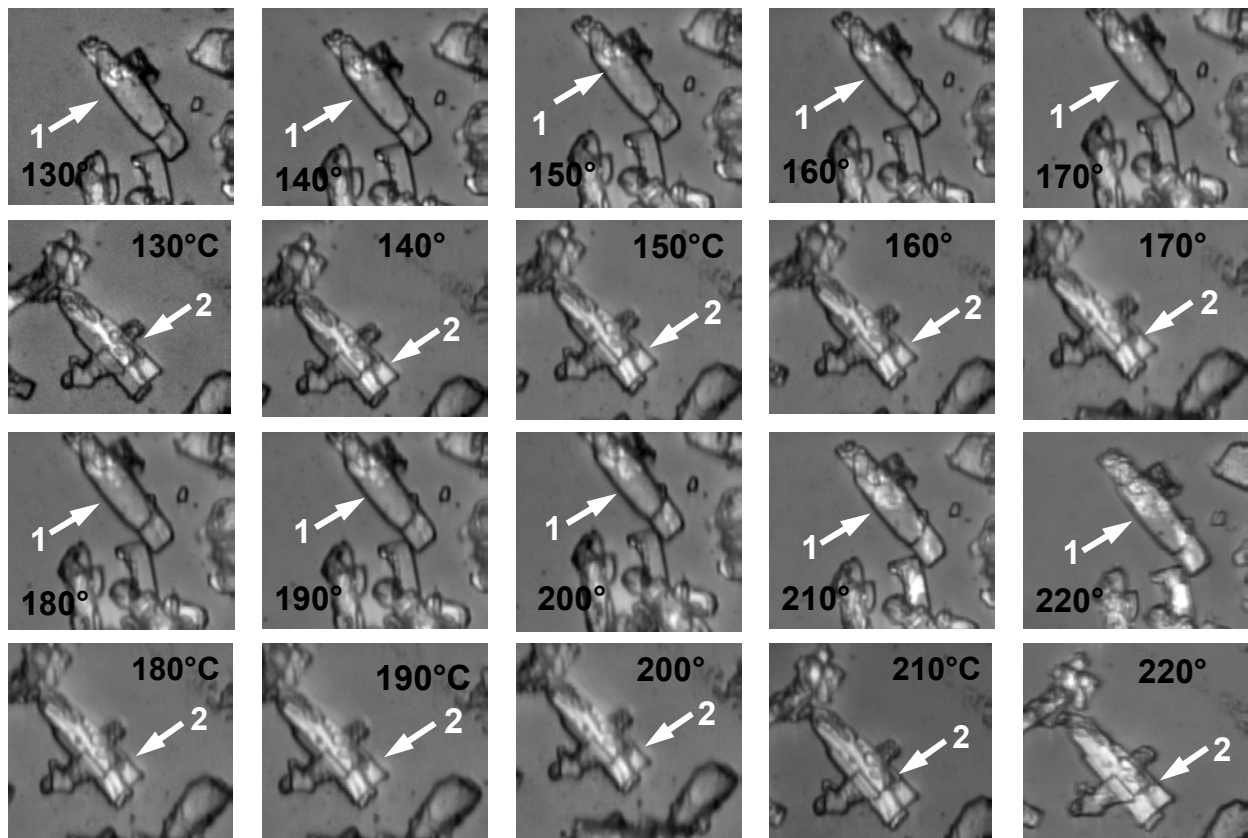


Figure 3.35: Polarized Light Microscopy pictures taken in reflection modus (zoom $\times 50$) of the dehydration of α -ZPT at 10 K.min^{-1} . This shows a surface change of contrast interpreted as an Avrami nucleation and growth mechanism on surface (011) on specific points (1 and 2).

In conclusion of this investigation about the thermal behaviour of ZPT polymorphs Figure 3.36 offers a schematic representation of the possible concurring dehydration mechanisms.

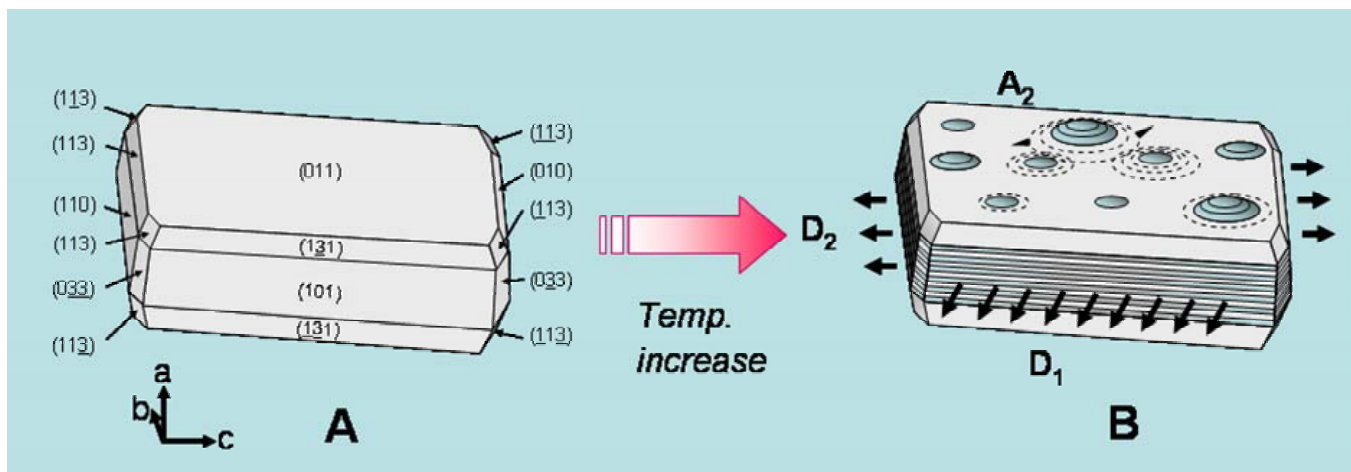


Figure 3.36: Schematic concurring mechanisms of dehydration upon heating: (A) stable α -ZPT at room temperature, (B) transforming α -ZPT above 130°C. The dehydration involves one and two-dimensional diffusion mechanisms (labelled as D1 and D2) and a two dimensional JMA Nucleation & Growth mechanism (A2).

3.6. Conclusion

In this chapter the fundamental understandings of the solid state thermodynamic and kinetic properties of dehydration of such a complex system as the zinc phosphate hydrates system was of major interest. In order to explain the unique thermal behaviour of the different polymorphs of zinc phosphate tetrahydrates, preliminary experimentations combining morphological (SEM) and structural (XRD) characterizations were undertaken and led to the discoveries of microchannels and striations of dehydration. Upon heating ZPT polymorphs (i.e. α - and β -modifications) release crystal water differently: while the α -form loses water two by two in two well defined stages, the β -form exhibits a dehydration pathway involving intermediary products of hydration, namely the dihydrate and the monohydrate. This phenomenon could be correlated with the respective hydrogen bonding pattern of each phase. Therefore dehydration of ZPT must be considered a multi-step irreversible heterogeneous solid state (solid-gas) reaction. On this basis and applying a “same final thermodynamic state” procedure, the thermodynamic stability phase diagram pointing out the possible interrelations between the various hydrate states and phases was built. By varying heating rates, the standard state functions, i.e. standard enthalpies ($\Delta H^{\text{dehydr.}}$), entropies ($\Delta S^{\text{dehydr.}}$) and free energies ($\Delta G^{\text{dehydr.}}$) of dehydration and of formation ($\Delta H^{\text{form.}}$, $\Delta S^{\text{form.}}$ and $\Delta G^{\text{form.}}$) have been generated statistically and successfully compared with reference values obtained from the solid-liquid reaction approach of Gardner et al. The following classification of decreasing stability can be made ZPT < ZPD < ZPA. The difference of free energy first between α - and β -ZPT and secondly between α - and β -ZPD were approximately 8 and 6 $\text{kJ}\cdot\text{mol}^{-1}$ and are essentially of entropic origin. By extrapolation to zero heating rate, the transition temperature between β -ZPT and α -ZPT was estimated around

170°C, lying well in the dehydration range. Therefore this phase transition is hardly observed. Similar transitions are observed between β -ZPD and α -ZPD. This interconversion mechanism may be described with the classical “activated complex” theory. Furthermore one could show that the transitions $ZPT \rightarrow ZPD$ and $ZPD \rightarrow ZPA$ were of thermodynamic second and first order respectively. This thermodynamic study of the zinc phosphate hydrates system, a requisite to a proper kinetic study, in combination with the characterization of the thermal behaviour of fine ZPT powders by XRD, SEM and Polarized Light Microscopy, allows the identification of the basic mechanisms involved during dehydration. Dehydration of ZPT is strongly influenced by the modulation of the heating rate and the morphology (i.e. thickness of the platelets) of the crystals. From DSC and DTGA curves in employing the Kissinger, Friedmann, Carroll and WFO (isoconversional method) methods, the activation energies of each step-reaction in dependence on the crystal modification could be determined around 145, 120, 110 and 98 kJ.mol⁻¹ for α -ZPD, β -ZPD, α -ZPA, β -ZPA respectively. Besides, Kissinger’s approach gave a reliable estimate of the apparent order of reaction and precious indications on the supposed mechanisms of dehydration, especially for the reaction $ZPT \rightarrow ZPD$ which is of industrial relevance. A critical heating rate of 7 K.min⁻¹ as the value at which the activation energy and the apparent order of reaction switch from one statistical value to another one has been found; this corresponds to concurring mechanisms of dehydration: on one hand at low heating rate a two dimensional JMA mechanism on the (011) surface, induced by surface crystal defects and starting preferentially from crystal edges is privileged, and on the other hand at high heating rate a two dimensional diffusion mechanism (D₂) first on the (101) plan and then on the (110) surface takes over, as nicely shown by the realized ex-situ SEM study. These mechanisms take place in both forms of ZPT but with different kinetics, i.e. β -hopeite tends to dehydrate faster and at lower temperature than α -hopeite. At higher temperature the α - and β -form of ZPD dehydrate following a purely two dimensional diffusion mechanism. Moreover for a deeper understanding of the complex phenomena here-above discussed, one should refer to monographs contributing to the general improvement of DSC theory. And because it is the nature of science to give only an approximation of reality, Šesták in his homage to the fundamental work of J.H. Flynn pleasantly discussed on the modern and conceptual pictures of the nature of kinetics in Solid State Chemistry and the relevance of the extensive use of isoconversional methods necessary for its accurate description (i.e. dichotomy between empirical models and basic kinetic mechanisms)*.

Conclusively, one should add that this thermodynamic and kinetic study settles the basis for a thoroughfull analysis of the chemical surface reactivity and solubility of zinc phosphate tetrahydrate polymorphs.

(*) J. Šesták, V. Šesták, *Thermochim. Acta* 203 (1992) xix

3.7. References

- [1] J.B. Harrison, *Corrosion and Coatings* **3** (1976) 11
- [2] M.F. Clay, J.H. Cox, *J. Oil Colour Chem. Assoc.* **56** (1973) 13
- [3] G. Meyer, *Farbe + Lacke* **3** (1965) 113
- [4] A. Kalendová, P. Kalenda, *Farbe + Lacke* **109** (2003) 62
- [5] G.E. Servais, L. Cartz, *J. Dent. Res.* **50** (1971) 613
- [6] O. Pawlig, *PhD Thesis*, University of Mainz, Germany (2001)
- [7] M.V. Goloshchapova, T.N. Filatova, *Russ. J. Inorg. Chem.* **14** (1969) 424
- [8] L. Perez, G.H. Nancollas, *J. Cryst. Growth* **66** (1984) 412
- [9] H.M.A. AL-Maydama, P.J. Gardner, I.W. Mc Ara, *Thermodyn. Acta* **196** (1992) 117
- [10] P.A. Sandormirski, C.P. Klientova, M.A. Simonov, N.V. Belov, *Dkl. Akad. Nauk. Cryst.* **236** (1977) 597
- [11] Y. Cudennec, A. Lecerf, A. Riou, Y. G erault, *C.R. Acad. Sci.* **301** serie II (1985) 93
- [12] R.J. Hill, J.B. Jones, *Am. Mineral.* **61** (1976) 987
- [13] A.R. Milnes, R.J. Hill, *Neues Jahrb. Mineral. Monatsh* **1** (1977) 25
- [14] S.A. Amirova, V.V. Pechkovskii, G.E. Tyuleneva, *Izv. Vyssh. Ucheb. Zaved., Khim. Khim. Tekhnol.* **10** (1967) 3
- [15] C. Calvo, *J. Phys. Chem. Solids* **24** (1963) 141
- [16] C. Calvo, *Can. J. Chem.* **43** (1965) 436
- [17] J.S. Stephens, C. Calvo, *Can. J. Chem.* **45** (1967) 2303
- [18] R.C. Mackenzie, *Thermochim. Acta* **28** (1979) 1
- [19] R.C. Mackenzie, *Isr. J. Chem.* **22** (1982) 203
- [20] W.W. Wendlandt, *Thermochim. Acta* **36** (1980) 393
- [21] J.G. Dunn, *Chem. Aust.* **47** (1980) 281
- [22] G. Liptay, *J. Thermal Anal.* **25** (1982) 235
- [23] C. Duval, *Inorganic Thermogravimetric Analysis*, 2nd Edition, Elsevier (Amsterdam) (1963)
- [24] W.L. De Keyser, *Nature* **172** (1953) 364
- [25] L. Erdey, F. Paulik, J. Paulik, *Nature* **174** (1954) 885
- [26] P.L. Waters, *Nature* **178** (1956) 324
- [27] J.G. Dunn, *Application Note 250*, Stanton Redcroft Ltd. (London)
- [28] J.G. Dunn, S.S.A. Jayweera, *Thermochim. Acta* **61** (1983) 313
- [29] C. Duval, *Anal. Chim. Acta.* **31** (1964) 301
- [30] E.L. Simons, A.E. Newkirk, *Talanta* **11** (1964) 549
- [31] A.E. Newkirk, *Anal. Chem.* **32** (1970) 1558
- [32] E.L. Simons, W.W. Wendlandt, *Thermochim. Acta* **2** (1971) 465
- [33] A.W. Coats, J.P. Redfern, *Analyst* **88** (1963) 906
- [34] K.J. DeVries, P.J. Gellings, *J. Inorg. Nucl. Chem.* **31** (1969) 1307
- [35] J.M. Criado, A. Ortega, F.J. Gotor, *Thermochim. Acta* **203** (1992) 187
- [36] J. Sestak, *Talanta* **13** (1966) 567
- [37] A. Richer, P. Vallet, *Bull. Soc. Chem. Franc.* (1953) 148
- [38] S.B. Warrington, G.W.H. H hne, *Thermal Analysis and Calorimetry in Ullmann's Encyclopedia of Industrial Chemistry*, Vol. **1**, Wiley VCH (2002)
- [39] W. Hemminger, G. H hne, *Calorimetry, Fundamentals and Practice*, Verlag Chemie, (Weinheim) (1984)
- [40] E. Gmelin, *Thermochim. Acta* **304-305** (1997) 1
- [41] F. Paulik, J. Paulik, *Analyst* (London) **103** (1978) 417
- [42] H. Gobrecht, K. Hamman, G. willers, *J. Physics E: Sci. Instr.* **4** (1971) 21
- [43] M.J. O'Neill, *Anal. Chem.* **36** (1964) 1233
- [44] A.P. Gray, in *Analytical Calorimetry*, R.F. Porter and J.M. Johnson Eds., Plenum (NY) (1968), p. 209
- [45] R.A. Baxter, in *Thermal analysis*, R.F. Schwenker and P.D. Garn Eds, Academic Press (NY), (1969), p. 65

- [46] J.H. Flynn, in *Status of Thermal Analysis*, O. Menis Eds., NBS special publications 338, Gov't Printing Office, (Washington), (Oct. 1970), p. 119
- [47] D.J. David, *J. Thermal Anal.* **3** (1971) 247
- [48] G.W.H. Höhne, *Thermochim. Acta* **330** (1999) 45
- [49] A.R. Salvador, E.G. Calvo, C.B. Aparicio, *Thermochim. Acta* **143** (1989) 339
- [50] S.M. Sarge, W. Hemminger, *Thermochim. Acta* **247** (1994) 129
- [51] D.J. David in W.E. Collins, *Analytical Calorimetry*, R.S. Porter and J.M. Johnson Eds., Vol. **2**, Plenum (NY) (1970), p 369
- [52] B.R. Curell, in *Thermal Analysis*, R.F. Schwenker and P.D. Garn Eds., Vol. **2**, Academic Press (NY) (1969), p. 1185
- [53] T. Ozawa, *Bull. Chem. Soc. Jpn.* **39** (1966) 2071
- [54] A. Hensel, C. Schick, *Thermochim. Acta* **304-305** (1997) 229
- [55] R. Melling, F.W. Wilburn, R.M. McIntosh, *Anal. Chem.* **41** (1969) 1275
- [56] P.D. Garn, *Thermoanalytical Methods of Investigations*, Academic Press (NY) (1965) p. 60
- [57] E.M. Barall, L.B. Rogers, *J. Inorg. Nucl. Chem.* **28** (1966) 41
- [58] H.E. Kissinger, *J. Res. Nat. Bur. Stand.* **57** (1956) 217
- [59] H.E. Kissinger, *Anal. Chem.* **29** (1957) 1702
- [60] H.T. Smyth, *J. Am. Ceram. Soc.* **34** (1951) 221
- [61] R. C. Wilhoit, *J. Chem. Educ.* **44** (1967) A571
- [62] W.P. Brennan, B. Miller, J.C. Whitnell, *Thermochim. Acta* **2** (1971) 354
- [63] G. Hakvoort, C.M. Hol, P.J. Van Ekeren, *J. Thermal Anal. Calorim.* **69**(1) (2001) 367
- [64] S. Speil, L.H. Berkerhamer, J.A. Pask, B. Davis, *US. Bur. Mines, Tech. Papers* **664** (1945)
- [65] P.F. Kerr, J.L. Kulp, *Am. Mineral.* **33** (1948) 387
- [66] V.B.F. Mathot, *Calorimetry and Thermal Analysis of Polymers*, Hanser Verlag (Munich) (1994) p. 67
- [67] I.M. Klotz, R.M. Rosenberg, *Chemical Thermodynamics: Basic theory and methods*, 5th Ed., Wiley Interscience, (NY) (1994), p. 196
- [68] S.C. Mraw, *Rev. Sci. Instrum.* **53** (1982) 228
- [69] Y. Saito, K. Saito, T. Atake, *Thermochim. Acta* **99** (1986) 299
- [70] Y. Saito, K. Saito, *Thermochim. Acta* **104** (1986) 275
- [71] I. Hatta, H. Ichikawa, M. Todoki, *Thermochim. Acta* **267** (1995) 83
- [72] R.F. Schwenker, J.C. Whitwell, in *Analytical Calorimetry*, R.F. Porter and J.C. Johnson Eds., Vol. **1**, Plenum (NY) (1968), p. 249
- [73] E. Sturm, *Thermochim. Acta* **4** (1972) 461
- [74] A. I. Volkov, V. N. Yaglov, G. I. Novikov, *Russian J. Phys. Chem.* **A48** (1974) 1697
- [75] V. N. Yaglov, *Khim. Khim. Tekhnol.* (Minsk) **13** (1978) 7
- [76] H. M. A. AL-Maydama, P.J. Gardner, *Electrochem. Acta* **194** (1992) 117
- [77] A. Whitaker, *J. Appl. Chem.* **6** (1973) 495
- [78] L. Herschke, V. Enkelmann, I. Lieberwirth, G. Wegner, *submitted to Chemistry- A Europ. J.* **10**(11) (2004) 2795
- [79] J. S. Stephens, C. Calvo, *Can. J. Chem.* **45** (1967) 2303
- [80] Y. Cudennec, A. Lecerf, A. Riou, Y. G rault, *C.R. Acad. Sci.* **301** serie II (1985) 93
- [81] J. Komrska, V. Satava, *Silikaty* **13**(2) (1969) 135
- [82] F. L. Katnach, F. A. Hummel, *J. Electrochem. Soc.* **105** (1958) 125
- [83] ICDS cards of α, β -Zn₃(PO₄)₂ N° 29- 1390 and 30-1489
- [84] A. G. Kotlova, N. I. Shcheepochkina, B. M. Kobsev, *Inorg. Mater.* (USSR) **11** (1976) 1247
- [85] Y. Arnaud, E. Sahakian, M. Romand, *Appl. Surf. Sci.* **32** (1988) 281
- [86] T. Kanazawa, in *Inorganic Phosphate chemistry*, edited by Kodansha Scientific, (Tokyo) (1985)
- [87] Y. Arnaud, E. Sahakian, J. Lenoir, A. Roche, *Appl. Surf. Sci.* **32** (1988) 296
- [88] H. Haidara, *PhD. Thesis*, University of Muhlhouse, (France), (1985)
- [89] E. A. Nikonenko, I. I. Olikov, I. N. Marenkova, L. N. Margolin, L. A. Reznikova, *Russ. J. Inorg. Chem.* **30** (1985) 25
- [90] J. Šest k, *Thermophysical Properties of Solids*, Academia (Prague) (1984), p. 112
- [91] J. Mu, D.D. Perlmutter, *Ind. Eng. Chem. Process. Des. Dev.* **20** (1981) 640
- [92] T.V. Lee, S.R. Beck, *AIChE J.* **30** (1984) 517

- [93] M.A. Stanish, D.D. Perlmutter, *AIChE J.* **29** (1983) 806
- [94] T.J.W De Bruijn, W.A. De Jong, P.J. Van Berg, *Thermochim. Acta* **45** (1981) 315
- [95] T.B. Tang, *Thermochim. Acta* **57** (1982) 195
- [96] P. O' Brian, S.D. Ross, *Thermochim. Acta* **53** (1982) 195
- [97] C. Guler, D. Dollimore, G.R. Heal, *Thermochim. Acta* **54** (1982) 187
- [98] V.M. Gorbachev, *J. Therm. Anal.* **20** (1981) 229
- [99] A. R. Salvador, E.G. Calvo, *Thermochim. Acta.* **107** (1986) 283
- [100] E. Segal, C. Popescu, M. Tucsnak, C. Oprea, *Thermochim. Acta* **107** (1986) 365
- [101] H. Tanaka, *Thermochim. Acta* **90** (1985) 101
- [102] A. R. Salvador, E.G. Calvo, J. M. Navarro, *Thermochim. Acta* **87** (1985) 163
- [103] E. Urbanovici, E. Segal, *Thermochim. Acta* **107** (1986) 339-363
- [104] A.E. Newkirk, *Anal. Chem.* **32** (1960) 1558
- [105] R.F. Melling, F.W. Wilburn, R.M. McIntosh, *Anal. Chem.* **41** (1969) 1275
- [106] Y. Saito, K. Saito, T. Atake, *Thermochim. Acta* **107** (1986) 277
- [107] P.D.Garn, *Thermoanalytical Methods of Investigation*, Academic Press (NY) (1965), p.32
- [108] N.B. Hannay in *Treatise on Solid State Chemistry*, Vol. **5**: Changes of State, N.B. Hannay Ed., Plenum (NY) (1975), p. 70
- [109] S.J. Ashcroft, *Thermochim. Acta* **2** (1971) 512
- [110] H. M. A. AL-Maydama, P. J. Gardner, I. W. Mc Ara, *Electrochim. Acta* **196** (1992) 117
- [111] V. S. Joshi, M. J. Joshi, *Cryst. Res. Technol.* **38**(9) (2003) 817
- [112] R. R. Kumar, M. Wang, *Mater. Letters* **49** (2001) 15
- [113] A. I. Volkov, V. N. Yaglov, G. I. Novikov, *Russ. J. Phys. Chem.* **48** (1974) 1697
- [114] A. I. Volkov, V. N. Yaglov, G. I. Novikov, *Russ. J. Phys. Chem.* **48** (1974) 1701
- [115] V. N. Yaglov, *Khim. Khim. Technol.* (Minsk) **13** (1978) 7
- [116] V. N. Yaglov, L. A. Marinova, G. I. Novikov, *Dokl. Akad. Nauk.* **B78** (1974) 624
- [117] D. D. Wagman, W. H. Evans, V. B. Parker, I. Halow, S.M. Bailey, R. H Schumm, *Natl. Bur. Stand. Tech. Note* **270**(3) (1968) 264
- [118] D. Dollimore, *Thermochim. Acta* **203** (1992) 7
- [119] D. D. Wagman, W. H. Evans, V. B. Parker, I. Halow, S. M. Bailey, R. H Schumm, *Natl. Bur. Stand. Tech. Note* **270**(4) (1969) 152
- [120] D. D. Wagman, W. H. Evans, V. B. Parker, I. Halow, S. M. Bailey, R. H Schumm, K. L. Churney, *Natl. Bur. Stand. Tech. Note* **270**(5) (1971) 49
- [121] I. R. Gibson, I. Rehman, S. M. Best, W. Bonifield, *J. Mater. Sci.: Mater. Med.* **12** (2000) 799
- [122] M. Tamai, M. Nakamura, T. Isshiki, H. Endoh, A. Nakahira, *J. Mater. Sci.: Mater. Med.* **14** (2003) 617
- [123] J.S. Stephens, C. Calvo, *J. Chem.* **45** (1967) 2303
- [124] J. JP. Valdes, J. O. Lopez, G. R. Morales, G. P. Malagon, V. P. Gortcheva, *J. Mater. Sci.: Mater. Med.* **5** (1997) 297
- [125] V. B. Parker, D. D. Wagman, W. H. Ewans, in Selected values of chemical thermodynamic properties, *Natl. Bur. Stand. Tech. Note* **270**(6) (1971) 119
- [126] J. D. Cox, D. D. Wagman, V. A. Medvedev, in CODATA Key Values for Thermodynamics, (Hemisphere Pub. Corp.) (London) (1989)
- [127] A. I. Volkov, *Khim. Khim. Tekhnol.* (Minsk) **14** (1979) 58
- [128] G. Y. Chao, *Z. Kristallogr.* **130** (1969) 261
- [129] E. Sahakian, Y. Arnaud, *C.R. Acad. Sci., Ser. 2* **306** (1988) 277
- [130] C. Calvo, *Can. J. Chem.* **43** (1965) 436
- [131] H.M.A. Al-Maydama, P.J. Gardner, I.W. McAra, *Thermochim. Acta* **196** (1992) 117
- [132] H.J. Borchardt. F. Daniels, *J. Chem. Educ.* **33** (1956) 103
- [133] H.J. Borchardt. F. Daniels, *J. Inorg. Nucl. Chem.* **12** (1960) 252
- [134] H.J. Borchardt. F. Daniels, *J. Am. Chem. Soc.* **79** (1957) 41
- [135] J. Sestak, *Talanta* **13** (1966) 567
- [136] E.S. Freeman, B. Carroll, *J. Phys. Chem.* **62** (1958) 394
- [137] C.D. Doyle, *J. Appl. Polym. Sci.* **5** (1961) 285
- [138] A.W. coats, J.P. Redfern, *Nature* **201** (1964) 68
- [139] H.H. Horowitz, G. Metzger, *Anal. Chem.* **35** (1963) 1464
- [140] A.E. Newkirk, *Anal. Chem.* **32** (1960) 1558

- [141] L. Reich, S.S. Stilava, *Thermochim. Acta* **24** (1978) 9
- [142] L. Reich, S.S. Stilava, *Thermochim. Acta* **34** (1979) 287
- [143] L. Reich, S.S. Stilava, *Thermochim. Acta* **59** (1982) 247
- [144] L. Reich, S.S. Stilava, *Thermochim. Acta* **60** (1983) 251
- [145] L. Reich, S.S. Stilava, *Thermochim. Acta* **62** (1983) 129
- [146] L. Reich, S.S. Stilava, *Thermochim. Acta* **36** (1980) 103
- [147] L. Reich, S.S. Stilava, *Thermochim. Acta* **73** (1984) 165
- [148] E.S. Freeman, B. Carroll, *J. Phys. Chem.* **62** (1958) 394
- [149] H.E. Kissinger, *Anal. Chem.* **29** (1957) 1702
- [150] H.E. Kissinger, H.F. McMurdie, B.S. Simpson, *J. Am. Ceram. Soc.* **39** (1956) 168
- [151] A.W. Coats, J.P. Redfern, *Nature* **201** (1964) 68
- [152] J.H. Sharp, S.A. Wentworth, *Anal. Chem.* **41** (1969) 2060
- [153] P.K. Galladher, D.W. Johnson, *Thermochim. Acta* **6** (1973) 67
- [154] J.M. Criado, J. Morales, Y. Rives, *J. Thermal Anal.* **14** (1978) 221
- [155] J. Vachuska, M. Voboril, *Thermochim. Acta.* **2** (1971) 379
- [156] H.A. Papazian, P.J. Pizzolato, R.R. Orrell, *Thermochim. Acta* **4** (1972) 97
- [157] Z. Andonyi, *Period. Polytech.* **11** (1967) 325
- [159] C.D. Doyle, *J. Appl. Polym. Sci.* **5** (1961) 285
- [159] J. Zsako, *J. Phys. Chem.* **72** (1968) 2406
- [160] H. Friedman, *J. Polym. Sci.* **C6** (1964) 183
- [161] T. Ozawa, *Bull. Chem. Soc. Jpn.* **38** (1965) 1881
- [162] T. Ozawa, *J. Thermal Anal.* **7** (1975) 601
- [163] T. Ozawa, *J. Thermal Anal.* **2** (1970) 301
- [164] T. Ozawa, *J. Thermal Anal.* **9** (1976) 217
- [165] J. H. Flynn, L.A. Wall, *J. Polym. Sci.* **B4** (1966) 323
- [166] T. Ozawa, *Bull. Chem. Soc. Jpn.* **38** (1965) 1881
- [167] L.F. Jones, D. Dollimore, T. Nicklin, *Thermochim. Acta* **13** (1975) 240
- [168] J.H. Sharp, G.W. Brindley, B.N.N. Achar, *J. Am. Chem. Soc.* **49** (1966) 379
- [169] J. Sestak, G. Berggren, *Thermochim. Acta* **3** (1971) 1
- [170] V. Satava, *Thermochim. Acta* **2** (1971) 423
- [171] F. Baitalow, H.G. Schmidt, G. Wolf, *Thermochim. Acta.* **337** (1999) 111
- [172] G.I. Senum, R.T. Yang, *J. Therm. Anal.* **11** (1977) 445
- [173] C. Criado, M. Gonzales, A. Ortega, C. Real, *J. Thermal Anal.* **29** (1984) 243
- [174] F. Baitalow, H.G. Schmidt, G. Wolf, *Thermochim. Acta* **1-2** (1999) 337
- [175] C. Rozycki, M. Maciejewski, *Thermochim. Acta* **122** (1987) 339
- [176] J. Málek, *Thermochim. Acta* **200** (1992) 257
- [177] J. Málek, *Thermochim. Acta* **236** (1994) 187
- [178] R.A.W. Hill, *Trans. Faraday Soc.* **54** (1958) 685
- [179] P.W.M. Jacobs, F.C. Tompkins, in *Chemistry of the Solids*, W.E. Gardner Ed., Butterworth (1955), Chap. 7, p. 184
- [180] S.F. Hulbert, *J. Brit. Ceram. Soc.* **6** (1969) 11
- [181] K.L. Mampel, *Z. Phys. Chem.* **A187** (1940) 43, 235
- [182] B.V. Erofeev, *C.R. Dokl. Acad. Sci. URSS* **52** (1946) 511
- [183] M. Avrami, *J. Phys. Chem.* **7** (1939) 1103
- [184] W.A. Johnson, R.F. Mehl, *Trans. AIME* **135** (1939) 416
- [185] M. Avrami, *J. Phys. Chem.* **8** (1940) 212
- [186] M. Avrami, *J. Phys. Chem.* **9** (1941) 177
- [187] J. Šesták, *Thermophysical properties of Solids, Their Measurements and Theoretical Analysis*, Elsevier (Amsterdam) (1984)
- [188] J. Málek, J.M. Criado, J. Šesták, J. Militký, *Thermochim. Acta* **153** (1989) 429
- [189] N.B. Hannay, *Treatise on Solid State Chemistry*, Vol. **5** – Changes of State, Chapters 2 and 3., Plenum Press (NY) (1975)
- [190] H. Schmalzried, *Chemical Kinetics of Solids*, Wiley VCH (Weinheim) (1995)
- [191] R.K. Agrawal, *Thermochim. Acta* **203** (1992) 111
- [192] D. Dollimore, *Thermochim. Acta* **203** (1992) 7
- [193] J. Málek, *Thermochim. Acta* **200** (1992) 257

- [194] G. W. Brindley, M. Nakahira, *J. Am. Ceram. Soc.* **42** (1959) 319
- [195] P. Murray, J. White, *Trans. Brit. Ceram. Soc.* **48** (1949) 187
- [196] P. Murray, J. White, *Trans. Brit. Ceram. Soc.* **54** (1955) 204
- [197] E. C. Sewell, *Clay Minerals. Bull.* **2** (1955) 233
- [198] E. C. Sewell, D.B. Honeyborne, in *The differential Thermal Investigations of Clays*, R.C. McKenzie Ed., Mineral Soc. (London) (1957) p.65
- [199] H. Friedman, *J. Polym. Sci.* **C6** (1964) 183
- [200] E. S. Freeman, B. Carroll, *J. Phys. Chem.* **62** (1958) 394
- [201] J.H. Flynn, L. A. Wall, *J. Polym. Sci.* **B4** (1966) 323
- [202] T.Ozawa, *Bull. Chem. Soc. Jpn.* **38** (1965) 1881
- [203] F. C. Hawthorne, *Geol. Ore Deposits* **45**(2) (2003) 88
- [204] A. Werner, *Ber.* **40** (1907) 1433
- [205] N. Rhodes, *Chem. News* **127** (1921) 85
- [206] V. I. Semishin, *Russ. J. Inorg. Chem.* **8**/1 (1963) 66
- [207] C. K. Hsu, *Thermochim. Acta* **392-393** (2002) 157
- [208] E.R. Lippincott, R. Schroeder, *J. Phys. Chem.* **23** (1955) 1099
- [209] H. Sachsenröder, E. Brunner, M. Koch, H. Pfeifer, B. Staudte, *Microporous Mater.* **6** (1996) 341
- [210] H.T. Heal, H. Misura, *Metal Treatment* (Autumn 1950) 129
- [211] J. Saison, J. J. Trillat, *Cr. Hebd. Acad. Sci.* **249**(2) (1959), 2562
- [212] P. Murray, J. White, *Trans. Brit. Ceram. Soc.* **54** (1955) 204
- [213] J. Holt, I.B. Cutler, M.E. Wadworth, *J. Am. Ceram. Soc.* **45** (1962) 133
- [214] J. Opfermann, E. Kaiserberger, *Thermochim. Acta* **203** (1992) 167
- [215] C. H. P. Lupis, *Chemical Thermodynamics of Materials*, Elsevier Publish. (Oxford) (1983) p. 87
- [216] R. S Berry, S. A. Rice, J. Ross, in *Physical Chemistry*, Wiley and Sons Eds (1980) p. 1147
- [217] A. Jha, H.A. Davis, *J. Non-Cryst. Solids* **113** (1989) 185
- [218] C. Wagner, *Z. Anorg. allg. Chem.* **236** (1938) 320
- [219] W. Jost, *Diffusion und chemische Reaktion in Festkörper*, Steinkopff Ed. (Dresden) (1937)
- [220] P. Murray, J. White, *Trans. Brit. Ceram. Soc.* **54** (1955) 204
- [221] J. Holt, I.B. Cutler, M.E. Wadworth, *J. Am. Ceram. Soc.* **45** (1962) 133
- [222] E. Sahakian, Y. Arnaud, JCPDS ICDD card N° 41-493 (1996).
- [223] S. Haussuhl, M. Friedrich, *Crystal Res. Technol.* **28**(4) (1993) 437
- [224] F.R.N. Nabarro, *Proc. Roy. Soc.* **A175** (1940) 519
- [225] J.C. Fisher, J.H. Hollomon, D. Turnbull, *Trans. AIME* **185** (1949) 691

4. Chemical reactivity of metal (Zn^{2+} , Ca^{2+}) phosphate hydrates at surfaces and interfaces

“In all things of nature, there is something marvellous”, *Aristote*, Parts of Animals, 384 BC

4.1. Introduction

Hopeite is of considerable importance since it has been observed as a stable phase growing on the surfaces of zinc phosphate dental cements [1]. Recently great advances have been achieved in combining hydroxyapatite with zinc phosphate cements [2]. Accordingly, an implant with desired long term biostability and low cytotoxicity can be obtained in controlling the crystal size and the hydration state of zinc (ZP) and/or calcium phosphate containing materials [3-5]. Therefore many studies focus on the synthesis of biphasic zinc phosphate ceramics through various raw materials [6] and processes [7-8]. However retention of dental restoration to the tooth substance and sealing of the marginal gap between the restoration and tooth are also dependent on the surface and bonding properties of ZP cements that critically control the adhesion stability and longevity of the restoration [9-12].

Thermal properties, phases changes at certain temperatures and resulting phase stabilities of zinc phosphate tetrahydrates have been already fully described in Chapters 2 and 3 using different thermal analysis techniques (DSC, TGA-MS) and vibrational analysis (XRD, Diffuse Reflectance Infrared Fourier Transform-DRIFT, FT-Raman) [13]. But crystal thermodynamics and dehydration kinetics offer only partial and unsatisfying explanations about recently reported observations that zinc phosphate tetrahydrates have a greater tendency for dissolution and degradation than zinc phosphate dihydrates in an aqueous environment, which will consequently decrease chemical stability and enhance degradation of ZP cements in vivo [14-17] and reduce the efficient life time of protective coatings against corrosion.

Therefore the purpose of this current chapter is to elucidate certain aspects of the highly complex chemical stability and surface reactivity of ZP polymorphs in correlation with their

crystal size distributions and their corresponding structural (bulk) properties emerging from different hydrogen bonding patterns. Furthermore this study may provide key information about the until now not investigated and possible polymer-crystal surface interactions, deeply needed to: (i) to understand the mechanism of crystal growth of pure hopeite in its pristine stages (ii) to govern efficiently the nucleation of zinc phosphate hydrate voluntarily heterogeneously in order to reduce the average crystal size and to narrow the crystal size distribution, thus allowing the obtaining of ZPT nanocrystals on a large scale (iii) to control the crystal growth and crystal morphology of ZPT thus giving discrimination criteria (regarding the chemical structure) for the selection of the adequate crystallization additives, (iv) to avoid, first, inorganic particle aggregation and, second secondary nucleation (i.e. self-seeding) during crystallization (v) to improve the wettability of ZP pigments and to increase their redispersability in aqueous (saline) media by crystal size reduction (direct approach) (vi) or by chemical modification of the crystal surface (indirect approach), (vii) to tune selectively the compatibility of crystal with latex particle either during the formulation of anticorrosion paint dispersions or in dried protective coatings, (viii) and finally to understand the first stages of the dissolution mechanism of ZPT pigments and the controlled release of zinc and phosphate ions. Biogenic Hydroxyapatite (HAP) and one of its metastable precursors, a calcium dihydrogen phosphate dihydrate (DCPD) or Brushite may be used to underline the resulting variation of chemical reactivity in zinc phosphates since hydroxyapatite and Brushite possess crystal structures very similar to basic zinc phosphate hydrate and zinc hydrogen phosphate trihydrate (a metastable precursor of hopeite) .

For convenience the investigation of crystal surface reactivity may be separated on one side in the evaluation of the physical surface properties and of the chemical surface properties on the other side. A solid interface is defined as a small number of atomic layers that separate two solids in an intimate contact with one another, where the properties differ significantly from those of the bulk material they separate. Albeit the surface of a solid is a particularly simple type of interface, at which the solid is in contact with the surrounding world, i.e. the atmosphere or a dispersion (liquid) medium, physical surface properties such as surface roughness, defect density (dislocations and point defects) and aggregation phenomena need, nevertheless, for precise detection using advanced techniques such as scanning electron microscopy on a micron scale and atomic force microscopy on a nanometric scale. Furthermore, Brunauer-Emmett-Teller (BET) technique [18] seems a particularly suitable and complementary method to follow solid-gas adsorption-desorption equilibrium as it is known to give valuable information about hypothetical surface microporosity and active site density at solid surfaces.

On the other hand the evaluation of chemical reactivity may be done simply by selective chemical etching of the crystal surface, i.e. on short exposure of a surface to diluted H_3PO_4 and

NH_4OH solutions. The development of the etch pattern can be easily visualized by SEM. Electron beam irradiation may induce surface chemical reactions and thus might also give hints for the relative structural stability of hopeite polymorphs compared to Brushite and Hydroxyapatite. Identification of chemical compositions of adsorbed species on crystal surfaces (hydroxyl, carboxyl, phosphate, hydrogen phosphate contaminations), partly generated during selective dissolution of etched surfaces and later reprecipitated, is of primary importance since it influences the wettability and stability of microcrystal dispersion in aqueous media. DRIFT spectroscopy in combination with surface-enhanced FT-Raman spectroscopy as described by Campion [19] provide a powerful basis for the identification of such weakly adsorbed species and demonstrated a possibility to fingerprint subtle changes of molecular orientation and surface bonding/locking [20]. Besides, the wetting phenomenon and the involved surface tensions and surface energies can be accurately described using contact angle measurement [21]. Capillary microelectrophoresis [22] via the evaluation of existing surface potentials reflected by the zeta potential value, offers an accurate view of the interfacial electrokinetic phenomena and of the overall stability of hopeite based pigment dispersions when subjected to salts of various compositions and to variations of salt concentration, pH and temperature.

4.2. Morphological studies

4.2.1. Morphology and structure (topology) of surfaces

To begin with it is useful to give a brief definition of the terms morphology and structure. The term morphology is generally associated with a macroscopic property of solids, and means form or shape of a surface or interface. Structure, on the other hand, is here associated more with a microscopic, atomistic picture and is used to denote the geometrical arrangement of atoms and their relative position at a surface or interface.

For instance SEM allows a fast characterization of the surface morphology and its topological fluctuations. Thus Fig. 4.1 A and Fig. 4.1 B show SEM micrographs of the α - and β -form of zinc phosphate tetrahydrate crystalline powders synthesized and used in this study. α -hopeite crystals (Fig. 4.1 A) present the classical plate shape and are reasonably uniformly sized of about $27 \times 6 \times 0.5 \mu\text{m}^3$, whereas β -hopeite crystals (Fig. 4.1 B) were not as well defined and slightly smaller ($24 \times 5.5 \times 0.5 \mu\text{m}^3$) and partially agglomerated (Fig. 4.3). The development of the faces of α -hopeite crystals is sometimes irregular and the crystals may simulate hemimorphic symmetry. In comparison the β -hopeite sample presents two different habits: tabular $\{011\}$ to prismatic $\{001\}$.

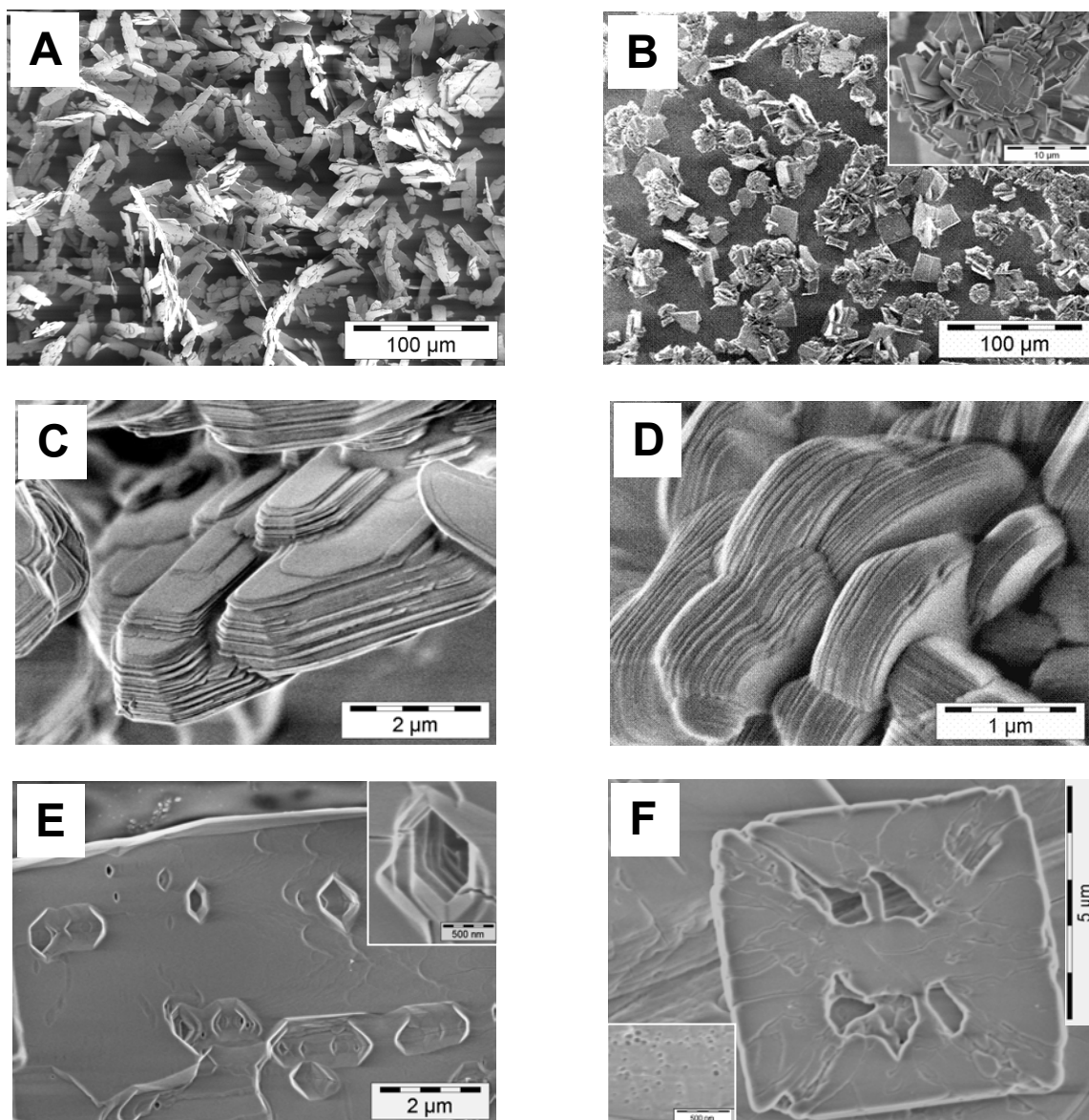


Figure 4.1 : SEM photographs of: (A) α -hopeite, (B) β -hopeite. Chemical etching of: (C) α -hopeite, (D) β -hopeite in $0.1 \text{ mol.L}^{-1} \text{ H}_3\text{PO}_4$ for 90 sec at room temperature (with powder recovery by drying overnight in oven at 75°C). Specific dissolution patterns are observed after 5 min immersion in $1 \text{ mol.L}^{-1} \text{ NH}_3$ solution for α -hopeite in the [011] plane (E) and β -hopeite in the [011] plane (F).

The plate-like habitus of hopeite crystals, whether α -form or β -form, corresponds to a layered structure; the b -axis being the crystal-plate normal [23]. A corresponding crystallographic representation is given in Fig. 4.4 A. In addition SEM images of α - and β -hopeite (Fig. 4.1 A, Fig. 4.1 B) suggest that secondary nucleation may occur with the appearance of small crystallites partially detached from the crystal surface, which continues to grow. Similarly Figure 4.2 A shows twinned platelike crystals of Brushite, with a shape similar to the one observed for the hopeite polymorphs.

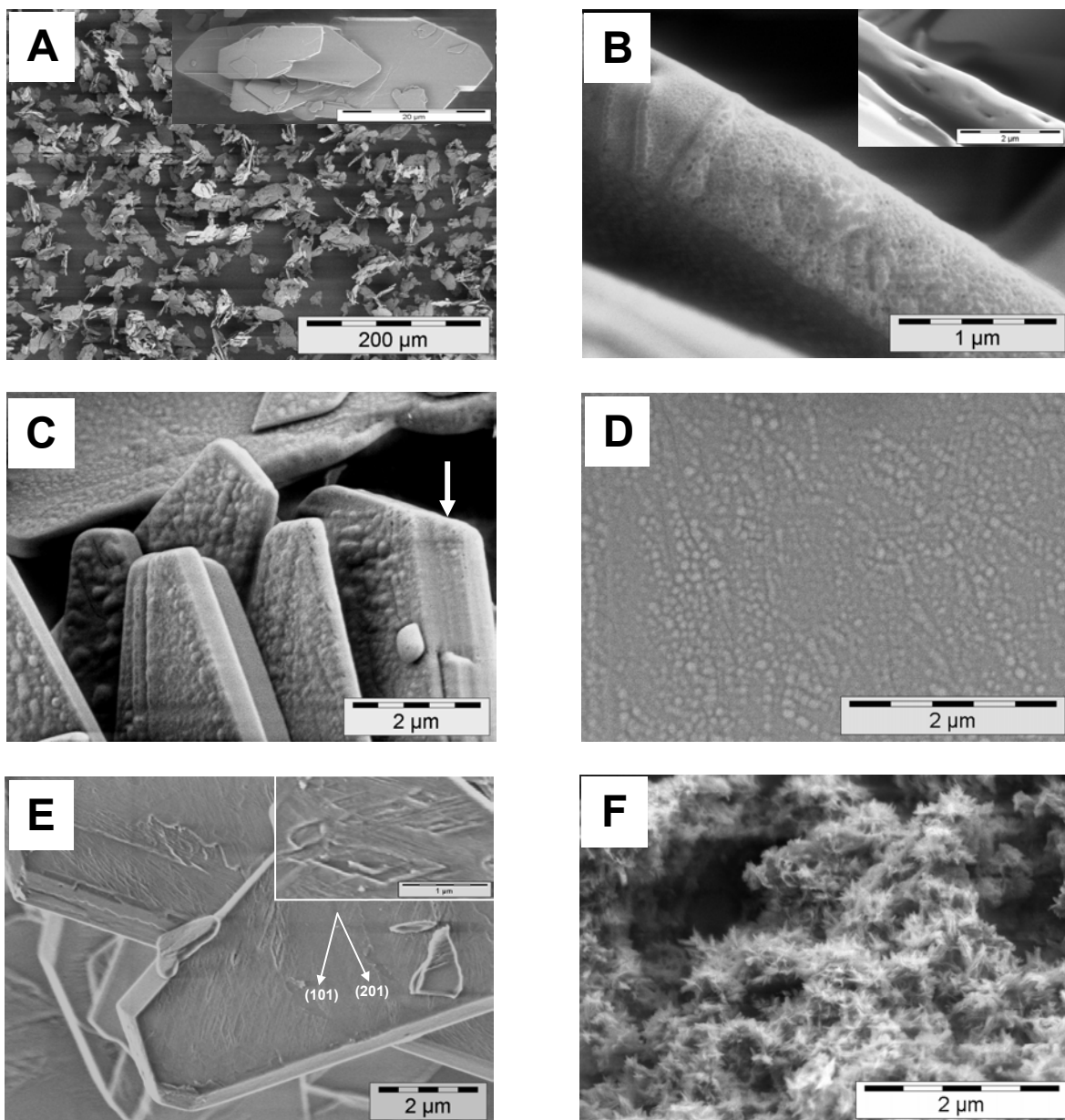


Figure 4.2 : SEM photographs of Brushite: (A) after crystallization, characteristic needle-plate shape in inlet , (B) e-beam etching of pure Brushite for 60 sec at 1.5 kV, (C) Chemical etching followed by e-beam irradiation (5 min, 3 kV), (D) periodically oriented OCP clusters on (010) Brushite surface, (E) Trapezoidal etch pit in the ac plane obtained by immersion 1 mol.L⁻¹ NH₃ solution, (F) needle like hydroxyapatite nanocrystals after precipitation at 40°C.

The insert in Fig. 4.2 A illustrates a characteristic view of the {011} surface of a single crystal, which is the major growth and principle cleavage plane. Furthermore, the sequence of HAP formation suggests that the process, under the conditions used here, follows Ostwald's rule, according to which the formation of HAP, because of its high activation energy and its high thermodynamical stability, occurs via one or more metastable intermediate stages [24-25]. So as comparison to Brushite, the microstructural arrangement of tiny uniform crystals of Hydroxyapatite are also shown in Fig. 4.2 D. Usually HAP crystallized from aqueous solution via precipitation at pH 11, forms a porous structure with blade shape, needle-like or rodlike

crystallites of 200 nm in length and a maximum of 60 nm in width and height with no preferential direction of crystallite orientation. This morphology is obviously compatible with the results of Aosaka et al [26]. But the formation of aggregates and the microchannel containing organization of HAP observed here may possibly originate from a spatial restriction due to the presence of organic tetramethylammonium hydroxide (TMAOH) as pH regulating agent in the mother liquor. For both hopeite polymorphs and calcium phosphate hydrates a precise evaluation of the agglomeration phenomena occurring on crystal powder recovery is required since Ostwald ripening reduces the specific surface area and thus strongly influences the dispersability of these pigments in aqueous medium. Lyklema [27] and Hogg [28] successively studied the colloidal aspects of agglomeration and examined the character of the interaction forces inside agglomerates and stressed its influence (reduction) on surface activity. This point will be considered in more details in § 4.3.

Figure 4.3 displays crystal size distributions (CSD) of zinc and calcium phosphate hydrates obtained from dynamic light scattering (DLS) at 90° after ultrasonic dispersion for 10 min in a 10 wt% solution of non ionic surfactant (Lutensol AT50, BASF AG). The so-obtained statistics were compared with size distributions obtained from REM images. Regarding the particle sizes and distributions determined from SEM images at least 250 crystals were measured per sample. To avoid errors due to projections of the three-dimensional crystal shape to a two-dimensional image, only crystals lying flat on the substrate were considered. Size histograms were calculated using a number based population balance approach [19] and the data were fitted using a Gaussian distribution [20]. Unlike the simple case of α -hopeite, which grows in two dimensions via a non-diffusion controlled mechanism [25] as shown in Fig. 4.1 A, it is necessary for β -hopeite and hydroxyapatite [26] (Fig. 4.1 B, Fig. 4.2 F) to disregard a number-based CSD and use a particle size distribution based on volume or sphere population analysis [27-28]. It is presumed that these two last systems exhibit strong aggregation partially due to a strong heterogeneous nucleation or the presence of TMAOH in the specific case of HAP. This is particularly well pointed out since the average value of the CSD obtained from DLS is circa 50% higher than the one deduced by SEM.

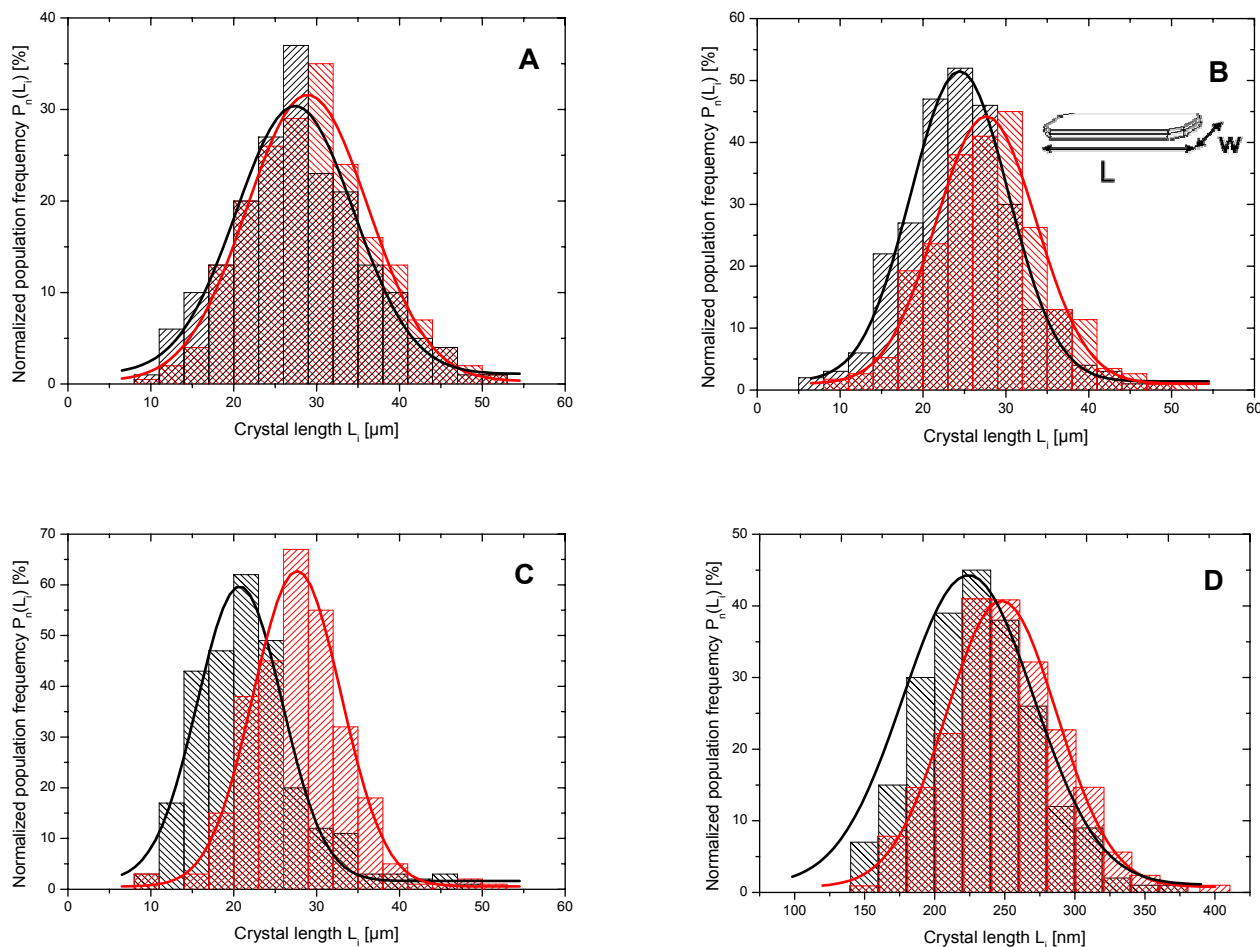


Figure 4.3 : Size distribution histograms of model samples displayed in Fig. 4.1 and Fig. 4.2: (A) α -hopeite, (B) β -hopeite, (C) Brushite, (D) Hydroxyapatite, obtained from SEM (■) and DLS (■). Inset b shows the definition of crystal length \underline{L} and crystal width \underline{w} .

This consideration about aggregation is of particular importance since it justifies the assumptions made in Chapter 3 as a first approach that, since α - and β -hopeite display similar dimensions, surface effects may be neglected for the determination of the thermodynamic parameters and interrelation between the different zinc phosphate hydrates.

Furthermore, aggregation phenomena resulting from pigment recovery, post-mineralization treatment and also occurring during pigment redispersion in a paint formulation can be accurately estimated by evaluating the difference between the specific surface area $\$$ obtained from BET adsorption isotherm and the geometric surface calculated from SEM photographs. It is also possible to evaluate the aggregation phenomena, the aggregation number (number of crystal per agglomerate) and the accessible crystal surface employing marker molecules of known molecular coverage and applying a Langmuir isotherm model. Brunauer, Emmet and Teller [34] initially developed a model describing gas-solid adsorption assuming a multilayer adsorption, i.e. that each molecule in the first adsorbed layer provides an adsorption site for the second layer, and so on. Molecules in the second and subsequent layers are assumed to

behave essentially as those in the bulk liquid with successive molecular layers of adsorbate forming at pressures well below the pressure required for the completion of a monolayer [35]. The extension of this model to liquid-solid adsorption in the frame of development of chromatographic methods with high resolution has been recently given by Gritti et al. [36]. This model is used to extract from experimental data the monolayer (coverage) capacity θ , and hence the surface area of many adsorbent surfaces such the (011) surface of ZPT powders. For the evaluation of the geometric surface from the PSD obtained by SEM, a sphere model was used for β -ZPT and HAP while a plate-like model was employed for α -ZPT and Brushite, thus better describing the observed morphologies in Fig. 4.1 and 4.2.

Powder sample	BET method	Geometric (SEM) method			
	S_{N_2} ($m^2 \cdot g^{-1}$) ^a	Geometric length ^b	density	model	Geometric surface S_{SEM} ^e
α -ZPT	0.27	27.410	3.05 ^c	plate	722
β -ZPT	0.54	24.433	3.13 ^c	sphere	39
Brushite	1.95	20.730	2.27 ^d	plate	808
HAP	35.81	0.338	3.16 ^d	sphere	8328

Table 4.1: Comparison of specific surface area of metal phosphate powders obtained from BET and SEM analysis.

- (a) obtained with 500 mg powder, estimated error $\pm 0.01 m^2 \cdot g^{-1}$.
- (b) corresponds to the plate length or a sphere diameter, given in microns.
- (c) refers to Chapter 2.
- (d) from ICSD crystallographic files 16132 (Brushite) and 203027 (hydroxyapatite).
- (e) given in $m^2 \cdot g^{-1}$ with an estimated error $\pm 1 m^2 \cdot g^{-1}$.

In Table 4.1, BET isotherms deliver a relatively small specific surface area lower than $5 m^2 \cdot g^{-1}$ and in good agreement with known values for nano- and microcrystalline powders such as $CaCO_3$, Al_2O_3 and TiO_2 [37]. However in accordance with the observed morphologies in Fig. 4.1 A and B, the β -ZPT exhibits an accessible area two times higher than the α -ZPT, since β -ZPT forms dense aggregates of maximum 6 μm plates in length (see insert in Fig. 4.1 B) compared to 27 μm for α -ZPT. This logically explains that one obtains a twenty times higher estimation of the geometric area for α -ZPT than for β -ZPT assuming spherical aggregates of 24 μm in diameter for β -ZPT and a densely packed plate structure for α -ZPT. Similar results are achieved with Brushite and hydroxyapatite, thus proving the pertinence of such an approach (Table 4.1) for the quantification of the aggregation phenomenon, which may partially govern the surface reactivity of metal phosphate powders.

4.2.2. Surface reactivity and chemical etching

There are only few reports on the relation between the surface chemistry and properties of metal phosphate hydrates and their structural characteristics. Tentative explanations were given

by Nancollas et al. for Brushite [38] and then by de Leeuw for Hydroxyapatite [39-40]. For instance, DFT calculations of hydroxyapatite revealed that two energetically favoured configurations coexist, with preferred arrangement of hydroxyl groups, all OH⁻ groups being lined up with oxygen and hydrogen ions alternating in column parallel to the *c*-axis (Fig. 4.30 C). These columns of aligned OH⁻ can of course be found in two directions, either up or down the *c*-axis, hence promoting a hydroxyapatite structure consisting of domains of well-ordered OH⁻ columns. A change in this ordering within these columns is possible either by thermal induction (only 42 kJ.mol⁻¹ per OH group) or by the presence of anionic impurities (F⁻, Cl⁻, acrylate polymeric derivatives). In order to obtain similar informations and also details about the stress induced crystal growth from a crystallographic point of view, in correlation with the surface reactivity and dissolution-precipitation mechanisms, the chemical etching of zinc phosphate and Brushite crystals was investigated.

4.2.2.1. Theory of etch pit formation applied to hopeite

4.2.2.1.1. *Thermodynamic approach*

Dissolution of a crystal surface is initiated at sites of high surface energy: edges, corners, cracks, scratches, and holes are favourable sites for fast dissolution. At micro-scale, trapped impurities, point defects, twin boundaries, and dislocations can cause enhanced dissolution. The formation of etch pits by dissolution at dislocations has been of particular interest to experimentalists motivated by testing and developing theories of dissolution, lattice strain and material dissolution. Frank [41], Cabrera et al. [42] and then Cabrera and Levine [43] developed the first theories of etch pits formation based on dislocation lattice strain (Burton-Frank-Cabrera BFC theory [44]). Historically Brantley et al. [45] in studying etch pits formation on quartz macrocrystals defined a critical concentration of etchants solution above which dislocation etch pits would not nucleate, and below it where dissolution occurs preferentially at edges, kinks and propagating dislocations at the crystal surface as shown in Figure 4.4. A brief outlook of the Frank-Cabrera etch pit theory applied on hopeite is given hereunder. If one considers a dissolution nucleus at a screw dislocation intersecting the surface which consists of a cylindrical hole of radius *r*, one atom layer deep (*d*) (definition of a *etch tube pit*) then the free energy of formation of this nucleus will be composed of a volume energy, surface energy and strain energy term, respectively as follows:

$$\Delta G = \pi r^2 d g + 2\pi r d \gamma - d \tau b^2 \frac{\ln(r/r_0)}{4\pi} \quad (4.1)$$

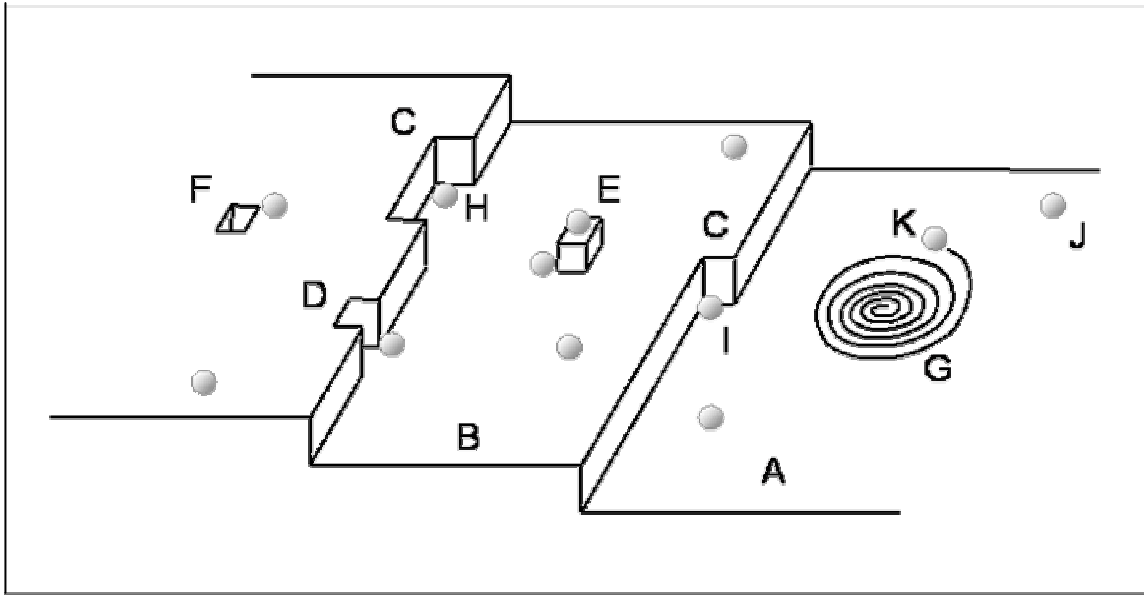


Figure 4.4: Kossel's model [46] of growing crystal surface showing flat surfaces (A), steps (B), kinks (C), edge vacancies (D), surface-adsorbed growth units (E), Surface vacancies (F) and propagating screw dislocations (G). Sites as identified by Davey and Mullin [47] for adsorption of impurities inducing etch pit formation on a growing crystal: kinks (H), steps (I), ledges (J) and dislocations (K).

where τ is the shear modulus, b is the Burger's vector, r_0 is the dislocation core radius, γ is the surface energy and g is the free energy of dissolution per unit volume. Equation (4.1) shows that opening a pit on a crystal surface is a competition between terms which decrease the free energy (dissolution of a volume of crystal into an undersaturated medium and release of dislocation strain energy) and a term which increases the free energy (creation of additional surface area). The cylindrical hole geometry is often chosen for simplicity. In order to predict whether an etch pit will form at a dislocation, one should determine the variation of ΔG with radius, r , and the free energy of dissolution, g , defining g as the chemical affinity per unit volume and neglecting activity corrections:

$$g = \frac{RT}{V} \ln\left(\frac{C}{C_0}\right) \quad (4.2)$$

where C is the concentration of the dissolving species, C_0 is the equilibrium solubility of the species, V is the molar volume, R is the gas constant and T the absolute temperature at which dissolution is observed. Equation (4.1) expresses the free energy in enlarging the pit from a radius r_0 to a radius r . The core radius r_0 is also the radius of the central volume of the dislocation where the continuum approximation breaks down and electronic energies become important. For $r < r_0$ the elastic strain term of equation (4.1) cannot adequately predict the dislocation energy. Therefore, following the recommendations of Wintsch and Dunning [48], one might choose to set $r_0 = b \approx 5.05 \text{ \AA}$ (corresponding to lattice parameter a of ZPT) and in the

case of ZPT one may also assume that a atomic monolayer corresponds also to a since in SEM screw dislocations are always observed in (bc) plan. For zinc phosphate cements Attar et al. [49] measured a shear modulus of 9.2 GPa, indicating a very high rigidity of such materials. Thanks to contact angle measurement (§ 4.3.1) the average surface energy may be estimated around 70 mJ.m^{-2} . From crystallographic data obtained in Chapter 1, the molar volume of α -ZPT is approximately 147.9 cm^3 . Thus it may be possible to calculate the values of ΔG as a function of r for different realistic values of the saturation index C/C_0 . In the case of screw dislocations, a typical graph obtained by Brantley [50] for quartz at 300°C , temperature where quartz readily dissolves, is shown in Figure 4.5. For edges dislocations, the strain energy term is modified by the factor $(1/(1-\nu))$ where ν is the Poisson's ratio. From the works of Haussühl and Friedrich [51] about the thermoelastic constants of hopeite, one can evaluate the Poisson's coefficient around 0.386 ($\nu = -S_{12}/S_{11}$ and $S_{ij} = C_{ij}^{-1}$), which is extremely high for such stable crystals. This means that that pits at growth edge are also favoured. Detailed consequences of this value of the Poisson's ratio regarding etch pits nucleation are amply discussed in § 4.2.2.

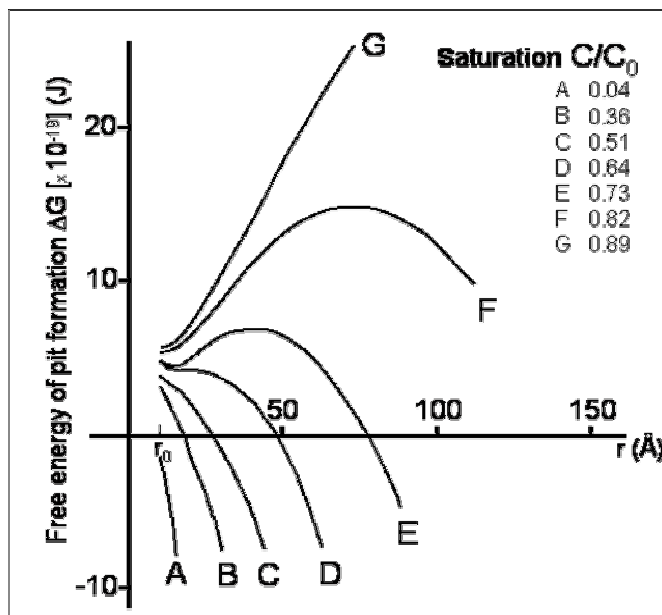


Figure 4.5: Free energy of formation of etch pits at a dislocation on a quartz surface in contact with water at 300°C as calculated by Haussühl et al. [51].

As Figure 4.5 and Figure 4.6 show, all the calculated ΔG curves display a minimum near r_0 and a maximum at large values of r , indicating a strong contribution of the surface energy at high undersaturation. These extrema are influenced by the formation of pits at edges (red curves in Fig. 4.6). At 0.7 times the saturation, i.e. a crystal of hopeite being chemically attached by a nearly saturated solution of zinc phosphate ($\sim 0.7 \mu\text{mol.L}^{-1}$ with K_s values of Chapter 6), dislocation pits and edges pits coexist with the same probability since the ΔG values are not affected by the Poisson's ratio (superposition of green curves in Fig. 4.3).

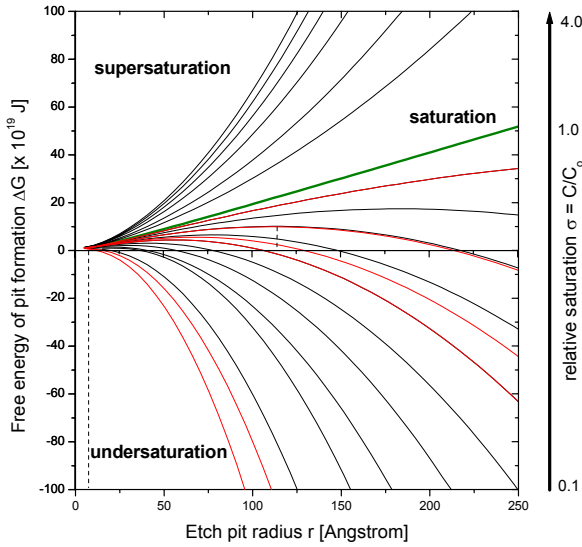


Figure 4.6: Calculated etch pits free energy curves plotted versus pit radius for hopeite at 25°C for increasing concentration (supersaturation) of the aggressive saline solution. Black lines correspond screw dislocation pits while red lines indicate the formation of edge pits for $\sigma \cong 0.05, 0.1, 0.6, 0.7, 0.9, 1$. The green line shows that saturation conditions are achieved.

The critical concentration at which the minimum and maximum in the ΔG curve disappear can be determined by deriving of equation 4.2 and solved for a critical value of r :

$$r_{crit.} = -\frac{\gamma}{2g} \left[1 \pm \frac{\tau b^2 g}{2\pi^2 \gamma^2} \right]^{\frac{1}{2}} \quad (4.3)$$

At $r_{crit.}$ a steady state solution of etching for Eq. 4.3 is obtained in contact with which the pit geometry will remain constant, while the rest of the crystal grows or dissolves depending on the chemical affinity (equation 4.2). From Figure 4.3 at $\sigma = 0.7$ the critical value of r is around 12 nm for α -ZPT at 25°C. In any case corresponding to $\tau b^2 g / 2\pi^2 \gamma^2 > 1$, no solution exists for equation 4.3 and there is no steady-state value of r , which indicates that a small pit nucleated at a dislocation core should spontaneously open up to form a macroscopic etch pit (supersaturation domain in Fig. 4.3). The critical concentration at which this occurs is:

$$C_{crit.} = C_o \cdot \exp\left(-2\pi^2 \gamma^2 V / RT \tau b^2\right) \quad (4.4)$$

And is around $85 \mu\text{mol.L}^{-1}$ or 8.6 times the solubility limit of hopeite at room temperature and neutral pH. For $C = C_{crit.}$, an inflexion point appears in the ΔG function as seen in Figures 4.5 and 4.6. Since there is no activation barrier to opening up the etch pit, any pit nucleated at a dislocation should open up into a macroscopic etch pit nucleate (see Fig 4.1 E). Similarly for $C < C_{crit.}$, no real solution of equation 4.3 is obtained. This means also that nucleated pits open up into etch pits. Above $C_{crit.}$ (i.e. Curves E and F in Fig. 4.5), there are two roots to the equation 4.2 corresponding to a minima and a maxima of ΔG function. If a pit is nucleated at a dislocation core, the pit should spontaneously open its radius fulfils the condition that ΔG is at a minimum ($\sim 5 \text{ \AA}$). Consequently an activation energy ΔG^* equal to $\Delta G_{max} - \Delta G_{min}$ exists toward

further opening of the pit into a macroscopic etch pit. The height of the activation barrier (ΔG^*) will determine the rate of formation of etch pits. If a metastable equilibrium is assumed, the rate of formation of etch pits per unit area J , for concentration above the saturation limit, should be expressed as follows:

$$J = A \cdot X_d \exp(-\Delta G^*/RT) \quad (4.5)$$

where X_d is the fraction of surface sites intersected by dislocations and A the frequency factor. Even if the core energy is included in the ΔG calculations, a small activation barrier exists for pit nucleation below $C_{crit.}$. Pit nucleation is highly dependent on dislocation density. The slope of the sides of the pits is governed by the ratio of the downward dissolution rate r_{down} (or r_n) to toward dissolution rate r_{up} (or $r_{surface}$), and must be high in order to visualize etch pits macroscopically. Since the hopeite surface is close-packed, holes nucleated in these surfaces consist of high-index faces composed of step edges, as fully observed by AFM in § 4.2.2. Anisotropy of $r_{surface}$ causes etch pits to have crystallographically-controlled non-cylindrical geometries. The rate r_n is the rate of formation of holes at a dislocation, and $r_{surface}$ is the ledge velocity or the rate of recession of ledges away from nucleated holes. Kinks in the ledge serve as sites for easier transfer of zinc phosphate molecules from the surface into solution (Figure 4.5). Johnston [52] suggested that the ratio $r_n/r_{surface}$ must be higher than 0.1 for an etch pit to become microscopically observable. When r_n is small compared to $r_{surface}$, the ledge spacing of the apex of the nucleated pit will be large, the wall of the pit will be large and as the ledges recede, the walls of the pit will be maintained at a very shallow angle. This defines *terraced etch pits*. Extends of the BFC model to situations where bulk diffusion (diffusion of solute molecules through a boundary layer) is the limiting step have been formulated by Chernov [53], Ohara and Reid [54] and lately by Nývlt et al. [55]. Sears et al. [56] pointed out that the adsorption of poisons onto the dissolving pit surface can decrease $r_{surface}$, producing a more visible pit. Based on etch pits observations in LiF, they concluded that poisons were essential for the formation of etch pits on crystal surface. A similar approach for gaining information of surface reactivity of zinc phosphate hydrates is retained. This requires the extensive use other interesting substances covering the pH-scale (HCl, NaOH, NH₃) or encountered in corrosive environments such as NaCl.

Besides, by measuring etch pit densities as well as pits dimensions on sequentially etched crystals, nucleation rate data and pit growth data may be collected, yielding attractive information about the rate limiting steps and mechanism of dissolution.

4.2.2.1.2. Kinetic approach and etch pit size distribution (PDS model)

The etch pit size distribution (EPSD) is currently calculated from a model adapted from the crystal size distribution (CSD) by MacInnis and Brantley [57]. Crystal size distribution was developed by Randolph and Larson [58] as a means of optimizing process parameters in order to produce specific particle size distributions in industrial crystallizers. The key to CSD is the population density function $n(L_i)$, and the derived cumulative frequency distribution of crystal size. Changes in the population density with time are determined by the continuity equation for the population balance, which might include terms for nucleation, the rate of crystal growth and dissolution, crystal fractionation and breakage and Ostwald ripening. Factors derived from the crystal growth kinetics are in turn related to chemical affinity and temperature [59].

The EPSD model is based on the pit population density function $n(L)$ ($\text{m}^{-1} \cdot \text{m}^{-2}$), the number $N(L)$ of pit per unit area per unit length (i.e. width) interval ΔL as defined by Marsh [60], the cumulative number of them per unit area with lengths $L_i \leq L$:

$$N(L) = \int_0^L n(L) dL \quad (4.6)$$

As pointed out by Marsh, the cumulative frequency function $N(L)$, is a more “stable” function statistically than the experimentally measured number density of pit population $n(L)$. Therefore its extensive use for data analysis is highly recommended.

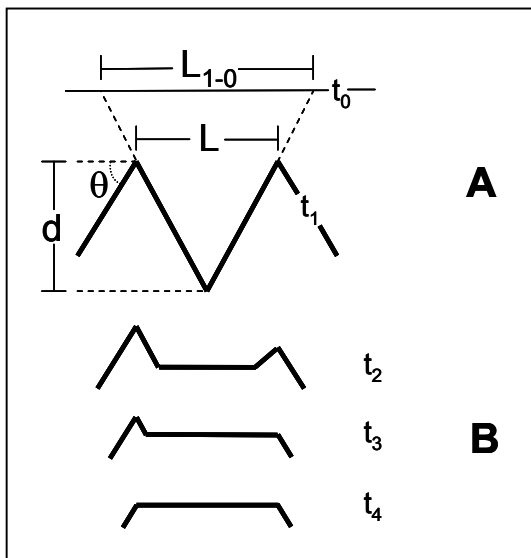


Figure 4.7: Schematic view of profile of pit intersection. (A) the observed length L of an intersecting pointed pit leads to the calculation of an apparent half-length opening rate v_b of propagating pits. The actual opening rate between t_0 and t_1 is calculated from L_{1-0} , the pit length relative to the original unetched surface at t_0 . This definition applies similarly to the pit width (W and W_{1-0}). The bulk dissolution rate is related to the average pit geometry (wall slope θ , and pit depth d). (B) the intersection of a flat pit with deeper pits ultimately results in annihilation (t_4); however individual pits commonly disappear at intermediate stages (t_3) due to random spacing of pits on the crystal surface.

First considering a population balance within a finite range of pit length (i.e. width) (ΔL) for a given area A , the observed etch pit distribution will depend on the number n , and the growth rate G ($\text{m} \cdot \text{s}^{-1}$), of pits growing into and out of this size window ($n_1 G_1$ and $n_0 G_0$, respectively). The population density will be decreased by the removal frequency of the entire population \dot{a} (s^{-1}), as pits intersect each other.

Albeit this derivation does not deal with the associated appearance of a larger pit that occurs in the case of coalescence, the removal of pits by annihilation will be considered. The change of population balance over the time interval dt is described by:

$$\frac{dn}{dt} + \frac{d(nG)}{dL} + n\dot{a} = 0 \quad (4.7)$$

The generally observed linear increase of the length of the pit population G_1 with time suggests that growth rates are independent of pit size. Substituting the mean pit lifetime ($\tau_p = 1/\dot{a}$) in steady-state conditions leads to:

$$n(L) = n_0 \exp\left(\frac{-L}{G\tau_p}\right) \quad (4.8)$$

where n_0 is the density of etch pit nucleation, or the population density at $L = 0$. PSD plot of Ln (n) against L produces a straight line with a slope ($-1/G\tau_p$) and an intercept at Ln (n_0). Linear plots result from the balance of nucleation rates and a size- and time-independent growth rate of pits. Kerrick et al. [61] have argued that the determination of solubility data in applying this linearization of the PSD model to systems where pits are not removed might be misleading. Instead one should use the moments of the CSD distribution. The PSD coefficients (n_0 , τ_p , G) are used to calculate the moments m_i of order i of the population (distributions in number for $i = 0$, 1 for length, 2 for area, 3 for volume), as a cumulative measure of the dimensions per unit area of all pits up to a given length:

$$m_i = \int_0^L L^i n(L) dL \quad (4.9)$$

Substituting for $n(L)$ from equation (4.8) in (4.9), one obtains:

$$m_i = i! n_0 (G\tau_p)^{i+1} \times \left[1 - \left\{ \sum_{p=0}^i \frac{1}{p!} \left(\frac{L}{G\tau_p} \right)^p \right\} \exp\left(\frac{-L}{G\tau_p}\right) \right] \quad (4.10)$$

And the total moment is given by $m_{i,T} = i! n_0 (G\tau)^{i+1}$ (4.11). It follows that the total number of pits $m_{0,T}$ is $n_0 G\tau_p$ and the average length of annihilation L_a is related to the total density of pits on the surface:

$$L_a = \frac{1}{\sqrt{m_{0,T}}} = \frac{1}{\sqrt{n_0 G\tau_p}} \quad (4.12)$$

Pairs of succeeding moments are used to evaluate the average pit length for a given dimension \bar{L}_i :

$$\bar{L}_i = m_{i,T} / m_{i-1,T} \quad (4.13)$$

which points out the significance of the PSD coefficient: $G\tau_p$ represents the average pit size based on length (\bar{L}_1).

The evolution of the PSD with time shows that two populations of pits coexist. While etch pits are nucleated at a defect-point or impurity cluster (G_1) they propagate on a terrace to larger flat-bottomed pits, located frequently at screw dislocations (G_2). Therefore early in the surfacial dissolution process, the population of pits ($\ln n(L)$ vs. L) appears as peak rather than a negatively sloped straight line, attributed to the process of Oswald ripening by Cashman and Ferry [62]. A negative slope represents a homogeneous initial distribution of point-defects while a negative slope results from preferential removal of small pits from the pit population in order to reduce the surface free energy of the system.

The contribution of these two pit populations to the bulk dissolution rate $R(L)$ depends on the etch pit density $n(L)$, the average pit geometry (pit of length L , depth d and wall slope θ), the etch pit half-length (i.e. half-width) opening rate v_b and the occurrence of the pit intersection phenomenon. The dissolution rates for pointed pits (population G_1) and flat pits (population G_2) are defined as follows:

$$R_{G_1}(L) = n_0 \exp\left(\frac{-L}{G\tau_p}\right) \cdot \frac{L^2 v_b \tan \theta}{V_m} \quad (4.14)$$

$$R_{G_2}(L) = n_0 \exp\left(\frac{-L}{G\tau_p}\right) \cdot \frac{4v_b(d \cdot L - d^2/\tan \theta)}{V_m} \quad (4.15)$$

where V_m is the molar volume. The average transition length from pointed to bottom-flat pit geometry L_F is also calculated as: $L_F = 2d/\tan \theta$ (4.16)

Thus the sum of the surface dissolution rates R_T gives an accurate quantification of the bulk dissolution rate of ZPT crystals in the early stage of the dissolution mechanism.

4.2.2.2. Chemical Etching of metal phosphate crystals followed by SEM

4.2.2.2.1. pH-dependence on the efficiency of treatment by chemical etching

Selective chemical etching of a stable zinc phosphate crystal is achieved in putting ZPT crystals into a 1 up to 10 mmol.L⁻¹ H₃PO₄ buffer solution of pH \approx 2. Time-dependent effects were observed and followed by scanning electron microscopy (Fig. 4.2 C and 4.2 D). During the first thirty seconds, no change in shape of the α - and β -ZPT crystals is observed, and the morphology is conserved except for a slight rounding of the edges. Fig. 4.2 C and 4.2 D show a characteristic “herringbone” texture on the (110) and ($\bar{1}\bar{1}0$) faces corresponding to an alternating layered structure of zinc phosphate and water containing layers [63-64]. The local pH around these planes also changes with dissolution. This was evident with 1 mmol.L⁻¹ H₃PO₄ buffer solution by adding a dye (bromocresol green) to the ZPT crystals maintained at pH \sim 3. At this pH bromocresol green is of yellow colour. However the colour of the dye turned green as

dissolution started, in the vicinity of the lateral faces of both zinc phosphates, first indicating that the solution around these dissolving planes became more basic, and secondly proving the release of phosphate anions. This marks the disappearance of the monocrystalline character of the ZPT tetrahydrate platelets. If the local pH reaches 4, redeposition or "chemically induced" secondary nucleation takes place and the surface roughness softens [65]. In contrast, the (010) planes show no trace of dissolution in H_3PO_4 . The absence of triangular etch pits on the flat terraces of the (011) surface shows that a homogeneous (hydrogen) bonding environment exists [66-68]. This can be tested by immersing hopeite crystals in $1 \text{ mol.L}^{-1} \text{ NH}_3$ solution for 5 min (Fig. 4.1 E and 4.1 F). Already after a few seconds, α -hopeite shows a specific quadratic dissolution pattern along the a - and c - axis, that transforms into an hexagonal shape after 5 minutes, due to truncations of the square summits in the $\{101\}$ and $\{10\bar{1}\}$ directions (angle of 45° with b and c -intersects) to come back to a quadratic shape at infinite time, indicating a crystallography-controlled etching mechanism. In good agreement with Wolfe's observations [69], Fig. 4.1 E emphasizes the fact that two preferential pitting orientations in the $\{010\}$ and $\{001\}$ directions coexist. Logically, β -hopeite crystals have different dissolution behaviour (Fig. 4.1 F). These crystals display occasional corrosion pits in the diagonals of the rectangular surfaces ($[011]$ plane) and along the crystal growth edges. This last observation may be correlated with the high Poisson's ratio, which suggests that pits at edges may also nucleate. Ammonia infiltrates in the sheets of β -hopeite parallel to the b -axis and triggers triangular etch pits (intersection of (011) and (0 $\bar{1}$ 1) direction in bc -plane, insert Fig. 4.1 F). From a crystallographic point of view, one should notice that each time, these corrosion patterns correspond point to point to one of the hydrogen bond direction, either in the α -hopeite or in the β -hopeite.

While more complex surface geometries are readily found in other metal phosphate crystals, Brushite and HAP exhibit similar sheet crystal structures as α - and β -hopeite with alternating hydration and calcium phosphate layers (Fig. 4.2 A). Thus, after 2 minutes exposure to a $10 \text{ mmol.L}^{-1} \text{ H}_3\text{PO}_4$ buffer solution, a slight striated morphology appears on the (110) and (1 $\bar{1}$ 0) planes of Brushite crystals (Fig. 4.2 C). None of the triangular etch pits bound by steps along $\{101\}$ and $\{201\}$ ((010) plane) mentioned by Ohta et al. [70-71] are found here, but a few are present only on the (401) lateral face, apparently along $\{001\}$ (see insert Fig. 4.2 B). This can be explained by the non-colinearity of oxygen pairs with the c -axis and their slight counter clockwise twisting from the $\{001\}$ direction (preferential orientation of hydrogen bonds), which provides the lack of rotational symmetry necessary for the dissolution process [72]. Similarly, as above-mentioned, when attacked by ammonia α -hopeite displays progressively trapezoidal and hexagonal pits, corresponding to a step-wise dehydration accompanied by an elementary rotation along the c -axis [73]. In that sense, it is possible to explain the controlled growth of thin

apatite crystals with hexagonal symmetry on [010] of Brushite [74]. This hypothesis is confirmed by the presence of characteristic trapezoidal etch pits (double triangular etch pits face to face along (201), (101) and (001)) in the *ac*-plane when Brushite crystals are chemically attacked by 1 mol.L⁻¹ NH₃ (Fig. 4.2 E).

4.2.2.2.2. *Time-dependence on the efficiency of treatment by NH₃ chemical etching*

Furthermore, the SEM technique allows the estimation of the etch pits density and the estimation of the pits average and critical sizes from the etch pit size distribution (PSD) [75] and the subsequent dislocation density on the (101) surface by applying the crystal size distribution that is population balance – (CSD) on dissolving α -, β -ZPT polymorphs.

A maximum is present in the PSD plots (Fig. 4.8) in the early stages of dissolution and appears to result from nucleation of pits at all available sites on the initial cleaved surface over the first 90 seconds where the (101) crystal surface stays in contact with a concentrated ammonia solution. As pits grow larger, a progression is observed in the individual etch pit shape from pointed (pyramid-shaped) (Fig. 4.9 C,D) to flat-bottomed (truncated pyramid) (Fig. 4.9 E,F) and finally terraced (insert in Fig. 4.9 D). The peak of the PSD (Fig. 4.8 C,D) moves to larger sizes and increases in magnitude from a few hundredth nanometers to tenths of microns. The smallest pits that can be visualized pointing downward are short-lived and have always a different source of surface defect for α - and β -ZPT. It seems that, while etch pits nucleate at ledges, point-defects and screw dislocations in α -hopeite crystals (Fig. 4.9 A), they nucleate at kinks and edges in β -hopeite crystals (Fig. 4.9 B). Flat pits result when pointed pits stop deepening (i.e. stop nucleating) but continue to grow laterally. Terraced pits result from nucleation and growth of smaller pits at the bottom of flat pits as nicely shown in Figure 4.9 E. Already after 5 minutes, one can distinguish in Figure 4.8 B-D a small number of large pits (> 7 μm), long-lived terraced and pointed pits that increase in size with elapsed time (group G₂) from a background of more numerous short-lived pits, having length smaller than 800 nm (group G₁). The development of this bimodal size distribution coincides with the attainment of a steady-state rate of ZPT dissolution after 10 min. The initial and final pit density allows an estimation of surface defects for both hopeite polymorphs. Therefore β -ZPT possesses a higher point-defects density than α -ZPT around $5 \cdot 10^{-13}$ point-defects/m² compared to $3.75 \cdot 10^{-13}$ point-defects/m² while on contrary α -ZPT exhibits a screw-dislocation density one orders of magnitude higher than β -ZPT, i.e. $1.8 \cdot 10^{-8}$ dislocations/m² compared to $1.4 \cdot 10^{-10}$ dislocations/m².

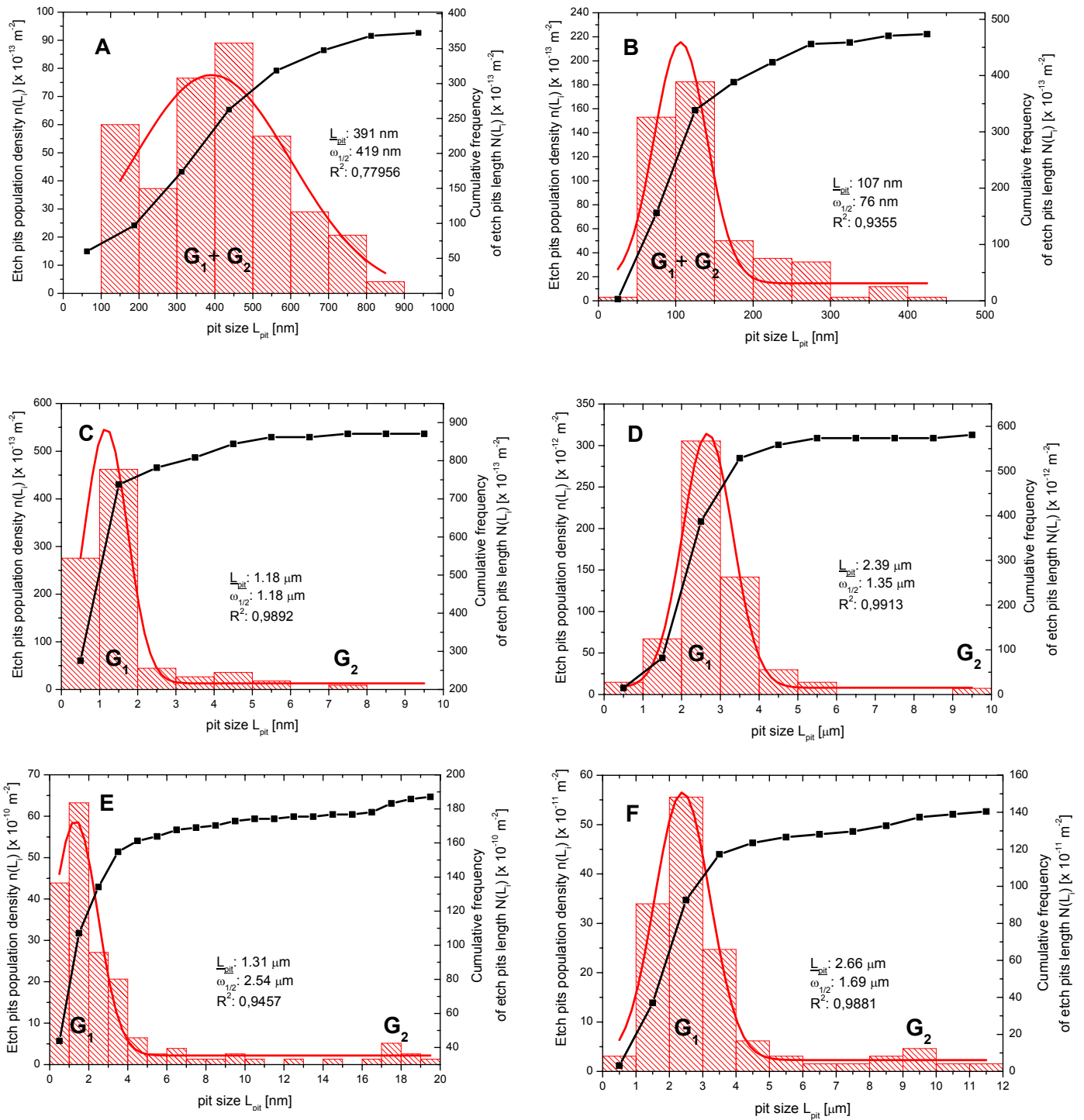


Figure 4.8: Time-dependence of the pit size (length) distribution or surface population density $n(L_i)$ and cumulative frequency function $N(L_i)$ successively for α -ZPT and β -ZPT: (A),(B) 90 sec, (C),(D) 5 min, (E),(F) 10 min. This illustrates the pit nucleation at a defect-point or impurity cluster and the etch pits propagation on a terrace ((101) plane) to larger flat-bottomed pits at screw dislocations (appearance of a second pit population around $10 \mu\text{m}$).

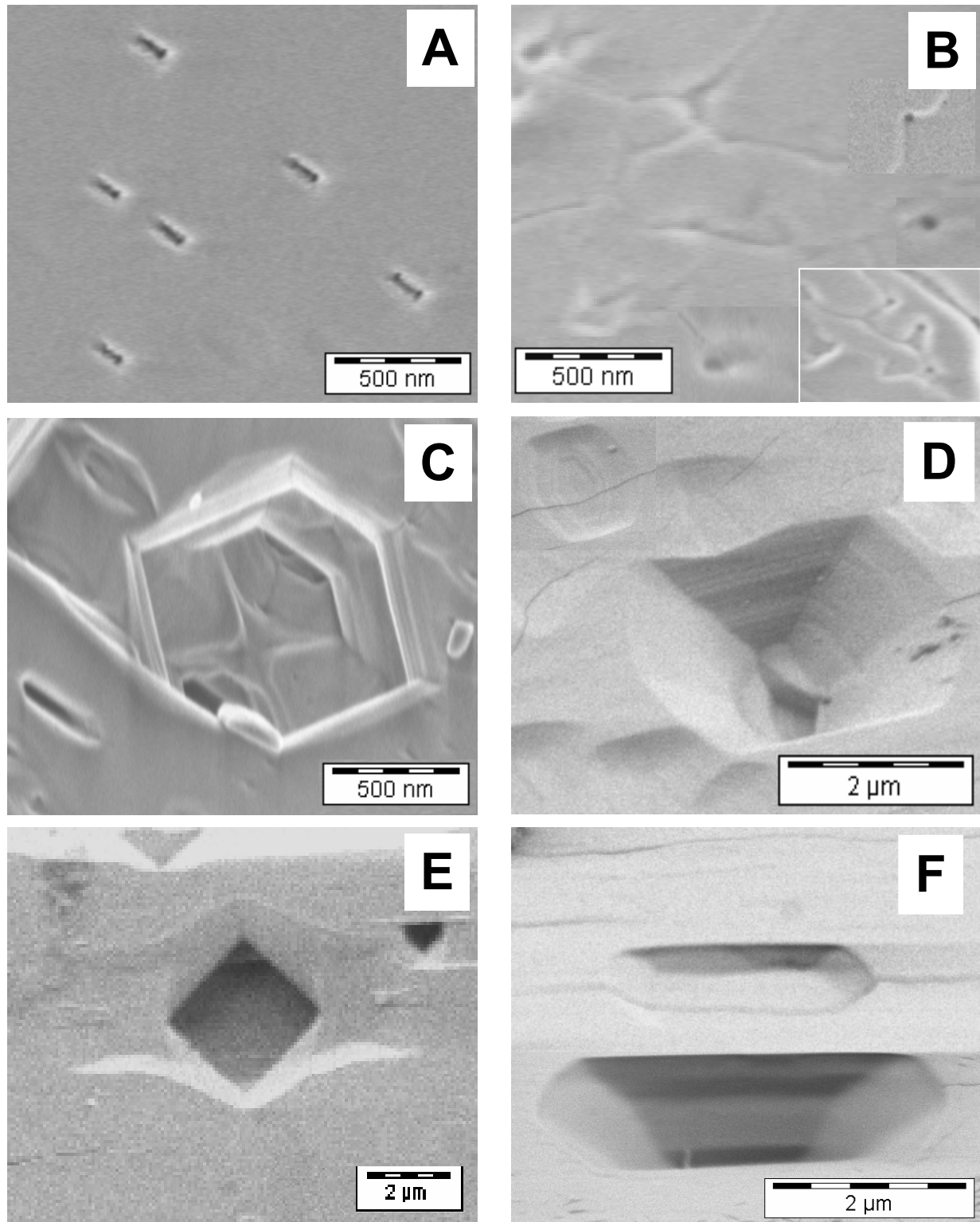


Figure 4.9: Progression of the individual etch pit shape for α -ZPT and β -ZPT: (A), (B) 90 sec, (C), (D) 5 min, (E), (F) 10 min. The hopeite polymorphs differ by their induced dissolution behaviour first in their nucleation source, i.e. at ledges or surface dislocations for α -ZPT and mainly at edges or kinks for β -ZPT and then in their propagation in having different pit opening rates corresponding to different attainment of a steady-state rate of dissolution.

From the calculated cumulated frequency distribution of pits, one may conclude that the relative population of terraced pits (G_2) to smaller pits (G_1) increases six times faster in α -ZPT than in β -

ZPT with a ratio of 1 to 0.18, indicating that destabilization of the surface lattice via leakage of hydrogen bonds is faster in α -ZPT than β -ZPT. This is in complete agreement with the observation of thermally induced destabilization of the crystal structure in Chapter 3.

However a small number of larger pits (G_2) exhibiting a “pipe” hole (pipe mechanism of dissolution) along the crystal a -axis, covers a large fraction of the ZPT crystal surface. Those pits also might perforate the surface eventually causing its rupture (Fig. 4.9 C). A growing etch pit may intersect other etch pits. In the case of a pointed pit, edge-to-edge intersection with other pits reduces the measured pit length and width (Fig. 4.7, t_1). The statistical geometries of etch pits are found in Table 4.1.

crystal phase	L^a [μm]	L_{1-0}^a [μm]	W^a [μm]	W_{1-0}^a [μm]	Depth ^a d [μm]	Slope ^b θ_b [$^\circ$]	Slope ^b θ_c [$^\circ$]	ν_b^c [$\text{nm}\cdot\text{s}^{-1}$]	ν_c^c [$\text{nm}\cdot\text{s}^{-1}$]
α -ZPT	1.400	2.165	1.025	1.600	1.605	45	32.8	2.543	1.926
β -ZPT	0.790	2.400	1.490	3.595	1.665	45	34.5	5.373	7.045

Table 4.1: Characteristic average parameters (length L , width W , depth d and estimated average slope (θ) of etch pits after 10 min immersion in $1 \text{ mol}\cdot\text{L}^{-1} \text{ NH}_3$ and surface oriented (plan $[101]$) propagation rates along crystal axes. Average of 250 pits.

- (a) geometric estimated error $\pm 5 \text{ nm}$
- (b) geometric estimated error $\pm 0.3^\circ$
- (c) estimated error $0.002 \text{ nm}\cdot\text{s}^{-1}$

The pits are on average smaller and less stretched in α -ZPT than in β -ZPT, as confirmed by SEM micrographs (Fig. 3.9 E,F). Although the width of the pit (W_{1-0}) of β -ZPT is two times bigger than its length (L_{1-0}), etch pits of α -ZPT and β -ZPT possess the same, hexagonal geometry with similar pit wall inclination θ and depth. Correcting the average measured pit length of the larger pits at 10min to the length at 5 min relative to the original cleavage surface L_{1-0} (see Fig. 4.7) gives the true half-length and true half-width opening rates ν_b and ν_c along b -axis and c -axis. The pits on the β -ZPT surface have the tendency to propagate three times faster ($\sim 6 \text{ nm}\cdot\text{s}^{-1}$) than on the α -ZPT surface ($\sim 2 \text{ nm}\cdot\text{s}^{-1}$). While the opening rate on the α -ZPT surface is 30% faster along b -axis than along c -axis, the inverse tendency is observed on the β -ZPT surface. This explains the shape of the pits in Fig. 4.7 F. This may be correlated with the fluctuation of surface defect density between α - and β -ZPT. This statement is confirmed in Table 4.2.

One may also notice that the bulk dissolution rate is then not exclusively governed by the surface dissolution rate and the average pit depth, but also by the type of pit (pointed (G_1) or flat (G_2)), which in turn is strongly dependent on the surface defect origin (point-defect or screw dislocation).

crystal phase	Pit population	Ln n°	τ G° [μm]	$R(G_1)^*$ [$\text{mol}\cdot\text{cm}^{-2}\cdot\text{s}^{-1}$]	$R(G_2)^*$ [$\text{mol}\cdot\text{cm}^{-2}\cdot\text{s}^{-1}$]
α -ZPT	G_1	3.797	0.4008	$1.327 \cdot 10^{-10}$	-
α -ZPT	G_2	5.061	0.0084	-	$1.553 \cdot 10^{-12}$
β -ZPT	G_1	1.142	1.1829	$0.811 \cdot 10^{-10}$	-
β -ZPT	G_2	4.711	0.0212	-	$1.732 \cdot 10^{-14}$

Table 4.2: Characteristic average parameters (density of etch pit nucleated n° , mean pit life-time τ and initial growth rate G°) after 10 min immersion in $1 \text{ mol}\cdot\text{L}^{-1} \text{ NH}_3$ and Bulk dissolution rates R calculated from PSD coefficients for pointed (G_1) and flat (G_2) pits

(*) estimated calculation error ± 0.005 of the given growth rate value

The bulk dissolution rate is 30% higher at initial time for α -ZPT than β -ZPT. This tendency dramatically evolves as time elapses, since for the G_2 population the bulk dissolution rate is two orders of magnitude higher α -ZPT than β -ZPT. This is not surprising since the solubility constant K_s at steady-state equilibrium and basic pH at room temperature is higher for α -ZPT than β -ZPT as demonstrated in Chapter 6. Since the etch pattern is crystallographically-controlled over a long time, the fluctuation of the $R(G_2)$ values between α - and β -ZPT may be also originate from the structural stability, i.e. the hydrogen bonding pattern (see Chapter 2). In Chapter 3 one had concluded that the three-dimensional hydrogen bond network of α -hopeite was easier to destabilize thermally than the two-dimensional hydrogen bond network of β -hopeite. This conclusion may extend to chemical attack of the ZPT crystal surface.

4.2.3. Topology, surface inhomogeneities and local disorder followed by AFM

In crystals, non-steady state component transport locally alters the number and sometimes even the kind, of point defects (irregular Structure Elements SE, vacancies, Frenkel defects [76], Schottky disorder [77]). As a consequence, the relaxation of defect concentrations takes place continuously during chemical diffusion and interdiffusion (homogeneous reaction) and solid state reaction of dehydration (heterogeneous reaction). Generally the rate of these relaxation processes determines how far local defect equilibrium can be achieved during chemical transport at interfaces. The Kirkendall effect in metals and ionic crystals, a local phenomenon, shows that during interdiffusion the relaxation time for local defect equilibration is often sufficiently short compared to the characteristic time of macroscopic component transport, to justify the assumption of local point defect equilibrium. In those cases the (isothermal, isobaric) transport coefficients (i.e. D_i , b_i) are a function only of chemical composition and time [78]. First a multi-component approach may be considered in the case of hopeite since either zinc or

phosphate groups occupy the crystal surface, but with local concentration fluctuations depending on the observed crystal face. However one should consider that in zinc phosphate hydrates sublattice positions are occupied by rather immobile components, only reactive when subject to intense dissolution by prolonged contact with polar media or when temperature is sufficiently high to break bonds. For example in ZnO component transport at a crystal-corrosive liquid interface occurs almost exclusively in the cation sublattices. It is mediated by the predominant point defects, which are cation vacancies. Thus surface defects and sudden change of topology serve as “diffusion pipe” for molecular transport and accordingly promote surface reactivity (wettability, interfacial solid-liquid diffusion process). Surface inhomogeneities (surface roughness due to climbs, edges, jogs or kinks, macroscopic inclusion, i.e. existence of adsorbed contamination such as $\text{ZnHPO}_4 \cdot x \text{H}_2\text{O}$ traces appearing during uncontrolled crystallization of hopeite) defects (punctual or two dimensional defects such as sliding or screw dislocations [79], grain boundaries [80] etc.) may be investigated by techniques precise on atomic scale such as Scanning Force Microscopy (SFM) or alternatively Atomic Force Microscopy (AFM) and their localisation facilitated by chemical etching (descriptive revealing technique).

Hence in Figure 4.10 a bare area of the (011) surface of α -hopeite before any chemical treatment was observed with AFM technique. Typical features of the surface are shown in evidence: in Fig. 4.10 A, Point 1 displays growth steps of 10.47 Å average heights and clearly corresponding to the height of a lattice unit cell along the a-axis, thus confirming the orientation of the observed surface as the (bc) plan. in Fig. 4.10 A, Point 2 shows two well defined surface vacancies 55 nm long corresponding to the length of thirty lattice cells, preferentially oriented along c-axis and separated by circa 100 nm or fifty unit cells. Point 3 (Fig. 4.10 C) displays two kinks separated by 450 nm or 250 unit cells, thus offering ample space for an etch pit to nucleate or a polymer to adsorb.

Numerous growth steps are shown in Fig. 4.11 B, thus allowing the application of the *kinematic theory* developed by Frank [81] for the evaluation of the average surfacial growth rate of α -ZPT. Two processes are involved in the layer growth of crystals, viz. the generation of steps at some source on the (011) surface followed by movement of layers across the surface. Consideration of the movement of macrosteps of unequal distance apart, the BFC theory considering a regular distribution of monoatomic steps, led Frank formulate his kinematic theory of crystal growth. The step growth velocity u depends on the proximity of the other steps since all steps are competing units (Fig. 4.11).

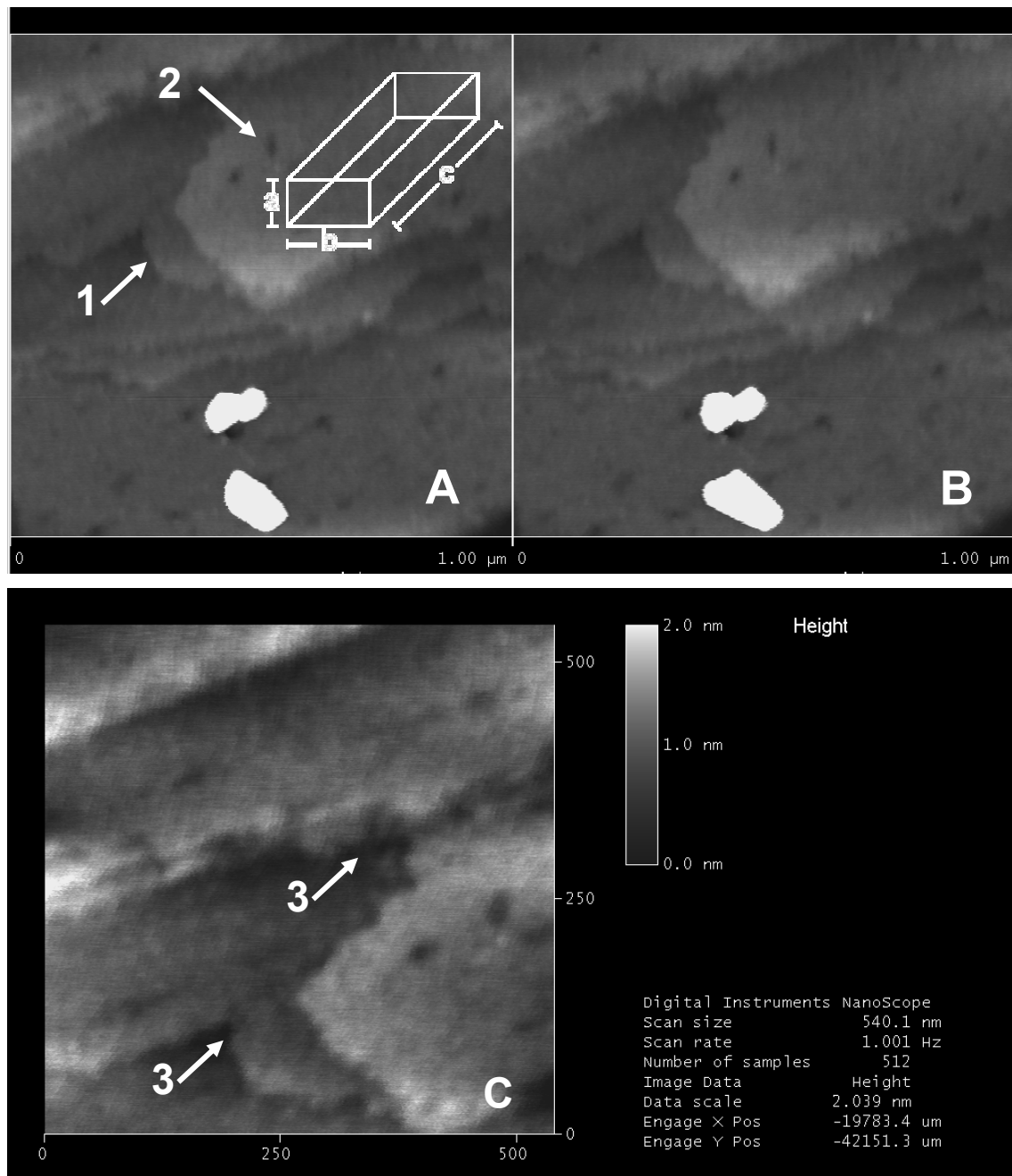


Figure 4.10: AFM images recorded with trace (A) and retrace (B) on a $1 \mu\text{m}^2$ area of the (011) surface of untreated α -ZPT. Point 1 indicates a point-defect and Point 2 illustrates a growth step. (C) zoom on a kink at a growth edge allowing the determination of the height of a growth step (Point 3).

Thus

$$u = q/n \quad (4.16)$$

Where q is the step flux (the number of steps passing a given point per unit time) and n is the step density (the number of steps per unit length in a give region) The distance between steps λ is defined as $\lambda = n^{-1}$. The slope of the surface p , with reference to the close packed surfaces, i.e. flat ledges, is given by:

$$p = \tan \theta = hn \quad (4.17)$$

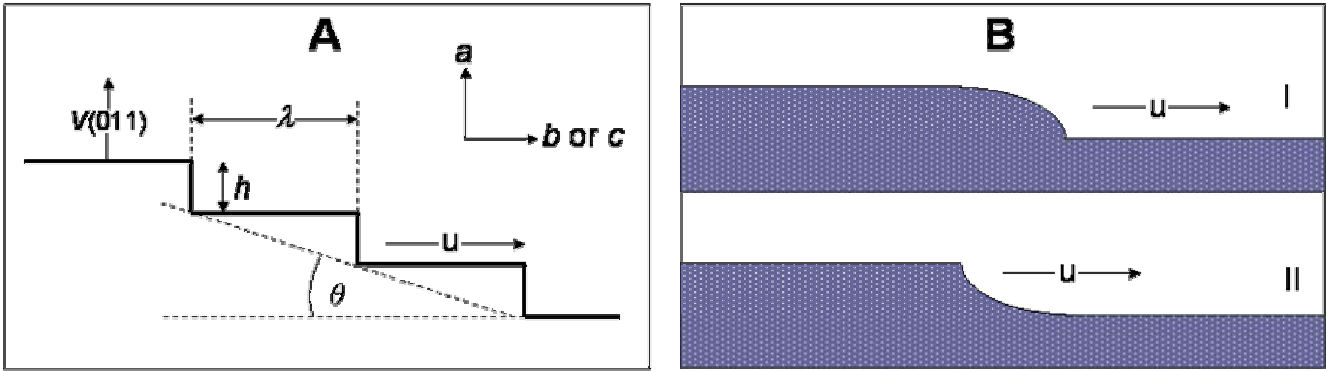


Figure 4.11: (A) two-dimensional diagrammatic representation of steps on the (011) surface. (B) Surface profiles arising from bunches with growth kinetics of type I, $d^2q/dn^2 < 0$ and type II $d^2q/dn^2 > 0$ respectively.

And the average surface growth rate or face growth velocity $v(011)$, normal to the reference surface is determined as follows:

$$v(011) = hq = hnu \quad (4.18)$$

where h is the step height. If the steps are far apart ($\theta \rightarrow 0$), and the diffusion fields do not interfere with one another, the velocity of each step u will be maximised. As the step spacing decreases and the slope increases, u decreases to a minimum at $hn = 1$ ($\theta = 45^\circ$). For the two dimensional case depicted in Fig. 4.12 another velocity C (C_b or C_c) in the (011) plane may be defined, which represents the motion of “kinematic waves”, i.e. the region of the surface with a constant slope p and velocity u , $u = v(011)/p$.

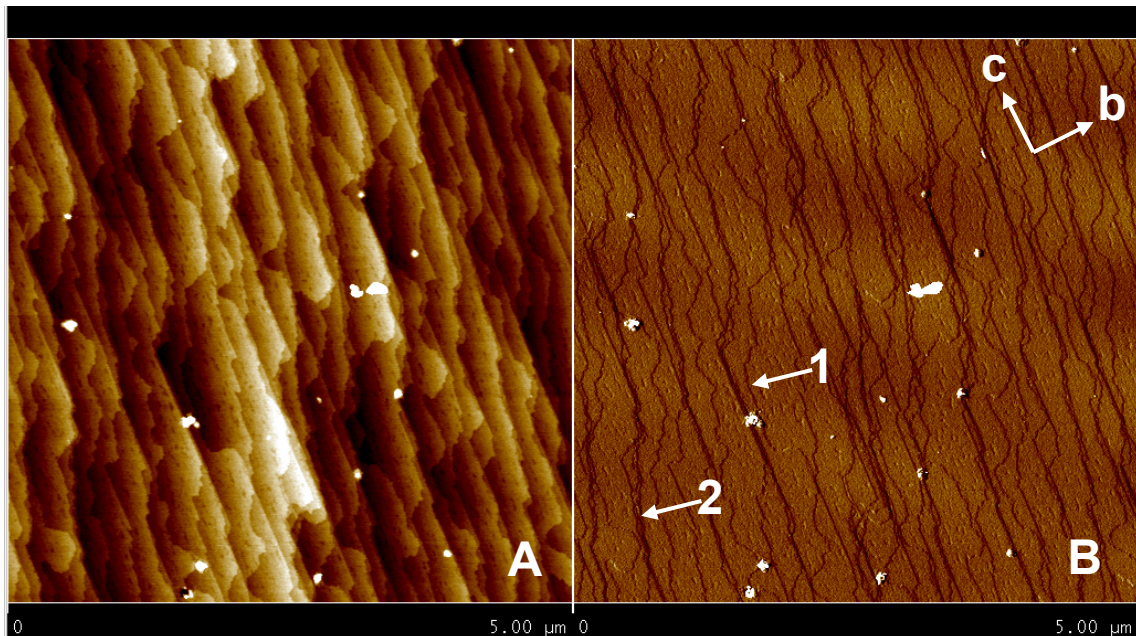


Figure 4.12: AFM image recorded in tapping mode (height) (A) with phase shift (B) as additional information of the topography on the chemically untreated (011) surface of a α -ZPT macrocrystal obtained after 2 days crystallization at 90°C . Points 1 and 2 describe two two-dimensional kinematic waves (G_1 and G_2) of different slopes ($\theta_{G_2} < \theta_{G_1}$). Contaminations appear as white spots on the photographs.

These waves do not contain the same monomolecular steps all the time, as the step velocity u can be greater or less than C . When two kinematic waves (1 and 2 in Fig. 4.12 B) of different slope meet, a discontinuity in slope occurs, giving rise to “shock waves” across the surface.

The analysis of Figure 4.12 B shows that two types of step growth coexist. The G_1 step population appears three times more frequently than the G_2 population, which in turn possesses a two time higher height (Table 4.3), for the reason that the G_2 step population propagates at a slower pace (1.49 \AA/s) than the G_1 step population (1.88 \AA.s^{-1}) along c -axis. Furthermore, because of an average crystal length of 30 \mu m obtained after 2 days (crystallization time) the average growth rate of the (011) surface is 1.73 \AA.s^{-1} and first corresponds to a growth rate of one lattice unit per second and secondly to the average step growth rate of population G_1 and G_2 . While the step growth rate along a -axis is approximately one sixth of the longitudinal velocity for the G_1 steps, it is reduced to one tenth for the G_2 steps, and corresponds to the incorporation of a half-cell every second. Thus it follows that the (011) surface (Figure 4.12 A or B) appears relatively smooth with a local roughness restrained to a height amplitude equivalent to one or two unit cell.

Growth step (wave type)	n [step/ μm]	h [nm]	λ [nm]	u ($\sim u_c$) [\AA.s^{-1}]	v [\AA.s^{-1}]
G_1	7.6	44	143	1.88	0.315
G_2	2.2	22	391	1.49	0.146

Table 4.3: Average step growth rates obtained from collected AFM data (Fig. 4.12) over 300 measures for a 30 \mu m long crystal of α -ZPT.

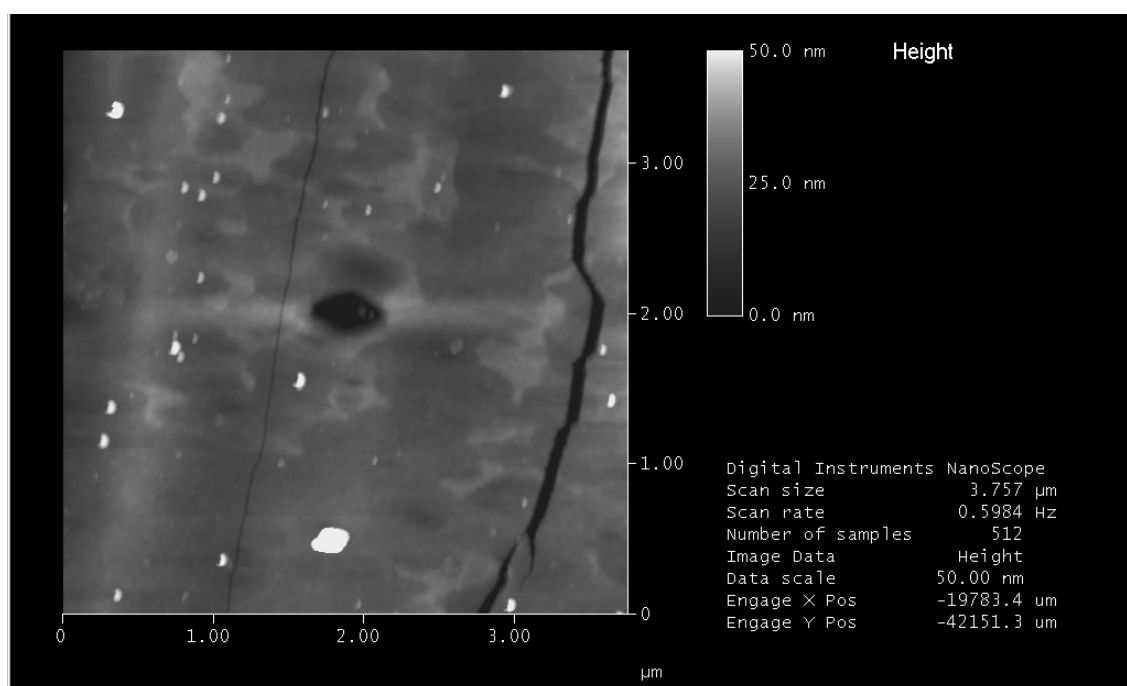


Figure 4.13: AFM image recorded in tapping mode of an etch pit on the (011) surface of a α -ZPT macrocrystal after 5 min immersion in $1M \text{ NH}_3$. This etch pit exhibits a hexagonal shape and corresponds to a G_1 pits population since it has nucleated at a surface vacancy.

Pores and changes of surface geometry (growth steps) are observed at or near the interdiffusion zone. Pore formation and missing unit cells at the crystal surface are witness of a certain point defect supersaturation and indicate that sinks and sources for point defects are not sufficiently effective to maintain local defect equilibrium and therefore promote the destabilization of the hopeite crystal surface on contacts with a $1 \text{ mol.L}^{-1} \text{ NH}_3$ solution. Figure 4.13 displays the (011) surface exposed to a $1 \text{ mol.L}^{-1} \text{ NH}_3$ solution during five minutes. One notices a small etch pit belonging to the G_1 pit population, as characterized in SEM (Fig. 4.8). One may assume that this etch pit may have nucleated at a surface vacancy (Fig. 4.13) since no surface defects are detected in AFM, excluding a surface crack originating from the crystal recovery method after etching (100°C air drying under vacuo). This etch pit exhibits a characteristic hexagonal shape, indicating a crystallography-controlled surface dissolution mechanism and is 207 nm long, 120 nm large and 123 Å or 22 lattice unit deep. During dissolution ZPT material is removed from the pit hole and may reprecipitate and readsorb either on the pit walls or farther on the surface. It should explain the source of numerous impurities (white spot in Fig. 4.13) observed. Assuming an impurity concentration distribution $\rho_n(L)$ in number at a distance L around the pit center, it is possible to define an average apparent diffusion coefficient D_{app}^s of impurities, corrected by $\rho_n(L)$ and evaluated at $650 \pm 10 \text{ nm/s}$ (Fig. 4.14). A subsequent question arises from the observation of large pit walls: what is the chemical nature of these adsorbed impurities and what material cover the pit wall, α -ZPT or condensed zinc hydrogen phosphate hydrates.

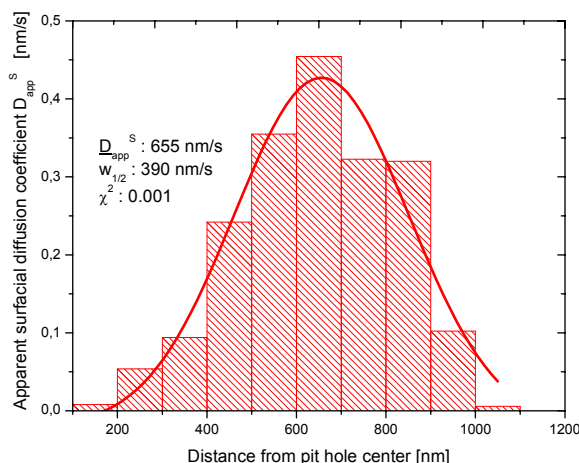


Figure 4.14: Estimated apparent (uniaxial, isotropic) diffusion coefficient D_{app}^s from AFM characterization of the (011) surface in Fig. 4.13.

In order to solve this ambiguities, Friction force microscopy (FFM) around an etch pit hole (Point 1) was employed as shown in Figure 4.15.

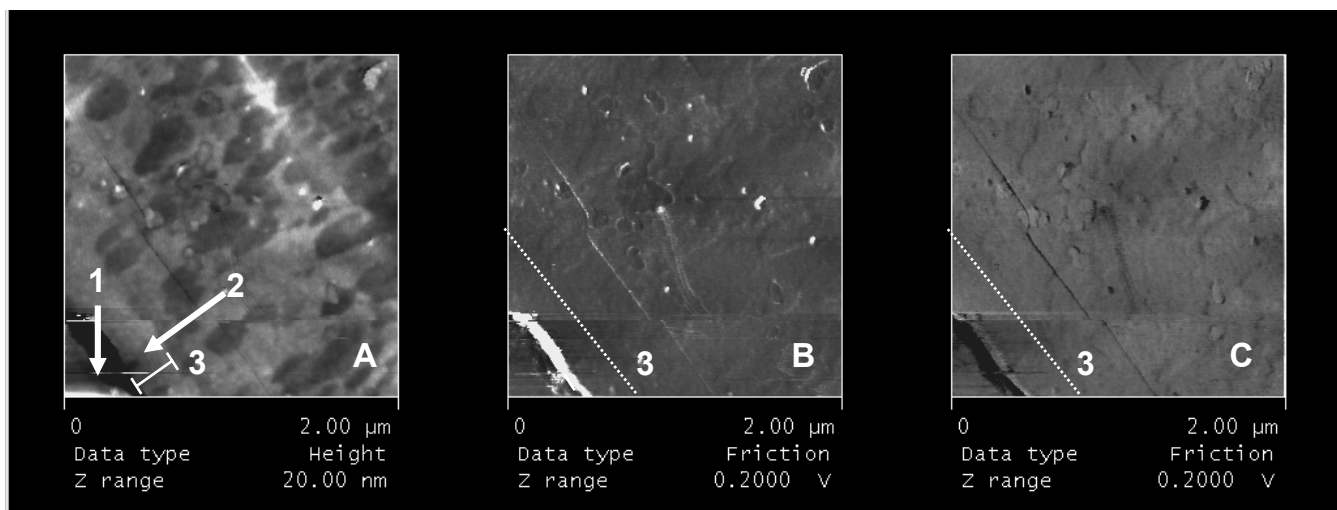


Figure 4.15: Friction force microscopy images (FFM) recorded in taping mode (A), direct (B) and reverse friction scanning (C) of the (011) surface of a α -ZPT macrocrystal after 5 min immersion in 1M NH_3 . Point 1 indicates the “hole” of an etch pit and Point 2 the pit wall of approximately 250 nm in height. Point 3 indicates (dot line) indicates the geometric limit of the etch pit. Since no contrast on the wall of the etch pit is observed between direct friction mode (white + grey colors) and reverse friction mode (complementary color, black and grey) one may conclude that the chemical compositions on the pit wall and the (011) surface are identical, suggesting a bare hopeite surface on the etch wall. This proves that all the material of the etch pit is removed (fickian diffusion) without redeposition in the pit hole or adsorption on the pit wall of zinc “hydrogen” phosphate hydrate explaining the existence of adsorbed impurities (in white on micrograph A) on the (011) surface.

Since in zone 2 (Fig. 4.15) no contrast on the wall of the etch pit is observed between direct friction mode (white + grey colors) and reverse friction mode (complementary color, black and grey) one may conclude that the chemical compositions on the pit wall and the (011) surface are identical, suggesting a bare hopeite surface on the etch wall. This proves that all the material of the etch pit is removed (fickian diffusion) without immediate redeposition in the pit hole or any adsorption on the pit wall, but farther on the surface, thus explaining the existence of adsorbed impurities (in white on micrograph A) on the (011) surface.

Characterization of the surface species before and after chemical etching is certainly required before any adequate interpretation of dynamics data can be given. On the other solubilisation dynamics as treated in Chapter 6 informs of how products form. However a simple observation of the morphology and chemical composition of the adsorbed impurities on the (011) surface can be easily and rapidly undertaken using a SEM, FT-Raman spectroscopy and XRD.

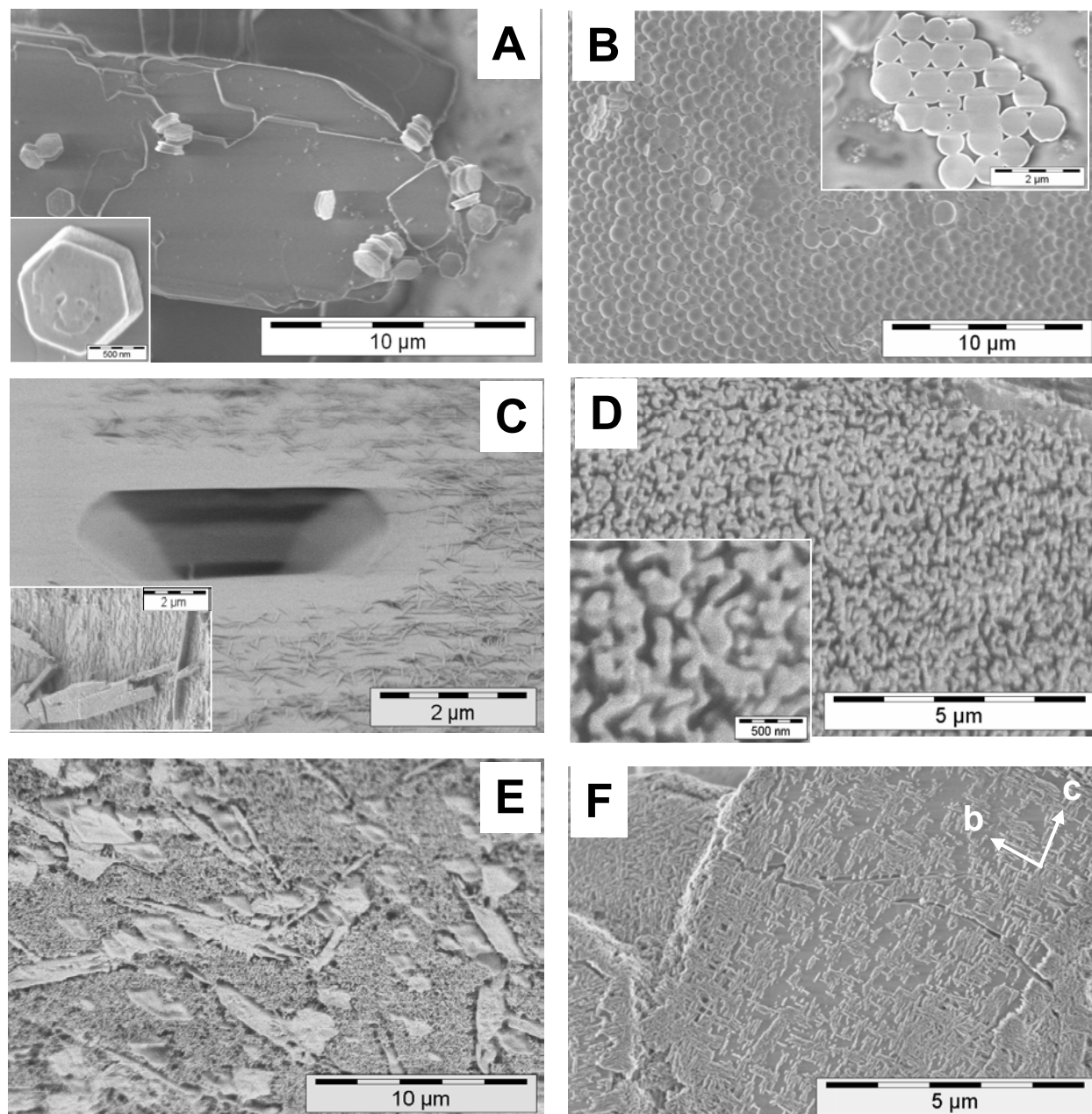


Figure 4.16: Time dependence of the chemical compositions and morphologies of adsorbed impurities stemming from $1 \text{ mol.L}^{-1} \text{ NH}_3$ chemical etching of the (011) surface of a macrocrystal of (A) α -ZPT after 90 sec, (B) β -ZPT after 90 sec, (C) α -ZPT after 5 min, (D) β -ZPT after 5 min, (E) α -ZPT after 10 min, (F) β -ZPT after 10 min, and followed by SEM. (A) shows the nucleation of ZnO crystal while (B) point out the formation of amorphous spheres of zinc hydrogen phosphate presumingly. After 10 min the adsorbed impurities organise preferentially along the crystal b- and c- axes and finally cover densely the (011) surface.

Thus Figure 4.16 illustrates the effect of time on the conversion of the first surface layers of zinc phosphate tetrahydrate as observed by SEM. The rapid appearance of hexagonal nanocrystals characteristic of zinc oxide (Fig. 4.16 A) [82-83], and followed successively by the generation of plate-like crystals (Fig. 4.16 B,C) of maximum $2 \mu\text{m}$ length assumingly belonging to an hydroxyl-phosphate hydrate homologue, indicates a strong but local variation of pH at the surface of α -ZPT, i.e. a decrease of pH due to the buffering effect of surface released phosphate groups.

Even so, the inorganic impurities adsorbed on the (011) surface of α -ZPT display a structural arrangement indicating not only a probable heterogeneous nucleation without induction time and diffusion to the surface – surface adsorption mechanism (Fig. 4.16 C), but that also fully covers the reactive surface of the α -ZPT crystals over a longer time (Fig. 4.16 E). Separately, the β -form of ZPT is rapidly destabilized when put in contact with an ammonia solution and is marked by the formation of numerous nanospheres of monodisperse distribution (Fig. 4.16 B), eventually attributed to the generation of unstable amorphous [84] zinc ammonium phosphate salts [85-86] via a liquid phase precursor [87], ammonium zincate salts [88] or zincite [89], that may agglomerate and crystallize (Fig. 4.16 D) via homogeneous nucleation as they adsorb on the reactive β -ZPT surface. These adsorbed species convert into a fibrile-like two-dimensional arrangement along b - and c -axis (Fig. 4.16 F) of basic zinc phosphates, i.e. Tarbuttite and Spencerite.

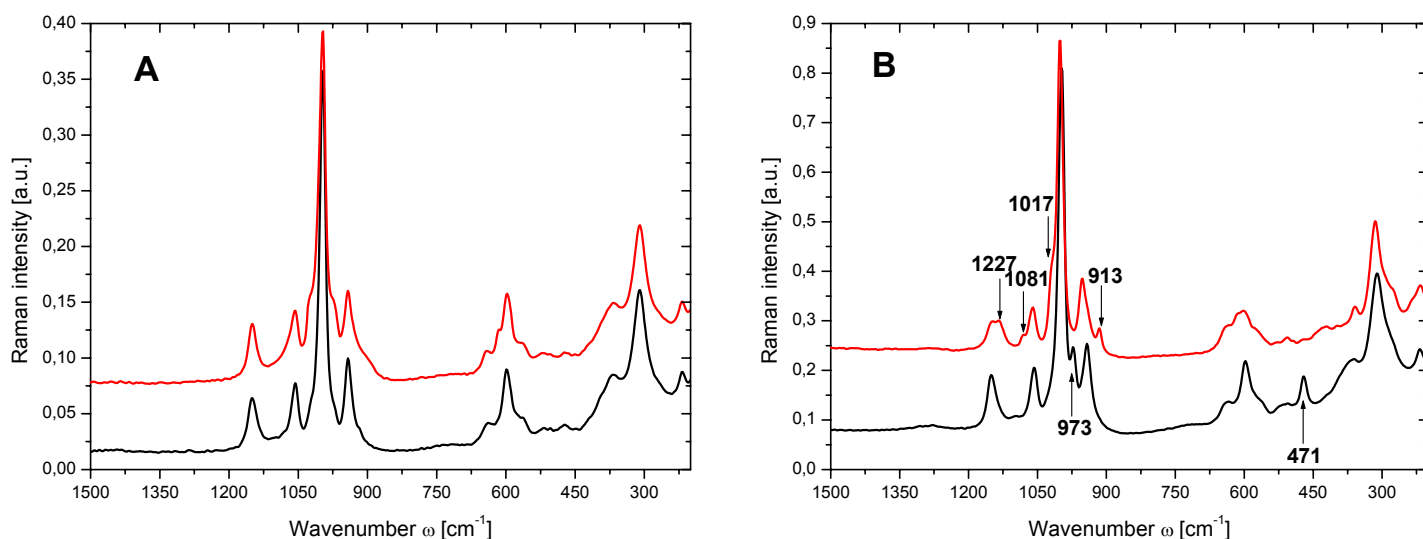


Figure 4.17: Effect of chemical etching of α -ZPT (red) and β -ZPT (black) on the local coordination of phosphate groups before (A) and after (B) after exposition with $1 \text{ mol.L}^{-1} \text{ NH}_3$ for 10 min followed by FT-Raman. The α -form of hopeite is apparently less stable than the β -form, since another form of strongly bound phosphate group appears with a shift of 20 cm^{-1} to higher energy, presumably belonging to a hydroxyphosphate compound.

These products are first detected by FT-Raman spectroscopy with a change in the sphere of coordination of structural phosphate groups, marked by the apparition of a second set of peaks corresponding to ν_1 (1017 cm^{-1}), ν_3 ($1227, 1081, 913 \text{ cm}^{-1}$) vibrations for α -ZPT and to an additional and pronounced ν_2 (471 cm^{-1}) libration for β -ZPT (Fig. 4.17 B). Furthermore the chemical transformations taking place at the crystal surface are easily spurred by XRD with the unambiguous detection of new diffraction peaks at $14.42, 16.03, 16.45, 27.26$ and 31.34° , characteristic of $\text{Zn}_2(\text{PO}_4)(\text{OH})$ for a transforming α -ZPT surface (Fig. 4.18 A) [90], and at 51.14° explaining the additional presence of $\text{Zn}_4(\text{PO}_4)_2(\text{OH})_2 \cdot 3\text{H}_2\text{O}$ (Fig. 4.18 B) [91] on the β -ZPT surface.

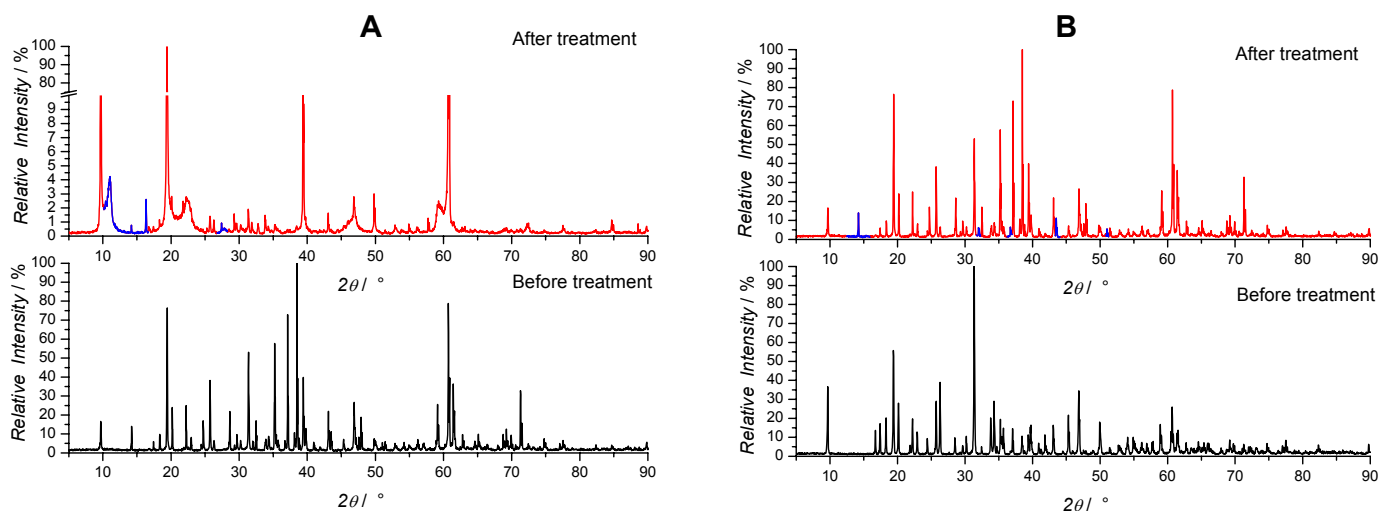


Figure 4.18: Chemical etching with $1 \text{ mol.L}^{-1} \text{ NH}_3$ exposition for 10 min of α -ZPT (A) and β -ZPT (B) followed by XRD. Drastic effects of surface texture changes and stemming from ammonia treatment are observed with the apparition of traces (blue) of Tarbuttite $[\text{Zn}_2(\text{PO}_4)(\text{OH})]$, Spencerite $[\text{Zn}_4(\text{PO}_4)_2(\text{OH})_2 \cdot 3\text{H}_2\text{O}]$ and adsorbed NH_4HCO_3 , thus accurately emphasizing the chemical surface reactivity of zinc phosphate hydrates.

Since the (011) surface of both polymorphs of hopeite present a high surface chemical reactivity in a broad range of acid-base conditions, it may be suspected also a severe transformation under e-beam irradiation, provoking a local dehydration of the crystal surface due to superheating, thus inducing the dehydration of a “destabilized”-ZPT to a ZPD structure, or similarly the conversion of a metastable metal hydrogen phosphate hydrate to a more condensed structure such as hydroxyapatite.

4.2.4. E-beam irradiation and electron induced chemical reaction

Thus dramatic changes are observed when the (010) surface of Brushite is exposed to a high energy electron beam as it occurs during Scanning Electron Microscopy (SEM), while the same surface of α - and β -ZPT crystals show a high stability (Fig. 4.1 A and Fig. 4.1 B). However if first chemically treated with ammonia, the (011) surface of α -ZPT displays the same e-beam induced crystallization patterns as on the Brushite surface, located only on the walls of growing etch pits as shown in Fig. 4.19. Besides, it was found that Brushite is a metastable precursor of hydroxyapatite with a general tendency for the following transformation sequence under a broad range of conditions: Brushite \rightarrow OCP \rightarrow HAP, where OCP denotes the octacalcium phosphate phase [92-95]. Because of its plate-like morphology (Fig. 4.2 A) in the (010) orientation, the calcium phosphate dihydrate (Brushite) is suitable for e-beam etching. After 5 min exposure (induction period), the (010) surface show rise of periodically organised nanospherules (40 nm in diameter, Fig. 4.2 D), forming a cluster-like morphology on further e-beam exposure (Fig. 4.2 C). Correlated with the results of Prosnier et al. [96] and later with the interpretation of Nancollas

and Mohan [97] for the transformation of amorphous calcium phosphate, we identify this “freshly generated” phase as octacalcium phosphate. This would be the first experimental evidence of OCP growth on Brushite surface caused by electron irradiation.

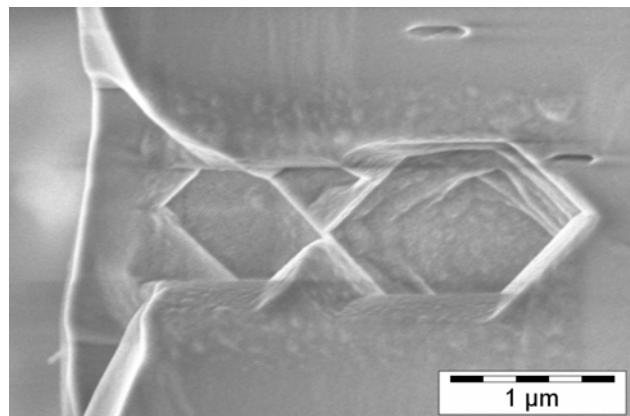


Figure 4.19: (011) surface of α -ZPT successively submitted to $1 \text{ mol.L}^{-1} \text{ NH}_3$ etching for 10 min and then to e-beam etching (5 min, 3 kV). The electron radiation induces the dehydration of ZPT to ZPD specifically on the highly reactive pit walls and hole bottom, emphasized by the homogeneous distribution of rounded ZPD nuclei of 90 nm diameter.

The idea that on exposure to an intensive electron beam on the SEM stage Brushite heats locally ((010) plane) and hence dehydrates via HPO_4^{2-} condensation and crystal water release (partial leaking of hydrogen bonds) was recently supported [98-99]. The Brushite surface becomes electroconductive and luminescent. The luminosity remanence ceased on stopping of the e-beam exposure [100]. In comparison, this electromolecular effect can not be observed for any of the hopeite polymorphs due to their higher thermodynamic stability. Subsequently in the [010] plane, oxygen radicals $\text{O}_2^{\bullet -}$ (superoxide anion radicals) are formed due to the presence of trapped electrons in the structure as reported successively by Monma et al. [101] and Kanai and coworkers [102-103]. This generates numerous structural atomic stresses with a depth of a few unit cells [104], necessary for the “epitaxial” growth of OCP islands on the (010) Brushite surface.

When there is a local lattice misfit of crystallographic parameters, the initially grown layers may display defects or imperfections inducing a less favourable direction for crystal growth.

The ability of one crystalline phase to grow on the surface of another is strongly dependent on the surface characteristics. The establishment of a defined orientation-relationship between the crystalline overgrowth and the substrate requires formation of at least one immobile monolayer of the building units of the new phase regularly organized on the nm-scale. It is suggested that there is a critical misfit threshold for an epitaxial monolayer in order to reach the same lattice spacing as the crystalline substrate [105-108]. A generally accepted value is 10-20%, which is commonly known as the Royer-Friedel rule [109]. Turbull and Vonnegut [110] developed a global theory in which the efficiency of primary heterogeneous nucleation is also related to lattice matching, i.e. to lattice misfit δ , between nucleus and substrate and predicted that nuclei

would most probably be created for values of δ below 0.015. Therefore, it is possible to consider the reactivity of the Brushite crystal surface in terms of lattice matching. Although Brushite and octacalciumphosphate (OCP) crystallize in different systems, namely monoclinic and triclinic (Table 4.4), both have a layered structure with alternating sheets of crystalline water and anionic tetrahedra of Ca^{2+} and PO_4^{3-} . While the “hydrated” layers of Brushite are oriented parallel to the (010) plane, the hydrated layers of OCP alternate with “apatitic” layers along the a -axis [111].

Structure name	Dicalcium phosphate dihydrate or Brushite (DCPD)	Octacalcium phosphate (OCP)
Crystal system	Monoclinic	Triclinic
Space group	$C2/2$	$P1$
a (Å)	5.812	19.625
b (Å)	15.180	9.629
c (Å)	6.359	6.830
α (°)	90.0	89.48
β (°)	118.52	92.68
γ (°)	90.0	107.48

Table 4.4 : Crystallographic data for Brushite and octacalcium phosphate (OCP).

If one considers an epitaxial approach through a change of axis in the Brushite ac plane (figure 4.20), where $\{100\}$ and $\{001\}$ become $\{101\}$ and $\{\bar{1}01\}$ respectively, one can observe δ -values of 5.1% and 5.3% with the b and c lattice parameters of OCP. This indicates a remarkably close fit between both lattice structures. On the other hand, this misfit could be the reason for the change of the layer growth mode to the famous Stranski-Krastanov model describing the transition from layer to island growth. Following this model, heating by the electron beam increases the stored elastic energy in the nearest layers below the (010) surface. This elastic energy is then the driving force for the growth mode change. A strong support to this hypothesis comes from the presence of typical nanospherules and coalescing double-spheres of OCP, when the hydrated (010) faces of Brushite crystals are exposed to an intensive electron beam (Fig. 4.2) [112].

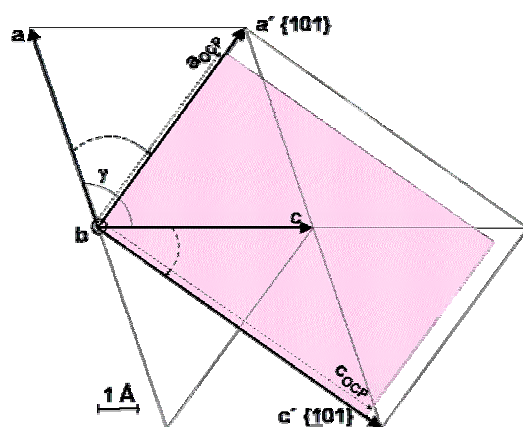


Figure 4.20: Representation of the epitaxial matching of ac planes of Brushite and OCP (approximately up to scale). The colored surface corresponds to the (ac) plane projection of a OCP unit cell.

4.3. From structural to surface properties

4.3.1. Wettability and contact angle measurement

The process of pigment dispersion consists of three distinguishable stages: wetting, mechanical disruption, and stabilization [113]. In wetting, the pigment surface is wetted by the solution, which penetrates into small gaps in the pigment agglomerates and reduces the cohesive forces between pigment particles. Since smaller particles tend to reaggregate (flocculate) more easily than larger particles, a stabilizing mechanism (electrostatic, steric and electrosteric stabilization) should operate during the process in order to achieve excellent pigment dispersion.

The determination of solid-vapor (γ_{SV}) and solid-liquid (γ_{SL}) interfacial tensions and subsequently the evaluation of solid surface energies is of utmost importance for modifying chemically or compatibilizing efficiently the solid surface of ZPT crystals with other substances, either in the liquid state in the case of anticorrosion paints such as latex particles in forming coatings or as solid reactants in the case of orthopaedic dental cements, since it completely reflects the wettability of the crystal surface. Several approaches have been developed to estimate interfacial energies (IFT) and surface tensions (SFT), including direct force measurements [114-118], contact angles [119-123] and film flotation [124], or from theoretical arguments in combination with the Gradient theory [125-126], the Lifschitz theory of Van der Waals forces [127] the theory of molecular interactions [128-129] and the Equation-of-state approach.

Contact angle measurement is easily performed by establishing the tangent (angle) of a liquid drop to a solid surface at the base. The possibility to determine contact angles was pioneered by Young [130]. The contact angle θ of a liquid drop on a solid surface is defined by the mechanical equilibrium of the drop under the action of the interfacial tensions: solid-vapor (γ_{SV}), solid-liquid (γ_{SL}) and liquid-vapor (γ_{LV}) as shown in Figure 4.21. The equilibrium equation is known as the Young's relation:

$$\gamma_{LV} \cos \theta_Y = \gamma_{SV} - \gamma_{SL} - \sigma \kappa_{GS} \quad (4.19)$$

where θ_Y is the Young contact angle, σ is the line tension and is κ_{GS} the geodesic curvature of the three-phase line, i.e. the curvature in the plane of the solid phase. Since γ_{SV} , γ_{SL} , γ_{LV} are thermodynamic properties, Eq. (4.19) implies a single unique contact angle θ , however due to the existence of a contact angle hysteresis H originating from the solid nature of the tested substrate, the roughness and heterogeneity of the surface as well as the existence of

metastable surface energetic states, values of θ different of θ_Y may be measured. On very rough surfaces, contact angles are larger than on chemically identical, smooth surfaces. Therefore on ideal solid surfaces, there is no contact angle hysteresis and the experimentally observed contact angle is equal to θ_Y . On smooth but chemically heterogeneous surface, θ is not necessarily equal to the thermodynamic equilibrium angle. Nevertheless the experimental advancing contact angle θ_a , can be a good approximation of θ_Y . In addition to these complexities, existence of an equilibrium spreading pressure π_e [131], penetration of a liquid into the solid, swelling of the solid by the liquid, and chemical reaction, all play a preponderant role. Thus most contact angle approaches rely on Young's equation for the determination of surface energetics. While these approaches are, logically and conceptually, mutually exclusive, they share some basic assumptions: (i) All approaches rely on the validity and applicability of Young's equation; (ii) pure liquids are preferred since liquid mixtures induce preferential adsorptions; (iii) the surface tensions γ_{SV} , γ_{SL} , γ_{LV} are assumed to be constant during the experiment, i.e. there should be no physical or chemical reactions between the liquid and the solid surface; (iv) the liquid surface tensions of the testing liquids should be higher than the anticipated solid surface tension, (v) the values of γ_{SV} , going from liquid to liquid are supposed to be constant, i.e. independent of the liquid used.

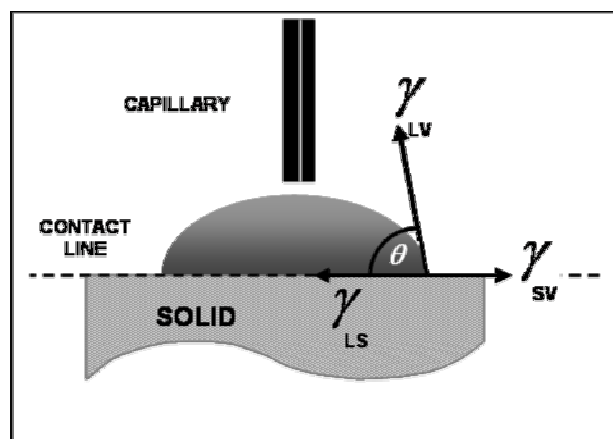


Figure 4.21: Schematic representation of a sessile-drop angle system based on Young's approach.

Besides basic assumptions required performing an automated axisymmetric drop shape analysis (ADSA) from direct contact angle measurements, some other widely accepted assumptions relative to the calculation of surface energies must be discussed. Obviously, contact angle interpretations of reactive solutions are expected to be more complicated than that of a pure liquid due to additional intermolecular effects. Thermodynamically, such systems have three degree of freedom and additional degrees of freedom arise from addition effects of the liquid component (acidity, polarity, ionic strength, etc.). If $\gamma_{LV} \approx \gamma_{SV}$ or $\gamma_{LV} < \gamma_{SV}$. Either complete wetting occurs or a change in γ_{SV} induced by the solid/liquid contact (autophobicity) is

observed. The last assumption of consistency of γ_{SV} going from liquid to liquid is strongly needed first for reason of procedure in deducing solid surface tensions and secondly because only γ_{SL} and θ are accessible parameters. A general review of other more subtle and negligible assumptions for the measurement of surface energies of ZPT powders was given by Neumann et al [132]. Nevertheless surface tension component approaches will be briefly discussed and tested.

4.3.1.1. Fowkes approach and extended Fowkes approach

The approach of surface components was first described by Fowkes [120]. It is postulated that the total surface tension can be expressed as a sum of different surface tension components, each of which arise due to a specific type of intermolecular forces:

$$\gamma = \gamma^d + \gamma^h + \gamma^{di} + \dots \quad (4.20)$$

where γ , γ^d , γ^h and γ^{di} are respectively, the total surface tension, dispersive surface tension component, and surface tension component due to hydrogen and dipole bonding. Eq. (4.22) is often rearranged into:

$$\gamma = \gamma^d + \gamma^n \quad (4.21)$$

i.e. the total surface tension is the sum of only the dispersive γ^d and non-dispersive γ^n surface tension components. The former is claimed to result from molecular interactions due to non-London forces. A geometric mean relationship is postulated for both of the solid-liquid and liquid-liquid interfacial tension, which combined with Young's relation yields:

$$\gamma_L \cos \theta_Y = -\gamma_L + 2(\gamma_S^d \cdot \gamma_L^d)^{1/2} \quad (4.22)$$

Typically, experimental contact angles of different liquids (see Table 4.5) with known γ_L^d on a dispersive solid surface ($\gamma_S = \gamma_S^d$) are employed to determine the surface tension of a solid. Therefore surface energy results stated in Table 4.7 with the Fowkes approach vary very much employing two liquids of nearly the same surface tension but with very different intermolecular forces, i.e a polar (non dispersive) liquid (1-octanol, $\gamma_L = 21.3 \text{ mJ.m}^{-2}$) and a dispersive liquid (NaCl, $\gamma_L = 20.0 \text{ mJ.m}^{-2}$). However the simple approach of Fowkes is not completely satisfying since it is obvious that $\gamma_L \cos \theta$ changes smoothly with γ_{LV} , independent of intermolecular forces and liquid structures. Owens and Wendt [133] extended Fowkes's concept to cases where both dispersion and hydrogen bonding forces may operate. They regarded the surface tension as being composed of two components:

$$\gamma = \gamma^d + \gamma^h \quad (4.23)$$

where γ^h denotes the component of surface tension due to both hydrogen bonding and dipole-dipole interactions. Combining Eq. (4.23) with the Young's Eq. (4.19), one obtains the *Owens-Wendt-Kaelble* relation [134]:

$$\gamma_L(1 + \cos \theta_Y) = 2\sqrt{\gamma_S^d \gamma_L^d} + 2\sqrt{\gamma_S^h \gamma_L^h} \quad (4.24)$$

This relation contains two unknowns (γ_S^d and γ_S^h) and implies the constancy of the solid surface tension from liquid to liquid. Thus water as non-dispersive liquid ($\gamma_L = 71.6 \text{ mJ.m}^{-2}$, $\gamma_L^d = 19.9 \text{ mJ.m}^{-2}$) and 1-octanol as dispersive liquid ($\gamma_L = 27.6 \text{ mJ.m}^{-2} \geq \gamma_L^d \approx 21.3 \text{ mJ.m}^{-2}$) are selected for surface energy calculations.

4.3.1.2. Lifshitz-van der Waals / Acid-Base (van Oss) approach (STC method)

Lifshitz-van der Waals / Acid-Base (van Oss) approach [122-123] is claimed to be a generalization of the Fowkes approach, by considering perceived acid-base interactions at the interface. Van Oss et al. divided the surface tension into different perceived components, i.e. the so-called Lifshitz-van der Waals (LW) acid (+) and base (-) components (surface tension components or STC), such that the total surface tension is given by:

$$\gamma_i = \gamma_i^{LW} + 2\sqrt{\gamma_i^+ \gamma_i^-} \quad (4.25)$$

where i describes a liquid or a solid. For a solid-liquid system combination of Eq. (4.25) with Young's relation (4.19) leads to:

$$\gamma_L(1 + \cos \theta_Y) = 2(\gamma_L^{LW} \gamma_S^{LW})^{1/2} + 2(\gamma_L^+ \gamma_S^-)^{1/2} + 2(\gamma_L^- \gamma_S^+)^{1/2} \quad (4.26)$$

This Acid-Base relation is often used to access solid surface components ($\gamma_S^{LW}, \gamma_S^+, \gamma_S^-$) from contact angles, using three simultaneous calibration liquids of known properties. Recently, Della Volpe [135] concluded that in spite of much controversy, the multi-component approach is still a reliable approach, in which "only substrate dependant" surface energies may be gained using Wu's procedure [136]. Besides, the "equation of state" approach defended by Kwok, Neumann et al. [137] offers an alternative to the STC method and appears to be of practical importance.

4.3.1.3. Equation of state approach (EQS method)

Two well known equation-of-state relations are the Antonow's [138] and Berthelot's [139] rules. Antonow's rule relates surface tensions for solid-liquid system in a simple manner ($\gamma_{SL} = |\gamma_{LV} - \gamma_{SV}|$) (2.27) which combined with Young's approach yields:

$$\cos \theta_Y = -1 + 2 \frac{\gamma_{SV}}{\gamma_{LV}} \quad (4.28)$$

Another equation-of-state relation can be obtained from Berthelot combining rule. Unlike Antonow's rule, Berthelot's (geometric mean) rule bases on molecular interactions of like pairs, from London theory of dispersion [140], the long range dispersion energy function for two identical molecules in combination with the thermodynamic definitions of free energies of cohesion and free energy adhesion per unit area of a solid-liquid pair (Dupré law). Explicitly this assumes the direct and reversible substitution between potential energy parameters for like and-unlike pair interactions ($\varepsilon_{ii}, \varepsilon_{ij}$) with the free energies of cohesion of the solid and the liquid (W_{SS}, W_{LL}) (*combination principle*). By definition it follows: $\gamma_{SL} = (\sqrt{\gamma_{LV}} - \sqrt{\gamma_{SV}})^2$ (4.29) which combined with Eq. (4.19) yields:

$$\cos \theta_Y = -1 + 2 \sqrt{\frac{\gamma_{SV}}{\gamma_{LV}}} \quad (4.30)$$

Thus solid-vapor tension can be easily determined from liquid-vapor tension and contact angle values. This relation also automatically implies that when measuring contact angles with low-energy solid surfaces, the surface tension γ_{SV} is expected to be constant and independent of γ_{LV} . Further developments of Berthelot's equation of state for solid-liquid interfacial tensions are given by Li et al. [141] under the form of a Lennard-Jones solid-fluid interaction potential for the used of liquid mixtures such as NaCl or NaOH solutions. A broadly used extension of Berthelot's rule takes the form:

$$\cos \theta_Y = -1 + 2 \sqrt{\frac{\gamma_{SV}}{\gamma_{LV}}} \cdot \exp\left(-\beta\{\gamma_{LV} - \gamma_{SV}\}^2\right) \quad (4.31)$$

where β is a constant that does not systematically depend on the tested solid surface. For polymer modified crystal surfaces and SAM (self-assembled monolayer), an average value of $12.47 \cdot 10^{-4} (\text{m}^2 \cdot \text{mJ}^{-1})^2$ for β may be considered as excellent [141] or can be evaluated using the Newton method [142]. In the case of very large $|\gamma_{LV} - \gamma_{SV}|$, Eq. 3.32 is approximated using a development in series of the exponential term. Thus from a single contact angle measurement on the same solid surface with various liquids, the equation-of-state approach is capable of accurately predicting solid surface energies with deviations as low as $0.1 \text{ mJ} \cdot \text{m}^{-2}$.

Moreover, each of the method above-described cannot exempt from the fact that one of the fundamental parameters needed to solve local fluid mechanics equations (drop receding effect) is the knowledge of the boundary condition of the fluid velocity at the solid surface. In his "Lectures of Physics" Feynman wrote: "It turns out – although this not at all self-evident – that in all circumstances where it has been experimentally checked, the velocity of a fluid is exactly zero at the surface of a solid" [143]. However in these contact angle experimentations the droplet interfaces of the applied fluids to the ZPT surface are apparently constantly mobile and evolving either due to fluid evaporation or by the continuous fluid absorption in the bulk, hence

deforming dramatically the tested surface. Another case emerges with the use of non-newtonian fluids such as polymers (latex decoration on ZPT crystal), where observed extent of slippage may be stress dependent [144]. Therefore a precise estimation of surface energies and the establishment of reliable wetting envelope curves for α - and β -ZPT require the use of varied approaches with different theoretical foundations.

4.3.2. Wetting envelop of ZPT polymorphs

Surface energies must in some way be connected to surface chemistry and is therefore an important determinant of ZPT material's functions. Contact angles for a set of test liquids (Table 4.5), some recognized to be inert (water, 1-octanol) and other to be aggressive (HCl, NaOH, NH₃) to the ZPT crystal (011) surface or of particular interest (NaCl) were used to measure the wettability characteristics of ZPT polymorphs.

Contact Liquid	H ₂ O	NaCl	HCl	NaOH	NH ₃	1-Octanol
Concentration (mol.L⁻¹)	pure	0.5	1	1	1	pure
pH	7.01	6.69	0.07	11.76	13.03	-
Conductivity κ^d	2.66 10 ⁻⁶	6.32	13.36	5.13	2.12	-
Surface tension (SFT) $\gamma_{LG}^{a,b}$	71.6	72.3	71.0	67.8	70.2	27.6
Disperse/LW part ^a	19.9	20.0	19.6	18.7	19.2	21.3
Polar/acid-base part ^a	52.2	52.3	51.4	49.6	50.7	6.3
Acid part ^a	52.2	52.3	51.4	49.6	50.7	6.3
Base part ^a	13.1	13.1	12.8	12.2	12.7	1.57
Interfacial tension (IFT) ^{a,e}	72.1	72.3	71.0	67.8	70.2	27.6
Average contact angle θ^c						
α-ZPT	13.8	9.8	13.7	9.1	8.1	15.4
β-ZPT	18.7	19.0	13.6	7.8	8.2	16.4

Table 4.5: Comparison of four classical approaches for the evaluation of the surface energy γ_{SL} zinc phosphate tetrahydrates.

- (a) estimated average error $\pm 0.5 \text{ mJ.m}^{-2}$
- (b) measured with a DuNouy ring method
- (c) tangential fitting method, estimated average error $\pm 0.1^\circ$
- (d) estimated error $\pm 0.10 \text{ mS.cm}^{-1}$. Value of water evaluated with Onsager-Hückel-Debye law
- (e) evaluated after Schulz

Interfacial tension of these liquid were first determined using a DuNouy ring method. The surface tension of salt mixtures and diluted solutions does not differ greatly of that of pure water as shown in Table 4.5. All contact angles obtained with these different test liquids are under 15° and tend to indicate either a strong hydrophilicity of ZPT surfaces or an underlying directing effect of the surface topology due to adsorption of the liquid (i.e. depend on internal compaction, thus on powder density) and slight surfacial dissolution reaction as already discussed in § 4.2.3. For this specific reason, ammonia and NaOH display the lowest contact angles for α -ZPT and β -ZPT respectively. On contrary, 1-octanol exhibits the highest values of contact angles due to

its low polarity, i.e. its inefficiency to interact with surface phosphate groups. Nevertheless, strong differences (doubling) in contact angle values arise in presence of NaCl, suggesting a high surface polarisation of the (011) surface of α -ZPT in contrast to a high chemical surface stability of β -ZPT. This may originate from the differences in the respective (bulk) hydrogen bonding patterns that control the surface stability and reactivity. Therefore the total surface energies calculated using the Equation-of-state method and the Lifshitz-van der Waals approach strongly differ. However both methods, albeit having different theoretical justifications, deliver an average difference for σ_s of 0.4 mJ.m⁻², but depending on the liquid properties and assumingly the equilibrium spreading pressure π_e [131].

MODEL	EQS ^{a,c}	LW ^{b,d}	Fowkes			Wu		
Contact liquid			Total energy ^e	Disperse part ^f	Polar Part ^f	Total energy ^e	Disperse part ^f	Polar part ^f
α-ZPT								
H ₂ O	70.1	253.7	69.5	19.2	50.3	74.2	32.9	41.3
NaCl	69.3	250.4	69.1	19.1	50.0	74.2	33.8	40.4
HCl	66.9	243.2	67.1	18.5	48.6	74.6	33.7	38.9
NaOH	69.5	250.2	69.5	19.3	40.2	74.5	33.8	40.7
NH ₃	71.3	258.2	71.5	19.8	51.7	71.5	31.8	39.7
1-Octanol	26.5	34.4	26.6	20.5	5.1	28.1	25.2	2.9
β-ZPT								
H ₂ O	69.6	252.4	68.9	19.0	49.9	68.3	18.9	49.4
NaCl	69.7	249.9	68.7	18.9	49.8	74.1	33.2	40.9
HCl	67.2	243.6	67.2	18.5	48.7	73.1	34.6	38.5
NaOH	69.5	259.2	69.5	19.3	50.2	74.4	33.8	40.6
NH ₃	71.5	258.7	71.6	19.8	51.8	69.5	19.3	50.2
1-Octanol	26.6	34.5	26.6	20.9	5.7	28.1	25.2	2.9

Table 4.6: Comparison of four classical approaches for the evaluation of the surface energy γ_{SL} (mJ.m⁻²) of zinc phosphate tetrahydrates.

- (a) EQS: Equation of State model
 (b) LW: Lifshitz-Van der Waals / acid-base (van Oss) model
 (c) estimated error ± 0.1 mJ.m⁻² (d) estimated error ± 5.0 mJ.m⁻²
 (e) estimated error ± 2.0 mJ.m⁻² (f) estimated error ± 1.0 mJ.m⁻²

Thus, it is instructive to compare the Fowkes and Wu approaches, to gain access to polar and disperse components of the surface energy. Both methods give ground to affirm that α -ZPT possesses a higher total surface energy than β -ZPT with values of 71.8 and 68.6 mJ.m⁻², confirming the higher stability of the β -ZPT in regards to the α -ZPT surface. Since the polar component represent a contribution of 72% (Fowkes method) and 55% (Wu's approach) to σ_s independent of the pH value of the test solution and independent of the form of ZPT, one might suggest that both ZPT polymorphs have nearly neutral surfaces (low dispersion ability) and highly polar surfaces. Plotting the polar part against the dispersive part of the surface tension for

various liquids allows the establishment of the wetting envelope curves as shown in Figure 4.25. The long-term water retention and polymer adsorption characteristics of the powders, depending on the polymer structure and composition (bloc, side chains, functional polar and/or charged side groups) can be ascertained using these wetting curves. Every surfactant of surface modifying molecule with polar and dispersive components located inside the wetting envelope will adsorb on the ZPT surface. Therefore it is important to note first that the shape of these curves is consistent with the Zisman fitting [145] made by Neumann [146] and secondly that Fowkes approach and Wu approach deliver similar results. In Fig. 4.25 A and B, one can observe that the Fowkes's approach predict the largest wetting envelop for both ZPT polymorphs in NaCl environment, indirectly indicating a complexation of emerging phosphate groups on the surface with free Na⁺ ions while in Fig. 4.25 C and Fig. 4.25 D Wu's approach suggests the largest wetting envelop in HCl environment, maybe due to the preferential dissolution in acidic conditions of ZPT crystals as proven in Chapter 6. In basic environment realized using NaOH or NH₃ solutions, β-ZPT displays an equivalent sensibility to polar and charged molecules while α-ZPT exhibit a smaller wetting envelop with a higher interaction probability for charged molecules. This implies a possible higher adsorption of polar block (PEO, PVP) of a polymeric surfactant and an equal surface reactivity regarding charged blocks (PSS, PAA) of a polymeric surfactant for β-ZPT comparing to α-ZPT [147].

Finally it is possible to estimate the enthalpy of wetting and its diminishing employing surface compatibilizers as duly reported by Douillard et al. [148]. The heat of wetting i.e. the adsorption enthalpy and the contact angles are directly related, knowing the specific surface area value with sufficient precision and the variation of the cosine of the contact angle with the temperature [149-150]. For example the cosine coefficients reported by Wu [151] vary between -0.00014 and -0.00226 for water deposited on solids far from solid phase transition.

Contact liquid	$\Delta H^{\text{wetting}}$	
	α-ZPT ^a	β-ZPT ^a
H₂O (pure)	95.6	94.1
NaCl (0.5 M)	98.1	94.9
HCl (1 M)	96.2	94.7
NaOH (1 M)	91.4	91.5
NH₃ (1 M)	94.7	94.7
1-Octanol (pure)	36.7	36.5

Table 4.7: Estimation of the enthalpy of wetting $-\Delta H^{\text{wetting}}$ (mJ.m⁻²) of ZPT polymorphs at 25°C in various saline environments with Douillard's method [35].

(a) Estimated error ± 0.2 mJ.m⁻².

Thus an estimation of the average enthalpy of wetting $-\Delta H^{\text{wetting}}$ is obtained from measured contact angles, combined with surface energy values accessed with Fowkes approach, and reported in Table 4.7

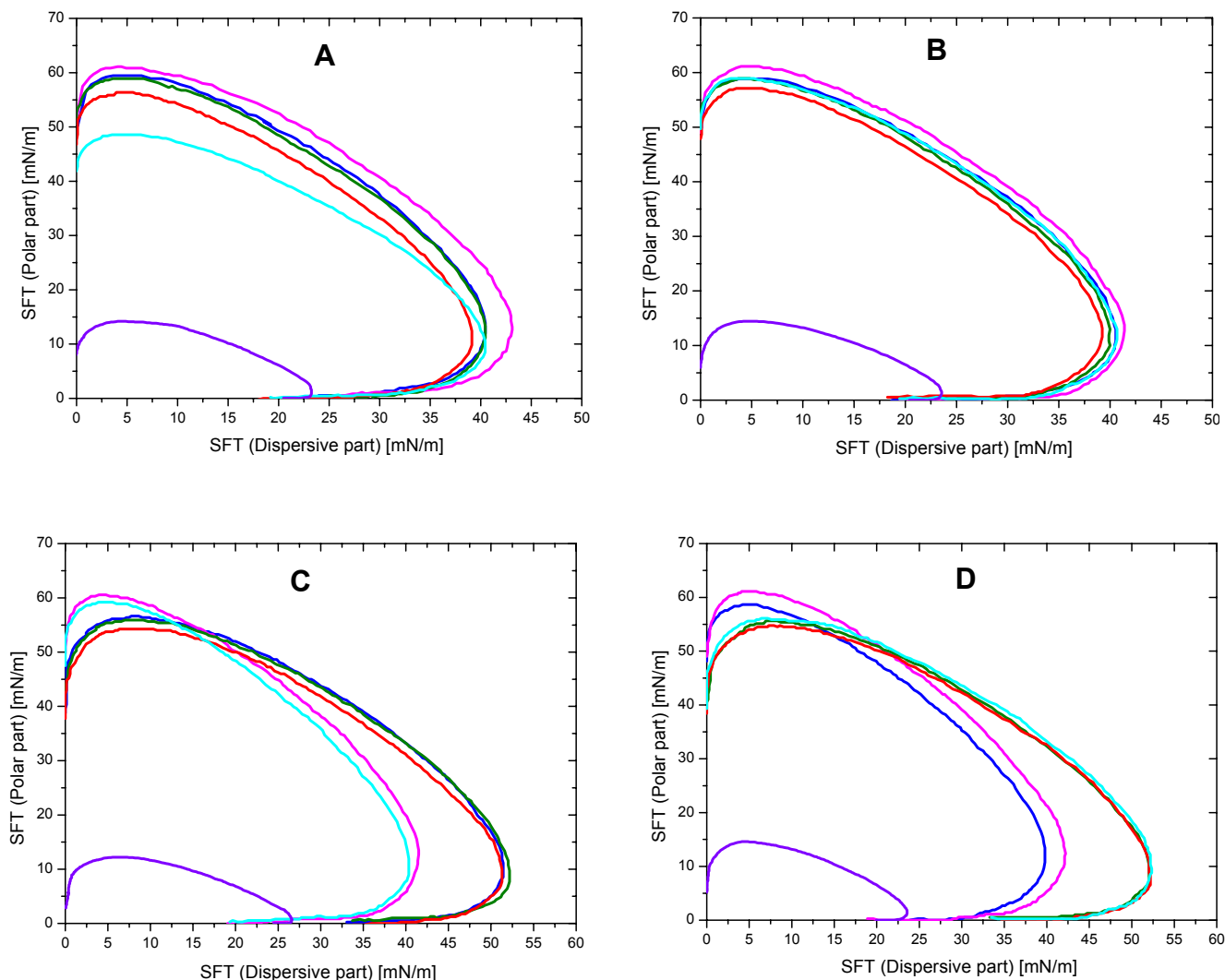


Figure 4.25: Wetting envelope curves generated according to Fowkes and Wu methods for α -ZPT (A,C) and β -ZPT (B,D) respectively, in contact with various liquid environments : ultrapure water (midnight blue), 0.1 mol.L^{-1} NaCl (pink), 1 mol.L^{-1} HCl (deep green), 1 mol.L^{-1} NaOH (red), 1 mol.L^{-1} NH_3 (blue), 1-octanol (violet). The area below the curves corresponds to chemically compatible liquids with the powder surface.

These values of $\Delta H^{\text{wetting}}$ strongly depend on the dispersing medium and are globally very low, with around one third of the value found by Douillard for talc microcrystals (-321.0 mJ.m^{-2}) dispersed in water [148] and the half of values measured by Médout-Marère [152] for calcite (-206.1 mJ.m^{-2}) but well in the accepted range for aggregated silica (-78 mJ.m^{-2}) and quartz (-104 mJ.m^{-2}) powders. The huge difference with results published by Douillard et al. originates from the choice of the measurement method (use of contact angle values / microcalorimetry)

and the use of an averaged value of $(\partial \cos \theta / \partial T)_p$, disregarding the chemical nature of the test fluid.

Thus the combined predictions of the wetting behaviour and surface energies of ZPT polymorphs in combination with zeta-potential measurements (§ 4.3.2) represent a starting point for the evaluation of the stability of an inorganic colloidal suspension and the use of effective additives for its enhancement (adsorption isotherm experiments).

4.3.3. Suspension stability and zeta-potential measurements

Another point to discuss is the influence of surface charge density on the surface chemical stability or reactivity of ZPT polymorphs in comparison with calcium phosphate hydrate materials. This question can be efficiently approached by measuring the electrophoretic mobility of microcrystalline particles suspended in aqueous medium and thus obtaining the zeta-potential as a function of pH.

4.3.3.1. Interfacial electrophoretic phenomena

A charged particle in an electrolyte solution moves in an applied static electric field E with a stationary velocity U . This interfacial electrokinetic phenomenon is called electrophoresis. If the dimension a of the particle is much larger than the Debye-Hückel length $1/\kappa$, then the particle surface can be considered planar ($\kappa a \gg 1$), and the particle moves in such a way that the applied field is parallel to the particle surface as shown in Fig. 4.26. The relative velocity u of the liquid is then zero at the particle surface (§ 4.3.1). This plane ($x = 0$) is called the *slipping plane* or *shear plane*. The charge density σ of the particle surface is bound to the surface potential ψ_0 in the slipping plane by:

$$\sigma = 4\pi \varepsilon \varepsilon_0 \psi_0 \kappa (1 + \kappa a) \quad (4.32)$$

where ε and ε_0 are respectively, the relative permittivity of the liquid and the permittivity of vacuum. By definition the electrophoretic mobility μ is the electrophoretic velocity per unit strength of applied electric field and is in general related to the surface charge density, thus to the potential at the slipping plane. This potential is called the zeta potential ζ of the particle, and is the only experimentally accessible surface potential.

However the slipping plane does not necessarily coincide with the particle surface. Only if the slipping plane is located at the particle surface does the zeta potential become equal to the surface potential ψ_0 (Fig. 4.26 B). Thus it comes,

$$\mu = \frac{\varepsilon \varepsilon_0}{\eta} \cdot \zeta \quad (4.33)$$

which is known as the Schmoluchowski expression of the electrophoretic mobility of a colloidal particle [153].

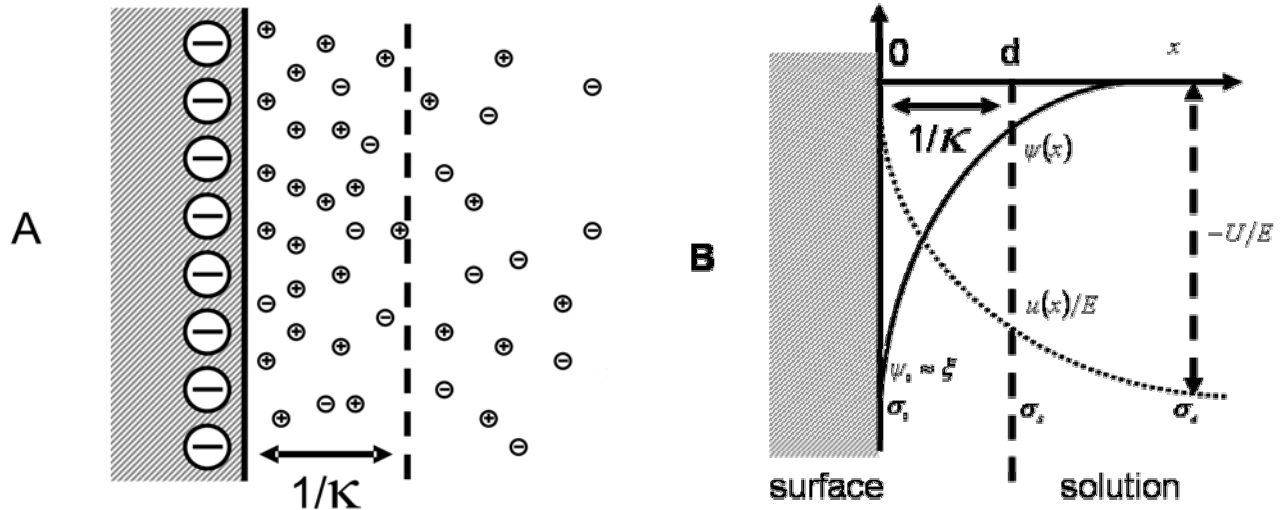


Figure 4.26: Schematic representation of the distribution of electrolyte ions (A), the electric potential distribution $\psi(x)$, the liquid velocity distribution $u(x)$ and the zeta-potential ξ (B) near a negatively charged planar solid surface. The electroneutrality condition of the electrical double layer at the water-solid interface is verified within the Gouy-Chapman-Stern model which is generally adopted in combination with Langmuir adsorption isotherms to analyse the surface charging process.

For very small spheres ($\kappa a \ll 1$), a factor of $2/3$ appears in the equation (4.33) and defines the Hückel's formula. In this case, the electrical double layer is thin and the electrolyte ions in the double layer experience a distorted field near the particle surface (electrophoretic *retardation effect*), which is larger than the original field by a factor of $3/2$. On the other hand when $\kappa a \gg 1$, the electric double layer is thick (i.e. large $1/\kappa$) and the ions experience an almost undistorted field (Fig. 4.27 A). Further, Henry derived mobility formulas for particles with non-spherical geometry and low values of ξ in introducing the Henry's function $f(\kappa a)$ in Eq. (4.33) in order to also take into account the distortion of the equilibrium double layer (*relaxation effect*).

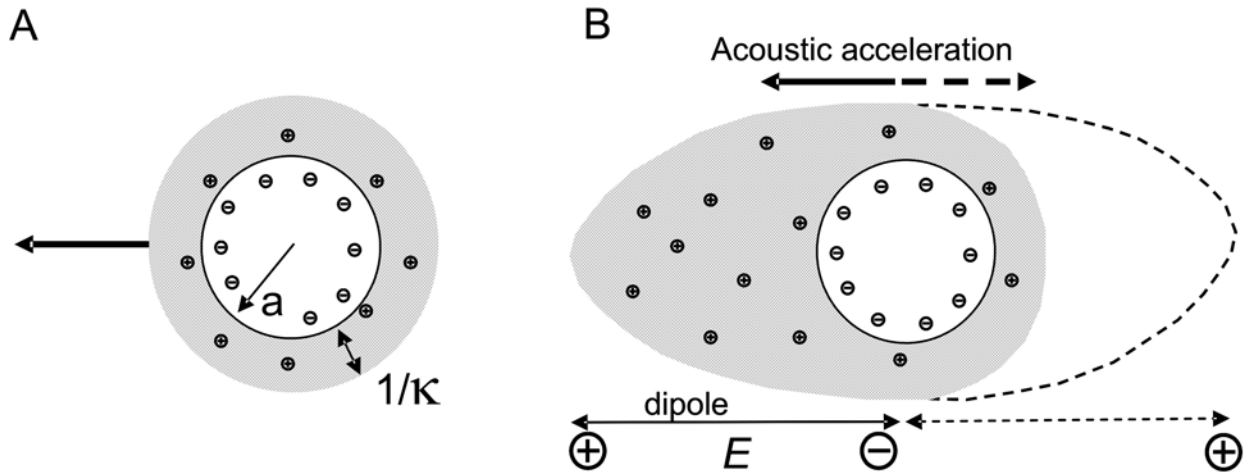


Figure 4.27: Illustration of the relaxation effect. The electrical diffuse double layer around a spherical particle is spherical (symmetrical counter ions distribution) for low zeta potential (A) but is no longer spherical for high zeta potentials (counter ions lag behind the particle) (B) in reason of a local polarization of the double layer (mechanism of colloidal vibration potential - CVP).

It follows:

$$\mu = \frac{\varepsilon \varepsilon_0}{\eta} \cdot \zeta \cdot f(\kappa a) \quad (4.34)$$

An accurate approximation of the Henry's function is given by Ohshima [154]:

$$f(\kappa a) = \frac{2}{3} \cdot \left[1 + \frac{1}{2(1 + 2.5/\kappa a [1 + 2 \exp(-\kappa a)])^2} \right] \quad (4.35)$$

When large colloidal particles have a charged surface structure, an ion penetrable surface layer of thickness d exists, in which ionisable groups of valence Z are distributed with a uniform density N . Then the slipping plane is located at $x = -d$. This case corresponds to ZPT microcrystals dispersed in alkaline (basic) aqueous solutions, and is fully described by the Ohshima theory [155]. A Smoluchowski equation [156] corrected for the effects of particle size distribution [157-158] and ionic strength of the suspension [159] are used in this context. Therefore for spherical particles with a thin double layer, O'Brien [160] showed that dynamic mobility is given by :

$$\mu_d = \frac{2\varepsilon\zeta}{3\eta} (1 + F(a)) \cdot G\left(\frac{\omega a^2}{\nu}\right) \quad (4.36)$$

where ε is the permittivity of the suspension medium and η its viscosity at a given temperature. If ζ is the average zeta-potential of the particles, F is a measure of the field strength near the particle surface, G is a measure of the effect of the inertia of the particles, and ν ($= \eta/\rho$) is the kinetic viscosity. In many cases the function F is set to 0.5 and consequently the particle size a enters only in the function G .

It is an important observation that exposure to an electric field as well as stirring may initiate sedimentation (Dorn effect) and thus affect the overall stability of the suspension [68]. From a

practical point of view in consequence of the large crystallite size of the Brushite and hopeite polymorphs (see Fig. 4.3) the presence of a non ionic surfactant (BASF, AT 50, $C_{18}-(CH_2-CH_2-O)_5H$) is required at constant ionic strength in order to evaluate the zeta-potential in delaying the destabilization of the suspension. However, this restricts the use of the DLVO theory [161-162] since the stability of the colloidal suspension depends strongly on the van der Waals interactions between the solid and the molecules of solvent in the case of a divided solid in suspension in a liquid, without a third component such as a surfactant molecule, a polymer or an electrolyte.

Nevertheless as stated by O'Brien [160], electroacoustic measurement is a "new" technique for the electrokinetic analysis of colloidal dispersion. The electrokinetic sonic amplitude (ESA) is proportional to the dynamic electrophoretic mobility of colloidal particles in an applied oscillating electric field. Mangeldorf and White [163] obtained the full electrokinetic equations governing the dynamic electrophoresis and succeeded in obtaining an approximate but accurate expression of the zeta potential, on which modern dynamic electrophoresis technique is based.

4.3.3.2. Electrokinetic properties of ZPT pigments and suspension stability

Thus zeta-potential values were calculated from electrophoretic mobility data using the Helmholtz-Smoluchowski equation with a $f(KA) = 1.5$, corrected by taking into account the particle size distribution of the powders (Henry equation) as above described (§ 4.3.2.1). The aqueous dispersing behaviour of ZPT powders compared to calcium phosphate pigments was also investigated through potentiometric titration. HNO_3 0.1 mol.L^{-1} and KOH 0.1 mol.L^{-1} were used to adjust the pH. The isoelectric point (IEP) was identified at the pH axis crossing point as shown in Figure 4.28.

The isoelectric point (IEP) of Brushite and Hydroxapatite occur at pH 6.16 and 6.44 respectively. This corresponds to reported values by Howie-Meyers [164] and Leach [165-167] as shown in Fig. 4.28. Under acidic conditions, a mixture of calcium deficient HAP, Monetite ($CaHPO_4$) or Brushite will form as suggested by Brown [168]. Solubility diagrams for calcium phosphate [169] show that HAP may convert or at least coexist with Brushite in an acidic environment at an approximate pH of 4.8. Below 4.8, Brushite and Monetite are the stable phases while above pH 4.8, HAP is the stable phase. In the light of the results mentioned by Lemaitre [170], the above measured IEP also correspond to vanishingly small concentration of free Ca^{2+} ions in the suspension and marks the onset of the precipitation reaction. Therefore at pH 6.9, the zeta-potential tends to stabilize Brushite and corresponds to its solubility minimum. However, at any given pH above of 4, Brushite exhibits a higher (30 orders of magnitude higher) solubility than HAP and similarly at pH above IEP a higher but negative zeta-potential [164].

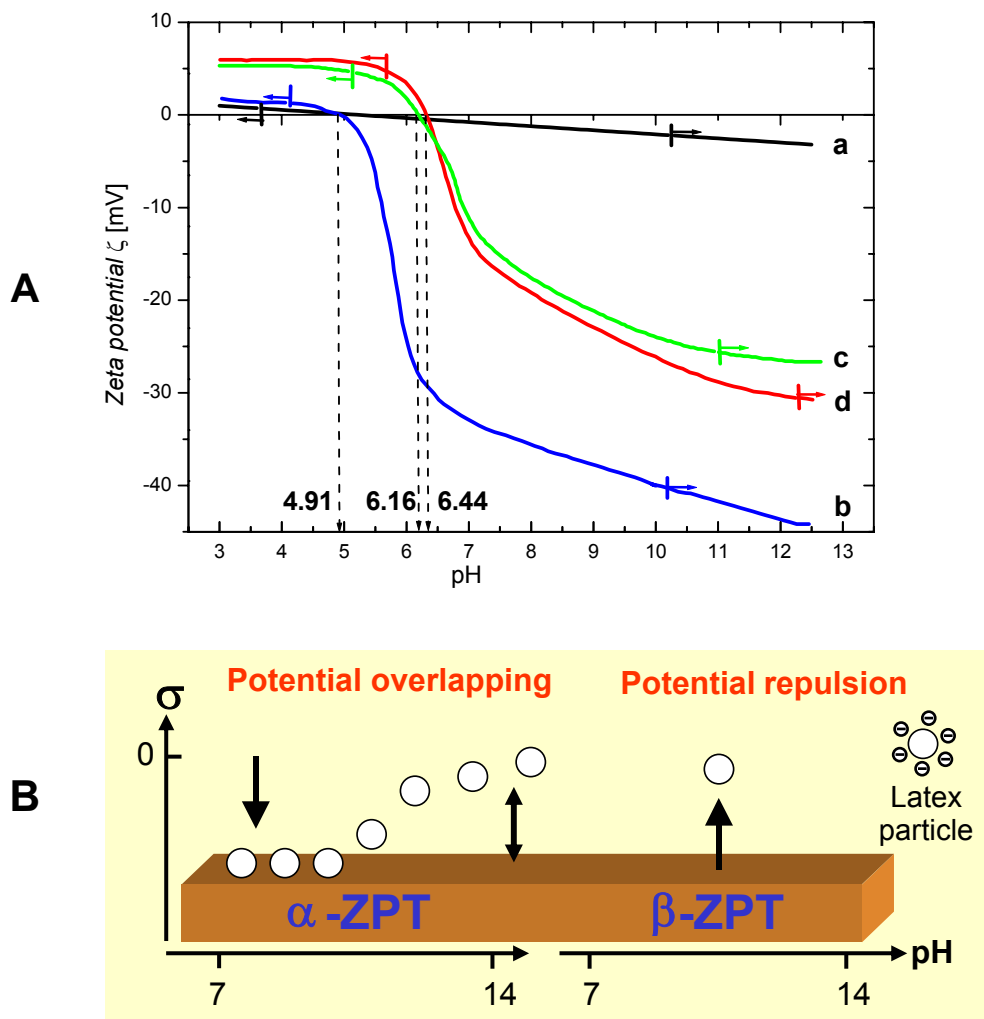


Figure 4.28 : Effects of pH on zeta potential (A) of (a) α -hopeite, (b) β -hopeite, (c) Brushite, (d) hydroxyapatite at 25°C under constant ionic strength ($I = 0.05 \text{ mol.L}^{-1}$). Vertical lines and arrows indicate pH initiation of the solubilisation process. (B) schematic representation of the adsorption behaviour of a negatively charged latex particle (carboxylated modified PS-based miniemulsion) on the (011) surface of both ZPT polymorphs.

In alkaline solution ($\text{pH} > 9$), a usual decrease of zeta potential followed by a plateau is attributed to dissolution of calcium phosphate, the release of Ca^{2+} in the aqueous medium, and the progressive adsorption of Na^+ at the dissolving surface (diffuse layer), mainly to compensate the buffering effect of surface phosphate groups (electroneutrality condition).

There is no significant difference between IEP obtained for hopeite and calcium phosphate samples in KCl, HNO_3 , NaOH or $(\text{CH}_3)_4\text{NOH}$ solutions. As one would expect, the cation $(\text{CH}_3)_4\text{N}^+$ and the anion NO_3^- are too large to exchange with surface ions and, as there would be little tendency for these ions to form complexes with the surface ions, it is reasonable to assume that these ions behave indifferently and act only as counterion for any surface charge. It is not surprising therefore, that upon equilibration the zeta potential reflects partially the surface charge density.

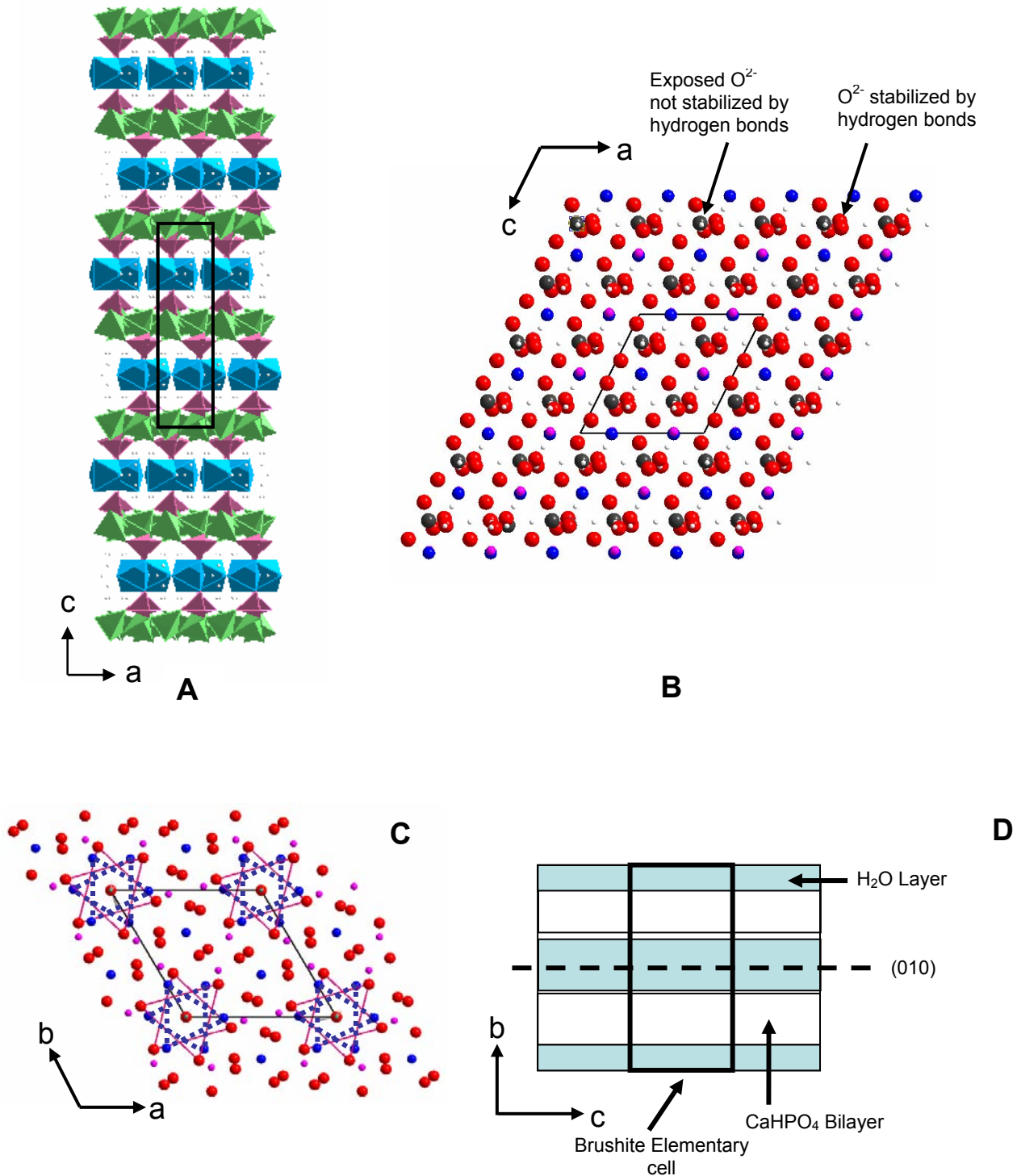


Figure 4.30: (a) Sheet arrangement of cation (Zn^{II})-centered polyhedra and phosphate tetrahedra in zinc phosphate tetrahydrate (hopeite). The framework is identical for α and β -hopeite. The connectivity is emphasized in projections along [010] (a). The (\blacklozenge) and (\blacklozenge) tetrahedra describe ZnO_4 (coordination 4) and PO_4 groups respectively. The (\blacklozenge) octahedra are relative to the ZnO_6 (coordination 6) groups. (b) Crystallographic representation of Brushite showing a similar alternate layered structure as the Hopeite (\bullet : Ca, $\color{magenta}\bullet$: P, \bullet : O, \circ : H) and emphasizing the orientation of phosphate hydrogen bonds along the c-axis, (c) Excerpt from the atomic structure of Hydroxyapatite illustrating the OH positions along the c-axis. Shown here are the columns of Ca (\bullet) and O (\bullet) involved in hydrogen bonding. (d) Schematic representation of Brushite viewed on the (001) plane, showing the water and $CaHPO_4$ bilayers along the b-axis.

Rodrigues-Clemente et al. [171] show that citrate exchanges selectively with phosphate groups at the solid-solution interface, caused by a higher affinity of citrate than phosphate species for Ca-sites on HAP surface. This adsorption may take place via a bidentate surface-chelate interaction. Nevertheless, adsorption kinetics depends not only of surface chemistry but also on surface topology. For example, albeit α - and β -hopeite have the same chemical composition and nearly the same particle size distributions, they display astonishing disparities in their electrophoretic behaviour.

Under acidic conditions, the conversion of both forms of hopeite to zinc hydrogen phosphate (ZHP) (structure similar to Brushite) is very interesting as suggested by Nriagu [172] and is marked by a positive zeta-potential, independent of pH ($\text{pH} < 5$), but below the IEP of 4.91. The isoelectric point is identical for α - and β -hopeite. ZHP acts as a protective barrier and prevents complete dissolution of the hopeite core particles, as shown in the chemical etching test, by functioning as a semi-permeable layer. At IEP, the concentration of zinc ions in equilibrium with β -hopeite is around 1 ppb and that with α -hopeite is about 0.2 ppb ($\text{p}K_s = 44$ and 48). Therefore, this solubility difference appears to provide favourable conditions for bulk precipitation of β -hopeite. In contrast surface conversion or surface precipitation is favoured in the case of α -hopeite. While both hopeite polymorphs display negative zeta potential above pH 5, the zeta-potential of α -hopeite decreases linearly with pH in a unique manner, and reaches only -3.8 mV at pH 12. In contrast, β -hopeite has already a high zeta potential up to -30 mV at pH 6.5. Above pH 7, the zeta-potential of β -hopeite also decreases linearly with pH. Many factors may influence the zeta potential, but this linear dependence on pH in basic medium may be explained in terms of dissolution-precipitation mechanism since at $\text{pH} > 6.3$ zinc hydroxide tends to form and may adsorb on hopeite surfaces [165, 173]. Furthermore, it is well known that sparingly soluble salt such as Brushite or hopeite dissolve easily at high undersaturation, under the present conditions [174]. However, this can not explain the global difference of electrophoretic behaviour of α - and β -hopeite. Ammonia and HNO_3 chemical etching experiments clearly suggest that surface potential and surface dissolution are correlated not only with the formation and propagation of etch pits as described by the "self-inhibition" model of Nancollas et al. [175], but also with the surface morphology and insofar with the overall crystal architecture. In that sense, α -hopeite possesses a three dimensional hydrogen bond network, inducing the formation of an isoenergetic layered structure (Fig. 4.30 A) with an high surface tension γ_{SL} toward H_2O and ensuring a high surface stability against dissolution [176]. This hydrogen pattern inhibits the formation of etch-pits and prevents their preferential propagation along {011}. Consequently α -hopeite display neutral or partially dissociated phosphate groups on the [011], [110] and [1 $\bar{1}$ 0] planes, as reflected by a very low negative zeta-potential above pH 5. In contrast, because of an hydrogen bonding pattern oriented along the crystallographic b -axis, β -hopeite displays under NH_4OH chemical etching a complete dissolution of all units in the

[011] planes, exposing bare phosphate groups as indicated by a strong negative zeta-potential above pH 5. The [110] and [1 $\bar{1}$ 0] planes are destabilized and etch pits can be specifically found on these planes (Fig. 4.9).

To some extent the zeta-potential curves let suggest that in basic pH, particularly above 10 while both ZPT polymorphs will dissolve, based on the DLVO theory they will adsorb mostly positively charged molecules or polymers due to their negative potentials, if one neglects first the fact that in paints polymeric dispersions are highly concentrated and secondly that no depletion effect and heterocoagulation occur [177] as shown in Fig. 4.28 B. Furthermore the combined zeta-potential measurements, conductivity and contact angle experiments give the basic understanding of ZPT surface chemistry needed to use ZPT pigments as vector of phosphate groups in corrosion science and for an improved compatibilization of the (011) surface with acrylic dispersion in paint formulation.

4.4. Conclusion

In synergy with classical methods such as XRD, DRIFT, FT-Raman and Solid State NMR, which are mainly used for the characterization of bulk properties of microcrystalline powders of zinc phosphate hydrates, scanning electron microscopy offers an in-situ analysis of the particle morphology, size distribution and aggregation phenomena, by comparison with BET solid-gas adsorption data. Targeted chemical etching experiments over the whole pH range proved to be successful in providing key information about the first stages of surface dissolution, needed to understand the mechanism of release of phosphate anions in the frame of the development of a new generation of corrosion inhibitors or in the improvement of ZPT based dental cements. α - and β -ZPT exhibit distinctive response in acidic and alkaline environments in direct correlation with their unique structural characteristics, i.e. hydrogen bonding patterns thus explaining the crystallographic controlled etch pit propagation and the coexistence of two etch pit populations. Thanks to e-beam irradiation, the first precise understanding of the surface stability of zinc phosphates was obtained. In addition, induced Brushite (calcium hydrogen phosphate dihydrate) conversion to HAP (calcium phosphate) by e-beam irradiation is reported for the first time and gives an outlook of the phase transformations (structure condensation in the most stable phase) presumably occurring during hydrothermal crystallization of metal phosphates. Complementary AFM and surface FFM experimentations pointed out the various types of surface defects (point defects, dislocations) and allow an interesting estimation of their surface density, thus offering access to a representative description of the surface topology. Using contact angle measurements, wetting phenomena were evaluated, first allowing the calculation of surface energies, and secondly providing the polar and disperse components of the surface tension following the Fowkes and Wu's approaches. The building of wetting envelope curves, in combination with zeta-potential measurements gives a discrimination criteria (regarding the chemical structure) for the selection of the adequate crystallization additives and efficient chemical modification of the crystal surface for an improved redispersability in paints and offer a starting point for further investigations of the possible polymer-crystal surface interactions, which knowledge is deeply required in polymer controlled mineralization for designing new zinc phosphate materials (with nanometric size, with incorporation of doping elements such as Na^+ , Ni^{2+} , MoO_6^{2-} , etc., and with tunable solubility).

4.5. References

- [1] G.E. Servais, L. Cartz, *J. Dent. Res.* **50** (1971) 613
- [2] M. Otsuka, S. Marunaka, Y. Matsuda, A. Ito, P. Layrolle, H. Naito, N. Ichinose, *J. Biomed. Mater. Res.* **52**(4) (2000) 819
- [3] M. Uo, G. Sjoren, A. Sund, F. Watari, M. Bergnman, U. Lerner, *Dent. Mater.* **19** (2003) 487
- [4] A. Piwowarezyk, H.C. Laue, *Oper. Dent.* **28**(5) (2003) 535
- [5] A. Ito, H. Kawamura, M. Otsuka, M. Ikeuchi, H. Ohgushi, K. Ishikawa, K. Onuma, N. Kanzaki, S. Sogo, N. Ichinose, *Mater. Sci. Eng. C –Bio. S.* **22**(1) (2002) 21
- [6] A.D. Wilson, J.W. Nicholson, *Phosphate bonded cements*, in A.D. Wilson and J.W. Nicholson Eds. *Acid-base cements: their biomedical and industrial applications*, University Press (Cambridge) (1993)
- [7] W.W. Brackett, S. Rosen, *Oper. Dent.* **19** (1994) 106
- [8] J. Li, S. Forberg, R. Söremark, *Acta. Otolol. Scand.* **52** (1994) 209
- [9] A.J. Coleman, H.H.D. Rickerby, L.R. Antonoff, *Quintessence Int.* **32**(10) (2001) 811
- [10] G.J.P. Fleming, O. Narayan, *Dent. Mater.* **19**(1) (2003) 69
- [11] M.M. Piemjai, *Int. J. Prosthodont.* **14**(5),(2001) 412
- [12] R. Nomoto, J.F. McCabe, *Dent. Mater.* **17**(1) (2001) 53
- [13] L. Herschke, J. Rottstegge, I. Lieberwirth, G. Wegner, *J. Mater. Sci.: Mater. Med.* (submitted)
- [14] A. Kalendová, P. Kalenda, *Farbe + Lacke* **109** (2003) 62
- [15] J.W. Nicholson, M.A. Amiri, *J. Mater. Sci.: Mater. Med.* **9**(10) (1998) 549
- [16] E.J. Van Miller, K.L. Donly, *Am. J. Dent.* **16**(5) (2003) 356
- [17] B. Czarnecka, H. Limanowska-Shaw, J.W. Nicholson, *J. Mater. Sci.: Mater. Med.* **14**(7) (2003) 601
- [18] M. Kruk, V. Antonchshuk, M. Jaroniec, A. Sayari, *J. Phys. Chem.* **B103**(48) (1999) 10670
- [19] A. Champion, *Raman spectroscopy of adsorbed molecules*, in *Chemistry and Physics of Solid Surfaces*, Vol. **6**, R. Vanselow and R. Howe Eds., Springer Series in Surface Sciences 5 (Heidelberg) (1986)
- [20] T. Zhu, H.Z. Yu, Y.C. Wang, Z.F. Liu, *Mol. Cryst. Liq. Cryst.* **337** (1999) 241
- [21] D.H. Kwok, A.W. Neumann, *Adv. Colloid Interfac.* **31**(3) (1999) 167
- [22] M. Matsumoto, in *Electrical Phenomena at Interfaces: Fundamentals, Measurements, and Applications*, 2nd Ed., H. Ohshima and K. Furusawa Eds., Marcel Dekker (Basel) (1998)
- [23] O.V. Yakubovich, O.V. Karmova, O.V. Dimitrova, W. Massa, *Acta. Cryst.* **C55** (1999) 151
- [24] K. Otha, M. Kikuchi, J. Tanaka, H. Eda, *Key. Eng. Mat.* **240**(2) (2003) 517
- [25] T. Nishino, M. Nagai, Z. Sakurai, et al, *J. Ceram. Soc. Jpn.* **104**(8) (1996) 729
- [26] N. Aosaka, S. Best, J. C. Knowles, W. Bonfield, *Characterization of HA precipitated from different reactants*, in J. Wilson, L. L. Hench and D. Greenspan Eds, *Bioceramics*, Proceeding of the 8th International Symposium on Ceramics in Medicine, Vol. **8** (Ponte Verda, FL), Elsevier (1995) p. 331
- [27] J. Lyklema, *The colloidal background of agglomeration*, 4th International Symposium on Agglomeration, L.G. Kuhn Ed., (Toronto, Canada) (1985) p.23
- [28] R. Hogg, *Role of colloid and interface science in agglomeration*, 5th International Symposium on Agglomeration, Brighton, UK, Institute of Chemical Engineering (Rugby, Engl.) (1989) p.483
- [29] R.J. Hunter, *Foundation of colloid science*, Oxford Science Publications (Oxford, UK) (1986), Vol. 1+ 2
- [30] L. Perez, G.H. Nancollas, *J. Cryst. Growth* **66**(2) (1984) 412
- [31] N.M. Hansen, R. Felix, S. Bisaz, H. Fleisch, *Biochim. Biophys. Acta* **451** (1976) 549
- [32] R.W. Hartel, A.D. Randolph, *AIChE J.* **32** (1986) 1136

- [33] G.H. Nancollas, J.A. Budz, *J. Dent. Res.* **69**(10) (1990) 1678
- [34] S. Brunauer, P.H. Emmet, E. Teller, *J. Am. Chem. Soc.* **60** (1938) 309
- [35] D.M. Ruthven, *Principles of adsorption and adsorption processes*, Wiley (NY) (1984)
- [36] F. Gritti, G. Guiochon, *J. Chromatogr. A* **1028** (2004) 121
- [37] R. Bown, *Physical and chemical aspects of the use of fillers in paper chemistry*, J.C. Roberts Ed., Blackie Publish. (Glasgow, UK) (1992) p. 162
- [38] A. Hina, G.H. Nancollas, M. Grynopas, *J. Cryst. Growth* **223** (2001) 213
- [39] N.H. de Leeuw, *Chem. Comm.* **17** (2001) 1646
- [40] N.H. de Leeuw, *Phys. Chem. Chem. Phys.* **4**(15) (2002) 3865
- [41] F.C. Frank, *Acta Cryst.* **4** (1951) 497
- [42] N. Cabrera, M.M. Levine, J.S. Plaskett, *Phys. Rev.* **96** (1954) 1153
- [43] N. Cabrera, M.M. Levine, *Phil. Mag.* **1** (1956) 450
- [44] W.K. Burton, N.Cabrera, F.C. Frank, *Phil. Trans. A* **243** (1951) 299
- [45] S.L. Brantley, S.R. Crane, D.A. Crerar, R. Hellmann, R. Stallard, *Dislocation etch pits in quartz, in Geochemical Processes at Mineral Surfaces*, Chapter 31, ACS Symposium series 323, E. Hayes and J.A. Davis Eds., Am. Chem. Soc. Washington, (1986)
- [46] W. Kossel, *Zur Energetik von Oberflächenvorgänge*, *Annalen der Physik* **21** (1931) 457
- [47] R.J. Mullin, M.J.L. Whiting, *Kristall + Technik* **11** (1976) 229
- [48] R.P. Winsch, J. Dunning, *J. Geophys. Res.* **90** (1985) 3649
- [49] N. Attar, L.E. Tann, D. McComb, *J. Prothet. Dent.* **89**(2) (2003) 127
- [50] S.L. Brantley, S.R. Crane, D.A. Crerar, R. Hellmann, R. Stellar, *Geochim. Cosmochim. Acta* **50**(10) (1986) 2349
- [51] S. Haussühl, M. Friedrich, *Cryst. Res. Technol.* **28**(4) (1993) 437
- [52] W.G. Johnston, *Prog. Ceram. Sci.* **2** (1962) 3
- [53] A.A Chernov, *Soviet Phys. Usp.* **4** (1961) 116
- [54] M. Ohara, C. Reid, *Modeling Crystal Growth Rates from Solutions*, Prentice-Hall, (Englewood Cliffs, NJ) (1973)
- [55] J. Nýlt, *Cell. Czech.* **46** (1981) 79
- [56] G.W. Sears, *J. Chem. Phys.* **32** (1959) 1317
- [57] I.N. McInnis, S.L. Brantley, *Chemical Geology* **105**(1-3) (1993) 31
- [58] C.I. Steefel, P. Van Cappellen, *Geochim. Cosmochim. Acta* **54** (1990) 2657
- [59] I.N. McInnis, S.L. Brantley, *Geochim. Cosmochim. Acta* **56** (1992) 1113
- [60] B.M. Marsh, *Contrib. Mineral. Petrol.* **99** (1988) 277
- [61] D.M. Kerrick, A.C. Lasaga, S.P. Raeburn, *Kinetics of heterogeneous reactions, in Contac Metamorphism*, D.M. Kerrick Ed., Mineral. Soc. Am., *Rev. Mineral.* **26** (1991) 583
- [62] K.V. Cashman, J.M. Ferry, *Contrib. Mineral. Petrol.* **99** (1988) 401
- [63] R.J. Hill, J.B. Jones, *Am. Mineralogist* **61**(9-10) (1975) 987
- [64] K. Sangwal, K. W. Benz, *Prog. Cryst. Growth and Charact.* **32** (1996) 135
- [65] J. Saison, J.J. Trillat, *Cr. Hebd. Acad. Sci.* **250**(13) (1960) 2374
- [66] F.C. Frank, *Acta Cryst.* **4** (1951) 497
- [67] N. Cabrera, M.M. Levine, J.S. Plaskett, *Phys. Rev.* **96** (1954) 1153
- [68] R. Tang, C.A. Orme, G.H. Nancollas, *J. Phys. Chem.* **B107** (2003) 10653
- [69] C. W. Wolfe, *Am. Miner.* **25**(12) (1940) 795
- [70] M. Otha, M. Tsutsumi, S. Ueno, *J. Cryst. Growth* **47** (1979) 135
- [71] M. Otha, M. Tsutsumi, *J. Cryst. Growth* **56** (1982) 652
- [72] L. Scudiero, S.C. Langford, J.T. Dickinson, *Tribol. Letters* **6** (1999) 41
- [73] K. Flade, C. Lau, M. Mertig, W. Pompe, *Chem. Mater.* **13** (2001) 3596
- [74] G.W. Johnson, *J. Appl. Phys.* **22** (1951) 797
- [75] A.D. Randolph, M.A. Larson, *Theory of Particulate Processes*, Academic Press (NY) 2nd Ed., (1988) p.369
- [76] J. Frenkel, *Z. Physik* **35** (1926) 652
- [77] W. Schottky, *Z. Phys. Chem. B* **21** (1935) 335
- [78] G. Kutsche, H. Schmalzried, *Solid State Ionics* **43** (1990) 43
- [79] D.J. Bacon, *Mater. Sci. and Technol.* Vol. **1**, R.W. Cahn, P. Haasen, E.J. Kramer Eds, Verlag Chemie (Weihnheim) (1993)

- [80] R.W. Balluffi, A.P. Sutton, *Grain Boundaries in Crystalline Solids*, Oxford Univ. Press, (Oxford, UK) (1993)
- [81] F.C. Frank, in *Growth and Perfection of Crystals*, R.H. Doremus, B.W. Roberts, D. Turnbull Eds., Wiley (NY) (1958), p.411
- [82] G. Wegner, P. Baum, M. Müller, J. Norwig, *Macromol. Symp.* **175** (2001) 349
- [83] A. Taubert, G. Glasser, D. Palms, *Langmuir* **18** (2002) 4488
- [84] M. Faatz, G. Wegner, *Adv. Mater.* **16**(12) (2004) 996
- [85] W.T.A. Harrison, *Acta Cryst.* **E57** (2001) i15
- [86] Z. Bircsak, W.T.A. Harrison, *Acta Cryst.* **E58** (2002) i44
- [87] M.J. Ostza, D.J. Odom, E.P. Douglas, L.B. Gower, *Connect. Tissue Res.* **44**, Suppl. 1 (2003) 214
- [88] W.T.A. Harrison, A.N. Sobolev, M.L.F. Phillips, *Acta Cryst.* **C57** (2001) 508
- [89] A. Taubert, G. Wegner, *J. Mater. Chem.* **12**(4) (2002) 805
- [90] E.A. Genuina, B.A. Maximov, O.K. Melnikov, *Dokl. Akad. Nauk. SSSR* **282**(2) (1985) 314
- [91] I. Fanfani, P.F. Zanazzi, A. Nunzi, *Mineral. Mag.* **38**(298) (1972) 687
- [92] J.S. Sørensen, H.E.L. Madsen, *J. Cryst. Growth* **216** (2000) 399
- [93] E.A.P. de Maeyer, R.M.H. Verbeeck, C.W.J. Vercruysse, *J. Biomed. Mater. Res.* **A52**(1) (2000) 95
- [94] J.C. Elliott, in *Structure and Chemistry of Apatites and other Calcium Orthophosphates*, Elsevier (Amsterdam) (1994)
- [95] G. Graham, P. W. Brown, *J. Cryst. Growth* **165** (1996) 106
- [96] A.S. Prosnier, N.C. Blumenthal, F. Betts, *Chemistry and structure of precipitated hydroxyl-apatites* in "Phosphate minerals", J.O. Nriagu and P.B. Moore Eds., Springer-Verlag (Berlin) (1984)
- [97] A. Nancollas, M.S. Mohan, *Arch. Oral. Biol.* **15** (1970) 731
- [98] S. Rößler, A. Sewing, M. Stölzer, R. Born, D. Scarnweber, M. Dard, H. Worch, *J. Biomed. Mater. Res* **A64**(4) (2003) 655
- [99] H. Monma, S. Ueno, Y. Tsutsumi, T. Kanazawa, *Yogyo Kyokai-Shi* **86** (1978) 590
- [100] X. Li, S. Q. Gu, E.E. Reuter, J.T. Verdeyen, S.G. Bishop, J.J. Coleman, *J. Appl. Phys.* **80** (1996) 2680
- [101] H. Monma, S. Ueno, T. Kanazawa, *J. Chem. Technol. Biotechnol.* **31** (1981) 15
- [102] Y. Matsumura, H. Kanai, J.B. Moffat, *J. Chem. Soc. Faraday Trans.* **93** (1997) 4383
- [103] H. Kanai, Y. Matsumura, J.B. Moffat, *Phos. Res. Bull.* **6** (1996) 293
- [104] D.L. Vezie, E. L. Thomas, *Polymer* **36**(9) (1995) 1761
- [105] G.P. Thomson, *Proc. Phys. Soc.* **61** (1948) 403
- [106] J.H. Van der Merwe, *Discuss. Faraday. Soc.* **5** (1949) 201
- [107] G.W. Johnson, *J. Appl. Phys.* **21** (1950) 1057
- [108] G.W. Johnson, *J. Appl. Phys.* **22** (1951) 797
- [109] H. Aoki in *Science and medical applications of hydroxyapatite*, JAAS (Tokyo) (1991) p. 46
- [110] D. Turnbull, B. Vonnegut, *Ind. Eng. Chem.* **44** (1952) 1291
- [111] W. E. Brown, J.P. Smith, J.R. Lehr, A W. Frazier, *Nature* **196** (1962) 1048
- [112] A. Bigi, E. Boanini, M. Borghi, G. Cojazzi, S. Panzavolta, N. Roveri, *J. Inorg. Biochem.* **75** (1999) 145
- [113] P.J. Koutsoukos, W. Norde, J. Lyklema, *J. Colloid. Interface Sci.* **95** (1983) 385
- [114] B.V. Derjaguin, V.M. Muller, Y.P. Toporov, *J. Colloid Interface Sci.* **73** (1980) 293
- [115] K.L. Johnson, K. Kendall, A.D. Roberts, *Proc. R. Soc. (London)* **A324** (1971) 301
- [116] V.M. Muller, V.S: Yushchenko, B.V. Derjaguin, *J. Colloid Interface Sci.* **92** (1983) 92
- [117] A. Fogden, L.R. White, *J. Colloid Interface Sci.* **138** (1990) 414
- [118] P.M. Pashley, P.M. McGuiggan, B.W. Ninham, D.F. Evans, *Science* **229** (1985) 1088
- [119] W.A. Zisman, *Contact angle, wettability and adhesion* in Advances in Chemistry series, Vol. **43**, Am. Chem. Soc. (Washington) (1964)
- [120] F.M. Fowkes, *Ind. Eng. Chem.* **12** (1964) 40
- [121] J.K. Spelt, D. Li, *The equation of state approach in interfacial tensions*, in A.W. Neumann, J.K. Spelt Eds., Applied Surface Thermodynamics, Marcel Dekker (NY) (1996) p. 239

- [122] C.J. van Oss, M.K. Chaudhury, R.J. Good, *Chem. Revs.* **88** (1988) 927
- [123] R.J. Good, C.J. van Oss, *The modern theory of contact angles and the hydrogen bond components of surface energies*, in *Modern Approaches to Wettability: Theory and Applications*, M. Schrader and G. Loeb Eds., Plenum Press (NY) (1992) p. 1
- [124] D.W. Fuerstenau, M.C. Williams, *Colloid Surf.* **22** (1987) 87
- [125] R. Guermeur, F. Biquard, C. Jacolin, *J. Chem. Phys.* **82** (1985) 2040
- [126] E. Moy, A.W. Neumann, *Theoretical approaches for estimating solid-liquid interfacial tension*, in A.W. Neumann, J.K. Spelt Eds., *Applied Surface Thermodynamics*, Marcel Dekker (NY) (1996) p. 333
- [127] A.E. van Giessen, D.J. Bukman, B. Widom, *J. Colloid Interface Sci.* **192** (1997) 257
- [128] D.E. Sullivan, *J. Phys. Chem.* **74** (1981) 2604
- [129] D.V. Matyushov, R. Schmidt, *J. Chem. Phys.* **104** (1996) 8627
- [130] T. Young, *Philos. Trans. R. Soc. (London)* **95** (1805) 65
- [131] R.J. Good, Adsorption at interfaces, K.L. Mittal Ed., ACS Symposium Series, Vol. **8** (1975)
- [132] D.Y. Kwok, A.W. Neumann, *Adv. Colloid Interface Sci.* **81** (1999) 167
- [133] D.K. Owens, R.C. Wendt, *J. Appl. Polym. Sci.* **13** (1969) 1741
- [134] D.H. Kaelble, *J. Adhesion* **2** (1970) 66
- [135] C. Della Volpe, D. Maniglio, M. Brugnara, S. Siboni, M. Marra, *J. Colloid Interface Sci.* **271** (2004) 434
- [136] S. Wu, *J. Adhesion* **5** (1973) 39
- [137] D.Y. Kwok, Y. Lee, A.W. Neumann, *Langmuir* **14** (1998) 2548
- [138] G. Antonow, *J. Chim. Phys.* **5** (1907) 372
- [139] D. Berthelot, *Comp. Rend.* **16** (1898) 1857
- [140] F. London, *Z. Phys. Chem. B11* (1930) 222
- [141] D. Li. A. W. Neumann, *J. Colloid Interface Sci.* **137** (1990) 304
- [142] E. W. Swokowski, *Calculus with analytical geometry*, 2nd Ed., Prindle, Weber & Schmidt, Boston (1979)
- [143] R. Feynman, *Lectures of Physics*, Vol. **2**, Addison Wesley Ed. (Reading, UK) (1965) 41
- [144] F. Brochard-Wyart, P.G. De Gennes, *Langmuir* **8** (1992) 3033
- [145] W.A. Zisman, *Contact Angle, Wettability and Adhesion*, R.F. Gould Ed., *Adv. Chem. Ser.* **43**, ACS (Washington), (1964), p.1
- [146] S. Siboni, C. Della Volpe, D. Maniglio, M. Brugnara, *J. Colloid Interface Sci.* **271** (2004) 454
- [147] P. Baum, *PhD Thesis*, Univ. Mainz (Germany) (2000)
- [148] J.M. Douillard, J. Zajac, H. Landrini, F. Clauss, *J. Colloid. Interface Sci.* **255** (2002) 341
- [149] G. Jura, W.D. Harkins, *J. Am. Chem. Soc.* **66** (1944) 1362
- [150] S. Partyka, F. Rouquerol, J. Rouquerol, *J. Colloid Interface Sci.* **68** (1979) 30
- [151] S. Wu, *J. Phys. Chem.* **74** (1970) 632
- [152] V. Médout-Marère, *J. Colloid Interface Sci.* **228**(2) (2000) 434
- [153] M. Von Smoluchowski, *Z. Phys. Chem.* **92** (1918) 129
- [154] H. Ohshima, *J. Colloid Interface Sci.* **168** (1994) 269
- [155] H. Ohshima, *Colloid Surf. A103* (1995) 249
- [156] J.H. Kennedy, A. Foissy, *J. Am. Ceram. Soc.* **60**(1-2) (1977) 33
- [157] Y. Zhang, C.J. Brinker, R.M. Brooks, *Mater. Res. Soc. Symp. Proc.* **271** (1992) 465
- [158] R. J. Hunter, in *Zeta potential in Colloid Science: Principles and Applications*, Academic Press (NY) (1981) p. 11
- [159] K. Yamashita, M. Matsuda, Y. Inada, T. Umegaki, M. Ito, T. Okura, *J. Am. Ceram. Soc.* **80** (1997) 1907
- [160] R.W. O'Brien, *J. Fluid Mech.* **190** (1988) 71
- [161] B.V. Derjaguin, I. Landau, *Acta Physiochim. USSR* **14** (1941) 633
- [162] E.J.W. Verwey, J.Th.G. Overbeek, *Theory of the Stability of Lyophobic Colloids*, Elsevier, Amsterdam (1948)
- [163] C.S. Mangelsdorf, L.R. White, *J. Chem. Soc., Faraday Trans.* **88** (1992) 3567
- [164] C.L. Howie-Meyers, D.L. Elliott, K.P. Ananthapadmanabhan, *Langmuir* **10** (1994) 320
- [165] S.A. Leach, *Arch. Oral. Biol.* **3** (1969) 48

- [166] L.C. Bell, A.M. Posner, J.C.P. Quirk, *J. Colloids. Interf. Sci.* **42**(2) (1973) 250
- [167] J. Ma, C.H. Lang, L.B. Kong, C. Wang, *J. Mater. Sci.: Mater. Med.* **14** (2003) 797
- [168] P.W. Brown, *J. Am. Ceram. Soc.* **75** (1992) 17
- [169] P. Somasundaran, J.O. Amankonah, K.P. Ananthapadmabhan, *Colloids Surf.* **15** (1985) 309
- [170] G. Vereecke, J. Lemaitre, *J. Cryst. Growth* **104** (1990) 820
- [171] A. López-Macipe, J. Gómez-Morales, R. Rodríguez-Clemente, *J. Colloids Interf. Sci.* **200** (1998) 114
- [172] J.O. Nriagu, *Geochim. & Cosmochim. Acta* **37** (1973) 2357
- [173] Solubility Data Series, edited by IUPAC, (Pergamon) (Oxford, UK) (1979) p. 250
- [174] R. Tang, C.A. Orme, G.H. Nancollas, *J. Phys. Chem.* **B107** (2003) 10653
- [175] R. Tang, C.A. Orme, G.H. Nancollas, *J. Am. Chem. Soc.* **123** (2001) 5437
- [176] A.E. Nielsen, *Pure Appl. Chem.* **53** (1981) 2025
- [177] P.R. Sperry, *J. Colloid Interface Sci.* **99** (1984) 97

5. Polymer controlled mineralization of zinc phosphate hydrates

“Truth is ever be found in the simplicity, and not in the multiplicity and confusion of things”,
Sir Isaac Newton (1642-1727)

5.1. Introduction

Nature is adept at controlling mineralization processes. Many living organisms synthesize simultaneously amorphous and polycrystalline organic/inorganic composite materials for the generation of protective structures, e.g. mollusc shells and coral skeletons [1]. They exert exceptional control over the gross morphology, physical properties and nanoscale organization of these materials, often creating shapes that defy the strict geometrical restrictions of the 230 classical space groups [2-3]. In recent years much interest in biomineralization has been generated due to the perspectives of unique combination of strength and elasticity, the resistance both to fracture and to drastic environmental conditions, and other desirable properties of biomaterials [4-5]. Additionally, the participation of biomolecules in the nucleation and growth of crystals raises interesting questions with respect to molecular recognition [6-7]. Most notably, the proteins involved in directing the shape of these biomaterials have often evolved to recognize and bind selectively to one or more faces of the growing crystal. Because of clear potential applications such as bone substitutes for hydroxyapatitic materials [8-10] and the opportunity to unravel this fascinating process (e.g. stabilization of intermediary phases: amorphous calcium carbonate (ACC) [11-14], amorphous calcium phosphate or calcium hydrogen phosphate dihydrate (brushite) [15-16]), research into the design of supramolecular, organic assemblies to assist the growth “in-vitro” of inorganic crystals has increased significantly in the last ten years [17-20].

Inspired from biomineralization, polymer-mediated mineralization of inorganic materials has been the subject of intense research, primarily for the same reasons as above-mentioned. Many authors have thoroughly investigated the influence of synthetic polymers [21-24] and biopolymers [25-27], supramolecular assemblies [28-32], ultrathin films [33-34], self-assembled films [35-36], crystal-

imprinted polymer surfaces [37], gels [38-39], polymer matrixes [40], foam lamellae [41] and inverse emulsions (i.e. nanoreactors) [42-44] on the mineralization process. However these studies are mainly restricted to simple model systems such as ZnO or BaTiO₃ mainly due to the presence of a single crystal phase [45]. Recently such studies were extended first to semi-conducting nanopowders and finally to the complex calcium carbonate and calcium phosphate systems (i.e. existence of three or more crystallizing phases) [46-51]. Notably, several descriptive studies have clearly shown that polymeric additives control not only the particle shape (e.g. morphology and surface topology), size and size distribution [21-22,26,46,52-58] but also the crystal phase [36,52,59-60] and the crystal state of hydration [61] and even the crystal chirality (introduced by the organic host) [62-64]. Hence, precipitation reactions from aqueous media in particular are a versatile and non-polluting method for the formation of monodisperse and uniform inorganic powders, and highly ordered composite architectures in the nanometer up to the micron scale. In addition to the chemical nature of the polymeric additive of mineralization, numerous “physical” parameters such as temperature, ionic strength and the pH of the reaction solution or the stirring process itself drastically influence the crystallization process and thus the resulting powder substances [65].

Although immense progress has been made in understanding the role of the polymeric additives on nucleation and crystal growth during precipitation, and aging process (e.g. aggregation, phase transformation) especially in dependence of the polymer composition [66-67] and concentration, few studies have carefully addressed the question of the precise crystal growth mechanisms [68-73] on the basis other than systematically investigating morphologies of the final products. In this line, a new class of functional polymers, the so-called double-hydrophilic block copolymers (polyelectrolytic DHBCs) has been recently developed for mineralization purpose [74-76]. These polymers consist of one charged and hydrophilic (e.g. poly(meth)acrylic acid) block designed to interact strongly with the appropriate inorganic materials and surfaces, and another hydrophilic block that does not interact (or only weakly and mainly promotes steric stabilization or solubilisation in water). The potential of poly(meth)acrylics and poly(meth)acrylates in nucleation and growth processes was identified rather early by the pioneering work of Henglein et al. [77] Owing to the separation of the solvating moieties, DHBCs are “improved or optimized versions” of the polyacrylics and turned out to be incredibly effective in the crystallization control for zinc oxide [67] and calcium carbonate [78], where tuned morphologies varying from rods, tubes, wires, cube, spheres, drumlike, to donuts and pancakes were easily achieved [79-80].

The present chapter offers primarily a new approach to polymer-controlled mineralization and crystal engineering [81-82] in using latex additives (i.e. structure controlling agents) for the first time. Especially, it seeks to determine how new crystallization additives, among them are a multitude of

chemically modified carboxylated-PS based latex beads [83-87] and polyester/polyurea/polyamide (e.g. PAMAM) based dendrimers [87-88], efficiently affect the particle formation and growth over time of a more complicated system than metal oxides (e.g. ZnO, α -Fe₂O₃ [38,89]) and metal carbonates (e.g. CaCO₃): the ZPT system (c.f. Chapter 2). Carboxylated-PS based latexes may represent a promising new generation of crystallization additives with many advantages, e.g. being well-defined, displaying a rigid and hydrophobic core (i.e. the entangled PS core has a transition temperature significantly (i.e. by 10-20°C) above the temperature range of crystallization (20°C-90°C)) and a flexible hydrophilic corona of known chemical composition (i.e. containing non charged polar PEO-based surfactants and positively or negatively charged acrylic-based polymers) [90-91] that may be stereoselective [92]. Such templates display also striking similarities with P(S-*b*-MAA) and P(EO-*b*-MAA) DHBCs [93] used in model crystallization systems. In addition, these latexes are conveniently produced by one-step synthesis, i.e. direct miniemulsion [94-97], which is a quite reliable process (e.g. high reproducibility [98], product stable over months [99-100], that delivers monodisperse structured particles [101] of adjustable size (range 50 nm - 1 μ m), composition (choice of the hydrophilic comonomer, especially on acrylics basis) and surface charge density. Furthermore, such latexes are obtained on industrial large scale and are currently used as the most promising substitute primer (waterborne) to more classical but toxic organic anticorrosive coatings.

Moreover, understanding the molecular and supramolecular processes that lead to a specific phosphate containing product is of paramount importance for enabling the design and fabrication on large scale of tailored materials, such as *basic* zinc phosphate based corrosion inhibitors (i.e. NaZnPO₄·1H₂O, Na₂Zn(PO₄)(OH)·2H₂O). Hence in a first step, the first four chapters of this thesis were realized in order to shed some necessary light on the reactivity of ZPT crystals at surfaces and interfaces (Chapter 4), depending on their polymorphism (chapter 2) and respective state of hydration (Chapter 3). In this study, the systematic investigation of the parameters governing an efficient latex-controlled mineralization is expected to offer key information regarding ZPT crystallization mechanism. Indeed, the synthesis of nanocrystalline ZPT powders is required to achieve first an improved pigment dispersion in the primer (e.g. avoidance of sedimentation on storage in a coating formulation and elimination of coating inhomogeneities caused by segregation on film application, i.e. primer compatibilization) and secondly an outstanding controlled release of phosphate anions (i.e. thanks to an increase of the specific surface) for optimal protection of metallic surfaces against corrosion.

Besides, Sarig et al. [102] pioneeringly reviewed the basic interaction mechanisms between a polymeric electrolyte and sparingly soluble salts, mineral class in which zinc phosphate hydrate is represented (Chapter 6). More recently Nancollas et al. [103] proposed various theoretical models

of interactions between DHBCs and calcium phosphate hydrates, on basis of a standard “train-loop” adsorbing structure (face-down model, brush configuration model, flat extended configuration model and multilayer adsorption model). However such configuration models only emphasize the primary role of DHBCs on crystal growth, disregarding completely the nucleation step. Therefore motivated by the general principle that latex particles may also be either a nucleation retardant (e.g. acting as Zn^{2+} reservoir by cation complexation and entrapment in the hydrophilic, negatively charged latex corona) or a nucleation promoter (e.g. nuclei stabilization of a kinetically favoured *metastable zeolitic* $NaZnPO_4 \cdot 1H_2O$ phase), tentative models, that are consistent with the characterization of the nascent solid phases (e.g. competitive complexation of Zn^{2+} and Na^+ followed by incorporation of Na^+ in the ZP crystal structure [104]) and the selective incorporation of fluorescent labelled latexes [105-106] in the growing crystal structures, will be proposed and then tested.

5.2. Selected crystallization additives

5.2.1. Latexes obtained by miniemulsion polymerization

Although there are a few overviews in the field of miniemulsion [107-108], the aim of this paragraph is to grab the exploding understanding and experimental developments, which occurred especially in the last years, to allow a current assessment of the possibility of radical miniemulsion polymerization to produce well-defined hard-soft core-shell (spherical) additives for mineralization purpose.

Some important prerequisites exist to the use of synthetic latexes as structure directing agent in the mineralization of zinc phosphate hydrate, regarding either their chemical nature or the synthesis route. First, it should stay intact (i.e. in a hard sphere form) during the precipitation reaction that occurs in aqueous medium at 90°C, in the same conditions as for the obtaining of chemically pure polymorphs of zinc phosphate tetrahydrates (c.f. Chapter 2) in order to efficiently influence the mineralization process. This means that the glass transition temperature (T_g) of the polymeric latex, while being reduced by the presence of water of hydration in the latex shell [109], should be higher than the crystallization temperature. Therefore, polystyrene based latexes were selected in favour of latexes displaying polymethylmethacrylate (PMMA) cores [110]. Secondly, Palms [111] gives clear indication that in the ZnO system a satisfying control of mineralization process could only be achieved if the effective specific surface of the latex is in the range $1-10 \text{ m}^2 \cdot \text{g}^{-1}$, i.e. if the latex diameter locates in the 50-500 nm range, which corresponds fortunately to the range of latex mean diameter achieved by miniemulsion polymerization.

5.2.1.1. Principle of miniemulsion polymerization

A system where small droplets with high stability in a continuous phase are created using high shear (e.g. ultrasonication (US), high pressure homogenization) [112-113] is classically called “a miniemulsion” [114]. The stability of a miniemulsion system is basically dictated by (i) suppression of Ostwald ripening (τ_1 mechanism) achieved by the use of an hydrophobe, and (ii) minimizing coalescence (τ_2 mechanism) enabled by a sufficient surface coverage by surfactants. The small droplets can be hardened either by subsequent radical polymerization or by decreasing the temperature (if the dispersed phase is a low temperature melting material). For a typical oil-in-water miniemulsion, an oil (styrene), a hydrophobic agent (or several), an emulsifier (polar / charged or not), and water are homogenized by high shear (ultrasound - US) to obtain homogenous and monodisperse droplets in the widely accepted range 50 nm - 500 nm [102,158], as shown in Figure 5.1.

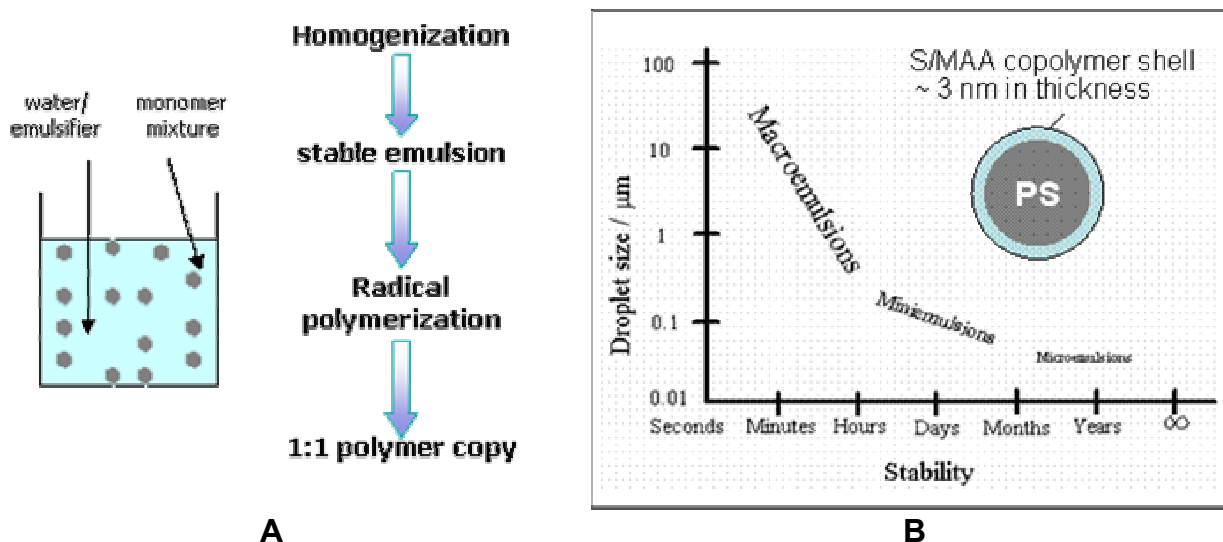


Figure 5.1: Schematic representation of (A) the miniemulsification process and (B) the miniemulsion strategy for the obtention of monodisperse lattices, suitable as mineralization templates.

5.2.1.2. Choice of the parameters of miniemulsion polymerization

In order to prevent the destabilization and breaking of the miniemulsion, the use of a surfactant is required. Stabilization can be obtained electrostatically or sterically. Landfester examined the nature and efficacy of the surfactant on the latex size and size distribution and long-term emulsion stability [91]. Presently, cationic (e.g. cetyl trimethylammonium bromide or CTAB) [116] and anionic (e.g. sodium dodecyl sulphate or SDS) surfactants are disregarded since they may introduce a chemical functionalization of the latex corona along with surface charges, other than those introduced by the use of a comonomer (e.g. acrylic acid). Therefore, a nonionic stabilizer such as a polyethylene

oxide derivate (i.e. Lutensol AT50, C₁₆/C₁₈-EO₅₀) or alternatively a polyvinylpyrrolidone (PVP) derivate was selected. Landfester also found a simple linear relation between the AT50 concentration S (i.e. S : surfactant to monomer ratio) and the final latex size [86].

Furthermore, by using hydrophobes for the preparation of miniemulsions, the stability of the emulsion can be significantly enhanced. Hydrophobes, also sometimes called a co-surfactants, suppress efficiently Ostwald ripening (i.e. monomer diffusion from small droplets to larger ones) by creating an osmotic pressure in each oil droplet. The most important requirement of the hydrophobe is its low water solubility. Landfester et al. [99,112] have investigated the chemical nature of the hydrophobic additive in the miniemulsification process. Consequently, hexadecane was selected for (i) its liquid form that allows a precise control of the added amount in the dispersed phase, (ii) its "neutral" or restricted effect as oligomeric plasticizer compared to silane, siloxane, crown ethers, alkyl mercaptans and cetylalcohol, since it remains in the final polymer particle, (iii) its compatibility with the dispersed phase and other substances (e.g. pyrene, pentane or octane [117]) that may be encapsulated in the latex particle.

A radical polymerization strategy was chosen based on the easy preparation of reproducible latexes on large scale without deterioration of the design of the carboxylated latex corona. Hence, Suzuki et al. [118] compared various radical initiators, either oil or water soluble. Thus, V59 (2,2'-azobis(i2-methyl-butyrionitrile) was selected as oil-soluble radical initiator since it presents the advantage of exhibiting a very low water solubility at 0.6 wt% and very high partition coefficient λ between the monomer phase (styrene) and the continuous phase (water), compared to AIBN (20 times higher) while offering the same efficiency and similar initiation constant (k_d) at ambient temperature.

Moreover, the chemical functionalization and the stability of latexes can be improved by adding small amount (i.e. maximum 6 wt% in respect to the oil phase) of acrylic acid (AA) to the recipe of a polystyrene (PS) emulsion polymerization reaction [119-120]. Carboxylic acid groups on the particle surface enhance the electrostatic repulsion between particles [121]. Slawinski et al. [122] studied the incorporation of AA in PS latexes as a function of pH and the addition moment for an emulsion polymerization initiated in the organic phase. They confirmed that AA is best incorporated at low pH when all carboxylic groups are protonated, minimizing the electrostatic effects, which prevent the effective entry of AA containing oligomer radicals and AA monomer molecules in the latex core [123-125]. Indeed, Slawinski et al. found that an addition of AA at styrene conversion above 0.5 had the advantage that most of the incorporated AA is located at the particle surface. Above styrene conversion of 0.5, the polymerization continues mainly inside the swollen particles and the particle diameter does not increase much [126]. Addition of AA at even higher conversions bears the risk that much AA remains in the water phase, forming water soluble chains, which may induce

flocculation at high pH or bridging at low pH [127-128] and more dramatically influence ZPO mineralization since beside the employed latex additives it is known to be a structure directing agent. In order to avoid such difficulties AA oligomeric radicals were extracted from the continuous phase and grafted on the latex corona by adding aliquots (10wt% of the organic initiator concentration) of water soluble initiator (e.g. ammonium persulfate, APO) at styrene conversion above 0.75 and increasing the polymerization temperature from 70°C (Landfester process) to 85°C. The grafting efficiency was twice evaluated above 95% by NMR after extraction in ethanol on the functionalized PS bead itself and on the unreacted oligomeric traces of acrylic acid in the disperse phase [129].

5.2.1.3. Standard synthesis of PS-g-PAA latexes by radical (direct) one-step miniemulsion polymerization

Following the composition given in Table 5.1, a standard latex (one-step) synthesis is obtained by adding an oil phase to a continuous phase after previous homogeneization.

Dispersed (oil) phase	Amount
<i>Styrene</i>	5.760 g
<i>Acrylic acid</i>	240 mg
<i>Hexadecane (Hydrophobe)</i>	250 mg
<i>V59 (Initiator)</i>	130 mg
Continuous phase	Amount
<i>Water (MilliQ)</i>	24 g
<i>AT50 (surfactant)</i>	1.5 g

Table 5.1: Standard formulation of P(S-g-AA) latex

It is worth mentioning that the stability of the resulting miniemulsion depends strongly on the degree of dispersion and the reaching of a steady state depends on the total shear applied to the system, i.e. the duration and the intensity of ultrasonication. Therefore after intense stirring (1h at 1200 rpm), as suggested by Landfester [130], the pre-emulsion is exposed to 5 min ultrasonication at 70% intensity (power 250 W) while kept at around 10°C by immersion in a cooling bath. After introduction of the miniemulsion in a two-necked flask or emulsion reactor, polymerization was conducted by gentle stirring at 70°C for 6h to 10h under reflux and inert gas atmosphere. After completion of the polymerization, the latex was purified by (dia-)filtration. By variation of the styrene to acrylic acid ratio, latexes with different surface charge density can be synthesized.

5.2.1.4. Standard synthesis of core-shell latexes based on PS-g-PNaSS copolymer by radical (direct) two-step miniemulsion polymerization

Sulfonate (e.g. Styrylsulfonate sodium salt, NaSS), phosphate (vinylphosphonic acid VPO), or alcoholate functionalized (vinylphenol, VPOH) latexes may successfully be synthesized in following a two stage “shot-growth” procedure developed by De las Niervas [131], El-Asser and al. [132-133]. Overall, this method offers the possibility to achieve a broad range of chemical functionalization of the latex surface without limiting the accessible particle size range, as found with the procedure described in § 5.2.1.3. Also a better defined core-shell structure may be obtained. Besides, positively charged latexes are potentially interesting in ZPO mineralization for their ability to coordinate and release phosphate ions through pH modulation. Such latexes can be obtained in the second-step of the reaction by copolymerization of styrene with 1-vinylbenzyl-6-trimethylammonium chloride salt (VBTMC), 2-(methacryloyloxy) trimethylammonium chloride salt (MATMAC) or cationic polyacrylamide [134].

5.2.1.5. Characterization of model latexes

Following the recommendations edited by German and al. [135] the emulsions were characterized by different means either morphologically or by their solid content on drying under vacuum as well as their surface charge density as well as the polymer architecture itself. From a proper latex architecture depends its efficiency as structure controlling agent in hydrothermal mineralization. Therefore, the morphology of the latex particles was confirmed as spherical by SEM (i.e. latex deposition of a silicium wafer) and dynamic light scattering at 90° (e.g. DLS, Mastersizer and Zetasizer series, Malvern Inst.). The polymer architecture along with the efficiency of the polymerization process (i.e. degree of conversion at 70°C) were thoroughly investigated by ¹H NMR and MALDI-Tof after polymer recovery by lyophilization and dissolution in chloroform. The dispersion medium (aqueous phase) was equally analysed for traces of ungrafted acrylic oligomers, indicating the efficiency of post-polymerization initiated in the aqueous phase in adding aliquots of a 10⁻³ mol.L⁻¹ K₂S₂O₈ solution. The effective polymer composition and PAA grafting were checked by ¹H NMR. In addition, the surface charge density σ in the different accessible layers of the latex corona and corona functionalization were evaluated thanks to total titration with 10⁻² mol.L⁻¹ NaOH solution, polyelectrolyte titration with 10⁻⁴ mol.L⁻¹ polyDADMAC, and indirectly by zetapotential measurements in reference to Oshima [136] and van Leeuwen's [137] studies of polymer colloids. As suggested by Russel et al. [138], the charge on the latex particle can be determined by measuring the concentration C_i of each monovalent counterion of type i in a deionized latex sample (Kozerny-Carman capillary model):

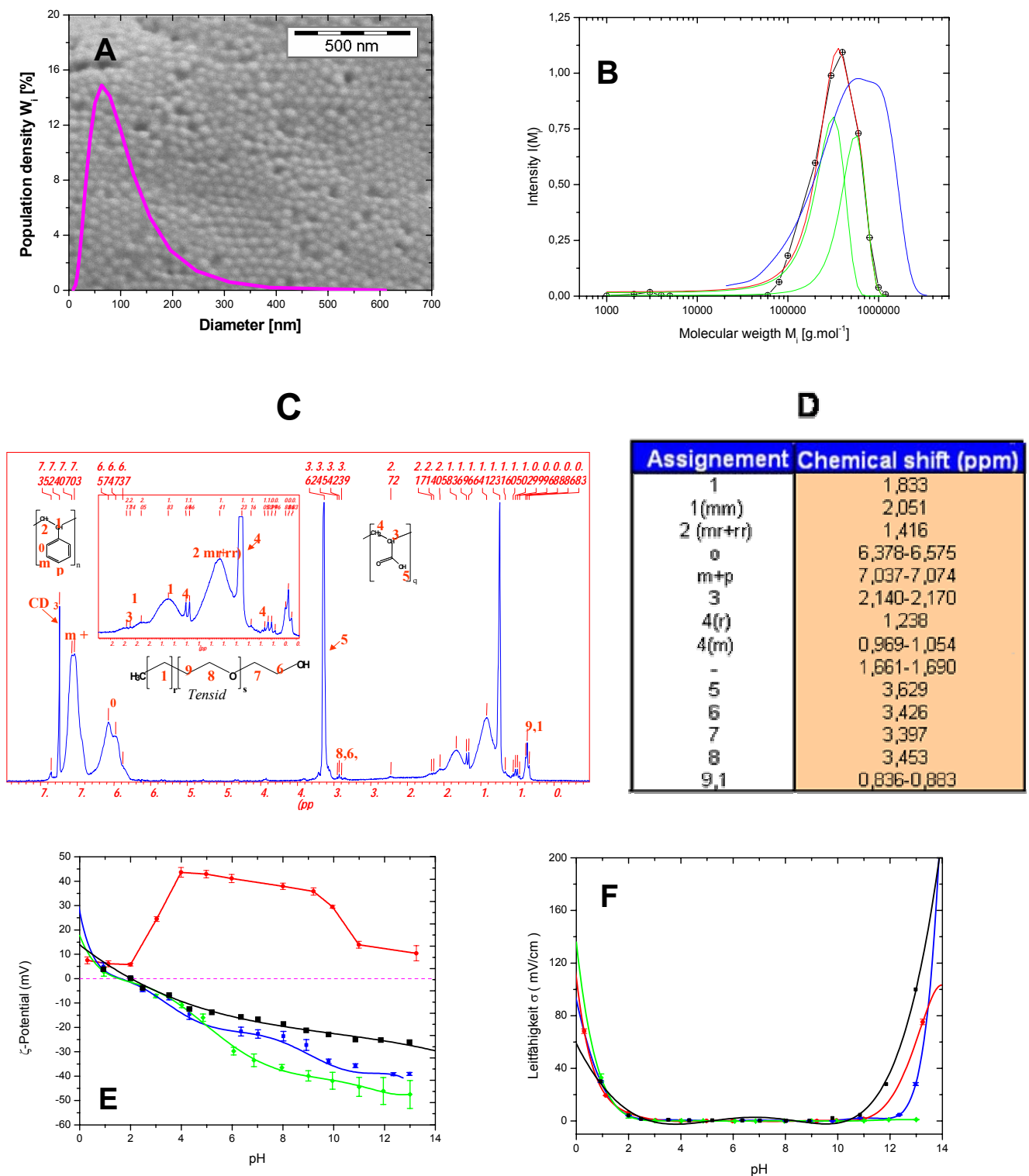


Figure 5.2: Standard characterization of latex based on *P(S-g-MAA)* employed in evaluation in controlled mineralization of ZPO by fast screening process: (A) SEM combined with DLS at 90° for latex size determination, (B) copolymer molecular weight determination by GPC (◆) and DLS (◆, 90°), (C) attributed ¹H NMR spectrum, allowing the determination of the latex corona functionalization, (E) Zeta-potential curves and (F) corresponding conductivity for four different latex functionalization: (◆) L-(CH₃)₃N⁺ Cl⁻, (◆) L-COOH, (◆) L-(COOH-CH₂-COOH), (◆) L-PO₄H₂.

$$\sigma = Fa \sum_i C_i (1 - \phi) / 3\phi \quad (5.1)$$

where F is the Faraday's constant, a is the latex particle radius, and ϕ (also denominated $D(1,0)$) is the measured particle volume fraction (determined from solid content value). Since zeta potential is related to the surface charge density, its measurement reflects to some extent the affinity of the latex for metal M^{2+} counterions. A systematic characterization is illustrated in Fig. 5.2 for a P(S-g-MAA) based latex.

Furthermore, Table 5.2 summarizes the generic physical and chemical properties needed for an efficient ZPO mineralization with latexes of different surface functionalities.

Latex N ^o	f ^a [wt%]	D(1,0) ^b [nm]	PDI(D) ^c	ζ-potential [mV]	Z ^d [function/particle]	σ ^e [μC.m ⁻²]
A ^g	26.14	76.3	0.089	-15.4	82	-7.16
B ^g	25.22	65.7	0.104	-18.1	45	-5.28
C ^g	26.20	92.1	0.063	-17.2	123	-7.41
D ^g	21.14	84.1	0.096	-8.2	66	-4.73
E ^g	17.18	81.1	0.112	-32.4	49	-3.83
F ^g	24.94	212.4	0.354	-18.3	129	-1.43
G ^g	19.20	94.1	0.154	-4.3	93	-14.34
H ^g	21.16	79.9	0.331	-	127	-
I ^g	10.84	31.1	0.088	-19.1	4	-2.11
J ^g	31.14	257.1	0.014	-38.1	1087	-8.39
K ^g	20.25	202.1	0.039	-28.6	569	-7.11
L ^g	21.59	152.9	0.064	-54.7	348	-7.59
M ^g	25.56	101.9	0.143	-105.9	66	-3.15
N ^f	23.57	80.1	0.078	+24.2	51	+4.01

Table 5.2: Summary of the physical and chemical properties of various functionalized latexes used as templates in ZPO mineralization.

- (a) f : solid content of the latex sample
- (b) D(1,0) : statistical latex diameter determined by DLS
- (c) PDI(D): associated polydispersity
- (d) Z : number of chemical functions bered by a latex particle.; mean value obtained from ¹H NMR and polytitration with NaOH and poly(DADMAC).
- (e) σ : average surface charge density of the latex evaluated from Z values
- (f) Latex used in § 5.3.5
- (g) Latexes uses in § 5.5.4

5.2.2. Dendrimers

Various dendrimers based on polyesteramide, polyurethans and polyurea, kindly supplied by the BASF AG were used for controlled mineralization of basic zinc phosphate hydrates (Fig. 5.3 A), and no special efforts were made to characterize them thoroughly. Nevertheless, as shown in Fig. 5.3 MALDI-tof and ¹H NMR were used to evaluate the approximate molecular weight and the terminal

functionality of the different samples. While the dendrimer reported in § 5.4 has an estimated molecular weight around $1780 \text{ g}\cdot\text{mol}^{-1}$ and a repeating unit of $81 \text{ g}\cdot\text{mol}\cdot\text{L}^{-1}$ (attributed to 1st dendrimer generation), it exhibits a broad polydispersity (i.e. large NMR peaks) and terminal alcohol groups, detected by FT-IR spectroscopy.

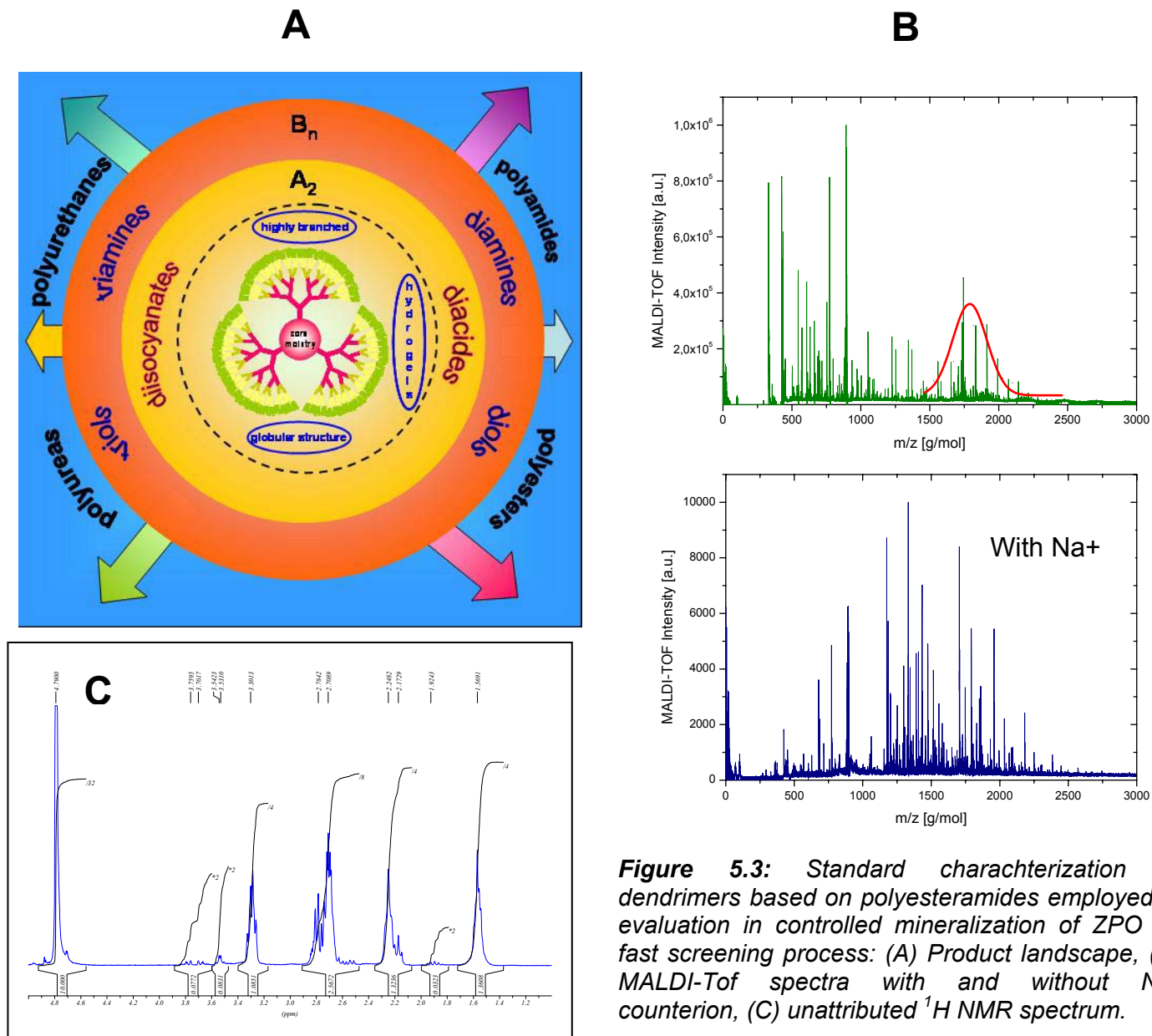


Figure 5.3: Standard characterization of dendrimers based on polyesteramides employed in evaluation in controlled mineralization of ZPO by fast screening process: (A) Product landscape, (B) MALDI-ToF spectra with and without Na^+ counterion, (C) unattributed ^1H NMR spectrum.

5.3. Polymer (Latex) controlled mineralization of zinc phosphate hydrates: 1st generation of basic ZPO

5.3.1. Effect of the addition of a carboxylated latex on ZPT crystallization

In a first approach, the effect of the latex composition (refer to Tables 5.1 and 5.2), i.e. of each of its component on the crystal phase and morphology has been systematically and qualitatively studied

by SEM, as depicted in Figure 5.4 and compared to chemically similar DHBCs structures (taken as references, Pluronic PE 8600 [139], EA3007). In order to obtain a direct comparison with the synthesis of α -ZPT, all mineralization experiments were conducted in similar conditions as for α -ZPT powders (Chapter 2), i.e. at 90°C and neutral pH (e.g. pH adjusted with 4 mol.L⁻¹ NaOH).

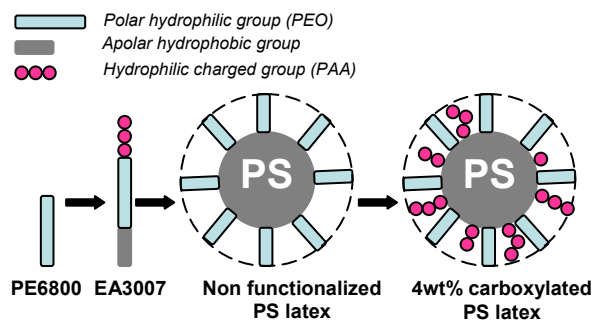


Figure 5.4: schematic representation of the different components that may constitute the corona (dashed line) of a carboxylated latex used as template agent in the mineralization of ZPT. These four polymeric additives correspond to those used in Fig. 5.10.

Without addition of any mineralization additive, Fig. 5.5 A shows the formation by “bulk” precipitation of characteristic platelets of crystalline α -ZPT of 16 x 2 μm^2 averaged dimension.

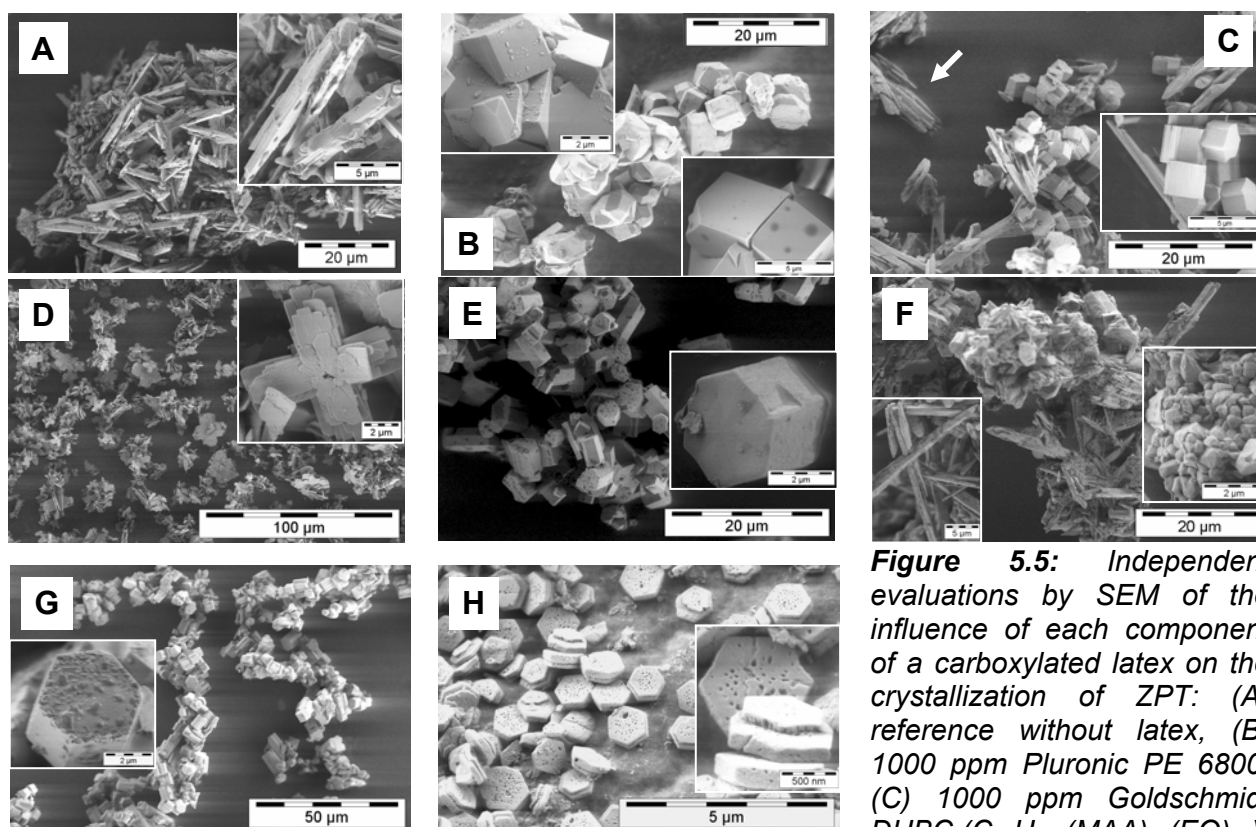


Figure 5.5: Independent evaluations by SEM of the influence of each component of a carboxylated latex on the crystallization of ZPT: (A) reference without latex, (B) 1000 ppm Pluronic PE 6800, (C) 1000 ppm Goldschmidt DHBC ($\text{C}_{12}\text{H}_{25}-(\text{MAA})_8-(\text{EO})_{68}$)

EA3007, (D) 700 ppm unfunctionalized (PS-PEO) latex, (E) 700 ppm of a 4 wt% carboxylated (PS-g-PAA) latex, (F) 700 ppm supernatant of the 4 wt% carboxylated (PS-g-PAA) latex, (G) 700 ppm of a latex (di)functionalized with 4 wt% maleic acid (Ps-g-PMA), (H) comparison to a test crystallization of ZnO with 700 ppm of a 4 wt% carboxylated (PS-g-PAA) latex.

In contrast the addition of 700 ppm of a carboxylated PS based latex (80 nm diameter) functionalized by 4 wt% acrylic acid induces after 3 hours mineralization the formation of recognizable monodisperse hexagonal crystals (Fig. 5.5 E), most probably of sodium zinc phosphate (refer to § 5.3.2). Consequently, one may conclude that the use of a acrylic functionalized latex as structure controlling agent implies a change of mineral phase, from α - $\text{Zn}_3(\text{PO}_4)_2 \cdot 4\text{H}_2\text{O}$ to $\text{NaZnPO}_4 \cdot 1\text{H}_2\text{O}$. However, since the synthesis procedure (§ 5.2.1.3) may result in the formation of a hairy layer of acrylic acid or oligomer [140] grafted onto the latex particle, this phase change may originate from the effects of some acrylic oligomers contained in the aqueous phase of the latex. Therefore, the influence of 700 ppm supernatant of the ultracentrifugated latex used previously was evaluated. Thus, Fig 5.5 F exhibits the simultaneous formation of aggregated nanoparticles (~700 nm diameter, refer to § 5.5.9) assumingly of sodium phosphate salt and the crystallization of twin platelets of α -ZPT, identical but of smaller size to those shown in Fig. 5.5 A. Furthermore, the use of 700 ppm of an unfunctionalized latex, i.e. a latex of PS core containing only a polyethylene oxide based surfactant (AT50) in the corona, produces uniform twin platelets of α -ZPT of even smaller dimension than those obtained in Fig. 5.5 F. In addition, 1000 ppm of an homopolymer of low molecular weight, based on polyethylene glycol (Pluronic PE 6800, $6800 \text{ g}\cdot\text{mol}^{-1}$) and a tribloc copolymer, namely EA3007 ($\text{C}_{12}\text{H}_{25}-(\text{MAA})_8-(\text{EO})_{68}$, $3300 \text{ g}\cdot\text{mol}^{-1}$), were employed separately for comparison with the effects of the PS-*g*-PAA latex. These two polymers were presently selected because Antonietti et al. [141-142] have exemplarily demonstrated on CaCO_3 mineralization that only DHBCs of low molecular weight, i.e. M_w lower than $15000 \text{ g}\cdot\text{mol}^{-1}$ could efficiently affect the morphogenesis of calcite. On one hand, the addition of PE 6800 as template indicates first the important role of the PEO chains in ZPT mineralization and the possibility of controlling both the morphology and mutual orientation of ZPO crystals. In that sense, the crystal growth control achieved using only PEO chains is unique to the ZPT system and singular and remarkable since it is not reported for reference systems such as ZnO or CaCO_3 . In fact, using 1000 ppm of pure PE 6800, cubes of polymer modified zinc phosphate are produced by isotropic growth (Insert left Fig. 5.5 B, average dimension: $2.5 \times 2.5 \times 2.5 \mu\text{m}^3$). The polymeric additive may be uniformly incorporated in these cubic crystals, and subsequently forming zeolitic structures [143] in reason first of the presence of dehydration channel of crystal water on specific faces (dark area in Fig. 5.5 B Insert right) and secondly due to the uniform kinetic control of the growing faces (e.g. [110], [011], [101] and [111] in Fig. 5.5 B insert left), phenomenon that may be explained for the high affinity of polar PEO chains for zinc ions [144-145]. On the other hand, EA 3007 was used directly as crystal modifier first for its ability to mimic of the corona of carboxylated latexes [146], which contains both PEO (surfactant) and PAA chains (copolymer) and secondly for its apparently low critical micellar concentration. Hence, Fig. 5.5 C emphasizes the simultaneous formation of platelets of α -ZPT and hexagonal $\text{NaZnPO}_4 \cdot 1\text{H}_2\text{O}$. This suggest that only the combination of two hydrophile segments, one polar and another charged, located in the latex corona effectively influence the crystallization of α -

ZPT by appearance of a new phase, i.e. $\text{NaZnPO}_4 \cdot 1\text{H}_2\text{O}$. This is further confirmed in employing 700 ppm of abicarboxylated latex functionalized with 4 wt% maleic acid. An absolutely monodisperse size distribution of $\text{NaZnPO}_4 \cdot 1\text{H}_2\text{O}$ is achieved ($4.1 \times 4.5 \mu\text{m}^2$, $\sigma^2: 1.4$), as duly shown in Fig. 5.5 G. For a definitive confirmation of the influence of a carboxylated latex on zinc containing crystals, i.e. its ability to coordinate and exchange zinc ions with the solvent and growing material, a precipitation of zinc oxide in presence of the same PS-*g*-PAA latex at the same concentration as in Fig. 5.5 E was realized in following the procedure developed by Taubert et Martin [147]. Fig. 5.5 G shows well formed hexagonal platelets (i.e. known as “tabular morphology”) of ZnO presenting intricated twin morphology. Therefore, as expected, such a latex is also effective at governing the morphology and internal structure of zinc oxide (i.e. “swiss cheese” structure marked by the presence of pores at the polar [001] surface, formed by latex inclusions) [113,148].

5.3.2. Effect of the size of a carboxylated latex on ZPT/ZPO crystallization

The addition of *small seed* particles to a saturated solution can greatly increase the rate at which ZPO crystals nucleate. This process is understood at least, when the seed have the same structure as the crystal that it spawns [149-150]. However, the microscopic mechanism of seeding by a “foreign” substance is not well understood. Recent advancements on CaCO_3 seeded with functionalized gold nanoparticles by Tremel et al. [151] and later on ZnO crystallization in presence of PS-based latex nanospheres [111] suggest that latex particles of size smaller than 80 nm might control efficiently the heterogeneous nucleation of ZnO as well as its growth by adsorption. Therefore, carboxylated PS-based latexes of approximately constant surface charge density and of increasing diameter have been prepared and used as template in ZPO mineralization.

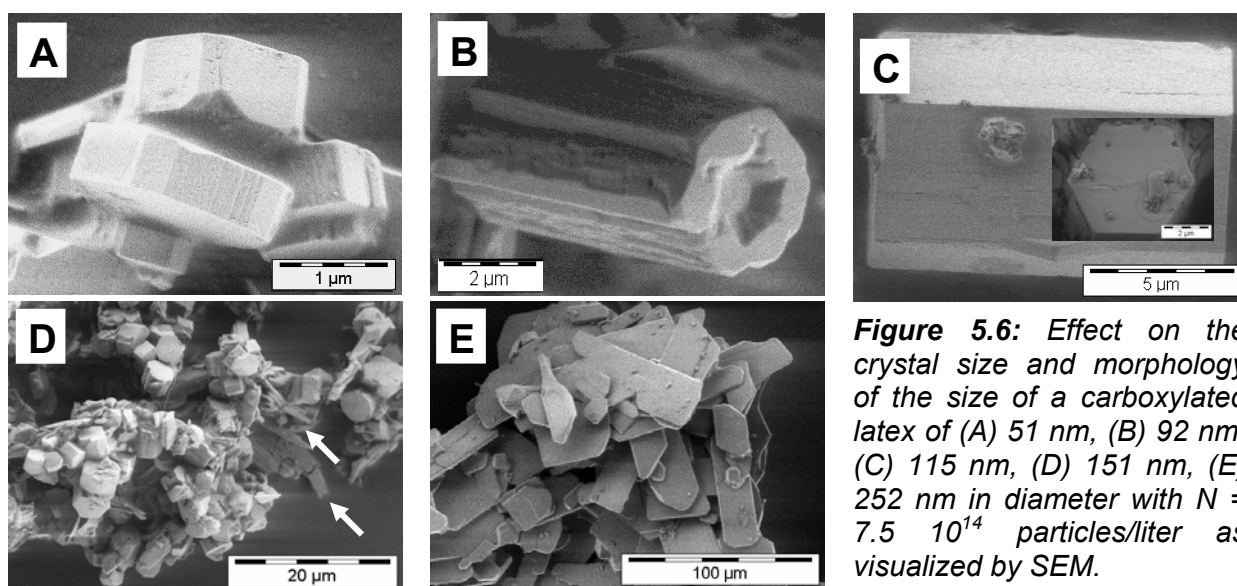


Figure 5.6: Effect on the crystal size and morphology of the size of a carboxylated latex of (A) 51 nm, (B) 92 nm, (C) 115 nm, (D) 151 nm, (E) 252 nm in diameter with $N = 7.5 \cdot 10^{14}$ particles/liter as visualized by SEM.

The effect of the surface charge density of a carboxylated latex on ZPO crystallization will not be

addressed in the frame of this work (*). At a precipitation temperature of 90°C, the latex particles should be considered as hard spheres with a soft surface (i.e. latex corona) of 3 nm maximum thickness. In the size range of a colloidal particle obtained by miniemulsion polymerization (e.g. 50 nm or more), the corona may be considered as a flat surface as far as ZPO nucleation is concerned. Kose [152] and later Dinsmore [153] show that such flat walls speed up nanoparticle crystallization by many orders of magnitude. Moreover, Cacciuto [154] affirms that at the other limit, where the ZPO nuclei have the same size as the colloids in the system, the latex particle should have no effect on the nucleation rate. However, crystallization can proceed spontaneously if a crystal seed (i.e. latex particle) that corresponds to the critical nucleus defined by the homogeneous nucleation theory, is added to a saturated liquid phase. Thus, even if carboxylated latex particles were not found to adsorb on hexagonal ZPO crystals during crystal growth, a marked effect regarding the achieved crystal dimensions is reported in Fig. 5.6 A-D, depending on the additive diameter. With a latex size of 252 nm (Fig. 5.6 E), the crystallization of the kinetically favoured $\text{NaZnPO}_4 \cdot 1 \text{H}_2\text{O}$ is inhibited and platelets of stable α -ZPT are generated, as confirmed by XRD in Fig. 5.9. This is the first major proof of the validity of the intra-corona latex nucleation mechanism described in § 5.3.11.

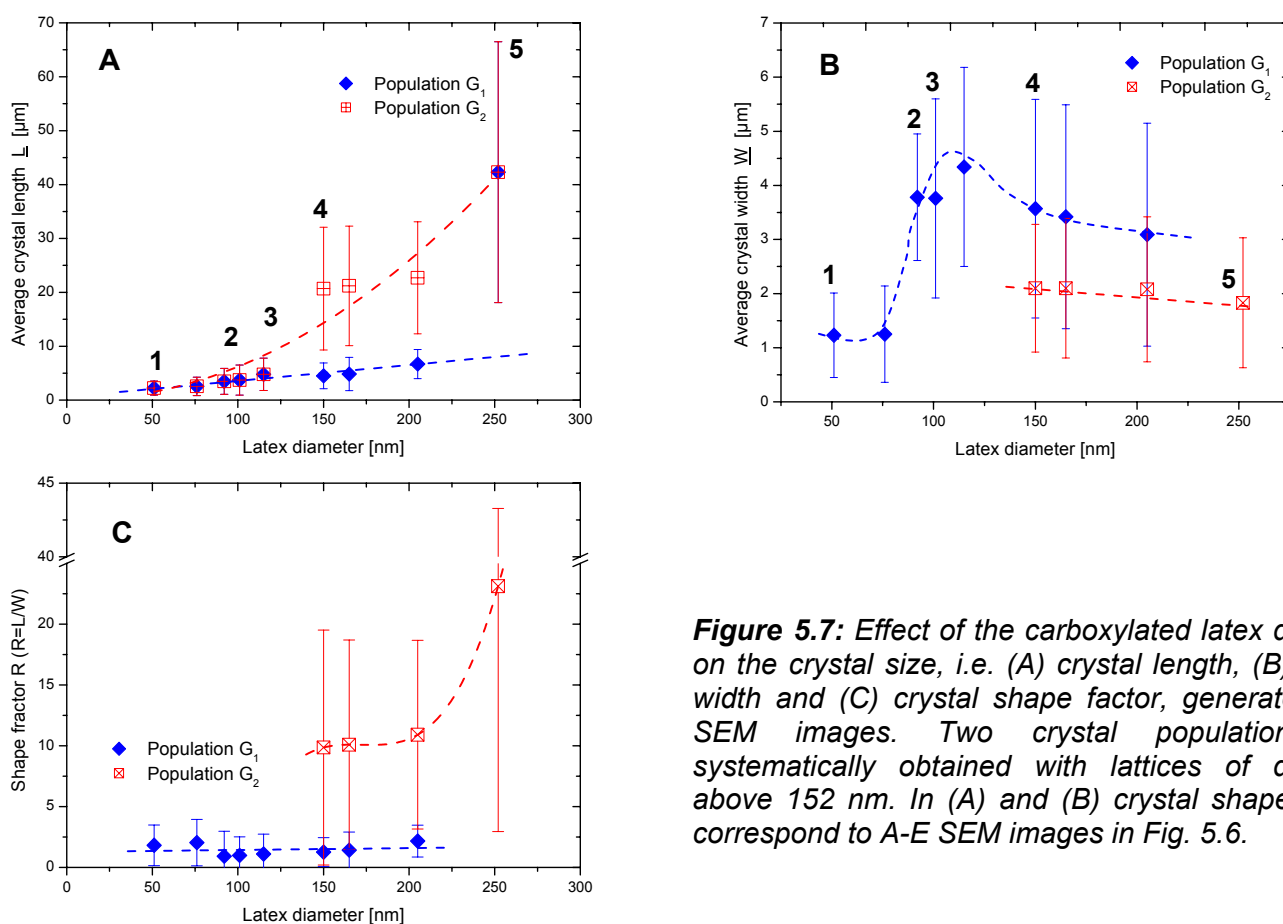


Figure 5.7: Effect of the carboxylated latex diameter on the crystal size, i.e. (A) crystal length, (B) crystal width and (C) crystal shape factor, generated from SEM images. Two crystal populations are systematically obtained with lattices of diameter above 152 nm. In (A) and (B) crystal shape 1 to 5 correspond to A-E SEM images in Fig. 5.6.

One might expect that nucleation speeds up monotonically with the size of the spherical seed but

(*) *Rafael Munoz-Espí, Private Communication (June 2004)*

this is not true. Because as pointed out by Hilton [155], crystals cannot grow on spheres without generating defects, nucleation of spherical particles on, or near a sphere with a very different size is inhibited (Fig. 5.8 E). Frenkel [156-157] found a dramatic increase of the crystal nucleation barrier in a system of polydisperse hard spheres. He discovered that the minimum size of a spherical seed R_s that can affect the rate of crystal nucleation started at five times the size of the crystal nuclei r_n . with the appearance of very small adsorbed nuclei on the latex corona, as shown in Fig. 5.6 (i.e. extra-corona nucleation). The nuclei adsorbed on the latex surface tend to grow radially outward until they either detach and move away into the bulk (i.e. catalytic nucleation) or engulf the latex particle (i.e. mechanism of 1 : 1 latex incorporation in a growing crystal). If the crystal in its first growth stage detaches from the latex corona, the latex becomes free to produce a new crystal-it can act as an “assembly line” for crystal nuclei. But even if a large latex particle may amply lower the energetic nucleation barrier, it can hardly be encapsulated into a growing crystal.

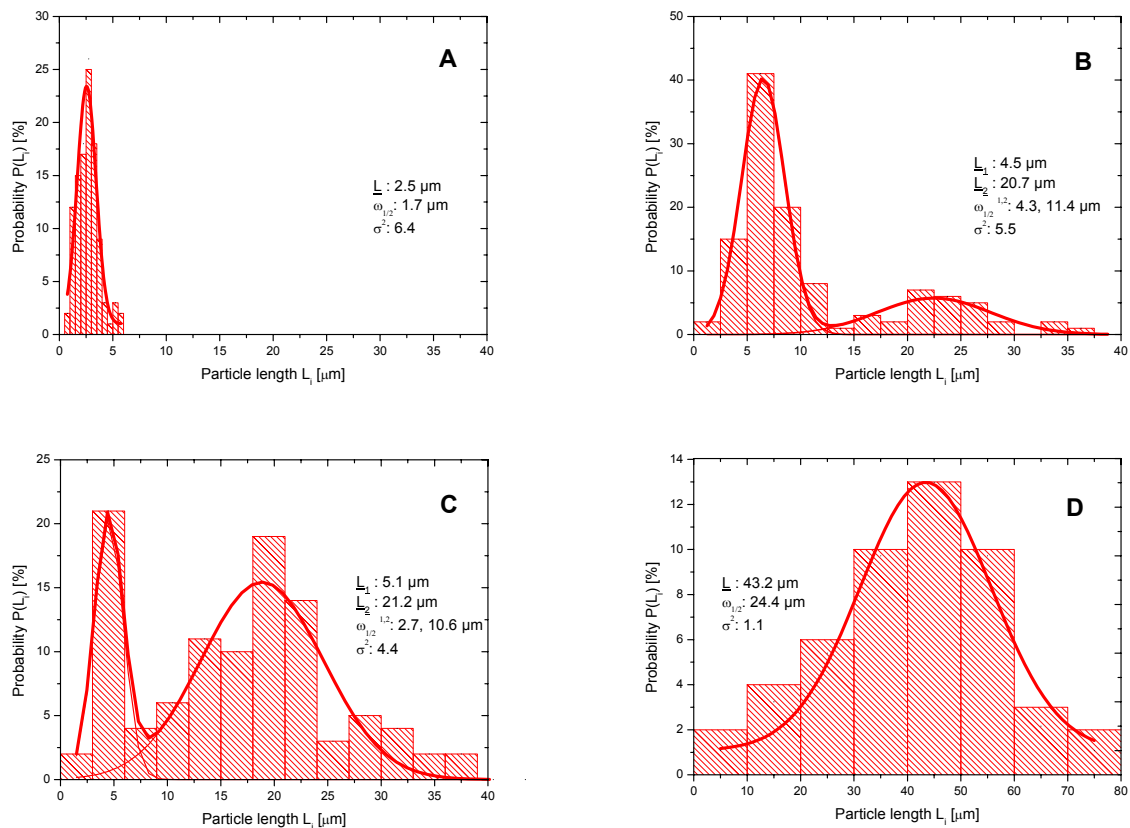


Figure 5.8: Influence of the size of a carboxylated latex on the size distribution histograms in length \underline{L} of $\text{NaZnPO}_4 \cdot 1 \text{H}_2\text{O}$ crystals obtained with latexes of (A) 76 nm, (B) 151 nm, (C) 205, (D) 252 nm in diameter. For a latex diameter above 151 nm, a bimodal distribution is obtained.

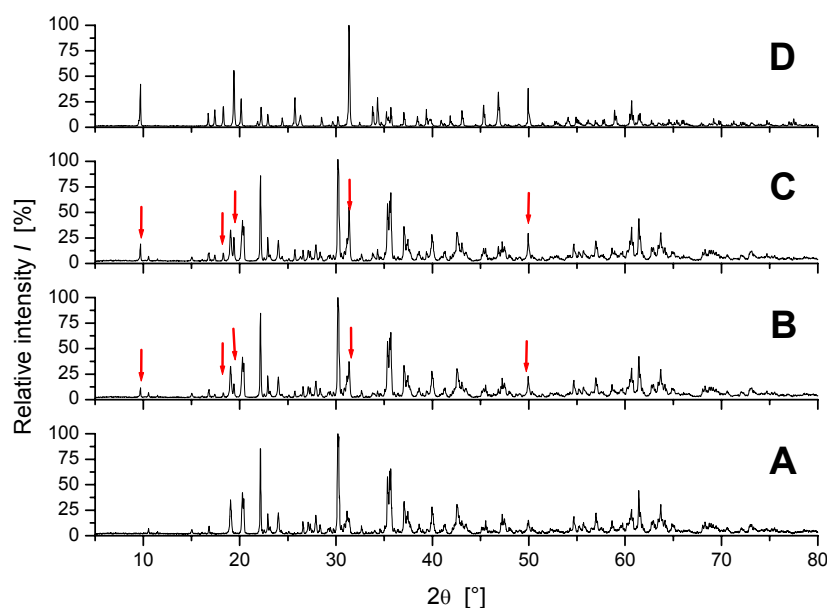


Figure 5.9: Influence of the size of the carboxylated latex on the precipitation reaction followed by XRD for a latex additive of (A) 76 nm, (B) 151 nm, (C) 205, (D) 252 nm in diameter and corresponding to the crystal size distributions given in Fig. 5.3.2.2. (A) indicates the mineralization of $\text{NaZnPO}_4 \cdot 1 \text{H}_2\text{O}$ while (D) illustrates the formation of α -ZPT. (C) and (D) show mixtures of $\text{NaZnPO}_4 \cdot 1 \text{H}_2\text{O}$ and α -ZPT crystals.

Thus Fig. 5.10 displays a computed sequence of altered crystal nucleation on spherical seeds of increasing size, and illustrates the catalytic nucleation approach proposed lately by Frenkel [157].

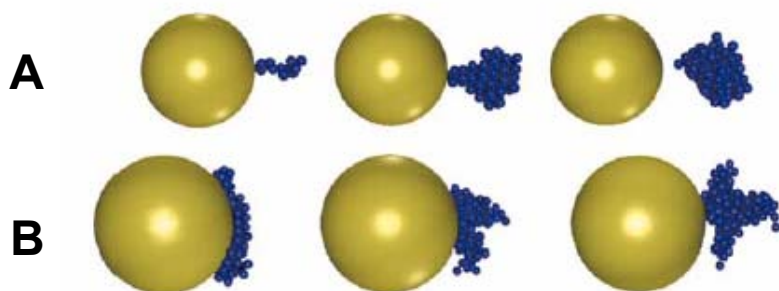


Fig. 5.10. Simulated snapshot sequence of $\text{NaZnPO}_4 \cdot 1 \text{H}_2\text{O}$ nucleation on carboxylated latex particles (spherical seed) of increasing size R_s , adapted from [155]. The seeds have radii $R_s = 5 r_n$ (A) and $7 r_n$ (B), respectively; r_n being the average size of the forming crystal nuclei. From left to right the number of the forming nuclei are respectively, $N \approx 10$, 50 and 100 for the case (A) and $N \approx 60$, 80 and 120 for the case B.

5.3.3. Effect of the corona thickness of a phosphonated latex on the crystallization mechanism of ZPO

Recently, Penczek [158] reviewed the efficiency of polyalkylene phosphate and phosphate and phosphonate functionalized ionic-non ionic DHBCs [159] to complex divalent metal ions (e.g. Mg^{2+} , Ca^{2+} , Ni^{2+} , Co^{2+}) and to control the crystal growth of calcium carbonate and calcium silicate hybrid materials [160]. These studies suggest control of crystal growth thanks to cation exchange between the PEO block and the phosphonate containing blocks of the DHBCs. In this line, the ability of the PEO blocks of increasing length contained in the phosphonate functionalized latex corona, to coordinate Zn^{2+} ions was investigated by SEM (Figure 5.11) on ZPO precipitation crystallization. In order to tune the PEO spacer length, non polymerizable phosphonate functionalized (i.e. end group) surfactants were selected and used as emulsifier in the radical miniemulsion polymerization of P(S-

g-AA) latex (1 wt% AA/S). Characteristic properties of the probing latexes are summarized in Table 5.3.

Latex	A	B	C
Surfactant	[164] RS-410E	RS-610E	RS-710E
[surfactant] (wt%)	1.43	1.43	1.43
Surfactant EO units	3	6	10
Latex diameter d (nm)	62	73	91
Solid content (wt%)	29.2	30.3	29.1
Latex pH	5.42	5.53	5.73
Total surface charge density σ [$C.m^{-2}$]	$1.21 \cdot 10^{-5}$	$1.36 \cdot 10^{-5}$	$1.285 \cdot 10^{-5}$
Zeta potential ζ (mV) at pH 12	-102	-105	-109
Electrophoretic mobility μ [$m^2.V^{-1}.s^{-1}$]	2.01	2.12	2.37
Conductivity K ($mS.cm^{-1}$)	2.12	1.13	0.31

Table 5.3: List of phosphonate functionalized latexes obtained with non polymerizable surfactant of increasing EO block length

Fig. 5.11 A shows $NaZnPO_4 \cdot 1 H_2O$ nuclei of 110 nm average diameter. By comparison to Table 5.3 and assuming the presence of just one latex particle pro nucleus, such value indicates a diameter increase of 18%. This suggests that Zn^{2+} ions are accumulated in the latex corona by dipole-ion interactions while the phosphonate end group condensate with zinc cation. One may conclude that the PEO block (3 units) is too short to affect the crystal growth. On contrary Insert in Fig. 5.11 C displays the effective stabilization of rather monodisperse hexagonal crystals of $NaZnPO_4 \cdot 1 H_2O$ when the PEO block length comprises a minimum of 10 EO units.

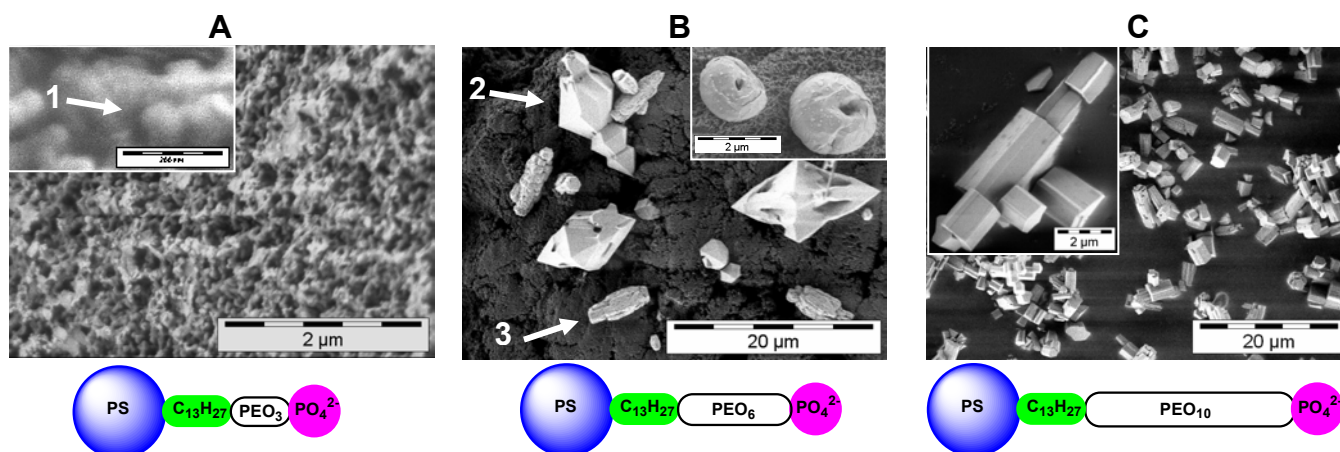


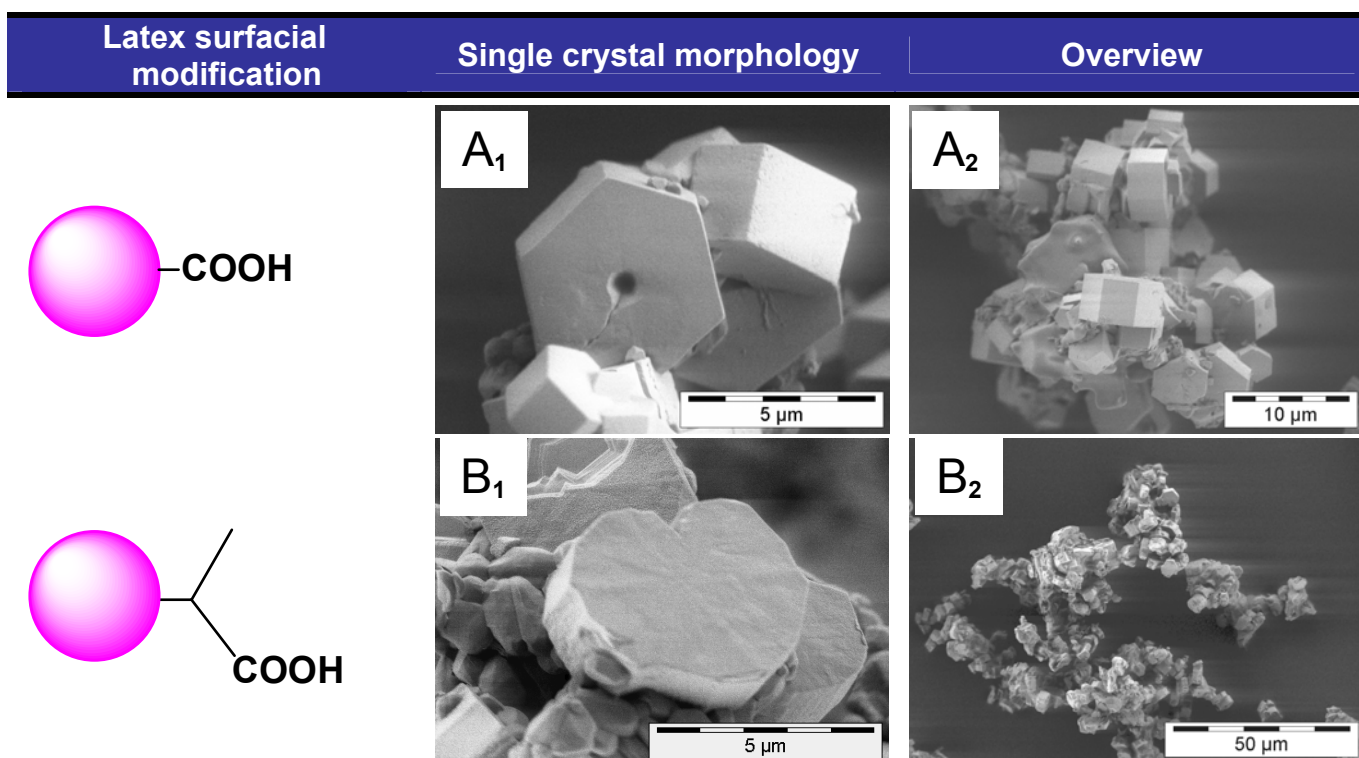
Figure 5.11: SEM investigation of the influence of the PEO spacer length that regulates the corona thickness of a phosphonate functionalized latex [161] (additive concentration: 1000 ppm) on ZPO crystallization: (A) 3 EO units, (B) 6 EO units, (C) 10 EO units. The corona functionalization stems from the surfactant used in the miniemulsion process. 1: amorphous zinc phosphate or spherical nuclei, 2: dendritic growth, 3: uncontrolled parallel growth of $NaZnPO_4 \cdot 1 H_2O$. Insert B: “donut” morphology also found in latex controlled mineralization of ZnO. An efficient control of $NaZnPO_4 \cdot 1 H_2O$ crystallization requires at least 10 EO units.

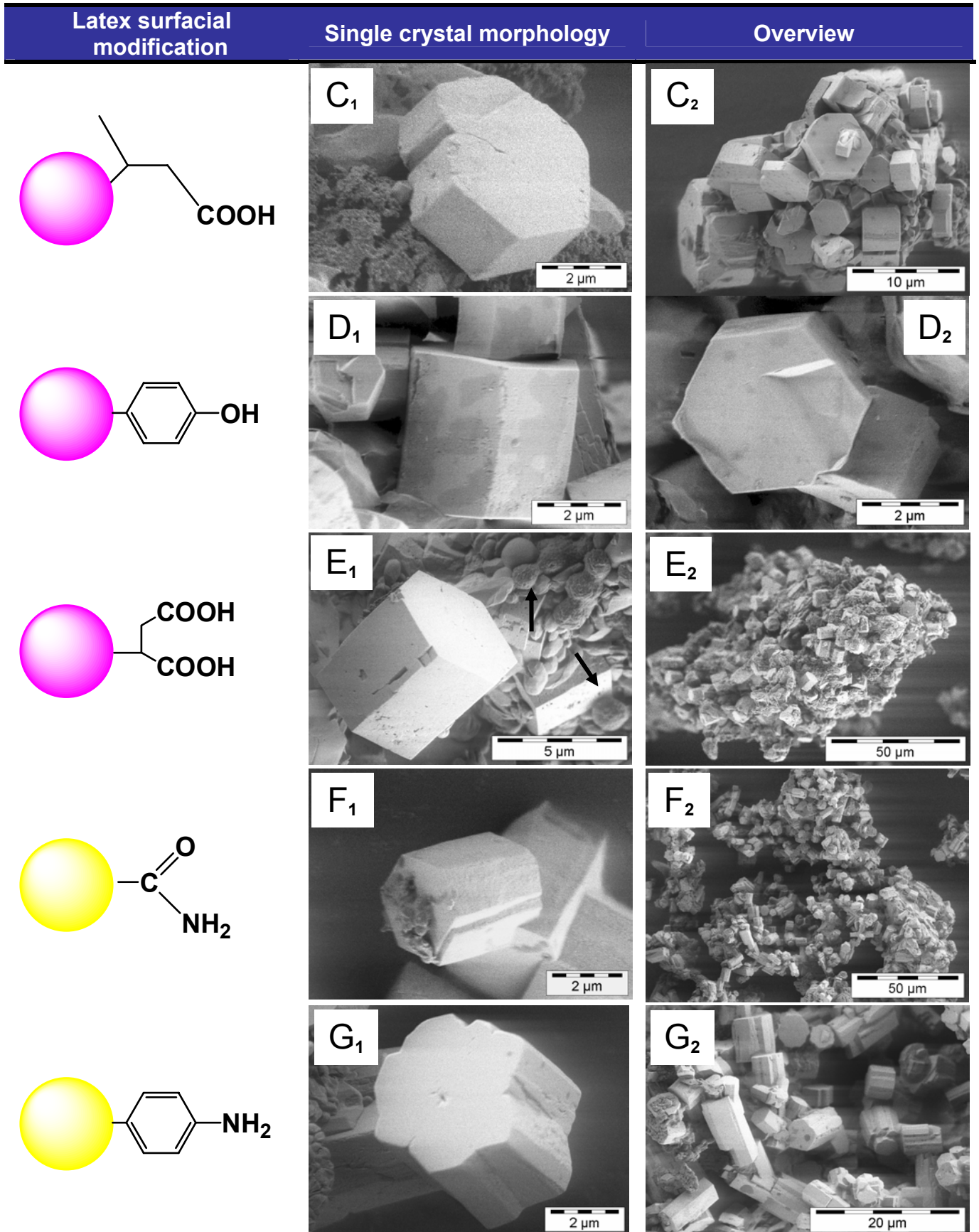
This first supports the use of AT50 (50 EO units) as standard surfactant of the functionalized latexes for ZPO mineralization, which is then long enough to ensure a nucleation control essentially via a intra-corona latex nucleation mechanism and secondly that the best ZPO binding efficiency (i.e. use

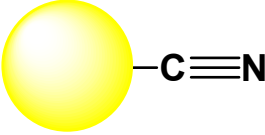
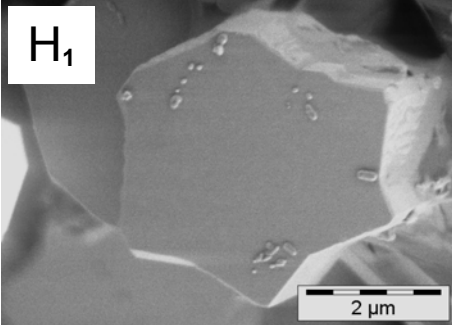
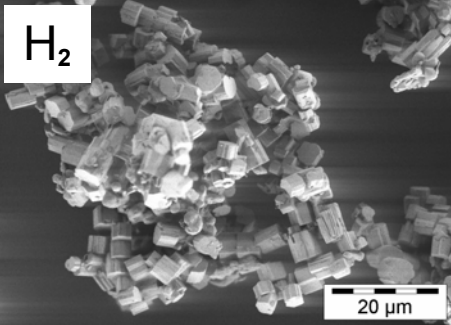
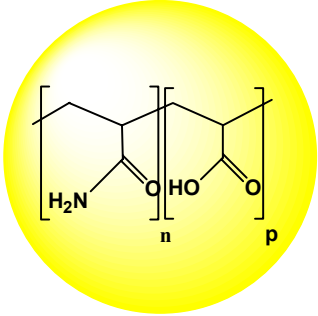
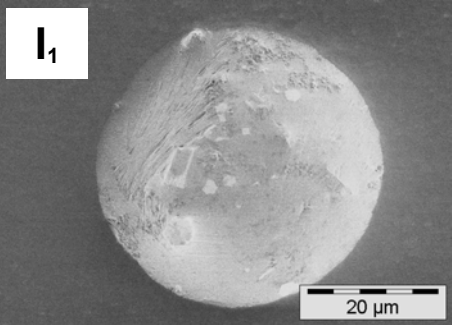
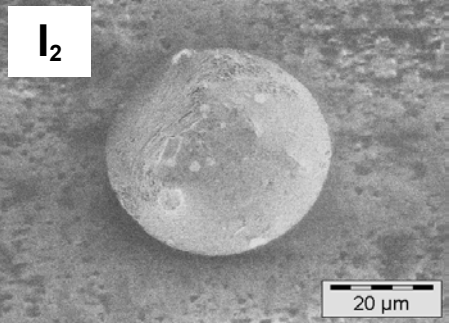
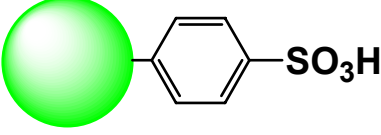
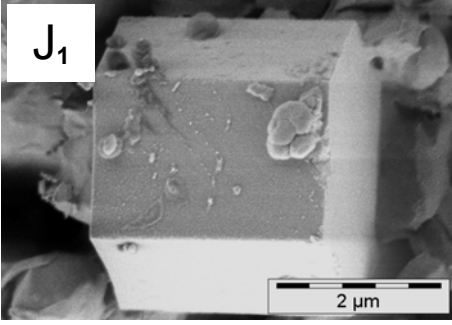
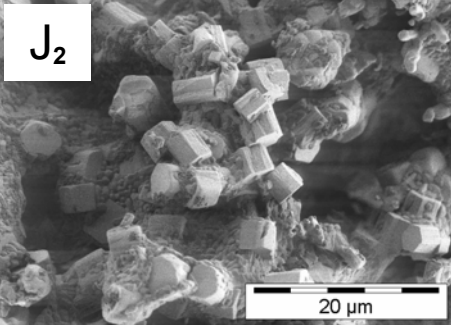
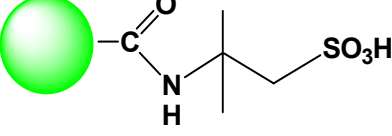
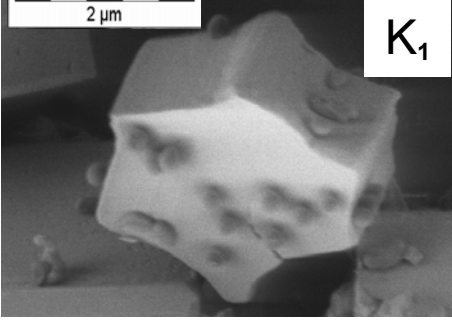
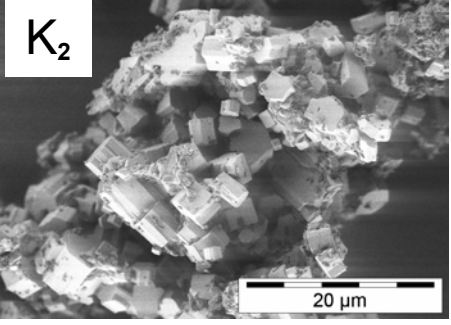
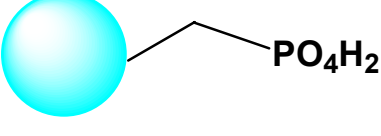
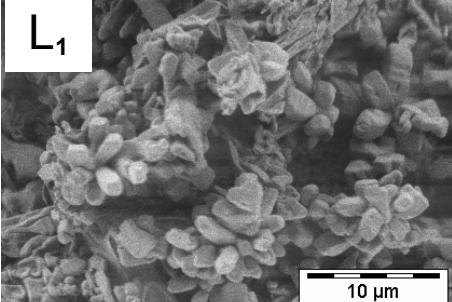
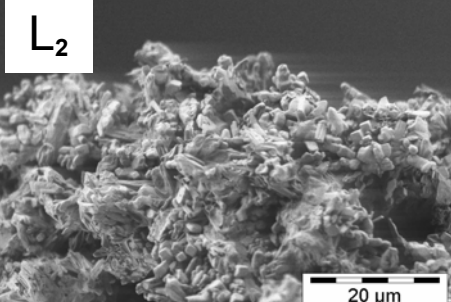
of phosphonate groups) does not necessarily lead to the best control of ZPO mineralization, in strong similarities with Cölfen's observations on CaCO_3 [162]. Furthermore, Cölfen et al. [163] pointed out that PEG-*b*-PMAA- PO_3H_2 could successfully block the solvent mediated vaterite-calcite transformation. Thus, arrow 2 in Fig. 5.11 B displays on one hand the hindered growth of $\text{NaZnPO}_4 \cdot 1 \text{H}_2\text{O}$ and arrow 1 in Fig. 5.11 B displays the stabilization of parallelly growing crystals (dendritic growth) of a sodium zinc phosphate phase, that also may adopt a "donut-like" shape.

5.3.4. Effect of the chemical function of latex on ZPT crystallization

The effects of the chemical functionalization, i.e. the hydrophilicity, the polarity and the surface charge density of a PS-based latex corona on the crystal size and morphology during ZPT mineralization may be conveniently monitored by SEM, as shown in Figure 5.12. For precise comparison, with AT50 as standard surfactant, identical amount of functionalized comonomer (4 wt%) during the latex synthesis, and identical amount of template agent during crystallization (800 ppm) were used. Hence, four classes of functions (i.e. phenolate, carboxylate, sulfonate and phosphonate are studied, since they often correspond to the chemical nature of the charged block of DHBCs and biopolymers used in polymer controlled mineralization and reported in the literature. In Fig. 5.12, characteristic hexagonal crystals are systematically obtained upon addition of different latexes.





Latex surficial modification	Single crystal morphology	Overview
		
		
		
		
		

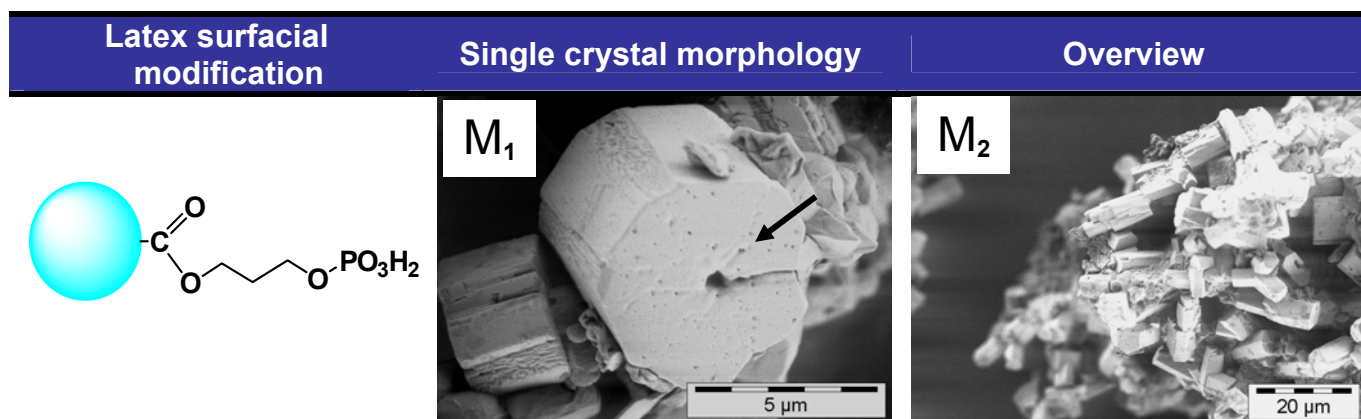


Figure 5.12: Summary of the effects of surface chemistry of 800 ppm functionalized latexes (latex diameter 80 nm) on ZPO morphology after 2h crystallization at pH 6.5 and 90°C. Various chemical modifications comprising phenolate (D), carboxylate (A,B,C,E), sulfonate (J,K) and phosphonate (L,M) functions are evaluated. While each latex additive stabilizes the $\text{NaZnPO}_4 \cdot 1 \text{H}_2\text{O}$ phase, different surfacial defects are obtained (arrows in sample M_1). Arrows in sample E_1 show crystal nuclei generated by latex particles.

This indicates that each of the latex used as a structure controlling agent induces the stabilization of the metastable $\text{NaZnPO}_4 \cdot 1 \text{H}_2\text{O}$ phase, disregarding the functionalization of the latex corona. Nevertheless, slight differences of shape and crystal size distribution have to be reported. Perfect hexagons are produced with the following “carboxylic” (i.e. functionalization of increasing pK_a) functionalization: phenolate (Fig. 5.12 D), acrylic (Fig. 5.12 A), maleic (Fig. 5.12 E).

Sample N°	Crystal length \underline{L} [μm] ^{e,f}	PDI σ_L^2	Crystal Width \underline{W} [μm] ^{e,f}	PDI σ_W^2	Shape Factor R	PDI σ_R^2	Distribution ^e	Morphology
A	3.66	1.85	6.54	1.87	0.56	0.98	monodisperse	hexagonal
B	1.68	4.00	4.59	5.70	0.36	0.71	monodisperse	heartlike
C	3.43	3.01	1.55	1.50	2.21	2.01	bidisperse ^{a,g}	heartlike
D	2.04	2.91	2.71	5.22	0.75	0.55	monodisperse	hexagonal
E	5.62	1.05	4.92	2.91	1.14	0.37	bidisperse ^{b,g}	hexagonal
F	1.81	5.39	1.52	4.20	1.19	1.28	bidisperse ^{c,g}	hexagonal
G	5.65	7.34	4.39	1.92	1.28	3.82	monodisperse	star
H	3.14	2.38	3.94	4.92	0.80	0.60	monodisperse	star
I	42.00	1.12	42.00	1.12	1.00	1.00	monodisperse	sphere
J	2.98	6.71	3.69	1.81	0.80	3.71	bidisperse ^{d,g}	hexagonal
K	2.11	4.39	2.81	1.46	0.75	3.00	monodisperse	star
L	3.99	5.01	1.43	5.22	2.79	0.96	monodisperse	hexagonal
M	7.82	2.88	4.77	3.20	2.71	0.90	monodisperse	hexagonal

Table 5.4: Summary of the crystal size distribution (CSD), shape factor and morphology obtained from SEM images (Fig. 5.X) with 800 ppm of various functionalized latexes.

- (a) particle size ≈ 1450 nm (c) particle size ≈ 840 nm
 (b) particle size ≈ 1200 nm (d) particle size ≈ 725 nm
 (e) distributions realized with 250 crystals min. Bimodal distribution with two populations
 (f) estimated error ± 0.05 μm
 (g) bimodal distribution with two populations of increasing size: G_1 and G_2 .

However, while monomodal distributions are achieved using phenolate and acrylic functions, a dicarboxylated function such as the maleic function produces a bimodal distribution of fully grown

crystals and spherical nuclei (arrows in Fig. 5.12 E), either originating from a secondary nucleation process or from stabilization by a latex particle, and subsequently not dissolved in return in solution due to partial Ostwald ripening occurring on aging. Recently, van der Leeden et al. [164] found that a copolymer of maleic acid and vinyl sulfonic acid stimulated the precipitation process of barium sulfate up to a concentration of 5 ppb. The retardation of the nucleation was enhanced with a further increase in the DHBC concentration. It was concluded that PMAI-co-PVS may be involved in a two dimensional nucleation process as an active center for nucleation. This may justify the presence of a bimodal distribution in sample E and J. Furthermore, the absence of latex particles on the different crystal faces also suggests the primary role of latex particles in the nucleation step. Besides, the acrylic functionalization (Fig. 5.12 A) displays the highest mineralization efficiency, i.e. the highest crystal length and shape factor reductions. On one hand, the crystal length diminishes in the following sequence: maleic > acrylic > phenolate (i.e. 5.62, 3.66 and 2.04 μm) and on the other hand the shape factor R decreases as follows: maleic > alcoholate > acrylic (i.e. 1.14, 0.75 and 0.56). The classification relative to the crystal length reduction might be explained by the efficiency of the comonomer incorporation in the latex corona since the maleic function has a higher solubility in water than the acrylic acid and the alcoholate function (stemming from 4-hydroxystyrene), and therefore exhibits a lower crystal length reduction. The sequence relative to the shape factor reduction is also related to the complexation constant of the comonomer. Thus the bimodal distribution obtained with the maleic function is strictly related to the nucleation step. However and surprisingly, the highest value of R is obtained with the maleic acid in comparison to the phenolate and acrylic functions.

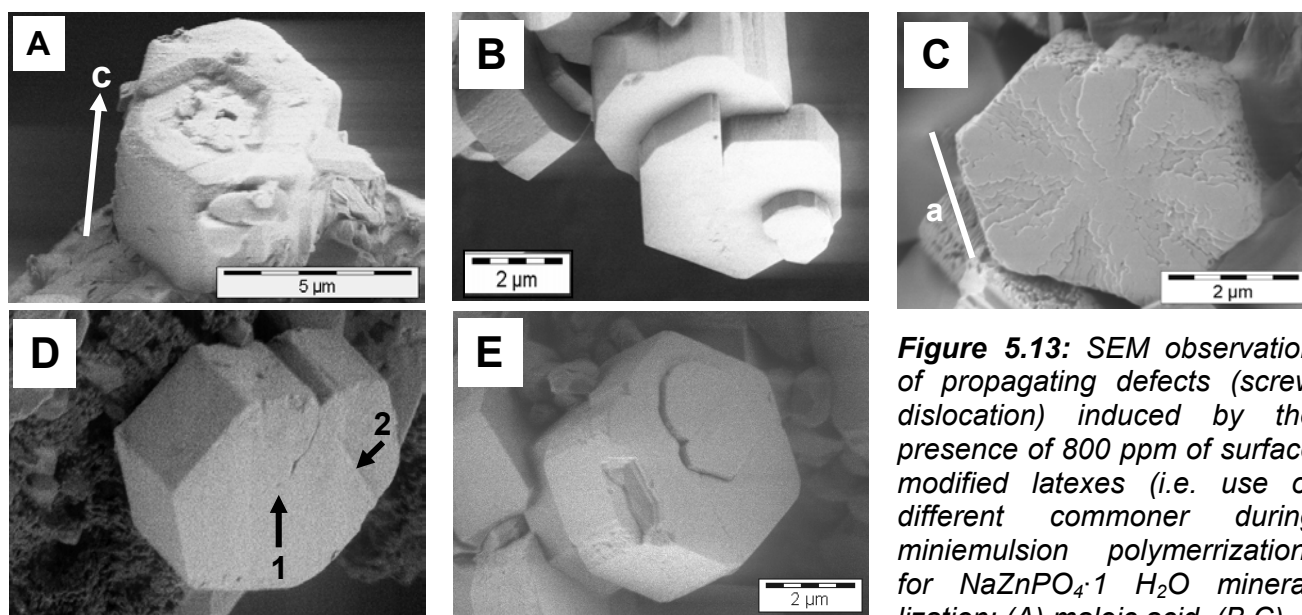


Figure 5.13: SEM observation of propagating defects (screw dislocation) induced by the presence of 800 ppm of surface modified latexes (i.e. use of different comonomer during miniemulsion polymerization) for $\text{NaZnPO}_4 \cdot 1 \text{H}_2\text{O}$ mineralization: (A) maleic acid, (B,C)

methacrylic acid, (D,E) crotonic acid. In image A, c describes the crystallographic c -axis, along which the spiral grows. In image C, a designs the length of a crystal edge and is a multiple of the unit cell dimension of $\text{NaZnPO}_4 \cdot 1 \text{H}_2\text{O}$. Arrows 1 and 2 in image D correspond to the core of a screw and a growth edge, respectively.

The low incorporation of acrylic based comonomers in the latex corona can be overruled in employing methacrylic based monomers. Thus, the influence of latexes containing methacrylic and crotonic functions is clearly shown in Fig. 5.12 B1 and Fig. 5.12 C1 respectively.

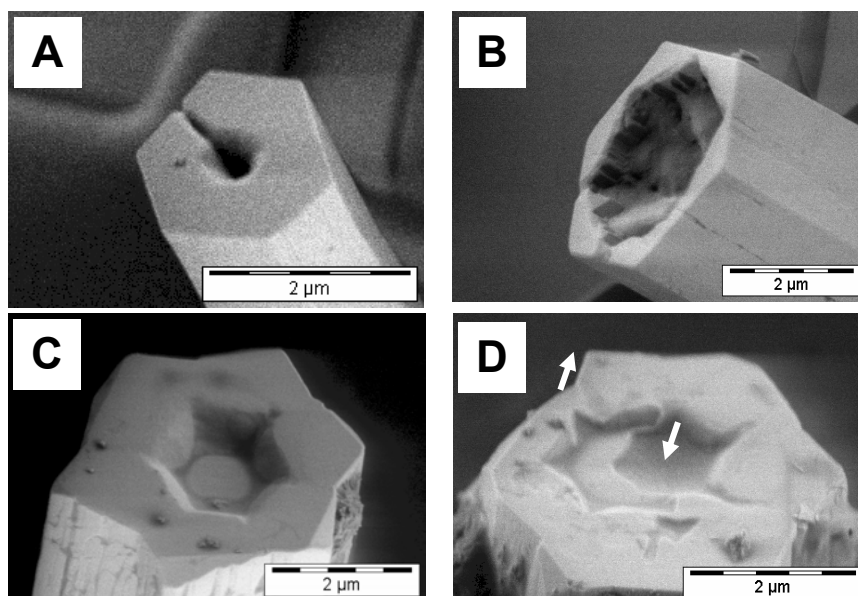


Figure 5.14: SEM observations of crystal dissolution emphasizing the formation mechanism of defects (screw dislocation) induced by the presence of 800 ppm of surface modified latexes for $\text{NaZnPO}_4 \cdot 1 \text{H}_2\text{O}$ mineralization: (A,B) acrylic acid, (C,D) styryl sulfonic acid. In D, arrow 1 indicates the core of screw and arrow 2 the growth edge of the screw.

Neglecting the difference of copolymerization kinetics in emulsion between acrylic and methacrylic comonomers [165], the comparison of the acrylic and the different methacrylic latex functionalizations suggests that the decrease of both shape factor and crystal length is in direct relation with the positive electron donor effect of the methyl group of methacrylic homologues, which increases the acidity of the functional group. In both B and C samples, a heart-like morphology is achieved. This is most probably due either to an intricate twin-crystal growth (Fig. 5.11 D) or to the presence of a growing screw dislocation more or less at the geometric center of the crystal (Fig. 5.11 A). The incorporation of latex, proven in § 5.3.10, leads to inhomogeneities around the absorption point (crystal nucleus) and remnant strains, that in turn govern the spiral growth along the c -axis of the hexagonal $\text{NaZnPO}_4 \cdot 1 \text{H}_2\text{O}$ crystal, as well illustrated in the case of PS latex functionalized with maleic acid in Fig. 5.13 A on a macroscopic scale. The inhomogeneities are not restrictively induced by latex adsorption (= impurities [166]) but also the intrinsic zeolitic structure of $\text{NaZnPO}_4 \cdot 1 \text{H}_2\text{O}$, that favors the intracavity diffusion of Na^+ and water of hydration, as pointed by Faux [167]. Figure 5.13 B to E shows successive stages of spiral growth on the [001] surface in presence of 800 ppm of PS latexes modified by 4 wt% of methacrylic and crotonic acids. The mechanism of formation of the screw is emphasized on aging when surfacel dissolution or controlled chemical etching occur (Fig. 5.14). Therefore, one notices the crystallographically controlled dissolution of the [001] surface along the a - or b -axis from the exact geometric center of the hexagon (Fig. 5.14 A and B). On contrary, for a heartlike morphology, the opening angles of the pseudo-hexagon corners, differ from ideality (120°) by $\pm 9^\circ$ precisely and the dislocation core is

located at 0.334 times a , i.e. the edge length of a single hexagon. Coincidentally, this distance corresponds from a crystallographic point of view in a unit cell to the plane (110), which contains the highest density in Na^+ ions (see Fig. 5.15 B) and all $\text{Zn}(2)$ ions. Furthermore, this can be interpreted from a classical crystallographic point of view using the “twinning law” along shared {100} plane in strong similarities to the Dauphiné law describing the quartz “right-turning” contact-twin formation (i.e. Schwalbenschwanz twin crystals) [168]. From these considerations, it is possible to propose a mechanism of formation of heartlike crystal as reported in Fig. 5.15 A.

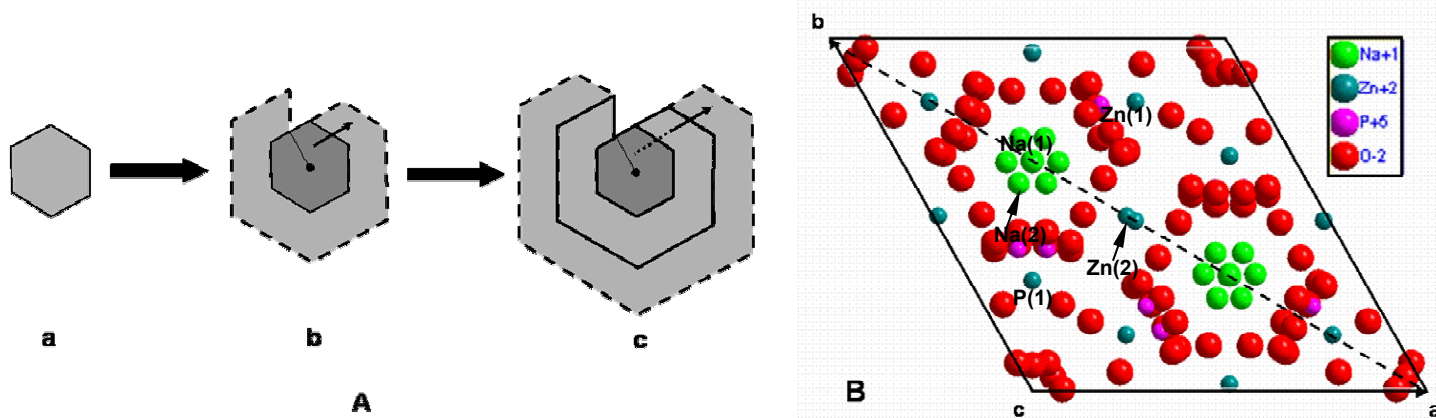


Figure 5.15: (A) Schematic representation of crystal spiral growth by propagation of a central screw defect deduced from morphological observations in Fig. 5.13 and Fig. 5.14 and explaining the obtained “heart-like” morphology upon addition of methacrylic-PS based latexes, (B) Ball and stick representation of a unit cell of an hexagonal crystal of $\text{NaZnPO}_4 \cdot 1 \text{H}_2\text{O}$ (A-form) displaying the [110] symmetry plane containing the maximal density of Na^+ ions (respecting the indexation of the structures described in § 5.3.9).

In addition, the samples J to M bear sulfonated and phosphonated functional groups, that exhibit stronger acidity than acrylic functions. This is well illustrated either by the appearance of a bimodal size distribution with decreasing crystal size from crotonic to styryl sulfonic acid, or by a systematic increase of shape factor from 0.96 to 0.80 and 0.56 (i.e. flattening effect) for phosphonic, sulfonic and acrylic acid. In fact, if the pK_a of the acid group is too low, the Zn^{2+} may be too strongly bound to the functional group and the latex possesses then a nucleation inhibiting effect. For identical reasons, traces of latex particle adsorbed or incorporated in the zinc rich [001] crystal face are found. Based on molecular-modeling calculation results, the dimensions of a zinc ion and phosphate ions are 1.2 and 2.5 Å and the active functional dimensions of the groups $-\text{PO}_3\text{H}_2$ and $-\text{COOH}$ are 3.5 and 2.2 Å, respectively. Therefore, a phosphate ion can be favourably replaced by a phosphonate group but not by a carboxylic group, which may explain the extraordinary affinity of phosphonated latexes for the hopeite and $\text{NaZnPO}_4 \cdot 1 \text{H}_2\text{O}$ crystal surfaces. These results imply that the latex do not only act by means of electrostatic interaction as latexes functionalized with styryl trimethylammonium chloride salt for example, but also apparently replace negative phosphate ions on the crystal surface. Because in strong polyelectrolytes such as poly(styrylsulfonic acid) electrostatic rather than chemical association govern the interaction between the polyelectrolyte and

the divalent metal [169], it may be speculated that the polymer/metal association takes place in the outer layer of the sulfonated PS-based latex. Moreover, this might explain as well the tendency in decrease of crystal length: phosphonic > acrylic > sulfonic acid (samples L,J,A in Table 5.4) which was observed by Taubert et al. [145] on ZnO crystallization for acrylic-sulfonic functionalized DHBCs and by Cölfen et al. [170] in BaCrO₄ crystallization with phosphonic-acrylic functionalized DHBCs. Besides, regarding each class of functional group, as the spacer length increases, the functional groups located in the outer layer of the corona become more accessible to Zn²⁺ ions, and thus may effectively inhibit or at least reduce notably the crystal growth. This tendency is observed in Table 5.4 for acrylic (samples A-B), sulfonic (sample K-J) and phosphonic (L-M) acids informs of the diminishing of the shape factor from 0.56 to 0.36, 0.80 to 0.75 and 0.96 to 0.90. A similar effect is found with a 40% reduction of the average crystal length with a sulfonic acid functionalization (sample J and K, Table 5.4).

Inspired from the numerous organic zinc phosphate zeolitic structures with open framework of different dimensionality [171-172] synthesized thanks to adequate use of polyamine derivatives [173-174], the potential of amine, amide and nitrile functionalized latexes [87,94] with increasing polarity and decreasing amphoteric or/and zwitterionic character was evaluated on ZPO crystallization. Thus comparing the nitrogen containing latexes, on one side the sample obtained with an acrylamide functionalized latex (sample F, Fig. 5.10) displays the shortest crystal length (1.81 μm) and the latex modified with p-aminostyrene (sample G, Fig. 5.12) the biggest \underline{L} value (5.65 μm), on the other hand. The decrease of the shape factor is directly proportional to the polarity of the function with the following sequence: p-aminostyrene > acrylamide > acrylonitrile, i.e. R decreasing from 1.28 to 1.19 and 0.8. Hanaki et al. [175] attributed such a classification to the kinetic stability of the chelating ring unit between terminal amine and a divalent metal ion (e.g. M²⁺ = Cu²⁺). Jansen et al. [176] studied the inherent reactivity of acrylate monomers during copolymerization and found that the propagation step of the radical polymerization is mostly influenced by hydrogen bonding and the intrinsic dipole moment of the monomer influences the termination rate. This suggests that the dipole moment defines the chemical architecture of the corona (i.e. leading to changes in grafting density of the hydrophilic comonomer on the latex corona) and thus might alter the control of the crystallization. Nevertheless this point of view is not absolutely relevant here, since a variation of the monomer polarity should be perceived as affecting proportionally and in the same manner both crystal length and shape factor. However this was not observed in samples F, G and H (Fig. 5.12). Thus, as stated by Pefferkorn [177], the grafted acrylamide functions on the PS latex surface can be either neutral, hydrolyzed in the sense of acrylic acid groups or complexed with zinc or sodium ions. The interaction of P(S-g-AM) latexes with ZPO crystal is very complex since electrostatic and van der Waals forces operate simultaneously. While hydrogen bonding between neutral PAM and hydrated zinc or zinc rich planes affects the kinetics of crystal growth, the

presence of positively charged, negatively charged and neutral segments in a complexed PAM latex corona confers to the latex a strong amphoteric character. This may explain the monodispersity of sample G and H in Fig. 5.12 compared to the bidisperse crystal size distribution of sample F, related to stabilization of small hexagonal crystals of 840 nm diameter.

In addition, the use of both sulfonated and amine functionalized latexes allows the achievement of a transition from a “six-petal flower” to a planar star-shaped morphology as shown in Fig. 5.12 G1, H1 and K1. On the contrary, a P(S-*g*-AM) latex has no marked influence as structure directing agent (refer to the morphology of sample F1), characterized by the production of hexagonal crystals of $\text{NaZnPO}_4 \cdot 1 \text{ H}_2\text{O}$. These particular morphologies can be described first from a structural point of view. Hence, the faces of the hexagonal crystals grow parallel to the three zinc rich [100], [010] and [110] planes. But the growing faces of star-shaped crystals grow along the sodium rich [110], [210] and [210] planes as shown in Fig. 5.16. The sodium rich planes should have a higher surface energy than the zinc containing planes, due first to the presence of sodium channels in the [110] cleavage / gliding plane [178] and secondly to the participation of $\text{Zn}^{2+}(\text{II})$ located in planes [100], [010] of the rigid $\text{NaZnPO}_4 \cdot 1 \text{ H}_2\text{O}$ framework. To some extent a satisfying description of this morphological transition from hexagonal to star shape upon addition of sulfonated (samples J-K) or amine (samples F-G-H) functionalized latexes can be discussed in the frames of the simple Wulff-Chernov approach (bulk dissolution model) [179] and then of the Hartman-Perdok theory [180], which directly relates the relative growth rate R_{hkl} of a face (hkl) to the attachment energy $E_{hkl}^{\text{attach.}}$, i.e. the energy to add or remove a growth unit from the surface (hkl). Completed with the energy of the broken bonds defining the crystal-solute interface (surface energy) E_{hkl}^{slide} this gives the crystallization energy, evaluated as low as $26 \text{ kJ}\cdot\text{mol}^{-1}$ for α -ZPT by Nancollas et al. [181]. It follows from the Hartman-Perdok theory that crystal will growth by F faces having the lowest R_{hkl} or the lowest $E_{hkl}^{\text{attach.}}$ and the highest E_{hkl}^{slide} . Furthermore, Zhanpeisov et al. [182] confirmed first that the formation of the ZPO structure was energetically highly favored when the building blocks that compose the crystal structure interacts according to a acid-base neutralization and secondly that the Lewis acidity of ZPO, pure ZPT and pure ZnO materials were nearly equivalent. The (metal) Lewis acid sites formed from the most metastable plane display high activity in binding with Lewis base molecule such as L-SO_3^- , L-COO^- , L-NH_2 and $\text{L-C}\equiv\text{N}$; L designating the latex particle. Secondly these particular heganonal and star-shape morphologies can be also described with the model of Sunagawa [183] and Pina and Putnis [184] (e.g. extended model combining a birth and spread (B+S) two-dimensional nucleation model and the Burton-Cabrera-Frank (BCF) equation for spiral growth), in which flat crystal faces grow according to two-dimensional nucleation and spiral growth mechanisms at moderate and low supersaturation (i.e. depending on the solid composition). This has been successfully employed for $\text{Ba}_x\text{Sr}_{1-x}\text{SO}_4$ solution crystallization by Pina and Putnis

[184]. In a third approach, these growth patterns are well described from a classical crystallographic point of view using the “twinning law” [185] and the combined Brasilian-Dauphiméer laws describing the quartz contact-twin formation as defined successively by Kleber and Fuksa [186]. Finally, based on these interpretations a mechanism of transition from hexagonal to star-shape morphology may be proposed in Fig. 5.16.

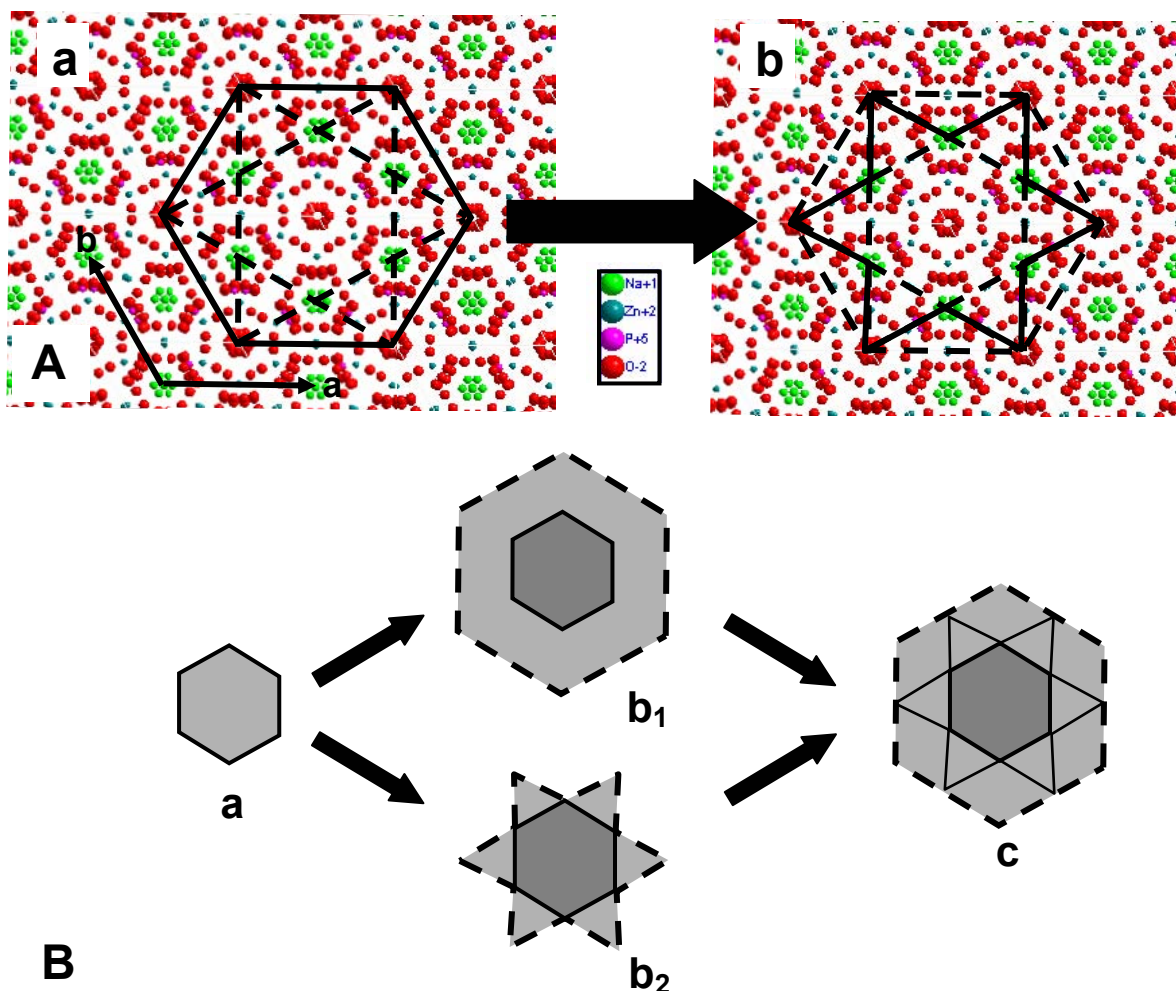


Figure 5.16 : Proposed schematic representation from a crystallographic approach (a) and kinetic approach (B) of the transition from an hexagonal (b1) to star-shape (b2) morphology observed upon addition of 800 ppm of sulfonate and/or amine functionalized latexes in the $\text{NaZnPO}_4 \cdot 1\text{H}_2\text{O}$ crystallization. Alternatively, the approach (B) can also be described employing the “twinning law” in the basal plane of an hexagonal system.

Following the strategy of Alkoy et al. [187] a sphere morphology of crystalline ZPO with monodisperse distribution was tentatively achieved using DHBCs poly(acrylic acid-stat-acrylamide) reticulated hydrogels [188] as Zn^{2+} reservoir and template obtained by inverse microemulsion polymerization and transferred in aqueous solution. In similarity to the work of Putnis et al. [189] on the interaction between polyacrylamide hydrogels and CaCO_3 , these results also suggest that SDA containing a polyacrylamide block may as well be incorporated in the crystal structure in an organised manner (e.g. Fig. 5.12 I₂). However, the obtained crystal size was even ten times higher than with acrylamide grafted (i.e. by on the PS-latex surface (samples FI and I in Figure 5.12) due

to the important water absorbing effect, i.e. well known swelling of PAM hydrogels [190-191]. In inverse microemulsion in toluene, the latex size was around 30 nm while after transfer into a 0.15 mol.L⁻¹ aqueous zinc solution a 20 µm average diameter was monitored. Nevertheless, this synthesis method opens new perspectives to design microstructured hybrid materials since the polymer serves not restrictively as crystallization template but also as organic matrix.

5.3.5. Effect of the presence of a positively charged latex on the fractal growth of ZPO – Crystal growth controlled by latex absorption mechanism

A positively charged latex might possess the ability to coordinate phosphate ions present in the reaction milieu and on the growing crystal faces, and thus take control of the NaZnPO₄·1 H₂O crystallization by polymer adsorption, since each of the carboxylated latexes used before was found to control the nucleation step of the mineralization process.

Therefore, Figure 5.17 describes the growth of anisotropic self-assembled hierarchical growth of NaZnPO₄·1 H₂O in presence of 1000 ppm of a highly positively charged latex (P(S-*g*-STMACl)). This shows immediate parallels to the topological branching criteria of the macromolecular starburst dendrimers. Moreover, this particular mineralization begins with an elongated hexagonal prismatic seed (Fig. 5.17 A) that adsorbs concentrically on a cylindrical latex aggregate (cross-section Fig. 5.17 I) up to 16 µm in length (Fig. 5.17 B) following a criteria of length/diameter of approximatively 1.6. Progressive stages of polymer controlled assembled (non crystallographic) upgrowth of needle-shaped hexagons (Fig 5.17 H) at both end of the seed (fractal branching) (Fig. 5.17. B and Fig. 5.17 C) lead to dumbbell-shaped aggregates (Fig. 5.17 D and Fig. 5.17 F). The dumbbells complete their shape by successive and self-similar upgrowth to give notched spheres (Fig. 5.17 G) with diameter up to 70 µm after about the 5th fractal generation. The fractal growth and final architecture is controlled by two noncrystallographic parameters, which are derived from SEM images at different growth stages: (i) the maximum aperture angle between the long axis of the seed and the needlelike units of the following generation is $45 \pm 3^\circ$ (Fig. 5.17 B) in two dimension and $90 \pm 3^\circ$ (Fig. 5.17 D) in three dimension, (ii) subsequent generation scale down in their length by a factor of ≈ 0.85 while their diameter is conserved.

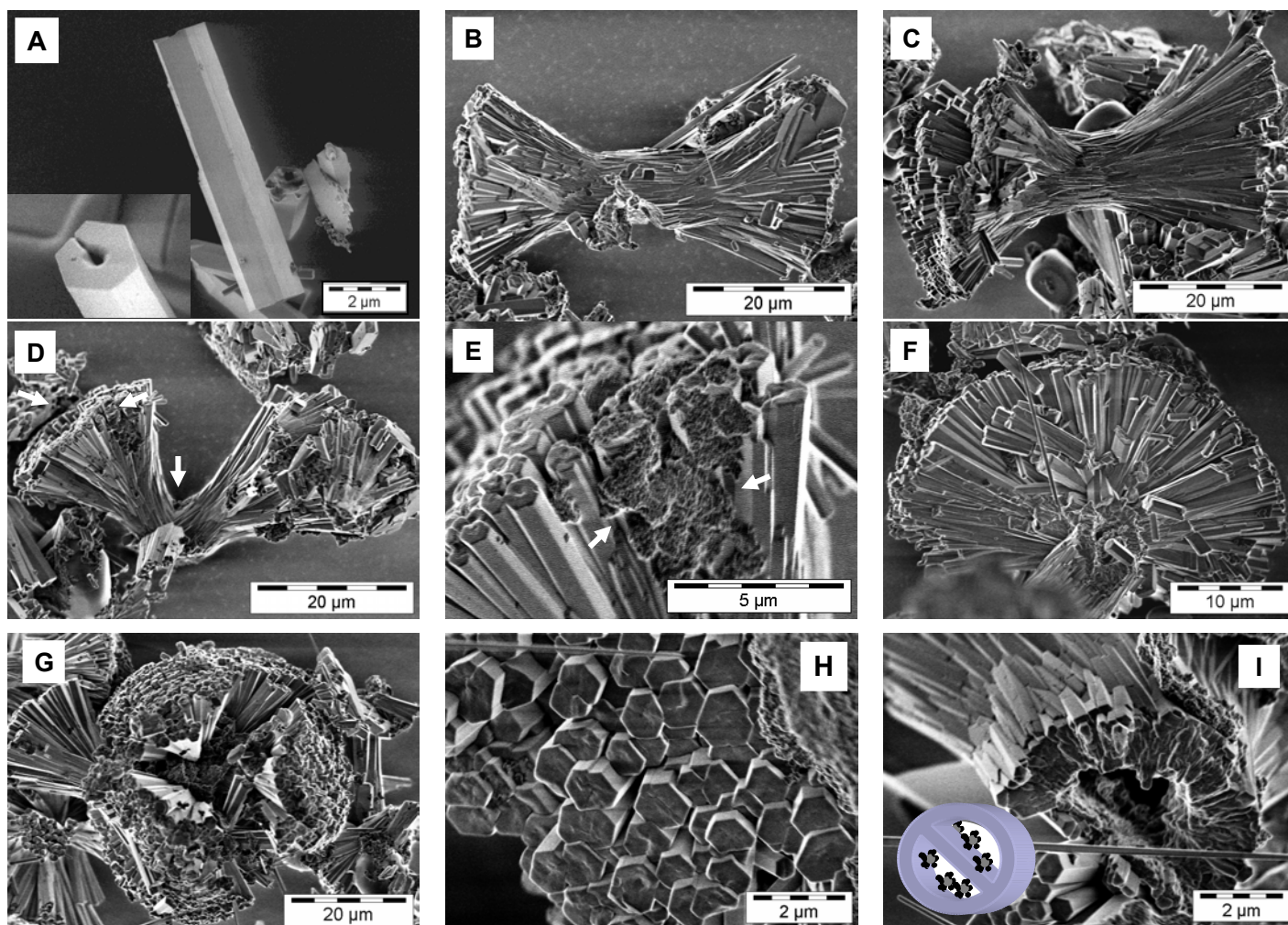


Figure 5.17: Selected sequence of SEM images of progressive polymer (positively charged latex, P(S-g-STMACl) controlled assembly (hierarchical) growth of $\text{NaZnPO}_4 \cdot 1 \text{H}_2\text{O}$ aggregates (morphogenesis) from an elongated hexagonal-prismatic seed (A) through dumbbell shape (B,C) to fully grown sphere (G), composed of six sectors separated by absorbed polymer; dumbbells displaying 2nd (B) and 3rd (C) generation (fractal) growth and a three fold splitting sector (D) of maximum opening angle measured at 90° precisely; sections of a connecting bar (I) displaying a hollow core and part of a growing dumbbell; section a growing dumbbell (F), which growth is limited by polymer absorption (E, arrows in D and E); surface of one of the six grown sectors consisting of hexagonal needlelike units (H) following the general principle of self-similarity.

As shown in Fig. 5.17 D and Fig. 5.17 E (arrows) the length reduction or limited growth of a rodlike unit is controlled by selective latex particle absorption. Inside the spherocrystal a torus-shaped cavity partitioned in three sectors forms around the elongated hexagonal seeding rod (Fig. 5.17 G). Maleev [192] and then Busch and Kniep [193] generated similar architecture by the geometrical model of a splitting needle of hydroxyapatite in presence of collagen fibrils at constant growth rate and constant splitting rate. The hexagonal to circular cross-section of the seed and the channel surrounding the seed is shown in Fig. 5.17 I. Furthermore, it is interesting to note that the cleavage area of the elongated hexagonal-circular seed is characterized by a radial structure separated in two hemispheres, starting from the middle (Model inserted in Fig. 5.17 I). This observation is in agreement with the idea of nucleation by cylindrical preorientation of macromolecular units (“liquid crystal seed”) [194].

this product for water vapour, i.e. its extremely high hygroscopicity, that proves to be reversible [201].

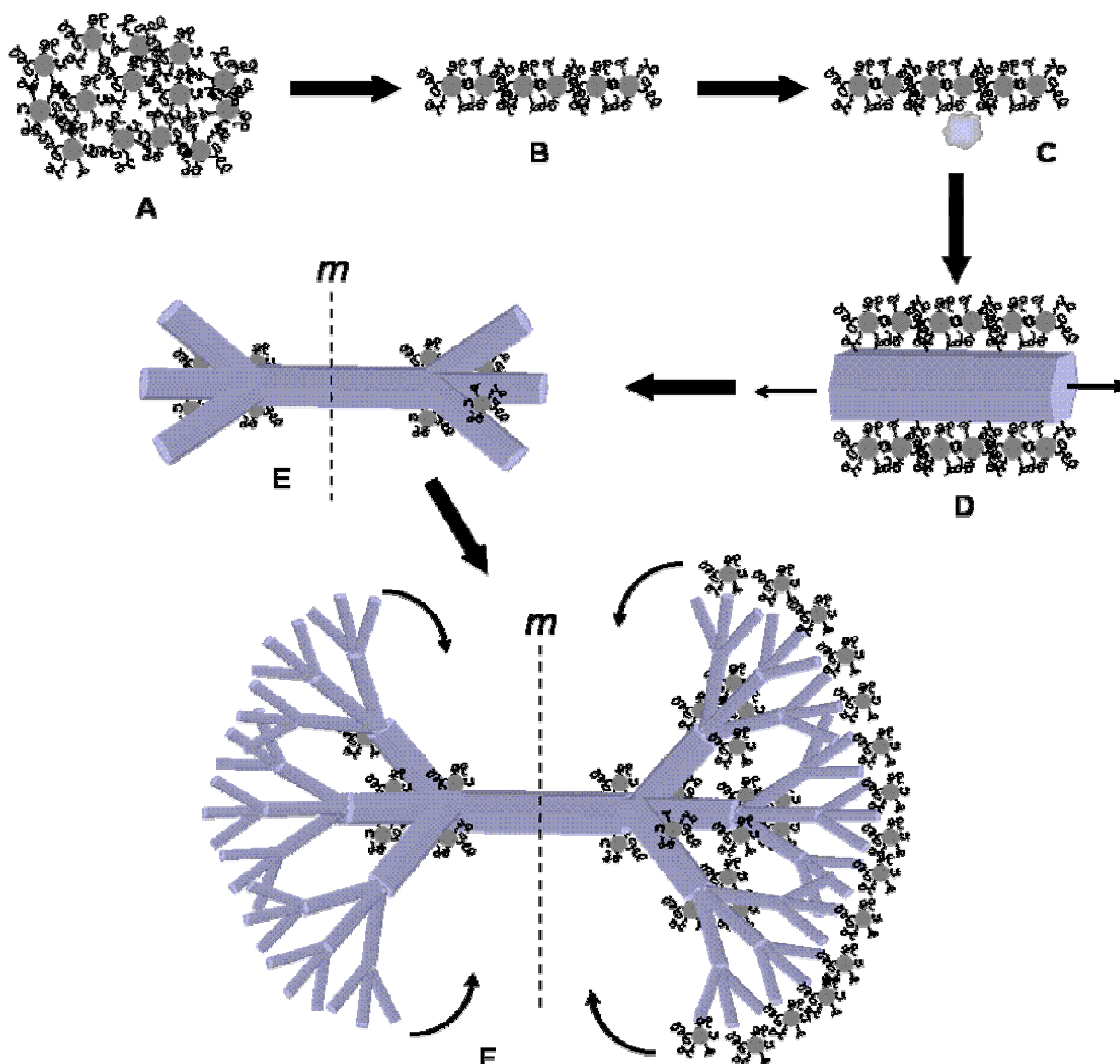


Figure 5.17: Suggested mechanism for the dendritic growth of a rod (D) formed from a nearly spherical nucleus (C) absorbed on a polymer aggregate (A,B) via dumbbell intermediate (E) to a final half-spherical structure (F), adapted from mechanisms introduced by Busch, Kniep [193, 195] and Antonietti [194]. (m) indicates the mirror plane of crystal growth.

Recently, Cölfen et al. [202] reported the controlled formation of similar mesostructured particles in presence of a polycation, poly(allylamine hydrochloride) of low molecular weight, that cannot be satisfyingly explained by the approach of Kniep et al. for negatively charged polyelectrolytes (e.g. PSS), i.e. the existence of intrinsic electric field. In contrast, elongated primary particle may well form by a dissolution-recrystallization process, which branches at both tips to form the observed dumbbell structures. The role of the polyelectrolyte appears to be fundamentally different depending on its intrinsic charge. In particular for $\text{NaZnPO}_4 \cdot 1 \text{ H}_2\text{O}$ crystallization, whereas a cationic polymer may promote crystallization of amorphous precursor particles within a spherical aggregate involving

particle bridging by the polymer, an anionic PSS will not bridge the primary particles so that crystallization of an elongated particle is favoured.

In addition, the combined but successive use of positively and negatively charged latexes [203] proves to be effective in reducing not the crystal size of $\text{NaZnPO}_4 \cdot 1 \text{H}_2\text{O}$ hexagonal crystal but the polydispersity and the shape factor to 1 (i.e. Length = width) since carboxylated latexes controls the nucleation process while highly positively charged latexes govern the crystal growth by selective absorption. This synergetic effect has been tested on ZPO crystallization but will not be reported here [204].

5.3.6. Effect of the pH and ionic strength on ZPO crystallization in presence of a negatively charged and polar latex template

pH as well as the ionic strength are known to be important parameters in hydrothermal crystallization [205]. The present study aims at developing conditions favourable to the latex controlled mineralization of basic zinc phosphate microcrystals of definite morphology, which do not extensively dissolve in neutral or basic pH conditions. Moreover, the deprotonation and subsequent coordination of Zn^{2+} ions in the latex corona is driven by pH buffering. Therefore, the solution pH may dramatically influence the ability of a latex particle to control the nucleation and growth of ZPO crystals. Since hopeite polymorphs and ZPO zeolite structures form by condensation of mixed or zinc hydrogen phosphate hydrates of low symmetry, the solution pH is thought to shift the reaction pathway by solubility modulation of the precipitating products (c.f. Chapter 6). In the pH range 4-10 (e.g. pH adjusted by addition of aliquot of 4 mol.L^{-1} NaOH and by the buffering effect of residual phosphate ions in solution), addition of a highly polar negatively charged latex P(S-g-MAN-g-MAA) to an undersaturated solution of zinc phosphate hydrate leads to unusual morphologies in the inorganic phase.

Figure 5.20 shows that at low pH, around 4, α -ZPT precipitates (c.f. Chapter 2). An increase of pH from 5 to 8 induces the formation of the kinetically favoured (metastable) hexagonal phase of $\text{NaZnPO}_4 \cdot 1 \text{H}_2\text{O}$. Spherulitic sodium zinc phosphate polyhydrate aggregates with one, two and three arm helical branches are systematically produced at 90°C above pH 9, as shown in details in Fig. 5.21. Similar crystal shapes have been mentioned by Gower [206] for CaCO_3 grown in solution of poly(aspartic/glutamic acid). As indicated by XRD (Fig. 5.22 A), in basic aqueous solution the hexagonal $\text{NaZnPO}_4 \cdot 1\text{H}_2\text{O}$ crystals convert to densely packed cubic $\text{Na}_6(\text{ZnPO}_4)_6 \cdot 8\text{H}_2\text{O}$, another analogue of hydrosoladite (ABW structure) [207].

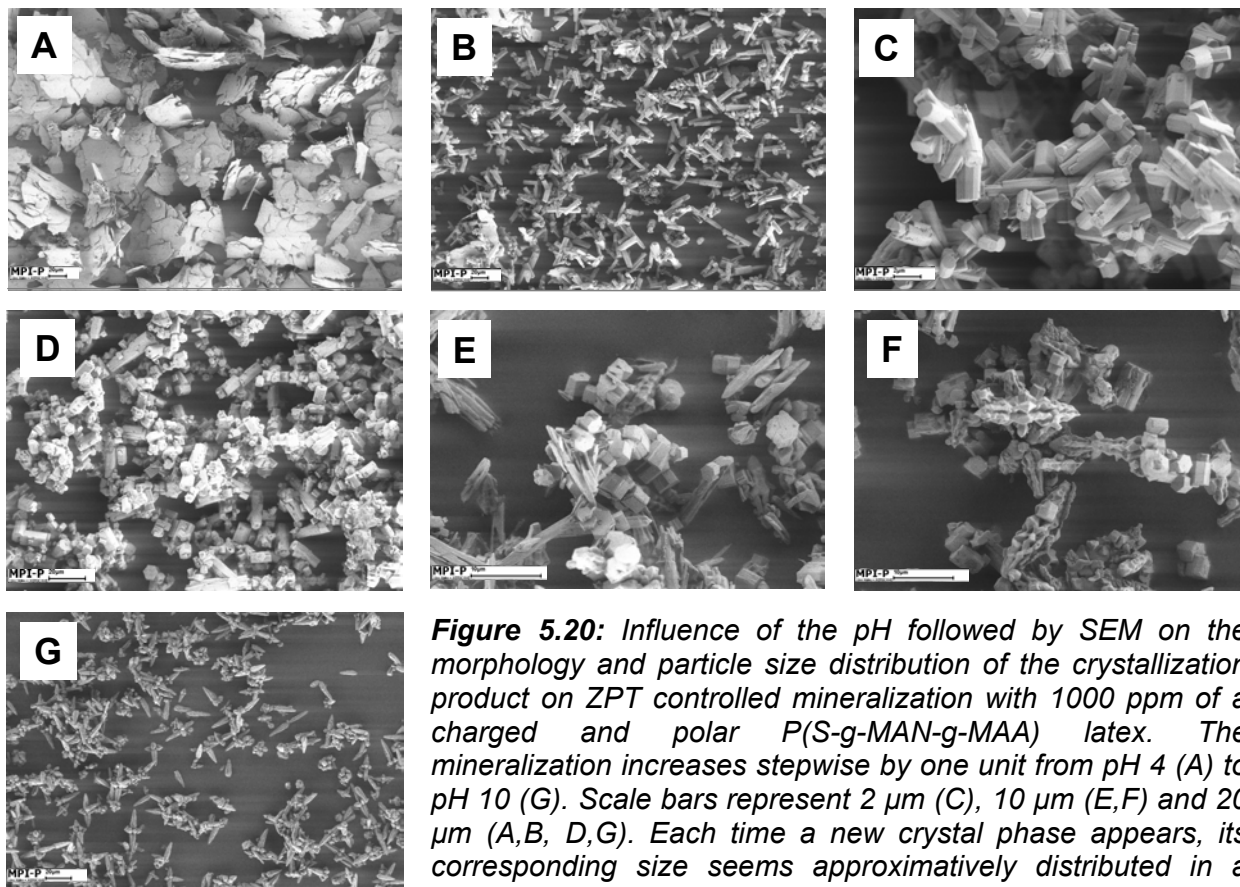


Figure 5.20: Influence of the pH followed by SEM on the morphology and particle size distribution of the crystallization product on ZPT controlled mineralization with 1000 ppm of a charged and polar $P(S-g-MAN-g-MAA)$ latex. The mineralization increases stepwise by one unit from pH 4 (A) to pH 10 (G). Scale bars represent 2 μm (C), 10 μm (E,F) and 20 μm (A,B, D,G). Each time a new crystal phase appears, its corresponding size seems approximately distributed in a monodisperse manner as shown in A, B, D and G.

Gier et al. [208] found that after crystal recovery the transformation $\text{Na}_6(\text{ZnPO}_4)_6 \cdot 8\text{H}_2\text{O} \rightarrow \text{NaZnPO}_4 \cdot \text{H}_2\text{O}$ was reversible upon heating at 200°C by loss of two crystal water. Sodium ions are inevitably present in the crystallization medium due to the necessity to increase the pH either in using an inorganic base (NaOH, KOH, etc.) or employing an organic base e.g. tetramethylammonium hydroxide, that unfortunately acts as mineralization template [209-210].

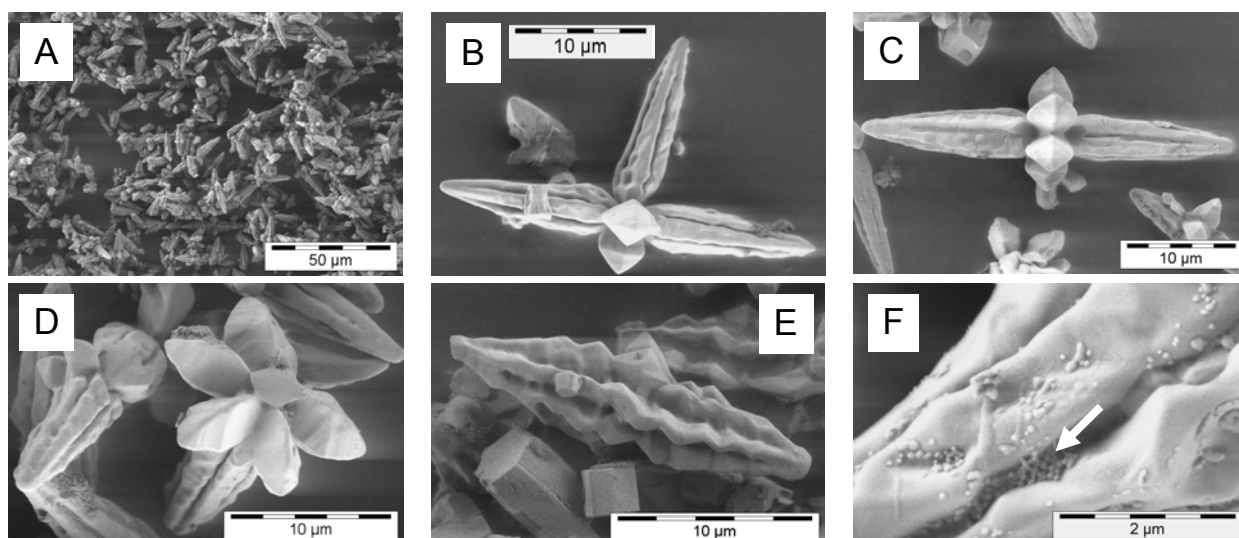


Figure 5.21: Characteristic morphologies achieved with 1000 ppm of charged, polar $P(S-g-MAN-g-MAA)$ latex for $\text{Na}_6(\text{ZnPO}_4)_6 \cdot 8\text{H}_2\text{O}$ at different stage of crystal growth: (A) overview, (B,C) planar two and three arm lancelet or helix (D) floret morphology, (E) dendritic twin crystal (F) adsorbed latex particle hindering crystal growth (arrow).

As shown in Fig. 5.21 E, latex particles are obviously adsorbed in the microchannels of two-arm lancet of $\text{Na}_6(\text{ZnPO}_4)_6 \cdot 8\text{H}_2\text{O}$. These latex particles may selectively adsorb on the edge of growing $\text{Na}_6(\text{ZnPO}_4)_6 \cdot 8\text{H}_2\text{O}$ cubes, by synergic interaction of functional groups contained in the latex corona (i.e. a highly polar group, acrylonitrile and charged group, methacrylic acid) with the crystal structure [211], and emphasizes by XRD (Fig. 5.20 A) via the presence of N- $\text{PO}_3\text{-H-X}$ (e.g. $\text{X} = \text{Na}^+, \text{Zn}^{2+}$) peaks, especially at 22.96° and 33.45° assumingly corresponding to crystallized organic amide [212]. As displayed in Fig. 5.22 B, sodium ions via their concentration are “linearly” proportionally incorporated in the forming zeolitic crystal structure as pH increases. This was first detected by a divergent reaction yield and the rapid formation of a gel, which transforms to a thick, creamy slurry on mild stirring above pH 8. It may be straightforwardly concluded that at low temperature ($20^\circ\text{C} < T_{\text{cryst.}} < 95^\circ\text{C}$) and under high ionic strength ($I \approx 0.3\text{-}0.5 \text{ mol.L}^{-1}$) such a system is fairly sensitive to the sodium to zinc molar ratio in the synthesis mixture.

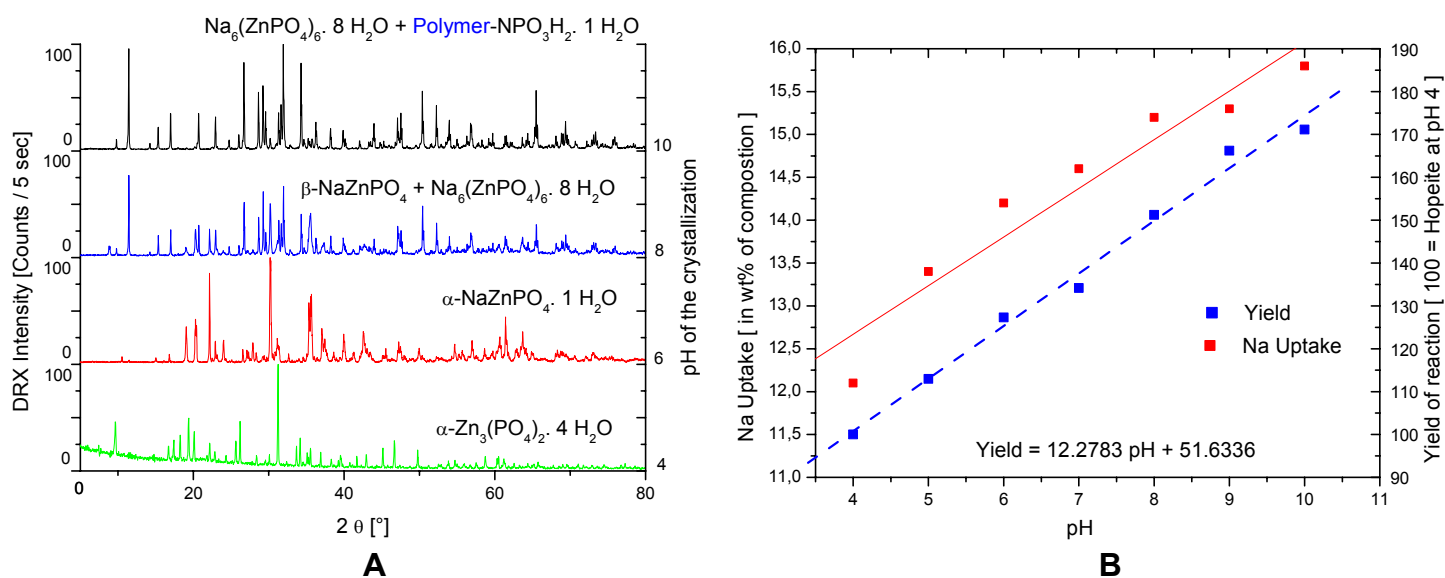


Figure 5.22: Influence of the pH regulated by addition of a 4 mol.L^{-1} NaOH solution, on the phase of the crystallization product on ZPT controlled mineralization with 1000 ppm of charged, polar P(S-g-MAN-g-MAA) latex. The formation of sodium containing zeolitic structures may be followed by XRD (A) and elemental analysis, thus explaining the divergence of the yield of crystallization from the synthesis of α -ZPT.

If less than 2/3, α -ZPT is formed, and if greater, until around 1, the latex particles stabilize (i.e. nucleate) an infinite variety of hydrated acid or basic sodium zinc phosphates (e.g. $\text{NaZn}_2(\text{HPO}_4)(\text{PO}_4)$ [213], $\text{Na}_2\text{Zn}(\text{H}_2\text{PO}_4)_4 \cdot 4\text{H}_2\text{O}$ [214], $\text{Na}_6\text{Zn}_3(\text{PO}_4)_4 \cdot 3\text{H}_2\text{O}$ [215], $\text{NaZn}(\text{HPO}_4)(\text{PO}_4)$ [216], $\text{NaZn}(\text{PO}_4)(\text{OH})$ in § 5.4) also observed, fully characterized but not reported here for the clarity of this chapter. But the synthesis route of a majority of these zeolitic structures involves extreme conditions (e.g. high temperature, low concentration, day long precipitation). Thanks to the up/down classification of Liebau [217], a common feature of all these multidimensional open-framework structures derives with the synergic presence of hydrogen

bondings and sodium ions intercalated in 4-to-8 membered ring forming channels (i.e. Na^+ invariably located in a distorted octahedral environment). Therefore it is tempting to speculate that the latex corona is the privileged location for cation (e.g. Na^+ , Zn^{2+}) exchange before ion condensation and (nucleus) precursor formation.

5.3.7. Kinetics of ZPO crystallization

The evolution of the crystal morphology along the crystal size distribution (CSD) [218] with the crystallization time at a fixed concentration of latex additive may help elucidate certain aspects of the important role of a semi-rigid template in the crystallization of zinc phosphate based zeolites.

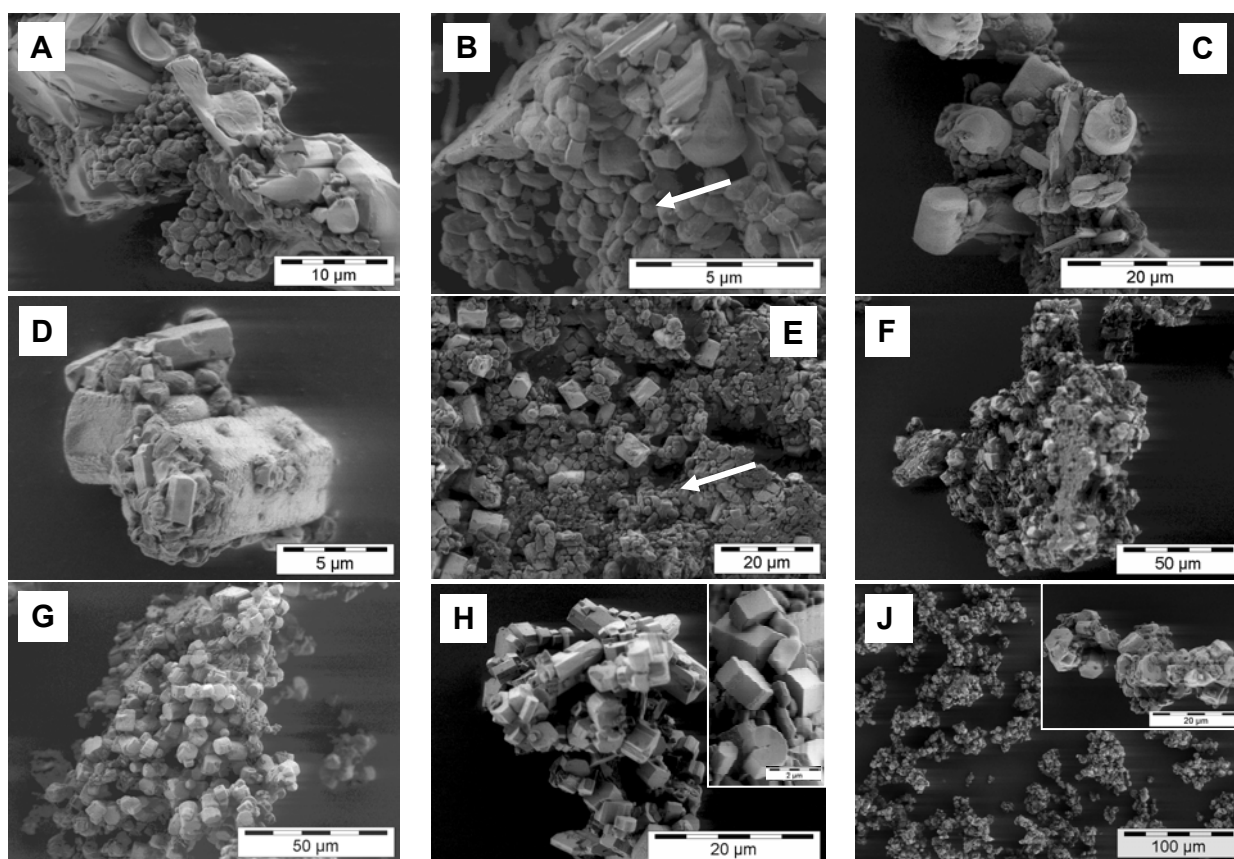


Figure 5.23 : Kinetics of crystal growth of $\text{NaZnPO}_4 \cdot 1\text{H}_2\text{O}$ grown in the presence of 1000 ppm of a carboxylated latex $\text{P}(\text{S-g-MAA})$ containing 4 wt% MAA/S followed by SEM: (A) 1 min, (B) 2 min, (C) 5 min, (D) 10 min, (E) 30 min, (F) 45 min, (G) 60 min, (H) 120 min, (I) 180 min. Arrows point out possible latex stabilized nuclei.

Figure 5.23 shows the crystallization kinetics as followed by SEM. The corresponding time dependence of the CSD in length L_1 is reported in Figure 5.24. Even with a latex concentration of around 900 ppm, a uniform and narrow distribution of G_1 particles is already obtained after one minute and rapidly transforms (i.e. approximately 5 minutes) in a bimodal distribution of small particles (population G_1) coexisting with growing hexagonal crystals (population G_2) as shown in Fig. 5.23 C. While the CDS of G_1 particles is becomes larger after 10 min and the population density

steadily centered around 800 nm decreases, the CDS in length becomes broader and dissymmetric. This suggests (i) first that nucleation takes place by cluster formation as mentioned by Taubert et al. [219] and Weller et al. [220], since the G_1 particles distribution is uniform; (ii) that the latex particles are powerful nucleation promoters for this first metastable (amorphous) precipitate [221] since a latex particle and $\text{NaZnPO}_4 \cdot 1\text{H}_2\text{O}$ nucleus measure around 70 nm and 10 nm respectively, compared to a pristine size of 800 nm observed by SEM; (iii) that the final crystal CDS is controlled essentially by the nucleation step, since it is dissymmetric with a tail of distribution oriented to higher size and that no latex particles are found adsorbed on crystal faces, as shown in Insert in Fig. 5.23 G.

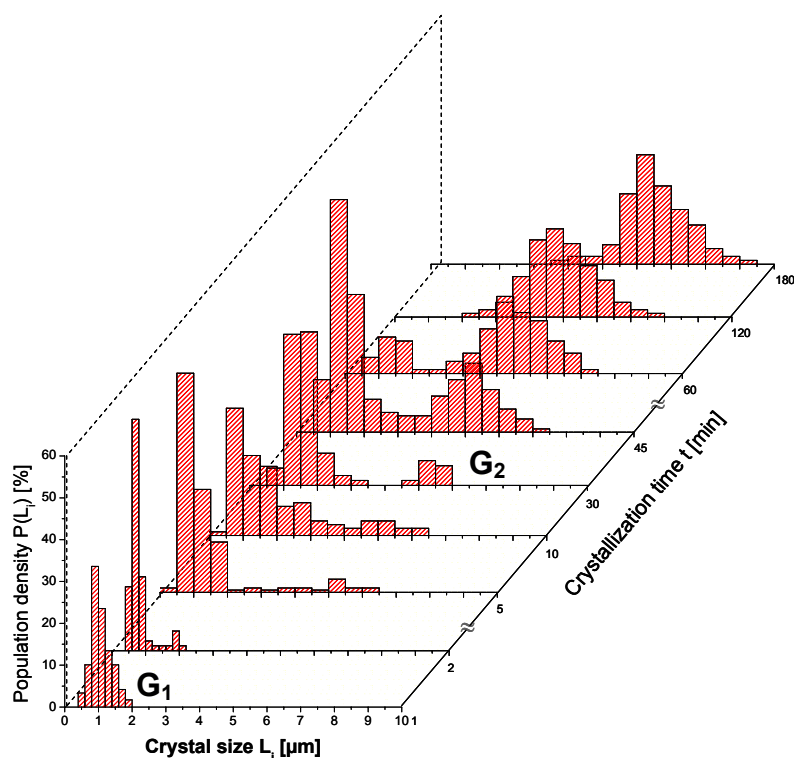


Figure 5.24: Transient particle size distribution in number (i.e. frequency analysis) for $\text{NaZnPO}_4 \cdot 1\text{H}_2\text{O}$ grown in the presence of 1000 ppm of a carboxylated latex P(S-g-MAA) containing 4 wt% MAA/S. At initial time a Gaussian distribution of particles (population G_1) is instantaneously achieved due to the presence of the latex, and rapidly transforms partly in growing crystals (population G_2) through a bimodal distribution, appearing after 5 min and predominating after 30 min.

This may be explained by strong coulombic repulsion between the negatively charged crystal surface and the carboxylated latex particles [222]. For example, while the first G_1 particles formed at the induction time of nucleation t_n (i.e. 1 min) transform in large crystals after 150 min, nuclei formed after 10 min deliver crystals of smaller size, if the growth rate is independent of the crystal size, i.e. if the surface energy is not modulated by the face area and the crystallographic nature of the growing crystal face, and if the growth rate is constant with time. The existence of a non oriented growth is proved by reporting the crystal length L , width W and aspect ratio (i.e. shape factor R) along with the crystallization time as given in Fig. 5.25 A. During crystal growth, the length and width of an individual crystal increase linearly with time:

$$L(t) = 4.971 + 0.00806 \cdot t \text{ in } \mu\text{m} \quad \text{and} \quad K_{app}^{growth}(L) : 8.06 \cdot 10^{-3} \mu\text{m} \cdot \text{min}^{-1} \quad (5.2)$$

$$W(t) = 3.791 + 0.001619 \cdot t \text{ in } \mu\text{m} \quad \text{and} \quad K_{app}^{growth}(W) : 16.19 \cdot 10^{-3} \mu\text{m} \cdot \text{min}^{-1} \quad (5.3)$$

The growth rate in width is two times higher than the growth rate in length, i.e. $K_{app}^{growth}(W) \approx 2 K_{app}^{growth}(L)$. In respect to the hexagonal crystal morphology, the crystal grows in the (110) crystallographic plane at the same rate $K_{app}^{growth}(L)$ along *a*- and *b*-axis or in other words along the directions [100], [$\bar{1}$ 00], [010] and [0 $\bar{1}$ 0]. This demonstrates that the crystal growth is homogeneous in each direction and crystallographically controlled with a rate of 8 nm.min⁻¹ or around 6 unit cell/minute. The calculated value of the growth rate constant is in good agreement with those obtained from the published and presently processed data of Taubert et al. [82] for the crystallization of ZnO at 90°C in presence of carboxylated and sulfonated DHBCs with $13.56 \cdot 10^{-3} \mu\text{m} \cdot \text{min}^{-1}$ and $2.23 \cdot 10^{-3} \mu\text{m} \cdot \text{min}^{-1}$ respectively.

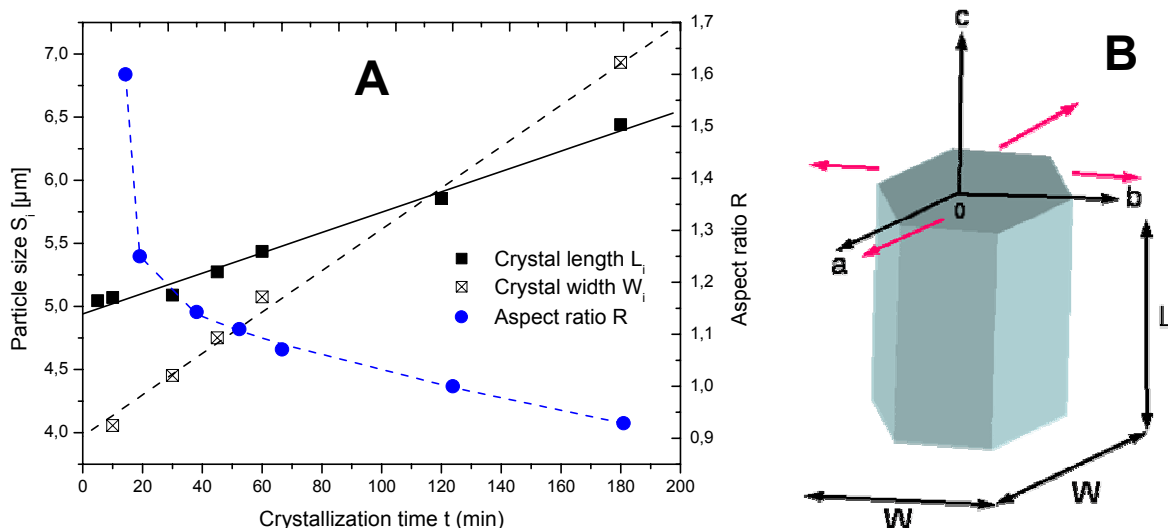


Figure 5.25: Time dependence of the crystal morphological characteristics (length *L*, width *W* and aspect ratio *R*, as defined in (B)) obtained from the SEM investigation of the crystallization kinetics of NaZnPO₄ · 1H₂O grown in the presence of 1000 ppm of a carboxylated latex P(S-g-MAA).

These values of $K_{app}^{growth}(L)$ fluctuate depending on the chemical nature of the functional group, which in turn depends on its overall ability to coordinate a M²⁺ ion. As crystallization proceeds, the aspect ratio *R* decreases asymptotically from a threshold clearly above one (around 1.6 shortly after nucleation) to a value of 0.9 after 150 min. These changes of *R* are directly related to its definition (i.e. $R = L / W$) and the linear dependence of both crystal length and width with reaction time. Therefore it may be concluded that the crystal growth of NaZnPO₄ · 1H₂O follows a three dimensional Johnson-Mehl-Avrami (JMA) growth mechanism and not a diffusion controlled one [223]. This is further supported by the fact that Nancollas et al. reported a bidimensional non diffusion controlled growth for the most stable zinc phosphate (pure α-ZPT) structure [224].

5.3.8. Effect of concentration of a carboxylated latex on ZPT crystallization

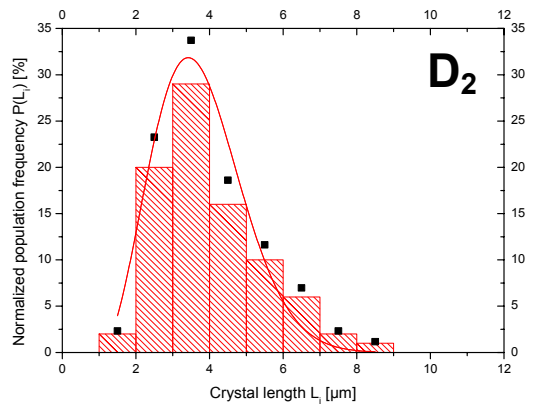
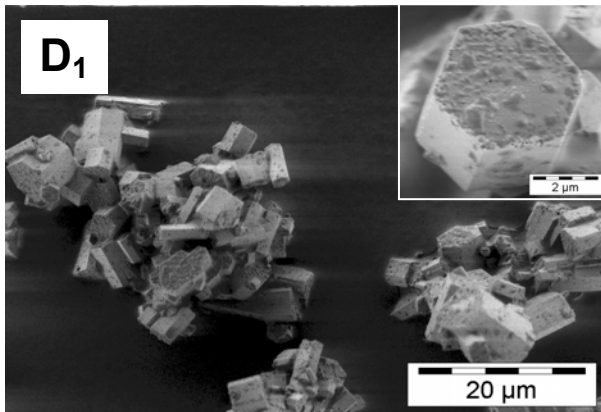
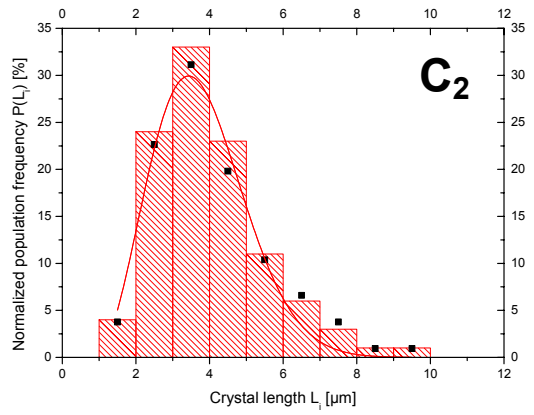
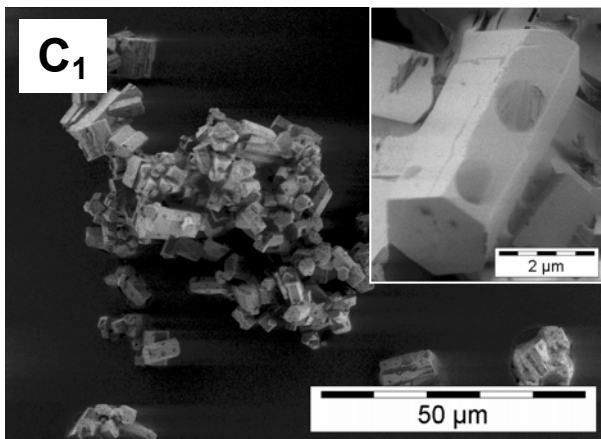
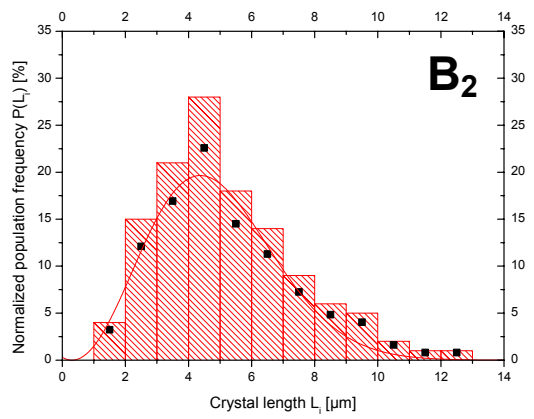
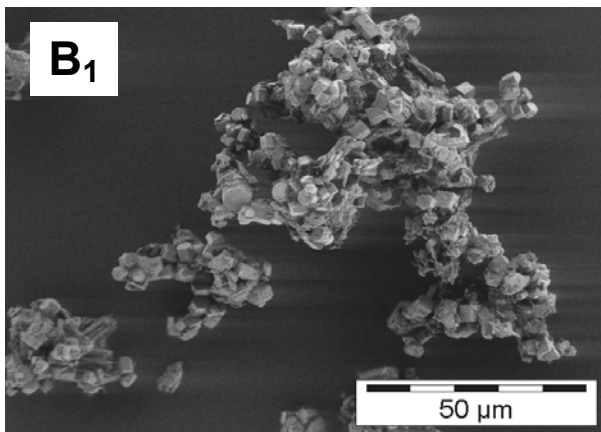
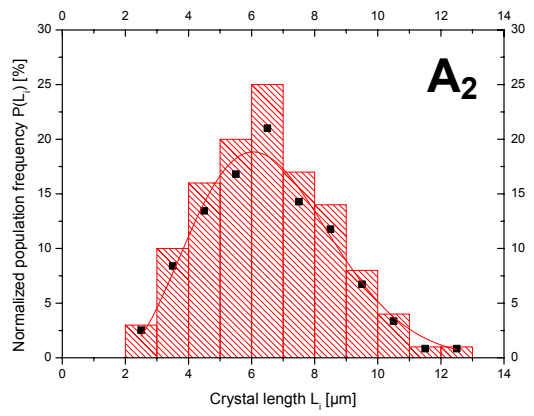
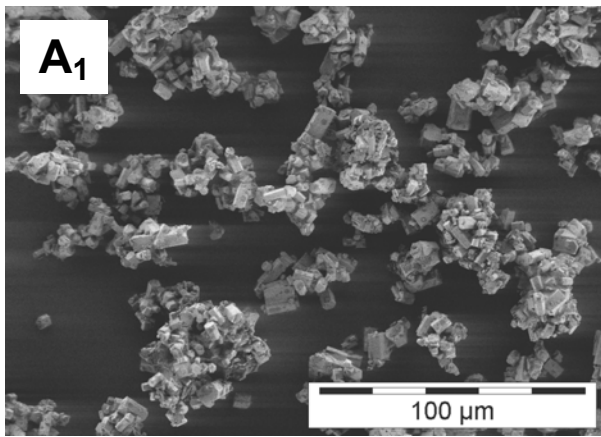
The importance of DHBCs additives functionalized with maleic acid and vinylsulfonic acid simultaneously on nucleation rate, crystal growth rate and induction time in unseeded precipitation of BaSO₄ has been theoretically described and validated by Van der Leeden et al. as early as 1992 [225]. Such a study could appropriately shed some light on the basic step mechanisms of crystallization involving a flexible polymer (e.g. cluster formation, nucleation, controlled growth by selective adsorption, aggregation by bridging, etc.). The difference between inhibiting and nucleation function of polyelectrolyte has been attributed by Füredi-Milhofer et al. [102] to the additional aspect of their activity besides their concentration [226]. It was already observed by Zettlemoyer et al. [227] and then Birchall et al. [228] 25 years ago that flexible polyelectrolytes act as crystal nucleation inhibitor, but when immobilized on suitable surfaces the same macromolecules can act as strong nucleator. For instance, Addadi et al. [229] reported the induced oriented nucleation of calcite by polyaspartate adsorbed in β -sheet conformation on sulfonated polystyrene surfaces. Such polymeric structures are very similar to the latex additives employed in ZPO crystallization. Therefore latexes may reasonably act as nucleation agent of ZPO crystals. One way of confirming this is to study the kinetics of ZPO crystallization at increasing latex concentration, therefore it is precisely the aim of the following study.

Furthermore, theoretical expressions for the induction time applicable to seeded and unseeded zeolitic precipitation systems, developed by Verdoes et al. [230] allow the separate determination of nucleation time and growth rate in dependence of the polymeric additive concentration, based on the size distribution of the final product [231-233].

When nucleation and growth steps are decoupled, the precise effect of the polyelectrolyte can be assessed. The suspension response in terms of change of crystal morphology to the addition of increasing concentration of a carboxylated latex P(S-*g*-MAA) in an undersaturated solution (ionic strength $I \approx 0.4 \text{ mol.L}^{-1}$) is presented in Figure 5.26(1) by SEM investigation of the final product. The crystal shapes stay of hexagonal type on increasing latex concentration as reported in § 5.3.5 for a fixed concentration. Fig. 5.26(2) compares the crystal size distribution of grown crystal determined from SEM images and statistically calculated by the following CSD equation:

$$P(L_i(t)) = \frac{n_i^{crystal}}{N_{tot}}(t) = A(L_i(t) - L_{min}(t))^2 \cdot \exp[-B \cdot (L_i(t) - L_{min}(t))^2] \quad (5.4)$$

where, at an observation (crystallization) time t , N_{tot} is the total number of crystal, $n_i^{crystal}$ is the number of crystals of length L_i , and L_{min} is the length of the smallest crystal.



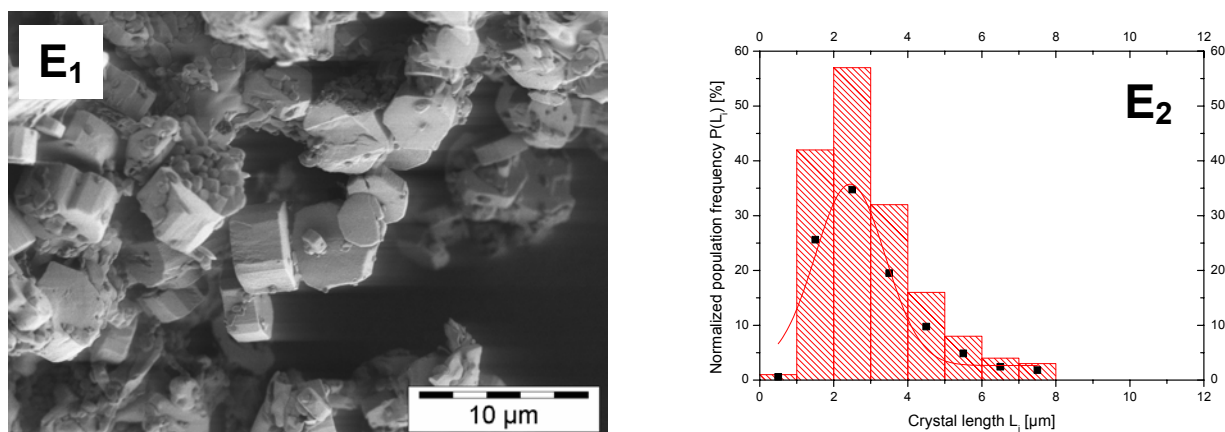


Figure 5.26: Influence of an increasing concentration of a P(S-g-MAA) latex on (1) crystal morphology and (2) on crystal length distribution [absolute (■) and normalized (■)] for (A) 229 ppm, (B) 458 ppm, (C) 687 ppm, (D) 916 ppm and (E) 1145 ppm.

This expression is modified from the well-known nucleation rate equation of zeolite $dn_i^{nuclei}/dt = At^3 \cdot \exp(-Bt^2)$ proposed by Barrer [231]. This statistical model fits perfectly the experimental distributions since it takes into account the distribution tail, corresponding to very large crystals. The characteristic shape of the distribution has already been discussed in § 5.3.5. In such a distribution adjustable parameters A and B are related to amplitude and width of distribution, respectively.

[Latex] (ppm)	CSD Amplitude A	CSD width B	L_{min} (μm)	Relative induction time ($t_{nf}-t_n$) (sec) ^a
229	2.596	0.0507	1.604	58.79
458	3.255	0.0609	1.014	48.85
687	11.578	0.1473	0.959	26.71
916	14.234	0.1644	0.829	23.52
1145	27.083	0.5453	0.311	8.63

Table 5.5: Summary of the parameters related to the crystal size distribution in length after 150 min and induction time of nucleation in dependence of the P(S-g-MAA) latex concentration.

(a) Determined from Fig. 5.28.

For increasing latex concentration, the CSD in length narrows and is shifted to lower size values (Fig. 5.26) and values of A and B increase, indicating a narrowing CSD and are summarized in Table 5.1. The length L_{min} of the smallest crystals is also shifted to lower values, from 1.6 μm at 229 ppm to around 310 nm at 1145 ppm. This is directly related to the control of the nucleation step by the particles. Nuclei are formed at the initial stage of the crystallization. If the nuclei grow to a certain size $L_i(t)$, they grow into crystal (c.f Chap. 4 and reference [234] on the thermodynamic approach of the homogeneous nucleation). However a certain fraction of them dissolve back to the solution before they grow to a certain size $L_i(t)$. Fig. 5.27 displays the evolution of the crystal length of the G_2 population (refer to Fig. 5.22) as crystallization proceeds in dependence of the latex concentration. First, the crystal length increases linearly with time for a given additive concentration

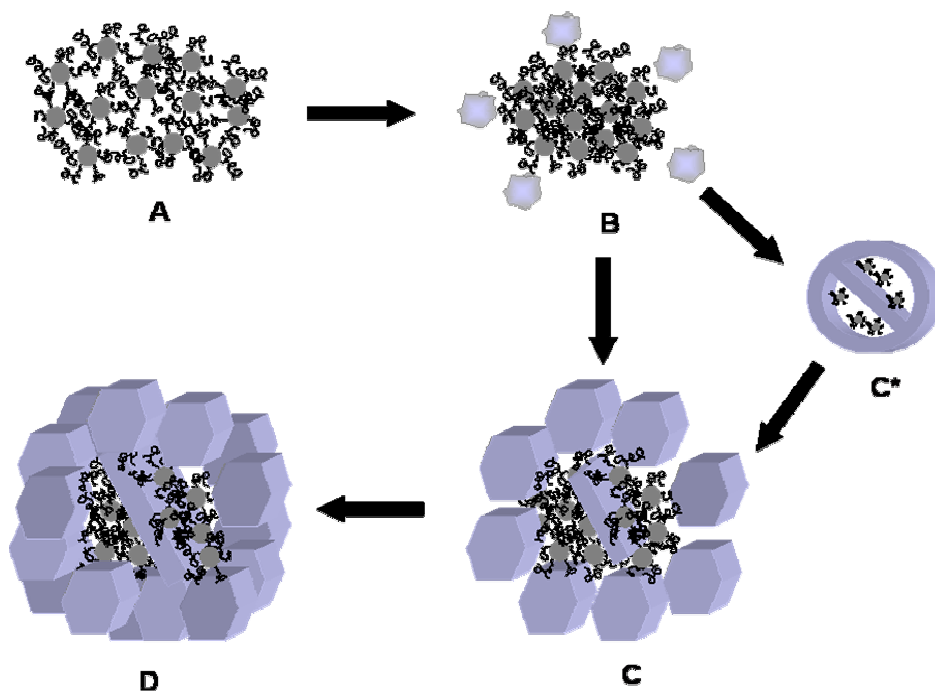


Figure 5.18: Proposition of simplified formation mechanism of a hollow (polymer filled) core of a dumbbell connecting bar: (A) aggregation of latex particle caused either by Zn^{2+} bridging or by salt screening effect, (B) formation of $NaZnPO_4 \cdot 1 H_2O$ precursor by extra-corona nucleation and absorption on polymer aggregate, (C) transformation of nuclei in hexagonal crystal, (D) crystal growth by self-similarity and secondary nucleation. (C*) represents the idealized splitting of the core in two hemisphere under influence of possible strong intrinsic electric fields stemming from the crystal structure itself.

Consequently, this leads to propose the seeding mechanism given in Fig. 5.18. The complex but symmetric structure of growth, i.e. existence of a (mirror plane perpendicular to the long axis of the connecting rod corresponds to a fractal growth model given in Fig. 5.19. Busch and Kniep [195] and then Cölfen et al. [196] give an interpretation for this noncrystallographic (fractal) splitting of crystal generations and for the overall polymer mediated / self-assembled core aggregates based on the existence of intrinsic electric fields and permanent dipole/quadrupoles, also observed by Antonietti et al. [197] on $BaCO_3$ and consistent not exclusively with the local asymmetry of the $NaZnPO_4 \cdot 1 H_2O$ internal structure (four ring square loop composed of a $ZnPO_4$ central unit bonded into an 8-ring of neighboring PO_4 groups, and growing in helix along c-axis) [198-199], but also with the possible charge nonuniformity at the latex surface, as suggested by Feick et al. [200]. The basic premise of this hypothesis is the presence of intrinsic electric fields which take control over the growth of the aggregates since the hexagonal seed, as well as the following generations, contain a permanent dipole, mainly due to the presence of highly disordered crystal water and Na^+ ions [200], partially occupying the six distinct atomic guest sites of this β -zeolitic structure. Finally, the absorbed latex, bearing polar and positively charged organic component and the inorganic material may act together (phosphate-ammonium ionic interaction) in the sense of an organized composite structure, which gives rise to the formation of a strong intrinsic (i.e. trapped inside the inorganic superstructure) permanent dipole. Therefore, this permanent dipole, combined with the high specific surface arising from this particular crystal morphology might well explain the extraordinary affinity of

and this tendency is similar for the whole range of concentration tested. The slopes of these curves K_{app} and the initial crystal length L_0 decrease concomitantly with increasing latex concentration.

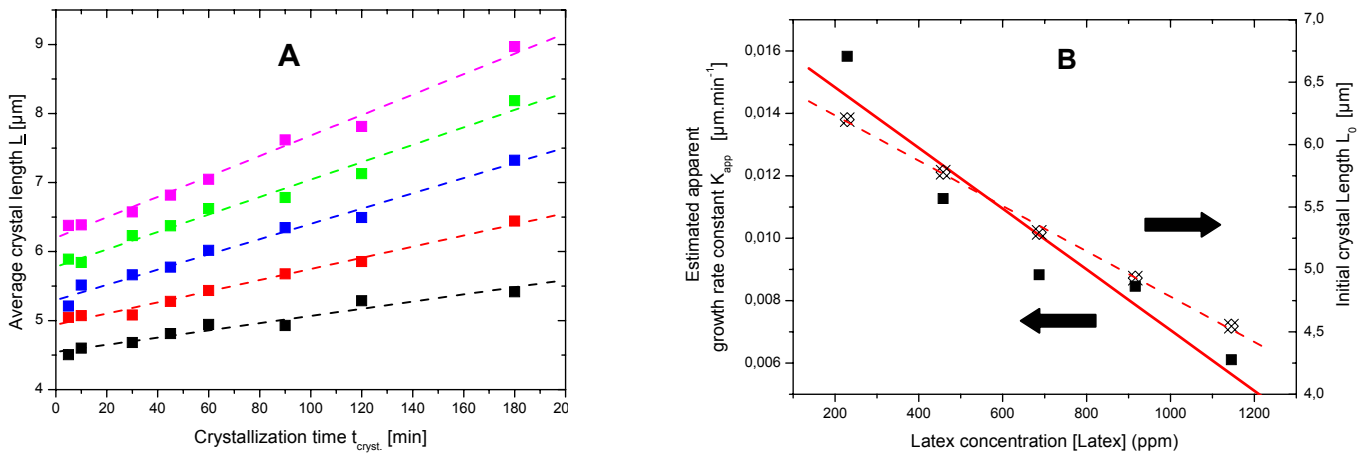


Figure 5.27 : Influence of an increasing concentration of a P(S-g-MAA) latex on (A) crystal growth and (B) crystal growth rate constant K_{app}^{growth} and the crystal length at the first instant of crystallization, determined from the kinetics of crystallization of $\text{NaZnPO}_4 \cdot 1\text{H}_2\text{O}$. Increasing latex concentration: (■) 229 ppm, (■) 458 ppm, (■) 687 ppm, (■) 916 ppm and (■) 1145 ppm.

If one assumes the primary role of latex particle on nucleation, the corona of a latex particle can deplete Zn^{2+} ions from the solution because of the water of hydration present in the corona [233]; the complexation efficiency (complex stability) depending on the chemical nature of the functions forming the latex corona and the ionic radius of the metal ion. Alternatively, since aqueous poly(ethylene oxide) solutions phase separate at high temperature [236] and weak polyacids nearly “irreversibly” complex divalent metal cations and subsequently precipitate, nucleation may not occur in solution but on or in the latex corona (phase separated polymer region) containing poly(acrylic acid) complexing Zn^{2+} . Hartgerink et al. [237] found that synthetic peptide amphiphile (PA) fibers showed increased electron density prior to precipitation of hydroxyapatite. This was interpreted as to be due to a high local ion supersaturation on the PA Fibers. In the present case, the latex leads to a local increase of Zn^{2+} concentration via complexation of the metal ions but the latex may also stabilize the crystal nuclei as they start appearing in the reaction medium. Thus local supersaturation in the latex corona (intra-corona nucleation mechanism) and undersaturation in the mother liquor is achieved more rapidly at higher than at lower latex concentration. Since the number of latex particle increases, less zinc ions are available in the surrounding medium for crystal growth. Thus growing crystals attain a smaller size as the latex concentration increases. This justifies the decrease of K_{app} , L_0 and L_{min} values with increasing latex concentration. As suggested by Eidelman et al. [238], it is also very likely that the increase of the growth rate constant K_{app} at low latex concentration might be related to a decrease of free energy for two dimensional surface

nucleation caused by nucleus adsorption on the latex corona (extra-corona nucleation). Furthermore, Nyvlt [239] proposed to relate the apparent crystal growth constant and the correct crystal growth constant by the supersaturation s as follows: $K_{app} = K_{cryst} \cdot s$. Samuelich et al. [240] and later Thompson et al. [241] proposed a method to deduce the rate of nuclei formation from the CSD obtained at the final time t_f (e.g. 150 min) since the nuclei grow to final product at a constant rate K_{app} . The nuclei formed at $t = t_{no}$ (initial time of nuclei formation) grow to crystals of length L_{max} at t_f . Therefore the length L_i of the crystal grown from the nuclei formed at t_{ni} ($t_{no} < t_{ni} < t_{nf}$), can be expressed as a function of the time of nuclei formation t_{ni} as follows:

$$L_i(t) = K_{cryst} \cdot s \cdot (t_{nf} - t) = K_{app} \cdot (t_{nf} - t) \text{ at a given } [Latex] = Cte \quad (5.5)$$

$$\Leftrightarrow t = t_{nf} - \frac{L_i(t)}{K_{app}} \quad (5.6)$$

The fraction s represents the solubility of ZPO at the crystallization temperature of 90°C (refer to Chapter 6) and is assumed to stay approximatively constant during nucleation. By substituting $L_i(t)$ in Eq. (5.3), the fraction of nuclei $P(n_{ni}(t))$ as a function of crystallization time can be expressed as follows:

$$P(n_{ni}(t)) = \frac{n_{ni}}{N_n^{tot}}(t) = AK_{app}^2 (t_{nf} - t)^2 \cdot \exp[-B \cdot K_{app}^2 (t_{nf} - t)^2] \text{ for } t \geq t_{ni} \quad (5.7)$$

where N_n^{tot} is the total number of nuclei formed and grown to final crystal and n_{ni} is the number of nuclei grown at t_{ni} . t_{nf} might be determined from the largest length L_{max} of final product and is taken constant at 150 sec (see Fig. 5.26 § 5.3.5). Figure 5.28 shows the rate of nucleation in function of time for increasing latex concentration. With increasing latex concentration the nucleation time decreases while the maximum rate of nucleation increases and the distribution of rate of nucleation broadens.

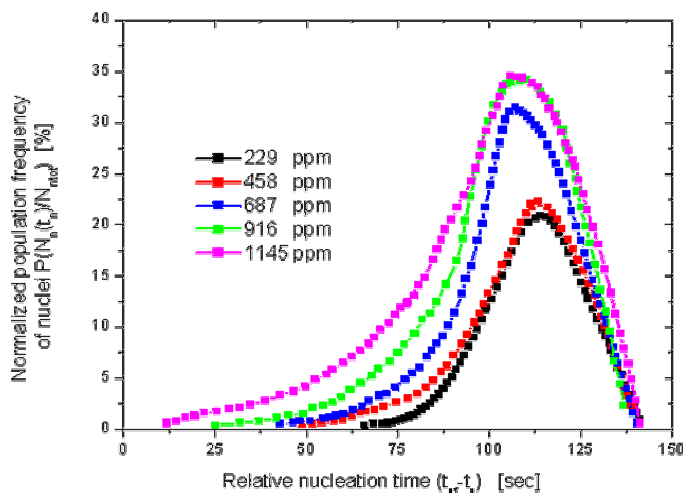


Figure 5.28: Influence of an increasing concentration of a P(S-g-MAA) latex simultaneously on the relative nucleation time and on the rate of nuclei formation of $\text{NaZnPO}_4 \cdot 1\text{H}_2\text{O}$ deduced from crystal size distribution of final product (180 min) at 90°C. After 150 sec, the nuclei either transform into growing crystals or redissolve on aging. The linear dependence of induction time and maximum rate of nucleation with additive concentration indicates that latex particles act as nucleation agent of hexagonal $\text{NaZnPO}_4 \cdot 1\text{H}_2\text{O}$ crystals.

The rate of nucleation should increase in presence of an increasing latex concentration since an increasing number of latex particles are available for potential nucleation. Nevertheless the rate of nucleation in presence of latex particles may be lower than that without latex particles (i.e. α -ZPT nucleation) since some platelets of hopeite are observed by SEM (Fig. 5.26) at the final stage of crystallization. Besides, on increase of latex concentration, the aggregation tendency of latex generated nuclei diminishes first due to a lowering of Zn^{2+} concentration in solution that may cause bridging or flocculation and secondly by a providential stabilization of subcritical nuclei by latex particles free of nuclei in their corona (i.e. extra-corona nucleation process). So the distribution of rate of nucleation should narrow as the latex concentration increases. On the contrary it diminishes due to contradictory effects, as indicated in relation (5.6). On one side, the CSD narrows as the latex concentration increases, but on the other side K_{app} decreases with increasing latex concentration. This results in a broad distribution of nucleation rate at increasing $[Latex]$. The maximum density of nuclei increases from 21 % at 229 ppm to 35 % at 1145 ppm and is shifted to shorter time, from 106 sec at 1145 ppm to 114 sec at 229 ppm at increasing $[Latex]$. Similarly, the induction time decreases from 59 sec at 229 ppm to less than 8 sec at 1145 ppm.

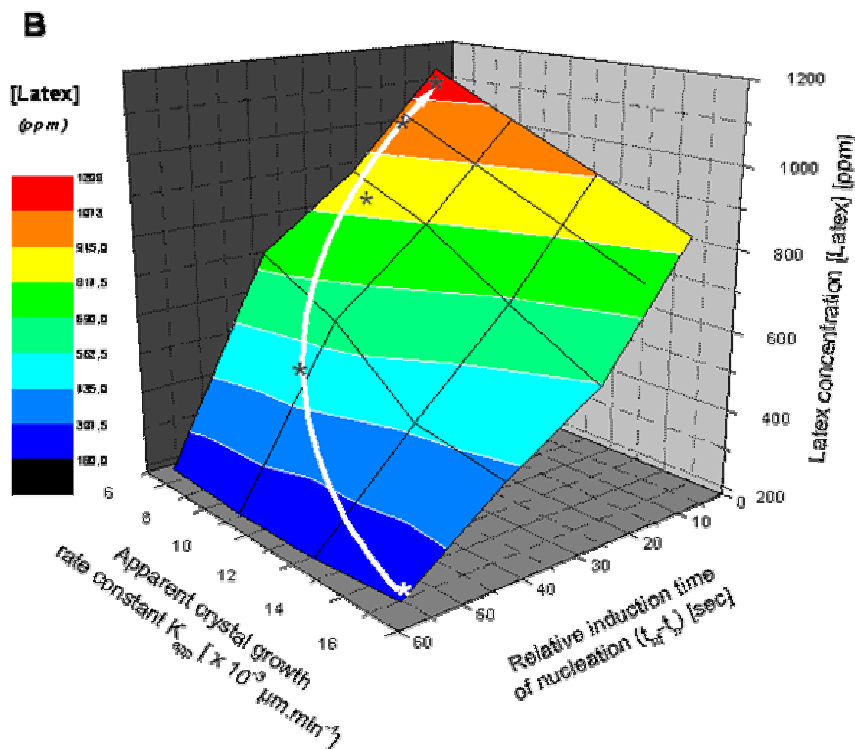


Figure 5.29 : Influence of an increasing concentration of a P(S-g-MAA) latex simultaneously on the elementary step of crystallization, i.e. on the relative nucleation time and on the apparent constant of crystal growth rate of $NaZnPO_4 \cdot 1H_2O$ deduced from crystal size distribution of final product (180 min) at $90^\circ C$, illustrating the prevalent role of latex particle on nucleation. Star labels refer to the preferential crystallization pathway controlled by the presence of carboxylated latex.

This proves irrefutably the primary role of rigid and negatively charged latex particles on the nucleation process of $NaZnPO_4 \cdot 1H_2O$. This is summarized on the three dimensional diagram of the

NaZnPO₄ · 1H₂O crystallization in Fig. 5.29, where the concurring influences of increasing latex concentration on both nucleation step and growth step are simultaneously depicted, thus giving an immediate overview of the efficiency of a latex additive on ZPO mineralization. Nevertheless the recent communication of Föderi-Milhofer [240] suggest that the influence of polyelectrolyte on each step of the crystallization, e.g. precipitation mechanism of hydroxyapatite via stabilization of amorphous calcium phosphate (ACP) and subsequent nucleation or conversion in calcium deficient hydroxyapatite (DA) or hydroxyapatite (HAP) should be observed not only at various additive concentration but also and necessarily at increasing ionic strength or at least the Ca²⁺ concentration, depending on the actual solution pH. Both parameters govern the ability of a given polyelectrolyte to induce or inhibit nucleation and were in this study neglected..

5.3.9. Characterization of 1st generation basic zinc phosphate and selective incorporation of latex particles

The formal identification of the precipitation products emerging from the latex controlled mineralization succeeded not only by SEM (§ 5.3.5) and XRD (§ 5.3.6) that confirms the belonging of the observed crystals to hexagonal NaZnPO₄ · 1 H₂O, an hydrated β-zeolite structure and analogue of NaBePO₄ · 1 H₂O beryllonite type [243-244] but also by other techniques of investigation in order to definitively conclude on the state of hydration [245-246] and the incorporation of latex particles during the nucleation step. A brief description of this unique zeolic structure is first given for a better understanding of the polymer-crystal interactions.

Although the geometrical principles and theoretical stabilities of tetrahedral open-framework structures are quite well understood, and the recent demonstration of selective chirality transfer [245] from incorporated (guest molecule) structure directing agents (CDA) [248-249], demonstrated during mineralization of various microporous zincophosphates [250-251], it was not possible until now to synthesize new *chiral* open-framework structures on “demand”.

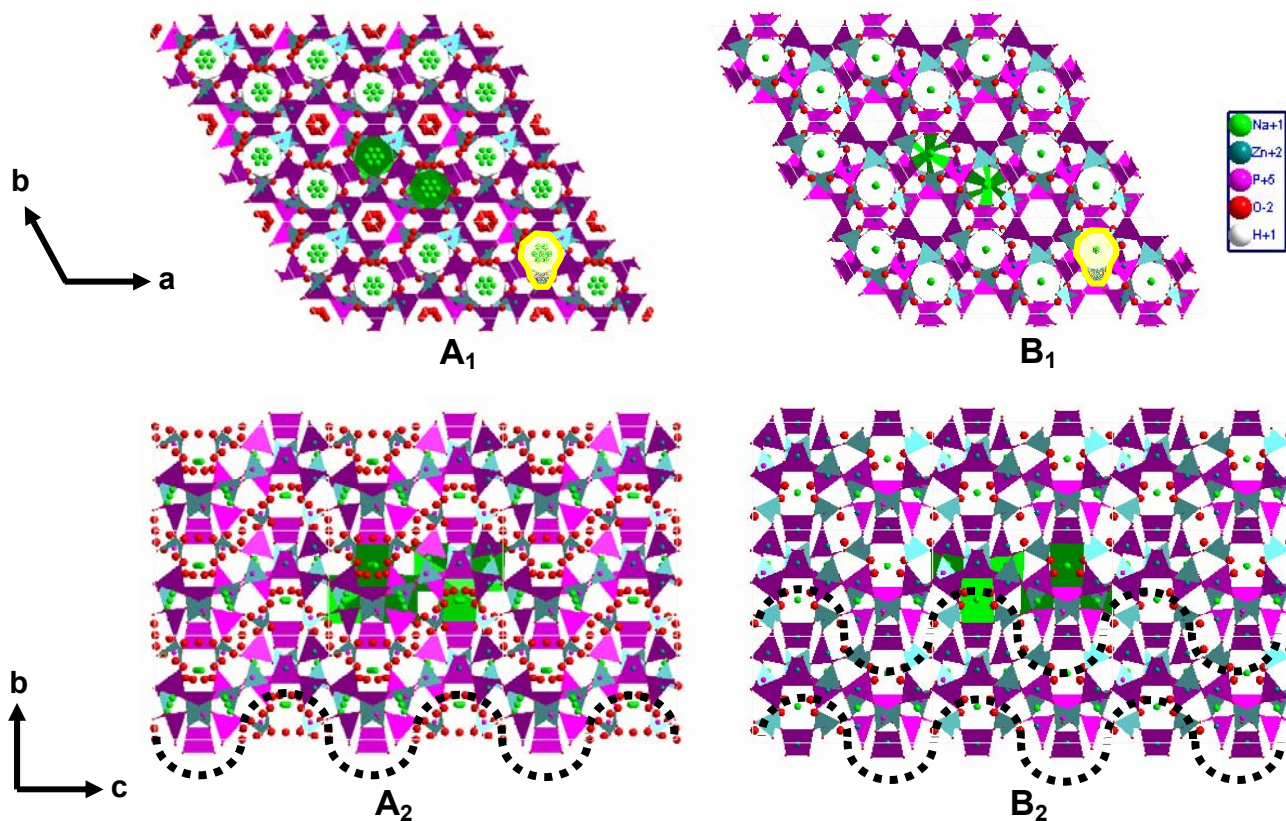


Figure 5.28: Schematic (polyhedral) representation of a triple unit cell of layered $\text{NaZnPO}_4 \cdot 1 \text{H}_2\text{O}$ enantiomers A and B, corresponding to the structures I and II described by Harrison et al. [242] and projected along c-axis (A_1, B_1) and a-axis (B_1, B_2). This polyhedral representation emphasizes (1) the connectivity first between ZnO_4 (●), $\text{Na}\cdots\text{O}_3(\text{H}_2\text{O})$ (●), and PO_4 (●) tetrahedra and secondly between the sodium channels (A_1, B_1) and (2) the propagation of tetrahedral helix (---) along [001] direction, with a periodicity equal to the c-unit cell dimension (A_2, B_2). The close oxygen environment of the different Na^+ ions that participate in hydrogen bonding and the sodium containing pear-shape cavities are described as (■) and (■) respectively.

Harrison et al. [198] made the first structural analysis of pure $\text{NaZnPO}_4 \cdot 1 \text{H}_2\text{O}$, and described it as a Zeolite- β . Zeolite- β [252] is a rare example of aluminosilicate with a helical pore structure. "Normal" zeolite- β (grown without any organic additives) consists of random or highly faulted intergrowth of two polymorphs (A and B) of opposite chirality [253] and is therefore used in catalysis [254]. The polymorphs A and B are generally found in a 60:40 ratio [255]. However, a third polymorph of zeolite- β has been recently detected experimentally by Corma et al. [256]. The structure of this last proposed polymorph C is closely related to those of polymorphs A and B but of higher symmetry (space group $P4_2/mmc$) and can be generated from polymorph A simply by recurrent application to the periodic building unit (PerBU-IZA nomenclature [257]) of a shear operation along a- and b-axes. In fact, the two enantiomeric phases of $\text{NaZnPO}_4 \cdot 1 \text{H}_2\text{O}$ (polymorphs A and B) belong to the enantiomorphic space group $P6_122$ and $P6_522$ respectively, and differ slightly by their extra-framework arrangement. The $\text{NaZnPO}_4 \cdot 1 \text{H}_2\text{O}$ (A-form) displays an asymmetric unit consisting of 7 framework atoms (2 Zn, 1 P, 4 O atoms) and 6 non-equivalent guest species (2 Na, 4 O of water molecules). The Zn and P framework atoms show typical

crystallographic behaviour, consistent with the environment in other tetrahedral zincphosphate structures (i.e. α - and β -ZPT). While the two zinc atoms, both of which occupy special positions of site symmetry 2, are tetrahedrally coordinated to their O atom neighbors, both ZnPO_4 tetrahedra are somewhat squeezed from regular $43m$ local symmetry, with Zn(2) (refer to atom indexation in § 5.3.4, Fig. 5.33) being more distorted as Zn(1) (i.e. standard deviation of 7° from Zn-O-P linkage). The single, crystallographically independent tetrahedral phosphorus atom forms bonds to 4 oxygen atom bridges [2 Zn(1) and 2 Zn(2)] (Fig. 5.30 A₁). Therefore, the Zn(1)O₄ and P(1)O₄, linked by non hydrogen bonding forming O-bridges, form one dimensional helix chains that propagate along the *polar c*-direction. Another unprecedented feature of this structural connectivity is the presence of squares of 4-rings, in which a rigid central Zn(1) tetrahedron is effectively surrounded by a “bonded into” 8-ring of alternating ZnO₄ and PO₄ groups [198]. Conversely, Zn(2) makes the linking between helices by forming two 4-rings and four 8-ring loops. The structural voids consist of six distinct partially vacant atomic sites that accommodate the two sodium atoms and the water molecule, or possibly a mixture of both. The difficulty of accurately modelling disordered sodium/water molecule sites in zeolite is well known [258] and the two species are mobile and interchangeable over all extra-framework sites, albeit they are confined in large interconnected pear-shaped cavities, consisting sodium channels parallel to the *c*-axis (Fig. 5.30 A₂).

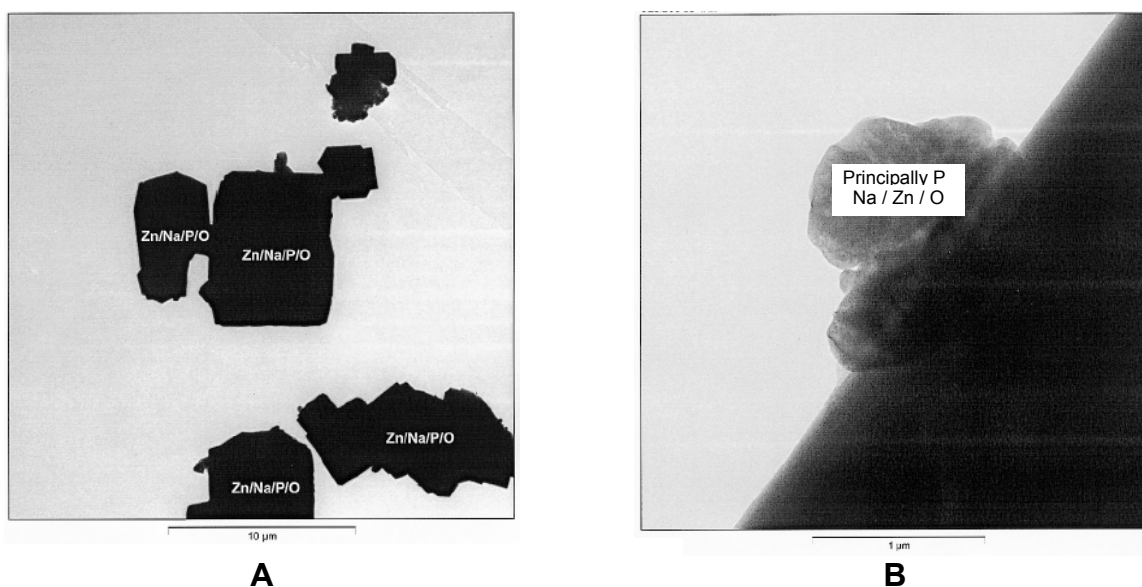


Figure 5.31: Characterization of the mineralization product by TEM (A) combined with elemental identification, i.e. Selected Area Diffraction (SAD). The crystallization of hexagonal sodium zinc phosphate monohydrate is confirmed by the observed crystal morphology and the measured stoichiometry (B) Zoom on absorbed traces on the crystal surface, most probably anhydrate NaZnPO_4 mixed with crystallized sodium phosphate salts.

In a strong parallel, the B-form of $\text{NaZnPO}_4 \cdot 1 \text{H}_2\text{O}$ is essentially the enantiomeric equivalent of form A above described (Fig. 5.30 B₁) with respect to the Zn/P/O framework species, but with 8-ring pore openings and highly puckered 12-ring with “side pockets” containing all hydrated sodium atoms. Because the water molecule has the same occupancy as the Na^+ atoms (coincidentally all

similar) the two are probably associated. The singular sodium coordination geometry is a highly disordered square prism with four short and four long Na-O distances, that indicates a disorder involving at least two adjacent sites (pear-like cavities in Fig. 5.30 B₁). Nevertheless, the sodium channels are interconnected and propagate infinitely along the *c*-axis (Fig. 5.30 B₂).

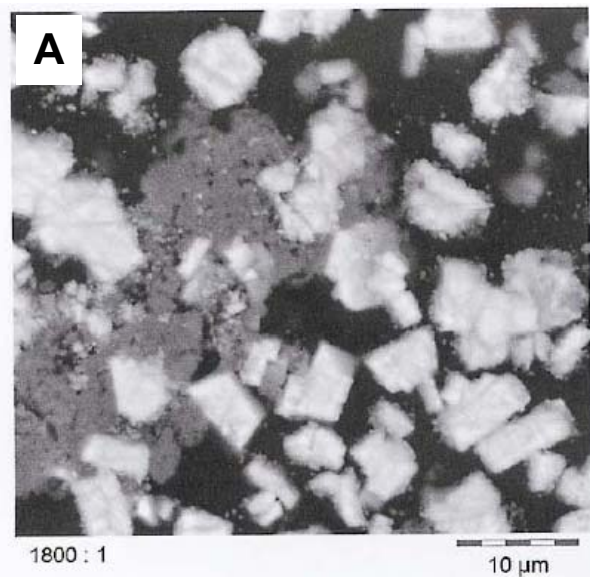
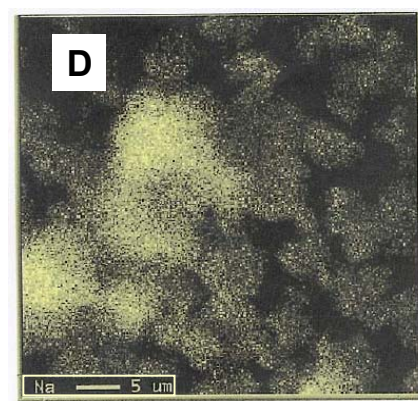
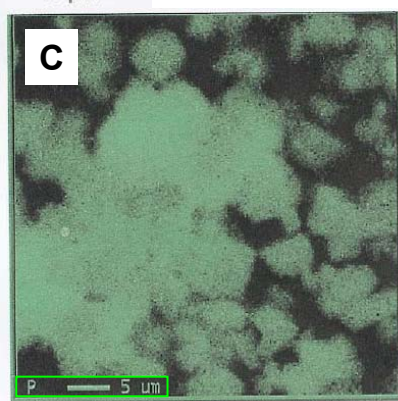
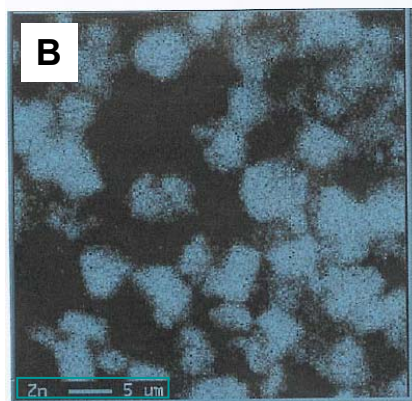


Figure 5.32: (A) SEM photographs of mineralization product (A) combined with elemental identification, i.e. EDX. (B), (C) and (D) display the density fluctuations of zinc, phosphorous and sodium, respectively



Morphological and structural chemical aspects of $\text{NaZnPO}_4 \cdot 1 \text{H}_2\text{O}$ are cleared by TEM combined with Selected Area Diffraction (SAD) (Fig. 5.31). Thus, the hexagonal shape in Fig. 5.30 A validates the SEM observations. The $\text{NaZnPO}_4 \cdot 1 \text{H}_2\text{O}$ stoichiometry, first determined by elemental analysis and TGA-MS (i.e. weight loss of 8.68 wt% giving an hydration state of 1 H_2O /unit for a predicted value of 8.91 wt%, Fig. 5.32 B) is confirmed in Fig. 5.31 A and B. Absorbed traces of not so well defined sodium hydrogen phosphate and monoclinic sodium zinc phosphate anhydrate, and generated by the crystal recovery procedure, are observed in Fig. 5.31 B. In addition, spatial elemental distribution of zinc, sodium and phosphorous is depicted in Fig. 5.31. An homogeneous repartition of principal elements in accordance with the crystal stoichiometry is found. Extra-framework water molecules, stabilizing Na^+ ions in the large pear-shape cavities (Fig. 5.30) by hydrogen bonding, is unambiguously detected at 134°C (Fig. 5.32 B), in good agreement with the thermal behaviour of the more compact α -ZPT phase (c.f. Chapter 3). This dehydration is irreversible and corresponds to the collapse of the zeolitic structure in a more condensed phase

NaZnPO_4 (ABW zeolite) [259]; thus proving the significant role of hydrogen bonding for stabilization of sodium atoms in the $\text{NaZnPO}_4 \cdot 1\text{H}_2\text{O}$ enantiomers. Besides, presence of incorporated latex particles in the crystalline structure is signaled by a characteristic but unusual high temperature CO_2 peaks at 347°C and 402°C (attributed to polymer combustion) and accompanied by a H_2O peak at 420°C (attributed to the departure of water of hydration confined in the latex corona) in TGA-MS. Similarly these endothermic peaks are detected at 335°C and 351°C in DSC (Fig. 5.33 A) and the degradation of phosphate in pyrophosphate groups starts around 493°C .

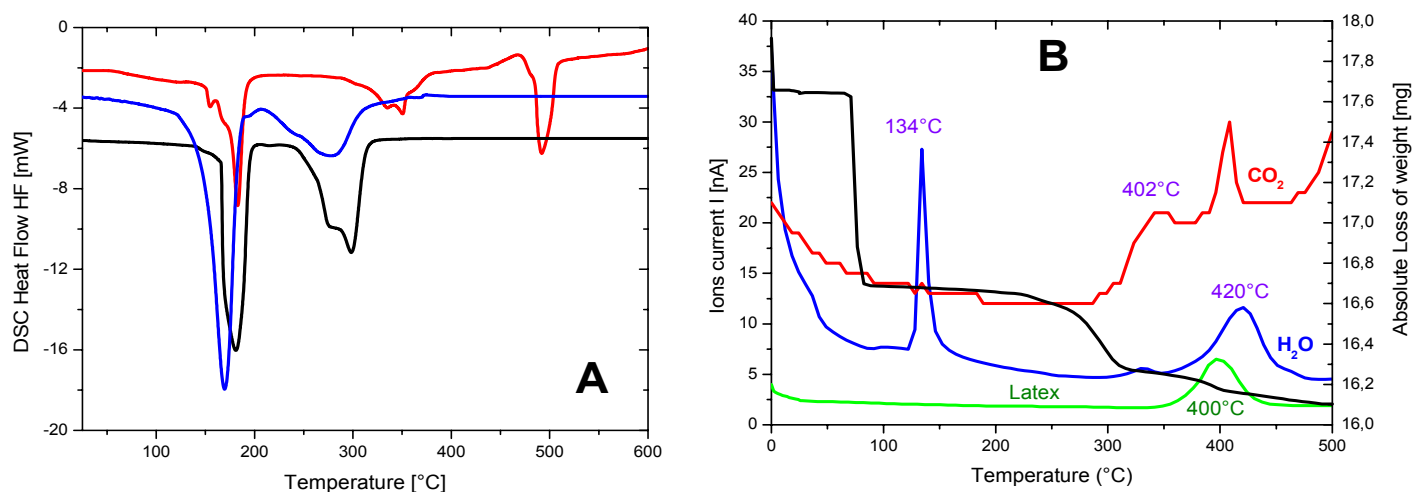


Figure 5.33: Incorporation of the carboxylated latex in hexagonal crystals of $\text{NaZnPO}_4 \cdot 1\text{H}_2\text{O}$ monitored by DSC (A) and TGA-MS (B) at a heating rate of $10\text{ K}\cdot\text{min}^{-1}$. For comparison, labels in (A) correspond to: (■) α -ZPT, (■) β -ZPT and (■) $\text{NaZnPO}_4 \cdot 1\text{H}_2\text{O}$.

More than ten years ago, Dutta et al. [260] had already proposed that cation-water complexes stabilize small aluminosilicate and/or phosphate anions that are responsible for forming unique zeolite structures primarily through electrostatic and steric factors [261]. In similarity, this may give ground to the interaction with the latex corona- $\text{Zn}^{2+}/\text{Na}^+$ ions and consecutive incorporation of latex in the crystal. This was easily verified by TEM of selected crystals, as shown in Fig. 5.34. Fig. 5.34 A and Fig. 5.34 B exemplarily show a cleavage plane that propagates along the c -axis on all the crystal length. A 30 nm spherical inclusion, found at the exact geometric center of the crystal under investigation may confirm the importance of latex particles as heterogeneous nucleation agent at the first stage of the controlled mineralization. Besides, a symmetric structural sheet/lamellar organization of 180-340 nm measured thickness is visualized in Fig. 5.34 B and corresponds to shear planes that may contain latex inclusions. Furthermore, as seen with other continuous zincophosphates nets linked by two-coordinate oxygen-atom bridges [262-263], complete ZnO_4/PO_4 ordering and alternation is maintained in these $\text{NaZnPO}_4 \cdot 1\text{H}_2\text{O}$ framework configuration, which contains only even-number of P atoms (4-, 6-, 8- and 12-ring). The voids observed in Fig. 5.34 C and D are non-circular, of maximum 200 nm length, and may form by dissolution, as stated in § 5.3.4. In addition, these defects are localized on the precise crystallographic position of O(2) atoms (Insert in Fig. 5.34 D), that are only involved in transversal stabilization (i.e. plane [110]) of the one

dimensional helix chains ($\text{Zn}(1)\text{O}_4$ and $\text{P}(1)\text{O}_4$ interconnection) by the two-coordinate oxygen-atom bridges above mentioned. This interpretation is supported by the significant changes observed in the phosphate region by DRIFT and FT-Raman spectroscopy (Fig. 5.35 and Fig. 5.36) compared to α - and β -ZPT. In fact, the presence of an infinitesimal quantity of latex particles is already responsible for immense distortions of the phosphate tetrahedral geometry, since PO_4^{3-} vibrational bands broaden independently of the latex concentration (Fig. 5.35 B).

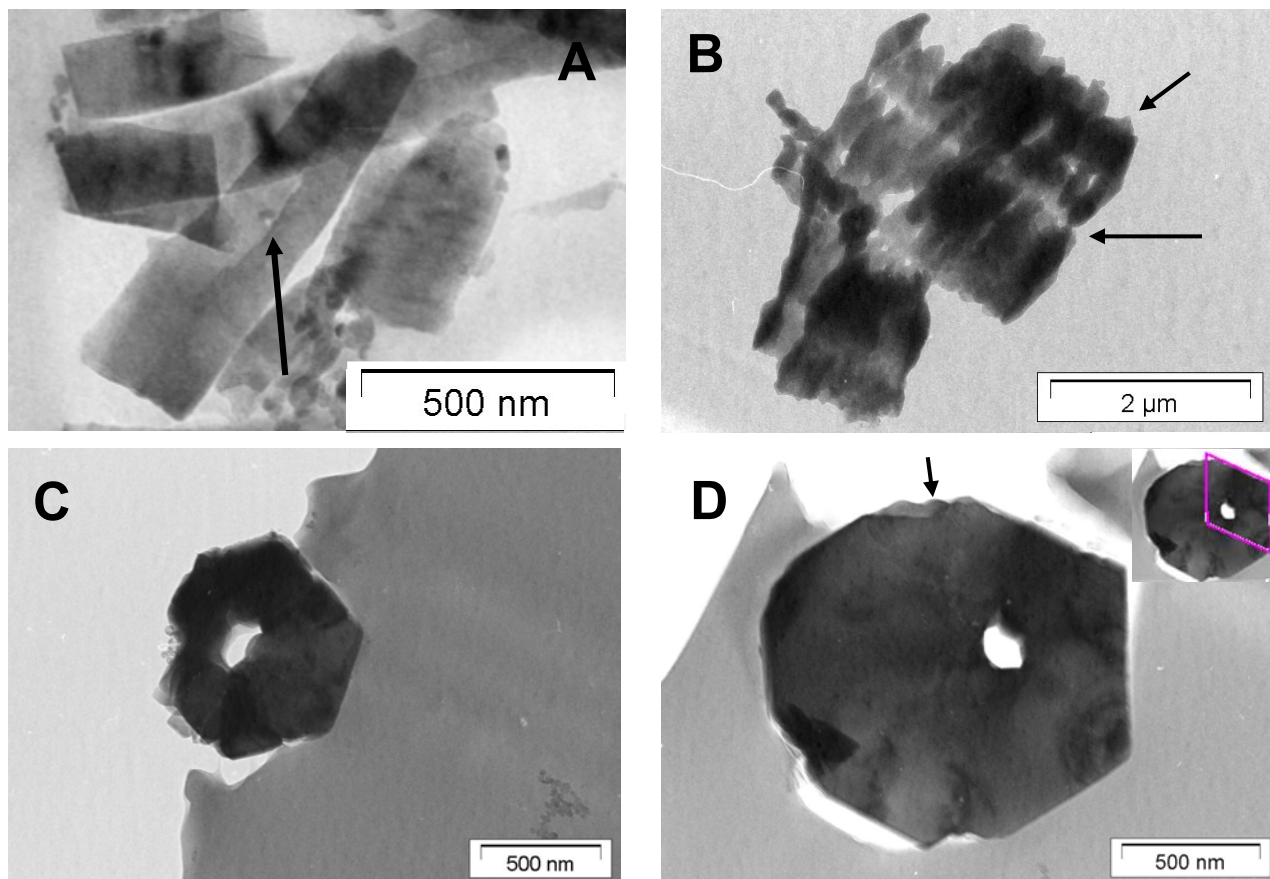


Figure 5.34 : TEM images of $\text{NaZnPO}_4 \cdot 1\text{H}_2\text{O}$ showing (A) the formation of screw defects along the crystallographic c -axis, starting from a 30 nm inclusion located at the geometric center of the crystal, (B) the same screw defect along with the delamination of the crystal structure in crystalline sheets of 180-340 nm thickness, (C,D) progressive formation of voids of maximum 200 nm diameter perforating the crystal structure on all its length and located at the structural $\text{O}(2)$ position (similar for both enantiomers, insert in D with unit-cell limits), suggesting the inclusion of a 90 nm latex particle that destabilizes the growing crystal structure. Arrows point at selected defects.

Dutta et al. [264] monitored by Time Resolved FT-Raman spectroscopy the progressive dissolution of faujasitic-like zincophosphates and concluded that the random Na^+ atom distribution leads to this reported band broadening effect and increases with incorporation of sodium in the extra-framework cages [265]. Similar effects are described by Nenoff et al. [266] for soladite-type phases such as $\text{Na}_3\text{Zn}_3(\text{PO}_4)_3 \cdot 4\text{H}_2\text{O}$, a sodium zinc phosphate of higher hydration state compared to $\text{NaZnPO}_4 \cdot 1\text{H}_2\text{O}$.

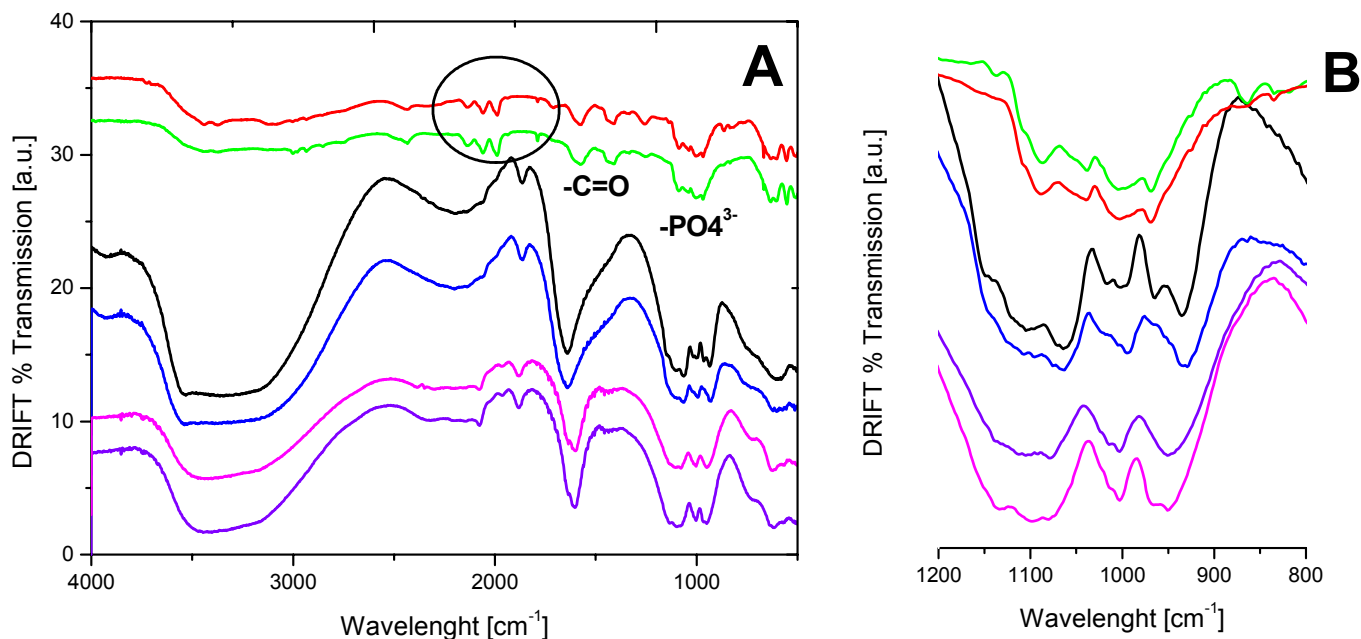


Figure 5.35: DRIFT spectra of: (■) α -ZPT, (■) β -ZPT, (■) α -ZPD, (■) β -ZPD, compared to (■) $\text{NaZnPO}_4 \cdot 1\text{H}_2\text{O}$ with 915 ppm and (■) $\text{NaZnPO}_4 \cdot 1\text{H}_2\text{O}$ with 1145 ppm carboxylated PS-latex in the range 4000-1500 cm^{-1} (A) and centered on the phosphate region (B). The incorporation of latex is emphasized by the presence of carbonyl related bands (1411, 1438, 1571 cm^{-1}) and results in a significant distortion of the PO_4^{3-} sphere of coordination (B)

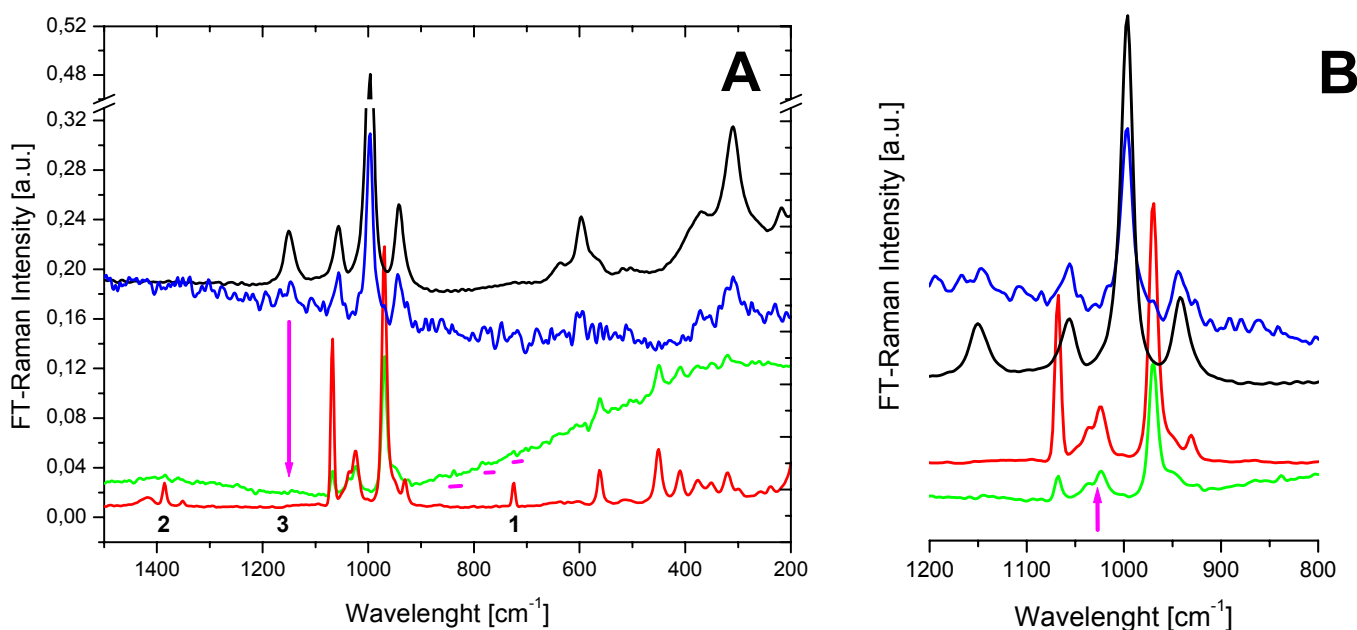


Figure 5.36: FT-Raman spectra of: (■) α -ZPT, (■) β -ZPT compared to (■) $\text{NaZnPO}_4 \cdot 1\text{H}_2\text{O}$ with 915 ppm and (■) $\text{NaZnPO}_4 \cdot 1\text{H}_2\text{O}$ with 1145 ppm carboxylated PS-latex in the range 1500-200 cm^{-1} (A) and centered on the phosphate region (B). The incorporation of latex is emphasized by the presence of carbonyl related bands (A, mark 2, around 1400 cm^{-1}) and Latex- PO_4Na band (A, mark 1 at 724, 787 and 838 cm^{-1}) and by the marked absence of $\nu_3(F_2)/g : 3$ (A, mark 3 at 1150 cm^{-1}) vibration along one of the PO_4^{3-} tetrahedron axis (arrow in A, B).

Fig. 5.36 A even shows the complete suppression of the $\nu_3(F_2)$ band of lowest energy, i.e. the peak of internal bending at 1150 cm^{-1} , and the appearance of small peaks at 724, 787 and 838 cm^{-1} ,

attributed to privileged Na-O bondings. A possible identification could be a strong squashing of the O(4)-P(1)-O(1) bonds to the benefit of O(1)-Na(1) or O(1)-Na(2) short (~ 2.30 Å) bondings, since the P(1)-O(1) bonds develop nearly parallel to the *c*-axis. This is further confirmed first by the simultaneous appearance of two peaks at 409 cm^{-1} (given to 408 cm^{-1}) and at 450 cm^{-1} (given to 448 cm^{-1}) and describing translational T and T' modes (refer to Chapter 2), and secondly by the emergence of small diffuse halos in the TEM diffraction pattern (Fig. 5.37 A) of a $\text{NaZnPO}_4 \cdot 1\text{H}_2\text{O}$ crystal containing a latex particle. In particular, these halos are centered on the scattering points relative to the (012) and (016) planes that contains the displaced O(2) and Na(1) atoms, thus destabilizing the entire structure along the *c*-axis by partial rupture of O(2)-atom bridges between the $\text{Zn}(1)\text{O}_4$ and $\text{P}(1)\text{O}_4$ elements of the helical chains as shown in Fig. 5.37 B.

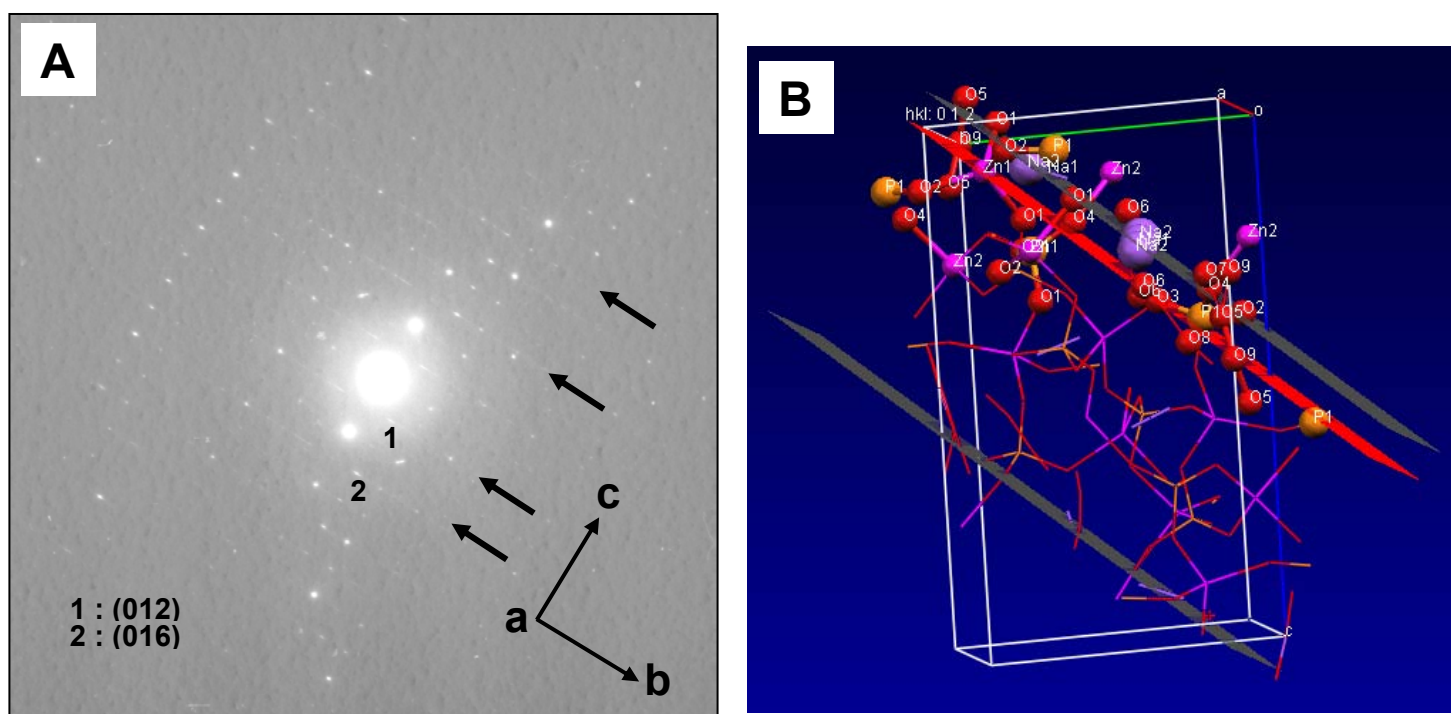


Figure 5.37: (A) TEM electron diffraction pattern of $\text{NaZnPO}_4 \cdot 1\text{H}_2\text{O}$ taken from crystals presented in Fig. 5.10 A showing the diffuse halos in the (*ab*) planes reflecting the one dimension of collapse/displacement of the zeolitic structure along the crystallographic *c*-axis consecutive to simultaneous distortion of PO_4 tetrahedra and displacement of Na(1) atoms and O(2)-atom bridges between the $\text{Zn}(1)\text{O}_4$ and $\text{P}(1)\text{O}_4$ elements of the helical chains. (B) Mixed Ball-Sticks/wireframe representation of a unit cell intersected by gliding planes (grey) parallel to the (012) plane (red), which contains the Zn(1), O(3), O(9) and Na(1), O(2) atoms.

In addition, solid state NMR is a unique tool for characterization of complex open-framework structures and highly suited for detection of the incorporation of latex particles in an inorganic matrix. Indeed, in the ^1H magic angle spinning NMR spectra at increasing spinning frequency of $\text{NaZnPO}_4 \cdot 1\text{H}_2\text{O}$ crystallized with 916 ppm of carboxylated PS-based latex (Fig. 5.38 A), the presence of latex particles and its individual components are unambiguously detected for example at 32 kHz at 1.15, 6.61, 7.28 and 8.32 ppm (latex PS-core) and 1.70, 3.92 and 4.42 ppm (latex corona containing PAA and PEO chains) [267]. The low MAS frequency spectrum in Fig. 5.38 A reveals also two types of

crystal water, one very rigid (i.e. broad band at 6.20 ppm) and one very mobile water species overlapped by the sharp latex signal (residual water of hydration localized in the latex corona and entrapped during nucleation step) at 4.37 ppm. In ^{31}P spectrum (Fig. 5.38 B) taken at 10 kHz, two well defined peaks at 10.74 and 11.17 ppm indicate two different types of PO_4 tetrahedra, distorted from their ideal geometry by hydrogen bonds. This is confirmed by the presence of two ^1H signals at 13.31 and 14.25 ppm in Fig. 5.38 A corresponding to two distinct acidic protons, one mobile (sharp peak at 14.25 ppm) and one rigid proton ($\text{H}\cdots\text{O}-\text{P}(1)\text{O}_3$) signalized by the broad peak ($w_{1/2}$: 1.18 ppm) at 13.31 ppm.

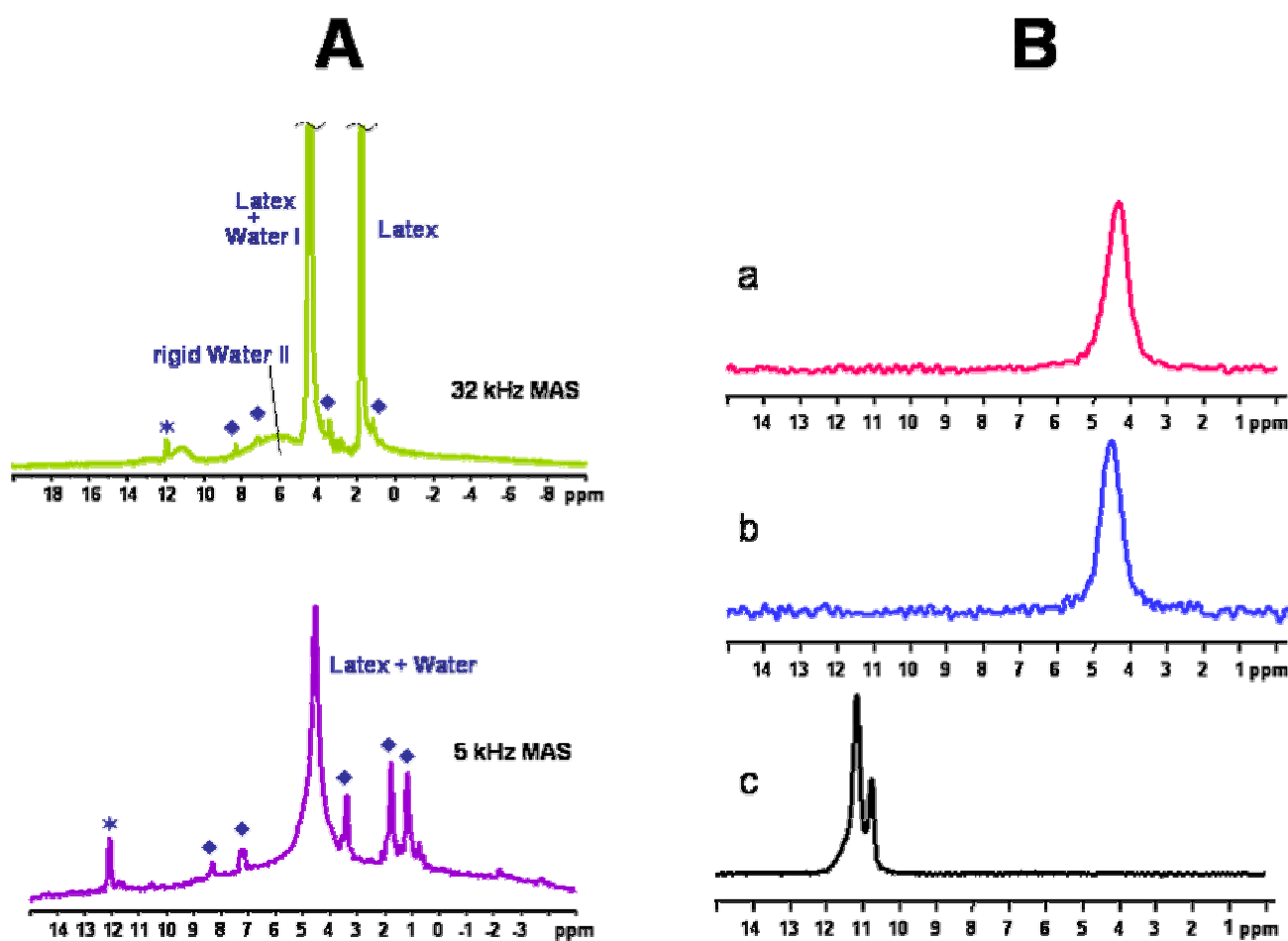


Figure 5.38: Slow spinning ^1H MAS NMR spectra (A) at low (5 kHz) and high (32 kHz) spinning frequency and ^{31}P MAS NMR spectra (B) taken at 10 kHz of (c) $\text{NaZnPO}_4 \cdot 1\text{H}_2\text{O}$ crystallized with 916 ppm of carboxylated PS-based latex, compared (a) α -hopeite and (b) β -hopeite. All ^{31}P NMR spectra were referenced with respect to 85% H_3PO_4 (0 ppm), with upfield shifts taken as negative at 10 kHz. Note that liquid water and latex components, i.e. surfactant (PEO chains) are generally found to resonate around 4.7 ppm (◆) in a sharp resonance, while acidic protons are presently found around 12.1 ppm (*).

Inspection of structural data from literature [268-269] and comparison with reference values of ZPT polymorphs (c.f. Chapter 2) suggest a strong effect of the latex corona and/or the water it contains on the phosphorous chemical shift ($\Delta\delta \approx 7. \text{ppm}$ compared to α -ZPT) that reflects a complete change of the PO_4 sphere of coordination since first only one structural P atom is identified in the

two known asymmetric $\text{NaZnPO}_4 \cdot \text{H}_2\text{O}$ unit cells [270] and secondly Rao et al. [271] showed that terminal phosphoryl groups are highly reactive. Furthermore, albeit one anhydrate NaZnPO_4 structure is reported by Elammari et al. [272] and might explain the presence of two ^{31}P peaks (i.e. mixture of hydrated and dehydrated sodium zinc phosphate), it does not contain crystalline water and cannot justify the emergence of two acid protons in the crystal structure. Alternatively, this ^{31}P doublet and the mobile proton peak could arise from the presence of significant amount of HPO_4^{2-} located in the latex corona during crystal nucleation (whose volume represents nearly 1 vol% of a single fully grown $\text{NaZnPO}_4 \cdot \text{H}_2\text{O}$ crystal). Nevertheless, another more convincing explanation is the above mentioned displacement of Na(1) and O(2) atoms in the (012) plane, that induces two non equivalent phosphorus spheres of coordination.

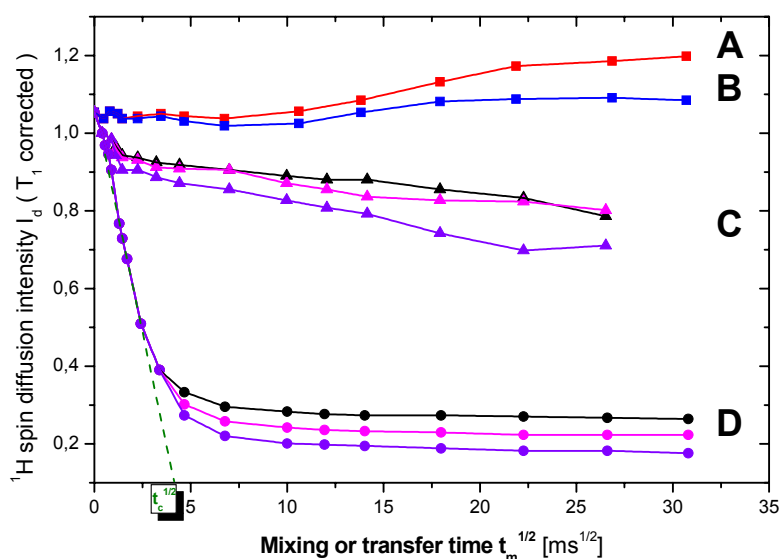


Figure 5.39: Spin diffusion curves at 500 MHz and increasing t_m , plotted as the normalized ^1H diffusion intensity I_d against the square root of the mixing time $\sqrt{t_m}$ at 25°C for (A) α -ZPT, (B) β -ZPT, (C) $\text{NaZnPO}_4 \cdot \text{H}_2\text{O}$ crystallized with carboxylated PS-based latex, (D) lyophilised with carboxylated PS-based latex.

Moreover solid-state NMR ^1H spin diffusion experiments in combination with transmission electron microscopy are usually used to elucidate highly complex latex-crystal nanocomposite structures [273] and were recently extended for both quantitative determination of monocrystalline domains and spatial localization of interfaces [274]. Remagnetization effects are detected in a four-component system with two different rigid and two soft phases, which are discriminated by their characteristic ^1H chemical shift. The remagnetization effects facilitate the interpretation of spin-diffusion experiments for a structure investigation, since the $\text{NaZnPO}_4 \cdot \text{H}_2\text{O}$ crystals precipitated with carboxylated PS-based latexes contain one very rigid (NaZnPO_4 framework) and more or less rigid component (PS latex core) spatially separated of the two very mobile components (crystal water anchored in the crystal structure by hydrogen bonding) and the residual water/PEO chains of the emulsion polymerization entrapped in the latex corona. A typical ^1H spin-diffusion experiment starts with selecting the proton magnetization of one of the components by application of magnetic filter (CPMG sequence), which destroys selectively the magnetization of the rigid component in a heterogeneous system with mobile and rigid phases. This generates a non-equilibrium distribution

of proton magnetization in the system that immediately afterward starts to re-equilibrate through spin-diffusion, propelled by the dipolar couplings between spins stemming from protons of crystal water and latex particles. Due to the density of hydrogen atoms in the crystal structure and latex particles, the spin diffusion process may be treated classically by assuming a continuous matrix of hydrogen atoms, and therefore described using Fick's second law of diffusion where $D_{\text{eff}}(r)$ is the spatially dependent spin-diffusion coefficient [275]. As Spiegel et al. [276] showed, $D_{\text{eff}}(r)$ can be simply determined from static ^1H NMR spectral line width or more accurately from transverse relaxation time T_2 [277]. A series of signal intensities of the mobile component is then observed after different spin-diffusion times. The subsequent application of monotone filter cycles with increasing strength yields characteristic decay curves with a linear slope and a plateau proportional to the ratio of mobile to rigid phases in the sample, i.e. T_1 (Fig. 5.39). The intercept of the decay dotted line with the X-axis (mixing time) gives the value of $\sqrt{t_m^{s,0}}$, which is a measure for the diameter of the mobile phase:

$$d_{\text{mobile}} = \frac{2\varepsilon}{\sqrt{\pi}} \sqrt{D_{\text{eff}} \cdot t_m^{s,0}} \quad (5.8)$$

if the geometry (morphology) of the magnetization phase (e.g. Latex spheres, $\varepsilon = 3$) is known.

In Fig. 5.39 the lyophilized PS-based latex (Fig. 5.39 D) delivers a mobile phase diameter of around 4 nm (i.e. $\sqrt{t_m^{s,0}} \approx 4.5 \text{ ms}^{1/2}$) corresponding to the latex corona, while references comprising α -ZPT and β -ZPT display unexpected positive remagnetization (Fig. 5.39 A and B). On contrary, $\text{NaZnPO}_4 \cdot 1\text{H}_2\text{O}$ crystals containing latex nuclei exhibit a spin diffusion domain of 180 nm approximately (e.g. $\sqrt{t_m^{s,0}} \approx 80 \text{ ms}^{1/2}$) which is in good agreement with published values [278]. While the incorporation of a small amount of latex additive in the zinc phosphate crystals is again confirmed, it is nevertheless not possible to conclude with certainty that the $\text{NaZnPO}_4 \cdot 1 \text{H}_2\text{O}$ domains are of monocrystalline character.

5.3.10. Quantitative determination of the incorporation of latex particles in $\text{NaZnPO}_4 \cdot 1 \text{H}_2\text{O}$, a basic zinc phosphate (1st generation ZPO)

So far, the strong involvement of carboxylated latex particles in the stabilization and nucleation of metastable ZPO phase, i.e. $\text{NaZnPO}_4 \cdot 1 \text{H}_2\text{O}$, has been demonstrated by numerous techniques. However, albeit latex particles have been found in the crystal structure, elusive questions remain: is the latex the single nucleation promoter, and is there a single latex particle pro crystal? Along this line, labelling by fluorescence tracers encapsulated in the carboxylic latex particles revealed to be an interesting approach.

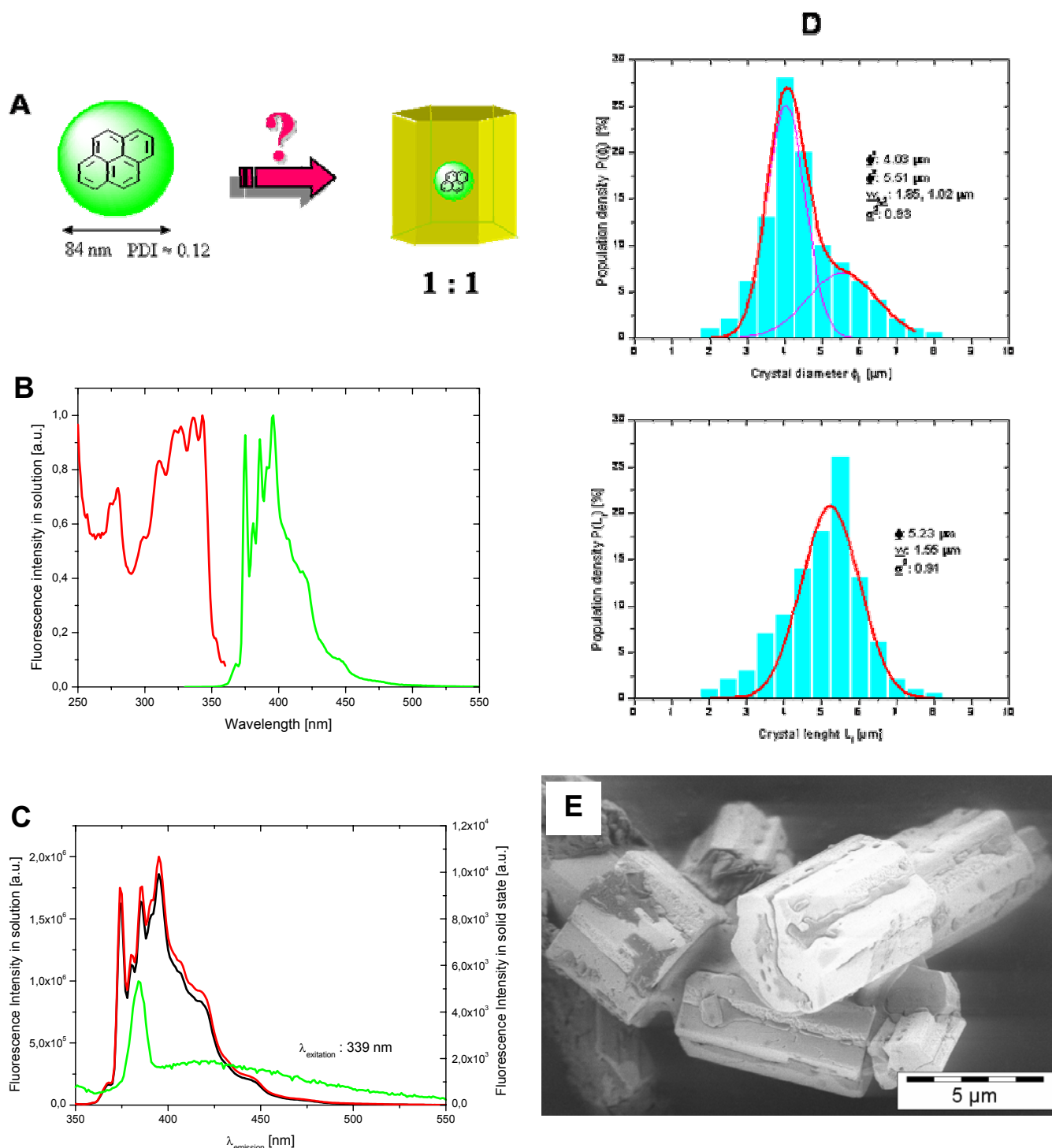


Figure 5.40: Quantitative measurement of the incorporation of a carboxylated latex particle in a $\text{NaZnPO}_4 \cdot 1\text{H}_2\text{O}$ crystal followed by fluorescence. (A) measurement strategy for a pyrene labelled latex, (B) excitation (■) and emission (■) spectra in fluorescence ($\lambda_{\text{excit}} : 339 \text{ nm}$) of the pyrene labelled latex, diluted ($\times 10000$) in aqueous solution, (C) Fluorescence spectra before (■) and after (■) ZPO mineralization in the supernatant compared to the fluorescence spectrum of the latex incorporated into the crystal and released by complete crystal dissolution in acidic medium (HCl, pH 3) (■), (D) crystal size distribution obtained from SEM after mineralization (E).

This strategy has been shown to be highly efficient for the determination of complex surfactant phase diagrams [279-280] and the investigation of transport phenomena through biomembranes

[281-282]. In accordance to Thomas's pioneering work [283-284], pyrene was selected principally for its good quantum yield, its emission wavelengths which do not interfere with the PS-latex matrix and its satisfying solubility in organic solvent (styrene monomer) in comparison to other potential fluorophores. Therefore, using 50 ppm of a fluorescence labelled latex functionalized with carboxylic groups hexagonal crystals of $\text{NaZnPO}_4 \cdot 1\text{H}_2\text{O}$ were synthesized, as shown in Fig. 5.40 C. The determination of the consumed amount of latex particle during mineralization succeeds either by measuring directly the relative fluorescence intensity of the continuous (aqueous) phase before and after precipitation reaction and thus in determining the exact number of labelled latex particles staying in the supernatant, that consequently are not incorporated in the precipitating crystals (Fig. 5.40 B (■) and (■)). Alternatively, a less efficient way consists of redissolution of a precise amount of the previously precipitated ZPO crystals in a given volume of solvent (typically 2 mol.L^{-1} NaOH solution or 3 mol.L^{-1} HCl, refer to Chapters 4 and 6) and consequently to measure the fluorescence activity of the obtained suspension (i.e. release of labelled latex particles incorporated in the $\text{NaZnPO}_4 \cdot 1 \text{ H}_2\text{O}$ crystals). This gives rise to remarkable features in the fluorescence emission spectrum (Fig. 5.40 B (■)). Similar features (e.g. excimer band) in the measured fluorescence spectra have been reported by Thomas et al. and interpreted in terms of spatial confinement in a latex particle [285]. The first peak at 384 nm may be attributed directly to the pyrene monomer itself and the broad peak at a higher wavelength (427 nm) to an *excimer* state, and therefore does not show vibronic bands as already reported by Birks and Christophorou in 1963 [286]. Excimer are dimers of an excited state (the term excimer results from the contraction of "excited dimer") and are formed by collision resulting from aggregation in the PS-latex core between an excited molecule of pyrene and an identical unexcited molecule. The formation of excimer is a diffusion-controlled process and a photophysical phenomena detected normally at relatively high concentration of pyrene (i.e. so that a sufficient number of collisions can occur during the excited-state lifetime, concentration presently used $1.65 \cdot 10^{-2} \text{ mol.L}^{-1}$) [287]. Assuming a density of 2.79 g.L^{-1} (pure $\text{NaZnPO}_4 \cdot 1 \text{ H}_2\text{O}$), the crystal size distribution from SEM (Fig. 5.40 B) allows the fast determination of the number of perfectly packed crystals in a given suspension volume. In measuring the relative intensities of the fluorescence emission peaks I and V ($\lambda_{\text{abs.}} \approx 339 \text{ nm}$, Fig. 5.40 C) at 374.5 and 395.4 cm^{-1} , respectively, the exact number of incorporated latex particles can be determined, as given by the following relation:

$$N = [P]_{\text{ads}} \propto N_o \left(1 - \frac{A_{I/V}^{\text{after}}}{A_{I/V}^{\text{before}}} \right)_{\text{crystallization}} \quad (5.9)$$

Thus, a statistical value of 10-50 latex particles per $\text{NaZnPO}_4 \cdot 1 \text{ H}_2\text{O}$ crystal was obtained. Alternatively, this quantitative determination was validated using tracers absorbing the visible light frequencies such as Cu(II) phthalocyanine complex and Red Oil O (Fig. 5.41). The incorporation of 20-100 latex particles per monocrystal was subsequently detected.

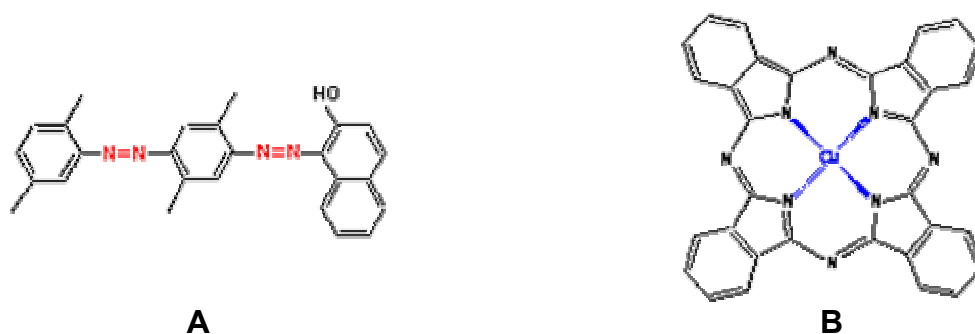


Figure 5.41 : Other possible oil soluble molecules evaluated for labelling a carboxylated latex particle : (A) Oil Red O ($\lambda_{\max}^{\text{abs}} = 525 \text{ nm}$), (B) Heliogene Blue B ($\lambda_{\max}^{\text{abs}} = 700 \text{ nm}$) [288-289] (absorption wavelength given for a dye labelled latex).

These two values are concurring and are in good agreement with the expected range of concentration of impurities generally involved in heterogeneous nucleation [290], an foremost implies that one latex particle or an aggregate or cluster of latex particles nucleates a $\text{NaZnPO}_4 \cdot 1 \text{ H}_2\text{O}$ crystal. A promising alternative technique [111,291] may consist of latex particles vectoring spherical magnetite nanoparticles and the measurement of induced magnetic field of $\text{NaZnPO}_4 \cdot 1 \text{ H}_2\text{O}$ crystals after controlled nucleation [292].

5.3.11. Mechanisms of interactions between a growing basic ZPT crystal and a latex particle

The field of organic-inorganic nano/micro-composites materials has been widely recognized as one of the most promising and rapidly emerging research area in Materials Chemistry. These systems can be perhaps best described as being organized into spatially identifiable domains of an organic and inorganic component. They are generally produced using various methodologies of “soft” inorganic chemistry in liquid and sol/gel media, exploiting either self-assembly mechanisms under the influence of structure-directing agents (template), controlled polymerization processes in media of directed assembly of nano-building blocks in solution or at the solid/liquid interface.

The spatial organization of dissimilar and commonly incompatible components in these hybrid materials produces a wealth of novel structure features, with physical-chemical properties and complex functions in demand, which arise from the synergistic interaction of each of the individual component (e.g. inorganic ZP framework and functionalized latex nanoparticles). A first general classification has been proposed by Sanchez [293], distinguishing “class I” materials, in which inorganic and organic component interact only weakly through hydrogen bonding, van der Waals contacts or electrostatic forces, from “class II” materials, in which the constituent are more strongly linked through ionic/covalent bond formation. Nevertheless, fundamental understandings of polymer assisted/mediated crystallization and related mechanisms, particularly those involving weak intermolecular forces still need to be elucidated. Therefore, on the basis of the here-above

accumulated results, simple mechanisms referring to coordination chemistry are tentatively proposed in order to highlight the primary role of negatively charged latex particles on ZPO mineralization.

In systems subjected to large undercooling or high supersaturation conditions such as zinc phosphate hydrates, crystal nucleation and growth limitations can expose ZPO material metastability due either to the suppression of an equilibrium phase or else by the formation of a kinetically favored metastable phase such as $\text{NaZnPO}_4 \cdot 1\text{H}_2\text{O}$ (i.e. in reference to Ostwald Law of stage [294]). For the case of an amorphous phase formation during mineralization processing the kinetic control may be analyzed in terms of nucleation limitations and growth restrictions. In due respect, numerous experimental *direct* evidences and the non detected latex adsorption of growing crystal faces have first proven that carboxylated latex particles are incorporated selectively during ZPO polymer controlled mineralization in infinitesimal amount (refer to § 3.5.9), that secondly suggests the preponderant role of latex particle during controlled heterogeneous nucleation of sodium containing ZPO zeolites. Thanks to TEM and spectroscopic methods sensitive to changes of sphere of coordination of Zn(II) and P(V) atoms, the detection of infinite stacking faults (*) and the disruption of $\text{ZnO}_4\text{-PO}_4$ helices propagating along the *c*-axis on atomic level and the systematic presence of microscopic screw defects developing nearly parallel to the *c*-axis (axis of privileged crystal growth) could be correlated by the incorporation of latex particles in the crystal structure. Further, Solid state NMR suggests the irremediable deformation of the latex corona during latex incorporation in $\text{NaZnPO}_4 \cdot 1\text{H}_2\text{O}$ crystals. Besides, Coker and Rees [297] and later Faux [167] observed that the existence of low electrostatic field strengths in zeolites render the interaction between divalent metal cation of high charge density (Ca^{2+} , Zn^{2+}) and the open-framework less important and diffusion of hydrated cation (e.g. Na^+ , K^+ , NH_4^+) through the voids of the framework dominates the exchange processes. In the same time, Subramanian et al. [298] has first proposed a mechanism of both synergetic exchange between Cu^{2+} ions and H_2O molecules of solvation and complexation with carboxylic groups of a PVP-*b*-PMAA dihydrophilic block copolymer. In this line, as depicted in Fig. 5.42 two latex-assisted mechanisms of nucleation are proposed:

- (i) Intra-corona latex nucleation mechanism
- (ii) Inter-corona latex nucleation mechanism

(*) Stacking faults [295] are planar defects in which atomic coordination across the (001) plane is not perfect. A stacking fault can be envisaged as being created by a dislocation moving across this basal plane, but with a Burger's vector not equal to a lattice translation vector (e.g. $1/3 \langle 11\bar{2}0 \rangle$ in an hexagonal unit cell). Thus stacking faults are bounded by imperfect or partial dislocations (e.g. Shockley and Frank partial dislocations) [296].

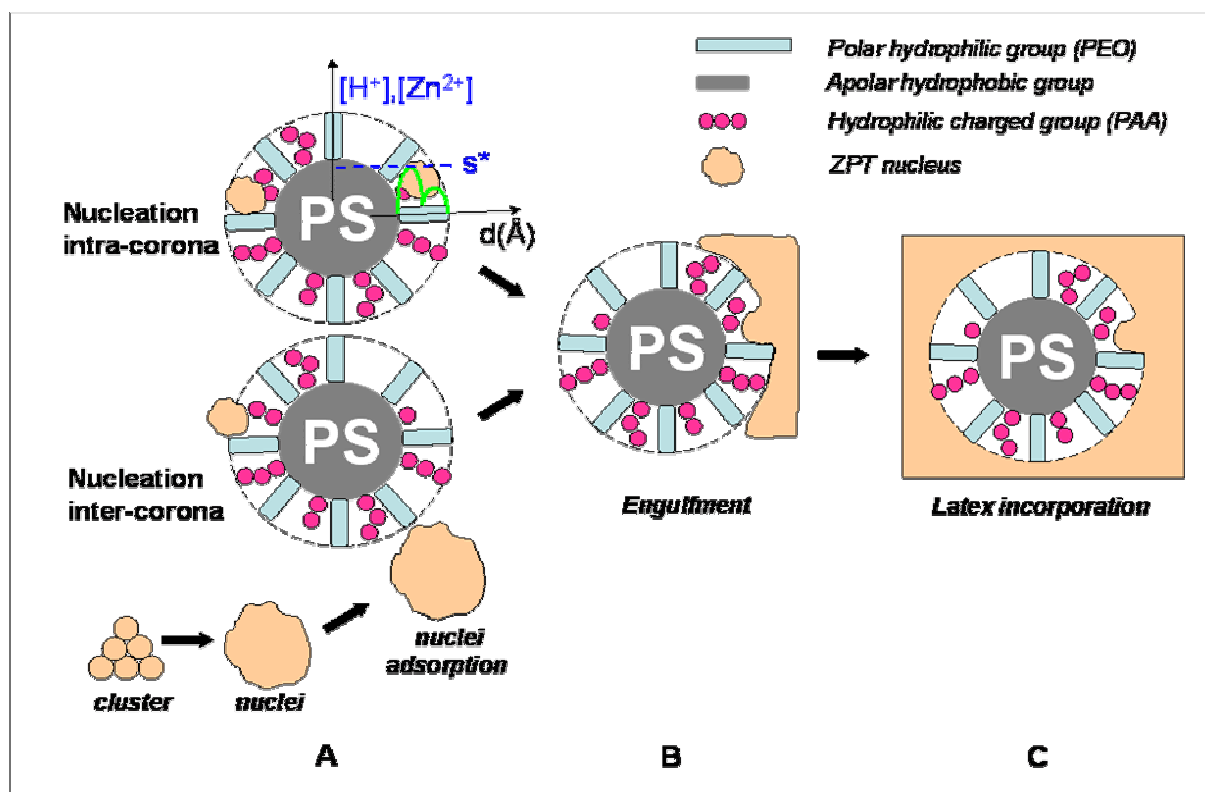


Figure 5.42: Schematic representation of the influence of a carboxylated latex particle on the nucleation of a zinc phosphate crystal in aqueous solution (A), leading to a selective latex incorporation (C) by engulfment (B). In the inter-corona nucleation pathway, the crystal nucleus adsorbs on the outer charged layer of the hydrophilic corona due to a minimization of the surface energy. The intra-corona nucleation occurs due to a fluctuation of the negative charge density and consequently of the local Zn^{2+} concentration caused by partial deprotonation of the PAA segments. ZPT nucleation takes place if the Zn^{2+} concentration reaches supersaturation condition s^* and PO_4^{3-} anions diffuse through the latex corona.

5.3.11.1. Intra-corona latex nucleation mechanism

Miniemulsion polymerization produces carboxylated latex particles with a not so well defined corona, where fluctuations of chains length and spatial distribution of PS-*g*-PMAA copolymers are generally detected. Particularly, Vandoremaele et al. [299] have characterized the microstructure of a poly(styrene-co-methylacrylate) copolymer, obtained by emulsion polymerization, in terms of triad fraction and tacticity (i.e. intramolecular structure), and in terms of a three-dimensional molar-mass chemical composition distribution (MMCCD) (i.e. intermolecular structure). The difference in water solubility appears to be one of the major factors determining the microstructure of the copolymers. Depending on conversion, monomer ratio and monomer-to-water ratio, they predicted either single or double-peaked MMCCDs. This suggests copolymers of different length more or less densely packed in the latex corona. Morcellet et al. [300] analyzed the deprotonation and complexation of a series of water soluble polyelectrolytes and the influence of the degree of polymerization (DP_n) or chain length by considering oligomeric subunits each containing eight monomeric units. In each case eighth distinct and successive ionization constants were obtained in relation with structural

features of the polymer, i.e. the nature of the side chain, tacticity and chain conformation, indicating that any fluctuation of polymer chain length leads to fluctuation of carboxylic group reactivity (i.e. affinity) toward Zn^{2+} and Na^+ ions. If one applies this observation to a PS-*g*-PAA emulsion copolymer, this fluctuation of chain length induces a gradient of concentration of zinc complexed with the acrylic acid units. Furthermore, in recent years the theory of cellular solidification and homogeneous nucleation from molar flux balance approach at a diffuse interface layer has been modified by Kotake [299] from the pioneering work of Chalmers [302] and might accurately describe the behaviour of the kinetically governed water and ion exchange taking place in a negatively charged latex corona before reaching supersaturation. Thus in the diffuse layer of the latex, the zinc concentration may well attain the critical concentration s^* necessary for crystal nucleation (i.e. supersaturation conditions). The nucleated crystal, anchored in the corona, first grows parallel to the latex surface until it matches the latex size, then grows radially to the latex surface. In this precise case, the latex plays the role of nucleating impurity that in consequence is progressively engulfed and then fully incorporated in the growing crystal. This defines a so-called ***Intra-coronona latex nucleation mechanism***. Antonietti et al. validated this complex approach for calcium phosphate mineralization in presence of simple linear PEO-*b*-PAA DHBCs [51].

5.3.11.2. Inter-coronona latex nucleation mechanism

A second approach, namely the ***inter-coronona latex nucleation mechanism***, may also be envisioned, in which $NaZnPO_4 \cdot 1H_2O$ nuclei are generated in the suspension medium in an uncontrolled manner (supposedly heterogeneous nucleation process) and stabilized by adsorption on the latex corona either by direct ionic bondings (e.g. $PAA^- \cdots Zn^{2+}$) hydrogen bondings following a surface energy minimalization principle. This is supported by the observation of drastic changes in turbidity at low polymer concentration during precipitation reaction (milky medium at the beginning of crystallization and transparent/clear solution at the end of the reaction), which indicates a complete incorporation of latex particles (i.e. depletion of latex particles in suspension). On one hand, this may give grounds to the estimated high value of incorporated latex particle / crystal, ranging between 20 and 100 in opposition to an expected value of 1 to 1 (i.e. homogeneous nucleation controlled by latex particles). On the other hand, this could justify the linear increase of crystal number density (i.e. number of crystals per unit volume) with increasing latex concentration and the observation that a latex radius of 150 nm is similarly effective for nucleation control of $NaZnPO_4 \cdot 1H_2O$. Besides, Rodionova et al. [303] first investigated the effects of M^{2+} electrolytes on hydration, stability of negatively charged latex particles sterically stabilized by PEO surfactants, and overall hydrophilicity (i.e. decrease of surface tension of the outer layers of the latex corona) depending on suspension temperature. The degree of hydrophilicity and the thickness of the hydrate shell are higher, the lower the degree of ethoxylation (i.e. $DP_n(PEO) < 6$) and the M^{2+}

concentration are. In addition, they [304] also observed a very high dehydration effect of Na_3PO_4 compared to NaCl (i.e. anion coagulating effect). Moreover, Roberts et al. [305] and later Behrend et al. [306] by advanced calculation/simulations confirmed the combined cation and H^+ coagulating effect, and the proton transport in the latex corona leading to the continuous replacement of H^+ in the Stern layer of the carboxylated latex particle by Na^+ and Zn^{2+} cations thanks to ^1H , ^{23}Na , ^{31}P NMR spectroscopy and steady-state voltametry employing the “latex cell model” developed by Jönson et al. [307]. These two last studies suggest that both inter- and intra-corona latex nucleation mechanisms occur simultaneously and concurrently due to inherent latex- M^{2+} complexation during precipitation crystallization of $\text{NaZnPO}_4 \cdot 1\text{H}_2\text{O}$.

5.3.11.3. M^{2+} -Latex coordination mechanisms

Within the framework of the Gibbsian thermodynamics, the early stages of crystal nucleation are sequentially governed by the formation of stable complexes between cations (Na^+ , Zn^{2+}) and anions (PO_4^{3-} , carboxylate functions originating from both the acetate ions and latex corona) that form clusters and subsequently condensate in a crystal nucleus on approaching supersaturation conditions [308-309]. Changes in coordination geometry and chemistry (i.e. exchange of ligands) may be monitored by spectroscopic methods [310-311]. Metal ion coordination generally causes (i) the appearance of new bands and splitting of the degenerate modes due to lowering of symmetry, (ii) frequency shifts of the bands and (iii) intensification of the spectra. Bellamy [312] and Nakamoto [313] have summarized the infrared and Raman absorption frequencies of carboxyl groups and the change of those frequencies when coordination of an organic ligand to metal ion occurs.

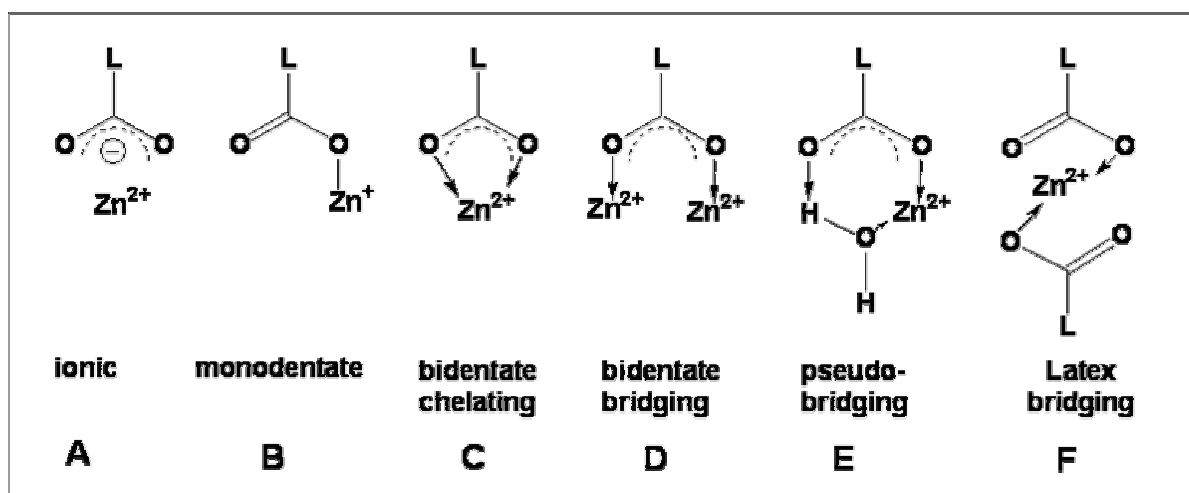


Figure 5.43: Main types of interaction between a carboxylate ligand grafted on a latex particle and a zinc cation. L describes the latex corona.

The carboxylate group of the latex corona can act as an uncoordinate anion (i.e. “ionic structure”) or form a monodentate ligand, a bidentate ligand or a bidentate bridging structure (Fig. 5.41). Recently, Milev et al. [312] fully reviewed these different coordination complex structures, distinguishing each

type of bonding by frequency shift and frequency separation of antisymmetrical and symmetrical carboxylate stretching vibrations ($\nu_{as}(\text{COO}^-)$ and $\nu_s(\text{COO}^-)$). A general trend may be summarized as follows in Fig. 5.43: Bidentate coordination (Fig. 5.43 C,D) of the COO^- group to Zn^{2+} downshifts the position of the $\nu_{as}(\text{COO}^-)$ band from that of free ionic carboxylate groups (seen in FTIR at $1580\text{--}1560\text{ cm}^{-1}$, Fig. 5.43 A) and upshifts to the respective $\nu_s(\text{COO}^-)$ stretching vibration. Monodentate (Fig. 5.43 B) coordination of the COO^- group to a Zn^{2+} upshifts the $\nu_{as}(\text{COO}^-)$ band from the position of the ionic band and downshifts the $\nu_s(\text{COO}^-)$. In the bridging coordination geometry D where one Zn^{2+} is bound to one of the two oxygen in the COO^- group and another divalent metal cation to the other oxygen, the $\nu_{as}(\text{COO}^-)$ is located essentially at the same position as the ionic $\nu_{as}(\text{COO}^-)$ band. It is also likely that a carboxylate group in a monodentate species is somewhat symmetrized by hydration (i.e. water contained in the latex corona, Fig. 5.43 E). Such coordination type, where the two C-O bonds bridge water hydrogen and Zn^{2+} is called "pseudobridging coordination" [315]. At high ionic strength and zinc concentration bridging between two latex particles via a L-COO-Zn-COO-L bridge can not be completely excluded (Fig. 5.43 F).

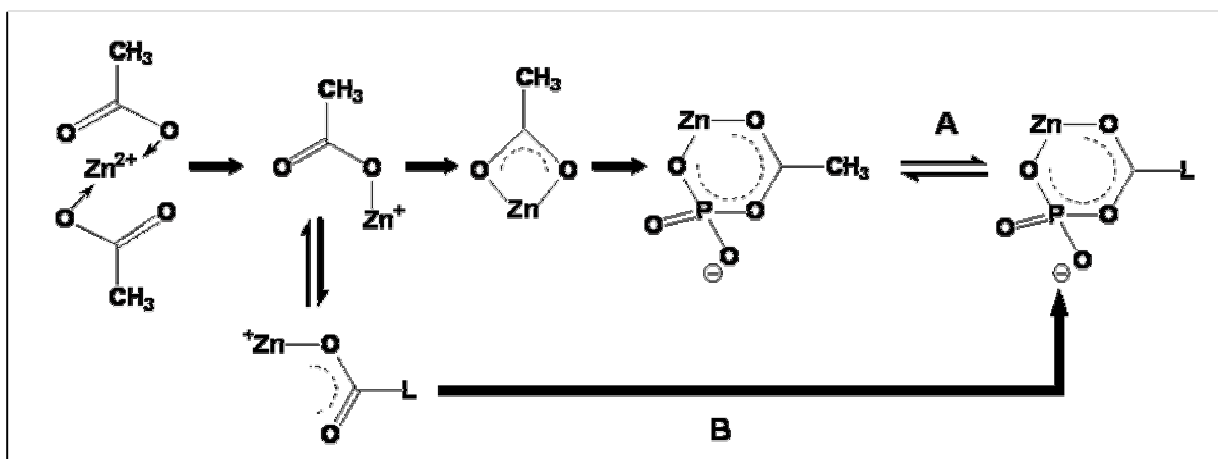


Figure 5.44: Possible pathways of ligand exchange occurring in the latex corona between acetate and a carboxylated latex (L) involved in ZPO mediated crystallization. Latex complexation before (A) and after (B) ion (Zn^{2+} and PO_4^{3-}) combination.

In addition, it is of foremost importance to stress the role of $\text{Zn}(\text{CH}_3\text{COO})_{2(\text{aq})}$ (i.e. ZnAc_2) played in the current synthesis of organic modified zinc phosphate (ZPO). Ac^- is a conventional ligand that has been widely used in coordination chemistry. However its coordinating function is always overlooked in materials science, which may be caused by the relatively weak interaction between Ac^- and the zinc ions. But compared with polymeric ligands, such as the acrylic based latexes presently used, Ac^- is characterized by its low binding stability at high temperature (90°C), rendering it especially suitable for hydrothermal synthesis of ZPT, and compatible with the presence of polymeric template agents, even at high concentration (i.e. no screening effect detected at ionic

strength $I > 0.5 \text{ mol.L}^{-1}$). Beside coordination effects, acetate ions function as buffer agent, keeping the pH value of the system around pH 7 at $I < 0.03 \text{ mol.L}^{-1}$. For large scale synthesis of ZPO, in direct correspondence with the synthesis procedure of pure ZPT polymorphs, NaOH is added to increase the solution of an initial value of 3 to pH 7, since ZPO formation is an H^+ releasing process (stemming from the H_3PO_4 concentrated solution). While pH 7 is required to sufficiently deprotonate the latex corona containing carboxylic groups, it implies the presence of non negligible quantities of sodium ions, that may either interfere with the ZPO crystallization or be fortunately partly trapped by Ac^- ions. Therefore acetate ions may participate in the latex/ Zn^{2+} complex formation prior to nucleation via two plausible pathways of ligand exchange: Latex complexation before (A) and after (B) ion (Zn^{2+} and PO_4^{3-}) combination, as shown in Fig. 5.44, via 4- to 6-membered ring geometry. Such a mechanism explains perfectly the incorporation of latex particle in a growing crystal and the nucleation activity of a carboxylated latex in ZPO mineralization.

5.4. Dendrimer controlled mineralization and ZPOs of 2nd generation: $\text{Na}_2\text{ZnPO}_4(\text{OH}) \cdot 2 \text{H}_2\text{O}$

In the light of the promising crystalline structures obtained by latex controlled hydrothermal mineralization regarding the morphology modifications, the phase stabilization of the overall decrease of crystal size and the diminishing of the CSD polydispersity of $\text{NaZnPO}_4 \cdot 1 \text{H}_2\text{O}$ on one hand, and the achievement of unsatisfying solubility behaviour of especially in alkaline medium above pH 10 (Chapter 6), efforts were focused on the development of a second generation of basic zincophosphates zeolites of defined morphology containing structural hydroxyl groups for superior surfacial stability on chemical aggression. Recently, synthetic anionic polypeptide analogue polymers have been found to be potent inhibitors or habit modifiers of calcium carbonate [305-306]. Systematic studies of $\text{NaZnPO}_4 \cdot 1 \text{H}_2\text{O}$ precipitation in presence of latex particles of diverse corona functionalization has shown that the selectivity for growth of certain faces as well as the efficient nucleation control appears to be highly dependent on the chemical organization of the corona and the secondary structure of the macromolecules (e.g. PS-*g*-PMAA of different block length). Levi et al. [318] reached similar conclusions regarding the stabilization of vaterite by poly-L-aspartate. As early as 1990, Tomalia et al. [319] candidly proposed poly(amidoamine) (PAMAM) dendrimers with alcoholate, carboxylate and amine groups at the external surface, denoted half-generation or $G = n.5$ dendrimers, as mimics of anionic micelles and proteins. The starburst structures are of disklike shape in the prime generations, whereas the surface branch cell becomes substantially more rigid and the structures are more spherical for later generations [320-321]. Upon chemical modifications (incorporation of carboxylate and hydrogen bonding groups at the primary amines) of PAMAM dendrimers, Birnbaum et al. [322] achieved an excellent anion selectivity and total binding capacity in aqueous medium. Lately, Mitra et al. [323] investigated the complex formation between

poly(amino amine) (PANAM) dendrimer of 4th generation and the phosphate groups of DNA chains in solution of ionic strength similar to the presently employed conditions for the dendrimer controlled synthesis of the new phase $\text{Na}_2\text{ZnPO}_4(\text{OH}) \cdot 2 \text{H}_2\text{O}$ and found significant conformational changes of the DNA chains. The dendrimer/DNA complexes formed aggregates and condensate in nanogels above a mixing ratio (i.e. number of NH_2 groups in dendrimer vs phosphate groups in DNA) of 0.2. Donners [324] even succeeded in stabilizing amorphous calcium carbonate and then generating hydroxyapatite nanocomposite of layered structure [325] with poly(propylene imine) dendrimers. Hence, owing to their unique and well defined secondary structures, PAMAM based dendrimers supplied by the BASF AG, should be good candidate for controlled mineralization of basic ZPO hydrid nanocrystals [326].

5.4.1. Effect of the chemical functionalization of PAMAM based dendrimers on ZPO crystallization

Upon addition of 1000 ppm of G = 1 PAMAM based dendrimer of different surface functionalization, under biological precipitation conditions (i.e. 20°C, pH 7, $I \approx 0.1 \text{ mol.L}^{-1}$) different morphologies and stabilization of crystal phases were achieved. In Fig. 5.45 either square shaped stacking pancakes of α -ZPT were obtained with such dendrimer of NH_2 -/OH-terminal functionalization (Fig. 5.43 A and B), or a cubic to hexagonal bipyramidal (HB) morphology was observed with zwitterionic dendrimer of NH_2 -/COOH-terminal functionalization Fig. 5.45 C and D).

In both cases monodisperse crystal size distributions were achieved and α -ZPT crystals were between 1.66 and 3.85 times larger than the size of those displayed in Fig. 5.45 C and D with 7.14 μm in averaged length versus 4.33 μm for the hexagonal bipyramidal morphology and 1.85 μm for the cubic morphology. This suggests a direct control of crystal growth by strong adsorption of dendrimer since adsorption of template additive onto specific surfaces of growing crystal alter the relative growth rate of the different crystallographic faces and leads to different crystal habits. In the light of the kinematic growth theory of Kossel and Stranski [327], observing that that the HB crystals are on average 2.34 times larger than the cubic crystals, an hexagonal bipyramid habit is *prevalent* in the selected experimental conditions (20.0°C, pH 7) (c.f. § 5.4.2). Therefore increasing concentrations of dendrimer from 500 ppm to 1000 ppm lead to stabilization of prismatic (rhombohedral) dodecahedrons, which undergo transformation in truncated hexagonal bipyramid and hexagonal bipyramid crystals of micrometric size (Fig. 5.45 C and D).

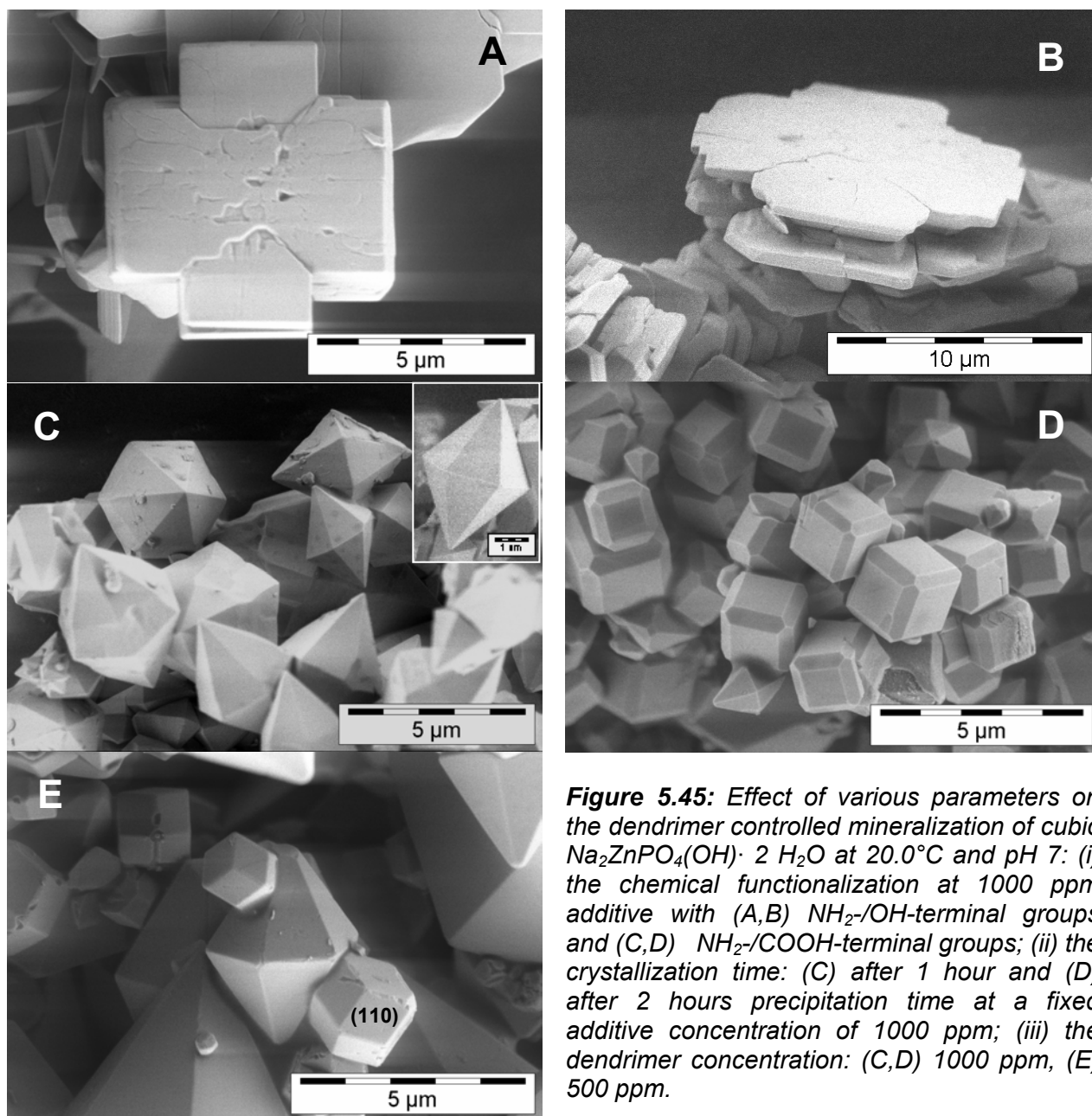


Figure 5.45: Effect of various parameters on the dendrimer controlled mineralization of cubic $\text{Na}_2\text{ZnPO}_4(\text{OH}) \cdot 2 \text{H}_2\text{O}$ at 20.0°C and $\text{pH } 7$: (i) the chemical functionalization at 1000 ppm additive with (A,B) NH_2 -/ OH -terminal groups and (C,D) NH_2 -/ COOH -terminal groups; (ii) the crystallization time: (C) after 1 hour and (D) after 2 hours precipitation time at a fixed additive concentration of 1000 ppm; (iii) the dendrimer concentration: (C,D) 1000 ppm, (E) 500 ppm.

This strongly suggests that this crystal phase is of cubic space group [328]. Besides, elemental analysis combined with thermogravimetry (TGA-MS) indicates the formation of organic-inorganic hybrid crystals of generic stoichiometry $\{(1-y) \text{Na}_x\text{Zn}_{(1-x)}(\text{OH})(\text{PO}_4) \cdot 2 \text{H}_2\text{O} + y \text{ Polymer}\}$ whereas $x = 2.11$ for the HB morphology and $x = 2.21$ for the cubic morphology. Huge amounts of dendrimer are incorporated in both morphologies with of 2.56 wt% and 3.18 wt% carbon content and 1.37 wt% and 1.71 wt% detected nitrogen content for the HB morphology and the cubic morphology, respectively. These crystal structures were analyzed by XRD as shown in Fig. 5.46. Both X-ray powder patterns are identical confirming that only the crystal habit between the two morphologies basically changed. The diffraction peaks do not correspond to any known single crystal structure. Recent crystallographic counter-analyses [329] deliver ambiguous results and tend to prove that the

precipitating material might be a mixture of hexagonal $\text{NaZnPO}_4 \cdot 1 \text{H}_2\text{O}$ and cubic $\text{Na}_6(\text{ZnPO}_4)_6 \cdot 8 \text{H}_2\text{O}$, thus explaining the determined average stoichiometry (2Na^+ and $2 \text{H}_2\text{O}$), albeit a single occurring morphology incompatible with an hexagonal one was observed at a time by SEM (refer to § 5.3). In addition, analogous and related zeolitic structures comprise sodium zinc phosphates of increasing state of hydration, i.e. $\text{Na}_2\text{ZnPO}_4(\text{OH})$ [330] and $\text{Na}_2\text{ZnPO}_4(\text{OH}) \cdot 7 \text{H}_2\text{O}$ [331] exist.

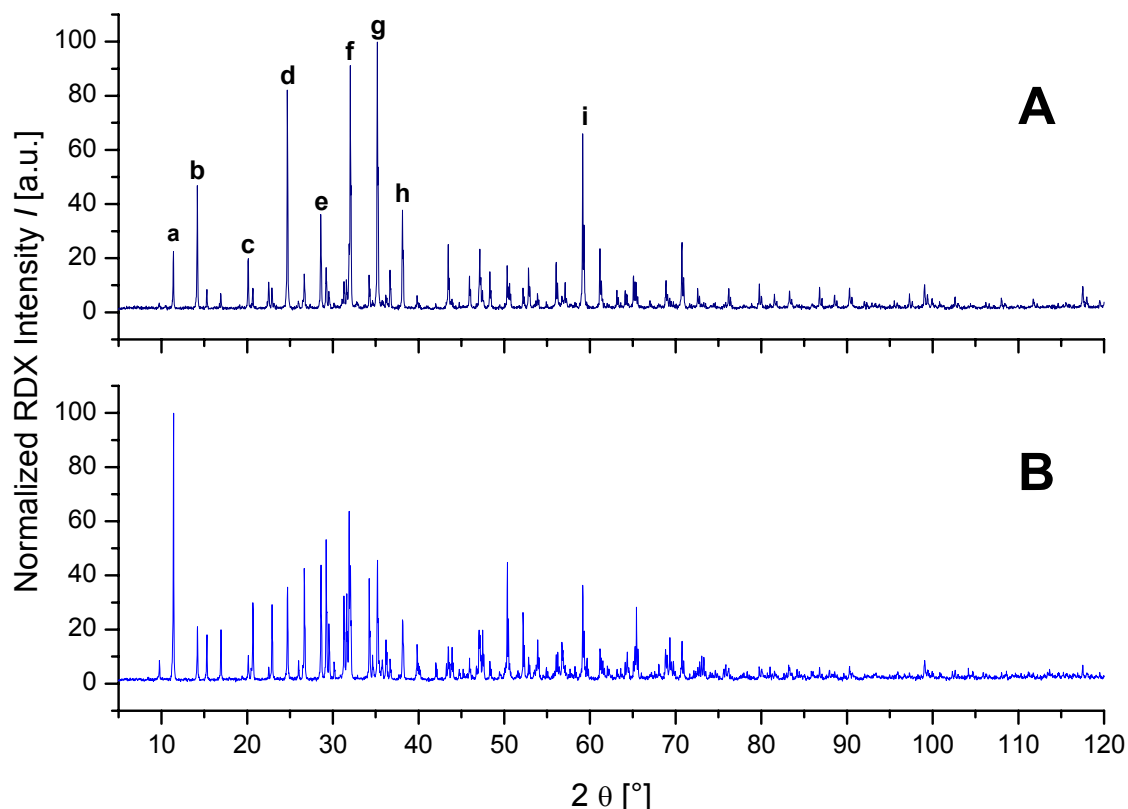


Figure 5.46: X-ray powder pattern of (A) cubic and (B) hexagonal bipyramidal (HB) morphologies of $\text{Na}_2\text{Zn}(\text{OH})(\text{PO}_4) \cdot 2\text{H}_2\text{O}$ zeolite obtained upon addition of 1000 ppm of NH_2 -/ COOH -end-functionalized dendrimer. Peak labels correspond to the following indexation sequence: a (100), b (110), c (120), d (021), e ($\bar{1}$ 02), f (230), g ($\bar{3}$ 21) and l (242) planes. Both structures are identified as $\text{Na}_2\text{Zn}(\text{OH})(\text{PO}_4) \cdot 2\text{H}_2\text{O}$ that crystallize in the monoclinic P12/C1 spacegroup. Intense reflexion of crystalline acetamide derivate (i.e. crystallized dendrimer layers) is observed in (B) at 27.25, 25.29 and 31.06°, indicating a strong polymer intercalation in the ZPO framework.

The generic structures synthesized here belong to odd-member ring zeolites and are characterized by high crystallographic disorder as the monoclinic space groups P121 /c1 and P21/a of the anhydrate and heptahydrate, respectively show. Brunner et al. [332] proposed that 3-ring containing systems may offer the lowest framework density possible, in terms of T (i.e. P) atoms per unit volume, in microporous systems. Coincidentally, the principal common features of these two sodium containing ZPOs are 3-ring grouping of PO_4 tetrahedra, which contain Zn-(OH)-Zn connections, and are part of one-dimensional chains or adjacent stacks of ZnO_4 and PO_4 groups, interconnected via a complex arrangement of sodium cations and water molecules. Such crystallographic consideration is strictly necessary for immediate perception of the complex dendrimer behaviour in solution during ZPO mineralization.

5.4.2. Effects of increasing polymer concentration and crystallization time on PAMAM based dendrimer controlled ZPO crystallization

In strong parallel to the effect of selective changes of dendrimer surfacial functionalization, the transition from a hexagonal bipyramidal to a cubic morphology is detected on doubling the crystallization time, via stabilization of prismatic dodecahedrons at increasing dendrimer concentration Fig. 5.45 C to E). Once again, this observation emphasizes the evident role of $\text{NH}_2^-/\text{COOH}^-$ functionalized dendrimers which may simultaneously coordinate Zn^{2+} and PO_4^{3-} (i.e. HPO_4^{2-}) ions at pH 7 and room temperature, and thus do not only control the crystal growth step by selective adsorption on growing faces but may also be instrumental for induction of $\text{Na}_2\text{ZnPO}_4(\text{OH}) \cdot 2\text{H}_2\text{O}$ nucleation.

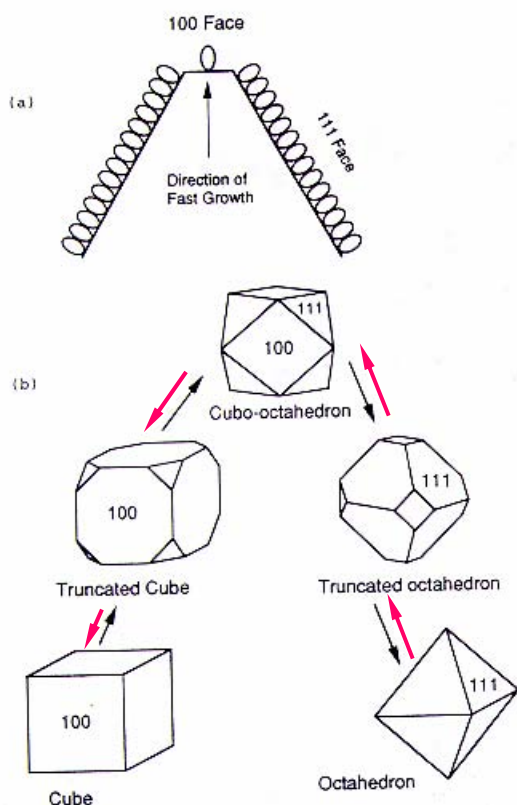


Figure 5.47: (A) Schematic representation of preferential adsorption of amino- carboxylated dendrimer at the (111) faces [e.g. (121), (231) and (321) faces] of $\text{Na}_2\text{Zn}(\text{OH})(\text{PO}_4) \cdot 2\text{H}_2\text{O}$, (B) transformation of crystal habit from hexagonal bipyramid (111) faces [e.g. (121), (231) and (321) faces] to cubic (100) due to selective adsorption of dendrimer (i.e. kinetic effect). From J.W. Mullin, *Crystallization*, 3rd Ed. CRC Press, (Boca Raton) (1993).

In due regard to the proposed mechanisms of latex controlled nucleation, this double chemical end-functionalization, and the planar geometry of the dendrimer may evidently facilitate his incorporation in layers perpendicular to the one-dimensional channels. As stated by Mullin [333] in Fig. 5.47, the adsorption of carboxylated dendrimer induces an increase of water adsorption water and thus a slowing of crystal growth. The magnitude of this phenomenon should increase with polymer concentration, on reminding that the cubic morphology contained 1.25 times more dendrimer in the corresponding framework than the HB morphology. This is precisely proven on exposing selected crystal faces to prolonged e-beam irradiation, as shown in Fig. 5.48. While the HB morphology

displays circular and concentric dehydration patterns, perpendicular to the observed surface plane, only sporadic and adventitious features are seen in the cubic morphology.

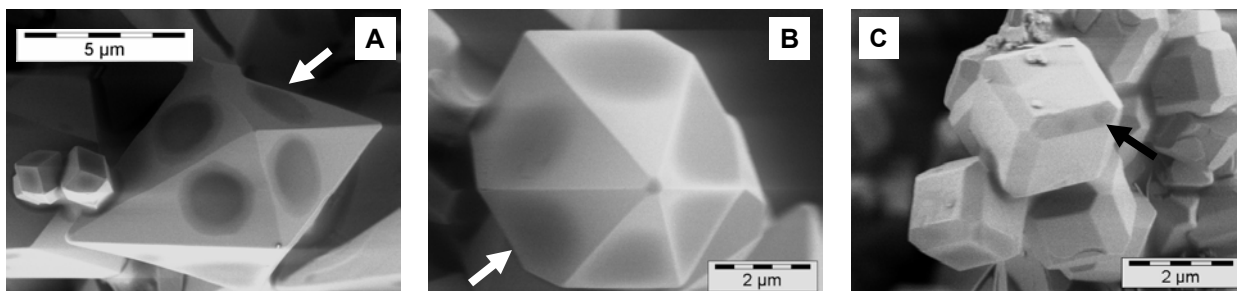


Figure 5.48: Dehydration channels (dark area marked by arrows) on the zeolitic structure of $\text{Na}_2\text{Zn}(\text{OH})(\text{PO}_4) \cdot 2\text{H}_2\text{O}$ as observed in SEM for various morphologies: (a), (B) hexagonal bipyramidal, (C) cubic.

On purpose, Fig. 5.49 and Fig. 5.50 give the TGA-MS and DSC curves of both ZPO morphologies. Huge differences in the thermal behaviour and water release have to be reported, depending on the crystal morphology, and thus denoting different insertion pathways of the dendrimer in the extra-framework structure.

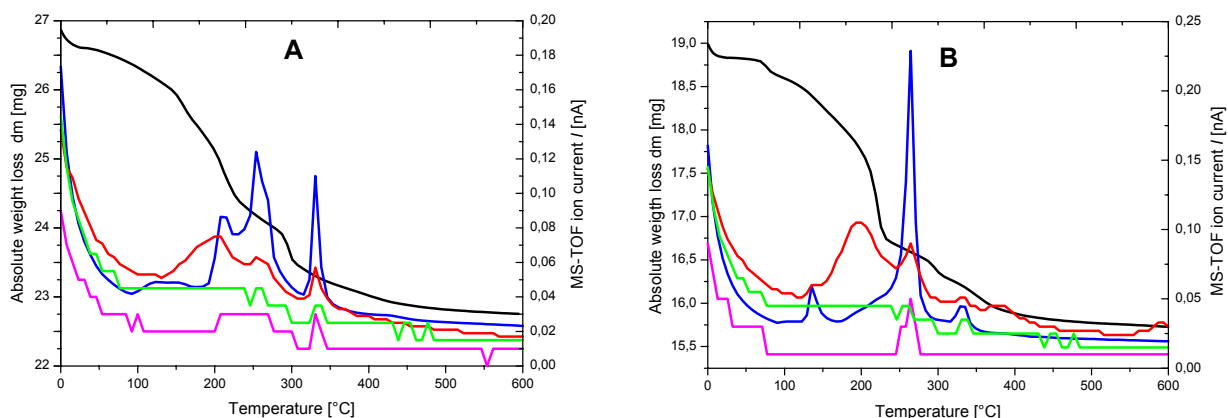


Figure 5.49: TGA-MS thermogravimetric curves (heating rate $10 \text{ K} \cdot \text{min}^{-1}$) of (A) cubic $\text{Na}_2\text{ZnPO}_4(\text{OH}) \cdot 2 \text{H}_2\text{O}$ (B) hexagonal bipyramidal $\text{Na}_2\text{ZnPO}_4(\text{OH}) \cdot 2 \text{H}_2\text{O}$ precipitated in presence of 1000 ppm NH_2 -/ COOH -end-functionalized dendrimer. The incorporation of the template agent is monitored by detection of (■) weight loss dm, (■) H_2O , (■) CO_2 [$\times 20$], (■) HCN [$\times 100$] and (■) NO/NO_2 [$\times 1000$] characteristic MS-signals. Huge differences in the water release are observed, depending on the crystal morphology.

Neglecting the release of adsorbed surface water of hydration, abrupt release of crystal water is observed by the presence of three successive sharp H_2O peaks at 207.6°C , 253.1°C and 330.7°C in the TGA-MS (m/z 18) curve of the $\text{Na}_2\text{ZnPO}_4(\text{OH}) \cdot 2 \text{H}_2\text{O}$ cubic morphology and correspond to a first release of $1.68 \text{ H}_2\text{O}$ at 253.1°C (Fig. 5.49.A), that is completed to $2 \text{ H}_2\text{O}$ (relative loss of 13.88 wt% for a theoretical yield of 13.87 wt%).

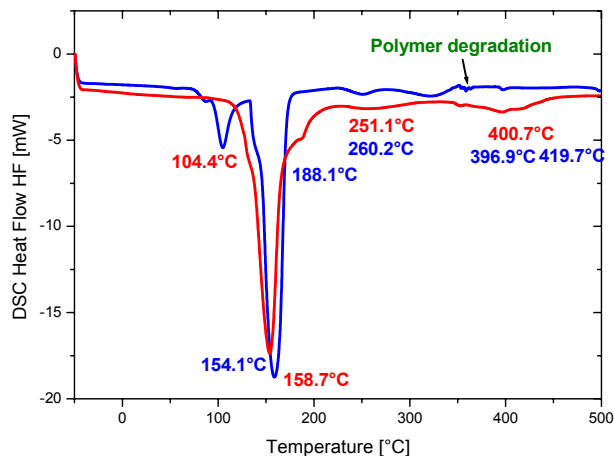


Figure 5.50: DSC curves taken at a heating rate of $10 \text{ K}\cdot\text{min}^{-1}$ of (■) hexagonal bipyramidal $\text{Na}_2\text{ZnPO}_4(\text{OH})\cdot 2 \text{H}_2\text{O}$ (■) cubic $\text{Na}_2\text{ZnPO}_4(\text{OH})\cdot 2 \text{H}_2\text{O}$ precipitated in presence of 1000 ppm NH_2 -/ COOH -end-functionalized dendrimer, showing a strong surface hydration effect for the cubic morphology. The incorporated dendrimer starts thermal degradation around 330°C ..

It can be concluded that a complete dehydration takes place on heating the crystals of cubic morphology. Moreover, the two last events are also related to some extent to the partial elimination of organic material (i.e. presence of CO_2 peaks at the same temperature as for H_2O MS signal). In opposition, the HB morphology has three peaks located at lower temperature, i.e. at 135.2°C , 264°C and 329°C respectively, suggesting a zeolitic structure of lower stability. These three steps correspond to the complete release of the two 2 structural water molecules at 264°C ; a release temperature 66°C lower than in the HB morphology. As temperature further increases, the $m/z = 18$ peak marks the release of 50% (3.14 wt% for a theoretical yield of 3.28 wt%) of the structural OH, and most probably indicates the beginning of the collapse of the zeolitic structure [334]. A transition peak that may correspond to the collapse of the crystal structure is detected at 400°C (Fig. 5.50). From a general point of view, the DSC curves confirm that each water release induces a phase transition, i.e. a structural reorganization of the sodium ions located in extra-framework guest sites since each peak appearing in DSC has is equivalent in the H_2O m/s signal detected in TGA-MS.

5.4.3. Selective incorporation of NH_2 -/ COOH -functionalized dendrimer in ZPO zeolitic structures

Spectroscopic methods highly sensitive to changes of the sphere of coordination of particular atoms such as FT-Raman, DRIFT and solid state MAS NMR help elucidate the formidable structural changes in the unit-cell at room temperature and the underlying transformations and atomic reorganizations upon heating of both cubic and HB complex morphologies of $\text{Na}_2\text{ZnPO}_4(\text{OH})\cdot 2 \text{H}_2\text{O}$ as recently demonstrated by Garcia-Serrano et al. for a chiral zincophosphates of Faujasite type [335].

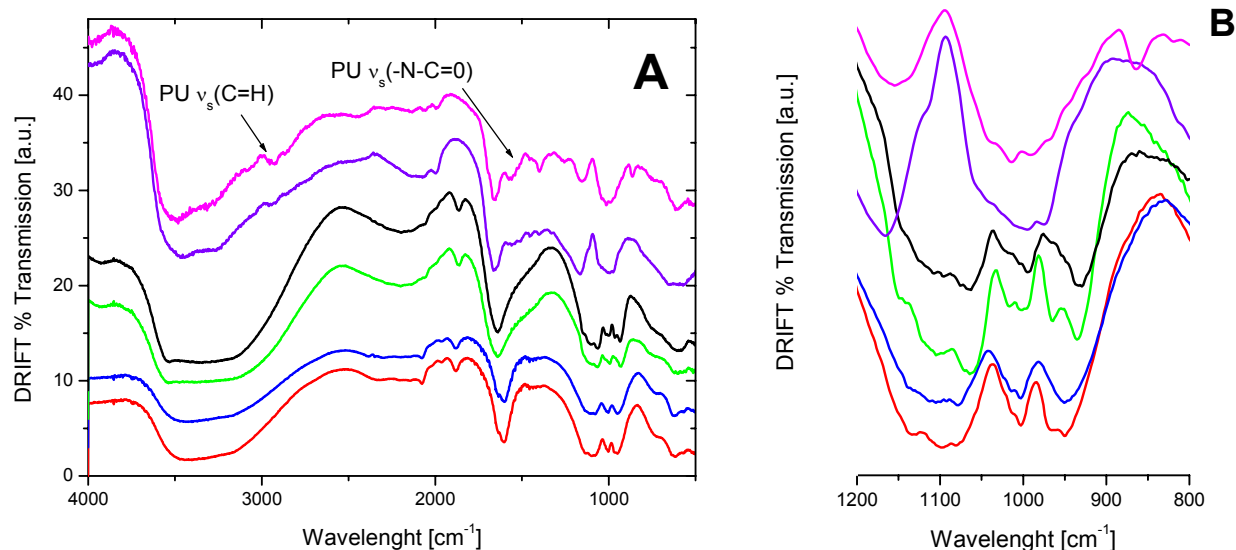


Figure 5.51: DRIFT spectra of: (■) α -ZPT, (■) β -ZPT, (■) α -ZPD, (■) β -ZPD compared to (■) hexagonal bipyramidal and (■) cubic $\text{Na}_2\text{ZnPO}_4(\text{OH}) \cdot 2 \text{H}_2\text{O}$ precipitated in presence of 1000 ppm NH_2 -/ COOH -end-functionalized dendrimer (A) overview and centered on the phosphate region (B). The incorporation of such a polyester amide dendrimer is emphasized by the presence of amide and alkyl related bands (A) and a strong distortion of phosphate groups (B).

Therefore, Figure 5.51 emphasizes the DRIFT spectra of the two morphologies of $\text{Na}_2\text{ZnPO}_4(\text{OH}) \cdot 2 \text{H}_2\text{O}$ compared to ZPT polymorphs. Characteristic bands of the polyester amide bonds constituting the PAMAM dendrimer are found in Fig. 5.49 A at $1622\text{--}1628 \text{ cm}^{-1}$ (N-H bending), 2923 cm^{-1} (ν_s C-H bond), and $1395\text{--}1580 \text{ cm}^{-1}$ (Dendrimer- $\text{COO} \cdots \text{Zn}^{2+}$ complex band) [336], further confirming the incorporation of dendrimer in the growing crystal structure. Similarly in the FT-Raman spectra (Fig. 5.52), for both morphologies the incorporation of the polyester amide dendrimer is well demonstrated in (A) with the appearance of characteristic peaks related to specific structural features of the dendrimer: OH band at 3231 cm^{-1} , C-H band at 2932 cm^{-1} , C-N band at 2731 cm^{-1} , C=O band at 1661 cm^{-1} , {amide}- $\text{ROCNI} \cdots \text{Zn}$ complex band at 1447 cm^{-1} ester amide bands at $1329/1296 \text{ cm}^{-1}$. This gives grounds to justify the observed slight distortion of the phosphate tetrahedra first in DRIFT (phosphate region, Fig. 5.51 B) between the hexagonal bipyramidal morphology of $\text{Na}_2\text{ZnPO}_4(\text{OH}) \cdot 2 \text{H}_2\text{O}$ and α -ZPT of 27 cm^{-1} maximum: 1037 vs 1010 cm^{-1} (ν_3 , g : 3), 1010 vs 1002 cm^{-1} (ν_3 , g : 2), 987 vs 968 cm^{-1} (ν_1) and 968 vs 950 cm^{-1} (ν_3 , g : 1) and secondly by FT-Raman spectroscopy (Fig. 5.51 B) with the observation of all compression modes (strong ν_2 and ν_4 at 473 cm^{-1} and 601 cm^{-1} respectively), one structural translation T mode at 558 cm^{-1} and the noticeable absence of one of the three shear mode $\nu_3(F_2)$ at 1150 cm^{-1} (shifted to 1109 cm^{-1}).

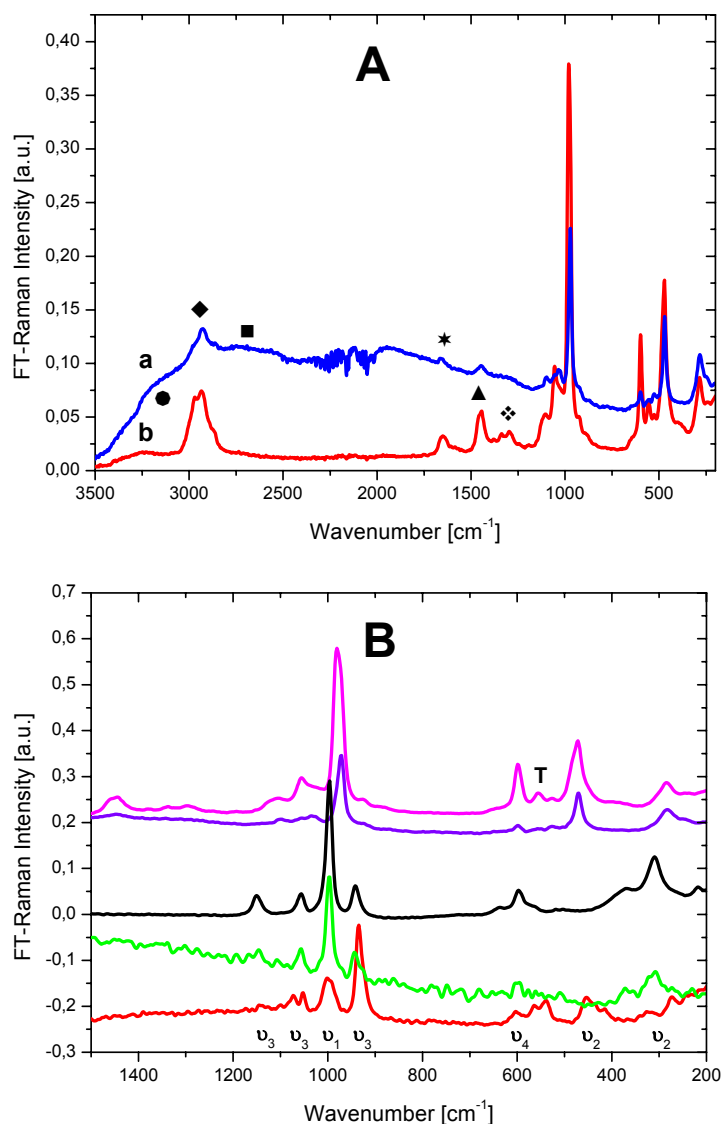
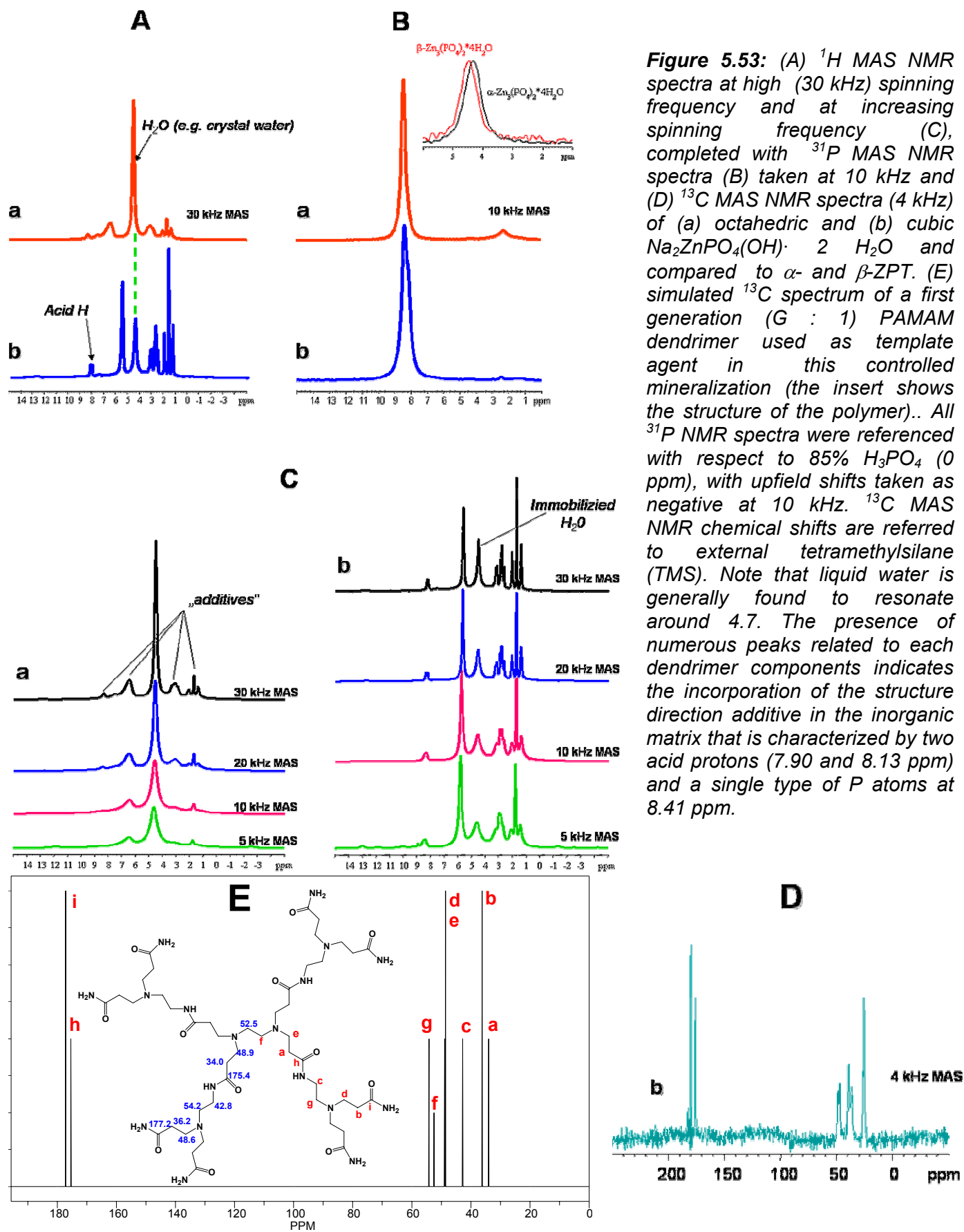


Figure 5.52: FT-Raman spectra of: (a) cubic $\text{Na}_2\text{ZnPO}_4(\text{OH}) \cdot 2 \text{H}_2\text{O}$ compared to (B) octahedral $\text{Na}_2\text{ZnPO}_4(\text{OH}) \cdot 2 \text{H}_2\text{O}$ precipitated in presence of 1000 ppm NH_2 -/ COOH -end-functionalized dendrimer. The incorporation of the polyester amide dendrimer is well demonstrated in (A) with the appearance of characteristic peaks related to specific structural features of the dendrimer: (●) OH band at 3231 cm^{-1} , (◆) C-H band at 2932 cm^{-1} , (■) C-N band at 2731 cm^{-1} , (★) C=O band at 1661 cm^{-1} , (▲) Amide-Zn complex band at 1447 cm^{-1} (◇) ester amide bands at $1329/1296 \text{ cm}^{-1}$. (B) Zoom on the phosphate region and the internal modes, i.e. ν_1 and ν_3 : symmetric and antisymmetric PO_4 stretching, ν_2 : bending, ν_4 : rocking and T: translational modes, for (■) α -ZPT, (■) β -ZPT, (■) $\text{Zn}_3(\text{HPO}_4)_3 \cdot 3 \text{H}_2\text{O}$, (■) octahedral $\text{Na}_2\text{ZnPO}_4(\text{OH}) \cdot 2 \text{H}_2\text{O}$, (■) cubic $\text{Na}_2\text{ZnPO}_4(\text{OH}) \cdot 2 \text{H}_2\text{O}$.

This may suggest that both morphologies of $\text{Na}_2\text{ZnPO}_4(\text{OH}) \cdot 2 \text{H}_2\text{O}$ are composed of inorganic layers alternated by intercalation of dendrimer layers, that may bridge the inorganic ZnO_4 - PO_4 framework and the sodium ions either by hydrogen bonding (possible due to the presence of strong symmetric OH-band at 3331 cm^{-1} in Fig. 5.52 A) or directly by amine-phosphate ion condensation. Besides, the most interesting difference between the cubic and the hexagonal bipyramidal morphologies of $\text{Na}_2\text{ZnPO}_4(\text{OH}) \cdot 2 \text{H}_2\text{O}$ lays not in the incorporation of the dendrimer additive itself but how it is done and how its pristine chemical structure is preserved upon intercalation.



On one hand, in the FT-Raman spectrum given in Fig. 5.52 A displays bands at $1329\text{-}1296\text{ cm}^{-1}$ and in the ^1H and ^{13}C MAS NMR spectra [337] of the cubic ZPO morphology (Fig. 5.53 A and D) the signaled presence of an acid proton a 8.0 ppm on the other hand, concordantly indicate that the structure of the $\text{NH}_2\text{-}/\text{COOH}$ -end-functionalized PAMAM dendrimer do not stay intact upon crystal nucleation, i.e. $\text{PO}_4\cdots\text{NH}_2$ -dendrimer (“amine”) condensation-like fashion takes place, generating some acidic protons (i.e. degradation of the dendrimer via saponification of the ester functions [338]) yielding for example and as described by Knecht et al. [339] silica nanospheres with distinct crystal size distributions (CSD) reminiscent of the structures produced during the early stages of nucleation. On the contrary, regarding the HD morphology the amido-function related bands nearly disappear simultaneously in Fig. 5.52 A, indicating only the restricted incorporation of the dendrimer in $\text{Na}_2\text{ZnPO}_4(\text{OH})\cdot 2\text{H}_2\text{O}$ crystal of this morphology, since XRD patterns still show crystalline organophosphate amide domains and possibly organized in layers reflecting at 27.25 , 25.29 and 31.06° [340].

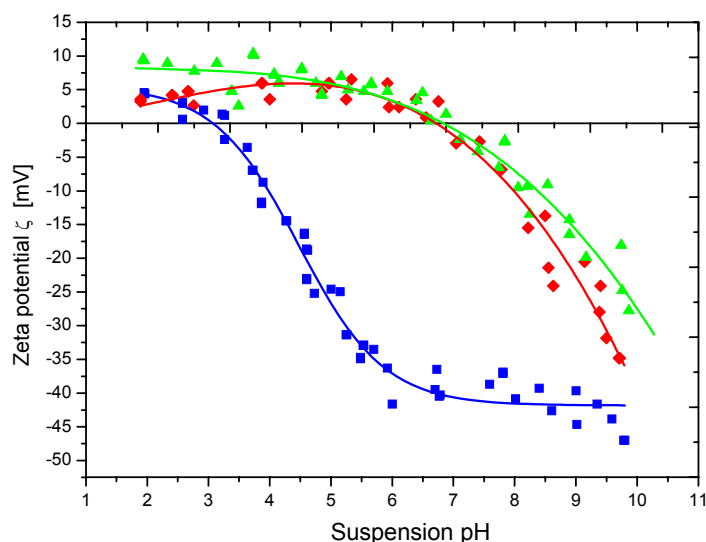


Figure 5.54: Effect of pH on zeta potential corrected from the particle size distribution and consequently on the surface charge density of basic zinc phosphates obtained by polymer controlled crystallization: (■) hexagonal $\text{NaZnPO}_4\cdot 1\text{H}_2\text{O}$, (▲) cubic $\text{Na}_2\text{Zn}(\text{OH})(\text{PO}_4)\cdot 2\text{H}_2\text{O}$, (◆) hexagonal bipyramide $\text{Na}_2\text{Zn}(\text{OH})(\text{PO}_4)\cdot 2\text{H}_2\text{O}$.

Furthermore, ^{31}P MAS spectra of both morphologies point out that the PO_4 environments are essentially the same in both structures, since a unique phosphorus atom type exists. This is in good agreement with the supposed crystal structure and no differences of chemical shift (peak at 8.41 ppm) has to be reported. In consequence, as verified by similar pH dependence of the zeta-potential of each morphology [341] of $\text{Na}_2\text{ZnPO}_4(\text{OH})\cdot 2\text{H}_2\text{O}$ (Fig. 5.52), while the surface reactivity of both morphologies of $\text{Na}_2\text{ZnPO}_4(\text{OH})\cdot 2\text{H}_2\text{O}$ should be identical, the bulk reactivity is expected to fluctuate greatly due to significant alteration of the dendrimer structure when the HB morphology is achieved.

In conclusion, the bulk solubility of these two morphologies of basic zinc phosphate, successfully synthesized on purpose in reasonable amount ($\approx 100\text{ g}$) by dendrimer controlled crystallization, can

be evaluated in dependence of the environmental conditions to which anticorrosion pigments are exposed in Chapter 6.

5.5. Conclusion

Among various research fields aimed at engineering complex nanostructures inspired from nature, organic-inorganic hybrid materials have opened a new horizon in the field of material science. Carboxylated PS-based latexes obtained by one-step radical miniemulsion polymerization offer a motivating and efficient alternative to expensive DHBCs currently used in polymer controlled (bio-) mineralization. This novel approach proved to be efficient at producing basic zinc phosphate microcrystals such as $\text{NaZnPO}_4 \cdot 1 \text{ H}_2\text{O}$ (1st generation ZPO) and $\text{Na}_2\text{ZnPO}_4(\text{OH}) \cdot 2 \text{ H}_2\text{O}$ (2nd generation ZPO), highly promising pigments for corrosion protection of steel surfaces.

Indeed, the addition of a 4 wt% COOH-functionalized latex in concentration as low as 700 ppm as structure controlling agent during hydrothermal precipitation (e.g. at 90°C and pH 7) induces the formation of hexagonal crystals of $\text{NaZnPO}_4 \cdot 1 \text{ H}_2\text{O}$, a metastable ZPO in respect to ZPT polymorphs. Uniquely latexes of 150 nm maximum diameter or lower could affect the rate of crystal “heterogeneous” nucleation without influencing the step of crystal growth by preferential adsorption on the polar [001] face. In this line, an effective latex in ZPO crystallization should exhibit a latex corona containing at least a non-ionic surfactant (e.g. PEO) of DP_n 10, i.e. a latex corona of 2 nm minimum thickness, so that cation exchanges (H^+ , Na^+ , Zn^{2+}) in the corona are favoured. Because as pointed out by Hilton, crystals cannot grow on spherical inclusions without generating defects, latexes of different surface functionalities and polarities, among them are represented -COOH, - SO_3H , - PO_4H_2 , - CONH_2 and $(\text{CH}_3)_3\text{N}^+ \text{Cl}^-$, but of constant surface charge density were synthesized. This leads first to different crystals morphologies such as hexagonal, heart-like, flowers, six arm star, spheres, etc., and secondly to a drastic change of aspect ratio R, characterized by a global flattening of the individual crystals (i.e. R decreases from 2 to 0.2). Each of these morphologies was obtained not only due to twinning and parallel growth, but also in reason of the intrinsic incorporation of a latex particle and its presence at the geometric center of the crystal as observed by TEM. In turn, this induces remnant strains around the absorption point (i.e. nucleation point) that consequently governs the growth on micron length scale of spiral dislocations along the c-axis, which were found to propagate coincidentally in one of the existing sodium channels of the $\text{NaZnPO}_4 \cdot 1 \text{ H}_2\text{O}$ zeolitic structure. On contrary, the addition of a positively charged latex emphasized separately both the control of nucleation and crystal growth step with the apparition of 70 μm wide dumbbells from hexagonal needle-like units following the principle of self-similarities (fractal growth). The connecting bar displays three-fold splitting sectors at both extremities and a hollow core filled

by latex aggregates. This strongly suggests a local inversion of permanent dipole in reference to Kniep's theory. In addition, the increase of pH and ionic strength in the crystallization medium produce zeolite β of increasing sodium and crystalline water content (i.e. $\text{Na}_6(\text{ZnPO}_4)_6 \cdot 8 \text{H}_2\text{O}$ at pH 10) in form of helical one, two and three arm lancers.

In addition, fundamental aspects of the crystallization kinetics were investigated. Thanks to a systematic increase of latex concentration during kinetics experiments, carboxylated latexes could not only monotonically decrease the crystal growth rate down to $8 \text{ nm} \cdot \text{min}^{-1}$ and also govern the induction time of nucleation, reduced to 8 sec at 1145 ppm. As expected latex particles revealed to be strong nucleation promoter. Moreover, negatively charged fluorescence labelled latexes were found to be selectively incorporated within a statistical ration crystal/latex particle ranging from 1:20 to 1:100. Solid state MAS NMR firstly confirmed the encapsulation of infinitesimal amount of latex in the crystal and secondly indicated a strong deformation of the latex corona via formation of $\text{L-COO}^- \cdots \text{Zn-PO}_4 \cdots \text{H}_2\text{O}_{\text{crystal}}$ coordination bridges. On this basis, two simple mechanisms referring to coordination chemistry (i.e. formation of a six-atom complex with ligand exchange) are tentatively proposed in order to highlight the primary role of negatively charges latexes on ZP nucleation (and mineralization by extension): an intra-corona nucleation mechanism and an extra-corona nucleation mechanism. The first mechanism settles on a fluctuation of PAA chain length (i.e. DP_n), and consequently on a fluctuation of corona affinity toward Zn^{2+} and Na^+ cations, which forces nucleation by attainment of local supersaturation inside the latex shell. In contrast, the extra-corona nucleation mechanism suggests an heterogeneous ZPO nucleation followed by adsorption on the outer layers of the hydrophilic corona due to a minimization of surface energy (i.e. nucleus stabilization).

A second generation of basic zinc phosphate hydrates containing crystalline hydroxyl groups in similarities to hydroxyapatite, of generic stoichiometry $\text{Na}_2\text{ZnPO}_4(\text{OH}) \cdot 2 \text{H}_2\text{O}$ was also successfully produced on large scale using polyesteramides dendrimers. A kinetic transition from a hexagonal bipyramidal (HB) to cubic morphology was observed on aging. Albeit no single crystal analysis was performed, this structure may belong to zeolite β of low symmetry (i.e. monoclinic space group) and present an arrangement in alternating *polymer-inorganic framework* layers. Such a conclusion was supported first by the detection of circular dehydration channels by SEM, secondly by the presence of huge concentration of dendrimer in the hybrid material as shown by ^1H and ^{13}C MAS NMR and thirdly by the combined presence of translation modulus and absence of one antisymmetric stretching modulus ($\nu_3(F_2)$) observed by FT-Raman. Nevertheless investigation by HRTEM and Raman confocal microscopy might be still necessary to finally conclude on this particular zeolitic architecture.

Finally, this study can be considered a first step toward deep understandings of the interactions polymer-crystal during hydrothermal precipitation, especially in the nucleation step (i.e. formation of coordination complexes and exchange of molecular units comprising latex functions such as L-COO⁻ groups, crystal water, water of hydration entrapped in the latex corona, diffusing Zn²⁺, PO₄³⁻ ions). In that sense, the synthesis of latexes of perfectly well defined architecture via the use of polymerizable surfactants bearing functional groups, applied on model ZnO mineralization could offer an interesting approach. The intra-corona latex nucleation mechanism may be sustained in studying the exact mechanisms of Mⁿ⁺ ions exchange and diffusion inside the corona layers by selective polytitration, atomic absorption spectroscopy (AAS), electrochemistry (i.e. conductometry and voltametry) and by complementary evaluation of the basicity of local extra-framework sites supposedly interacting with the latex corona thanks to ²³Na⁺ (e.g. metal cluster basicity) and ¹⁷O (e.g. hydroxyl functions: Brønsted base sites, basic oxygen: Lewis base site) MAS-NMR. Moreover, the corona-crystal interaction, the polymer-crystal interphase along with the structural organization of such ZPO “hybrid” materials could be advantageously investigated using latexes as vectors, e.g. containing magnetite nanoparticles. For industrial applications ZPO nanoparticles may be produced via the controlled thermal expansion (e.g. 200°C) of latexes charged with heptane that are selectively incorporated in ZPO crystals (“popcorn” effect).

5.6. References

- [1] C.M. Zaremba, D.E. Morse, S. Mann, G.D. Stucky et al., *Chem. Mater.* **10** (1998) 3813
- [2] S. Mann, J. Webb, R.J.P. Williams, *Biomaterialization: Chemical and biochemical perspectives*, Wiley VCH (NY) (1989) p. 541
- [3] H.A. Lowenstrom, S. Weiner, *On biomineralization*, Oxford University Press (NY) (1989)
- [4] S. Mann, D.D. Archibal, J.M. Didymus, T. Douglas, B.R. Heywood, F.C. Meldrum, N.J. Reeves, *Science* **261** (1993) 1286
- [5] S. Mann, *J. Chem. Soc.: Dalton Trans.* **21** (1997) 3953
- [6] L. Addadi, S. Weiner, *Stereochemical and structural relations between molecules and crystals in biomineralization*, S. Mann Ed, Wiley VCH (NY) (1989) p. 133
- [7] R.J. Davey, S.N. Black, L.A. Bromley, D. Cotter et al., *Nature* **353** (1991) 549
- [8] J.E. Barrelet, K.J. Lilley, L.M. Grover, D.F. Farrar, C. Ansell, U. Gbureck, *J. Mater. Sci.:Mater. Med.* **15**(4) (2004) 407
- [9] (a) M. Kikuchi, T. Ikoma, S. Itoh, H.N. Matsumoto et al., *Compos. Sci. Tech.* **64**(6) (2004) 819; (b) F. Watari, A. Yokoyama, M. Omori, T. Hirai et al., *Compos. Sci. Tech.* **64**(6) (2004) 893
- [10] S. Kim, H.S. Ryu, F.S. Jung, K.S. Hong, *Met. Mater. Int.* **10**(2) (2004) 171
- [11] E. Loste, R.M. Wilson, R. Seshadri, F.C. Meldrum, *J. Cryst. Growth* **254**(1-2) (2003) 206
- [12] L. Addadi, S. Raz, S. Weiner, *Adv. Mater.* **15**(12) (2003) 960
- [13] E. Loste, R.M. Wilson, R. Seshadri, F.C. Meldrum, *J. Cryst. Growth* **154**(1-2) (2003) 206
- [14] S. Weiner, P.M. Dove, *Rev. Mineral. Geochem.* **54** (2003) 1
- [15] R.K. Tag, C.A. Ormes, G.H. Nancollas, *J. Phys. Chem. B* **107**(38) (2003) 10653
- [16] (a) L.M. Grover, J.C. Knowles, G.J.P. Fleming, J.E. Barrelet, *Biomaterials* **24**(23) (2003) 4133; (b) R. Alvarez, L.A. Evans, P.J. Milham, M.A. Wilson, *Geoderma* **118**(3-4) (2004) 245
- [17] S. Mann, *Angew. Chem. Int. Ed.* **39** (2000) 3392
- [18] L.A. Estroff, A.D. Hamilton, *Chem. Mater.* **13** (2001) 322
- [19] S. Weiner, E. Levi-Kalisman, S. Raz, L. Addadi, *Connect. Tissue Res.* **44** (2003) 214
- [20] L.A. Estroff, C.D. Incarvito, A.D. Hamilton, *J. Am. Chem. Soc.* **126**(1) (2004) 2
- [21] C.G. Göltner, M. Antonietti, *Adv. Mater.* **9** (1997) 431
- [22] (a) H. Cölfen, M. Antonietti, *Langmuir* **14** (1998) 582; (b) H. Cölfen, Q. Limin, *Chem. Eur. J.* **7** (2001) 106
- [23] L. M. Qi, H. Cölfen, M. Antonietti, *Chem. Mater.* **12** (2000) 2392
- [24] H. Cölfen, *Macromol. Rapid. Commun.* **22** (2001) 587
- [25] J. Aizenberg, J. Hanson, T.F. Koetzle, S. Weiner et al., *Chem. Eur. J.* **1** (1995) 414
- [26] S. Weiner, L. Addadi, *J. Mater. Chem.* **7** (1997) 689
- [27] (a) N. Kröger, G. Lehmann, R. Rachel, M. Sumper, *Eur. J. Biochem.* **250** (1997) 99; (b) N. Kröger, R. Deutzmann, M. Sumper, *Science* **286** (1999) 1129
- [28] B.R. Heywood, S. Mann, *Adv. Mater.* **6** (1994) 9
- [29] (a) S. Mann, *J. Mater. Chem.* **5** (1995) 935; (b) S. Mann, S.L. Burkett, S.A. Davis, C.E. Fowler et al., *Chem. Mater.* **9** (1997) 2300
- [30] J.D. Hartgerink, E. Beniash, S.I. Stupp, *Science* **294** (2001) 1684
- [31] C. Feldmann, *Adv. Mater.* **13** (2001) 1301
- [32] C. Feldmann, C. Metzmacher, *J. Mater. Chem.* **11** (2001) 2603
- [33] D. Rautaray, A. Banpurkar, S.R. Sainkar, A.V. Limaye et al., *Adv. Mater.* **15**(15) (2003) 1273
- [34] L. Vaissieres, K. Keis, A. Hagfeld, S.E. Lindquist, *Chem. Mater.* **13**(12) (2001) 4395
- [35] J. Kuether, M. Bartz, R. Seshadri, G.B.M. Vaughn, W. Tremel, *J. Mater. Chem.* **11** (2001) 503
- [36] P.A. Ngankam, P. Lavalley, J.C. Voegel, L. Szyk, G. Decher et al., *J. Am. Chem. Soc.* **122** (2000) 8998
- [37] S.M. D'Souza, C. Alexander, S.W. Carr, A.M. Waller et al., *Nature* **398** (1999) 312
- [38] G. Falini, S. Fermani, M. Gazzano, A. Ripamonti, *J. Chem. Soc.: Dalton Trans.* **21** (2000) 3983

- [39] C.Z. Lu, J.Y. Cho, H.J. Chang, S.W. Joo et al., *Mater. Sci. Forum* **449**(4) (2004) 1009
- [40] (a) E. Loste, F.C. Meldrum, *Chem. Commun.* **10** (2001) 901; (b) R.J. Park, F.C. Meldrum, *Adv. Mater.* **14** (2002) 1167
- [41] B.D. Chen, J.J. Cilliers, R.J. Davey, J. Garside et al., *J. Am. Chem. Soc.* **120** (1998) 1625
- [42] M. Willert, R. Rothe, K. Landfester, M. Antonietti, *Chem. Mater.* **13** (2001) 4681
- [43] (a) M.P. Pileni, *Cryst. Res. Technol.* **33** (1998) 1155; (b) M. Antonietti, E. Wenz, L. Bronstein, M. Seregina, *Adv. Mater.* **7** (1995) 1000
- [44] J.P. Cason, M.E. Miller, J.B. Thompson, C.B. Roberts, *J. Phys. Chem. B* **105**(12) (2001) 2297
- [45] (a) A.F. Hollemann, N. Wiberg, *Lehrbuch der anorganische Chemie*, 91-100th Ed., W. DeGruyter (Berlin) (1985); (b) A.R. West, *Grundlagen der Festkörperchemie*, Wiley VCH (Weinheim) (1992)
- [46] J.M. Marentette, J. Norwig, E. Stockelmann, W.H. Meyer, G. Wegner, *Adv. Mater.* **9**(8) (1997) 647
- [47] M. Oner, J. Norwig, W.H. Meyer, G. Wegner, *Chem. Mater.* **10**(2) (1998) 460
- [48] H. Cölfen, *Z. Anorg. All. Chem.* **629** (2003) 2305
- [49] F. Peters, M. Epple, *J. Chem. Soc.: Dalton Trans.* **X** (2001) 3585
- [50] A. Becker, W. Becker, J.C. Marsen, M. Epple, *Z. Anorg. Allg. Chem.* **629** (2003) 2305
- [51] M. Antonietti, M. Breulmann, C.G. Göltner, H. Cölfen, *Chem. Eur. J.* **4**(12) (1998) 2493
- [52] H. Kawaguchi, H. Hirai, K. Sakai, S. Sera et al., *Colloid. Polym. Sci.* **270** (1992) 1176
- [53] L. Qi, H. Cölfen, M. Antonietti, M. Li et al., *Chem. Eur. J.* **7** (2001) 3526
- [54] A. Bigi, E. Banini, G. Cojazzi, G. Falini et al., *Cryst. Growth Des.* **1** (2001) 239
- [55] J.H. Adair, E. Suvaci, *Curr. Opin. Colloid Interface Sci.* **5** (2000) 160
- [56] (a) E. Matijevic, *Chem. Mater.* **5** (1993) 412; (b) E. Matijevic, *Curr. Opin. Colloid Interface Sci.* **1** (1996) 176
- [57] M. Sastry, A. Kumar, C. Damle, S.R. Sainkar et al., *CrystEngComm.* **1** (2001) 21
- [58] M. Sedláč, H. Cölfen, *Macromol. Chem. Phys.* **202** (2001) 587
- [59] (a) C. M. Zaremba, A. M. Belcher, M. Fritz, Y. Li et al., *Chem. Mater.* **8** (1996) 679; (b) C.M. Zaremba, D.E. Morse, S. Mann, P.K. Hansma et al., *Chem. Mater.* **10** (1998) 3814
- [60] J.B. Thompson, G.T. Placzi, J.H. Kindt, M. Michenfelder et al., *Biophys. J.* **79** (2000) 3307
- [61] J. Nyvlt, J. Ulrich, *Admixtures in Crystallization*, Wiley VCH (Weinheim) (1995)
- [62] Y. Mastai, M. Sedláč, H. Völfen, M. Antonietti, *Chem. Eur. J.* **8**(11) (2002) 2430
- [63] Y. Wang, J. Yu, Y. Li, Z. Shi et al.; *Chem., Eur. J.* **9** (2003) 5048
- [64] E. Yahima, K. Maeda, T. Nishimura, *Chem. Eur. J.* **10** (2004) 42
- [65] (a) E. Matijevic, *Langmuir* **2** (1986) 12; (b) E. Matijevic, *Chem. Mater.* **5** (1993) 412
- [66] P. Baum, *PhD Thesis*, University of Mainz (Germany) (2000)
- [67] G. Wegner, P. Baum, M. Muller, J. Norwig et al., *Macromol. Symp.* **175** (2001) 349
- [68] R.L. Penn, J.F. Banfield, *Science* **281** (1998) 969
- [69] A.P. Alivisatos, *Science* **289** (2000) 736
- [70] S. Bush, H. Dolhaine, A. DuChesne, T. Weiland et al., *Eur. J. Inorg. Chem.* **10** (1999) 1643
- [71] J.F. Banfield, S.A. Welch, H. Zhang, T. Thomsen-Ebert et al., *Science* **289** (2000) 751
- [72] J. Rieger, J. Thieme, C. Schmidt, *Langmuir* **16** (2000) 8300
- [73] N. Bouropoulos, S. Weiner, L. Addadi, *Chem. Eur. J.* **7** (2001) 1881
- [74] S. Förster, M. Antonietti, *Adv. Mater.* **10**(3) (1998) 195
- [75] C. Seitz, *PhD. Thesis*, University of Mainz (Germany) (1999)
- [76] P. Kašparová, *PhD Thesis*, University of Potsdam (Germany) (2002)
- [77] (a) M. Gutierrez, A. Henglein, *J. Phys. Chem.* **100**(18) (1996) 7656; (b) G.B. Ershov, A. Henglein, *J. Phys. Chem. B* **102**(52) (1998) 10663 and thereafter
- [78] S.H. Yu, H. Cölfen, M. Antonietti, *J. Phys. Chem. B* **107**(30) (2003) 7396
- [79] A. Taubert, D. Palms, Ö. Weiss, M.T. Piccini, *Chem. Mater.* **14** (2002) 2594
- [80] A. Taubert, G. Glasser, D. Palms, *Langmuir* **18**(11) (2002) 4488
- [81] D. Braga, *J. Chem. Soc.: Dalton Trans.* **21** (2000) 3705
- [82] B.Z. Putlitz, K. Landfester, H. Fischer, M. Antonietti, *Adv. Mater.* **13**(7) (2001) 500
- [83] H. Xiao, Z. Liu, N. Wiseman, *J. Colloid Interfaces Sci.* **216** (1999) 409
- [84] G. Baskar, K. Landfester, M. Antonietti, *Macromolecules* **33**(25) (2000) 9228
- [85] K. Landfester, *Macromol. Rapid. Commun.* **22** (2001) 896

- [86] K. Landfester, M. Antonietti, *Macromol. Rapid Comm.* **21**(12) (2000) 820
- [87] J.J.J.M. Donners, B.R. Heywood, E.W. Meijer, R.J.M. Nolte et al., *Chem. Commun.* **19** (2000) 1937
- [88] S.H. Liu, X.F. Qian, J. Yin, L. Hong et al., *J. Solid State Chem.* **168** (2002) 259
- [89] L. Vaissieres, N. Beermann, S.E. Lindquist, A. Hagfeldt, *Chem. Mater.* **13**(2) (2001) 233
- [90] K. Landfester, N. Bechthold, F. Tiarks, M. Antonietti, *Macromolecules* **32**(8) (1999) 2679
- [91] S. Kirsch, K. Landfester, O. Schaffer, M.S. El-Aasser, *Acta Polym.* **50**(10) (1999) 347
- [92] D. Vaihinger, K. Landfester, I. Kräuter, H. Brunner et al., *Macromol. Chem. Phys.* **203** (2002) 1965
- [93] M. Willert, K. Landfester, *Macromol. Chem. Phys.* **203**(5-6) (2002) 825
- [94] N. Bechthold, F. Tiarks, M. Willert, K. Landfester et al., *Macromol. Symp.* **151** (2000) 549
- [95] M. Antonietti, K. Landfester, *Prog. Polym. Sci.* **27** (2002) 689
- [96] J.M. Asua, *Prog. Polym. Sci.* **27** (2002) 1283
- [97] K. Landfester, *Top. Curr. Chem.* **227** (2003) 75
- [98] K. Landfester, N. Bechthold, F. Tiarks, M. Antonietti, *Macromolecules* **32**(16) (1999) 5222
- [99] K. Landfester, N. Bechthold, S. Förster, M. Antonietti, *Macromol. Rapid Commun.* **20**(2) (1999) 81
- [100] K. Landfester, *Macromol. Symp.* **150** (2000) 171
- [101] K. Landfester, F.J. Scherk, V.A. Kuscima, *C.R. Chimie (France)* **6** (2003) 1337
- [102] H. Füredi-Milhofer, S. Sarig, *Prog. Crystal Growth and Charact.* **32** (1996) 45
- [103] A. Tsortos, G.H. Nancollas, *J. Colloid Interface Sci.* **250** (2002) 159
- [104] K. Meuwis, N. Boens, F.C. De Schryver, M. Ameloot et al., *J. Phys. Chem.* **102**(3) (1998) 641
- [105] (a) Ö. Pekcan, M. Canpolat, E. Arda, *Polym. Int.* **47**(4) (1998) 451; (b) F. Tiarks, K. Landfester, M. Antonietti, *Langmuir* **17** (2001) 908
- [106] K. Landfester, L.P. Ramirez, *J. Phys. Condens. Mater.* **15**(15) (2003) 1345
- [107] P.L. Tang, E.D. Sudol, M.E. Adams, C.A. Silebi, M.S. El-Asser, in *Polymer Latexes*, E.S. Daniels, E.D. Sudol, M.S. El-Asser Eds., *American Chemical Society* (Washington) (1992) p. 72
- [108] E.D. Sudol, M.S. El-Asser, in *Emulsion Polymerization and Emulsion Polymers*, P.A. Lovell and M.S. El-Asser Eds., *Wiley & Sons* (Chichester) (1997) p. 699
- [109] (a) P. Moy, F.E. Karasz, *Polym. Eng. Sci.* **20** (1980) 315; (b) T.S. Ellis, F.E. Karasz, *Polymer* **25** (1984) 664
- [110] *Polymer Handbook*, J. Brandrup, E.H. Immergut and E.A. Grulke Eds., 4th Ed., *Wiley VCH* (Weinheim) (1999) pp. V88, V91
- [111] D. Palms, *PhD Thesis*, University of Mainz (Germany) (2003)
- [112] P.J. Blythe, E.D. Sudol, M.S. El-Asser, *Macromol. Symp.* **150** (2000) 179
- [113] F.J. Schork, G.W. Poehlein, S. Wang, J. Reimers, J. Rodrigues, C. Samer, *Colloid Surf. A : Physicochem. Eng. Asp.* **153** (1999) 39
- [114] K. Landfester, *Adv. Mater.* **13**(10) (2001) 765
- [115] K. Landfester, N. Bechthold, F. Tiarks, M. Antonietti, *Macromol. Rapid. Comm.* **20** (1999) 81
- [116] B. Zu Pulit, H.P. Hentze, K. Landfester, M. Antonietti, *Langmuir* **16** (2000) 3214
- [117] T. Feng-Shong, A. Dubault, J.L. Halar, *J. Appl. Polym. Sci.* **73** (1999) 2463
- [118] (a) K. Suzuki, A. Goto, M. Takayama, A. Muramatsu et al., *Macromol. Symp.* **155** (2000) 199; (b) K. Suzuki, M. Nomura, *Macromol. Symp.* **179** (2002) 1
- [119] G. Fritz, V. Schädler, N. Willenbacher, J.N. Wagner, *Langmuir* **18** (2002) 6381
- [120] X.E.E. Reynhout, J. Meuldijk, B.A.H. Drinkenburg, *Prog. Colloid Polym. Sci.* **124** (2004) 64
- [121] D.C. Brackley, *Sci. Technol. Polym. Coll.* **1** (1983) 203
- [122] M. Slawinski, J. Meuldijk, A.M. Van Herk, A.L. German, *J. Appl. Polym. Sci.* **78** (2000) 875
- [123] E.M. Cohen, R.A. Lyons, R.G. Gilbert, *Macromolecules* **29** (1996) 5128
- [124] A.M. Dos Santos, T.F. McKenna, J. Guillot, *J. Appl. Polym. Sci.* **65** (1997) 2343
- [125] M. Slawinski, M.A.J. Schellekens, J. Meuldijk, A.M. Van Herk et al., *J. Appl. Polym. Sci.* **76** (2000) 1186
- [126] I. Verala de la Rosa, E.D. Sudol, M.S. El-Aasser, A. Klein, *J. Polym. Sci.* **A37** (1999) 4054, and thereafter

- [127] (a) W. Liang, Th.F. Tadros, *Langmuir* **10** (1994) 441; (b) P. Jenkins, M. Snowden, *Adv. Colloid Interf. Sci.* **68** (1996) 57
- [128] A. Sharma, S. Nee Tan, J.Y. Walz, *J. Colloid Interf. Sci.* **190** (1997) 392
- [129] (a) V.A. Kabanov, D.A. Topchiev, T.M. Karaputadze, *J. Polym. Sci.: Polym. Symp.* **42**(1) (1973) 173; (b) G.L. Shoaf, G.W. Poehlein, *J. Appl. Polym. Sci.* **42** (1991) 1169
- [130] K. Landfester, M. Willert, M. Antonietti, *Macromolecules* **33** (2000) 2370
- [131] F.J. de las Niervas, E.S. Daniels, M.S. El-Aasser, *Colloids and Surfaces* **60** (1991) 107
- [132] (a) J.H. Kim, M.S. El-Aasser, A. Klein, J.W. Wanderhoff, *J. Appl. Polym. Sci.* **35** (1988) 2117; (b) J.H. Kim, M. Chainey, M.S. El-Aasser, J.W. Wanderhoff, *J. Polym. Sci.* **A30** (1992) 171
- [133] D. Bastos, F.J. de las Niervas, *Coll. Polym. Sci.* **271** (1993) 860
- [134] H. Xia, Z. Liu, N. Wiseman, *J. Colloid. Interface Sci.* **216** (1999) 409
- [135] A.L. German, A. M. van Herk, H.A.S. Schoonbrood, A.M. Aerdts, in *Emulsion Polymerization and Emulsion polymers*, Chapter 11, P.A. Lovell, and M.S. El-Aasser Eds., Wiley (NY) (1997) p. 343
- [136] H. Oshima, in *Electrical phenomena at interfaces: Fundamentals, Measurements and Applications*, Chapter 1 and 2, Surfactant Science Series Vol. 76, 2nd Ed., H. Oshimma and K. Furusawa Eds., Marcel Dekker (NY) (1998) p. 1
- [137] L.P. Yezek, H.P. van Leeuwen, *J. Colloid Interface Sci.* (2004), *in press*.
- [138] W.B. Russel, D.A. Saville, W.R. Schowalter, *Colloidal Dispersions*, Cambridge University Press (Cambridge) (1989)
- [139] (a) Pluronic PE Trademarks, *BASF Technical Information Datasheet*, TI/ES 1026d (2002); (b) P. Alexandridis, J.F. Holzwarth; T.A. Hatton, *Macromolecules* **27**(9) (1994) 2414; (c) D. Zhao, J. Feng, B.F. Chmelka, G.D. Stucky et al, *Science* **279** (1998) 548
- [140] A.M. Puertas, F.J. de las Nieves, *J. Colloid Interface Sci.* **216** (1999) 221
- [141] S.H. Yu, H. Cölfen, M. Antonietti, *Chem. Eur. J.* **8** (2002) 2937
- [142] S.H. Yu, H. Cölfen, M. Antonietti, *Adv. Funct. Mater.* **12** (2002) 541
- [143] X.H. Bu, T.E. Gier, W.T.A. Harrison, G.D. Stucky, *Acta Cryst.* **C53** (1997) 1517
- [144] (a) A. Wenddio, J. Lindgren, J.O. Thomas, G.C. Farrington, *Solid State Ionics* **53**(6) (1992) 1077; (b) H. Kasemagi, M. Klintonberg, A. Aadloo, J.O. Thomas, *Electrochim. Acta* **48**(14-16) (2003) 2273
- [145] (a) C.Z. Yu, B.Z. Tian, D.Y. Zhao, G.D. Stucky, *J. Phys. Chem.* **B107** (2003) 13375; (b) T. Liu, C. Burger, B. Chu, *Prog. Polym. Sci.* **28** (2003) 5
- [146] M. Antonietti, M. Breulemann, C.G. Göltner, H. Cölfen et al, *Chem. Eur. J.* **4**(12) (1998) 2493
- [147] A. Taubert, C. Kübel, D.C. Martin, *J. Phys. Chem.* **B107** (2003) 2660
- [148] N. Jedrecy, M. Sauvage-Simkin, R. Pinchaud, *Appl. Surf. Sci.* **162-163** (2000) 69
- [149] W.E. Ostwald, *Z. Phys. Chem.* **22** (1897) 289
- [150] K.E. Kelton, *Solid State Physics*, Vol. **45**, H. Ehrenreich and D. Turnbull Eds., Academic Press (NY) (1991)
- [151] (a) J. Kühther, R. Seshadri, W. Tremel, *Angew. Chem. Int. Edit.* **37**(21) (1998) 3044 (b) D. Schwahn, M. Balz, M. Bartz, A. Fomenko, W. Tremel, *J. Appl. Crystallogr.* **36**(3) Sp. Iss. 1 (2003) 583
- [152] A. Kose, S. Hachisu, *J. Colloid. Interface Sci.* **55** (1976) 487
- [153] A. Dinsmore, P. Warren, W. Poon, A. Yodh, *Europhys. Lett.* **40** (1997) 337
- [154] A. Cacciuto, S. Auer, D. Frenkel, *Nature* **428** (2004) 404
- [155] P. Hilton, J. Pederson, *Am. Math. Mon.* **103** (1996) 121
- [156] S. Auer, D. Frenkel, *Phys. Rev. Lett.* **91** (2003) 015703
- [157] S. Auer, D. Frenkel, *Nature* **413** (2001) 711
- [158] S. Penczek, 1st Plenary lecture, *NATO ASI Symposium* (6-16th October 2003, Tirrenia, Italy)
- [159] S. Penczek, J. Pretula, K. Kaluzynski, *J. Polym. Sci.* **A42**(3) (2004) 432
- [160] S. Penczek, E. Kaluzynski, Z. Bartczak, W. Zielenkiewicz et al., *E-polymers* (2002) Art. No. 055
- [161] *Non polymerizable phosphate ester emulsifier*, Polymer System Specialties, Rhodia SA, HPCII (July 2002).

- [162] M. Seldak, M. Antonietti, H. Cölfen, *Macromol. Chem. Phys.* **199**(2) (1998) 247
- [163] H. Cölfen, M. Antonietti, *Langmuir* **14** (1998) 582
- [164] M.C. Van der Leeden, G.M. Van Rosmalen, *J. Crystal Growth* **130** (1993) 221
- [165] K. Plochova, *J. Macromol. Sci. – Rev. Macromol. Chem.* **C20**(1) (1981) 67
- [166] J.W. Noor, B. Dam, *J. Crystal Growth* **76** (1986) 243
- [167] D.A. Faux, *J. Phys. Chem.* **B102** (1998) 10658
- [168] (a) C. Frondel, *Miner. Mag. – J. Min. Soc.* **36**(282) (1968) 8618; (b) W. Kleber, *Einführung in die Kristallographie*, WEB Verlag Technik (Berlin) (1970) p. 111
- [169] I. Sabbaugh, M. Delsanti, *Eur. Phys. J. E1* (2000) 75
- [170] S.H. Yu, H. Cölfen, M. Antonietti, *Chem. Eur. J.* **8**(13) (2002) 2937
- [171] (a) A.K. Cheetham, G. Ferey, T. Loiseau, *Angew. Chem. Int. Ed.* **38**(22) (1999) 3268; (b) P.M. Forster, A.K. Cheetham, *Top. Catal.* **24**(1-4) (2003) 79
- [172] S. Mandel, S. Natarajan, *Inorganic Chim. Acta* **357**(5) (2004) 1437
- [173] S. Natarajan, *Z. Anorg. Allg. Chem.* **629**(14) (2003) 2548
- [174] (a) S. Neeraj, P.M. Forster, C.N.R. Rao, A.K. Cheetham, *Chem. Commun.* **18** (2001) 1716; (b) S. Neeraj, A.K. Cheetham, *Chem. Commun.* **16** (2002) 1738
- [175] A. Hanaki, T. Ozawa, Y. Funashashi, A. Odani, *Bull. Chem. Soc. Jpn.* **77** (2004) 699
- [176] J.F.G.A. Jansen, A.A. Dias, M. Dorsch, B. Coussens, *Macromolecules* **36**(11) 3861
- [177] E. Pefferkorn, *J. Colloid Interface Sci.* **216**(2) (1999) 197
- [178] V. Gerold, *Material Science and Technology: A Comprehensive Treatment*, Vol. **1**, R.W. Calm, P. Haasen & E.J. Kramer Eds, Wiley VCH (Weinheim) (1993) p. 464
- [179] S.B. Gadewar, H.M. Hofmann, M.F. Doherty, *Cryst. Growth Des.* **4**(1) (2004) 100
- [180] P. Bennema, *J. Crystal Growth* **166**(1-4) (1996) 17
- [181] L. Perez, G.H. Nancollas, *J. Crystal Growth* **66**(2) (1984) 412
- [182] N.U. Zhanpeisov, M. Anpo, *Structural Chem.* **12**(5) (2001) 399
- [183] I. Sunagawa, *Morphology of minerals*, in *Morphology of Crystals*, Vol. **2**, I. Sunagawa Ed., Terra Scientific Publishing (Tokyo) (1987) p. 511
- [184] C.M. Pina, A. Putnis, J.M. Astilleros, *Chem. Geology* **204** (2004) 145
- [185] (a) F.D. Bloss, *Crystallography and Crystal Chemistry: An Introduction*, Chapter 10, Holt, Rinehart & Winston Eds. (NY) (1971) p. 324
- [186] (a) W. Kleber, *Einführung in die Kristallographie*, WEB Verlag Technik (Berlin) (1970) p. 112; (b) J. Fuksa, *Ferroelectrics* **222**(1-4) (1999) 325; (c) J. Fuksa, *Ferroelectrics* **240**(1-4) (2000) 1275
- [187] S. Alkoy, A.C. Hladky, A. Dogan, J.K. Cochran, R.E. Newnham, *Ferroelectrics* **226**(1-2) (1999) 11
- [188] (a) J. Barton, *Macromol. Symp.* **179** (2002) 189; (b) F. Candau, Y.S. Leong, R.M. Fitch, *J. Polym. Sci. A23* (1985) 193 (c) M.T. Carver, E. Hirsch, J.C. Wittmann, F. Candau et al., *J. Phys. Chem.* **93** (1989) 4867
- [189] O. Grassman, N.B. Neber, A. Putnis, P. Lobmann, *Am. Mineralogist* **88**(4) (2003) 647
- [190] E.B. Nyquist, *Functional monomers: Their preparation, Polymerization and Application*, Vol. **1**, R.H. Yocum and E.B. Nyquist Eds., Marcel Dekker (NY) (1973) p. 1
- [191] Y.G. Guo, J.S. Hu, H.P. Lang, L.J. Wan et al., *Chem. Mater.* **15**(22) (2003) 4332
- [192] N.M. Maalev, *Tschemmaks Min. Petr. Mitt.* **18** (1972) 1
- [193] S. Busch, H. Dolhaine, A. DuSchene, S. Heinz et al., *Eur. J. Inorg. Chem.* (1999) 1643
- [194] G.A. Ozin, H. Yang, I. Sokolov, N. Coombs, *Adv. Mater.* **9** (1997) 662
- [195] R. Kniep, S. Busch, *Angew. Chem. Int. Ed. Engl.* **35** (1996) 2624
- [196] H. Cölfen, L. Qi, *Prog. Colloid Polym. Sci.* **11** (2001) 200
- [197] S.H. Yu, H. Cölfen, M. Antonietti, *J. Phys. Chem.* **B107**(30) (2003) 7396
- [198] W.T.A. Harrison, T.E. Gier, G.D. Stucky, R.W. Broach et al., *Chem. Mater.* **8** (1996) 145
- [199] L.B. McCusker, *Acta Cryst.* **A47** (1991) 297
- [200] J.D. Feick, N. Chukwumah, A.E. Noel, D. Valegol, *Langmuir* **20** (2004) 3090
- [201] J.S. Oh, W.G. Shim, J.W. Lee, J.H. Kim et al., *J. Chem. Eng. Data* **48** (2003) 1458
- [202] S.H. Yu, H. Cölfen, A.W. Xu, W. Dong, *Cryst. Growth Des.* **4**(1) (2004) 33
- [203] H. Xiao, Z. Liu, N. Wiseman, *J. Colloid Interface Sci.* **216** (1999) 409
- [204] L. Herschke, BASF semestrial report, *GKD Dept.* (15th October 2002)

- [205] A.S. Myerson, *Handbook of industrial crystallization*, Butterworth-Heinemann Series in Chemical Engineering, (London) (1993) p. 220
- [206] L.A. Gower, D.A. Tirrell, *J. Crystal Growth* **191** (1998) 153
- [207] J. Felsche, S. Kuger, Ch. Baerlocher, *Zeolites* **6** (1986) 367
- [208] T.E. Gier, G.D. Stucky, *Nature* **349** (1991) 508
- [209] G. Harvey, W.M. Meier, in *Studies in Surface Science and Catalysis*, **49A**, P.A. Jacobs and R.A. van Santen Eds., Elsevier (Amsterdam) (1989) p 413
- [210] S. Natarajan, C.N.R. Rao, *Solid State Sci.* **2**(1) (2000) 87
- [211] R. Vaidhyanathan, S. Natarajan, C.N.R. Rao, *J. Mater. Chem.* **9**(11) (1999) 2789
- [212] (a) G. Turrell, *Infrared and Raman spectra of crystals*, Academic Press (London) (1972) p. 214; (b) K. Bouma, G. de Wit, J.H.G.M. Lohmeijer, R.J. Gaymans, *Polymer* **41**(11) (2000) 3965; (c) M. Remko, S. Scheiner, *J. Pharmaceutical. Sci.* **77**(4) (1988) 304
- [213] A. Echavarria, A. Simon-Masseron, J.L. Paillaud, V. Grämlich et al., *Inorg. Chim. Acta* **343** (2003) 51
- [214] W.T.A. Harrison, T.M. Nenoff, T.E. Gier, G.D. Stucky, *J. Solid State Chem.* **113** (1994) 168
- [215] X. Bu, T.E. Gier, W.T.A. Harrison, G.D. Stucky, *Acta Cryst.* **C53** (1997) 517
- [216] J. Yamakawa, I. Watanabe, A. Kawahara, *Acta Cryst.* **C50** (1994) 979
- [217] F. Liebau, *Structure chemistry of silicates*, Springer (NY) (1985)
- [218] G.H. Nancollas, J.A. Budz, *J. Dent. Res.* **69**(10) (1990) 1678
- [219] A. Taubert, G. Wegner, *J. Mater. Chem.* **12** (2002) 805
- [220] D.V. Talapin, A.L. Rogach, E.V. Shevchenko, H. Weller et al., *J. Am. Chem. Soc.* **124** (2002) 5782
- [221] D.V. Talapin, A.L. Rogach, E.V. Shevchenko, H. Weller et al., *J. Am. Chem. Soc.* **125** (2003) 9090
- [222] E.L. Heeley, C. Kit Poh, W. Li, A. Maidens et al., *Faraday Discuss.* **122** (2002) 343
- [223] D. Zhou, E.A. Schmitt, G.H. Zhang, D. Law et al., *J. Pharm. Sci.* **92**(9) (2003) 1779
- [224] L. Perez, G.H. Nancollas, *J. Crystal Growth* **66** (1984) 412
- [225] M.C. van der Leeden, D. Kaschiev, G.M. Van Rosmalen, *J. Crystal Growth* **130** (1993) 221
- [226] H. Füredi-Milhofer, P.B.Y. Ofir, M. Sikiric, N. Garti, *Bioceramics* **16** - *Key Eng. Mat.* **254**(2) (2004) 11
- [227] (a) M.P. Aronson, A.C. Zettlemoyer, R. Codell, M.C. Wilkinson, *J. Colloid Interface Sci.* **52**(1) (1975) 1; (b) J.H. Shen, K. Klier, A.C. Zettlemoyer, *J. Atmos. Sci.* **34**(6) (1977) 957
- [228] J.D. Birchall, R.J. Davey, *J. Crystal Growth* **54** (1981) 323
- [229] L. Addadi, J. Moradian, E. Shay, S. Weiner et al., *Proc. Natl. Acad. Sci. USA* **84** (1987) 2732
- [230] D. Verdoes, D. Kaschiev, G.M. Van Rosmalen, *J. Crystal Growth* **118** (1992) 401
- [231] R.M. Barrer, in *Hydrothermal Chemistry of zeolites*, Chap. 4, Academic Press (London) (1982)
- [232] K. Chung, K. Kim, G. Seo, *Korean J. of Chem. Eng.* **9**(3) (1992) 144
- [233] R. Mohan, A.S. Myerson, *Chem. Eng. Sci.* **57** (2002) 4277
- [234] R.V. Rodionova, V.A. Volkov, *Colloid J. Russ. Acad. Sci.* **54**(6) (1992) 875
- [235] S. Bekiranov, R. Bruijmsma, P. Pincus, *Phys. Rev.* **E55** (1997) 577
- [236] I. Sabbagh, M. Delsanti, *Eur. Phys. J.* **E1** (2000) 75
- [237] J.D. Hartgerink, E. Beniash, S.I. Stupp, *Science* **294** (2001) 1684
- [238] N. Eidelman, R. Azoury, S. Sarig, *J. Crystal Growth* **74**(1986) 1
- [239] J. Nyvlt, *Industrial crystallization from solutions*, Butterworth (London) (1971) p. 108
- [240] S.P. Zhdanov, N.N. Samuelich, *Proc. 5th Int. Conf. Zeolites*, Heydn (London) (1980) p. 75
- [241] A. Giaya, R. W. Thompson, *AIChE* **50**(4) (2004) 879
- [242] P.B.Y. Ofir, R. G. Govrin-Lippman, N. Garti, H. Füderi-Milhofer, *Cryst. Growth Des.* **4**(1) (2004) 177
- [243] X. Bu, P. Feng, T.E. Gier, G.D. Stucky, *Zeolites* **19** (1997) 200
- [244] H.Y. Ng, W.T.A. Harrison, *Micropor. Mesop Mater.* **23** (1998) 197
- [245] M. Andratschke, K.J. Range, *Mater. Sci. Forum* **378**(3) (2001) 659
- [246] R. Hammond, J. Barbier, C. Gallardo, *J. Solid State Chem.* **141**(1) (1998) 177
- [247] Y. Wang, H.H. Yu, Y. Li, Z. Shi et al., *Chem. Eur. J.* **9**(20) (2003) 5048
- [248] M.E. Davies, R.F. Lobo, *Chem. Mater.* **4** (1992) 756

- [249] Y. Mastai, M. Sedlák, H. Cölfen, M. Antonietti, *Chem. Eur. J.* **8**(11) (2002) 2429
- [250] J.P. Arhancet, M.E. Davis, *Chem. Mater.* **3** (1991) 567
- [251] Y. Xing, Y. Liu, G. Li, Z. Shi et al., *Chem. Lett.* **32**(9) (2003) 802
- [252] (a) M.M.J. Treacy, J.M. Newsam, *Nature* **332** (1988) 249; (b) J.B. Higgins, R.B. LaPierre, J.L. Schlenker, A.C. Rohrman et al., *Zeolite* **8** (1988) 446
- [253] M.M.J. Treacy, J.M. Newsam, W.T. Koetsier, C.B. De Gruyter, *Proc. R. Soc. London*, **A420** 81988) 375
- [254] M.A. Aramendía, V. Borau, C. Jiménez, J.M. Marinas et al., *J. Catalysis* **151** (1995) 44
- [255] J.M. Newsam, M.M.J. Treacy, W.T. Koetier, C.B. de Gruyter, *Proc. R. Soc. London* **A420** (1988) 375
- [256] A. Corma, M.T. Navarro, F. Rey, J. Rius et al., *Angew. Chem. Int. Ed.* **40**(12) (2001) 2277
- [257] (a) Ch. Baerlocher, W.M. Meier, D.H. Olson, *Atlas of Zeolite Framework Types*, 5th Ed., Elsevier (Amsterdam) (2001); (b) <http://www.iza-structure.org/databases/Catalog/beta.pdf>
- [258] L.B. McCusker, *Acta Crystallogr.* **A47** (1991) 297
- [259] X.Bu, P. Feng, T.E. Gier, G.D. Stucky, *Zeolite* **19** (1997) 200
- [260] P.K.Dutta, M. Pur, D.C. Shieh, *Mater. Res. Soc. Symp. Proc.* **111** (1988) 101
- [261] A.V. McCormick, A.T. Bell, *Catal. Rev. Ser. Eng.* **31** (1988) 97
- [262] T.M. Nenoff, W.T.A. Harrison, T.E. Gier, G.D. Stucky, *Chem. Mater.* **3** (1991) 27
- [263] T.M. Nenoff, W.T.A. Harrison, T.E. Gier, G.D. Stucky, *J. Am. Chem. Soc.* **113** (1991) 378
- [264] M.J. Castagnola, P.K. Dutta, *Micropor. Mesopor. Mater.* **42** (2001) 235
- [265] (a) R. Singh, J. Doolittle, P.K. Dutta, *J. Phys. Chem.* **B106**(9) (2002) 21; (b) P.K. Dutta, *Abstr. Pap. Am. Chem. Soc.* **226** (2003) 040
- [266] T.M. Nenoff, W.T.A. Harrison, T.E. Gier, G.D. Stucky et al., *Inorg. Chem.* **33** (1994) 2472
- [267] J. Rottstegge, K. Landfester, M. Wilhelm, H.W. Spiess, *Colloid Polym. Sci.* **278**(3) (2000) 236
- [268] S. Natarajan, L. Van Wullen, W. Klein, M. Jansen, *Inorg. Chem.* **42** (2003) 6265
- [269] A. Echavarria, A. Simon-Masseron, J.L. Paillaud, V. Gramlich et al., *Inorg. Chim. Acta* **343** (2003) 51
- [270] A.J. Norquist, D. O'Hare, *J. Am. Chem. Soc.* **126** (2004) 6673
- [271] C.N.R. Rao, S. Natarajan, A. Choudhury, S. Neeraj et al., *Acc. Chem. Res.* **34** (2001) 80
- [272] L. Elammari, J. Durand, L. Cot, B. Elouadi, *Z. Kristallogr.* **180** (1987) 137
- [273] K. Schmitt-Rohr, H.W. Spiess, *Multidimensional Solid State NMR and Polymers*, Academic Press (London) (1994)
- [274] K. Landfester, C. Boeffel, C. Lambla, H.W. Spiess, *Macromolecules* **29** (1996) 5972
- [275] F. Mellinger, M. Wilhelm, K. Landfester, H.W. Spiess et al., *Acta Polym.* **49** (1998) 108
- [276] S. Spiegel, K. Schmitt-Rohr, C. Boeffel, H.W. Spiess, *Polymer* **34** (1993) 4566
- [277] F. Mellinger, M. Wilhelm, H.W. Spiess, *Macromolecules* **32** (1999) 4686
- [278] M. Gaborieux, *PhD Thesis*, University of Strasbourg (France) (2004)
- [279] A. Lachawesky, F. Mallwitz, J.F. Baussard et al., *Macromol. Symp.* **15**(2) (2004) 135
- [280] J. Lee, Y. Moroi, *Langmuir* **20** (2004) 4376
- [281] P.R. Crippy, J.A. Fornes, A.S. Ito, *Colloid Surface* **B35**(2) (2004) 137
- [282] M. Raytchev, E. Mayer, N. Amann, H.A. Wagenknecht et al., *ChemPhysChem.* **5**(5) (2004) 706
- [283] K. Kalyanansundaram, J.K. Thomas, *J. Am. Chem. Soc.* **99**(7) 2039
- [284] T.S. Chen, J.K. Thomas, *J. Polym. Sci. Pol. Chem.* **17**(4) 81979) 1103
- [285] A. Thomas, S. Polarz, M. Antonietti, *J. Phys. Chem.* **B107**(21) (2003) 5081
- [286] (a) J.B. Birks, L.G. Christophorou J.B. Birks, *Nature* **194** (1962) 4827; (b) L.G. Christophorou, *Spectrochim. Acta* **19**(2) (1963) 401; (c) K. Siomos, G. Kourouklis, L.G. Christophorou, J.G. Carter, *Radiation Phys. Chem.* **17**(2) (1981) 75; (d) J.M.G. Martinho, J.C. Conte, *J. Chem. Soc.: Faraday Trans.* **II78**(7) (1982) 975; (e) A. Jover, F. Meijide, E. Rodríguez-Néñez, J. Vázquez-Tato et al., *Langmuir* **12** (1996) 1789
- [287] (a) M. Pope, C.E. Swenberg, *Electronic processes in organic crystals and polymers*, Monograph on the physics and chemistry of materials, Oxford University Press (1999); (b) B. Valeur, *Molecular Fluorescence: Principle and Applications*, Wiley-VCH (Weinheim) (2002) p.94

- [288] P. Erk, H. Hengelsberg, *Application of phtalocyanines in The porphirin Handbook*, K.M. Kadish, K.M. Smith and R. Guillard Eds, Vol. **19**, Elsevier (2003) p 105
- [289] C.H. Chern, C.H. Lin, *Polymer* **40** (1998) 139
- [290] J. Kuther, R. Seshadri, G. Nelles, W. Tremel et al., *Chem. Mater.* **11**(5) (2003) 1317
- [291] (a) L.P. Ramirez, K. Landfester, *Macromol. Chem. Phys.* **204**(1) (2003) 22; (b) K. Landfester, L.P. Ramirez, *J. Phys. Condens. Mater.* **15**(15) (2003) 1345
- [292] M. Pannetier, C. Fermon, G. Le Goff, J. Simola et al., *Science* **304** (2004) 1648
- [293] C. Sanchez, F. Ribot, *New J. Chem.* **18** (1994) 1007
- [294] W. Ostwald, *Grundniss der allgemeinen Chemie*, Leipzig (1899)
- [295] V. Gerold, *Material Science and Technology: A comprehensive treatment*, Vol. **1**, R.W. Cahn, P. Haasen & E.J. Kramer Eds, Wiley VCH (Weinheim) (1993) pp. 456 and thereafter
- [296] (a) A. Serra, D.J. Bacon, *Z. Metallkunde* **95**(4) (2004) 242; (b) R.C. Pond, A. Serra, D.J. Bacon; *Acta Mater.* **47**(5) (1999) 1425
- [297] E.N. Coker, L.V.C. Rees, *Faraday Trans.* **88**(2) (1992) 263; (c) E.N. Coker, L.V.C. Rees, *Faraday Trans.* **88**(2) (1992) 273
- [298] R. Subramanian, P. Natarajan, *J. Polym. Sci.* **A22** (1984) 437
- [299] G.H.J. Vandoremaele, F.H.J.M. Geert, L.A. Demeulen, A.L. German, *Polymer* **33**(7) (1992) 1512
- [300] M. Morcellet, M. Wozniak, *Macromolecules* **24**(3) (1991) 745
- [301] S. Kotake, *J. Crystal Growth* **266** (2004) 289
- [302] J.W. Rutter, B. Chalmers, *Can. J. Phys.* **31** (1953) 15
- [303] (a) R.V. Rodionova, V.A. Volkov, *Colloid J. USSR* **52**(5) (1990) 831; (b) N.M. Shevereva, R.V. Rodionova, V.A. Volkov, *Colloid J. USSR* **53**(6) (1991) 937
- [304] R.V. Rodionova, V.A. Volkov, *Colloid J. USSR* **54**(6) (1992) 875
- [305] J.M. Roberts, P. Linse, J.G. Osteryoung, *Langmuir* **14** (1998) 204
- [306] S.H. Behrens, D. Iso Christl, R. Emmerzael, P. Schurtenberger, *Langmuir* **16** (2000) 2566
- [307] B. Jönssen, H. Wennerström, P.G. Nilsson, P. Linse, *Colloid Polym. Sci.* **264** (1986) 77
- [308] F.F. Abraham, *Homogeneous nucleation Theory*, Academic Press (NY) (1974)
- [309] I.H. Leubner, *J. Imaging Sci. Technol.* **42**(4) (1998) 355
- [310] Y.S. Djikaev, I. Napari, A. Laaksonen, *J. Phys. Chem.* **120**(20) (2004) 9752
- [311] D. Kashchiev, *J. Chem. Phys.* **120**(8) (2004) 3749
- [312] L. Bellami, *The infrared spectra of complex molecules*, Wiley (NY) (1958) p.315
- [313] K. Nakamoto, *Infrared and Raman spectra of inorganic and coordination compounds*, 4th Ed., Wiley (NY) (1986) p.189
- [314] A.S. Milev, G.S. Kamali Kannangara, M.A. Wilson, *Langmuir* **20**(5) (2004) 1888
- [315] M. Nara, H. Torii, M. Tasumi, *J. Phys. Chem.* **100**(51) (1996) 19812
- [316] N. Ueyama, T. Hosoi, Y. Yamada, M. Doi et al., *Macromolecules* **31** (1998) 7119
- [317] L.A. Gower, D.A. Tirell, *J. Crystal Growth* **191** (1998) 153
- [318] Y. Levi, S. Albeck, A. Brack, S. Weiner et al., *Chem. Eur. J.* **4** (1998) 389
- [319] D.A. Tomalia, A.N. Naylor, W.A. Goddard III, *Angew. Chem. Int. Ed. Engl.* **29** (1990) 138
- [320] M. Francesca, D.A. Tomalia, *J. Am. Chem. Soc.* **116** (1994) 661
- [321] K. Naka, Y. Chujo, *Chem. Mater.* **13** (2001) 3245
- [322] E.R. Birnbaum, K.C. Rau, N.N. Sauer, *Separ. Sci. Technol.* **38**(2) (2003) 389
- [323] A. Miraa, T. Imae, *Biomacromolecules* **5**(1) (2004) 69
- [324] J.J.J.M. Donners, B.R. Heywood, E.W. Meijer, R.J.M. Nolte et al. *Chem. Commun.* **19** (2000) 1937
- [325] J.J.J.M. Donners, R.J.M. Nolte, N.A.J.M. Sommerdijk, *Adv. Mater.* **15**(3) (2003) 313
- [326] K. Naka, Y. Tanaka, Y. Chujo, *Langmuir* **18** (2002) 3655
- [327] (a) G. Wolff, G. Gross, I.N. Stranski, *Z. Elektrochem.* **56** (1942) 420; (b) W. Kleber, *Einführung in die Kristallographie*, VEB Verlag Technik (Berlin) (1971) p.118
- [328] W. Kleber, *Einführung in die Kristallographie*, 17th Ed., H.J. Bausch, J. Bohm and I. Kleber Eds., Verlag Technik GmbH (Berlin) (1990) p.86
- [329] Characterization report N° 30130, GKP/A, BASF AG, (08.2003)
- [330] J.K. Kabanov, M.A. Simonov, N.V. Belov, *Dokl. Akad. Nauk. USSR* **202** (1972)823
- [331] W.T.A. Harrison, T.M. Nenoff, T.E. Gier, G.D. Stucky, *Inorg. Chem.* **32** (1993) 2437

- [332] G.O. Brunner, W.M. Meier, *Nature* (London) **337** (1989) 146
- [333] J.W. Mullin, *Crystallization*, 3rd Ed. CRC Press, (Boca Raton) (1993)
- [334] M. Newsam, M.M.J. Treacy, W.T. Koetsier, C.B. DeGruyter, *Proc. Soc. London A***420** 81988) 375
- [335] L.A. García-Serrano, F. rey, J. Pérez-Paciente, E. Sastre, *Thermochim. Acta* **376** (2001) 155
- [336] G. Xu, N. Yao, I.A. Aksay, J.T. Groves, *J. Am. Chem. Soc.* **120** (1998) 11977
- [337] C.E. Webster, R.S. Drago, M.C. Zerner, *J. Phys. Chem. B***103**(8) (1999) 1242
- [338] B. Jayakumar, M. Rajkumar, R. Nagendran, S. Nanjundan, *J. App. Pol. Sci.*, Vol. **85** (2002) 1194
- [339] M.R. Knecht, D. W. Wriqth, *Langmuir* **20**(11) (2004) 4728
- [340] (a) B.J. McCoy, *J. Colloid Interface Sci.* **216**(2) (1999) 235; (b) S. Neeraj, A.K. Cheetham, *Chem. Commun.* **16** (2002) 1738
- [341] M. Kosmulski, *J. Colloid Interface Sci.* **275** (2004) 214

6. Solubility and dissolution kinetics of zinc phosphate hydrate based pigments for anticorrosion and potential biomedical applications

“Let there be light”, *Genesis*, Part 1:4, RSV

6.1. Introduction

The use of paints is an effective way to protect metallic surfaces against aggressive environments. Red lead and zinc chromate are the most extensively used pigments due to their excellent corrosion inhibition properties. Nevertheless, such compounds are hazardous and highly toxic. For that reason, their use has been discouraged since 1990 [1]. In this line, the manufacture effort is focused on their replacement with new generations of “environmental friendly” pigments [2-5].

Among several non-toxic anticorrosive pigments developed so far, zinc phosphate types represent the most widely employed alternative. To this end, in the present work, highly promising microsized pigments regarding their anticorrosion efficiency, of tailored morphology and surface reactivity (c.f. Chap. 4) and based either on pure *acid zinc phosphate* hydrate (α -, β -ZPD, α -, β -ZPD, c.f. Chap. 2) or on *basic zinc phosphates* hydrates ($\text{NaZnPO}_4 \cdot 1\text{H}_2\text{O}$, $\text{Na}_2\text{Zn}(\text{PO}_4)(\text{OH}) \cdot 2\text{H}_2\text{O}$, c.f. Chap. 5) have been successfully synthesized on a large enough scale. Although their anticorrosive action is still not yet understood, it seems that the protective mechanisms result from a combination of metal substrate phosphatization (formation of a passive layer) [6-7] and formation of complex substances with the binder components, as already recognized by Meyer in 1965 [8-9]. Such compounds react with oxidation products yielding an adherent layer of Phosphophyllite, $\text{FeZn}_2(\text{PO}_4)_2 \cdot 2\text{H}_2\text{O}$, on the metal surface [10-11]. Accordingly their anticorrosive efficiency depends on a “barrier effect”, in which microcrystals embedded in a protective organic coating can stop the water diffusion onto a steel surface [12-

13]. Recently, Kalendova and Kalenda [14] even suggested that only the zinc phosphate dihydrate may be an *active* corrosion inhibitor, since it might have the capacity to take water up in a broad range of environmental conditions (temperature, pH [15-16], salinity [12]) before dissolving as water penetrates the protective coating. Moreover, modern industrial waterborne anticorrosion coatings use mainly carboxylic based emulsions (BASF process), whose deprotonation and thus their steel adherence [17] are tuned by the selective addition of ammonia. In this precise case Ledheiser et al. [18] suggested that an immense advantage of zinc phosphate pigments are their ability not only to stop water diffusion but also to reduce the rate of diffusion of ammonium ions through the basecoats, presumably originating from the high stability of ammonium zinc hydrogen phosphate complexes [19-21] adsorbed on ZPT (011) surface (c.f. Chapters 3 & 4). In that sense, it has been pointed out that some of the major limitations of zinc phosphate pigments as corrosion inhibitors are the difficulties to control the desired hydration state [22], the presence [23-26] and amount [27-29] of added impurities ($\text{Zn}(\text{OH})_2$, Ca^{2+} as HAP, Co^{2+} , Ni^{2+} , Mn^{2+} , MoO_4^{2-} , organic phosphates, zinc nitrophthalates [29], etc.) and their poor solubility [31-32]. Therefore, the clear lack of published fundamental studies from a strictly physical and chemical point of view, of the solubility and stability in aggressive environments of such zinc phosphate based anticorrosion pigments is the primary motivation of this study.

In addition to its application in metal protection and its common use in coating technology, hopeite is also one of the main crystalline reaction products of dental cement [33-34] and leads to a new generation of dental ceramics formulations: the zinc phosphate cements (ZPC) [35-37]. Active research has been recently conducted in dental medicine to obtain materials suitable for the fabrication of esthetic single crowns or fixed partial dentures as permanent restoration of teeth [38-39]. Zinc phosphate based cements or glass ionomer/phosphate cements generally perform well because of high fracture toughness [40-41], low solubility in an aggressive biological environment (pH range 6-8) [42], as well as a high bonding strength with any other adhesive cement or with bone substrate conferring a good chemical stability, durability and low cytotoxicity, i.e. excellent biocompatibility, governed by the presence of zinc [43]. However, some clinical studies comparing different dental materials show that an optimization of long-term chemical resistance accompanied by a drastic lowering of the solubility, are still necessary [44-46].

Thus, precipitation and dissolution of zinc phosphates are processes of considerable importance in a broad field of industrial applications. Although there is no general agreement concerning the mechanism of zinc phosphate precipitation, the consensus is that the chemistry of the aqueous phase from which precipitation takes place is of paramount importance. Furthermore the knowledge of the solubility is a key information in crystallization process since it will determine

the amount of cooling and the cooling rate required first to achieve supersaturation conditions and secondly to obtain a reasonable crystallization yield of monodisperse product. But model studies are scarce and very often restricted to precise conditions depending on the application scope and therefore needed for the assessment of the most appropriate conditions of phosphate release in anticorrosion coating technology. In this respect, the simple solubility models successively developed by Jurinak and Inouye [47], Sillen and Martell [48] and later of Nriagu [49] have neither considered the polymorphic nature of hopeite nor the effect of pH, temperature and ion-pair and complex formations on the solubility equilibria. Lately Nancollas [50] in a preliminary report on corrosion protection even recommended that the effect of zinc hydroxide on zinc phosphate precipitation mechanism should not be neglected. Therefore such challenging studies should be firstly based on accurate thermodynamic considerations which only then may be used as guides for appropriate dissolution kinetics experiments, especially followed by EIS (Electrical Impedance Spectroscopy) in paint formulation (automated pigment screening by slurry method) and storage before use [51-52] on one hand and in industrial corrosion tests (salt spray and humidity chamber tests, adhesion test (Kelvin probe method)) [53] on the other hand. Thus the primary purpose of this chapter is the development of reliable thermodynamic solubility models for ZPT and the proposal of adapted phosphate dissolution mechanisms in correlation with the pigment state of hydration, the hopeite polymorphism and the overall pigment composition (*composition dependent models*). Besides and to some extent this study might well shed some light on the mechanism of dissolution-precipitation (metamorphism) and the primordial role of sodium ions in the corrosion efficacy of acid and basic zinc phosphate pigments. e.g. $\text{NaZnPO}_4 \cdot 1\text{H}_2\text{O}$, $\text{Na}_2\text{Zn}(\text{PO}_4)(\text{OH}) \cdot 2\text{H}_2\text{O}$, generated by polymer controlled mineralization. Furthermore this study may provide key values of the solubility product constants of ZPT and its relative zinc hydrogen phosphate hydrates on the full pH (0-14) and temperature range (0-100°C). For convenience, two main strategies have been developed here: a *leaching method* (thermodynamic approach), where pigment suspension are let equilibrated for months in a buffered solution, and a *pH response method* (kinetic approach), where phosphate release to a pH pulse is monitored, either by electrochemistry or by conductometry, gravimetry after filtrate recovery and also complete supernatant analysis.

6.2. Solubility models

6.2.1. Sparingly soluble salts, supersaturation and dissolution process

6.2.1.1. Basic concepts of solubility

A solution is formed by the addition of a solid solute to the solvent, typically a liquid under the

conditions of interest. The solid dissolves, forming an homogeneous solution. At a given temperature, there is a maximum amount of solute that can dissolve in a given amount of solvent. When this maximum is reached the solution is said to be saturated. The amount of solute required to obtain a saturated solution at a given condition (temperature, pH) is called the solubility. Solubilities of common materials vary widely, even when materials appear to be similar, as stated by Mullin [54]. Moreover inorganic salts are generally classified regarding their respective solubility range at saturation in standard conditions.

Soluble salt:	many mol.L ⁻¹ of salt may dissolve at saturation (e.g. ZnSO ₄ , Zn(NO ₃) ₂ , Zn(CH ₃ COO ₂) ₂)
Sparingly (slightly) soluble salt:	10 ⁻⁵ -10 ⁻² mol.L ⁻¹ of salt are present in solution at saturation (e.g. ZnCO ₃ , ZnCrO ₄ , Zn ₃ (PO ₄) ₂)
Insoluble salts:	less than 10 ⁻⁵ mol.L ⁻¹ of salt may dissolve at saturation (e.g. ZnS, Zn(OH) ₂)

The solubility of a material depends strongly on temperature. In the majority of the cases the solubility increases with the temperature, though the rate of increase varies principally with the chemical composition of the observed substances. However solubility can also decrease with increasing temperature, especially for sparingly soluble salts such as metal (Zn²⁺, Ca²⁺) phosphate hydrate minerals. Solubility may also be affected by the use of solvent mixtures or by the presence of additional species. In fact Like and Seidel have proven that the solubility of a sparingly soluble salt increases with increasing ion concentration in solution. This is commonly known as the *salt effect* [55].

6.2.1.2. Unusual dissolution and solubility phenomena

It is much more convenient to approach solubility equilibrium through dissolution rather than crystal growth [56-61]. In most kinetic studies, dissolution has been expressed analogously to the surface diffusion of the crystal growth [62-63], implying that the dissolution rate should be constant when the undersaturation is maintained and that dissolution continues until equilibrium is reached. However it has been found that this simple representation of dissolution is unsatisfactory for many sparingly soluble biominerals and metal phosphate compounds. In numerous studies released by Nancollas et al., some minerals were even found to be resistant to dissolution in undersaturated solutions, and the concept of an intermediate metastable state [64-68] was introduced, with solubility directly related to particle size and particle size distribution [69], in exact analogy to crystal growth. Recently, *constant composition method*, a highly reproducible technique for kinetic studies of crystallization and dissolution of sparingly soluble

salts, has shown that calcium phosphate dissolution rates decrease markedly with time despite of sustained undersaturation, eventually resulting in effective reaction suppression even though the solution remained undersaturated [70-71]. For octacalcium phosphate $[\text{Ca}_8\text{H}_2(\text{PO}_4)_6 \cdot 5\text{H}_2\text{O}]$, OCP] dissolution, Tang et al. [72] have shown that the reaction was effectively suppressed before all the solid phase had dissolved in the undersaturated medium, with only 55 wt% of the seed crystals undergoing dissolution at $S = 0.475$. This limit further decreased with increase of S , and similar phenomena were reported for other calcium phosphate minerals [73]. Furthermore dissolution rate is strongly dependant on the exposed crystal surface. Thus in the first stage of dissolution, the increase of surface roughness results in the creation of numerous reactive dissolution sites, in an increase of the solid-liquid interfacial energy inducing the formation of surface etch pits, which contributes to the dissolution reaction in dependence of their size.

Although the Ostwald-Freundlich equation [74-75] expresses the variation of solubility as a function of particle size and interfacial tension, it is generally accepted that neither the amount of excess solid nor the size of the particles investigated will change the position of the equilibrium, and thermodynamic considerations are applicable in aqueous solutions [76-77]. On the contrary it influences only the kinetics of dissolution [78], as firmly established in Chapter 4. On this basis, a first but simple approach of crystal dissolution employing solution thermodynamics may be appropriate and therefore will be considered.

6.2.1.3. Solution Thermodynamics

For a solution to be saturated it must be in equilibrium with the solid solute as show in Eq. 6.1:



Thermodynamically this means that the chemical potential of the solute in the solution is the same as the chemical potential of the species in the solid phase:

$$\mu_{solid} = \mu_{solution} \quad (6.2)$$

If the solute is an electrolyte that completely dissociates in solution (strong electrolyte), Eq. (6.2) can be rewritten as:

$$\mu_{solid} = v_c \mu_c + v_a \mu_a \quad (6.3)$$

where v_c (i.e. v_+) and v_a (i.e. v_-) are the stoichiometric numbers in a formula unit of the dissolving phase, and μ_c and μ_a are the chemical potentials of the cation and the anion respectively. The chemical potential of a species is related to the species activity by:

$$\mu_i(T) = \mu_{aq}^0 + RT \ln(a_i) \quad (6.4)$$

where a_i is the activity of species i and μ_{aq}^0 is an arbitrary reference state chemical potential.

The activity coefficient is defined as $a_i = \gamma_i m_i$ (6.5) where m_i is the molal concentration in

solution. In electrolyte solution, because of the condition of electroneutrality, the charges (valencies) of the anion z_a (i.e. z^-) and the cation z_c (i.e. z^+) will balance:

$$v_a z_a = v_c z_c \quad (6.6)$$

When a salt dissolves, it dissociates into its component ions. This led to the definition of a mean ionic activity coefficient and mean ionic molality defined as:

$$\gamma_{\pm} = (\gamma_c^{v_c} \gamma_a^{v_a})^{1/v} \quad (6.6)$$

$$m_{\pm} = (m_c^{v_c} m_a^{v_a})^{1/v} \quad (6.7)$$

Thus the chemical potential can be expressed as follows:

$$\mu_{salt(aq)} = \mu_{aq}^0 + vRT \ln(\gamma_{\pm} m_{\pm}) \quad (6.8)$$

where μ_{aq}^0 is the sum of the two ionic standard state chemical potentials of the anion and cation.

For sparingly soluble salts in a saturated solution, solubilities are always defined by solubility equilibrium (i.e thermodynamic solubility product) constant K_s (i.e. K_{sp}), as W. Nernst, one of the founders of modern physical chemistry, showed historically by measuring the solubility of silver acetate solutions:

$$K_s = \prod a_i^{v_i} \quad (6.14)$$

considering that the starting solid material is a stable crystal form at atmospheric pressure (standard state) so that its activity equals unity. For the pure component of a strong electrolyte (e.g. KCl), Eq. (6.9) reduces to:

$$K_s = \gamma_{\pm}^2 m_{\pm}^2 \quad (6.10)$$

The thermodynamic solubility product can also be calculated from standard state Gibbs free energy of formation data. It yields

$$K_s = \exp(-\Delta G_{form}^0 / RT) \quad (6.11)$$

As supersaturation is the fundamental driving force for crystallization and is metastable state, the undersaturation is the driving force for dissolution and also metastable [79]. Accordingly, the degree of supersaturation S and relative supersaturation σ are given as follows:

$$S = \left(\frac{IP}{K_s} \right)^{1/\sum_i v_i} \quad \text{and} \quad \sigma = 1 - S \quad (6.12) \text{ and } (6.13)$$

where IP is the ionic activity product, expressed using the electroneutrality equation. Cases where $S > 1$, $S = 1$ and $S < 1$ represent respectively supersaturation, saturation and undersaturation. Slight variations of notations of the supersaturation and relative supersaturation may be found in the modern literature [80]. For most common systems, the dependence of the equilibrium constants and of the supersaturation can be taken into consideration for calculations at temperatures other than 25°C, using the values of the crystallization enthalpy, reported by

Krishnam et al. [81] and the Van't Hoff equation. Thus in the particular case of a solid surface in thermodynamic equilibrium with an aqueous or electrolyte solution, since the chemical potential is related to the ΔG of dissolution and consequently to the supersaturation S , the variation of chemical potential between solution and crystal surface in undersaturating conditions $\Delta\mu$, is the driving force (see § 2.2.1.1) for the dissolution and dissolution occurs until an equilibrium state is reached. As illustrated in Figure 6.1 additional contribution to the change of chemical potential stems from remnant surface stresses (i.e. dependent of the dislocation density) [72] (refer to Chapter 4).

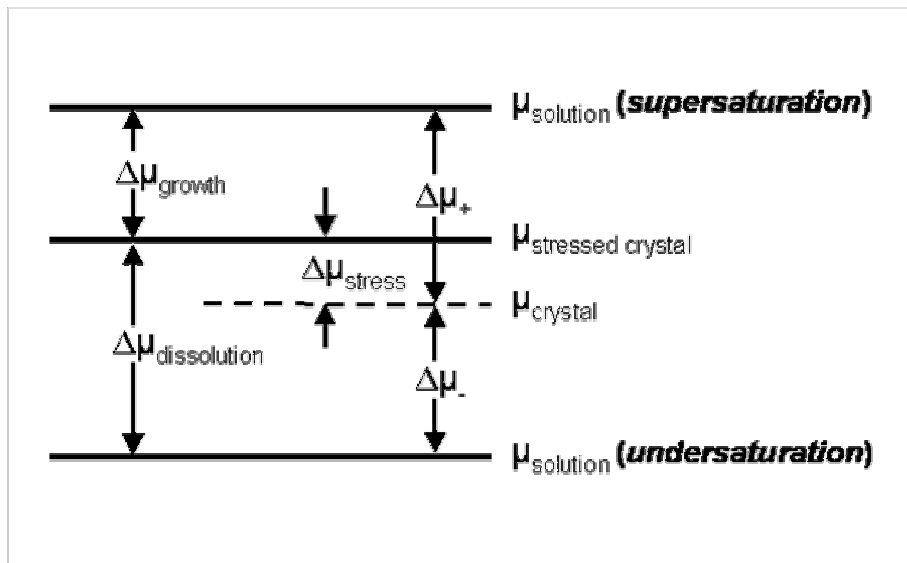


Figure 6.1: Chemical potentials of the ideal crystal, $\mu_{crystal}$, and solution, $\mu_{solution}$, at supersaturation S and undersaturation; $\Delta\mu_+$ and $\Delta\mu_-$ are the change of chemical potential for the ideal crystals during growth and dissolution, respectively. $\Delta\mu_{stress}$ is the increase of chemical potential in the stressed (real) crystal; making the value of $\Delta\mu$ in real growth ($\Delta\mu_{growth}$) and dissolution ($\Delta\mu_{dissolution}$) processes lower or higher, respectively, than “ideal”. The variation of surfacial chemical potential $\Delta\mu$ is the driving force for crystal dissolution.

Furthermore the calculation of the thermodynamic solubility product of mixtures of strong electrolytes or sparingly soluble salts is of utmost importance for an accurate evaluation of the thermodynamical solubility constants and thus requires knowledge of both ionic strength of the solution and the activity coefficients of all species that may precipitate. Thus the ionic strength I is defined by IUPAC [82] as follows:

$$I = \frac{1}{2} \cdot \sum z_i^2 a_i \quad (6.14)$$

where z is the charge of the ion i present at the molar concentration C_i and with activity a_i .

Generally, the activity coefficients are lower than unity when polar interactions with water are important, with a resulting increase in solubility of compounds compared with the ideal solubility. Numerous approaches and related equations have been developed. However in many instances the activity constants can be rapidly evaluated with the help of the Debye-Hückel (DH) theory,

which postulates that all deviations from ideal behaviour by ionic solutions arise from electrostatic interactions between ions. For very dilute solutions the DH theory yields:

$$\log \gamma_i = -\frac{e^3 z_i^2}{(\epsilon k_B T)^{3/2}} \cdot \left(\frac{2\pi N_a I}{1000} \right)^{1/2} = -A z_i^2 \sqrt{I} \cong -0.509 z_i^2 \sqrt{I} \quad \text{at } 25^\circ\text{C} \quad (6.15)$$

where e is the electronic charge ($1.6022 \cdot 10^{-19}$ C), ϵ is the dielectric constant of the medium, k_B is the Boltzman constant, N_a is the Avogadro number and T is expressed in Kelvin. At low ionic strength ($I \leq 0.1 \text{ mol.L}^{-1}$), the DH theory has been adapted by Guggenheim and Schindler (extended DH theory) [83] and leads to the following approximation:

$$\log \gamma_i = -A z_i^2 \frac{\sqrt{I}}{1 + \sqrt{I}} \quad (6.16)$$

Besides, for sparingly soluble salts with a ionic strength up to 0.2 mol.L^{-1} (i.e. diluted solutions) Davies [84-85] expressed satisfyingly the activity coefficients, and developed successively two expressions of the activity coefficients, where the first one is the prevalent relation for solubility studies of sparingly soluble salts :

$$\log \gamma_i = -A z_i^2 \left(\frac{\sqrt{I}}{1 + \sqrt{I}} - BI \right) \quad (\text{Davies 1962}) \quad (6.17a)$$

$$\log \gamma_i = -A z_i^2 \frac{\sqrt{I}}{1 \pm \sqrt{I}} + BI \quad (\text{Davies 1965}) \quad (6.17b)$$

where A and B (≈ 0.3 at 25°C) are DH constants characteristics for each ionic species [86-87].

Furthermore, on the basis of electrostatic and ion-pairing interaction theory, actually known as the regular solution theory of Prausnitz [88-89], first Pitzer and Mayorga [90] and then Bromley [91-92] developed a method for multicomponent electrolytes with concentrations up to 6 mol.L^{-1} , expressly taking into account ionic interactions:

$$\text{Log } \gamma_i = \frac{-A z_i^2 \sqrt{I} + F_i}{1 + \sqrt{I}} \quad (6.18)$$

where A = Hückel constant (≈ 0.511 at 25°C)

I = Ionic strength

i = any ion present

z_i = number of charges of ion i

F_i is an interaction parameter term defined as $F_i = \sum_j B_{ij} z_i^2 m_j$ (6.19)

where j indicates all ions of opposite charge to i, with:

$$z_{ij} = \frac{z_i + z_j}{2} \quad (6.20)$$

$$B_j = \frac{\left((0.06 + 0.6B) |z_i z_j| \right)}{\left(1 + \frac{1.5}{|z_i z_j|} I \right)^2} + B \quad (6.21)$$

where B is a constant for ion interactions tabulated by Zemaitis et al. [93], and that takes the value 0.024 for KCl at 25°C. Good examples of the iteration calculations necessary to identify the correct value of the activity coefficients that are then employed in the evaluation of the solubility product are given by Nancollas et al [94] and Barone et al. [95]. Even more complexed models have been recently developed by Liu et al. [96-97] for concentrated mixed electrolytes, that may be useful in the case of metamorphic systems. Nevertheless for describing the temperature dependence of the activity coefficients, Wilson [98-99] originally modified Eq. 6.18 using the quadratic temperature dependence of the excess free energy and enthalpy of dissolution. The Wilson approach has been modified by Novák [100] for partially miscible mixtures and further extended by Hiranuma [101] for ternary liquid-liquid systems. The choice of the best experimental data fitting approach of the activity coefficients and their respective temperature dependence is critical for an accurate evaluation of the solubility of complex pigment formulations based on ZPT and for a satisfying estimation of phosphate ion release in a broad range of pH and temperature conditions.

6.2.2. Turbidity phase diagram and metastability domain

Before beginning to approach any complex solubility equilibrium, one should first establish all the species present in the solution at a given pH and temperature. Then one must list all reactions encountered in the system and governing the concentration of the various ion species. One way of doing this is to consider the stoichiometry of the reactions forming the equilibrium species, and is known as “method of the principal reaction”. A more fruitful, but perhaps more complicated approach is to use mass and charge balances. However some prerequisite are necessary like the determination of solubility limits, which may be approached by crystal growth (c.f. Chapter 4) and/or controlled dissolution.

6.2.2.1. Thermodynamic approach of supersaturation

As explained previously in § 2.1, supersaturated and undersaturated solutions are metastable. In particular this means that in supersaturating a solution some amount will not necessarily result in crystallization due to effects of nucleation. It has long been recognized that precipitation does not occur instantaneously upon the creation of very low supersaturation. There is a metastable zone in which the solution remains stable, and only after a period of time τ , commonly designed as

induction time, are aggregates and then precipitating crystals detected. If one assumes that these aggregates or nuclei are spheres of radius r and of interfacial energy γ_{SL} , the free energy involved in crystal formation (homogeneous nucleation) is:

$$\Delta G_{form.} = 4\pi\gamma_{SL}r^2 - \left(\frac{4\pi r^3}{3V_m}\right) \cdot RT \ln(1+S) \quad (6.22)$$

where V_m is the molecular volume. The first term of Eq. (6.20) is the Gibbs free energy change for forming the surface ΔG_s , and the second term is for the volume and related to the supersaturation S . For small numbers of molecules, the total Gibbs free energy is positive. This means that the clusters are unstable and will dissolve (undersaturation). A plot of $\Delta G_{form.}$ as a function of cluster size (Fig. 6.1) shows that as the cluster size increases, a point is reached where the total Gibbs free energy of the system becomes negative and the cluster will grow spontaneously; and nucleation occurs.

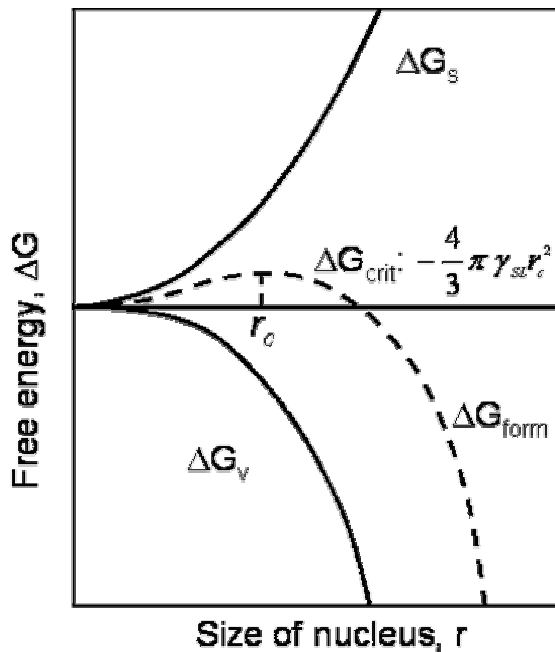


Figure 6.1: Representation of the free energy versus cluster radius in homogeneous nucleation. Under a critical size r_c , crystals dissolve spontaneously.

Thus the reason for the metastability of supersaturated solutions is the need for a critical sized cluster to form. The dependence of the Gibbs free energy on r passes through a maximum $\partial\Delta G/\partial r = 0$, corresponding to the critical size r_c :

$$r_c = 2V_m\gamma_{SL}/RT \ln(1+S) \quad (6.23)$$

Every solution can be supersaturated till a maximum concentration c^* before it becomes unstable. The zone between the saturation curve and this unstable boundary is called the *metastable zone*. The boundary between the unstable and metastable zones has a thermodynamic definition: the *spinodal curve*. There are four main methods to generate supersaturation (i.e. undersaturation), (1) temperature change, (2) evaporation of solvent, (3) chemical reaction (precipitation), (4) changing the solvent composition (e.g. effect of pH). Figure

6.2 illustrates the achievement of supersaturation by slowly cooling a solution, from point A to point B (saturation) until point C (supersaturation, appearance of the first nuclei). As crystallization occurs in the unstable domain, the solvent composition changes and crystals grow until the concentration diminishes to the equilibrium solubility (Point D)

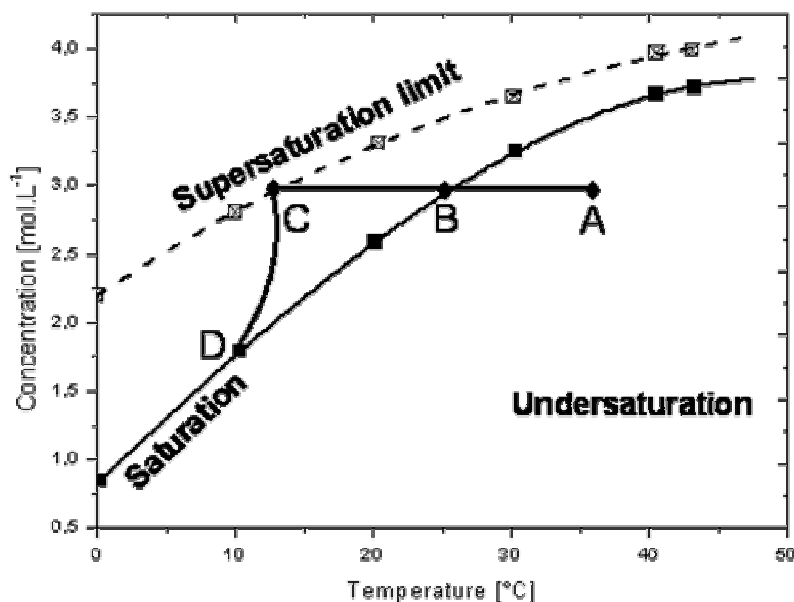


Figure 6.2: Representation of the metastable width for KCl-water system, showing the generation of the supersaturation conditions (C) on cooling in the absence of initial solid phase. In the presence of initial solid phase, seeding crystal tend to dissolve in undersaturation conditions (A). After data from Chang [102].

Evaluation of the metastable zone width obtained for a large variety of simple salts and inorganic materials are found in the monographs of Nývlt et al. [103-104]. It is worth to note that qualitative classification of inorganic substances for “stable” supersaturated solutions, i.e. the stability of a solution increases with the width of the metastable zone, was first developed by Matusevich, on the basis of the generalization of the Van’t Hoff rule. In other words, the stability of a solution increases with the magnitude of the ionic product of the crystallizing salt, and at constant product, the stability increases with increasing number of molecules of water of hydration incorporated in the salt crystal. Thus ZPT belongs to the class IV (di- and multivalent salts crystallizing with 3 or 4 molecules of water). Further Matusevich [105] introduced the logarithm of the temperature solubility coefficient, the absolute solubility and the type of lattice of the solid salt as complementary criteria. Besides, numerous empiric correlations have been established to evaluate the width of the metastable zone, corresponding to a fluctuation of temperature ΔT_{\max} or concentration ΔC_{\max} (Tovbin and Krasnova [106], Synowiec [107]) and more recently in function of the heat of dissolution (Gopal [108], Söhnel [109]). In general, there are two methods for measuring the metastable limit. In a first approach developed by Preckshot and Brown [110] and then Khamski [111], solutions are cooled to a given temperature rapidly and then the time required for the crystallization to occur is acquired (*isothermal method*). When this time becomes

short, i.e. a few minutes, then the effective metastable limit has been approached (Powers and Konak) [112-113]. A second method is to cool a solution at some rate and observe the temperature at which the first crystals form. The temperature at which the first crystals form will increase with the cooling rate used. This briefly describes the *polythermal method* developed by Mullin et al. [114] and Nývlt et al. [115]. Moreover, a third method uses an increase of pH to reach supersaturation conditions. This approach was selected in this study for reason of its high accuracy and sensitivity regarding transient regions and the buffer effect of hydrogen phosphate ions, in similarities with the well documented study of HAP (hydroxyapatite) stability on pH changes.

6.2.2.2. Experimental determination of supersaturation limits

For the precise and systematic determination of the width of metastable zone of solubility, applied isothermal methods yield reliable results only, if the induction period is much longer than the time necessary for cooling the solution. Thus rigorously determined conditions were employed. In that way a dilute dispersion (e.g. 2 g.L^{-1}) of pure $\alpha\text{-Zn}_3(\text{PO}_4)_2 \cdot 4 \text{ H}_2\text{O}$ previously synthesized (Chapter 2) was immersed in a solution containing $0.1 \text{ mol.L}^{-1} \text{ NaNO}_3$ as inert electrolyte for maintaining a constant ionic strength ($I \approx 0.05 \text{ mol.L}^{-1}$) [116] and introduced in a temperature equilibrated reactor and let equilibrate for at least one hour. pH values were controlled in successively adding aliquots of $0.1 \text{ mol.L}^{-1} \text{ HNO}_3$ and NaOH solutions, which choices were principally motivated by the avoidance of the introduction of new ion species in the system. Thus by optical measurements of the turbidity of a $\alpha\text{-ZPT}$ suspension, pH-T solubility diagram pointing out the limits of the metastable domains could be obtained. As shown in Figure 6.3 the dissolution (i.e. formation) of zinc phosphate salts in aqueous solutions takes place following the development of undersaturation (i.e. supersaturation), which may be obtained by first decreasing the aqueous medium content in zinc and/or phosphate ions and by diminishing the pH below 3.74 at 20°C under mild agitation (Fig. 6.3 B) as duly stated by Pawlig et al. around 4 [117], or by lowering the temperature. Thus at 20°C the system while stirred at 200 rpm exhibits a metastable zone width (ΔpH) of 1.39 and 2.06 in acidic and basic conditions, accompanied by an increase of ionic strength of approximately 0.02 and 0.04, corresponding exactly to the complete dissolution of the suspended amount of crystals. In fact, temperature decrease contributes strongly to the solution undersaturation because sparingly soluble zinc phosphate salts, in similarity to calcium phosphate salts [118-120], have *reverse solubility* as illustrated by the negative slope of curves **a** (undersaturation) and **b** (saturation) in Fig. 6.3 A and B. Since the pH represents the total concentration of protons H^+ in the solution, which reflects first the concentration of dissolved phosphate ions and then the overall $\alpha\text{-ZPT}$ solubility, the pH dependence of dissolving crystals with the temperature can be analyzed on the basis of the

Gibbs-Helmholtz relation and the Clausius-Clapeyron equation at temperature above 80°C, where water starts evaporating [121-122]. Thus Fig. 6.3 suggests that the enthalpy of dissolution is negative and consequently that the solubility decreases with increasing temperature. This is in complete agreement with the early observation by Perez and Nancollas [123] in the limited range 20-40°C. In Figure 6.3 for any temperature in the range 0-100°C but in isothermal conditions, starting from the stability region (zone III) where no crystal dissolves, lowering or increasing the pH value conducts to observe the partial and then total dissolution of α -ZPT, respectively in zones II and IV on one hand and in zones I and VI on the other hand. These regions are limited by the curves **a** and **d** (point of cloudiness: last dissolving crystal, solubility limit $S = 1$) on one hand and **b** and **c** (first dissolving crystal, supersaturation $S > 1$) on the other hand in acidic and basic conditions. Curve **e** indicates the basic pH limit of cloudiness, under which (zone V) zinc phosphate may presumably convert to zinc hydroxide since $\text{Zn}(\text{OH})_2$ forms above pH 6.13 ($\approx \text{p}K_1$) [124] and precipitates dominantly but simultaneously with ZnO around pH 9.5-10.2 ($\approx \text{p}K_2$) at 25°C [125]. Besides, mechanical action may dramatically influence, i.e. narrows the width of the metastable zone. This effect is precisely exhibited in Fig. 6.3 B. Moreover Mullin and Osman [126] concluded that without exception, any unstirred solution must have broader metastable zone than stirred solutions since the τ and S_{max} values decrease logarithmically with increasing intensity.

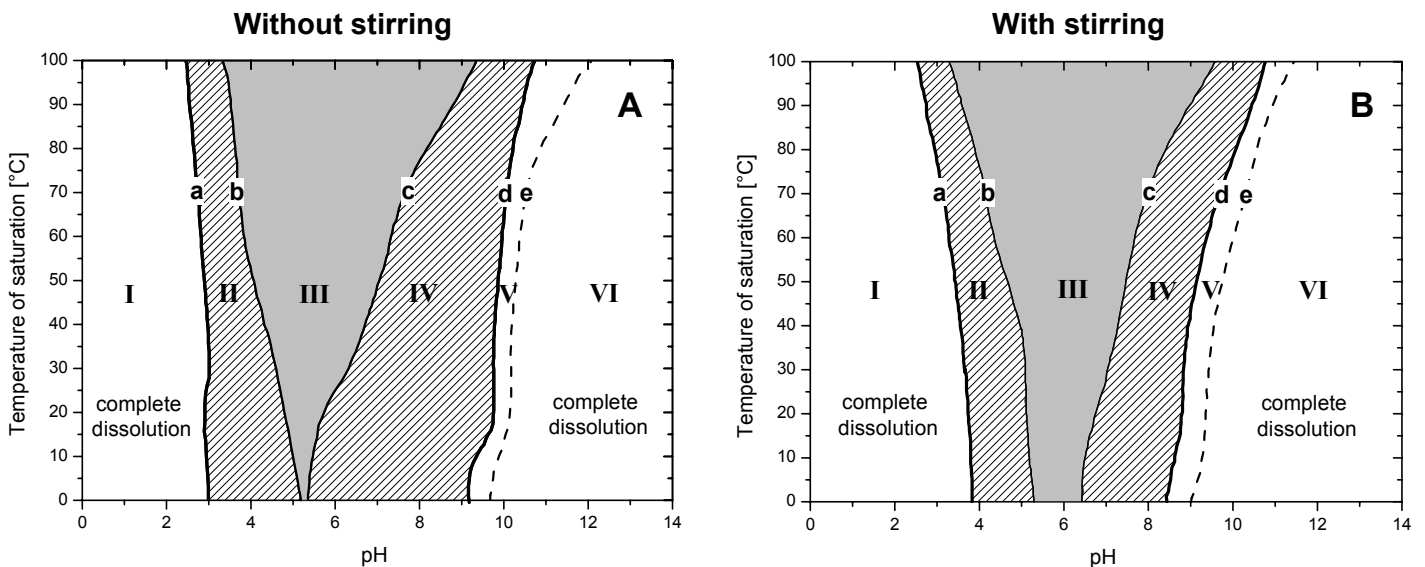


Figure 6.3: α -Zinc phosphate tetrahydrate isobaric dissolution diagram in dependence of the pH of the solution with (B) and without (A) stirring (200 rpm). This shows the saturation (b,c) and supersaturation (a,d) boundary curves in acidic and alkaline conditions respectively. Curve (e) indicates the pH-T domain above which zinc hydroxide equilibrium plays a major role on the dissolution of α -ZPT. Zone III represents the domain of insolubility (stability) of α -ZPT, while domains II and IV indicate dissolving regions in acidic and basic conditions.

Thus they interpreted this effect as being directly correlated with the diminishing probability of nucleus formation of critical size (semi-quantitative statistical model of Nývlt, Skřivánek, Gottfried et al. [127]).

6.2.3. Predominance diagrams of ions species

The speciation analysis of zinc phosphate tetrahydrate and the estimation of the free zinc ions either available for ZPT crystallization or originating from ZPT dissolution in various environmental conditions is a first but necessary step in the study of the solubility diagram in dependence of temperature and the presence of impurities (e.g. Ca^{2+} , Fe^{2+} , Ni^{2+}). Therefore Table 6.1 summarized nearly all solubility constants and ion-pairing stability constants known until now for the $\text{Zn}_3(\text{PO}_4)_2 \cdot 4\text{H}_2\text{O}-\text{H}_3\text{PO}_4-\text{H}_2\text{O}$ system.

Table 6.1: Equilibria involved in the $\text{Zn}_3(\text{PO}_4)_2 \cdot 4\text{H}_2\text{O}-\text{H}_3\text{PO}_4-\text{H}_2\text{O}$ system and the corresponding stability constants used for the computation of the solution speciation at 25°C and $I = 0 \text{ mol}\cdot\text{L}^{-1}$.

Equilibrium	Educt state ^a	pK_i ^b	Refs.
$\text{H}_2\text{O} \Leftrightarrow \text{H}^+ + \text{OH}^-$	sln	13.99	[128]
$\text{H}_3\text{PO}_4 \Leftrightarrow \text{H}_2\text{PO}_4^- + \text{H}^+$	sln	2.15	[129]
$\text{H}_2\text{PO}_4^- \Leftrightarrow \text{HPO}_4^{2-} + \text{H}^+$	sln	7.20	[129]
$\text{HPO}_4^- \Leftrightarrow \text{PO}_4^{3-} + \text{H}^+$	sln	12.37	[129]
$\text{Zn}_3(\text{PO}_4)_2 \cdot 4\text{H}_2\text{O} \Leftrightarrow 3 \text{Zn}^{2+} + 2 \text{PO}_4^{3-} + 4 \text{H}_2\text{O}$	s	35.29	[49]
$\text{Zn}_3(\text{PO}_4)_2 \cdot 4\text{H}_2\text{O} + 4 \text{H}^+ \Leftrightarrow 3 \text{Zn}^{2+} + 2 \text{H}_2\text{PO}_4^- + 4 \text{H}_2\text{O}$	s	-3.81	[130]
$\text{Zn}_3(\text{PO}_4)_2 \cdot 4\text{H}_2\text{O} \Leftrightarrow 3 \text{Zn}^{2+} + 2 \text{H}_2\text{PO}_4^- + 4 \text{OH}^-$	s	52.2	[49]
$\text{Zn}_3(\text{PO}_4)_2 + 4 \text{H}^+ \Leftrightarrow 3 \text{Zn}^{2+} + 2 \text{H}_2\text{PO}_4^-$	s	7.06	[131]
$\text{ZnH}_2\text{PO}_4^+ \Leftrightarrow \text{Zn}^{2+} + \text{H}_2\text{PO}_4^-$	sln	1.61	[132]
$\text{ZnHPO}_4^0 \Leftrightarrow \text{Zn}^{2+} + \text{HPO}_4^{2-}$	sln	-3.91	[133]
$\text{Zn}_2(\text{PO}_4)(\text{OH}) \Leftrightarrow 3 \text{Zn}^{2+} + 3 \text{PO}_4^{3-} + \text{OH}^-$	s	26.6	[134]
$\text{Zn}_4(\text{PO}_4)_2(\text{OH})_2 \Leftrightarrow 4 \text{Zn}^{2+} + 2 \text{PO}_4^{3-} + 2 \text{OH}^-$	s	52.8	[134]
$\text{Zn}_5(\text{PO}_4)_3(\text{OH}) \Leftrightarrow 5 \text{Zn}^{2+} + 3 \text{PO}_4^{3-} + \text{OH}^-$	s	63.1	[134]
$\text{Zn}(\text{OH})_2 + 2 \text{H}^+ \Leftrightarrow \text{Zn}^{2+} + 2 \text{H}_2\text{O}$	s	-10.84	[124]
$\text{Zn}(\text{OH})_2 + \text{H}^+ \Leftrightarrow \text{Zn}(\text{OH})^+ + \text{H}_2\text{O}$	s	-3.41	[124]
$\text{Zn}^{2+} + \text{OH}^- \Leftrightarrow \text{Zn}(\text{OH})^+$	sln	-6.31	[135]
$\text{Zn}^{2+} + 2 \text{OH}^- \Leftrightarrow \text{Zn}(\text{OH})_2$	sln	-11.19	[135]
$\text{Zn}^{2+} + 3 \text{OH}^- \Leftrightarrow \text{Zn}(\text{OH})_3^-$	sln	-14.31	[135]
$\text{Zn}^{2+} + 4 \text{OH}^- \Leftrightarrow \text{Zn}(\text{OH})_4^{2-}$	sln	-17.70	[135]
$\text{Zn}(\text{OH})_{2\text{s}} \Leftrightarrow \text{Zn}(\text{OH})_{2\text{sln}}$	s	5.53	[124]
$\text{Zn}(\text{OH})_2 \Leftrightarrow \text{Zn}^{2+} + 2 \text{OH}^-$	s	16.82	[124]
$\text{Zn}(\text{OH})_2 + \text{OH}^- \Leftrightarrow \text{Zn}(\text{OH})_3^-$	s	-0.99	[124]
$\text{Zn}(\text{OH})_2 + 2 \text{OH}^- \Leftrightarrow \text{Zn}(\text{OH})_4^{2-}$	s	1.39	[124]
$\text{ZnO} + \text{H}_2\text{O} \Leftrightarrow \text{Zn}^{2+} + 2 \text{OH}^-$	s	16.82	[124]
$\text{ZnO} + \text{H}_2\text{O} + \text{OH}^- \Leftrightarrow \text{Zn}(\text{OH})_3^-$	s	3.22	[124]
$\text{ZnO} + \text{H}_2\text{O} + 2 \text{OH}^- \Leftrightarrow \text{Zn}(\text{OH})_4^{2-}$	s	2	[124]

- (a) the educt state refers to the formation of ion-pair complexes in solution (sln) or to the dissolution of solid zinc phosphate compounds (s).
 (b) the estimated error from literature is on average $\text{pK}_i \pm 0.02$.

For more extend of Table 6.1, other solubility constants relative to the ternary system $\text{NH}_3\text{-H}_3\text{PO}_4\text{-H}_2\text{O}$ may be found in the monograph summarized by Eyssetlová and Dirke [136].

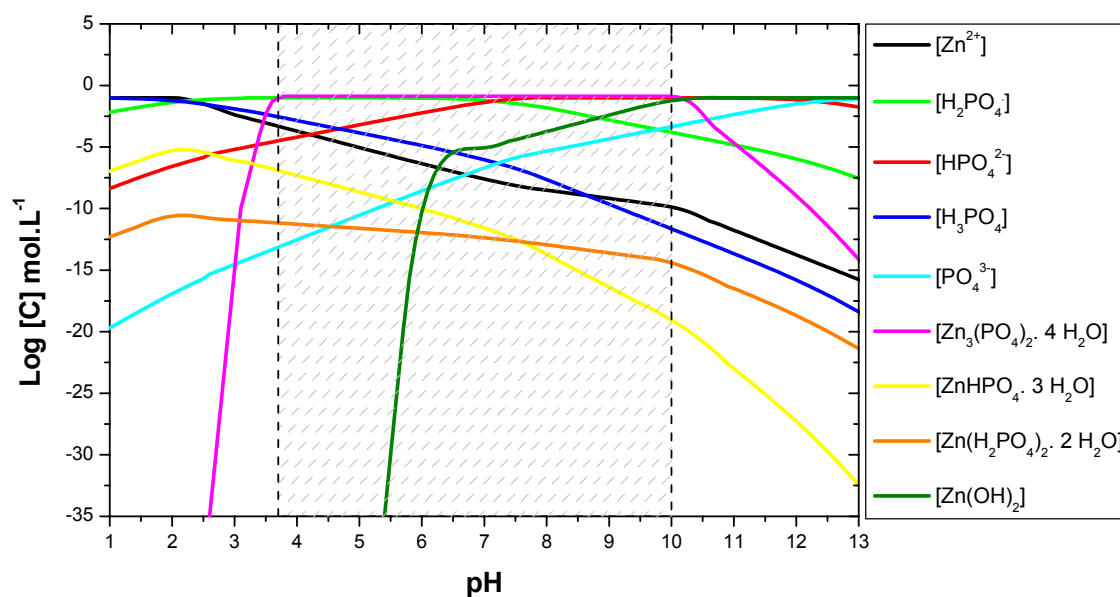


Figure 6.4: Logarithmic zinc phosphate tetrahydrate (ZPT) solubility and ion speciations versus pH at 25°C at $I = 0.2 \text{ mol.L}^{-1}$ in the system $\text{Zn}(\text{CH}_3\text{CO}_2)_2 \cdot 2\text{H}_2\text{O}\text{-H}_3\text{PO}_4\text{-H}_2\text{O}$. The grey area exhibits simultaneously the precipitation and stability regions of $\alpha\text{-ZPT}$.

Most ion species involved in the precipitation of the most stable zinc phosphate hydrate, namely hopeite, and also the complexation and hydrolysis reactions of free zinc ions in solution are taken into account using solubility constants summarized in Table 6.1 for the calculations of the ion predominance diagram on the full range of pH values at 25°C. In solutions where low ionic strength exists ($I = 0.2 \text{ mol.L}^{-1}$) it appears that zinc phosphate tetrahydrate (ZPT) forms mainly in the pH-domain 3.6-9.7 at room temperature, but dissolves rapidly below pH 3.6 and above pH 9.7. These observations are in complete agreement with the turbidity measurements in Fig. 6.3. However at high pH values, starting at pH 9 zinc hydroxide precipitation competes with the dissolution-precipitation equilibrium of ZPT independently of the ionic strength and becomes the dominating process at pH 10. Similar observations have been reported with calcium hydroxide [137-138] and other metal hydroxides by Nilson [139], Zemaitis [140] and Nriagu [141] in hydroxyapatite crystallization. Furthermore, the study of the $\text{ZnO-P}_2\text{O}_5\text{-H}_2\text{O}$ system by Goloshchapova and Filatova [7] has shed some light on the stability relations involving $\text{Zn}_3(\text{PO}_4)_2 \cdot 4\text{H}_2\text{O}$ polymorphs. Compiled with their results, the phase diagrams of $\alpha\text{-ZPT}$ in the range 0-90°C (refer to Chapter 2) suggest that $\alpha\text{-ZPT}$ is formed during the incongruent dissolution of $\text{Zn}(\text{H}_2\text{PO}_4)_2 \cdot 2\text{H}_2\text{O}$ and that parahopeite may be occasionally formed as an intermediary product in the decomposition of $\text{ZnHPO}_4 \cdot \text{H}_2\text{O}$. However Nriagu [49] has only estimated the formation of the stability constants of these zinc hydrogen phosphate in solution and not their real dissolution

(i.e. precipitation) constants. It is also particularly important to note that three polymorphs of ZPT are found in nature (Chapter 2) and that their solubility may dramatically vary with their ability to form surfacial zinc hydrogen phosphate complexes, i.e. depending on the features of their respective crystal structure (crystal symmetry hopeite/parahopeite, hydrogen bonding pattern α -ZPT/ β -ZPT).

Finally thanks to the preliminary knowledge of the various ion speciations and neglecting corresponding ions of extremely low concentration, the precise description of dissolution mechanisms through combination of multiple solubility equilibria on the whole aqueous pH range may be successfully achieved.

6.2.4. Zinc phosphate dissolution mechanism and chemical composition dependent models

6.2.4.1. Hopeite dissolution model

The simple solubility models successively developed by Jurinak and Inouye [142], Sillen and Martell [47] and later of Nriagu [49] have neither considered the polymorphic nature of hopeite nor the effect of pH, temperature and ion-pair and complex formations on the solubility equilibria. The various equilibria generally observed in the congruent dissolution of hopeite and considered in this thermodynamic model are listed in Table 6.2 with their corresponding equilibrium constants. This model is extended to the full range of pH and thus includes the formation of zinc hydroxide and zinc hydrogen phosphate complexes.

Table 6.2: List of equilibria observed in the hopeite dissolution model.

Equilibrium	Constant K_i	Equation i
Dissociation equilibria		
$H_iPO_4^{i-3} \Leftrightarrow i H^+ + PO_4^{3-}$	β_i, K_{ai}	(9)-(12) [i = 1-3]
Main solubility equilibria		
$Zn_3(PO_4)_2 \cdot 4H_2O_{(s)} \Leftrightarrow 3 Zn^{2+} + 2 PO_4^{3-} + 4 H_2O$	K_{S1}	(1)
$Zn_3(PO_4)_2 \cdot 4H_2O_{(s)} \Leftrightarrow 3 Zn^{2+} + 2 H_2PO_4^- + 4 OH^-$	K_{S2}	(2)
$Zn_3(PO_4)_2 \cdot 4H_2O_{(s)} \Leftrightarrow 3 Zn^{2+} + 2 HPO_4^{2-} + 2 OH^-$	K_{S3}	(3)
$Zn_2(PO_4)(OH) \Leftrightarrow 3 Zn^{2+} + 3 PO_4^{3-} + OH^-$	K_4	(4)
$Zn_4(PO_4)_2(OH)_2 \Leftrightarrow 4 Zn^{2+} + 2 PO_4^{3-} + 2 OH^-$	K_5	(5)
$Zn_5(PO_4)_3(OH) \Leftrightarrow 5 Zn^{2+} + 3 PO_4^{3-} + OH^-$	K_6	(6)
$Zn(OH)_{j(s)} \Leftrightarrow j OH^- + Zn^{2+}$	ω_j or K_j	(13-16) [j = 1-4]
Ion-pairing equilibria		
$ZnH_2PO_4^+ \Leftrightarrow Zn^{2+} + H_2PO_4^-$	K_7 or $K_{ZnH_2PO_4^+}$	(7)
$ZnHPO_4^0 \Leftrightarrow Zn^{2+} + HPO_4^{2-}$	K_8 or $K_{ZnHPO_4^0}$	(8)

$$\text{Where } \beta_i = \prod_i K_{a(3-i)} \cdot \quad (6.24)$$

If $[Zn^{2+}]_{total}$ and $[PO_4^{3-}]_{total}$ represent the measured global concentrations in the supernatant, and pK_w represents the logarithmic water product at a given temperature, the measurements of the solution pH leads to the determination of the phosphate ions individual concentrations. It then yields:

$$[H^+] = 10^{-pH} \quad (6.25)$$

$$[OH^-] = 10^{pH-pK_w} \quad (6.26)$$

$$[PO_4^{3-}]_{total} = [H_3PO_4] + [H_2PO_4^-] + [HPO_4^{2-}] + [PO_4^{3-}] \quad (6.27)$$

$$[H_2PO_4^-] = [PO_4^{3-}]_{total} / (1 + 10^{pH-pK_{a2}}) \quad (6.28)$$

$$[HPO_4^{2-}] = [PO_4^{3-}]_{total} \cdot 10^{pH-pK_{a2}} / (1 + 10^{pH-pK_{a2}}) \quad (6.29)$$

$$[H_3PO_4] = [H_2PO_4^-] \cdot 10^{pK_{a1}-pH} \quad (6.30)$$

$$[PO_4^{3-}] = [HPO_4^{2-}] \cdot 10^{pH-pK_{a3}} \quad (6.31)$$

In addition, assuming the activity coefficients of water and the solid phase equal to unity and considering a solution saturated with respect to hopeite, the following mass balance reaction can be written from reaction (1):

$$K_s = (a_{Zn^{2+}})^3 \times (a_{PO_4^{3-}})^2 \quad (6.32)$$

Using the definition of the activity of an ion *i* (Eq. 6.5), one obtains:

$$K_s = \gamma_{Zn^{2+}}^3 \cdot \gamma_{PO_4^{3-}}^2 [Zn^{2+}]^3 \times [PO_4^{3-}]^2 \quad (6.33)$$

where the activity coefficients of each ion species are determined in dependence of the pH using the Davies equation (Eq. 6.17a). The molar solubility *s* can also be described as follows :

$$s = [Zn^{2+}]_{total} = [Zn^{2+}] + \sum_{j=1, \neq 2}^4 [Zn(OH)_j^{2-j}] \quad (6.34)$$

$$\text{or } s = [PO_4]_{total} = [H_3PO_4] \cdot \Phi_1 + \alpha_1 \quad (6.35)$$

where the parameter Φ_1 is:

$$\Phi_1 = \frac{1}{\gamma_{PO_4^{3-}}} + \frac{(\gamma_{H^+} [H^+])}{\gamma_{HPO_4^{2-}} \cdot K_{a3}} + \frac{(\gamma_{H^+} [H^+])^2}{\gamma_{H_2PO_4^-} \cdot K_{a2} \cdot K_{a3}} + \frac{(\gamma_{H^+} [H^+])^3}{\gamma_{H_3PO_4} \cdot K_{a1} \cdot K_{a2} \cdot K_{a3}} \quad (6.36)$$

Defining respectively α_1 and α_2 as the immobilized phosphate and zinc amounts, i.e. the molar concentrations of phosphate and zinc forming ion-pair complexes or combined with hydroxides:

$$\alpha_1 = [ZnHPO_4^0] + [ZnH_2PO_4^+] + [Zn_2(PO_4)(OH)] + [Zn_4(PO_4)_3(OH)_2] + [Zn_5(PO_4)_3(OH)] \quad (6.37)$$

$$\alpha_2 = \alpha_1 + [Zn(OH)^+] + [Zn(OH)_2] + [Zn(OH)_3^-] + [Zn(OH)_4^{2-}] \quad (6.38)$$

Using known variables, it leads to:

$$\alpha_1 = [Zn^{2+}] \times \left\{ \frac{[HPO_4^{2-}]}{K_8} + \frac{[H_2PO_4^-]}{K_7} + [Zn^{2+}] \left[\frac{[PO_4^{3-}][OH^-]}{K_4} + \frac{[Zn^{2+}]^2 [PO_4^{3-}][OH^-]}{K_5} + \frac{[Zn^{2+}]^3 [PO_4^{3-}]^2}{K_6} \right] \right\} \quad (6.39)$$

$$\alpha_2 = \alpha_1 + [Zn^{2+}] \times \left\{ \frac{[OH^-]}{K_{13}} + \frac{[OH^-]^2}{K_{14}} + \frac{[OH^-]^3}{K_{15}} + \frac{[OH^-]^4}{K_{16}} \right\} \quad (6.40)$$

Here the first approximation encountered is the neglecting of the zinc quantity involved in the formation of ion-pair complex in the expression of the solubility on zinc ion. Thus over all the pH range the ionic strength of the present solution, derived from Eq. 6.39, becomes:

$$I = 2\gamma_{Zn^{2+}} ([Zn^{2+}]_{total} - \alpha_2) + \frac{1}{2} \left\{ \gamma_{H^+} [H^+] + \gamma_{OH^-} [OH^-] + \frac{\Phi_2 \cdot \gamma_{PO_4^{3-}} ([PO_4^{3-}]_{total} - \alpha_1)}{\Phi_1} \right\} \quad (6.41)$$

$$\text{with } \Phi_2 = \frac{9}{\gamma_{PO_4^{3-}}} + \frac{4(\gamma_{H^+} [H^+])}{\gamma_{HPO_4^{2-}} \cdot K_{a3}} + \frac{9(\gamma_{H^+} [H^+])^2}{\gamma_{H_2PO_4^-} \cdot K_{a2} \cdot K_{a3}} \quad (6.42)$$

Finally it comes,

$$K_s = \gamma_{Zn^{2+}}^3 \cdot \gamma_{PO_4^{3-}}^2 \cdot ([Zn^{2+}]_{total} - \alpha_2)^3 \times \left(\frac{[PO_4^{3-}]_{total} - \alpha_1}{\Phi_1} \right)^2 \quad (6.43)$$

The appropriate solubility constants of hopeite using reaction schemes (2) and (3) are:

$$K_{s2} = \gamma_{H_2PO_4^-}^2 \cdot \gamma_{PO_4^{3-}}^{-2} \cdot K_{s1} \cdot \frac{K_w^4}{K_{a2}^2 \cdot K_{a3}^2} \quad (*) \quad (6.44)$$

$$K_{s3} = \gamma_{HPO_4^{2-}}^2 \cdot \gamma_{PO_4^{3-}}^{-2} \cdot K_{s1} \cdot \frac{K_w^2}{K_{a3}^2} \quad (*) \quad (6.45)$$

It is noteworthy to mention that the calculated values of the solubility constants K_s , K_w and K_3 for the three reaction routes (1)-(3) in dependence on the pH, are only reliable after correcting the ionic strength with the determined activity coefficients of all charged species in solution by iteration process until the value of I in Eq. 6.66 becomes stable, i.e. constant, starting with an initialization of all activity coefficients equals to unity. This procedure was first suggested by Nriagu for the dissolution mechanism of Vivianite, an iron phosphate octahydrate [143]. The activity coefficients calculated in this manner are then used to obtain the activities of all ion species in solution and consequently the solubility constants. Moreover, the optimized values of activity coefficients, generated to obtain the best correspondence between the measured and calculated set of observables (pH, $[Zn^{2+}]_{total}$ and $[PO_4^{3-}]_{total}$) depends completely on the selected expression of the ionic strength, based either on empirical models (e.g. Davies equation, 1962) or theoretical basis (i.e. Bromley equation).

(*) N.B.: This defines pseudo-equilibrium constants, since the solubility product constants do not depend directly on the activity coefficient of the various ions in solution (c.f. Eq. 1-3 in Table 6.2).

However this model delivers satisfactory values of solubility constants in dependence of the solution pH and temperature only in the case of pure hopeite, and therefore is restricted to the evaluation of the influence of the polymorphism and state of hydration of zinc phosphate tetrahydrates on the solubility constants.

6.2.4.2. Composition dependent dissolution model

Since industrial pigments based on zinc phosphate exhibit extremely complex formulations, with traces of various additives corresponding to some desired anticorrosion effects [144-145], especially in the alkaline pH domain, the simple hopeite solubility model must be adapted in order to take into account these "impurities". In addition, basic zinc phosphates obtained by polymer controlled mineralization contain non negligible amounts of Na⁺ that are released during initial pigment dissolution, and may form metastable complexes (derivatives of sodium hydrogen phosphates, sodium zinc hydroxyphosphates) or precipitate again in the form of zeolites of lower compacity (e.g. Na₆Zn₃(PO₄)₃·3H₂O [146], Na₂Zn(HPO₄)₂·4H₂O [147], NaZn₂(HPO₄)(PO₄) [148]), that finally condensate in the most stable zinc phosphate hydrate, hopeite, thus strongly influencing the overall solubility equilibrium of the investigated pigments. Therefore a composition dependent dissolution model for those pigments has been developed. The added reactional pathways relative to NaZnPO₄·1H₂O, and Na₂Zn(PO₄)(OH)·2H₂O are described in Table 6.3.

Table 6.3: List of equilibria observed in the composition dependent dissolution model

Equilibrium	Constant K_i	Equation i
Added main solubility equilibria		
$\text{NaZnPO}_4 \cdot 1\text{H}_2\text{O}_{(s)} \Leftrightarrow \text{Na}^+ + \text{Zn}^{2+} + \text{PO}_4^{3-}$	K_{S4}	(17)
$\text{NaZnPO}_4 \cdot 1\text{H}_2\text{O}_{(s)} \Leftrightarrow \text{Na}^+ + \text{Zn}^{2+} + \text{H}_2\text{PO}_4^- + 2 \text{OH}^-$	K_{S5}	(18)
$\text{NaZnPO}_4 \cdot 1\text{H}_2\text{O}_{(s)} \Leftrightarrow \text{Na}^+ + \text{Zn}^{2+} + \text{HPO}_4^{2-} + \text{OH}^-$	K_{S6}	(19)
$\text{Na}_2\text{Zn}(\text{PO}_4)(\text{OH}) \cdot 1\text{H}_2\text{O}_{(s)} \Leftrightarrow 2 \text{Na}^+ + \text{Zn}^{2+} + \text{PO}_4^{3-} + \text{OH}^-$	K_{S7}	(20)
$\text{Na}_2\text{Zn}(\text{PO}_4)(\text{OH}) \cdot 1\text{H}_2\text{O}_{(s)} \Leftrightarrow 2 \text{Na}^+ + \text{Zn}^{2+} + \text{H}_2\text{PO}_4^- + 3 \text{OH}^-$	K_{S8}	(21)
$\text{Na}_2\text{Zn}(\text{PO}_4)(\text{OH}) \cdot 1\text{H}_2\text{O}_{(s)} \Leftrightarrow 2 \text{Na}^+ + \text{Zn}^{2+} + \text{HPO}_4^{2-} + 2 \text{OH}^-$	K_{S9}	(22)
Ion-pairing equilibria		
$\text{NaH}_2\text{PO}_4 \Leftrightarrow \text{Na}^+ + \text{H}_2\text{PO}_4^-$	$K_{23} = 10^{2.43}$ [149]*	(23)
$\text{Na}_2\text{HPO}_4 \cdot 12\text{H}_2\text{O} \Leftrightarrow \text{Na}_2\text{HPO}_4 \Leftrightarrow 2 \text{Na}^+ + \text{HPO}_4^{2-}$	$K_{24} = 10^{-2.34}$ [150]*	(24)

(*) Solubility constants given at 25°C.

Hence the solubility of sodium phosphate hydrate soluble salts highly depends on dissolution temperature [150], and therefore can not be neglected in the reaction scheme. As well, the congruent dissolution of NaZnPO₄·1H₂O may be used to derive the equilibrium constant for the

metamorphic reaction leading to β -ZPT (Figure 6.5) at ambient temperature via the evaluation of K_{s4} :

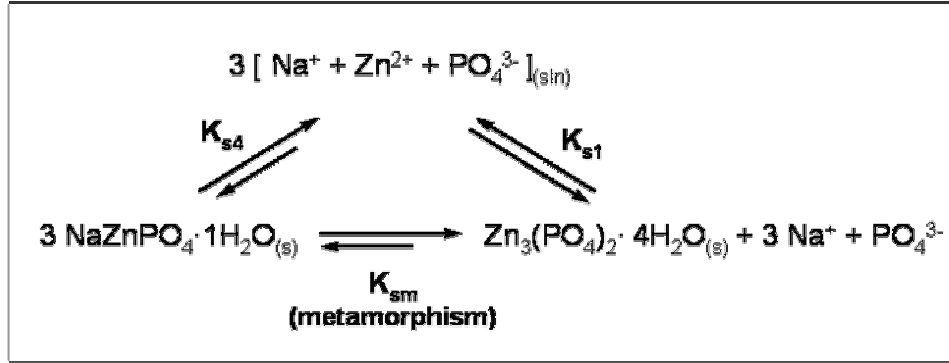


Figure 6.5: Reaction scheme displaying the progressive conversion of $\text{NaZnPO}_4 \cdot 1\text{H}_2\text{O}$ to β -ZPT at ambient temperature in an anticorrosion coating, accompanied with the release of one effective phosphate group, available for steel repairing.

From mass balance relation for the reaction (17), it comes:

$$K_s = \gamma_{\text{Na}^+} \cdot \gamma_{\text{Zn}^{2+}} \cdot \gamma_{\text{PO}_4^{3-}} \cdot [\text{Na}^+] \times [\text{Zn}^{2+}] \times [\text{PO}_4^{3-}] \quad (6.46)$$

In analogy to § 6.2.7.1, one may define respectively α_1 , α_2 and α_3 as the immobilized sodium, phosphate and zinc amounts, i.e. the molar concentrations of sodium, phosphate and zinc forming ion-pair complexes or combined with hydroxides:

$$\alpha_1 = [\text{Na}_2\text{HPO}_4] + [\text{NaH}_2\text{PO}_4] \quad (6.47)$$

$$\alpha_2 = [\text{ZnHPO}_4^0] + [\text{ZnH}_2\text{PO}_4^+] + [\text{Zn}_2(\text{PO}_4)(\text{OH})] + [\text{Zn}_4(\text{PO}_4)_3(\text{OH})_2^{3-}] + [\text{Zn}_5(\text{PO}_4)_3(\text{OH})] + \alpha_1 \quad (6.48)$$

$$\alpha_3 = \alpha_2 + [\text{Zn}(\text{OH})^+] + [\text{Zn}(\text{OH})_2] + [\text{Zn}(\text{OH})_3] + [\text{Zn}(\text{OH})_4^{2-}] \quad (6.49)$$

Using known variables, it leads to:

$$\alpha_1 = [\text{Na}^+] \times \left\{ \frac{[\text{HPO}_4^{2-}]}{K_{24}} + \frac{[\text{H}_2\text{PO}_4^-]}{K_{23}} \right\} \quad (6.50)$$

$$\alpha_2 = \alpha_1 + [\text{Zn}^{2+}] \times \left\{ \frac{[\text{HPO}_4^{2-}]}{K_8} + \frac{[\text{H}_2\text{PO}_4^-]}{K_7} + [\text{Zn}^{2+}] [\text{PO}_4^{3-}] [\text{OH}^-] \left\{ \frac{1}{K_4} + \frac{[\text{Zn}^{2+}]^2 [\text{PO}_4^{3-}] [\text{OH}^-]}{K_5} + \frac{[\text{Zn}^{2+}]^3 [\text{PO}_4^{3-}]^2}{K_6} \right\} \right\} \quad (6.76)$$

$$\alpha_3 = \alpha_2 + [\text{Zn}^{2+}] \times \left\{ \frac{[\text{OH}^-]}{K_{13}} + \frac{[\text{OH}^-]^2}{K_{14}} + \frac{[\text{OH}^-]^3}{K_{15}} + \frac{[\text{OH}^-]^4}{K_{16}} \right\} \quad (6.51)$$

And the molar solubility of the system successively on the sodium, zinc and phosphate ions yields:

$$s = [\text{Na}^+]_{\text{total}} = [\text{Na}^+] + \alpha_1 \quad (6.52)$$

$$s = [\text{PO}_4]_{\text{total}} = [\text{H}_3\text{PO}_4] \cdot \Phi_1 + \alpha_2 \quad (6.53)$$

$$s = [Zn^{2+}]_{total} = [Zn^{w+}] + \alpha_3 \quad (6.54)$$

Thus over all the pH range the ionic strength of the present solution, derived from Eq. 6.39, becomes:

$$I = 2\gamma_{Zn^{2+}} ([Zn^{2+}]_{total} - \alpha_3) + \frac{1}{2} \left\{ \gamma_{H^+} [H^+] + \gamma_{OH^-} [OH^-] + \gamma_{Na^+} ([Na^+] - \alpha_1) + \frac{\Phi_2 \cdot \gamma_{PO_4^{3-}} ([PO_4^{3-}]_{total} - \alpha_2)}{\Phi_1} \right\} \quad (6.55)$$

$$\text{with } \Phi_2 = \frac{9}{\gamma_{PO_4^{3-}}} + \frac{4(\gamma_{H^+} [H^+])}{\gamma_{HPO_4^{2-}} \cdot K_{a3}} + \frac{9(\gamma_{H^+} [H^+])^2}{\gamma_{H_2PO_4^-} \cdot K_{a2} \cdot K_{a3}} \quad (6.56)$$

Finally it comes,

$$K_s = \gamma_{Na^+} \gamma_{Zn^{2+}} \gamma_{PO_4^{3-}} \cdot ([Na^+]_{total} - \alpha_2) \cdot ([Zn^{2+}]_{total} - \alpha_3) \times \left(\frac{[PO_4^{3-}]_{total} - \alpha_2}{\Phi_1} \right) \quad (6.57)$$

The appropriate solubility constants of $NaZnPO_4 \cdot 1H_2O$ using reaction schemes (17) and (18) in Table 6.3 and the supposed scheme for the metamorphic reaction (Fig. 6.5) are:

$$K_{s5} = \gamma_{H_2PO_4^-} \cdot \gamma_{OH^-} \cdot \gamma_{PO_4^{3-}} \cdot K_{s4} \cdot \frac{K_w^2}{K_{a2} \cdot K_{a3}} (*) \quad (6.58)$$

$$K_{s6} = \gamma_{HPO_4^{2-}} \cdot \gamma_{OH^-} \cdot \gamma_{PO_4^{3-}} \cdot K_{s4} \cdot \frac{K_w}{K_{a3}} (*) \quad (6.59)$$

$$K_{sm} = K_{s4} \times K_{s1} \quad (6.60)$$

A similar approach by composition dependent dissolution model is highly recommended in the case of other basic zinc phosphate pigments such as $Na_2Zn(PO_4)(OH) \cdot 2H_2O$.

6.3. Methods developments

6.3.1. Strategies for the investigation of dissolution mechanisms: forced release and achievement of a thermodynamic equilibrium

For the study of the dissolution mechanisms and the evaluation of solubility equilibrium constants two main strategies have been presently considered as shown in Figure 6.6. The first strategy consists of a *leaching method* (thermodynamic approach), where pigment suspensions are let to equilibrate for months in a buffered solution. This method may highlight the formation of metastable ion-pair complexes that may precipitate and/or dissolve as saturation is reached. A second strategy, more precise than the first one, consists of a *pH response method* (kinetic

(*) N.B.: This defines pseudo-equilibrium constants, since the solubility product constants do not depend directly on the activity coefficient of the various ions in solution (c.f. Table 6.3).

approach), where phosphate release to a pH pulse is monitored until a solubilization equilibrium is also reached. This approach allows the released phosphate ions in function of the initially imposed pH and elapsed time to regulate the pH of the solution as buffer solution, since kinetic consideration are of paramount importance in determining the nature of the phase that forms initially, in analogy to the calcium phosphate system [50, 151-152]. These two strategies are implemented on a broad range of pure and modified zinc phosphates, and their solubilisation is either followed by electrochemistry or by conductometry, gravimetry after filtrate recovery and also complete supernatant analysis. All these techniques have special requirements (i.e. calibration, choice of the experimental conditions) that first need to be identified.

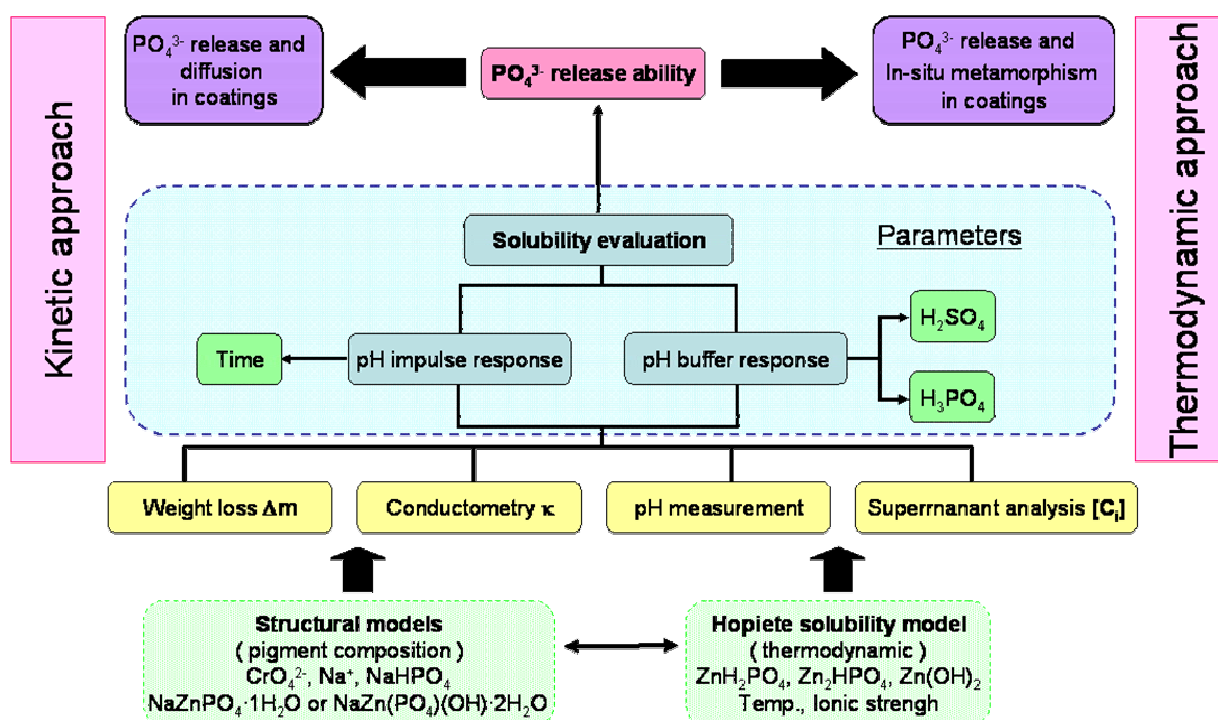


Figure 6.6: Schematic representation of the strategies developed for the investigation of the dissolution mechanisms of zinc phosphate hydrates based pigments

6.3.2. Dissolution conditions: Choice of the experimental parameters

The time scale for reaching solubility equilibrium as well as the buffer solution selected to achieve it are key parameters in the investigation of the dissolution mechanism of zinc phosphate pigments.

Moreover as suggested by Koutsoukos et al. [153], the dependence of the induction periods for dissolution (i.e. crystallization [154]) may be easily measured by gravimetry or conductivity at different solute concentrations, ionic strengths and temperatures. The time to reach the thermodynamic solubility equilibrium depends completely of the solid solute concentration that governs the relative supersaturation at infinite time. From the experimental methodology employed, i.e. the *leaching method*, it is obvious that the i^{th} measured induction time of

dissolution τ , includes both the time needed for dissolution to proceed τ_n and the time τ_g , required for the crystal to dissolve to a critical nucleus size (i.e. time required for a surfacial etch pit to grow to a critical size) which would correspond to the extent of ion release needed by the conductivity probe to give an appropriate change of specific conductance of the undersaturated solution, i.e.

$$\tau = \tau_n + \tau_g \quad (6.61)$$

The strong dependence of induction times of dissolution on the solution undersaturation (i.e. supersaturation) which is more pronounced at low temperature (25°C) should be ascribed to the sensitivity of pit nucleation on both supersaturation and temperature and the negative value of the enthalpy of ZPT dissolution. Assuming the achievement of a steady-state, the dependence of induction time on undersaturation may be expressed [2] as in Eq. 6.62 :

$$\text{Log } \tau = \frac{C_1}{T^3 \log^2 S} - C_2 \quad \text{and} \quad C_1 = \frac{\beta \gamma_{sl}^3 V_m^2}{(2.303)^3 \nu^2} \quad (6.62)$$

where C_1 and C_2 are constants related to the shape factor β (also denominated R , $R = L/l$, ratio of the length to the width of platelike crystals), the shape of the dissolving nuclei C_2 [155], k is the Boltzmann's constant and ν is the number of ions in the zinc phosphate crystals ($\nu = 5$).

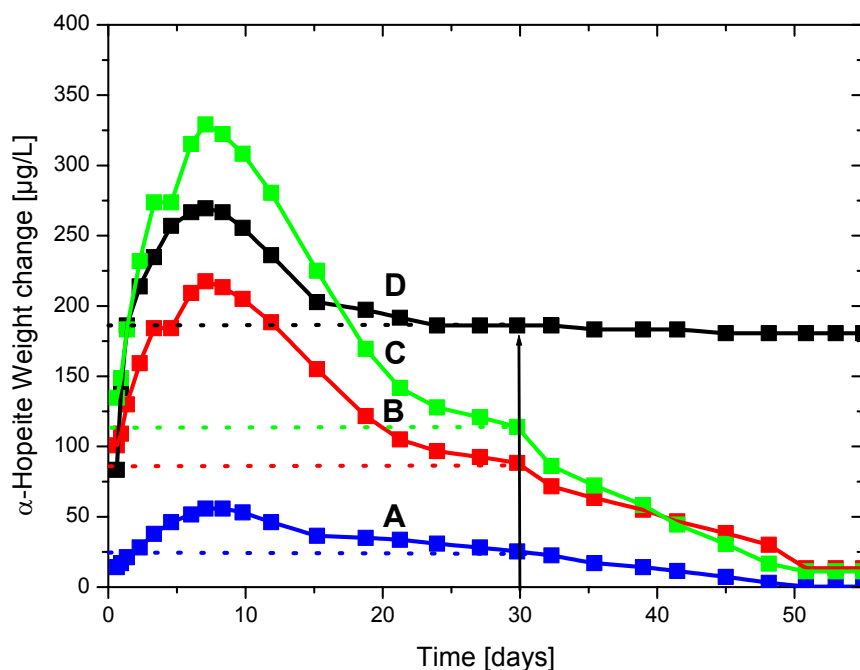


Figure 6.7: Kinetics of dissolution of a 2 g.L⁻¹ suspension of α -zinc phosphate tetrahydrate pigment in (A) water, (B) a 10⁻⁴ mol.L⁻¹ H₂SO₄ solution, (C) a 10⁻⁴ mol.L⁻¹ HNO₃ solution, (D) 10⁻⁴ mol.L⁻¹ H₃PO₄ solution under mild agitation (250 rpm) at 25°C. The final pH of the mother liquors establishes around 6.5.

The recent publication of Kashiev [156] of the in-depth analysis of the thermodynamics and kinetics of homogeneous and heterogeneous nucleation, in extension of the critical review of Söhnel and Garside [157] is noteworthy for further both evaluations of the induction time of dissolution, and of the time to reach thermodynamic solubility equilibrium. Thus, Figure 6.7 presents the kinetics of dissolution on immersion of zinc phosphate pigments followed by the

determination of the zinc concentration in the mother liquor by Atom Absorption Spectroscopy (AAS) at increasing elapsed time.

In all dissolution media, Because of the large size of the investigated α -ZPT pigment and a negligible supersaturation, any induction time of dissolution could be determined. After 30 days on average, the thermodynamic equilibrium (saturation) of dissolution is considered attained, and this independently of the dissolution medium. However, more precisely after an initial dissolution at its maximum 7 days, a slight solubility decrease is observed in HNO_3 and H_2SO_4 due to a precipitation of the species in solution as the pH of the mother liquor stabilizes around 6.5. In water and phosphoric acid, this phenomenon is not expected presumably due to buffer effects. The estimation of the time limit for achieving solubility equilibrium is consistent with the values found for industrial zinc phosphates manufactured either for anticorrosion [158] or for orthopaedic [42] and optical [159] applications.

6.3.3. Conductivity measurements

The solubility of sparingly soluble electrolytes in water may be in first approach easily determined from conductivity measurements and pH monitoring (i.e. screening method of pigment anticorrosion efficacy) on their saturated solutions at varying temperatures as proposed successively by Findlay [160] and Matthews [161]. Recently such a method was successfully applied to CaCO_3 by Carmona et al [162-164]. However complex reactions schemes as described in § 6.2.7 cannot be here directly considered, so that first ion-pair complex formations are excluded and only the dissolution route (1) (Table 6.2) for ZPT dissolution, i.e. $\text{Zn}_3(\text{PO}_4)_2 \cdot 4\text{H}_2\text{O}_{(s)} \Leftrightarrow 3 \text{Zn}^{2+} + 2 \text{PO}_4^{3-} + 4 \text{H}_2\text{O}$ is taken into account. Considering the potential dissolution routes of ZPT independently, as established in Table 6.2, it then yields a direct relationship between the measured conductivity and the thermodynamic solubility product, summarized in Table 6.4:

Table 6.4: Evaluation: solubility-solubility constants relationships applied in conductimetry in first approach without refinement procedure

precipitate	Solubility constant	Approximated equation
$\text{Zn}_3(\text{PO}_4)_2 \cdot 4\text{H}_2\text{O}$	Ks_1	$108 s^5$
	Ks_2	$432 s^7$
	Ks_3	$82944 s^{11}$
	Ks_4	s^3
$\text{NaZnPO}_4 \cdot \text{H}_2\text{O}$	Ks_5	$4 s^4$
	Ks_6	s^4

Thus, the measured conductivity K can be expressed as the product of the equilibrium saturated concentration s and the molar conductivity Λ_0 of the solution at infinite dilution. Even

a saturated solution of sparingly salt is still very diluted ($s < 10^{-2}$ mol.L⁻¹), so that it may be assumed that $\Lambda \approx \Lambda_0$, where Λ_0 is the molar conductivity of the solution at infinite dilution. For the considered sparingly salt in solution, the global molar conductivity at infinite dilution is the sum of the contribution of the Λ_0 of all ion species in solution. From the Kohlrausch-Onsager relation, it comes:

$$\Lambda_0^{suspension} = \sum_{ion i} \Lambda_0^i \quad (6.63)$$

$$K = g(s) = \Lambda_0 s - (A + B\Lambda_0) s^{3/2} \quad (6.64)$$

where A and B are coefficients characteristic of the electrolyte in a given concentration range.

The first approximation of this method (i.e. employing the relationships given in Table 6.4) is that in basic pH, the precipitation of zinc hydroxide diminishes the pristine amount of Zn²⁺ delivered by zinc phosphate dissolution, $[Zn^{2+}]_{total}$. Using known values of K_{14} of Zn(OH)₂ at different temperatures and the measured pH value, a correction on the original zinc concentration delivered by ZPT dissolution may be established:

$$[Zn^{2+}]_{total} \approx s + K_{14} / (4 \cdot 10^{2(pK_w - pH)}) \quad (6.65)$$

The second approximation relates to the determination of all phosphate species in solution from the restricted knowledge of pH and K, that may be either neglected by application of K_s equations as summarized in table 6.4, or considered and precisely determined by an iteration procedure (of convergence) on the measured solution conductivity $K_{measured}$. A such procedure is described as follows. Firstly from the pH value one may gain access to the distribution of phosphate ions summed on unity (c.f. Eqs. 6.25-6.31) using well known phosphoric acid equilibria constants. Then supposing that $[PO_4^{3-}]_{total}$ equals s , an initial molar concentration of all phosphate ions in solution may be obtained, offering approximate values of $K_{s_{1-3}}$ (i.e. $K_{s_{4-6}}$). By the means of a backcalculation of K, $K_{calculated}$ its comparison to the measured conductivity of the saturated solution K, and then minimization of the difference $\Delta K^i = K_{measured} - K_{calculated}^i$ by iteration (step i), exact concentrations of all species present in the solution can be determined. Finally this delivers directly nearly exact values of the solubility constants $K_{s_{1-3}}$ (i.e. $K_{s_{4-6}}$). The best correspondence between measured and estimated values of the conductivity is given by:

$$K_{calculated}^{i+1} = K_{measured} + \Delta K^i \quad (6.66)$$

$$\Delta K^i = K_{measured} - K_{calculated}^i \quad (6.67)$$

$$K_{calculated}^i(s^i) = f(s^i) = g(s_{OH^-}^i) + g(s_{H^+}^i) + g(s_{Zn^{2+}}^i) + g(s_{H_3PO_4}^i) + g(s_{H_2PO_4^-}^i) + g(s_{HPO_4^{2-}}^i) + g(s_{PO_4^{3-}}^i) \quad (6.68)$$

$$s_{Zn^{2+}}^i = s^i + K_{14} / (4 \cdot 10^{2(pK_w - pH)}) \quad (6.69)$$

Assuming $[PO_4^{3-}]_{total} = s^i$, it yields

$$s_{H_3PO_4}^i = s^i \cdot 10^{pK_{a1}-pH} / (1 + 10^{pH-pK_{a2}}) \text{ using Eq. 6.55} \quad (6.70)$$

$$s_{H_2PO_4^-}^i = s^i / (1 + 10^{pH-pK_{a2}}) \text{ using Eq. 6.53} \quad (6.71)$$

$$s_{HPO_4^{2-}}^i = s^i \cdot 10^{pH-pK_{a2}} / (1 + 10^{pH-pK_{a2}}) \text{ using Eq. 6.54} \quad (6.72)$$

$$s_{PO_4^{3-}}^i = s^i \cdot 10^{2pH-pK_{a2}-pK_{a3}} / (1 + 10^{pH-pK_{a2}}) \text{ using Eq. 6.56} \quad (6.73)$$

where $s_{OH^-}^i$ and $s_{H^+}^i$ are independent on s^i and therefore directly evaluated with Eq. 6.25-6.26

This refinement procedure of the conductivity is strenuous and does not consider the effect of the activity coefficients on the thermodynamic solubility products, albeit all necessary ionic concentrations are determined and an estimation of the corresponding activity coefficients thanks to the evaluation of the ionic strength and the application of the Davies equations (c.f. 6.42) is still possible. Therefore a more precise method, based on systematic investigation all free ionic species in the supernatant at saturation is required.

6.3.4. Supernatant analysis and complexometric measurements

The precise identification of all ionic species released in solution (supernatant) during dissolution of zinc phosphate pigments, and also their corresponding concentrations on equilibration in given pH and temperature conditions is unavoidable in order to first evaluate their corresponding activity coefficients and then to estimate very accurately the thermodynamic solubility constants by direct application of the solubility models developed in § 6.2.4.

6.3.4.1. Determination of the zinc concentration $[Zn^{2+}]_{total}$

Since at high pH (>7) the precipitation of $Zn(OH)_2$ competes with the dissolution of ZPT, the quantification of Zn^{2+} concentration becomes essential; the zinc ions being either a free species (aqua-complex) or forming not so stable hydrogen phosphate complexes in solution. This may be done either by Inductively Coupled Plasma Mass Spectroscopy (ICP-MS) and Atom Absorption Spectroscopy (AAS) for low concentrations ($\mu\text{mol.L}^{-1}$), by potentiometric or even by complexometric methods (mmol.L^{-1} concentration range). Albeit the potentiometric method is rapid and efficient, it relies on the formation and precipitation of potassium-zinc-hexacyanoferrat (II) complex. However sodium ions are known to strongly perturbate the $K_2Zn_3[Fe(CN)_6]_2$ formation and therefore is not further considered [165]. Besides, complexometric method while still attractive, are time consuming (numerous dilutions required), temperature dependent and

expensive, since they generally rely on the use of a zinc selective complexing agent, zincon (2-carboxy-2 μ -hydroxy-5 μ -sulformazylbenzene) [166-167]. Consequently, flame methods such as the AAS [168] have preferentially been chosen. This method was also selected for the determination of sodium delivered by the dissolution of polymer modified zinc phosphate (e.g. $\text{NaZnPO}_4 \cdot 1\text{H}_2\text{O}$).

6.3.4.2. Determination of the total phosphate concentration $[\text{PO}_4^{3-}]_{\text{total}}$

The total amount of free phosphate ions in solution can be conveniently determined colorimetrically either by the stannous chloride method ($\lambda = 690\text{ nm}$) [169] or by a more performing molybdate blue method according a procedure originally recommended by Harwood et al. [170-171], and presently extended to higher concentrations without any dramatic reduction in the sensitivity (estimated systematic error: 1 % $[\text{PO}_4^{3-}]_{\text{total}}$). Ascorbic acid, in combination with antimony as catalyst ($[\text{KSbOC}_4\text{H}_4\text{O}_6]_2 \cdot 1\text{ H}_2\text{O}$, conc. max. $1.2\text{ g}\cdot\text{L}^{-1}$) was selected as reducing agent of the molybdophosphoric acid formed, in reason of a slow but constant colour development, without perturbations caused by impurities present in the supernatant (Na^+ , CrO_4^{2-} , etc.) as displayed in Figure 6.8 B, where no departure of the linearity is observed, even above a concentration $[\text{PO}_4^{3-}]_{\text{total}}$ of $6\text{ mg}\cdot\text{L}^{-1}$ [172-173]. However noticeable difference with the results of Harwood et al. may be presumingly attributed to temperature fluctuations, since a tempered ($20^\circ\text{C} \pm 0.1^\circ\text{C}$) quartz cell was employed in the present method.

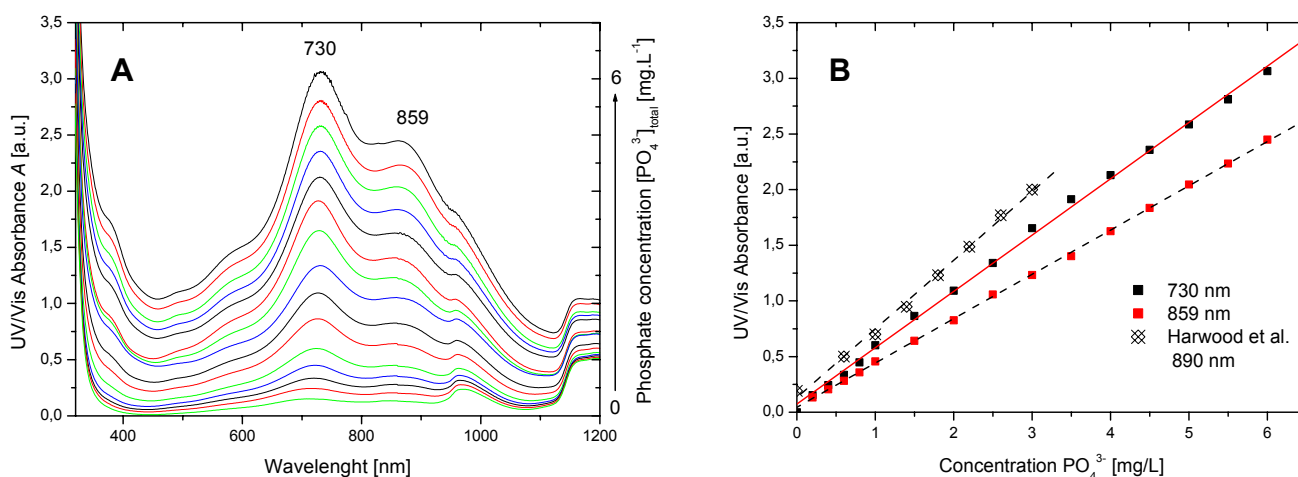


Figure 6.8: Sensitive detection of phosphates by the molybdate blue method (A) at high concentrations ($6\text{ mg}\cdot\text{L}^{-1}$) in water at 20°C and calibration curves at 730 and 859 nm (B).

Thus linear correlations of the Beer Lambert law obtained at 730 nm and 859 nm yield:

$$A_{730\text{ nm}} = 0.07349 + 0.50595 \cdot [\text{PO}_4^{3-}]_{\text{total}} \quad (6.74a)$$

$$A_{859\text{ nm}} = 0.04401 + 0.39818 \cdot [\text{PO}_4^{3-}]_{\text{total}} \quad (6.74b)$$

$$[PO_4^{3-}]_{total}^{avg} = (A_{730nm} + A_{859nm} - 0.1175)/0.90413 \quad (6.74c)$$

The total phosphate concentration is then averaged on both values obtained at the two wavelengths above mentioned. Combined with pH measurement of the supernatant, and in applying Eqs. 6.51-6.56, the exact concentration of all ion species, free or complexed ones, are successfully determined, thus allowing the evaluation of the ionic activity coefficients at a given ionic strength and temperature, and finally the calculation of the solubility constants K_{s1-6} with high precision and reliability on the whole pH range.

6.4. Solubility isotherms and pH dependence of dissolution profiles

6.4.1. Solubility isotherms

The dissolution behaviour in dependence of pigment composition and environmental conditions such as pH, and also the different relative mechanisms of dissolution-precipitation have been investigated on a wide range of zinc phosphate based pigments, listed in Table 6.5. While pure α - and β -ZPT are used as model pigments, highly modified pigments synthesized by polymer controlled mineralization, namely NaZP and NaZPOH, contain various contaminations, e.g. sodium ions and hydroxyl groups, and are thus expected to exhibit a lower solubility in basic pH range.

Table 6.5: Summary of investigated pigment formulations based mainly on inorganic zinc phosphate hydrates

Product label	Extended formulation name	Main components	Measured additives concentration [wt%]
α -ZPT	acid α - $Zn_3(PO_4)_2 \cdot 4 H_2O$	α -ZPT	none
β -ZPT	acid β - $Zn_3(PO_4)_2 \cdot 4 H_2O$	β -ZPT	none
NaZP	basic $NaZnPO_4 \cdot 1H_2O$	NaZP	11.5 wt% Na ^a
Na ₂ ZPOH	basic $Na_2Zn(PO_4)(OH) \cdot 2 H_2O$	NaZPOH	17.8 wt% Na, 6.5 wt% OH ^a
ZP-1	organic-inorganic modified basic zinc phosphate tetrahydrate	ZPT	0.2 wt% sodium zinc chromates ^a 0.5 wt% organic phosphates ^b
ZP-2	zinc calcium strontium phosphate silicate hydrate	ZPT	40.0 wt% CaO, SiO ₂ , SrO ^a 0.1 wt% organic phosphates ^b
ZP-3	mixed zinc phosphate tetrahydrate-dihydrate	ZPT	42 wt% ZPD ^{c,d}

- (a) detected by atomic absorption spectroscopy (AAS).
 (b) detected by solid state NMR.
 (c) detected by X-ray diffraction (XRD).
 (d) ZPD: zinc phosphate dihydrate.

Moreover, industrial pigments present as mixtures of zinc phosphates with known organic-inorganic active inhibitors of corrosion are used for comparison, and for this precise reason may display very different solubility products in regard to hopeite polymorphs, especially at pH 4 (acidic conditions) and above pH 10 (alkaline conditions).

6.4.1.1. pH fluctuations

The achievement of saturation conditions in response to a pH pulse of the above summarized pigments and in extension of Kalendova's studies of neutralizing effects of zinc containing anticorrosive pigments [174] the effective dissolution is easily monitored by measuring pH changes after 30 days in the pigment suspension, as shown in Fig. 6.10. While a marked departure from linearity indicates strong pigment dissolution, a stabilization of the final pH in the range 7-9 suggests a buffering of the released phosphate anions. Thus already in acidic conditions, α - and β -ZPT display complete solubilization behaviour, which tends to disappear as pH increases to neutrality. At pH 9.2 both hopeite polymorphs dissolve equally. Since basic zinc phosphates, such as NaZP and Na₂ZPOH do not exhibit any pH fluctuation to an initial pH value of 8, either dissolution does not take place or dissolution is accompanied by a strong buffering effect with probable formation of neutral sodium phosphate complexes in solution. All pigments (Fig. 6.10 A,B) display the highest departure from linearity at pH 9.5, indicating a nearly complete pigment dissolution and a strong release of phosphate ions. In addition, the linear dissolution of ZP-1 probe to a pH stimulation may be attributed first to the specific presence of chromates in the pigment formulation, as first suggested by Szaklarska-Smialowsha [175] and more recently by Sinko [176], and secondly to common ion effect. In fact Sinko measured linear pH dependence of solubility for various metal chromates and concluded that the intercept of the curve $pH_{final} = f(pH_{impulse})$, in similarity to the curve $\text{Log } C_{\text{saturation final}} = -k \cdot pH + C$ depends on the metal counterion chemical identity (Ba²⁺, Ca²⁺, Sr²⁺, Zn²⁺). In this line, it is also expected from the different curves shapes given in Fig. 6.10 B that the slope of this function $pH_{final} = f(pH_{impulse})$ does not uniquely depend on the employed buffer chemistry to regulate the pH pulse (H₃PO₄, HNO₃, H₂SO₄) but is also strongly affected by the anion chemical identity (e.g. chromates [177], phosphates [178], molybdates [179-181], silicates [182], hydroxides [183], etc.), since the measured slopes in the range 4 < pH < 8 vary very much from those obtained for chromate based pigments.

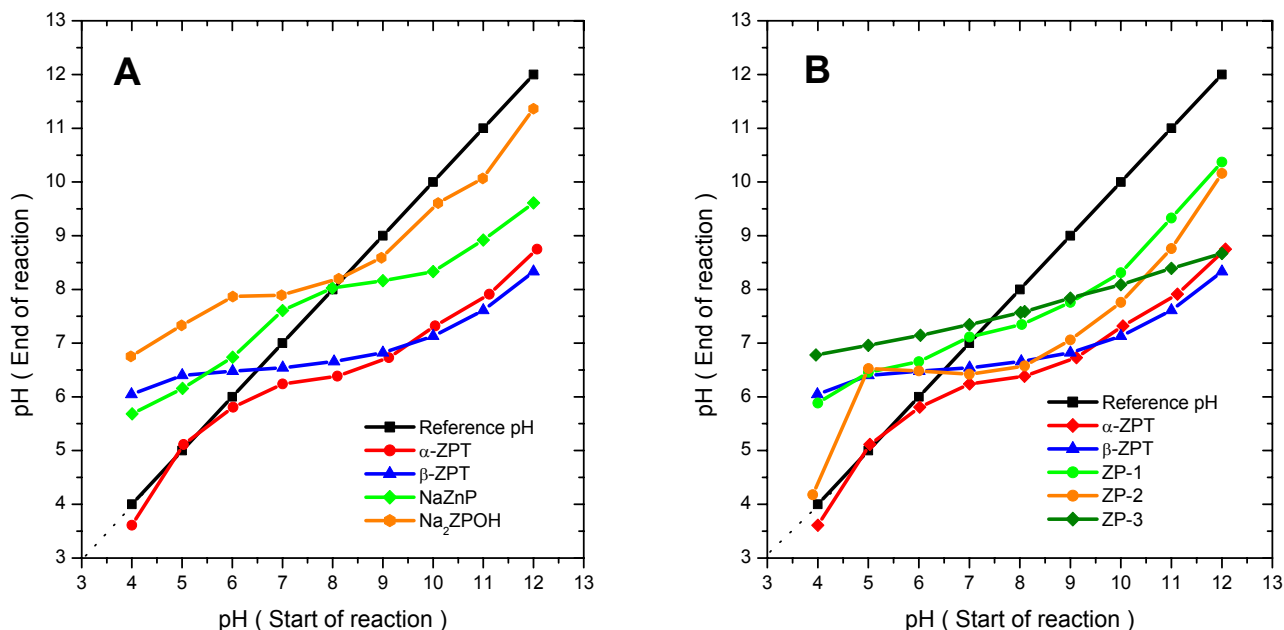
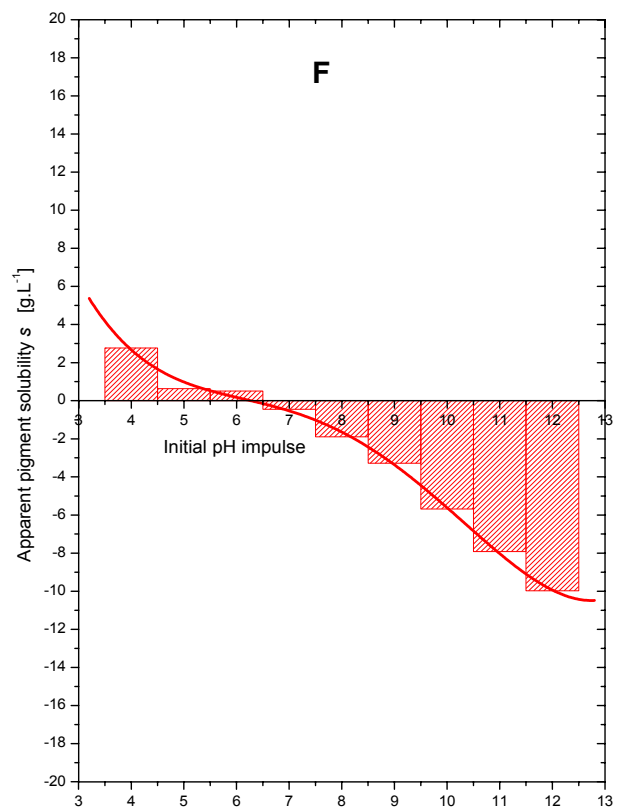
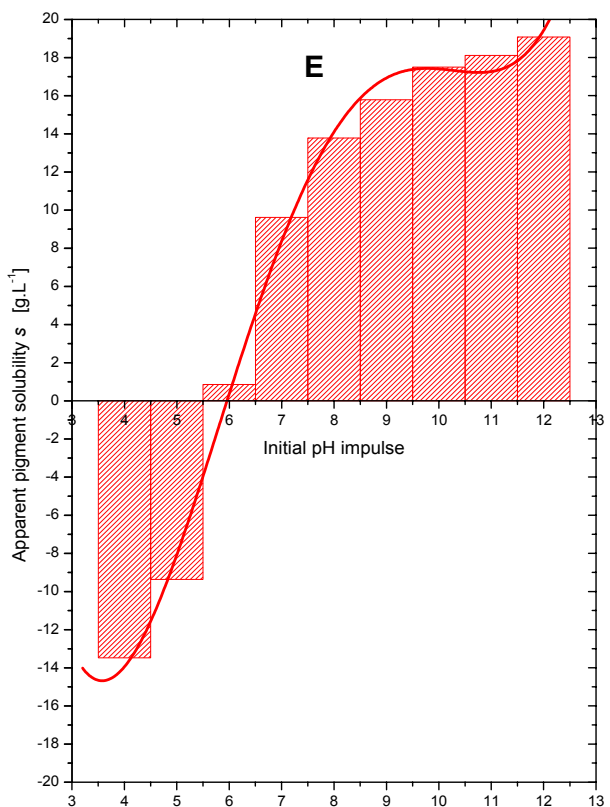
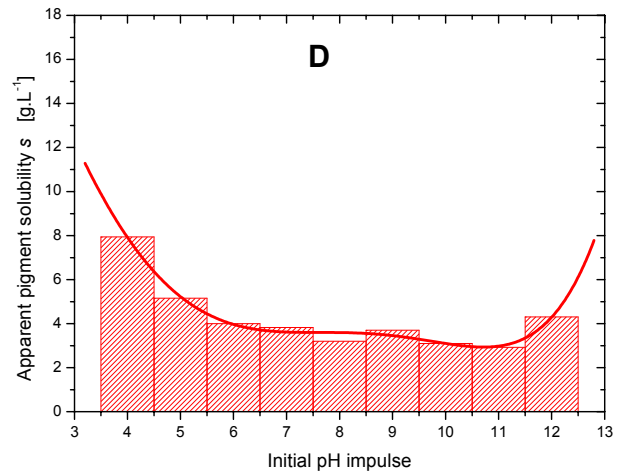
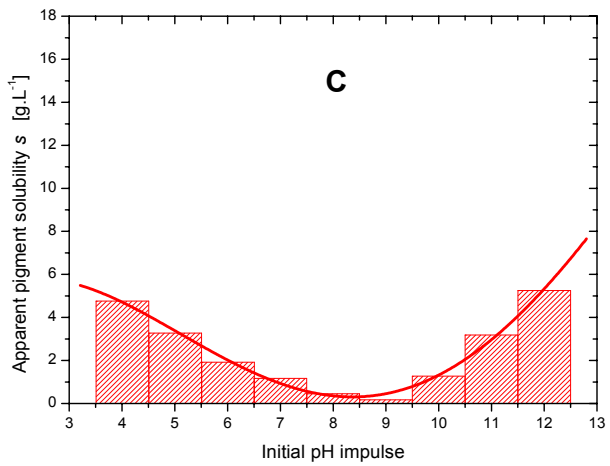
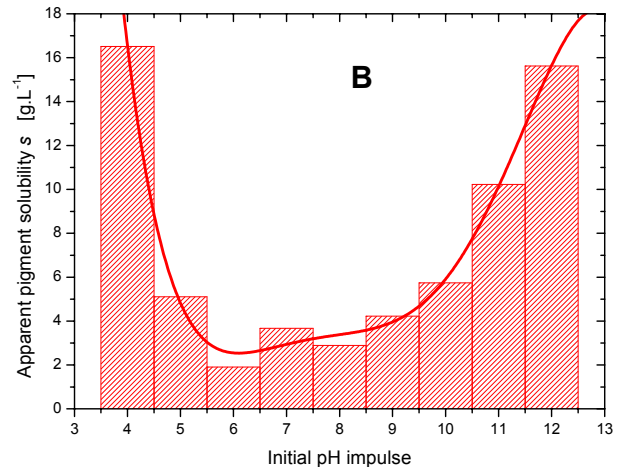
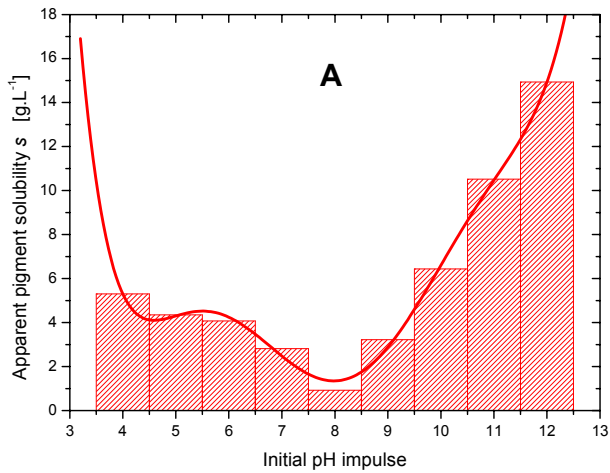


Figure 6.10: Monitoring of the pH reached in after 30 days in the pigment suspension in response to a pH impulse for (A) pure ZPT and modified ZPT by polymer controlled mineralization and (B) industrial ZP pigments in comparison with α - and β -hopeite. While a marked departure from linearity indicates strong pigment dissolution, a stabilization of the final pH in the range 7-9 suggests a buffering of the released phosphate anions.

6.4.1.2. Gravimetric monitoring of ZP dissolution

Furthermore, Figure 6.11 offers a comparison of the apparent solubility isotherms at 25°C in dependence of the suspension pH and pigment composition for a 37.5 g.L⁻¹ suspension as obtained gravimetrically. Firstly, the maximum solubility is achieved on both extrema of the pH range. None of the pigments are resistant to chemical aggression at pH 4 and pH 12. However on the whole tested pH range, they exhibit low dissolution, i.e. solubility within the accepted limits of the classification as sparingly soluble salts (10⁻⁵-10⁻² mol.L⁻¹ or 10 mg.L⁻¹- 10 g.L⁻¹). Moreover these obtained solubility values are consistent with known solubilities of metal phosphates [184], such as apatitic derivatives [185], in these conditions of very low ionic strength ($I \approx 10^{-3}$ mol.L⁻¹) [186] and temperature (25 °C); the ionic strength being controlled only by the amount of NaOH or HNO₃ strictly sufficient to impose a pH pulse. However, the inappropriate detection limits of this method do not allow the accurate observation of solubility below 400 mg.L⁻¹, which is the estimated boundary value of solubility expected for nearly insoluble zinc phosphate hydrates around pH 7. Model samples display a characteristic pH dependence of the solubility in “W-shape”, indicating a dissolution process governed essentially by the acidity constants K_{a_i} (i.e. β_i) of phosphoric acid (buffering effect). A clear influence of polymorphism of zinc phosphate tetrahydrate is shown in Fig. 6.11 A and Fig. 6.11 B. It appears that while α -ZPT has a three

times lower solubility on pH 4 than β -ZPT (16.4 g.L^{-1}) at around 5.4 g.L^{-1} , and both are equally soluble in highly alkaline media with solubilities up to 16 g.L^{-1} .



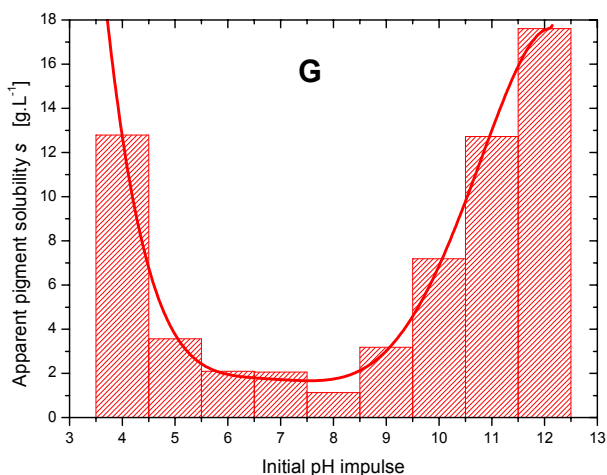


Figure 6.11: Apparent solubility isotherms at 25°C in dependence of the suspension pH ($I = 10^{-3} \text{ mol.L}^{-1}$) and pigment composition for a 37.5 g.L⁻¹ suspension of: (A) pure α -ZPT, (B) pure β -ZPT, (C) pure NaZP, (D) pure Na₂ZPOH, (E) ZP-1, (F) ZP-2, (G) ZP-3. Regarding industrial E, F, G samples, the negative apparent solubility measured by mass changes after 30 days equilibration, corresponds most probably to the dissolution-precipitation process of metal hydroxyphosphate hydrates of higher molecular weight than the original formulation.

Therefore it is thought that the published value of Bittner [184] of 15.8 g.L⁻¹ at pH 4 for a pure zinc phosphate hydrate, similar to the above mentioned result (Fig. 6.11 B and G) in nearly identical experimental conditions may be attributed directly to the pigment composition tested: either this sample was a mixture of α - and β -ZPT or a mixture of zinc phosphate tetrahydrate and dihydrate. Moreover, while α -ZPT displays two solubility minima at pH 4.5 and 8, β -ZPT displays the same minima with a pH shift of at least one pH unit at pH 6 and pH 9. Since this effect may be correlated with the pK_{ai} of ionic phosphate species released from the dissolving pigment surface, this may also and most probably depend on the surface crystal stability that is governed by the bulk hydrogen bond pattern (crystallographically-controlled etching-dissolution mechanism), as proved in Chapter 4. Besides, Chapter 2 and 3 inform on the relative structural stability of hopeite polymorphs, pointing out that since β -ZPT has only a two-dimensional hydrogen bonding pattern, ensuring mechanical and thermal stability preferentially along a -axis and c -axis, while α -ZPT has a three-dimensional hydrogen bonding pattern, the β -form of hopeite may be more sensitive to a chemical attack along b -axis and therefore dissolves easier, i.e. at higher acidic pH. Such a variation in the structural stability and its consequence on chemical etching were also reported in Chapters 3 and 4 for zinc phosphate of corresponding hydration state, i.e. tetrahydrate, dihydrate and anhydrate. Particularly, the ZP-3 (Fig. 6.11 G) sample shows an increased solubility (12.8 g.L⁻¹) at pH 4, compared to α -ZPT (Fig. 6.11A). By means of XRD, it was shown that ZP-3 represents a mixture of α -ZPT and α -ZPD in the ratio 58/42 wt%. Fig. 6.11 G also suggests that the hydration state of zinc phosphate pigments does not have a major influence on the apparent solubility in alkaline medium, since even higher solubilities are reported for ZP-3 in comparison to α -ZPT at pH above 9. Besides, impurities such as sodium ions and hydroxyl groups, incorporated in the zinc phosphate structure by polymer controlled mineralization seem to play a very important and positive role regarding the achieved solubility in conditions of very low ionic strength. On one hand, Figure 6.11 C and Fig. 6.11 D indicate that NaZP and Na₂ZPOH possess four times lower solubility than α - and β -ZPT at pH above 9. NaZP exhibits even the lowest pigment solubility at pH 9 with less than 170 mg.L⁻¹, of

all compared formulations and a single solubility minimum, probably in reason of the formation sodium monohydrogen phosphate complexes in solution, combined with the precipitation of zinc hydroxide, whose solubility minimum is around pH 9.5-10. This suggests the overall capability of the polymer controlled mineralization process to efficiently modify the zinc phosphate crystal structure in order to tune the pigment solubility, especially in basic conditions. Notably, Sinko [187] concluded that increasing the basicity of pigments to pH = 8-9 in select cases could help to improve significantly the corrosion inhibitive efficiency, by reducing conveniently the solubility and solubility rate of core component phases of multi-component anticorrosion pigments. Albeit the incorporation of easily soluble species in acidic conditions may in consequence increase the solubility of such modified pigments, astonishingly, no inauspicious effect has to be reported around pH 4. Unfortunately such a favourable control of the pigment solubility vanishes if NaZP and Na₂ZPOH are exposed to drastic conditions of solubilisation (high ionic strength 0.1-1 mol.L⁻¹ at critical pH [188]) as reported later in Fig. 6.13. Regarding industrial E, F, G samples, the negative solubility measured by mass changes after 30 days equilibration, corresponds most probably to the dissolution-precipitation process of metal hydroxyphosphate hydrates, of higher molecular weight than the original formulation. Therefore the definition of an *apparent solubility* is proposed in this context. Similarly Montle [189] introduced the concept of *specific relative solubility* in following the effect of the pH on solubility of organic modified zinc phosphate pigment using standard procedures (e.g. ASTM D 2448-73), however due to his apparent inability to justify the difference between found solubilities of zinc and phosphate ions on one side and of total soluble matter on the other side. This may be either due to the presence of ion-pair complexes in the supernatant or to the fact that the tests were not conducted after thermodynamic equilibrium may be achieved. The negative apparent solubility of ZP-1 below pH 6 may be explained by the chemical nature of the inorganic additives present in the formulation, as follows. As a unique feature of the chromate (CrO₄²⁻) and dichromate (Cr₂O₇²⁻) anticorrosion mechanism, i.e. strong oxidant in acidic medium, it appears that CrO₄²⁻ inhibits effectively the Fe, Al, Cu and Zn corrosion in acidic and reductive conditions by combinatorial formations of nearly insoluble mixed oxides based on Cr₂O₃ [190], and Fe₃Cr(OH)₁₂ [191] or Zn₃Cr(OH)₁₂ [192] by decomposition of HCrO₄⁻ (redox process in acidic and near neutral conditions). On the opposite, in alkaline medium, chromates are significantly weaker oxidant than below pH 6, albeit it is claimed to be efficient for steel corrosion protection up to pH 11 [193]. Hence they might promote rapidly high pigment dissolution as low as pH 7 and up to 18 g.L⁻¹ at pH 11 as shown in Fig. 6.11 E. In comparison to ZP-1, ZP-2 sample displays a symmetrical pH dependence of the solubility centered in pH 6, with negative apparent solubility reaching - 8 g.L⁻¹ at pH 11. This expected effect should be interpreted in terms of strong pigment dissolution followed by formation and subsequent precipitation of hydroxyapatite (Ca₅(PO₄)₃(OH)) [194] and parascholzite derivatives (CaZn₂(PO₄)₂· 2H₂O) [195], since both components, first are known to be more stable than

hopeite polymorphs [196] and secondly exhibit extremely low solubility with solubility minima at pH 8.5 [197] and 7.5 [198-200], respectively.

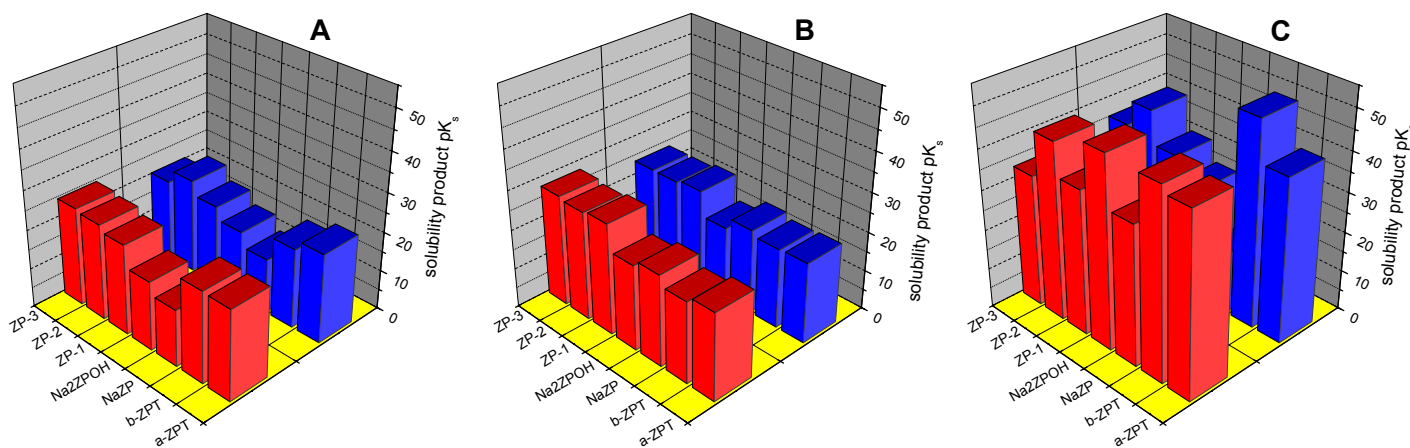


Figure 6.12: Comparison of solubility product $pK_{s,1,4}$ obtained at 25 °C and pH 4 (ionic strength $I \approx 0.1 \text{ mol.L}^{-1}$) by pH pulse (blue) and leaching (red) approaches using (A) gravimetry, (B) conductometry, (C) complexometric supernatant analysis and applying the best fitting model : hopeite model to α -ZPT, β -ZPT, ZP-3; and composition dependent model to: NaZP, Na₂ZPOH, ZP-1, and ZP-2.

6.4.1.3. Comparative techniques for monitoring ZP dissolution

Recent technique developments in the evaluation of pigment anticorrosion efficiency have shown that the obtaining of reliable and accurate solubility values and solubility constants could only succeed if the way to obtain them was strictly taken into consideration [198], as well illustrated in Fig. 6.12. In fact, Figure 6.12 compares the solubility product $pK_{s,1,4}$ obtained at 25°C and pH 4 by pH impulse and Leaching approaches using the three analytical methods described in § 6.3.1, i.e. gravimetry, conductometry, and complexometric supernatant analysis and applying the best fitting model : hopeite model to α -ZPT, β -ZPT, ZP-3; and composition dependent model to: NaZP, Na₂ZPOH, ZP-1, and ZP-2. In this line, the kind of acid used for a selected approach seems to be important: H₃PO₄ (leaching method) or HNO₃ (pH impulse method), since notable variations of pK_s are achieved between α - and β -ZPT with the supernatant analysis method. This emerging difficulty is disastrously exhibited in the case of basic zinc phosphates (e.g. Na₂ZPOH), for which the $pK_{s,4}$ fluctuates between 17 (gravimetry) and 47 (supernatant analysis). This clear effect was also duly mentioned by Bittner [184] in applying sulphuric acid for both leaching test and pH impulse method. Nevertheless huge discrepancies in the solubilities and solubility products of zinc phosphate pigments in dependence of the slurry pH reported by Bittner cannot only be attributed to the pigment chemistry but also to the way tests are conducted, since most probably the ionic strength,

another parameter of utmost importance was not taken into account. This may well explain the incredible fluctuations of solubility in the ZP-1 sample (17 g.L^{-1} at pH 4 and $6 \cdot 10^{-3} \text{ g.L}^{-1}$ at pH 7). In this context an increasing precision regarding the analytical method employed may be achieved. Furthermore, all these method do not deliver the same information about pH dependence of solubility. While gravimetric and conductometric methods give average and apparent solubility products, complexometric supernatant analysis emphasizes the different competing precipitation mechanisms through the formation of various soluble zinc hydrogen phosphate complexes.

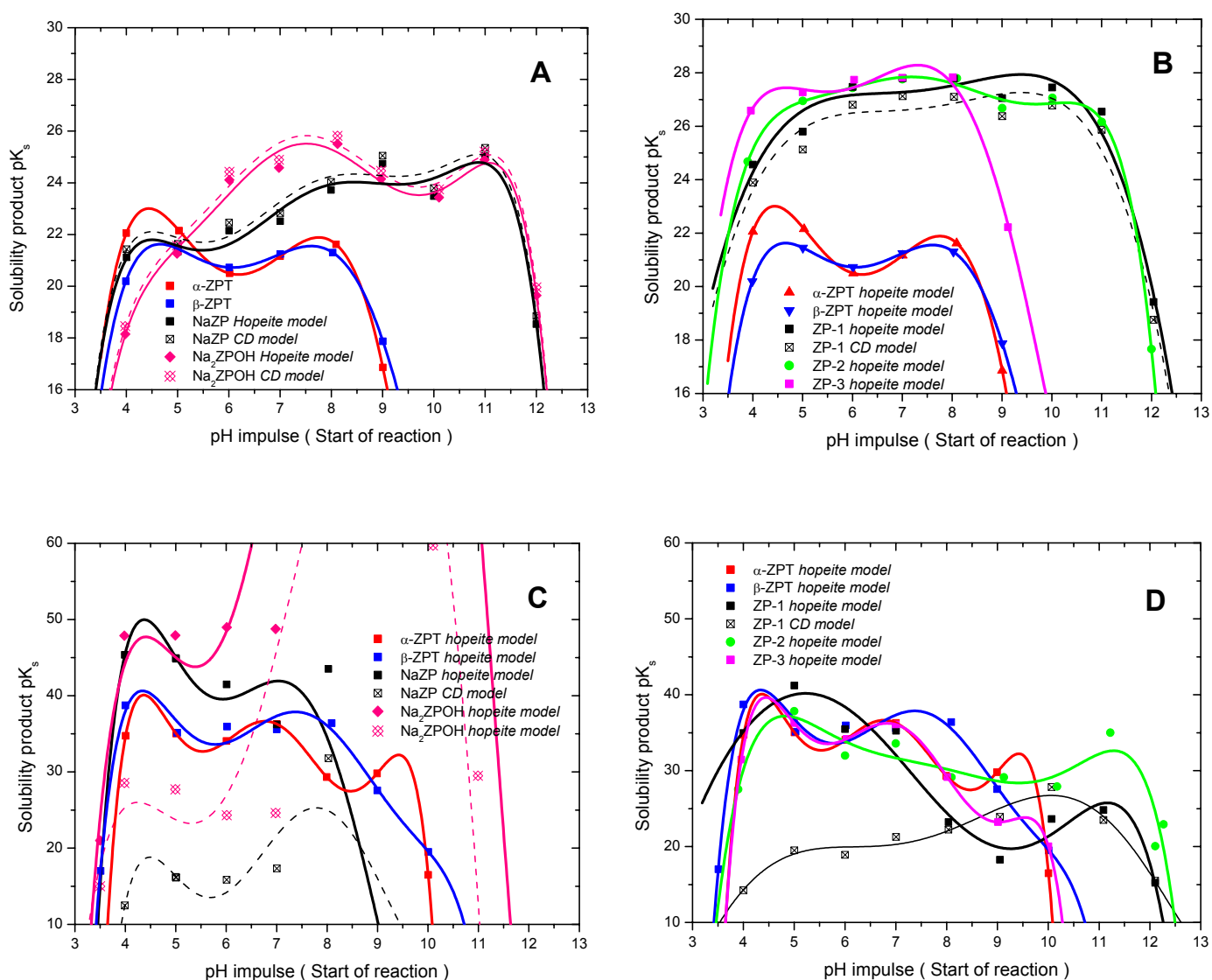


Figure 6.13: Comparison of solubility product $pK_{s,4}$ (solubility isotherms at 25°C) in dependence of the imposed pH, obtained by pH impulse approach using, (A,B) conductometry, (C,D) complexometric supernatant analysis and applying the "best fitting" dissolution model (hopeite model or/and composition dependent model) to zinc phosphate hydrate based pigments synthesized by polymer controlled mineralization (A,C) and industrial pigments (B,D)

6.4.1.4. Hopeite model and composition dependent dissolution model

Figure 6.13 displays a comparison of solubility product $pK_{s1,4}$ (solubility isotherms at 25°C) in dependence of the imposed pH, obtained by pH pulse approach for different analytical methods, conductometry (Fig. 6.13 A,B) and complexometric supernatant analysis (Fig. 6. 13 C,D) and applying the “best fitting” dissolution model (hopeite model or/and composition dependent model) to zinc phosphate hydrate based pigments either synthesized by polymer controlled mineralization (Fig. 6.13 A,C) or produced on large scale (Fig. 6.13 B,D). While employing the hopeite dissolution model the pK_{s1} -pH curves generated by conductometry have clearly the same shape and minima at the same pH as obtained gravimetrically (Fig. 6. 11 A,B) for α -ZPT and β -ZPT, noticeable differences between α -ZPT and β -ZPT are detected by precise analysis of the supernatant composition (Fig. 6.13 C), with a marked solubility maximum (local minimum of pK_{s1}) at 8.5 for α -ZPT and a not so well defined solubility maximum around pH 9.5 for β -ZPT. These observations can be interpreted in terms of formation of zinc monohydrogen phosphate aqua-complexes, adsorbed on the dissolving crystal surface, that subsequently form precipitating zinc hydroxide clusters, especially well illustrated in the case of α -ZPT with the until now not detected presence of a third solubility minimum at pH 9.5. Regarding β -ZPT, the wider pH range of dissolution, extended to basic pH values may originate from the increased surface stability controlled by its specific two dimensional hydrogen bonding pattern reported earlier, rendering the formation of surfacial zinc hydroxide species harder. Simply by conductometry in conditions of high ionic strength, i.e. being regulated between 0.1 and 1 mol.L⁻¹ depending of the targeted pH, it is also possible to visualize a general solubility decrease achieved by high ionic strength (common salt effect). The invoked effect of ionic strength is interesting, since this represents most of the conditions encountered in standard corrosion cases, either for acidic rains or in marine environment. Besides, at pH 4 (Fig. 6.13 C) the calculated pK_{s1} value of α -ZPT by supernatant analyses reaches 35.4, which is confirming the average value of 35.2 obtained by Nriagu [49] in similar conditions. Usually the presence of impurities is adventitious and undesirable but sometimes may be intentionally used as additives or even major components in order to change the dissolution conditions such as the rate of dissolution [201] or the phase stability to pH or temperature changes. Applying this last mentioned analytical technique, one can observe precisely the wished effect of impurities incorporation in the pigment formulation, with a controlled diminishing of the pK_s values of four orders of magnitude for basic zinc phosphate (Fig. 6. 13 A) and six orders of magnitude for commercial products (ZP-1 and ZP-2) to approximatively 27 (Fig. 6.13 B), in comparison to ZPT polymorphs. Unfortunately it is not possible to apply a composition dependent model for an accurate evaluation of the solubility product of ZP-2, since its formulation is extremely complex and may involve more than one

competing dissolution-precipitation mechanism (e.g. pK_i , $l = 4-6$) in addition to zinc phosphate hydrate dissolution and various intermediary products such as pure or mixed calcium phosphate phases [201-202] and particularly metastable brushite ($\text{CaHPO}_4 \cdot 2\text{H}_2\text{O}$, DCPD), octacalcium phosphate ($\text{Ca}_8\text{H}_2(\text{PO}_4)_6 \cdot 5\text{H}_2\text{O}$, OCP), whitelockite (beta tricalcium phosphate, $\beta\text{-Ca}_3(\text{PO}_4)_2$, TCP) and hydroxyapatite ($\text{Ca}_5(\text{PO}_4)_3(\text{OH})$, HAP). Precisely for that purpose, an intensive investigation of the dissolution products by means of XRD, ESCA (direct identification of precipitated phase from saturated solution) and FT-Raman or Solid State MAS-NMR (monitoring of the local fluctuations of the coordination sphere of phosphate groups) may be required. Therefore treatment of the solubility data using a composition dependent model is not considered. Nevertheless, the corrections brought by a composition dependent dissolution model in the case of the monitoring of a solubility isotherm by conductometry are restricted ($\Delta pK_s \approx 0.25$ units), since an average solubility is measured. But this gets its full meaning using a complete chemical analysis of the supernatant. Even huge variations of pK_s are achieved for basic zinc phosphate, if one takes the sodium contaminations into consideration, as shown in Fig 6.14 and Fig. 6.13 C. In these plots, using the hopeite model one estimates the pK_{s4} of NaZP and Na_2ZPOH to be 5 ($pK_{s4} \approx 41$) and 40 times ($pK_{s4} \approx 81$) higher than $\alpha\text{-ZPT}$ or $\beta\text{-ZPT}$ ($pK_{s1} \approx 36$) at 25°C and pH 7, respectively.

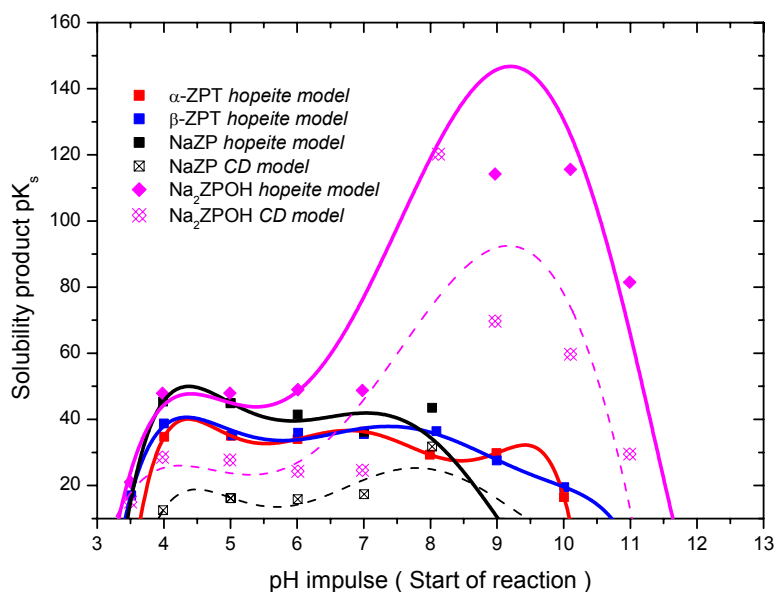


Figure 6.14: Comparison between the solubility product $pK_{s1,4}$ (solubility isotherms at 25°C) of hopeite polymorphs and pigments obtained by polymer controlled mineralization, in dependence of the imposed pH obtained by pH impulse approach using the best fitting dissolution model (hopeite model or/and composition dependent model). The selective incorporation of sodium ions in the zinc phosphate hydrate crystal structure improves the resistance to dissolution in alkaline medium at ambient temperature of Na_2ZPOH while on the contrary drastically lowering it for the NaZP sample

This means that NaZP and Na_2ZPOH should be by far more insoluble than pure hopeite polymorphs. However, using the composition dependent dissolution model, the opposite effect is observed with a pK_{s4} of only 21 for NaZP and still 42 for Na_2ZPOH . These results justify on one hand the development of solubility models, adapted to the pigment chemistry and formulation, and on the other hand confirm the results obtained for these pigments in humidity chamber and

salt spray test [204], where the incorporation of sodium in Na_2ZPOH induces extremely high solubility, while the intercalation of polymeric material (Na_2ZPOH) and the addition of hydroxyl groups decrease drastically the solubility of those compounds in alkaline medium. Similar beneficial effects on the solubilisation process are observed for commercial pigments, either by conductometry (Fig. 6. 13 B) or by supernatant analysis (Fig. 6.13 D). These two methods deliver different information. In fact, ZP-1 and ZP-2 exhibit pKs_{1-4} seven orders of magnitude higher than the model compounds, albeit the conductometric technique tends to over-evaluate the solubility products. The conductometric method (Fig. 6. 13 B) might point out that the effects of mixed additives on solubility is just to decrease it, as suggested by Bittner [184], while the supernatant analysis method might also well point out that the solubility stays constant (i.e. $\text{pKs}_{1-4} \approx 33$, Fig. 6. 13 D) on a broader pH range, i.e 4-12 instead of 4-9 or 4-10, as stated by Leidheiser [190].

6.4.2. Synergy of competing dissolution-precipitation mechanisms

While Figures 6.11 to 6.13 compare accurately for each compound listed in Table 6.5 the solubility product pKs_1 or pKs_4 of the main dissolution reaction, and its dependence on the pH and ionic strength, do not deliver adequate information about the various concurring dissolution route in dependence of the solution pH. Therefore, Figure 6.15 proposes a comparison of the pH dependence of the three possible dissolution routes for model compounds and products obtained by polymer controlled mineralization. As one can observe in Figures 6.15 A and B for the zinc phosphate tetrahydrate polymorphs, the thermodynamically favoured dissolution mechanism certainly involves a “free PO_4^{3-} ” pathway, since pKs_1 has the lowest value on all the investigated pH range, but also a monohydrogen phosphate pathway since first the difference between pKs_1 and pKs_3 is not so high (i.e. 38 and 41 at pH 4) and secondly appreciably lower than pKs_2 (i.e. 38 versus 56.1 at pH 4). In addition, the calculated value of pKs_2 of 56.1 at pH 4 for α -ZPT is acceptably concordant with a value of 52.2 reported by Nriagu [49] in similar conditions, because the study of Nriagu completely neglects the dissolution of α -ZPT by a monohydrogen phosphate pathway (pKs_3). This is consistent with the relative phosphate ions distribution in the tested pH range, and completely justifies the fact that the form of the solubility isotherms for example for α - β -ZPT was previously attributed to the buffer effect of phosphate system as it is described by Butler [204], since the various possible dissolution mechanisms are compared. One can also describe the dissolution route (1) and (2) (i.e. pKs_1 and pKs_2) as synergetic since the evaluated corresponding constants values are very similar. Identical conclusions are settled for NaZP in Fig. 6.15 C. However independent of the considered or most probable dissolution mechanism, NaZP stays more soluble than ZPT samples, with pKs_{4-6} at least 15 order of magnitude lower than the corresponding pKs_{1-3} , except at pH 8, where values

are very close. More balanced results are obtained for Na_2ZPOH at basic pH, as shown in Fig. 6.15 D. In opposition to NaZP at pH 8, a dissolution pathway involving dihydrogen phosphate may be favoured due to the higher value of pKs_6 compared to pKs_5 .

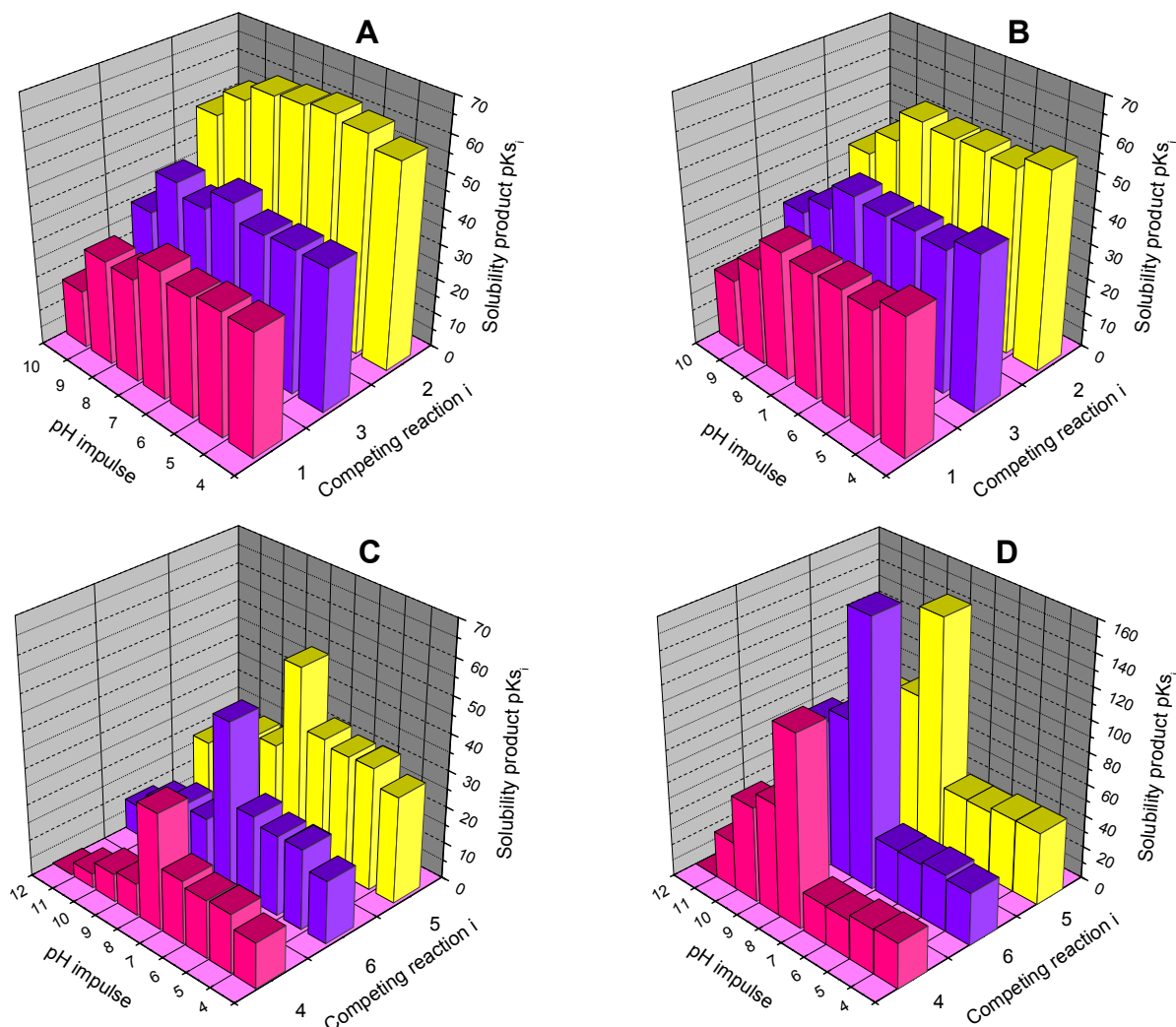


Figure 6.15: Comparison of the solubility products pKs_i of competing dissolution-precipitation at 25°C generated from pH impulse methodology for (A) $\alpha\text{-ZPT}$, (B) $\beta\text{-ZPT}$, (C) NaZPO_4 and (D) Na_2ZPOH and in applying the most consistent dissolution model: (A,B) Hopeite model, (C,D) Composition dependent model.

In the case, the preponderance of this dissolution route on the others, especially at a pH value, where the dihydrogen phosphate species is not present in majority, finds its justification by the fact that dissolution takes place at a given pH (e.g. acidic conditions), liberating phosphate ions in solution, that by a buffer effect shift the solution pH to higher values (neutral to basic pH), corresponding either to a solubility minimum or maximum. Therefore Jenkins [206] introduced for convenience the concept of *critical* pH, the pH value or less strictly the pH shift that distinguishes between dissolution and formation of zinc phosphates (mineralization) for the description of the demineralization of plaque enamel apatite. This concept is quite useful for a precise description of the dissolution mechanisms of NaZP and Na_2ZPOH .

6.4.3. Metamorphism of basic zinc phosphates: $\text{NaZnPO}_4 \cdot \text{H}_2\text{O}$, $\text{Na}_2\text{Zn}(\text{PO}_4)(\text{OH}) \cdot 2\text{H}_2\text{O}$

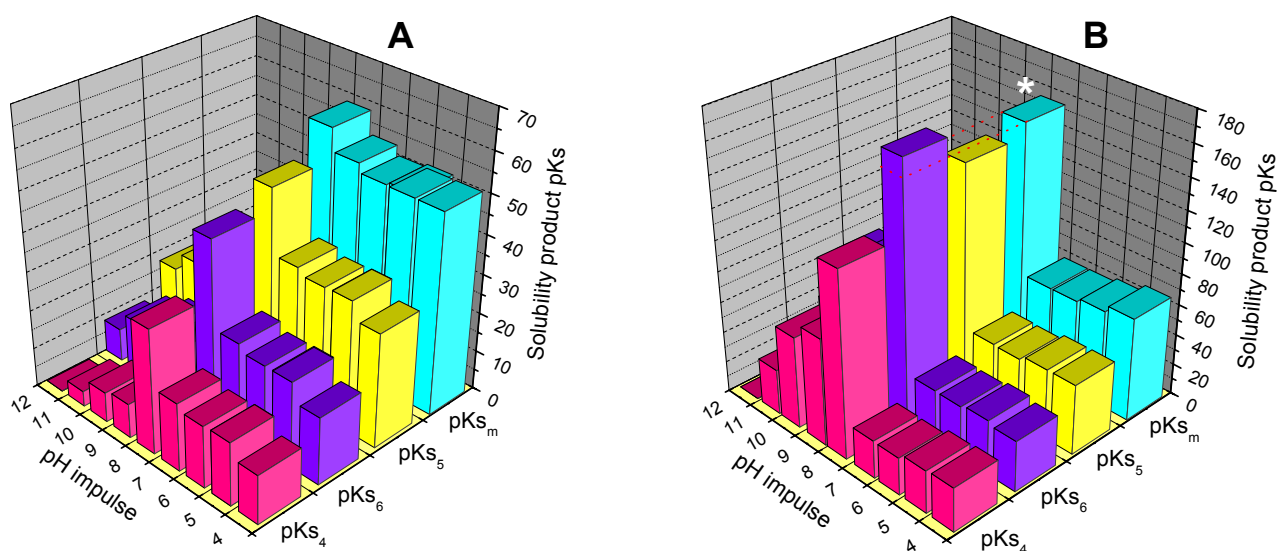


Figure 6.16: Comparison of the solubility products of competing dissolution reactions pKs_{1-3} , and metamorphism, pKs_m , at 25°C generated from pH pulse methodology ($I \approx 0.1-1 \text{ mol.L}^{-1}$) for (A) NaZPO_4 and (B) Na_2ZPOH and in applying the most consistent dissolution model: composition dependent model (pKs_{1-3}) and metamorphism (pKs_m). In the pH stability domain of β -ZPT, a synergic dissolution via formation of zinc monohydrogen phosphate complexes in solution and precipitation into β -ZPT occur up to pH 9 for NaZPO_4 (A) and pH 7 for Na_2ZPOH (white star, B). The mechanism of metamorphism first generates one free phosphate anion pro molecular entity, PO_4^{3-} available for corrosion inhibition and secondly induces a pH shift by local buffering effect, i.e. acidic dissolution and neutral or basic reprecipitation of hopeite. However above pH 9, both basic zinc phosphate hydrates are progressively but surely dissolving ($pKs < 15$).

Figure 6.16 shows the comparison of the solubility products of competing dissolution reactions pKs_{4-6} , and for the reaction of metamorphism, pKs_m , at 25°C generated from pH pulse methodology for (A) NaZPO_4 and (B) Na_2ZPOH in applying the most consistent dissolution model: composition dependent model (pKs_{1-3}) and metamorphism (pKs_m). In the pH stability domain of β -ZPT, a synergic dissolution via formation of zinc monohydrogen phosphate complexes in solution and precipitation at ambient temperature into β -ZPT occur up to pH 9 for NaZP (Fig. 6.16 A) and as low as pH 7 for Na_2ZPOH (Fig. 6.16 B). The mechanism of metamorphism first generates one free phosphate anion pro molecular entity, PO_4^{3-} available for corrosion inhibition and secondly induces a pH shift by local buffering effect, i.e. acidic dissolution and neutral or basic reprecipitation of hopeite. However above pH 9, both basic zinc phosphate hydrates are progressively but surely dissolving ($pKs < 15$). Furthermore in the restricted case of Na_2ZPOH , at pH 8, a marked change in the mechanism of reprecipitation takes

place. At this precise pH, reprecipitation changes from a metamorphic route (i.e. $pK_{sm} > pK_{4-6}$) to a dihydrogen phosphate route ($pK_{s6} > pK_{sm} > pK_{s5} > pK_{s4}$).

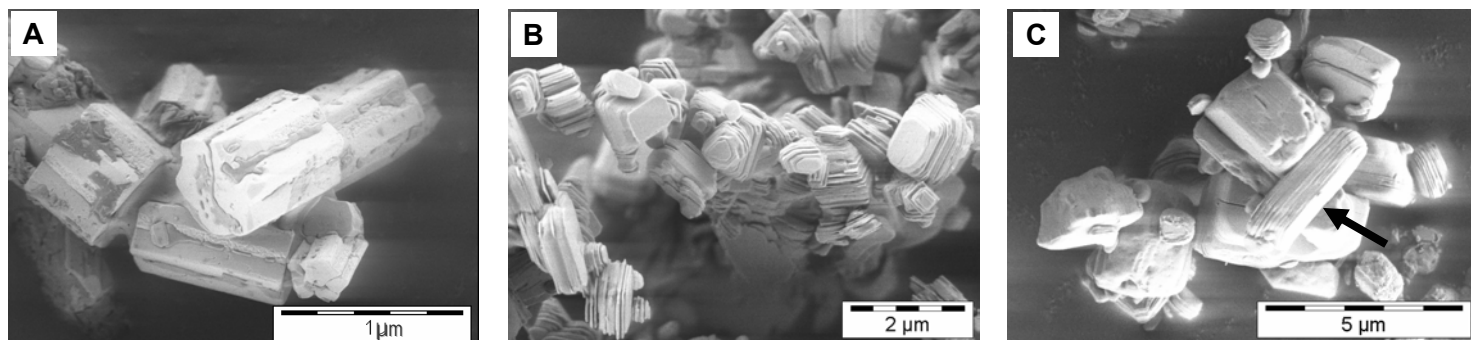


Figure 6.17: Effect of dissolution at pH 5 (ionic strength $I \approx 0.5 \text{ mol.L}^{-1}$) for 30 days at room temperature monitored by SEM for (B) β -ZPT and (C) NaZP. Image (A) shows pristine NaZP crystal with characteristic hexagonal morphology before pH pulse, which dissolves and reprecipitates in a zinc phosphate tetrahydrate (black arrow, (C)), presumably β -ZPT.

This confirms unambiguously the proposed reaction scheme of dissolution-precipitation given in Figure 6.5, and is highly relevant for the basic understanding of mechanisms of anticorrosion and the overall efficiency of zinc phosphate based pigments. Therefore, while α - and β -ZPD dihydrates work in adsorbing water penetrating the basecoat, the efficiency of such chemically modified ZP pigments such as $\text{NaZnPO}_4 \cdot 1\text{H}_2\text{O}$ as corrosion inhibitors certainly stems from this dissolution-precipitation mechanism or metamorphism.

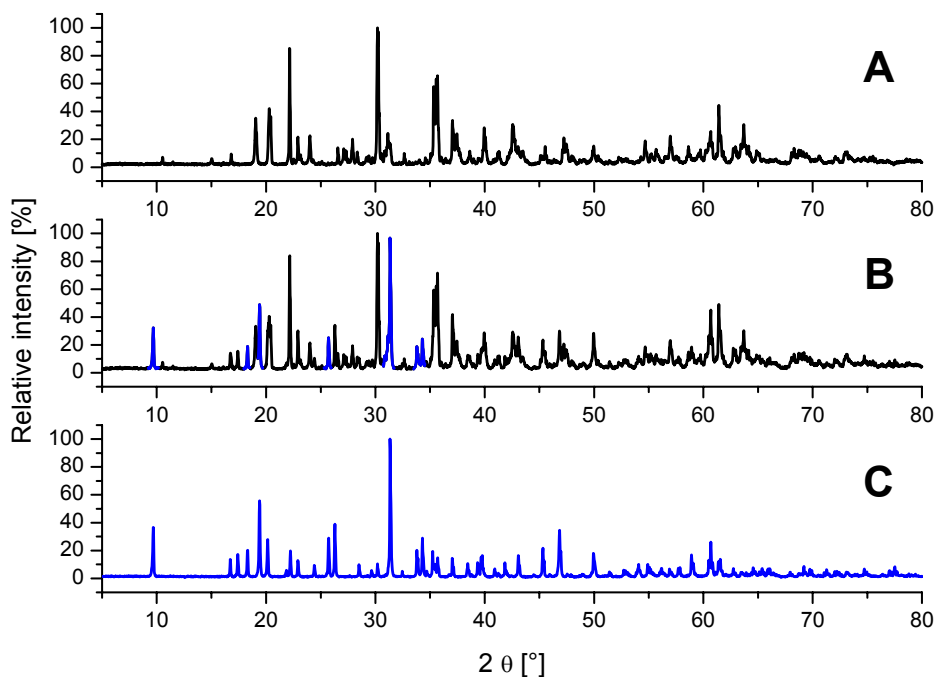


Figure 6.18: Effect of dissolution at pH 5 (ionic strength $I \approx 0.5 \text{ mol.L}^{-1}$) for 30 days at room temperature monitored by XRD. (A) NaZP before dissolution, (B) NaZP after dissolution, (C) β -ZPT before dissolution. The thoroughgoing comparison of powder spectra in the range 10–45° of NaZP before and after exposure to a solution of pH 5 in saturating conditions clearly demonstrates the partial conversion of NaZP in β -ZPT.

After dissolution, NaZP reprecipitates most probably in the β -form of hopeite, since the corrosion is likely to take place in standard conditions, i.e. room temperature. On the contrary, mixed composition of α -ZPT and β -ZPT may be achieved by pH induced dissolution at higher temperature. This can be easily visualized by SEM (Fig. 6. 17). The parallel dissolution of NaZP and unambiguous identification of forming of a β -ZPT crystalline phase succeeds by a precise analysis of the powder spectra of NaZP samples before and after exposure to a pH 5 solution for 30 days in saturation conditions, as shown in Figure 6.18.

Complementarily, Figure 6.19 depicts the further presence of precipitating $\text{ZnHPO}_4 \cdot 1\text{H}_2\text{O}$ ion-pair complex, that is verified by DSC and FT-Raman by identification of disappearing and emerging peaks in Figure 6.19 A and B, respectively.

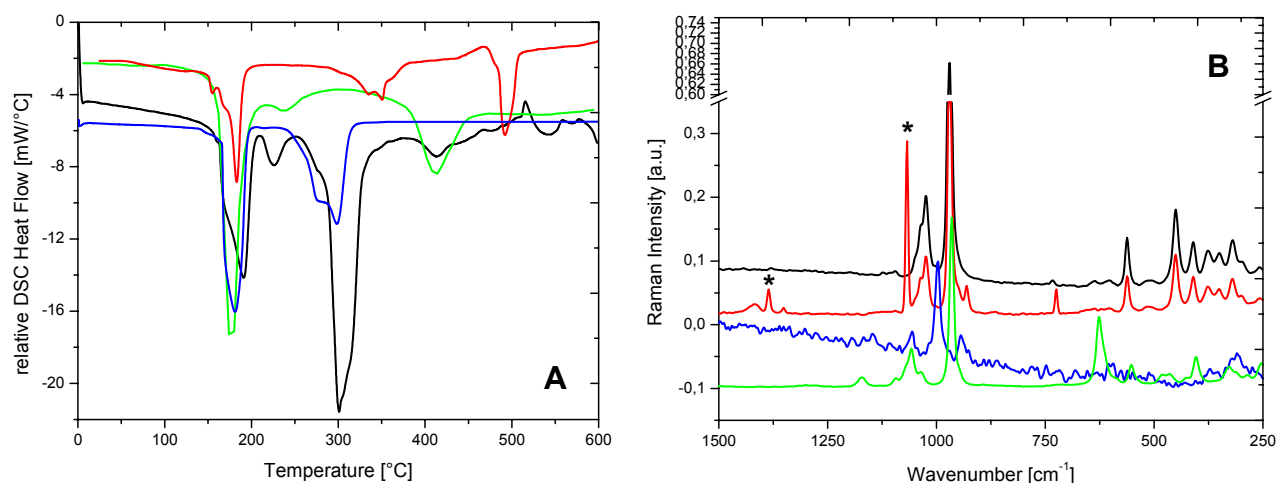


Figure 6.19: Effect of dissolution obtained by pH pulse at pH 5 (ionic strength $I \approx 0.5 \text{ mol.L}^{-1}$) for 30 days at room temperature (condition of saturation) as monitored by (A) DSC (10 K.min^{-1}) and FT-Raman spectroscopy in the phosphates frequency domain (B) for NaZP sample: NaZP before dissolution (red), NaZP after partial dissolution (black), β -ZPT before dissolution (blue), precipitating $\text{ZnHPO}_4 \cdot 1\text{H}_2\text{O}$ ion-pair complex (green) .

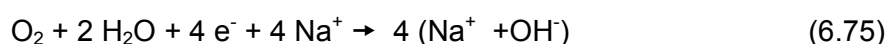
Regarding anticorrosion coatings (primers) containing zinc phosphate hydrate pigments obtained by polymer controlled mineralization, one free phosphate anion per NaZP entity (i.e. Na_2ZPOH) is delivered by metamorphic reaction to the surrounding steel-polymeric interface. Once at ambient temperature NaZP (i.e. Na_2ZPOH) is fully converted in β -ZPT, as it may be achieved by cyclic chemical exposition (aggression) of the primer, the pigment corrosion inhibition effects stem from barrier effects of the huge ZPT platelets and overall low ZPT solubilities in acidic conditions. However the release of Na^+ may affect the coating stability and generates undesirable side effects regarding the anticorrosion efficiency of such pigments.

6.4.4. Applications: standardized corrosion inhibition tests

6.4.4.1. Sodium effect in basic zinc phosphate pigments

By polymer controlled mineralization, a new generation of basic zinc phosphate hydrates as corrosion inhibitors has been developed. Among the various beneficial and synergic effects of such newly developed pigments regarding anticorrosion applications, two are of utmost importance and above illustrated. Firstly, the metamorphic reaction delivers one phosphate group per NaZP (i.e. Na₂ZPOH) entity, which is available for complexation with corrosion products, e.g. Fe²⁺ ions, thus precipitating and forming a passive layer of Phosphophyllite at the coating-steel interface. Secondly, the dissolving NaZP (i.e. Na₂ZPOH) entity that converts certainly to β-ZPT, which exhibits an appreciable low solubility in the pH range 4-9 and interesting barrier effects, due to its platelike morphology. Therefore, standard corrosion tests such as prolonged exposure to salt spray [206-207] and humidity chamber exposure [209-210] were conducted on the samples ZP-1, ZP-2 and NaZP as depicted by Figure 6.19. Test probes were prepared by applying on conventional steel plates a 50 μm (humidity chamber test) or a 100 μm (salt spray test) thick coating layer of a formulation (red lacquer) comprising of the mixture of a carboxylic-PS based dispersion (white lacquer) and 40 wt% tested pigments at pH 9.5. The coated specimens were pre-damaged with a scratch in order to allow a satisfactory description of the macroscopic corrosion behaviour.

Regarding the efficiency of these sodium-containing pigments for anticorrosion, two major and unexpected difficulties also arise. Firstly, in the inner layers (primer) of the anticorrosion coating a fixed volume, stemming from the space occupied by a single crystal or pigment aggregate before dissolution, is only accessible for dissolution and reprecipitation reactions. Thus the metamorphic conversion from NaZP to β-ZPT generates a change of crystal geometry, that consequently may induce uncontrolled delamination of the protective coating. This is well illustrated by the exposed bare steel surface in Fig. 20 C (Test 1), obtained after a prolonged stay in humidity chamber (continuous condensation) of a NaZP coating in comparison to an intact and therefore humidity resistant coating loaded with pigment ZP-1. Secondly, parallel to the advantageous release of PO₄³⁻ anions, a dramatic release of huge quantities of Na⁺ ions is observed. According to Stratmann et al [211], upon surfacial corrosion, cation transport (such as Na⁺) takes place from the generated coating voids and discontinuities, representing an aqueous environment [212-213], toward cathodic sites, notably along the interfacial gap [214], and neutralize locally produced OH⁻ ions, as follow:



If a coating / water interface exists, the above process yields highly alkaline conditions in the limited volume gap and results in localized cathodic disbondment of organic coating by leaching.

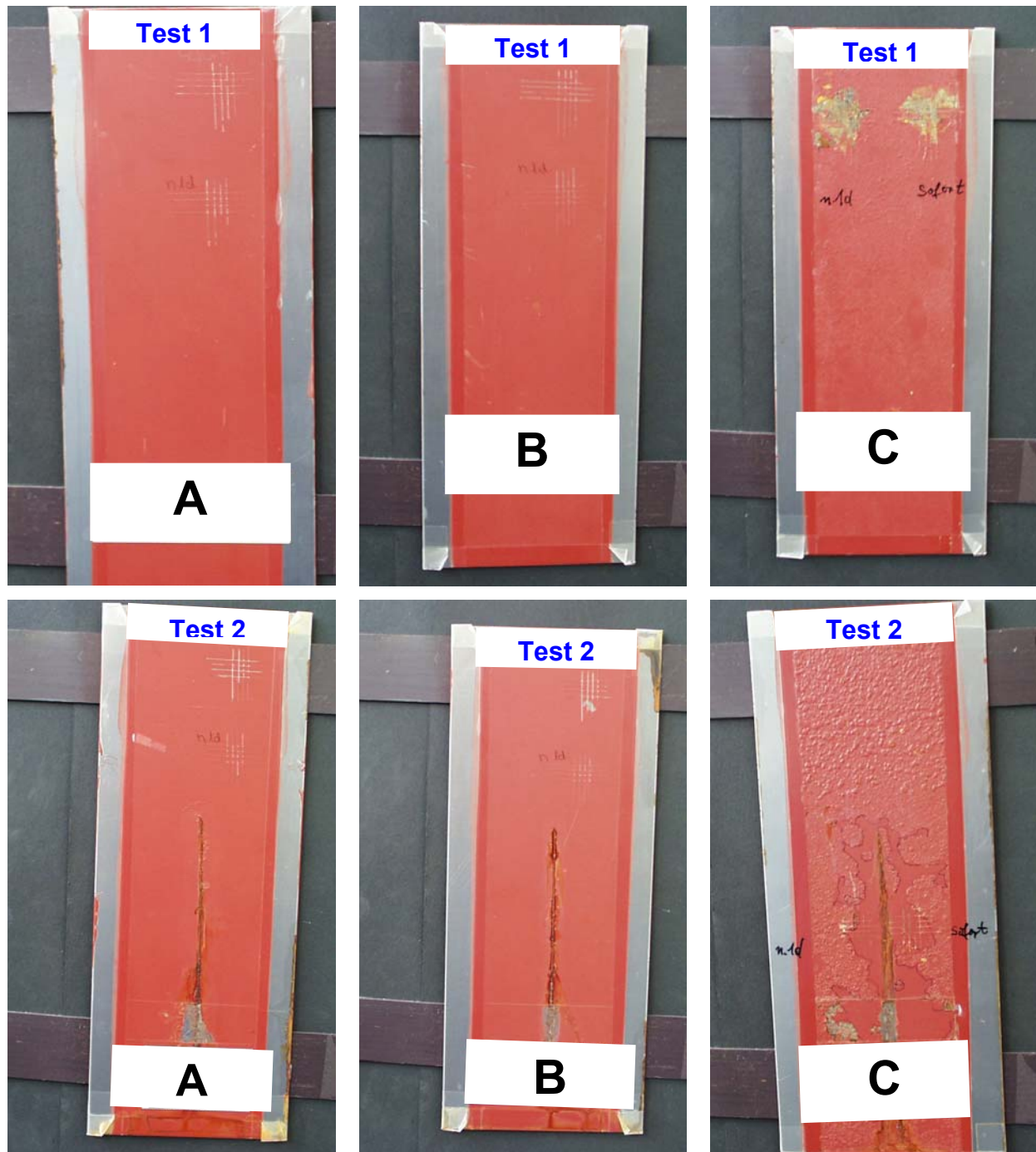


Figure 6.20: compared anticorrosion efficiency measured by humidity chamber exposure for 240 hours (Test 1) and salt spray test (Test 2) for ZP-1 (A), ZP- 3 (B) and NaZP (C) samples.

Due to the high affinity for water of the electrolytes accumulated at cathodic sites, osmotic water transport takes place, resulting in dramatic blister formation or cathodic blistering. [215]. A similar mechanism of coating degradation, osmotic blistering is caused by effective amounts of sparingly soluble, however generally neutral, organic or inorganic species (precipitated ion-pair

complexes) present at the substrate (steel) / coating interface [216], or notably inside the coating, such as NaZP. These dramatic blistering effects are well described in Fig. 6.20 C (Test 2), where an extreme blister density and total undercutting rusting are unsatisfactorily achieved. Undercutting rusting is also indicated by the presence of a discontinuous red oxide film in Fig. 6.20 C (Test 1). Anyway in both blistering cases, the blistering phenomenon is driven by the differences in water activity existent between blisters and their environment and the unfortunate presence of sodium ions. In this respect, it might be highly recommended to exchange the Na⁺ ions with other inorganic [217] or organic cations (e.g. alkyl ammonium, alkoxy phosphonium salts)[218-219] in the pigment formulation or directly in the crystal structure of pigments obtained by polymer controlled mineralization, and so that the selected additives do not disastrously interfere with the targeted corrosion inhibition mechanisms or finally devoid the on purpose synthesized pigment of any inhibitive properties.

6.4.4.2. Combined effects of the state of hydration and polymorphy on ZP anticorrosion efficiency

Being well documented, water penetration along inherent inhomogeneities of pigmented organic coatings is the primary step of the degradation process. The direct consequence of water uptake is the formation of interconnected pathways and transport by diffusion of corrosion promoter ionic species (such as Cl⁻) from the environment to the coating/substrate interface and ultimately the onset of the corrosion process. Therefore, in order to avoid the inopportune (previously described) effects of sodium-containing zinc phosphate pigments, and taking advantage of the widely recognized barrier effects of zinc phosphate pigments, the anticorrosion efficiency of zinc phosphate hydrates regarding both their unique dissolution behaviour in acidic conditions and their state of hydration, was evaluated employing cyclic humidity chamber exposure and standardized salt spray test.

Therefore, Table 6.6 illustrates precisely the influence of the state of hydration and the pigment polymorphy of absolutely pure zinc phosphate hydrates. Prolonged salt-spray tests indicate that the β -form of zinc phosphates perform better than the α -form, disregarding their respective state of hydration. On the contrary the humidity cabinet test let suggest that α -zinc phosphate hydrates perform better than β -zinc phosphate hydrates. Such differences may be first explained in term of barrier effect, strongly related to the pigment distribution inside the binder. If one assumes a uniform pigment distribution, the smaller size of β -zinc phosphate hydrates platelets, and their possible aggregation (c.f. Chapter 3) strongly reduces their respective barrier effects. Furthermore, β -ZPT displays not only a lower bulk dissolution rate (Chap. 4) but also a lower solubility product (pK_{s1}) at pH 9, thus releasing less phosphate groups on dissolution, i.e. less

free PO_4^{3-} being available for anticorrosion. In that sense, a strong indication is the preferential formation of zinc oxide, as dissolution product in the case of α -ZPT (see Chapter 4) and amorphous zinc phosphate in the case of β -ZPT.

Anticorrosive Pigment	Test duration (h)	Painted panel								
		Cut					Surface			
		Corrosion in scribe (mm)	Blister front (mm)	Normalized Blister front/coating density (a) (m / g)	Delamination (mm)	Under-rusting (mm)	Normalized Blister front/coating density and affected area (m / g) – (%)	Corrosion at cross-cut scratch (b)	Film thickness [μm]	Anticorrosion efficiency
ZP-1	504	0-8	0 - 18	1	0-15	0-15	1-2.5 25%	0-4/ 0	72-80	reference
ZP-3 $\alpha\text{-Zn}_3(\text{PO}_4)_2 \cdot 4 + 2 \text{H}_2\text{O}$	240	0	0-7	1-1.5	2-7	2-5	1.3-1.5 5%	1/1	90-95	-
$\alpha\text{-Zn}_3(\text{PO}_4)_2 \cdot 2\text{H}_2\text{O}$	504	(c)	2 - 10	1-2.5	complete	complete	1-2.5 50%	0-1/ 0-1	71-88	-
$\beta\text{-Zn}_3(\text{PO}_4)_2 \cdot 2\text{H}_2\text{O}$	504	0	1 - 10	1-1.2	4-9	0-9	1-2.5 5%	0-2/ 0-1	69-80	+++
$\alpha\text{-Zn}_3(\text{PO}_4)_2$	504	(c)	0.5 - 17	1.25-2.5	7-20	7-20	1.25-2 10%	0-1/ 0	61-81	+
$\beta\text{-Zn}_3(\text{PO}_4)_2$	504	0	0 - 12	1.2-1.5	5-10	5-10	1-2 15%	0-1/ 0-1	65-85	+++

Anticorrosive Pigment	Test duration (h)	Painted panel					
		Surfacial coloration change	Orange peeling (%)	Normalized Blister front/coating density (m/g)	Corrosion at cross-cut scratch (b)	Film thickness [μm]	Anticorrosion efficiency
ZP-1	504	whitening waterfleck	0	0	Gt 0-1/ 0-2	67-81	reference
ZP-3 $\alpha\text{-Zn}_3(\text{PO}_4)_2 \cdot 4 + 2 \text{H}_2\text{O}$	240	slight whitening waterfleck	0	0	Gt 1/1	60-80	---
$\alpha\text{-Zn}_3(\text{PO}_4)_2 \cdot 2\text{H}_2\text{O}$	504	whitening waterfleck	75%	0	Gt 0/ 0	60-88	-
$\beta\text{-Zn}_3(\text{PO}_4)_2 \cdot 2\text{H}_2\text{O}$	504	whitening - strong waterflecking	80%	Some flakes along the edges 1-1.5	Gt 0-1/ 0-1	69-88	--
$\alpha\text{-Zn}_3(\text{PO}_4)_2$	504	whitening waterfleck	70%	0	Gt 0-/ 0	64-77	-
$\beta\text{-Zn}_3(\text{PO}_4)_2$	504	whitening white layer	80%	Some flakes along the edges 1-1.5	Gt 0-1/ 0-1	61-88	--

Table 6.6: Comparison of water-reducible pigmented coatings (primer with topcoat) based on PS-acrylic emulsion (BASF AG) charged with pure zinc phosphate hydrates in dependence of the state of hydration and polymorphism two accelerated tests: (A) salt spray test, (B) humidity chamber test

(a) ISO 4628-2

(b) ISO 2409

(c) no identification possible due to complete blister coverage

Corrosion efficiency: +/-: better anticorrosion performance than reference at pH 9-10

Besides, β -ZPT is highly hydrophobic compared to α -ZPT, since it displays higher surface energy, especially at basic pH (in NaOH and NH_3 , solutions, Chapter 4) and is strongly negatively charged in these conditions while α -ZPT surfaces are nearly neutral. It may well explain the strong coating whitening observed in the humidity chamber test, since penetrating

water is not absorbed by dissolving β -ZPT crystals and therefore accumulates at pigment-coating interface. Nevertheless, if the pigment solubility of the inhibiting pigment is higher than a certain value, blistering occurs. This might be the case of α -ZPT in comparison to β -ZPT, with blister density visualized in the salt spray test two times higher for the α -modification than β -form of zinc phosphate. Also regarding the β -ZPT dissolution-precipitation mechanism, after a first contact with adsorbed water the generated nanoparticles of amorphous zinc phosphate may block diffusion path through the coating before dissolving again. This can not take place initially employing a α -ZPT charge, since dissolution product resume to highly stable zinc oxide at pH 9-10. Current investigation by humidity chamber test alone and its interpretation in term of relative pigment solubility point out that the protective properties of zinc chromate (ZP-1 coated sample) can not be achieved with zinc phosphate tetrahydrates. However in parallel to the conclusion of Romagnoli et al. [220] with alkyd binders, on the basis of the present salt spray test it may be shown that β -ZPT provide anticorrosive performance better or equal to that of paints pigmented with zinc chromate containing formulations. Moreover, zinc phosphate dihydrates and anhydrates are significantly more hygroscopic than the zinc phosphate tetrahydrates, since they induce an important formation of foam on application in paint formulations, and this may have better dispersability than zinc phosphate tetrahydrates, as reported by Burkill et al. [12]. In addition zinc phosphate of lower hydration state, having lower solubility products at pH 9, may also convert to tetrahydrate either by dissolution-precipitation process inside the coating or simply on storage [3]. Notably, this may explain the reduced efficiency of zinc phosphate tetrahydrate with achievement of similar bleach corrosion at cross-cut scratches after 240 hours compared to 504 hours for ZPD and ZPA pigments. This confirms Kalendova's recent observations [14]. But astonishingly, albeit its high solubility α -ZPT do not attack the coating integrity (orange peeling) [222] in opposition to α -ZPD and α -ZPA pigmented primers. This strongly suggests additional beneficial effects of pigment-coating (i.e. crystal-polymer) interactions.

6.5. Conclusion

It is recognized that the same spontaneous processes which promote corrosion at coating/steel interfaces, that is water adsorption into organic coatings filled with active corrosion inhibitors, local dissolution and transport by diffusion of ionic species in situ of organic coatings, also allow the action mechanisms of corrosion inhibitor species (controlled phosphate anions release resulting from pigment solubilisation) to operate. Similar unfortunate deterioration processes are widely observed in zinc phosphate based dental cements, albeit intensive technological developments currently focused on the improvement of long-term thermo-mechanical stability. Therefore this chapter focused on the systematic and meticulous investigation of the solubility and dissolution mechanisms potentially involved in steel corrosion in dependence of environmental conditions, among which ionic strength, pH and temperature are considered of utmost importance, for a broad range of pigments, ranging from pure zinc phosphate tetrahydrate polymorphs to organic modified pigments and zinc phosphate based pigments developed by polymer controlled mineralization.

Two approaches of the solubility equilibrium have been presently selected: a *leaching method* (thermodynamic approach), where pigment suspension are let equilibrated for months in a buffered solution until saturating conditions are achieved, and a *pH response method* (kinetic approach), where phosphate release to a pH impulse is monitored, either by electrochemistry or by conductometry, gravimetry after filtrate recovery and also complete supernatant analysis. Processing of the gained data succeeded using successively on purpose developed solubilisation models: a basic *hopeite model*, accounting the polymorphy and the state of hydration of the tested pigments and a composition dependent model that considers the chemical composition of the pigment formulation.

Albeit gravimetric and conductometric techniques tend to overevaluate the solubility products, these methods deliver precious information regarding an efficient screening and precise classification of tested compounds. In that sense, the classification of all zinc phosphate based pigments, even those of non-conventional formulations as sparingly soluble salts was confirmed. While gravimetric and conductometric allow a rapid but approximate evaluation of the temperature and pH dependence of the pigment solubility, only a thorough chemical analysis of the species present in the supernatant delivers satisfying values of the solubility product. For this precise reason this study could successfully shed lights first on the three competing mechanisms of ZPT dissolution on the whole pH range (1-13), involving not only free phosphate, mono- and dihydrogen phosphate anions but also ion-pair phosphate and hydroxo- complexes such as ZnHPO_4 , $\text{ZnH}_2\text{PO}_4^+$ and $\text{Zn}(\text{OH})^+$, $\text{Zn}(\text{OH})_2$ that also might precipitate in saturating conditions.

While at *the critical* pH 4 α -ZPT and β -ZPT exhibit very similar solubility products pK_{s1} with 35.4 and 38.4 respectively, in alkaline medium (pH 8) α -ZPT significantly distinguishes from β -ZPT with marked fluctuations in pK_{s1} values ranging from 36.1 to 29.3. Nevertheless both model pigments display characteristic pH dependence of the solubility in “W-shape”, indicating a dissolution process governed essentially by the acidity constants K_{a_i} (i.e. β_i) of phosphoric acid (buffering effect). In this line, unambiguous confirmation of the dependence of the dissolution of the ionic strength reigning in the aqueous medium of immersion and its nature (dilute solutions of H_2SO_4 , HNO_3 , H_3PO_4 , $NaOH$ and $NaCl$) was given. Furthermore the overwhelming mechanism of dissolution-reprecipitation (metamorphism) and the primordial role of sodium ions in the corrosion efficacy of acid and basic zinc phosphate pigments e.g. $NaZnPO_4 \cdot 1H_2O$, $Na_2Zn(PO_4)(OH) \cdot 2H_2O$ appear conspicuously in employing first a composition dependent dissolution model, and secondly further validated (i.e. emphasis of blistering effects governed by the sodium concentration in the coating) by combined salt spray tests and humidity chamber test. Besides, the incorporation of sodium in Na_2ZPOH induces extremely high solubility, while the intercalation of polymeric material (Na_2ZPOH) and the addition of hydroxyl groups decrease drastically the solubility of those compounds in alkaline medium. Similar beneficial effects of intentionally added impurities (e.g. chromates, CaO , SiO_2) in commercial pigment formulations on the solubilisation process are observed for ZP-1 and ZP-2. In fact these products exhibit pK_{s1-4} seven orders of magnitude higher than the model compounds thanks either to synergic release of chromates stemming from zinc or calcium chromates and mixed zinc phosphate hydrates with intrinsic low solubility, or to the presumed formation of highly stable dissolution products such as $CaZn_2(PO_4)_3 \cdot 2 H_2O$. Therefore while conductometry might point out that the effects of mixed additives on solubility is just to decrease it, as suggested by Bittner, the supernatant analysis method might also well point out that the solubility stays constant (i.e. $pK_{s1-4} \approx 33$) on a broader pH range, i.e. 4-12 instead of 4-9 or 4-10, as stated by Leidheiser.

In addition, this systematic study of the dissolution of zinc phosphate based pigments comes in concinnity of Chapter 4, focused especially on surfacial pigment dissolution mechanisms and dissolution kinetics. In consequence, this work may either help design pigments with adapted chemistry for anticorrosion or at least improve existing pigment formulations, in the sense of Sinko, who defined the *inhibitor activity parameter* I_i , i.e. the ratio of solubility to minimum concentration of an inhibitor of distinct inhibitor species necessary to promote passivity (against corrosion) of metal substrates exposed to aqueous phases. Besides the basic understanding of the dissolution mechanisms and the knowledge of the thermodynamic solubility constants/products in dependence of pH and temperature might also authorize the conception of reconstructive orthopaedic dental cements with drastically reduced solubility and high stiffness, thus improving their service lifetime.

6.6. References

- [1] D. Darling, R. Rakshpal., *Mater. Perform.* **37** (1998) 42
- [2] I.M. Zin, S.B. Lyon, S.J. Badger, J.D. Scantlebury, V.I. Pokhmurskii, *J. Corros. Sci. Eng.* **2** (1999) 21
- [3] L. Veleva, J. Chin, B. Del Amo, *Prog. Org. Coat.* **36** (1999) 211
- [4] C.H. Hare., *J. Prot. Coat. Minings* **15** (1998), 31
- [5] G.A. Howard, *Pigment Resins Tech.* **29** (2000) 325.
- [6] O. Pawlig, *PhD. Thesis*, University of Mainz, Germany (2001)
- [7] M.V. Goloshchapova, T.N. Filatova, *Russ. J. Inorg. Chem.* **14** (1969) 424
- [8] G. Meyer, *Farbe + Lacke* **69** (1963) 528
- [9] G. Meyer, *Farbe + Lacke* **71**(1965) 113
- [10] G. Adrian, A. Bittner, *J. Coatings. Technol.* **58**(740) (1986) 59
- [11] R. Romagnoli, V.F. Vetere, *Corrosion* **51**(2) (1995) 116
- [12] J.A. Burkill, J.E.O. Mayne, *J.O.C.C.A. - Surf. Coating Int.* **71**(9) (1988) 273
- [13] N.L. Thomas, *Prog. Org. Coat.* **19**(2) (1991) 101
- [14] A. Kalendová, P. Kalenda, *Farbe + Lacke* **109** (2003) 62
- [15] U. Nürnberger, *Korrosion und Korrosionsschutz im Bauwesen*, Vol. **1**, Bauverlag (Wiesbaden) (1995)
- [16] S. Turgoose, *Polym. Paint Color J.* **178** (1988) 108
- [17] R. Romagnoli, V.F. Vetere, B. Del Amo, *Surf. Coat. Int.: Coat. Trans.* **B86**(4) (2003) 301
- [18] H. Leidheiser, W. Funke, *J.O.C.C.A. - Surf. Coating Int.* **70**(5) (1987) 121
- [19] L.N. Shchegrov, N.M. Antrapsteva, I.V. Rudyi, *Zh. Neorg. Khim.* **32**(11) (1987) 2838
- [20] Z. Bircsak, W.T.A. Harrison, *Acta. Cryst.* **C54** (1998) 1383
- [21] (a) J. Eysseľtová, T.P. Dirkse, *IUPAC solubility data series*, Vol. **66** Pergamon Press (Oxford,UK) (1998); (b) J. Eysseľtová, T.P. Dirkse, *J. Phys. Chem. Ref. Data* **27**(6) (1998) 1289
- [22] H.M.A. Al-Maydama, P.J. Gardner, I.W. McAra, *Thermochim. Acta* **192** (1992) 117
- [23] G. Zsiklai, I. Szucs, E. Megyerikanya, *Hung. J. Chem.* **10**(2) (1982) 215
- [24] M. Morcillo, M.P. Mateo, *Europ. Coating. J.* **4** (1988) 170
- [25] T. Sugama, R. Broyer, *Surf. Coat. Technol.* **50** (1992) 89
- [26] L. Li, J.T. Guthrie, J.W. He, *Surf. Coat. Int.: Coat. Trans.* **B84**(1) (2001) 35
- [27] L. Chromy, E. Kamińska, *Prog. Org. Coatings* **18** (1990) 319
- [28] U. Nürnberger, *Korrosion und Korrosionsschutz im Bauwesen*, Vol. **2**, Bauverlag (Wiesbaden) (1995)
- [29] V. I. Pokhmurskyi, I.M. Zin, S.B. Layon, L.M. Bilyi, *J. Mater. Sci.* **39**(2) (2003) 153
- [30] S. Pietsch, *Plaste Kautsch.* **35**(7) (1989) 246
- [31] A. Amidurin, C. Barreau, R. Hellouin, D. Thierry, *Prog. Org. Coat.* **25** (1995) 339
- [32] B. Del Amo, R. Romagnoli, V.F.Vetere, L.S. Hernández, *Prog. Org. Coat.* **33** (1998) 28
- [33] M. Eisenberger, M. Addy, A. Rossbach, *J. Dentistry* **31**(2) (2003) 137
- [34] R. Nomoto, K. Uchida, Y. Momoi, J.F. McCabe, *Dent. Mater.* **19**(3) (2003) 240
- [35] R.G. Craig in *Restorative Dental Materials*, 11th Ed., R.C. Vraig and J.M. Powers Eds., Mosby Publish. (St Louis) (1993)
- [36] A.D. Wilson, J.W. Nicholson, in *Chemistry of Solid State Material*, Vol.**3: Acid-based cements, their biomedical and industrial applications, University Press (Cambridge) (1993)**
- [37] C.L. Davidson, *Adv. Eng. Mater.* **3**(10) (2001) 763
- [38] F. Bohlsen, M. Kern, *Quintessence Int.* **34**(7) (2003) 493
- [39] R.S. Squier, J.R. Agar, J.P. Duncan et al., *Int. J. Oral Max Impl.* **16**(6) (2001) 793
- [40] N. Attar, L.E. Tam, D. McComb, *J. Prothet. Dent.* **89**(2) (2003) 127
- [41] K.A. Proos, M.V. Swain, J. Ironside et al, *Int. J. Prosthodont.* **16**(1) (2003) 82
- [42] B. Czarnecka, H. Limanowska-Shaw, J.W. Nicholson, *J. Mater. Sci.-Mater. Med.* **14**(7), (2003) 601
- [43] G. Lusvardi, L. Menabue, M. Saladini, *J. Mater. Sci.: Mater. Med.* **13** (2002) 91

- [44] K. Sunnegardh-Gronberg K, A. Peutzfeldt, J.W.V. van Dijken, *J. Dent. Res.* **81** - Sp. Iss. B (2002) 361
- [45] E. Mezzomo, F. Massa, S. Libera, *Quintessence Int.* **34**(4) (2003) 301
- [46] M. Eisenberger, M. Addy, A. Roszbach, *J. Dent.* **31**(2) (2003) 137
- [47] L.G. Sillén, A.E. Martell, *Stability Constants of Metal-Ion Complexes*, Special Publ. 17, The Chemical Society (London) (1964)
- [48] J.J. Jurinak, T.S. Inouye, *Sol. Sci. Soc. Amer. Proc.* **26** (1962) 144
- [49] J.O. Nriagu, *Geochim. Cosmochim. Acta* **37** (1973) 2357
- [50] G.H. Nancollas, *Corrosion* **39**(3) (1983) 77
- [51] L.S. Hernández, G. Garcíá, C. López, B. Del Amo, R. Romagnoli, *J.O.C.C.A. - Surf. Coating Int.* **81**(1) (1998) 19
- [52] M. O'Donoghue, R. Garrett, V. Datta, P. Roberts, T. Aben, *Mater. Perform.* **42**(9) (2003) 36
- [53] D.A. Jones, *Principles and Prevention of Corrosion*, 2nd. Ed., Prentice-Hall (Upper saddle River, NJ) (1996)
- [54] J.W. Mullin, *Crystallization*, 4th Ed., Butterworths (London) (1972).
- [55] (a) W.R. Linke, A. Seidell, *Solubilities, Inorganic and Metal-Organic Compounds*, Vol. 1 (1958) American Chemical Society, ACS Ed. (Washington); (b) W.R. Linke, A. Seidell, *Solubilities, Inorganic and Metal-Organic Compounds* Vol. 2 (1965) American Chemical Society, ACS Ed. (Washington)
- [56] T.M. Gregory, E.C. Moreno, W.E. Brown, *J. Res. Natl. Bur. Stand.* **A74** (1970) 461
- [57] H. McDowell, W.E. Brown, J.R. Sutter, *Inorg. Chem.* **10** (1971) 1683
- [58] L.C. Bell, H. Mika, B.J. Kruger, *Arch. Oral. Biol.* **23** (1978) 329
- [59] G.H. Nancollas, L.J. Shyu, Y. Yoshikawa, J.P. Barone, D. Svrjcek, *Am. Inst. Chem. Eng.* **78** (1978) 26
- [60] R.M.H. Verbeek, H. Steyaer, H.P. Thun, F. Verbeek, *J. Chem. Soc.: Faraday Disc.* **76** (1980) 209
- [61] M.S. Tung, N. Eidelman, B. Sieck, W.E. Brown, *J. Natl. Bur. Stand.* **A93** (1988) 613
- [62] P. Hartman, *Crystal Growth: An Introduction*, North Holland Ed. (Amsterdam) (1975)
- [63] A.A. Chernov, *Prog. Cryst. Growth Charact. Mater.* **26** (1993) 121
- [64] F.C.M. Driessens, R.M. Verbeek, *Z. Naturforsch.* **35** (1980) 262
- [65] A. Chettry, Z.R. Wang, J.L. Fox, A.A. Baig, H. Zhuang, W.I. Higuchi, *J. Colloid Interface Sci.* **218** (1) (1999) 47
- [66] J. Barralet, M. Akao, H. Aoki, *J. Biomed. Mater. Res.* **49** (2000) 176
- [67] H. Zhuang, A.A. Baig, J.L. Fox, Z.R. Wang, S.J. Colby, A. Chettry, W.I. Higuchi, *J. Colloid Interface Sci.* **218**(1) (1999) 57
- [68] A.A. Baig, J.L. Fox, Z. Wang, W.I. Higuchi, S.C. Miller, A. M. Barry, M. Otsuka, *Calcif. Tissue Int.* **64**(5) (1999) 437
- [69] A.A. Baig, J.L. Fox, Z. Wang, J. Hsu, W.I. Higuchi, A. Chettry, H. Zhuang, M. Otsuka, *Calcif. Tissue Int.* **64**(4) (1999) 329
- [70] J. Zhang, G.H. Nancollas, *J. Cryst. Growth* **123** (1992) 59
- [71] R. Tang, G.H. Nancollas, *J. Cryst. Growth* **212** (2000) 261
- [72] R. Tang, G.H. Nancollas, *J. Am. Chem. Soc.* **123** (2001) 5437
- [73] R. Tang, W. Wu, M. Hass, G.H. Nancollas, *Langmuir* **17** (2001) 3480
- [74] W. Ostwald; *Z. Phys. Chem.* **34** (1900) 495
- [75] H. Freundlich, *Colloid and Capillary Chemistry*, Dutton Ed. (NY) (1923) p. 123
- [76] R. Defay, I. Prigogine, *Surface Tension and Adsorption*, Wiley (NY) (1966)
- [77] W. Wu, G.H. Nancollas, *J. Sol. Chem.* **27** (1998) 521
- [78] F. Christoffersen, M.R. Christoffersen, *J. Cryst. Growth* **53** (1981) 42
- [79] A.S. Myerson, *Handbook of Industrial Crystalization*, 2nd Ed., Butterworth-Heinemann (Boston) (2002)
- [80] N. Spanos, V. Deimede, P.G. Koutsoukos, *Biomaterials* **23** (2002) 947
- [81] R.U.G. Krishnan, G. Atkinson, *J. Chem. Eng. Data* **35** (1990) 361
- [82] *IUPAC Compendium*, Goldbook **50**(68) (1996) 977
- [83] E.A. Guggenheim, T.D. Schindler, *J. Phys. Chem.* **38** (1934) 533
- [84] C.W. Davies, *Ion Association*, Butterworths (Washington) (1962)

- [85] C.W. Davies, V.E. Malpass, *Trans. Faraday Soc.* **60**(503P) (1964) 2075
- [86] R.A. Robinson, H.S. Harned, *Multicomponent Electrolyte Solutions*, Pergamon Press (Oxford, UK) (1968)
- [87] J.W. Ball, D.K. Nordstrom, *WATERQ4F-Program for Calculation in Seawater*, USGS (Washington) (1987)
- [88] J.M. Prausnitz, R.N. Lichenthaler, E. Gomez de Azevedo, *Molecular Thermodynamics of Fluid Phase Equilibria*, 2nd. Ed. Prentice-Hall (Engelwood Cliffs, NJ) (1986)
- [89] R.C. Reid, J.M. Prausnitz, B.E. Poling, *The Properties of Gases and Liquids*, 4th Ed., McGraw-Hill (NY) (1987)
- [90] K.S. Pitzer, G. Mayorga, *J. Phys. Chem.* **77** (1973) 2300
- [91] L.A. Bromley, *J. Chem. Thermo.* **4** (1972) 669
- [92] L.A. Bromley, *AIChE J.* **20** (1974) 336
- [93] J.F. Jr. Zemaitis, D.M. Clark, M. Rafal, N.C. Scrivner, *Handbook of Aqueous Electrolyte Thermodynamics*, Am. Institute. Chem. Eng. Ed., AIChE (1986)
- [94] G.H. Nancollas, G.L. Gardner, *J. Cryst. Growth* **21** (1974) 267
- [95] J.P. Barone, G.H. Nancollas, *J. Colloid Interf. Sci.* **62**(3) (1977) 421
- [96] J. Liu, M. Wimby, U. Grén, *Comput. Chem. Eng.* **13**(4-5) (1989) 405
- [97] J. Liu, U. Grén, M. Wimby, *Fluid Phase Equilib.* **53** (1989) 269
- [98] I. Nagata, T. Yamada, *J. Chem. Eng. Data* **18** (1973) 87
- [99] I. Nagata, K. Miyamoto, *Thermochim. Acta* **205** (1992) 307
- [100] J.P. Novák, J. Matouš, J. Pick, *Liquid-Liquid Equilibria*, Elsevier (Amsterdam) (1987)
- [101] M. Hiranuma, *Ind. Eng. Chem. Fundam.* **22** (1983) 364
- [102] Y.C. Chang, A.S. Myerson, *AIChE J.* **31** (1984) 890
- [103] J. Nývlt, *Industrial Crystallization from Solution*, Butterworths (London) (1971) p.34 and thereafter.
- [104] J. Nývlt, O. Söhnel, M. Matuchova, M. Brout, *The Kinetics of Industrial Crystallization*, Elsevier (Amsterdam) (1985), p. 1
- [105] G.V. Medvedev, L.N. Matusevich, *Ind. Lab.* **35**(2) (1969) 302
- [106] (a) M.V. Tovbin, S.I. Krasnova, *Zhur. Fiz. Khim.* **23** (1949) 963; (b) M.V. Tovbin, S.I. Krasnova, *Fiz. Khim.* **25** (1951) 161
- [107] J. Sinowiec, *Krist. Technik* **8** (1973) 701
- [108] (a) R. Gopal, *J. Ind. Chem. Soc.* **23** (1946) 87; (b) R. Gopal, *J. Ind. Chem. Soc.* **27** (1950) 43
- [109] O. Söhnel, J. Nývlt, *Krist. Technik* **11** (1976) 141
- [110] G.W.: Preckshot, G.G. Brown, *Ind. Eng. Chem.* **44** (1952) 1314
- [111] E.V. Khamiski, N.D. Sedelnikova, *Zhur. Prikl. Khim.* **43** (1970) 2547
- [112] H.E.C. Powers, *Ind. Chem.* **39** (1963) 351
- [113] A.R. Konak, *Krist. Tech.* **9**(7) (1974) 779
- [114] J.W. Mullin, S.J. Jančić, *Trans. Inst. Chem. Eng.* **57** (1979) 188
- [115] J. Nývlt, V. Pekárek, *Z. Phys. Chem.* **122** (1980) 199
- [116] P. Anderson, F.R.G. Bollet-Quivogne, S.E.P. Dowker, J.C. Elliott, *Arch. Oral. Biol.* **49**(3) (2004) 199
- [117] O. Pawlig, R. Trettin, *Mat. Res. Bull.* **34**(12-13) (1999) 1959
- [118] G. Berger, R. Gildenhaar, *Materialwiss. Werkst.* **26**(7) (1995) 379
- [119] P.G. Koutsoukos, G.H. Nancollas, *J. Crystal Growth* **53** (1981) 10
- [120] W.E. Brown, L.C. Chow, *J. Cryst. Growth* **53** (1981) 31
- [121] E. Königsberger, *Pure Appl. Chem.* **74**(10) (2002) 1831
- [122] P.G. Klepetsanis, E. Dalas, P.G. Koutsoukos, *Langmuir* **15** (1999) 1534
- [123] L. Perez, G.H. Nancollas, *J. Cryst. Growth* **66**(2) (1984) 412
- [124] T.P. Dirkes, *IUPAC Solubility Data Series*, Vol. **23**, A.S. Kertes Ed., Pergamon Press (Oxford,UK), p. 172
- [125] T.P. Dirkes, *IUPAC Solubility Data Series*, Vol. **23**, A.S. Kertes Ed., Pergamon Press (Oxford,UK), p. 250
- [126] J.W. Mullin, M.M. Osman, *Krist. Technick* **8** (1973) 471
- [127] (a) J. Nývlt, J. Skřivánek, J. Gottfried, J. Křičova, *Collect. Czechosl. Chem. Commun.* **31** (1966) 2127; (b) J. Nývlt, O. Söhnel, M. Matuchova, M. Brout, *The Kinetics of*

- Industrial Crystallization*, Chemical Eng. Monograph **19**, Elsevier (Amsterdam) (1985) p. 99
- [128] L.W. Marshall, E.U. Franck, *J. Phys. Chem. Ref. Data* **10** (1981) 295
- [129] (a) A.E. Martell, R.M. Smith, R. Motekaitis, *Critically Selected Stability Constants of Metal Complexes*, NIST Standard Reference Database **46**, Vol. 5, Texas A&M Univ. (1998); (b) R.G. Bates, S.F. Acree, *J. Res. Nat. Bur. Stand.* **30** (1943) 129; (c) C.E. Vanderzee, A.S. Quist, *J. Phys. Chem.* **65** (1961) 118
- [130] F.G. Zharovsii, The solubility of phosphates, *Trudy. Kom. Anal. Khim. AKad. Nauk. USSR* **3** (1951) 101
- [131] R.M. Smith, A.E. Martell, *Critically Selected Stability: Inorganic Complexes*, Vol. **4**, Plenum Press (NY) (1976) p. 257
- [132] C.W. Childs, *Inorg. Chim.* **9** (1970) 2465
- [133] H. Sigel, Becker, D.B. McCormick, *Biochim. Biophys. Acta* **148** (1967) 655
- [134] A.V. Shevade, L. Erickson, G. Pierzynski, S. Jiang, *J. Hazard. Subst. Res.* **3** (2001) 2-1
- [135] A.O. Gubeli, J. Ste. Marie, *Can. J. Chem.* **46** (1968) 1707
- [136] J. Eysseletová, T.P. Dirke, *Ammonium Phosphates, IUPAC-NIST Solubility data Series* **66**, *J. Phys. Chem. Ref. Data* **27**(6) (1998) 1
- [137] L.C. Bell, H. Mika, B.J. Kruger, *Arch. Oral. Biol.* **23**(5) (1978) 329
- [138] E. Levlin, *Water Sci. Technol.* **46**(4-5) (2002) 435
- [139] R. Nilsson, *Water Res.* **5** (1971) 51
- [140] J.F. Zemaitis, D.M. Clark, M. Rafal, N.C. Scrivner, *Handbook of Aqueous Electrolyte Thermodynamics*, Am. Institute. Chem. Eng. Ed., AIChE (1986)
- [141] J.O. Nriagu, E. Nieboer, Chromium in the natural and human environments, *Adv. Environ. Sci.* **20**, Wiley (NY) (1988)
- [142] J.J. Jurinak, T.S. Inouye, *Sol. Sci. Soc. Amer. Proc.* **26** (1962) 144
- [143] J.O. Nriagu, *Geochim. Cosmochim. Acta* **36** (1972) 459
- [144] <http://www.heubachcolor.de>
- [145] R. Romagnoli, B. Del Amo, V.F. Vetere, L. Veleva, *J.O.C.C.A.-Surf. Coat. Int.* **83**(1) (2000) 27
- [146] X.H. Bu, T.E. Gier, W.T.A. Harrison, G.D. Stucky, *Acta Cryst.* **C53** (1997) 1517
- [147] W.T.A. Harrison, T.M. Nenov, T.E. Gier, G.D. Stucky, *Solid State Chem.* **113** (1994) 168
- [148] T.M. Nenov, W.T.A. Harrison, T.E. Gier, J.C. Calabrese, G.D. Stucky, *J. Solid State Chem.* **107** (1993) 285
- [149] M. Nadifiyine, El Madami Bel Madami, A. Mokhlisse, B. Tanouti, *Solid State Sci.* **2** (2000) 495
- [150] R.C. Weast, M.J. Astle, W.H. Beyer, *Handbook of Chemistry & Physics*, 66th Ed., CRC Press (Boca Raton, FL) (1985) **B144**
- [151] G.H. Nancollas, M.S. Mohan, *Arch. Oral. Biol.* **15** (1970) 731
- [152] G.H. Nancollas, B.B. Tomazic, *J. Phys. Chem.* **78** (1974) 2218
- [153] P.G. Klepetsanis, E. Dalas, P.G. Koutsoukos, *Langmuir* **15** (1998) 1534
- [154] O. Söhnel, J.W. Mullin, *J. Colloid Interface Sci.* **123** (1988) 43
- [155] A.E. Nielsen, O. Söhnel, *J. Crystal Growth* **11** (1971) 233
- [156] D. Kashchiev, *Nucleation*, Butterworth-Heinemann (Oxford,UK) (2000) p. 20
- [157] O. Söhnel, J. Gardside, *Precipitation*, Butterworth-Heinemann (Oxford,UK) (1992) p. 66
- [158] J.A. Burkill, J.E.O. Mayne, *J.O.C.C.A. - Surf. Coating Int.* **9** (1988) 273
- [159] Y.V. Roshchina, T.S. Tsehkomskaia, G.P. Roskova, I.S. Ivanovskaya, *Glass Phys. Chem.* **21**(5) (1995) 371
- [160] A. Findlay, *Practical Physical Chemistry*, 9th Ed., B.P. Levitt Ed., Longmans Green Publish. (London, UK) (1973)
- [161] G.P. Matthews, *Experimental Physical Chemistry*, Clarendon Press (Oxford,UK) (1985)
- [162] K. Johannsen, S. Rademacher, *Acta Hydrochim. Hydrobiol.* **27**(2) (1999) 72
- [163] J. Garcíá-Carmona, J.G. Morales, R.R. Clemente, *J. Cryst. Growth* **249** (2003) 561
- [164] J. Garcíá-Carmona, J.G. Morales, J.F. Sáinz, E. Loste, R.R. Clemente, *J. Cryst. Growth* **262** (2004) 479

- [165] G. Jander, K. Fr. Jahr, *Massanalyse: Theorie und Praxis der Titration mit chemischen und physikalischen Indikatoren*, 15th Ed., G. Schulze and J. Simon Eds., Walter de Gruyter Publish. (Berlin) (1989) p. 217
- [166] K. Yoshimura, H. Waki, S. Ohashi, *Talanta* **25** (1978) 579
- [167] J. Perutka, J. Havel, L. Jancar, *Collect. Czech. Chem. Commun.* **59** (1994) 1951
- [168] M.C. Yebra, A. Moreno-Cid, S. Candela, R.M. Cespon, *Atom Spectrosc.* **24**(6) (2004) 218
- [169] E. Arnold, *Standard methods for the examination of water and waste wafer ALPHA*, AWWA, WPCF, 16th Ed., E. Arnold Ed. (Washington) (1985) p. 446
- [170] J.E. Harwood, R.A. Van Steenderen, A.L. Kuehn, *Water Res.* **3** (1969) 417
- [171] J.E. Harwood, R.A. Van Steenderen, A.L. Kuehn, *Water Res.* **3** (1969) 425
- [172] H.E. Ungnade, I. Ortega, *J. Am. Chem. Soc.* **73** (1951) 1564
- [173] C.V. Smith, D.G. Norton, S.A. Ballard, *J. Am. Chem. Soc.* **73** (1951) 5270
- [174] A. Kalendová, *Prog. Org. Coat.* **38** (2000) 199
- [175] S. Szklarska-Smialowska, *Inhibition of pitting corrosion*, **I-9-1**, in A. Raman and P. Labine Eds., *Reviews on Corrosion Inhibitor Science and Technology*, NACE (Houston) (1993)
- [176] J. Sinko, *Prog. Org. Coat.* **42** (2001) 267
- [177] H.H. Uhlig, *Corrosion and Corrosion Control*, 2nd Ed., Wiley Interscience (NY) 1971
- [178] M. Cohen, *Corrosion* **32** (1976) 12
- [179] M.A. Stranick, *Corrosion* **40**(6) (1984) 296
- [180] M.S. Vukasovich, *Molybdate: the versatile inhibitor*, **II-12-1**, in A. Raman and P. Labine Eds., *Reviews on Corrosion Inhibitor Science and Technology*, NACE (Houston) (1993)
- [181] M.H.L. Garnaud, *Polymers Paint Colour J.* **174**(4) (1984) 268
- [182] M. Cohen, *Dissolution of iron*, in G.R. Brubaker, P. Beverley and P. Phipps Eds., *Corrosion Chemistry*, *ACS Symposium Series* **89** (1979), p.8
- [183] J.G.N. Thomas, T.J. Nurse, *Br. Corros. J.* **2** (1967) 1
- [184] A. Bittner, *J. Coat. Technol.* **61**(777) (1989) 111
- [185] J.O. Nriagu, P.B. Moore, *Phosphate Minerals*, Springer Verlag (Berlin) (1984) p.176
- [186] M.J. Larsen, E.I.F. Pearce, *Archs. Oral. Biol.* **42**(7) (1991) 475
- [187] J. Sinko, US Patent 5,948,147
- [188] Y. Ericsson, *Acta Omdot. Scand.* **8**, Suppl. 3 (1949) 1
- [189] J.F. Montle, *J. Protect. Coat. Linings* **6** (1987) 38
- [190] H. Leidheiser, *J. Coating Technol.* **53**(678) (1981) 29
- [191] I.J. Buerge, S.J. Hug, *Environ. Sci. Technol.* **31** (1997) 5
- [192] M. Seo, N. Sato, *Inhibition in the context of passivation*, **I-7-1**, in A. Raman and P. Labine Eds., *Reviews on Corrosion Inhibitor Science and Technology*, NACE (Houston) (1993)
- [193] D.A. Jones, *Principles and Prevention of Corrosion*, MacMillan (NY) (1992)
- [194] V.I. Pokhmurs'kyi, I.M. Zin, S.B. Layon, L.M. Bilyi, *J. Mater. Sci.* **39**(2) (2003) 153
- [195] G. Lusvardi, L. Menabue, M. Saladini, *J. Mater. Sci.: Mater. Med.* **13** (2002) 91
- [196] J.O. Nriagu, P.B. Moore, *Phosphate Minerals*, Springer Verlag (Berlin) (1984) p. 325
- [197] M. Bohner, *Biomaterials* **25** (2004) 741
- [198] B. Gade, H. Pöllmann, A. Heindl, H. Westermann, *Environ. Geol.* **40**(3)(2001) 248
- [199] B. D. Sturman, R.C. Rouse, P.J. Dunn, *Am. Mineralogist* **66** (1981) 843
- [200] R.A. Barrea, C.A. Pérez, A.Y. Ramos, *J. Synchrotron Rad.* **8**(2) (2001) 990
- [201] G.H. Nancollas, *Biological mineralization and demineralization*, Springer-Verlag (Berlin) (1982)
- [202] R. Tang, M. Haas, W. Wu, S. Gulde, G.H. Nancollas, *J. Colloid Interface Sci.* **260** (2003) 379
- [203] J. Wang, P. Layrolle, M. Stigter, K. de Groot, *Biomaterials* **25** (2004) 583
- [204] BASF AG, *Internal report*, GKD dept. (2004)
- [205] N.J. Butler, *Solubility and pH calculations*, Principles of chemistry series, Addison-Wesley Publish. (London,UK) (1964) p.68
- [206] G.N. Jenkins, *The Physiology and Biochemistry of the Mouth*, Blackwell Publish. (Oxford,UK) (1978)
- [207] H. Hoche, C. Rosenkranz, A. Delph, M.M. Lohrengel, E. Broszeit, C. Berger, *Materialwiss. Werkst.* **35**(2) (2004) 82

- [208] E. Ramoskiene, M. Gladkovas, M. Salkaukas, *Accredit. Qual. Assur.* **8**(5) (2003) 235
- [209] F. de Fragata, J.E. Dopici, *J.O.C.C.A. - Surf. Coating Int.* **3** (1991) 92
- [210] B. Del Amo, R. Romagnoli, V.F. Vetere, *Prog. Org. Coat.* **33**(1) (1998) 28
- [211] M. Stratmann, *Encyclopedia of Electrochemistry*, Vol. **2**, *Interfacial kinetics and mass transport phenomena*, A.J. Bart and M. Stratmann and E.J. Calvo Eds., Wiley-VCH (Weinheim) (2003)
- [212] M. Stratmann, R. Feser, A. Leng, *Electrochim. Acta* **39**(8-9) (1994) 1207
- [213] T. Nguyen, J.B. Hubbard, G.B. McFadden, *J. Coatings Technol.* **63**(794) (1991) 43
- [214] H. Leidheiser, W. Wang, I. Igetoft, *Prog. Org. Coat.* **11** (1983) 19
- [215] T. Nguyen, J.B. Hubbard, *J. Coatings Technol.* **68**(855) (1996) 45
- [216] L.A. Van der Meer-Lerk, P.M. Herertjes, *J. Oil Colloid. Chem. Assoc.* **62** (1979) 253
- [217] R.V.S.S.N. Ravikumar, K. Ikeda, A.V. Chandrasekhar, Y.P. Reddy, P.S. Rao, *J. Phys. Chem. Solids* **64**(12) (2003) 2433
- [218] M.S. Morad, *J. Appl. Electrochem.* **29**(5) (1999) 619
- [219] M.S. Abdel-Aal, M.S. Morad, *Brit. Corros. J.* **36**(4) (2001) 253
- [220] B. Del Amo, R. Romagnoli, V.F. Vetere, L.S. Hernandez, *Prog. Org. Coat.* **33** (1988) 28
- [221] P.J. Gardner, I.W. McArn, V. Barton, G.M. Seydt, *J.O.C.C.A. - Surf. Coating Int* **1** (1990) 16
- [222] R.A. Burgess and M.M. Morrison, Chemical Engineering Progress, Wiley VCH Sept. 1995 pp 63-69, in Common Coating Failures: Causes and Remedies, *Corrosioneering Newsletter* **3**(1) (2004)

7. Summary and further outlook

“All truths are easy to understand once they are discovered. The point is to discover them”,
The aim of sciences, Galileo Galilei

Materials research devoted to the development of new or improved materials based on zinc phosphate hydrate cements with enhanced mechanical and chemical stability, suitable as “environmental friendly” corrosion inhibitor for partial or permanent restoration of bone and teeth attracts much interest at the interface between medicine, inorganic and physical chemistry and ceramic science.

Reference probes, namely α - and β -hopeite (i.e. α -, β -ZPT) have been synthesized by hydrothermal crystallization from aqueous solution at 20°C and 90°C respectively. The crystal structure of these polymorphic forms of zinc phosphate tetrahydrate (ZPT) $Zn_3(PO_4)_2 \cdot 4 H_2O$ has been completely resolved. Single crystal analysis proves that the main difference between the α - and β -form of zinc phosphate tetrahydrate stems from two different hydrogen bonding patterns. The respective three dimensional and two dimensional hydrogen bonding patterns of α - and β -ZPT induce unique thermal behaviour. Upon heating ZPT polymorphs release crystal water differently: while the α -form loses water two by two in two well defined stages, the β -form exhibits a dehydration pathway involving intermediary products of hydration, namely the dihydrate and the monohydrate. This corresponds to concurring mechanisms of dehydration: on one hand at low heating rate a two dimensional JMA mechanism on the (011) surface, induced by surface crystal defects and starting preferentially from crystal edges is privileged, and on the other hand at high heating rate a two dimensional diffusion mechanism (D_2) first on the (101) plan and then on the (110) surface takes over. Furthermore, considering dehydration of ZPT a multistep irreversible heterogeneous solid state (solid-gas) reaction and applying a “same final thermodynamic state” procedure, the thermodynamic stability phase diagram pointing out the possible interrelations between the various hydrate states and phases was built and an intermediary activation state (transformation from β - to α -ZPT at 170°C) was introduced. Besides, targeted chemical etching with diluted H_3PO_4 and NH_3 solutions proved to be successful in providing key information about the first stage of surface dissolution. Indeed, α -

and β -ZPT display characteristic hexagonal to cubic etch pits propagating under crystallographic control. Complementary AFM and surface FFM experiments/analysis point out various types of surface defects (point defects, screw dislocations) and allow the simultaneous evaluation of the defect density and of the bulk dissolution rates of both α - and β -ZPT, thus offering a representative description of their surface topology and chemistry.

Moreover, a novel approach of polymer controlled mineralization employing functionalized latexes obtained by radical miniemulsion polymerization and PAMAM based dendrimers proved to be efficient at producing basic zinc phosphate pigments of 1st and 2nd generation (i.e. $\text{NaZnPO}_4 \cdot 1 \text{ H}_2\text{O}$ and $\text{Na}_2\text{ZnPO}_4(\text{OH}) \cdot 2 \text{ H}_2\text{O}$). These zeolitic (ZPO) structures of increasing sodium and water contents exhibit different morphologies: hexagonal, cubic, heart-like, six-arm star, multidimensional lancets, etc. Using fluorescence labelled particles, carboxylated PS-based latexes were shown not only to reduce monotonically the crystal growth rate to around $8 \text{ nm} \cdot \text{min}^{-1}$ but also revealed to be strong nucleation promoter. On this basis, two simple mechanisms referring to coordination chemistry (i.e. formation of a six-atom complex $\text{L-COO}^- \cdots \text{Zn-PO}_4 \cdots \text{H}_2\text{O}_{\text{crystal}}$ with ligand exchange) are tentatively proposed in order to highlight the primary role of negatively charged latexes on ZP nucleation: an intra-corona nucleation mechanism and an extra-corona nucleation mechanism.

Finally, the short and long-term anticorrosion efficiency of the tailor-made ZPO/ZPT pigments and the controlled release of phosphate ions was evaluated using two approaches of the solubility equilibrium: a *leaching method* (thermodynamic approach), and a *pH response method* (kinetic approach). To this respect, each pigment displayed characteristic pH dependence of the solubility in “W-shape”, indicating a dissolution process governed essentially by the acidity constants K_{a_i} (i.e. β_i) of phosphoric acid (buffering effect). Furthermore the overwhelming mechanism of dissolution-reprecipitation (metamorphism) and the primordial role of sodium ions in the corrosion efficacy of acid and basic zinc phosphate pigments appeared conspicuously in employing first a *composition dependent dissolution model* (CDD model) developed on purpose and secondly further validated (i.e. emphasis of blistering effects governed by the sodium concentration in the coating) by combined salt spray tests and humidity chamber tests.

Further, the studies described in this thesis demonstrate the capability of the functionalized latex (polymer) controlled mineralization process to produce tailor-made materials on zinc phosphate basis. Such organic/inorganic hybrid materials are urgently needed to develop both advanced formulations of “environmental friendly” anticorrosive pigments and reconstructive orthopaedic dental cements with improved service lifetime.

8. Acknowledgements

Chapter 8

Acknowledgements

Curriculum Vitae

Education and Academic studies

2001-2004 *Max Planck Institute for Polymer Research, Mainz, Germany*
Johannes Gutenberg University, Mainz, Germany
Doctorate's degree in Physical Chemistry obtained in close collaboration with the BASF AG (Polymer labs, Ludwigshafen) and the Max Planck Institute for Iron Research (Interface Chemistry Dept., Düsseldorf). Title of thesis: Polymer controlled mineralization of zinc phosphate and applications in Corrosion protection, Catalysis and Biomedicine. Marks: *Summa Cum Lauda*

Polymer Synthesis Laboratory supervisor at MPIP during two years.

1999-2001 *University Louis Pasteur, Strasbourg, France.*
Chemist, engineer specialised in polymer sciences and plastics processing from the European School of Chemistry, Polymers and Materials of Strasbourg (E.C.P.M – i.e. trilingual school). MSc. in Polymer Sciences. Grade A⁺, Rank: 1/ 24.

Prize of excellence H. Davy

1995-1999 *University Claude Bernard, Lyon, France.*
Maîtrise de Chimie-Physique – MSc. in Physical Chemistry. Grade A⁺, Rank: 1 / 60
Licence de Chimie-Physique – BSc. in Physical Chemistry. Grade A⁺, Rank: 1 / 60.
DEUG de Chimie – Associate's degree in Chemistry. Grade B⁺

1994-1995 *Lycée Stendhal (French – Italian High School), Milano, Italy.*
Baccalauréat – equivalent to High School Diploma. Grade : A.
Subjects : French, Maths, Physics and Chemistry.

Languages

- English (written and spoken).
Diploma : TOEFL (Test of English as a foreign language), TOEIC - Average mark : 118 / 150.
- German (fluent). French – German High School, Freiburg / Breisgau, Germany - from 1991 to 1993.
German Section (10th to 12th year).

Diploma : Goethe Institute Certificate in Advanced German Studies (ZMP, evening class study).
Grade: B⁺ , German Language Proficiency - Ständige Konferenz der Kultusminister der Länder der Bundesrepublik Deutschland Niveau I (KMK I).
- Italian (intermediate), French (native speaker).

Computer skills

- Microsoft Office '97 (MS-Word, Excel, Powerpoint), Origin and ADCs soft., use of Internet.
 - Programming in Turbo-Pascal, Fortran 97 and Visual Basic (intermediate level).
 - Applied programming : Mathcad 6.0, Maple V-3, Origin 7.5, Hyperchem, Polyflow, analytical softwares (i.e. Malvern Inst.).
-

Work Experience

- 2001 *Max-Planck-Institute for Polymer Research*
Six month partnership at MPIP Research Center in Mainz (Germany) within the Solid State Chemistry of Polymers Department under Prof. Dr. G: Wegner (MPIP) and Prof. G. Decher (ICS Strasbourg) supervisions. Title of the project: Controlled chemical modifications of functional macromonomers of vinylpyrrolidone for biomedical applications.
- Institut Charles Sadron (EPR 22 / Centre National de Recherches Scientifiques, Strasbourg, France).*
Research coworker. Title of the project: Development of a brand-new process of microencapsulation in supercritical carbon dioxide via interfacial polymerization (Prof. L:Danicher).
- 2000 *Henkel KGaA*
Four month internship at Henkel KGaA Corporate Research Center in Düsseldorf (Germany) within the Ressort VTR / Colloids & Interface Department under Dr. W. Ribinsky's supervision. Title of the project: Synthesis of tailored polymers for controlled release applications (cosmetics and health care). Responsibility for the development of a brand new polymerization process (miniemulsion based on epoxy resins).
- 2000 *Rhom & Haas Subsidiary - Compagnie des Salins du Midi et des Salines de l'Est S.A.*
Technical consultancy, project management and supervision of a team of four staff, redesigning the packaging system to incorporate a new PVC film printing machinery, resulting in major improvements of the products quality.
- 1999 *Rhodia S.A.*
Four month internship at Rhodia main Research Center CRA in Paris (France) in the Physical & Chemical Analysis Department. Title of the project: Introduction of colloidal particles in an organic medium within a low temperature process - Analytical studies. Supervision of the cross-applications of this research (catalytic pipe – Eolys process, pharm. vaccine substrate). *Internal Research Award Year 2000 hold.*
-

Achievements

- 2000 Coordination of ECPM Representatives travel to the International Trade Fair « Interplastica 2000 » in Moscow, Russia. Ground representation of Plastic Omnium S.A. Bulk contract negotiations with major Russian plastic industries and academic institutions (Russian Academy of sciences, Prof. S. Patlazan).
- 1999 Co-organisation and ground representation of Clariant France S.A at the "Forum Horizon 2000" (College meeting involving graduate students in chemistry and French businessmen).
- 1996 Participation in the reconstruction of a farm complex in Barstädt (East Germany) as skilled worker (volunteer experience).
-

Interests

- ♦ Travelling: commuting between Frankfurt and San Francisco (CA, USA), Moscow (2000), UK (1998-1999).
- ♦ Extreme sports: NAUI Advanced Scuba Diver (Key Largo, Florida 2003), Altitude + desert mountain biking (Moab, 2001-2003), skiing, & free climbing (Chamonix, 2002), mountaineering (Mount Rainier Expedition 2003).
- ♦ Photography of aircrafts (Farnborough 2004, Royal Air Tatoo 1998, Whiteman AFB, JPL 1997), assembling of scale models of military aircrafts, reading (Tom Clancy's and Stendhal books).

Full clean international driving licence held.

Publications

- 1 L. Herschke, V. Enkelmann, I. Lieberwirth, G. Wegner, The role of hydrogen bonding in the crystal structures of zinc phosphate hydrates, *Chem. Eur. J.* 10(11) (2004) 2795.
 - 2 L. Herschke, I. Lieberwirth, G. Wegner, Zinc Phosphate: a solution against heavy corrosion ? From polymer controlled mineralization to industrial applications, e-Polymers [P-001(2004)], NATO-ASI Symposium Macromolecules 2003 (Tirrenia, Italy 06-16/10/2003).
 - 3 L. Herschke, J. Rottstegge, I. Lieberwirth, G. Wegner, Zinc phosphate as versatile material for potential biomedical applications, Part 1, *J. Chem. Mater.: Mater. Med.* (accepted).
 - 4 L. Herschke, I. Lieberwirth, G. Wegner, Zinc phosphate as versatile material for potential biomedical applications, Part 2, *J. Chem. Mater.: Mater. Med.* (accepted).
 - 5 J. Rottstegge, M. Arnold, L. Herschke, G. Glasser, M. Wilhelm, H.W. Spiess, W.D. Hergeth, Solid state NMR and electron microscopy studies of latex modified tile mortar systems, *Macromol. Chem. Phys.* (accepted).
-

References available on request